HIPER

9^{TH} INTERNATIONAL CONFERENCE

ON HIGH-PERFORMANCE MARINE VEHICLES

ATHENS, GREECE

3 – 5 DECEMBER 2014

NATIONAL TECHNICAL UNIVERSITY OF ATHENS

SCHOOL OF NAVAL ARCHITECTURE & MARINE ENGINEERING

Published by: National Technical university of Atthens
School of Nval Architecture & Marine Engineering

Publication: December 2014

Editorial Processing: Gr. J. Grigoropoulos

TABLE OF CONTENTS

HULL DIMENSIONS OPTIMIZATION OF MEDIUM-SPEED MONOHULL PASSENGER FERRIES

Wolter Roberth HETHARIA[1], Andre HAGE[2] and Philippe RIGO[3]

[1]University of Liege - ANAST, Liege, Belgium, hethariawr@yahoo.com
[2]University of Liege - ANAST, Liege, Belgium, ahage@ulg.ac.be
[3]University of Liege - ANAST, Liege, Belgium, ph.rigo@ulg.ac.be

ABSTRACT

This paper deals with the optimization process of medium-speed monohull passenger ferries. Since those ships operate at the service speeds beyond the hump speed (Froude number Fn > 0.50), they need the higher engine power. To minimize the power or resistance the ship dimensions and geometrical hull form should be considered. The first part of the study presented here is the optimization of resistance due to the ship dimensions. Some constraints required during the optimization process were the stability parameters at a large angle of inclination. A parent ship was designed and modified due to its dimensions length L, beam B and draft T. To compute the resistance and stability at a large angle of inclination the dimensions and shape of the hull were defined. This process was executed by Maxsurf. The results were transferred to Excel to develop the regression models. The optimization models were provided and executed by using Excel. The optimization models can be used to select the optimum ship dimensions.

1. INTRODUCTION

Recent development of medium-speed passenger ferries has brought a new challenge in the maritime fields. Such ships operate in some regions of the world where the service speeds range from 18 to 25 knots. The use of light hull materials such as Aluminium and composite recently gives some benefits to those ships. Those ships operate at the range of Froude numbers *Fn* from 0.55 to 0.80 which is beyond the hump speed (*Fn* > 0.50). Therefore, they need a high engine power to maintain their speed and the efforts should be done to minimize the engine power. To minimize the engine power (or resistance) the ship dimensions and geometrical hull forms should be considered. In fact the dimensions and hull forms affect the other ship parameters. From the existing data of ships, it was found that for a given payload (number of passengers) those ships have different dimensions and engine power.

Some experts work with the optimization of any ships type with the objective of minimizing the resistance or power. In fact, one constraint that represents the stability parameters in their works is the initial metacentre GMt (Wolf, 2004; Abramowski, 2010; Ayob, 2010; Pecot, 2012). Also in their works, the stability parameters are considered when the ship is at departure condition. Early studies executed by the author (Hetharia, 2011; Hetharia, 2012) found that the stability parameters at a large angle of inclination such as: severe wind and rolling (weather) criterion “area b/ area a” and “angle of GZ_{max}” are more critical compared to the initial metacentric GMt. Medium-speed passenger ferries have a light displacement which causes a higher value of radius metacentric radius BM or higher initial metacentric GMt. Therefore considering a single value of GMt as a stability constraint in the optimization problems is not the good strategic. In addition, the passenger ships at the arrival condition should be evaluated. All the stability parameters should satisfy the criteria required by the rules (HSC Code 2000; IMO MSC 36(63) HSC Code; IMO Resolution A. 749(18).

In this study, a parent ship was designed and modified due to its main dimensions (length L, beam B and draft T). The modification process was conducted based on the layout of the parent ship. The layout was arranged due to the passenger distribution along the ship length (main deck and upper deck) and ship beam. This arrangement ended-up with the variations of ship length and beam. Also for a fixed length and beam of the ship the variation of the draft was considered. To compute the stability parameters at a large angle of inclination, the ship dimensions and geometrical hull forms are required. Also the weight components and their centers are required to define the loading conditions.

The ship configurations (dimensions and hull forms) for all variations of dimensions were developed by Maxsurf. The resistance of the ship and the stability parameters were also obtained from Maxsurf. From this tool the results were transferred to the Excel. Furthermore the data were developed to regression models. The regression models were applied for the optimization process. Furthermore, the objective function of minimum resistance may be found from this optimization models with respect to the constraints of the stability at the large angle of inclination and ship dimensions. This optimization model may be used by the users at the initial phase of design or other applications. Furthermore, the study is continuing for hull form optimization based on the selected hull dimensions.

2. THEORETICAL BACKGROUND.

2.1. Design of parent ship

The passenger ships have particular characteristics compared to the other commercial ships. In designing a passenger ship a designer has to pay attention concerning the spaces, accommodations, access and services for the passengers. This is important to provide the comfort and safety of the passengers during the travel. Also the layout of the ship should be arranged to ensure the movement of the passengers during the embarkation, travelling and safety operation. The arrangement of ship is fixed to fulfil the safety standard regulations. The facilities are provided to support the operation of the ship. Those requirements are described further in the references of Knox (2003), Levander (2003), Calhoun (2003), Gale (2003) and Olson (1990). In general, the design parameters should fulfil the design requirements. The parent ship has the input parameters such as:

- Type of ship: passenger ferry/class B — Navigation range: 200 n.m
- Number of passengers/crews: 254/5 — Service speed: 20 knots
- Pax distribution, main-upper deck: 70-30% — Type of pax accommodation: seat
- Type of pax room: passenger saloon — Number of seats in a row: 10

The input design parameters were computed and analyzed during the design process. The process is finished when the outputs meet the design requirements. The layout of the ship was determined to fit the rules of International Code of Safety for HSC (2000). The structure components of the ship were determined based on the Rules for the Classification of High Speed Craft, Bureau Veritas (2002). The hull material of the ship is Aluminium Alloy. The types of alloys used for the ship are 5083 H111 for plating and 6082 T6 for profiles.

The dimensions of the ship are as follows:

Length overall, L_{OA}	: 32.00 m	Length of waterline, L_{WL}	: 29.01 m
Beam of ship, B	: 7.00 m	Beam of waterline, B_{WL}	: 6.693 m
Draft of ship, T	: 1.40 m	Deck height, D	: 2.600 m
Chine height	: 1.25 m	Beam of chine	: 6.654 m
Upper deck height	: 2.25 m	Displacement, Δ	: 107.3 tones

2.2. Assessment of ship weight, resistance, stability and seakeeping.

2.2.1 Assessment of ship weight

To explore the parameters of ship stability with a large angle of inclination the details of weight items and their centers are required. The weight items may be obtained from the existing ships but the best way is to develop them from the parent ship which is designed in this study. By this way the weight items and their centers are determined properly. For the parent ship the weight items and their centers were computed manually. The weight items and their centers are presented at Table 1. A margin weight of 5% is added to the ship lightweight. In addition, a margin of VCG of 0.150 m is added for the VCG of the ship lightweight (Parson, 2003).

Table 1. Weight items and centres of weight of the parent ship

No	Items weight	Departure				Arrival			
		Weight (tone)	LCG (m)	VCG (m)	TCG (m)	Weight (tone)	LCG (m)	VCG (m)	TCG (m)
1	Structural weight	38.261	-0.863	2.913	0.000	38.261	-0.863	2.913	0.000
2	Machinery & systems	18.421	-2.193	1.345	0.000	18.421	-2.193	1.345	0.000
3	Ship outfit	16.490	-0.693	3.528	0.000	16.490	-0.693	3.528	0.000
	Sum lightweight	73.172	-1.159	2.807	0.000	73.172	-1.159	2.807	0.000
4	Deadweight (pax & fluids)	34.099	0.890	3.234	0.000	26.359	0.293	3.988	0.000
	Total weight	107.270	-0.410	2.947	0.000	99.530	-0.461	3.170	0.000

The ratios of weight items and centers obtained from the parent ship are presented at Table 2. In addition, the data obtained from the existing ship (Report No. SPO.1.11.15706Y/STB-1, Singapore 12 October 2011) are presented also as comparison to the parent ship. The existing ship has the features as follows, ship name: MV. Pacific 271, capacity: 266 passengers, service speed: 28 knots, dimensions: L_{OA} x B x T = (38.00 x 7.40 x 1.20) m. From Table 2, It is seen that the ratios of weight items of the parent ship are close to the existing ship. The results of weight items of the parent ship may be used for further applications.

Table 2. The ratios of weight items and centers

No	Item weight	Ratio item weight/ total weight	Ratio VCG/ deck height	Ratio item weight/ total weight	Ratio VCG/ deck height
A	Parent ship			B. Existing ship	
1	Structure	0.357	1.120		
2	Machinery	0.172	0.517		
3	Outfit	0.154	1.357		
4	Lightweight	0.682	1.079	0.691	1.002
5	Deadweight	0.318	1.244	0.310	0.971
6	Total weight		1.133		1.085

2.2.2. Assessment of ship resistance and power

The resistance of the parent ship was computed based on the method derived by Mercier and Savitsky (Lewis, 1988). This method is suitable for the semi-planning ships. The general form of the resistance equation adopted by Mercier and Savitsky is as follows:

$$R_T/W = A_1 + A_2X + A_4U + A_5W + A_6XZ + A_7XU + A_8XW + A_9ZU + A_{10}ZW + A_{15}W^2 + A_{18}XW^2 + A_{19}ZX^2 + A_{24}UW^2 + A_{27}WU^2 \quad (1)$$

where: $X = \nabla^{1/3}/L$; $Z = \nabla/B^3$; $U = \sqrt{2i_E}$,; $W = A_T/A_X$.

The values of the coefficients A_1 to A_{27} and correction factors are presented in Lewis (1988).

Two statistical methods were applied for this parent ship design, i.e. Holtrop (1978) and WUMTIA (Wolfson Unit for Marine Technology and Industrial Aerodynamics) (Molland, 2011). It was found that the method of Holtrop was out of range and the other two methods are in good pattern (Hetharia, 2012). For the next computation, the resistance is computed based on Savitsky pre-planning method which is provided in the Maxsurf software. The engine power (brake power P_B) is computed in relation with the effective power P_E (Parsons, 2003).

$$P_B = P_E / (\eta_h\ \eta_o\ \eta_r\ \eta_s\ \eta_b\ \eta_t) \quad (2)$$

The effective power of the ship is computed as:

$$P_E = R_T \times V \quad (3)$$

where: R_T = total resistance; V = speed of the ship

η_h = hull efficiency; η_o = propeller efficiency

η_s = seal efficiency; η_r = relative rotative efficiency

η_b = line shaft bearing efficiency; η_t = transmission efficiency

The values of coefficients η_r η_s η_b η_t may be found from Parsons (2003) while the coefficients η_h η_o are computed based on the parameters of ship hull and screw propeller. The maximum continuous rating (MCR) of the main engine is determined by adding a power service margin as 10% to the brake power. Two units for the main engines are selected for the propulsion system of the ship. It would be better to select the existing types of main engine to be used for the ship. However, for this preliminary study, the main engine and following characteristics were selected.

Type of main engine	: MTU Marine Diesel Engine 10V 2000 M72
Rated power	: 1205 bhp
Rated speed	: 2250 rpm,
Gearbox	: ZF 3000, i = 2.0

Two screw propeller units are used for the parent ship. The screw propellers are evaluated based on the propeller data from the Wageningen B-Screw Series (Lewis 1988). The parameters of selected screw propeller are presented as follows:

Type	: B 4-70	BAR	: 0.70	No. of blade	: 4
P/D	: 0.81	Diameter	: 1.119 m	Efficiency	: 0.592
Maximum ship speed			: 20.1 knots	Resistance	: 95.41 kN

2.2.3. Assessment of ship stability

The parameters of ship stability were computed by using Maxsurf software. The criteria that have been used for the ship stability are based on HSC Code 2000 MSC 97(73)- Annex 8 Monohull Intact, HSC Code 2000 Chapter 2 Part B Passenger Craft Intact, IMO MSC 36(63) HSC Code Monohull Intact and IMO Resolution A. 749(18) – Adopted on 4 November 1993. Some input data are required for computation of stability at large angle of inclination. Those data include items of weight and centers, down flooding points, wind speed, wind area and center and vertical lever for high speed turning. The maximum wind speed for weather criterion is set at 40 knots. The load case of the ship is separated from liquids, deadweight and lightweight. The free surface effects of liquids in tanks are considered in the stability computation. When the ship is at arrival condition the amount of liquids is fixed at 10%. The criteria of ship at the large angle of inclination according to the rules are presented as follows:

Area b/area a (%)	> 100	Area 0 to 30 (m.rad)	> 0.055
Area 30 to 40 (m.rad)	> 0.030	Max GZ at 30 or greater (m)	> 0.200
Angle of GZ max (deg.)	> 15.00	Initial metacentric GMT (m)	> 0.15
Angle Eq. Pax Crowd (deg)	< 10	Angle Eq. HS Turning (deg)	< 10
Angle Eq. Wind Hell (deg)	< 16		

2.2.4. Assessment of ship seakeeping

The sea keeping parameters for the initial design phase were evaluated for rolling, pitching and heaving natural periods. From those three natural periods, the rolling period is very important. The rolling period is required by the rules of IMO Resolution A. 749(18) – Adopted on 4 November 1993: Code on Intact Stability for All Types of Ships Covered by IMO Instruments. Chapter 3: Design Criteria Applicable to All Ships. 3.2 Severe Wind and rolling criterion (weather criterion). One important parameter that relates to the rolling period is angle of roll (θ_1). Angle of roll (θ_1) to windward due to wave action should be calculated as follows:

$$(\theta_1) = 109\ k\ X_1\ X_2\ \sqrt{(r\ s)},\ \text{degree} \tag{4}$$

$$r = 0.73 \pm 0.6\ OG/d \tag{5}$$

where the coefficients of k, X_1, X_2, s are presented at the tables of the rules.

OG = distance between the centre of gravity of ship and the waterline (m)

d = mean moulded draught of the ship (m)

The value of X_1 depends on the ratio B/d where the value of X_2 depend on block coefficient C_B and the value of s depend on the rolling period (Tr). Then the angle of roll (θ_1) to windward due to wave action may be determined. Furthermore the parameter of "area b/area a" is computed based on the minimum value of angle of roll (θ_1). According to the rules, the angle of heel under action of steady wind (θ_0) should be limited to 16 degree. The rolling period is determined by the formula:

$Tr = 2\ C\ B\ /\ \sqrt{GM}$ (second) (6)

The coefficient $C = 0.373 + 0.023\ (B/d) - 0.043\ (L/100)$ (7)

where: L = waterline length of the ship (m) B = moulded breadth of the ship (m)
d = moulded draught of the ship (m) C_B = block coefficient
GM = metacentric height corrected for free surface effect (m)

The natural periods of pitch and heave may be found in many references. For example, Parsons (2004) suggested the formula as follows:

Pitch natural period: $T_\Theta = 1.776\ C_{WP}^{-1}\ \sqrt{T\ C_B\ (0.6 + 0.36\ B/T)}$ (8)

Heave natural period: $T_h = 2.007\ \sqrt{T\ C_B\ (B/3T + 1.2)/C_{WP}}$ (9)

For the evaluation of seakeeping parameters, Parsons (2004) stated that early design checks typically try to avoid having those three natural periods are at the same phase which could lead to significant mode coupling.

2.3. Modification of ship dimensions

In this study, the modification (increasing or decreasing) of ship length and beam was executed based on the parent ship. The parent ship has the capacity of 254 passengers. The numbers of passenger seat in a row are 10. The parent ship is called S10. The passenger distribution on main deck and upper deck is 70-30%. The modification of beam was executed by adding or reducing one seat in a seat row. The modification of the ship length was executed by adding or reducing one seat row along the ship length. This modification of ship length and beam gave a certain percentage of passengers on main deck and upper deck. The modified ship with 9 seats per seat row is called S9 and the modified ship with 11 seats per seat row is called S11. Those ship configurations are presented at Figure 1.

During the modification of ship length and beam the structural weight was changed due to addition or reduction of the total structural components required for the enclosed passenger space. For example, to add one meter of the longitudinal structure for S10, the structural weight increases of 2.59 % for the structure at main deck and 0.94% for the structure at upper deck. In addition, the modification of ship beam will increase or decrease the total structural weight. During the modification process the ship deadweight (passengers, luggage and liquids) was kept to be constant. The distribution of passengers was done by shifting each seat row from main deck to upper deck or vice versa. It was noticed that during the modification process, the centre of passenger weight was the changing of vertical and longitudinal. The changing of length and beam causes the changing of structural where affects total ship weight.

Another ship dimension which affects the performance of the ship is the draft (T). The major effects of the changing of the draft are the stability and resistance (or power) of the ship. In this study the draft is also modified in order to evaluate the performance of the ship. The modification of draft was executed by increasing or decreasing the chine height of the ship hull. As a result the draft of the ship was changed. It is noticed that the modification of the draft is limited by the requirements of the ship displacement. The maximum draft is limited by the condition when the ship is in arrival condition. In this condition also the height of chine is kept to be below the designed waterline to maintain the stability of the ship. The minimum draft is limited when the parameters of ship stability are in the limit of satisfying the rules.

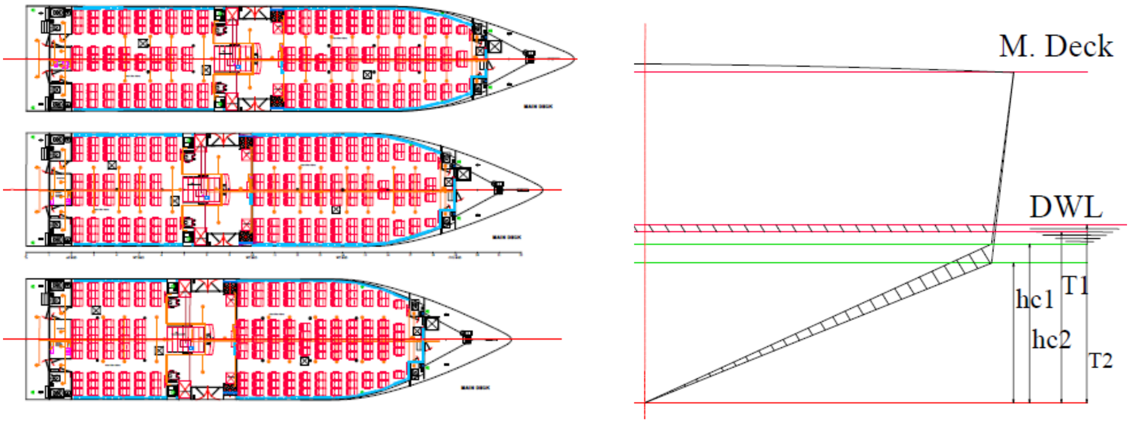

Figure 1. The modification of the length, beam and draft

The draft depends on the chine height. Therefore to modify the draft the chine height should be moved higher or lower. As shown at Figure 1 the original draft of the ship is T_1 and chine height is hc_1. To increase or decrease the draft (T_2) the chine height (hc_2) should be increased or decreased. During the process of modification the sectional areas along the ship length are kept constant. The purpose of this process is to keep constant the ship displacement. In fact, changing the chine height will reduce the side construction and increase the bottom construction. The net construction weight during the draft modification is less than 1% of the ship structural weight. Therefore this changing of structural weight was not taken into account during modification process. It is noticed also that during this process some ship dimensions are kept constant such as the deck height and chine offset. The changing of draft causes some parameters are changing, such as midship sectional area, midship coefficient, block coefficient, freeboard, wind area and center, center of lateral resistance and other hydrostatics and stability parameters.

The modification of ship length was executed by using the Maxsurf software. Using the parametric transformation command the length of ship is made longer or shorter. The modification of ship beam and draft was executed by using Maxsurf but some manual works are needed to fix the required ship displacement and hull form. During the modification of ship dimensions, some hull form parameters are kept constant such as angle of bow is set for 40 degree, the position of LCB is set for -2% Lwl and the area of transom stern is set for 23% of midship area. In addition, for the modification of ship draft the ship displacement is kept constant.

2.4. Parametric models development.

2.4.1. Regression analysis

The results of ship parameters obtained from Maxsurf were transferred to the Excel. Then the results of ship parameters are developed to provide the parametric models. The Microsoft Excel provides a solver to solve this regression analysis. The existing data points are fitted by a minimum least squares error curve of a particular form. The curve provides the model that presents the general relationship between dependent and independent variables. In fact the effectiveness of the curve should be considered to define the model. Parsons (2003) stated that the effectiveness (goodness of fit) of the modelling can be assessed by looking at the statistical measures of coefficient of correlation R, coefficient of determination R^2 and standard error SE. The value of $0 \le R \le 1$ with $R = 1$ indicates that all data is on the curve and $0 \le R^2 \le 1$ with $R^2 = 1$ indicates that all variation is reflected in the curve. The results of parameteric models are presented at Table 3. It is noted that the independent variables x_1, x_2 and x_3 represent the ship length, beam and draft respectively. It is noticed also that for the computation of ship resistance the speed is fixed for 20.1 knots.

Table 3. Regression models of the ship

No	Ship parameters	Unit	Regression models	R^2
			Departure condition (ship speed = 20.1 knots)	
1	Resistance	kN	$f(x_1,x_2,x_3)= 270.02-5.224\ x_1+ 4.840\ x_2 - 29.958\ x_3$	0.977
2	Area b/ area a	%	$f(x_1,x_2,x_3)= -1177.323 + 9.463\ x_1 + 122.335\ x_2 + 175.560\ x_3$	0.981
3	Area 0-30 or GZ_{max}	m.rad	$f(x_1,x_2,x_3)= 1.303+0.014\ x_1-0.631x_2+0.059x_2^2–0.159x_3+0.14x_3^2$	0.952
4	Area 30 - 40	m.rad	$f(x_1,x_2,x_3)= 0.163+0.005x_1-0.155x_2+0.017x_2^2+0.082x_3–0.028x_3^2$	0.998
5	GZ_{max} at 30 deg or >	m	$f(x_1,x_2,x_3)= 2.619+0.021x_1-1.077x_2+0.106x_2^2–0.443x^3+0.149x_3^2$	0.995
6	Angle of GZ_{max}	degree	$f(x_1,x_2,x_3)= - 53.265 + 1.020\ x_1+7.911\ x_2 –40.277\ x_3+27.483\ x_3^2$	0.934
7	Initial GMt	m	$f(x_1,x_2,x_3)= 8.755+0.157x_1-5.633x_2+0.566x_2^2+1.636x_3–0.551\ x_3^2$	0.993
8	Angle eq. pax crowd	degree	$f(x_1,x_2,x_3)= 41.967 - 0.283\ x_1 - 3.132\ x_2 – 10.236\ x_3 + 4.615\ x_3^2$.	0.959
9	Angle eq. HS turning	degree	$f(x_1,x_2,x_3)=74.687-0.316x_1-13.868x_2+0.81x_2^2–5.994x_3+ 2.176x_3^2$	0.950
10	Angle eq. wind heel	degree	$f(x_1,x_2,x_3)=58.70-0.156x_1-11.819x_2+0.688x_2^2–3.213x_3+1.023x_3^2$	0.942
			Arrival condition (ship speed = 20.1 knots)	
11	Resistance	kN	$f(x_1,x_2,x_3)= 234.018 - 4.549\ x_1 + 5.107\ x_2 - 27.309\ x_3$	0.975
12	Area b/ area a	%	$f(x_1,x_2,x_3)= -1234.973 + 9.887\ x_1 + 129.368\ x_2 + 131.051\ x_3$.	0.968
13	Area 0-30 or GZ_{max}	m.rad	$f(x_1,x_2,x_3)= 2.625+0.012x_1-0.971x_2+0.082x_2^2–0.209x_3+0.145\ x_3^2$	0.906
14	Area 30 - 40	m.rad	$f(x_1,x_2,x_3)= 0.169+0.005x_1-0.171x_2+0.018x_2^2+0.085x_3–0.029\ x_3^2$	0.997
15	GZ_{max} at 30 deg or >	m	$f(x_1,x_2,x_3)= 2.881+0.019x_1-1.134\ x_2+0.109x_2^2–0.371x^3+0.08\ x_3^2$	0.995
16	Angle of GZ_{max}	degree	$f(x_1,x_2,x_3)= - 47.179+0.799\ x_1+8.237\ x_2–44.526\ x_3 + 27.939\ x_3^2$	0.885
17	Initial GMt	m	$f(x_1,x_2,x_3)= 10.092+0.167x_1-6.226x_2+0.62x_2^2+1.744x_3–0.663\ x_3^2$	0.993
18	Angle eq. pax crowd	degree	$f(x_1,x_2,x_3)= 50.378 - 0.319\ x_1 - 3.742\ x_2 – 16.732\ x_3 + 8.324\ x_3^2$	0.964
19	Angle eq. HS turning	degree	$f(x_1,x_2,x_3)= 97.618-0.355x_1-19.424x_2+1.18x_2^2–7.868x_3+3.232x_3^2$	0.955
20	Angle eq. wind heel	degree	$f(x_1,x_2,x_3)=68.514-0.166x_1-13.896x_2+0.824x_2^2–6.30x_3+2.574\ x_3^2$	0.933
21	Percentage pax MD	%	$f(x_1, x_2) = -164.317 + 4.070\ x_1 + 14.862\ x_2$	0.995

In developing these regression models the coefficient of significance level is fixed for $\alpha = 0.05$. It was found from the regression equations that the coefficients of significance F for all equations of $f(x_1,x_2,x_3)$ are less than a coefficient of significance of 5 %. This means that the regression models are suitable to be used. It was found also that the values of P-value of the intercept coefficients x_1, x_2, x_3, x_2^2 and x_3^2 are less than the significance level of 5 %. This means that the independent variables have a strong contribution to the dependent variable.

2.4.2. Verification of regression models

The results of regression models presented at Table 3 give also the good values of the coefficients R, R^2 and SE. Also the values of coefficient of significance F and p-value of independent variable coefficients are less than the coefficient of significant level $\alpha = 0.05$. This indicates that the regression models are suitable to be used. Furthermore, the regression models were verified by introducing the independent variables x_1, x_2 and x_3. The results are then compared to the real values obtained from direct computations. An example of the results of computation are presented at Table 4.

Table 4. An example of comparison of the real values to regression model

No	Ship parameters	Unit	Departure condition			Arrival condition		
			Regression	Real	Difference (%)	Regression	Real	Difference (%)
1	Dimensions (L_{OA}xBxT)	m	32.0 x 7.0 x 1.40 (parent ship)			34.91 x 6.50 x 1.118		
2	Resistance	kN	94.78	95.41	-0.66	77.89	79.92	-2.60
3	Area b/ area a	%	227.6	225.5	0.93	97.59	98.76	-1.19
4	Area 0 to 30	m.rad	0.247	0.24	3.93	0.119	0.113	4.07
5	Area 30 to 40	m.rad	0.107	0.11	-0.19	0.065	0.063	2.47
6	GZ_{max} at 30 or greater	m	0.622	0.62	1.03	0.466	0.462	0.82
7	Angle of GZ_{max}	degree	32.24	33.20	-2.94	19.38	19.10	1.44
8	Initial GMt	m	3.319	3.32	-0.02	2.775	2.698	2.78
9	Angle eq. pax crowd	degree	5.694	5.80	1.86	6.627	6.410	3.28
10	Angle eq HS turning	degree	3.027	3.00	0.90	4.078	3.93	3.63
11	Angle eq. wind heel	degree	2.210	2.20	0.44	3.353	3.28	2.18

It is found that the difference of the values of ship parameters obtained from the regression equations compared to those from the results obtained from Maxsurf are less than 5%. Therefore the regression equations can be used further for the optimization process.

2.5. Optimization of ship resistance

2.5.1. Optimization models

Since the medium-speed passenger ferry operates with the higher engine power then there should be an effort to minimize the engine power or the resistance. The objective of this study is to find the minimum resistance of the modified parent ships. Here, the length of ship (L_{OA}), ship beam (B) and ship draft (T) become the control (design) variables and are represented by x_1, x_2 and x_3 respectively. Set the length, beam and draft as the control variables x_1, x_2 and x_3 respectively, the resistance as the objective function $f(x_1, x_2, x_3)$ used as the solution of the single criterion optimization problem are stated as:

For departure condition:

Minimize: $f(x_1,x_2,x_3)= 270.02 - 5.224\, x_1 + 4.840\, x_2 - 29.958\, x_3$ (10)

Subject to the constraints:

$-1177.323 + 9.463\, x_1 + 122.335\, x_2 + 175.560\, x_3 \geq 100$

$1.303 + 0.014\, x_1 - 0.631\, x_2 + 0.059\, x_2^2 – 0.159\, x_3 + 0.140\, x_3^2 \geq 0.055$

$0.163 + 0.005\, x_1 - 0.155\, x_2 + 0.017\, x_2^2 + 0.082\, x_3 – 0.028\, x_3^2 \geq 0.03$

$2.619 + 0.021\, x_1 - 1.077\, x_2 + 0.106\, x_2^2 – 0.443\, x^3 + 0.149\, x_3^2 \geq 0.2$

$- 53.265 + 1.020\, x_1 + 7.911\, x_2 – 40.277\, x_3 + 27.483\, x_3^2 \geq 15$

$8.755 + 0.157\, x_1 - 5.633\, x_2 + 0.566\, x_2^2 + 1.636\, x_3 – 0.551\, x_3^2 \geq 0.15$

$41.967 - 0.283\, x_1 - 3.132\, x_2 – 10.236\, x_3 + 4.615\, x_3^2 \leq 10$

$74.687 - 0.316\, x_1 - 13.868\, x_2 + 0.809\, x_2^2 – 5.994\, x_3 + 2.176\, x_3^2 \leq 10$

$58.700 - 0.156\, x_1 - 11.819\, x_2 + 0.688\, x_2^2 – 3.213\, x_3 + 1.023\, x_3^2 \leq 16$

$x_{1min} < x_1 < x_{1max}$

$x_{2min} < x_2 < x_{2max}$

$x_{3min} < x_3 < x_{3max}$

For arrival condition:

When the ship is at arrival condition some ship parameters should be evaluated particularly the stability at a large angle of inclination. This is due to reducing of the liquids on board during the travel. The ship dimensions (particularly the draft), displacement, resistance, hydrostatics and stability parameters are changing compared to those at the departure condition. In this case the effect of changing the ship parameters depends on the draft. In fact, the changing of stability parameters should satisfy the criteria stated by the rules. The changing of ship parameters at the arrival condition can be evaluated according to the following equations:

Resistance: $f(x_1, x_2, x_3)= 234.018 - 4.549\, x_1 + 5.107\, x_2 - 27.309\, x_3$ (11)

Area b/area a:

$f(x_1, x_2, x_3)= -1234.973 + 9.887\, x_1 + 129.368\, x_2 + 131.051\, x_3 \geq 100$

Area 0 to 30:

$f(x_1, x_2, x_3) = 2.625 + 0.012x_1 - 0.971x_2 + 0.082x_2^2 – 0.209\, x_3 + 0.145x_3^2 \geq 0.055$

Area 30 to 40:

$f(x_1, x_2, x_3) = 0.169 + 0.005\, x_1 - 0.171x_2 + 0.018x_2^2 + 0.085x_3 – 0.029x_3^2 \geq 0.03$

Maximum GZ at 30 or greater:

$f(x_1, x_2, x_3) = 2.881 + 0.019x_1 - 1.134x_2 + 0.109x_2^2 – 0.371x^3 + 0.080x_3^2 \geq 0.2$

Angle of GZ maximum:

$f(x_1, x_2, x_3) = - 47.179 + 0.799\, x_1 + 8.237\, x_2 – 44.526\, x_3 + 27.939\, x_3^2 \geq 15$

Initial metacentric GMt:

$f(x_1, x_2, x_3) = 10.092 + 0.167x_1 - 6.226x_2 + 0.620x_2^2 + 1.744x_3 – 0.663x_3^2 \geq 0.15$

Angle equilibrium of passenger crowd:

$f(x_1, x_2, x_3) = 50.378 - 0.319\, x_1 - 3.742\, x_2 – 16.732\, x_3 + 8.324\, x_3^2 \leq 10$

Angle equilibrium of high speed turning:

$f(x_1, x_2, x_3) = 97.618 - 0.355x_1 - 19.424x_2 + 1.180x_2^2 – 7.868x_3 + 3.232x_3^2 \leq 10$

Engle equilibrium of wind heel:

$f(x_1, x_2, x_3) = 68.514 - 0.166x_1 - 13.896x_2 + 0.824x_2^2 – 6.301x_3 + 2.574x_3^2 \leq 16$

The values of ship resistance and stability parameters when the ship is at arrival condition are obtained by introducing the values of x_1, x_2 and x_3 into the Equation (11). It is notice that the value of ship draft (x_3) is the draft when the ship is at arrival condition.

The constraints for the parameters x_1 (length), x_2 (beam) and x_3 (draft) should be limited during the modifications. In general the values of x_1 are ranging from 27.15 m to 36.85 m. The values of x_1 for the ship code S9 are from 30.06 m to 36.85 m while for S10 are from 28.12 m to 34.910 m and S11 are from 27.15 m to 32.97 m. The values of x_2 are ranging from 6.50 m to 7.48 m. The values of x_2 for the ship code S9 is 6.50 m, S10 is 7.00 m and S11 is 7.48 m. The values of x_3 for departure condition are ranging from 0.956 to 1.366 and for arrival condition are ranging from 0.903 to 1.306 m. In addition, these values differ for each ship configuration (S9, S10 and S11) due to the requirements to fulfil the ship displacement.

Another parameter that should be considered also is the number of passengers on the main deck. This is determined due to the arrangement of the passengers on the main deck and upper deck. According to the arrangement, the percentage of passengers on the main deck are ranging from 55 to 83 %. With these values the lengths of the ship are limited. The percentage of passengers on main deck is function of ship length and beam and is presented as:

$$f(x_1, x_2) = -164.317 + 4.070\, x_1 + 14.862\, x_2.\ (R^2 = 0.995) \qquad (12)$$

3. RESULTS AND DISCUSSION

3.1. Results of optimization

The optimization problem in this study was solved by using the Excel solver which is applicable to solve the nonlinear optimization problem. The results of parameters of resistance and stability are presented at Table 5. The results of optimization for all ship configurations for departure condition and evaluation of ship parameters at arrival conditions are presented. It is seen that the minimal value of the optimization problems in the feasible space is constrained by the value of “ship dimensions”. To reach the minimum resistance due to the objective function the ship dimensions tend to be longer, narrow beam and higher draft. In fact, higher draft gives better stability and lower resistance. Meanwhile, the lower draft is critical for the stability parameters at large angle of inclinations. It is seen that the parameters of “area b/area a” and “angle of GZmax” are more critical than the parameter initial metacentric GMt when the draft is lower.

From the results at Table 5 the minimum value of resistance is found at the ship with configuration S9, i.e. 68.05 kN. In addition for other two configurations of S10 and S11 the minimum resistance are 80.82 kN and 93.39 kN respectively. The dimensions and other stability and seakeeping parameters are presented in Table 5. The results obtained from the direct computations from Maxsurf for those ship configurations are 71.43 kN, 83.13 kN and 91.91 kN respectively. The difference of the results of optimization compared to the direct computations from Maxsurf are 4.73 %, 2.78 % and -1.60 % respectively. Those three ship configurations give a significant reducing of resistance compared to the parent ship (S10) with the resistance of 95.41 kN.

Table 5. Results of optimization of ship dimensions

No	Ship parameters	Unit	Departure			Evaluation at arrival			Criteria	Status
1	Ship configurations		S9	S10	S11	S9	S10	S11		
2	Ship Dimensions L_{OA}	m	36.85	34.91	32.97	36.85	34.91	32.97		
	B	m	6.50	7.00	7.48	6.50	7.00	7.48		
	T_{min}	m	1.366	1.358	1.348	1.325	1.317	1.308		
3	Resistance	kN	68.05	80.82	93.38	63.42	75.01	86.54		
4	Area b/ area a	%	206.4	247.2	286.4	143.9	188.4	230.1	≥ 100.0	Pass
5	Area 0 to 30	m.rad	0.226	0.277	0.353	0.172	0.214	0.291	≥ 0.055	Pass
6	Area 30 to 40	m.rad	0.095	0.120	0.152	0.078	0.104	0.137	≥ 0.030	Pass
7	GZ_{max} at 30 or >	m	0.549	0.683	0.864	0.467	0.600	0.776	≥ 0.200	Pass
8	Angle of GZ_{max}	degree	32.02	33.68	35.20	25.84	28.18	30.32	≥ 15.00	Pass
9	Initial GMt	m	3.071	3.760	4.698	3.125	3.874	4.871	≥ 0.150	Pass
10	Angle eq. pax crowd	degree	5.801	4.781	3.790	6.755	5.460	4.236	≤ 10.0	Pass
11	Angle eq. HS turning	degree	2.964	2.120	1.690	3.396	2.330	1.890	≤ 10.0	Pass
12	Angle eq. wind heel	degree	2.729	1.783	1.191	3.027	1.958	1.332	≤ 16.0	Pass
13	Roll period	second	3.373	3.283	3.199	3.390	3.278	3.186		
14	Pitch period	second	2.205	2.287	2.331	2.141	2.221	2.261		
15	Heave period	second	2.545	2.605	2.639	2.453	2.512	2.541		
16	Check percentage of Passengers on MD	%	80.32	81.90	81.50	80.32	81.9	81.50	≥ 0.55 ≤ 83.0	

The dimension of the drafts at arrival condition presented at Table 5 are due to reducing of fuel and fresh water during the travel. The real draft of the ships at arrival condition varies between 95 % to 97 % from those of departure condition. For example the ship configuration S9 with the dimensions of L x B x T = (36.85 x 6.50 x 1.366) m, the real draft when arriving is 0.97 x 1.366 m = 1.325 m. In fact, all ship configurations with the minimum resistance have the stability parameters which satisfy the rules as shown at Table 5.

3.2. Discussion

In this optimization process, the variation of ship configurations are limited by their dimensions. The minimum ship resistance is obtained at the dimensions with longer length, narrow beam and higher draft. In addition, a ship with a higher draft T (deep-V section) has lower resistance and better stability performances. From the results of optimization it is seen that the resistance of ship may be decreased up to the certain level. However the dimensions of ship tend to be longer length, narrow beam and higher draft. In addition, when the draft becomes higher or the length becomes lower the ship has critical stability parameters particularly the severe wind criteria “area b/area a” and “angle of GZmax”.

The seakeeping parameters of roll natural period (Tr), pitch natural period (Tp) and heave natural period (Th) are evaluated. It was found that the values of those three natural periods are not the same.

In fact, those equations presented before may be used by the users in order to get some information concerning the ship parameters at the initial design stage. As stated before that the minimum ship resistance may be obtained at the ship with longer length, narrow beam and higher draft.

The equations presented in this study may be applied by the users at initial design phase or for other applications. By using these equations the users may get the information concerning the ship dimensions, resistance of ship and stability parameters. The ship dimensions should be selected with considering other ship parameters such as economy, seakeeping, etc. These equations can be applied for medium-speed passenger ferries with the capacity of around 250 passengers.

4. CONCLUSIONS

Some conclusions may be drawn as follows:

- A ship with lower resistance may be obtained when the dimensions are longer length, narrow beam and higher draft.
- By applying the regression models for the optimization problems the value of ship resistance may be determined with considering the ship stability parameters.
- The stability parameter “area b/ area b” is more critical than the initial metacentric GMt for stability requirements when the draft tends to be lower.
- The regression models may be used to select the ship dimensions at the initial design phase or for other applications.

The results obtained from the regression models in this study are given for the modification of ship dimensions. In fact the resistance of the ship depends also on the geometrical hull forms. The study is continuing for selecting the proper hull form to minimize the resistance. The model tests will be executed to confirm the optimization results.

References

Abramowski, T. (2010). ‘Combining Artificial Neural Networks and Simulated Annealing Algorithm for Increasing Ship Transport Efficiency’. Proceedings of the 9th International Conference on Computer and IT Applications in the Maritime Industries COMPIT’10. Gubbio, Italy.

Ayob, A. F., Ray, T. & Smith, W. F. (2010). ‘A Framework for Scenario-Based Hydrodynamic Design Optimization of Hard Chine Planing Craft’. Proceedings of the 9th International Conference on Computer and IT Applications in the Maritime Industries COMPIT’10. Gubbio, Italy.

Bureau Veritas (2002). The Rules for the Classification of High Speed Craft. Bureau Veritas – Edition February 2002.

Calhoun, S. R. & Steven, S.C. (2003). ‘Human Factor in Ship Design’. Ship Design and Construction. Writen by an International Group of Authorities, Thomas Lamb, Editor, SNAME Publication, Jersey City, New York, USA. Vol. 2, Ch. 15, pp.15.1– 15.26.

Gale, P. A. (2003). ‘The Ship Design Process’. Ship Design and Construction. Written by an International Group of Authorities, Thomas Lamb, Editor, SNAME Publication, Jersey City, New York, USA. Vol. 2, Ch. 5, pp. 5.1–5.22.

Hetharia, W. R., Hage. A. & Rigo, Ph. (2011). ‘Preliminary Study of Medium Speed Monohull Passenger Ferries’. Proceedings of International Conference on Technologies, Operations, Logistics and Modelling for Low Carbon Shipping LCS 2011, Glasgow, Scotland, UK.

Hetharia, W. R., Hage. A. & Rigo, Ph. (2012a). ‘Preliminary Design Study on Medium Speed Passenger Ferries’. Proceedings of 8th International Conference on High-Performance Marine Vehicles HYPER. Duisburg, Germany.

Hetharia, W. R., Hage, A., & Rigo, Ph. (2012b). ‘The Effects of Hull Modification on Design Parameters of Medium-Speed Monohull Passenger Ferries’. Proceedings of The International Conference ICSOT: Developments in Ship Design & Construction. The Royal Institution of Naval Architects (RINA), Ambon, Indonesia.

HSC Code 2000 MSC 97(73)- Annex 8 Monohull Intact, HSC Code 2000. Chapter 2 Part B Passenger Craft Intact, IMO MSC 36(63) HSC Code Monohull Intact.

Holtrop, J. & Mennen, G.G.J. (1978). ‘A Statistical Power Prediction Method’. ISP, Vol. 25.

IMO Resolution A. 749(18) – Adopted on 4 November 1993. ‘Code on Intact Stability for All Types of Ships Covered by IMO Instruments’. Chapter 3: Design Criteria Applicable to All Ships. 3.2 Severe Wind and rolling criterion (weather criterion).

Knox, J. (2003). ‘Ferries’. Ship Design and Construction. Written by an International Group of Authorities, Thomas Lamb, Editor, SNAME Publication, Jersey City, New York, USA, Vol. 2, Ch. 38, pp. 38.1–38.29.

Larsson, L. & Hoyte C. R. (2010). Ship Resistance and Flow. The Principles of Naval Architecture Series’, J. Randolph Paulling, Editor, Published by The SNAME, Jersey City, New Jersey, USA. pp. 178-210.

Levander, K. (2003). ‘Passenger Ships’. Ship Design and Construction. Written by an International Group of Authorities, Thomas Lamb, Editor, SNAME Publication, Jersey City, New York, USA, Vol. 2, Ch. 37, pp. 37.1–37.38.

Lewis, E.V. (1988). ‘Resistance, Propulsion and Vibration’. Principles of Naval Architecture. SNAME, Jersey City, NJ, USA. Vol. 2, pp. 93–105.

Molland, A. F., Turnock, S.R. & Hudson, D.A. (2011). Ship Resistance and Propulsion. Cambridge University Press, 32 Avenue of the Americas, New York, N.Y, USA, pp. 208-216.

Nawari. (2010). Analisis Regresi dengan MS Excel 2007 dan SPSS 17. PT Elex Media Komputindo, Jakarta, Indonesia.

Olson, H. A. (1990). ‘Trends in Modern Ferry Boat Design’. Paper Presented at the Meeting of The Northern California Section of The SNAME, pp. 6–37.

Parsons, M. G. (2003). ‘Parametric Design’. Ship Design and Construction. Written by an International Group of Authorities, Thomas Lamb, Editor, SNAME Publication, Jersey City, New York, USA, Vol. 2, Ch. 11, pp. 11.1–11.34.

Pecot, F., Yvin, C., & Buiatti, R. (2012). ‘Shape Optimization of a Monohull Fishing Vessel’. Proceedings of The 11th International Conference on Computer and IT Applications in the Maritime Industries – COMPIT’ 12, Liege, Belgium, pp. 11-12.

Report No. SPO.1.11.15706Y/STB. (2011). PT Palindo Marine Shipyard, Singapore.

Watson, D. G. M. (1998). Practical Ship Design. Elsevier Ocean Engineering Book Series, Volume I, ELSEVIER, pp. 155–360.

Wolf, R., Dickmann, J. & Boas, R. (2004). ‘Ship Design Using Heuristic Optimization Method’. AIAA-2004-xxxx. Massachusetts Institute of Technology, USA.

SIMULATION-BASED DESIGN AND OPTIMIZATION FOR NAVY VESSELS AND MEGAYACHTS

Volker Bertram[1] and Nikolaos M.P. Kakalis[2]

[1] DNV GL, Brooktorkai 18, D-20457 Hamburg, Germany, Volker.Bertram@dnvgl.com
[2] DNV GL, 5 Aitolikou Street, GR-18545 Piraeus, Greece, Nikolaos.Kakalis@dnvgl.com

ABSTRACT
This paper highlights some recent applications of advanced simulations in concept exploration and design of advanced monohull navy vessels and megayachts. Concept exploration is performed before actual design to elucidate customer requirements or priorities. Multi-criteria optimization builds on concept exploration using the insight to specify objectives and constraints. Advanced simulations encompass CFD, FEA, but most recently also dynamic simulations of machinery and electric systems. Applications are shown for navy vessels and megayachts, taken from industry and R&D projects of DNV GL.

1. INTRODUCTION

Ship design is increasingly supported by sophisticated analyses. Traditionally, ship design is based on experience. This is still true to some extent, but increasingly we rely on “tailored experience” from dedicated and well-chosen simulations. Scope and depth of these simulations guiding our decisions in design and operation of ships are continuing to develop at a very dynamic pace. We describe here the state of the art as reflected in our work, with particular focus on applications for megayachts and navy ships.

Simulations mimic processes using computer models. The general approach is familiar from video games, e.g. for flying simulators. Unlike video games, engineering applications require generally better engineering models, but can accept simpler visualization and do not require real-time response. “All models are wrong, but some models are useful”, is a time-honoured adage in engineering. All simulation models introduce simplifications:

- Physics – the physical models are based on assumptions which simplify reality in the attempt to approach it, even in the most sophisticated approaches, e.g. assuming perfect homogeneity or perfect smoothness. Many approaches introduce linearizations assuming that some key parameter is small. Boundary and initial conditions determine a physical model in a simulation. If only part of the system is considered the numerical model has artificial boundaries that introduce inherent error sources.
- Numerics – Simulation techniques typically involve discretization schemes. The modelled surface or volume is then decomposed into many elements which have associated simplifications, e.g. constant or linear distributions of normal vectors, pressures, etc. The type and number of elements drive accuracy and required computer resources.

For hydrodynamics, our industry is familiar with model tests. Model tests have their own associated error sources. Models have scaling errors for all viscous effects (flow in aftbody, roll damping, etc.), surface tension (spray formation), surface roughness and stiffness (slamming). The errors in predictions for full-scale are often higher than for carefully performed CFD simulations.

Full-scale measurements are a possible source of insight, but often too expensive and plagued by uncertainties of ambient conditions.

Simple design estimates on statistical regression remains a popular design approach. The employed simple formulas are also models with associated errors. Simple formulas with very few input parameters can only give "order of magnitude" estimates. For example, coefficients for wind resistance of ships have given errors of typically 30% compared to wind tunnel tests.

Engineering is the art of choosing the right model. This involves experience and awareness of strength and limitations of various modelling approaches. Increasingly, the best choice is numerical simulation, especially for high-performance vessels such as megayachts and navy vessels.

2. COMPUTATIONAL FLUID DYNAMICS (CFD)

2.1. Resistance & Propulsion

CFD is used for the analyses of flows around hull, propellers, and appendages. Most recently, we have used CFD analyses also to gain insight into resistance penalties of such details as welds, *Ciortan and Bertram (2014).* The trend is from individual design assessment to concept exploration models and formal optimization.

Hull lines can be formally optimized for fuel efficiency or other criteria, *Oossanen et al. (2009), Hochkirch and Bertram (2012).* Parametric modelling, free-surface flow simulations and formal optimization are combined with massively parallel computer architectures to improve hull shapes in short turn-around times. Similar procedures can be used to minimize wave making and associated noise above sonar domes. Optimization of the aftbody lines requires considerably higher computer resources due to the dominant effects of viscosity and turbulence. However, such applications are by now state of the art and regularly applied for many ship types.

In a recent project for a Latin American navy, the hull for a new OPV (offshore patrol vessel) project was optimized for power requirements, considering a representative operational profile (six combinations of speed and draft). Constraints came in the form of several hard points for the hull and lower thresholds for initial stability (KM values). In total, 14000 design variants were considered. The selected hull shape was analyzed by high-fidelity CFD (free-surface RANSE code with fine grid, investigating both model-scale and full scale-conditions). Overall power requirements were reduced by more than 20%, Fig.1. Such savings are unusually high. They can be partially explained by the longer cycles for ship replacement in many smaller navies (sometimes exceeding 30 years). Such large savings are also found for very unusual designs where the designers have no intuitive knowledge or base geometries.

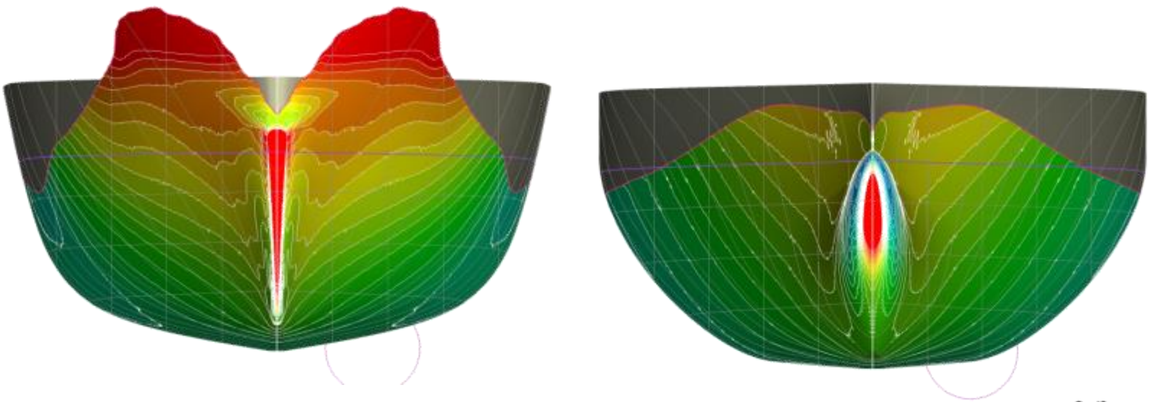

Fig.1. Hull lines optimisation for OPV design; bow wave and bow pressures for original hull (left) and optimized hull (right)

Very early design decisions have large impact on later performance. The more freedom you have, the more you can gain from making the best choices. Often, hull optimization starts with the main dimensions and displacement largely given. Then 4-6% improvement in yearly fuel consumption is typically achieved. But we can do better – if we start earlier. For high-performance vessels, both navy vessels and megayachts, there is significant potential for improvement in design requirement elucidation. Concept exploration model studies should then be performed first. The core objective of concept exploration is requirements elucidation, exploring what may be possible when varying key parameters (such as length, beam, block coefficient). Concept exploration studies typically cover several hundred variants. While we would not call such studies an "optimization", systematic concept exploration is very useful to understand the available options and can in itself improve designs significantly.

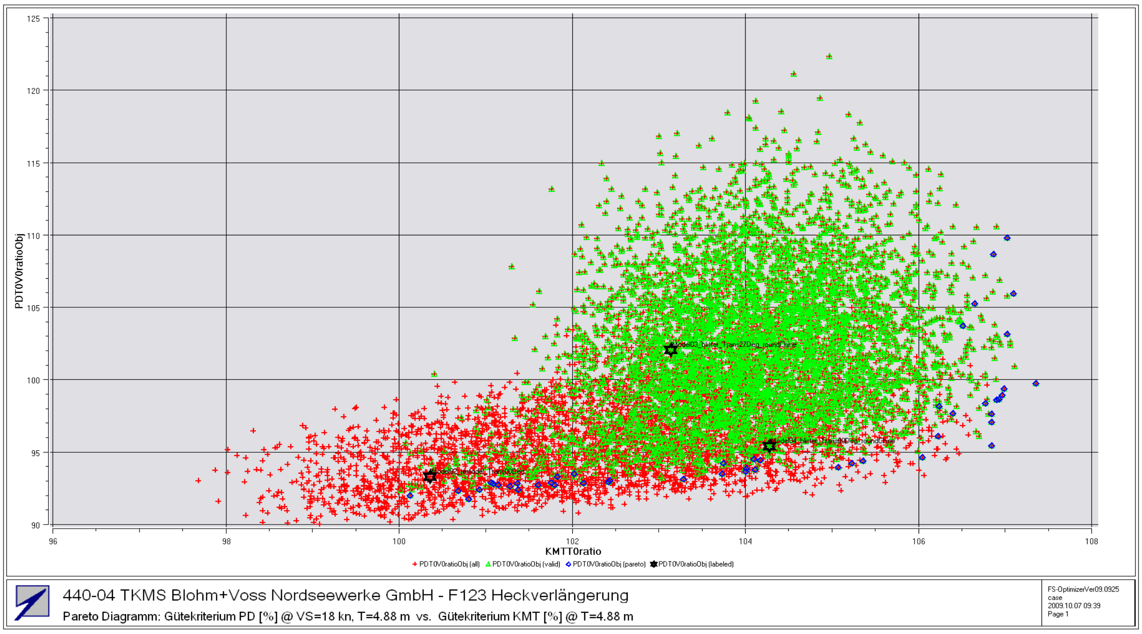

Fig.2. Pareto-diagram of required power (y-axis) and KM-values (x-axis). Each dot represents an investigated variant. Red dots violate a constraint, green dots are permissible variants.

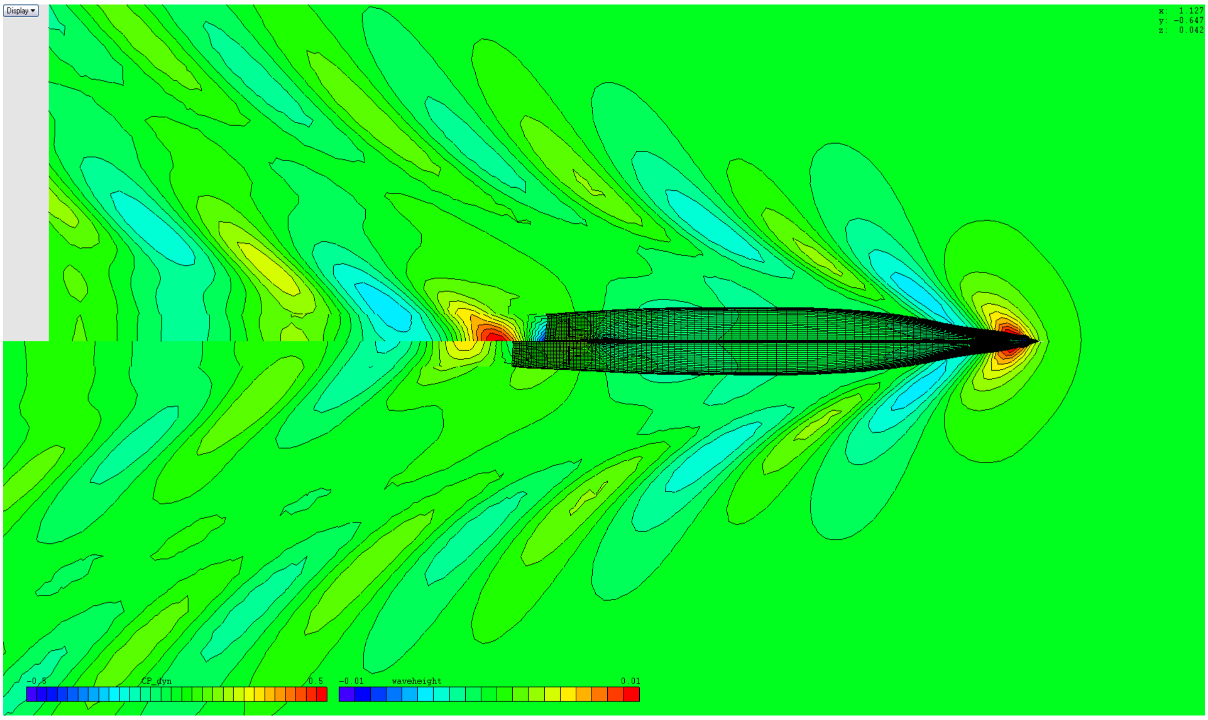

Fig.3. Wave pattern for original hull (top) and recommended extended version (bottom)

We performed such a design exploration study for an envisioned hull extension of the German Navy frigate F123. Key objectives were stability (to be increased) and power performance (to be decreased). Some 10000 variants of the new aftbody were investigated numerically, Fig.2 and Fig.3. Based on the resulting design knowledge, we recommended a detailed geometry with significantly improved stability and no hydrodynamic penalty.

2.2. Seakeeping

Bertram and Couser (2014) discuss the state of the art for computational methods for seakeeping and added resistance in waves. For many seakeeping issues, linear analyses (assuming small wave height or small wave steepness) are appropriate and frequently applied due to their efficiency. The advantage of this approach is that it is very fast and allows thus the investigation of many parameters (frequency, wave direction, ship speed, metacentric height, etc.). Non-linear computations employing time-domain approaches are usually necessary for the treatment of extreme motions. These simulations require massive computer resources and allow only the simulation of relative short periods (seconds to minutes). Combining intelligently linear frequency-domain methods with nonlinear time-domain simulations allows exploiting the respective strengths of each approach. The approach starts with a linear analysis to identify the most critical parameter combination for a ship response. Then a non-linear CFD (Computational Fluid Dynamics) analyses determines motions, loads and free surface (green water on deck), Fig.4.

Added power requirements in waves are due to added resistance, induced resistance to compensate drift forces, and reduced propeller efficiency. Recent progress in computational methods has improved prediction capabilities especially for short waves. The progress allows much better assessment of added power requirements, e.g. for appropriate definition of sea margins or speed loss in given sea states.

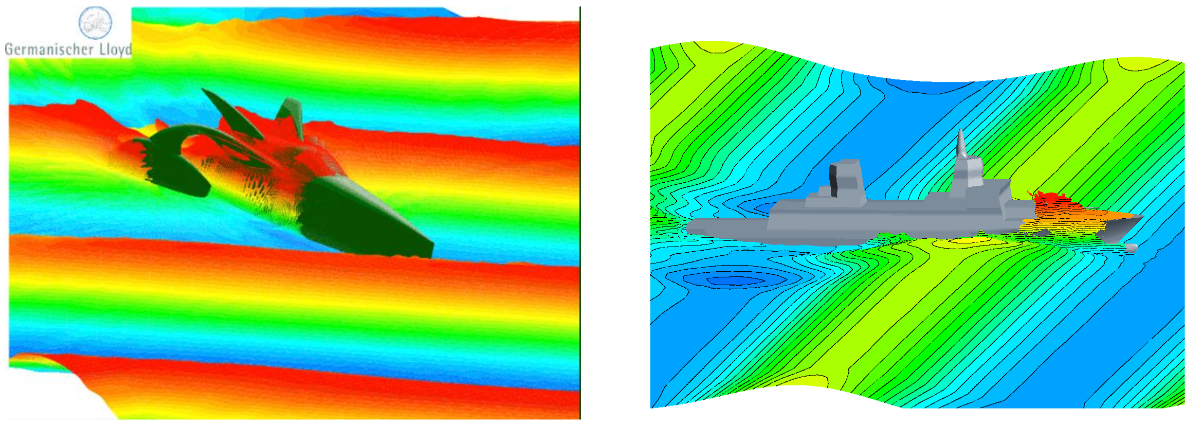

Fig.4. CFD simulation of ships in extreme waves; left: fast trimaran; right: frigate

2.3. Aerodynamics, HVAC and fire simulations

Aerodynamic flows around ship superstructures can be computed by CFD, Fig.5. Although wind tunnel tests remain to be popular, CFD offers the advantage of overcoming scale effects which can be significant if thermodynamic processes are involved, *El Moctar and Bertram (2002)*. HVAC (heat, ventilation, air condition) simulations involve the simultaneous solution of fluid mechanics equations and thermodynamic balances, often involving concentrations of different gases. Navy applications include for example the smoke and heat (buoyancy and turbulence) conditions on helicopter decks affecting safe helicopter operation. *Harries and Vesting (2010)* present how such simulations may be integrated in formal optimization, e.g. varying funnel geometries to minimize smoke dispersion on the helicopter deck.

For fire simulations, zone models and CFD tools are employed. Zone models are suitable for examining more complex, time-dependent scenarios involving multiple compartments and levels, but numerical stability can be a problem for scenarios involving multi-level ship domains, HVAC systems and for post-flashover conditions. CFD models can yield detailed information about temperatures, heat fluxes, and species concentrations, Fig.6. Applications have graduated from preliminary validation studies to more complex applications for typical ship rooms.

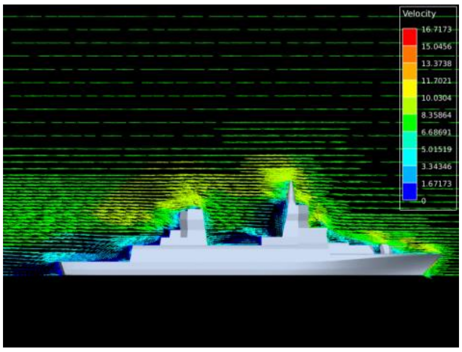

Fig.5. CFD aerodynamic simulation

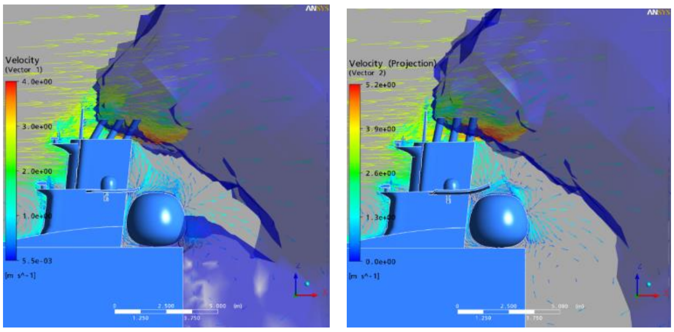

Fig.6.4 Funnel optimization for minimum smoke dispersion

3. FINITE ELEMENT ANALYSES (FEAs)

3.1. Global & local strength

FEA for global strength within the elastic material domain have been standard for a long time, Fig.7. These simulations were the starting point for more sophisticated analyses, e.g. fatigue strength assessment, ultimate strength assessment, etc. Navy specific simulations include assessing the effect of blast pressures near the hull on ship structure and equipment. The hull as a whole has to withstand the shock loads e.g. stemming from the global hull whipping response. For equipment and foundations, sufficient shock resistance against impulsive loads must be proven. The same is true for hull appendages directly exposed to shock waves, Fig.8.

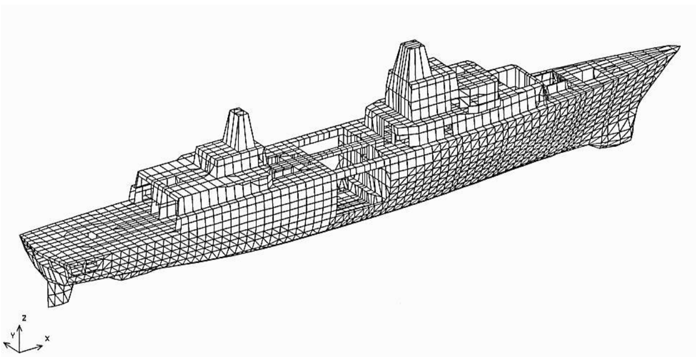

Fig.7. Residual strength analysis for frigate

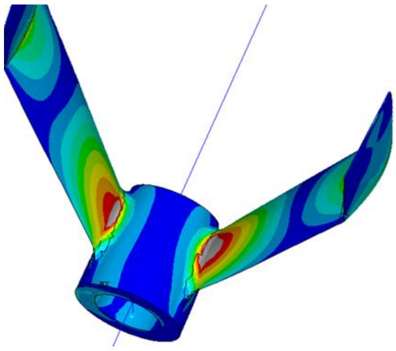

Fig.8. Shock analysis of shaft bracket

A variety of methods and calculations is applied to solve such diverse problems. For almost all calculations, FEA is used. Typically Shock Response Spectra (SRS), taken from navy standards or dedicated simulations, determine shock loads for equipment including supporting structures. The simulations combine hydrodynamic aspects (shock propagation under water) and structural aspects (FEA for hull and equipment). Decoupling the solution of the fluid problem and the solution of the structural problem reduces the calculation times dramatically.

Composite materials are increasingly used in high-performance vessels. The combination of light weight, high strength and mouldability make these materials highly attractive for designers. However, classical "cook-book" approaches in structural design do not work for high-performance light-weight designs, *Bertram et al. (2010)*. Prescriptive rules are often too inflexible; especially for advanced composite designs. Instead, first-principle analyses should be employed. Advanced FEA techniques for composite structures are available, Fig.9, but these analyses require particular attention and understanding. Early involvement of designers, owners and experts from classification society is vital for success.

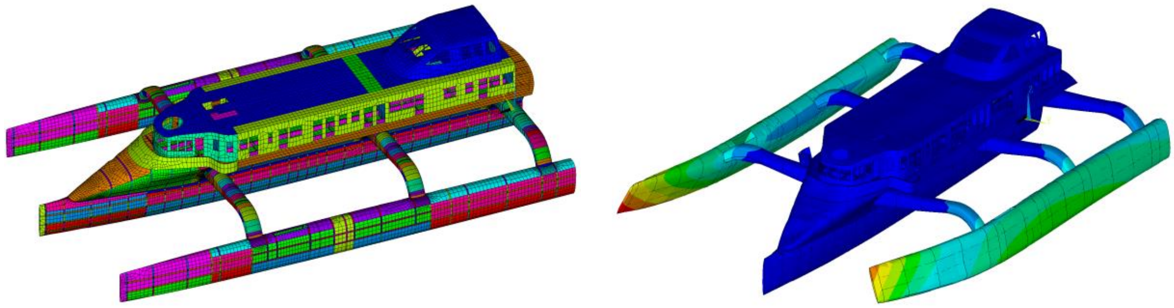

Fig.9. FEA model (left) and results (right) for composite material trimaran

3.2. Noise & Vibration

Advances in computer methods have made 3-d FEA today the standard choice for ship vibration analyses, Fig.10. The problem is complicated by the vicinity of fluids that change the vibration characteristics of the structures. The coupling to the fluid dynamics (so-called added mass and damping) may be based on experience or on more or less sophisticated hydrodynamic simulations. For local vibrations analyses, Fig.11, added mass needs to be considered only if the structures border on tanks or the outer hull plating. Because of the high natural frequencies of local structures, FEA models must be detailed including also the bending stiffness of structural elements. The source of ship vibrations is relatively easy to detect for engine and propeller induced vibrations. For hydrodynamic excitation, the identification of the problem source is in itself a good part of the problem. For vortex induced vibrations (VIV), the exciting frequency does not tell where the vortex shedding is generated. Consequently, this type of problem has been approached by expensive trial-and-error procedures, starting with alterations of the most likely appendages as V-brackets, fins, sea chests, etc. *Menzel et al. (2008)* show another approach, employing dedicated vibration and CFD analyses, before one single measurement trip pinpoints the area of hydrodynamic excitation. Here the time-domain CFD computations reveal locations of vortex shedding with associated frequencies. This allows pinpointing rapidly the source of the vibration problem. Then the problematic appendage can be redesigned and its new vortex pattern analysed again. The pressure fluctuations are used as input in FEA vibration analyses, quantifying vibration amplitudes in the ship structure.

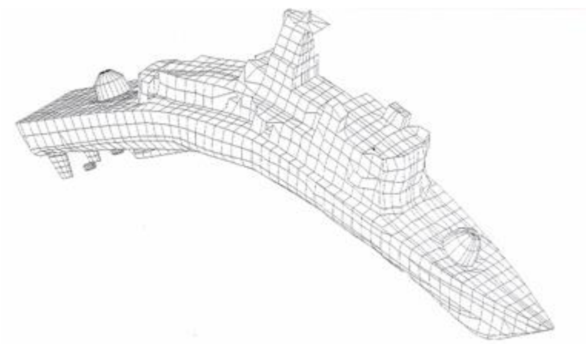

Fig.10. Global FEA of vibrations for gunboat

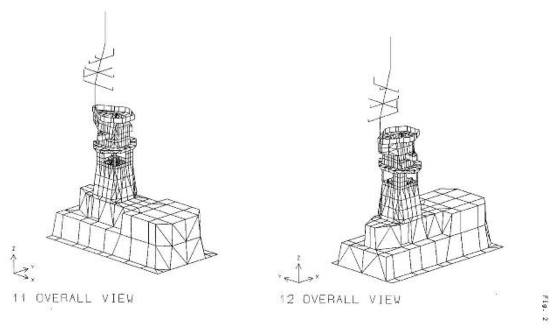

Fig.11. Local FEA mast and antennae

For very high frequencies (structure-borne noise), the standard FEA approach to vibration analyses is impossible due to excessive computational requirements. For a typical passenger vessel for a frequency of 1000 Hz, a FEA vibration model would lead to several million degrees of freedom. However, information is required only averaged over a frequency band. This allows alternative, far more efficient approaches based on statistical energy analysis (SEA). The Noise Finite Element Method of DNV GL is based on such an approach, Fig.12. Validation with full-scale measurements shows that the accuracy is sufficient for typical structure-borne sound predictions for the frequency range between 80 Hz and 4000 Hz. Accurate structure-borne noise is a requirement for underwater noise radiation. Navy vessels have been interested in acoustic signatures for a long time. Our procedures to predict underwater noise have been extensively validated in collaboration with the German Navy, Fig.13. Underwater noise is expected to become a design issue for megayachts in the future, if operating in environmentally sensitive regions, e.g. the Glacier Bay.

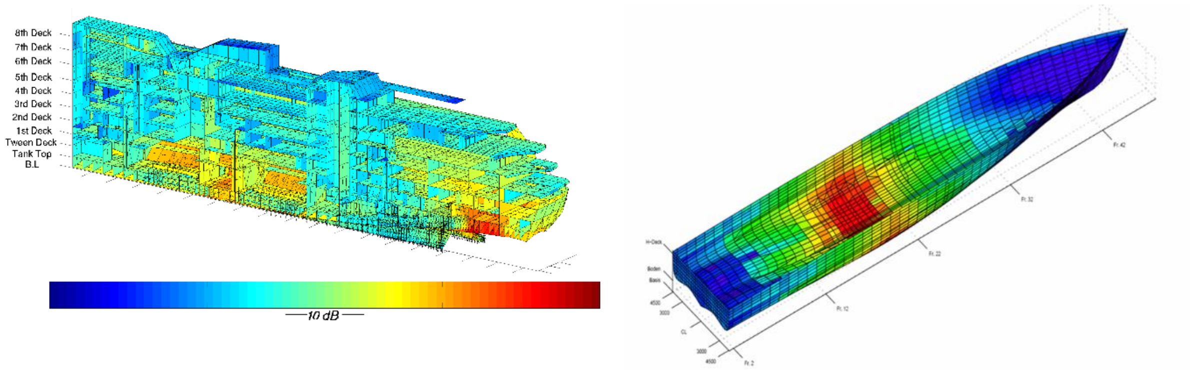

Fig.12. Structure-borne noise computation for Blohm&Voss cruiseship (left) and mine hunter (right)

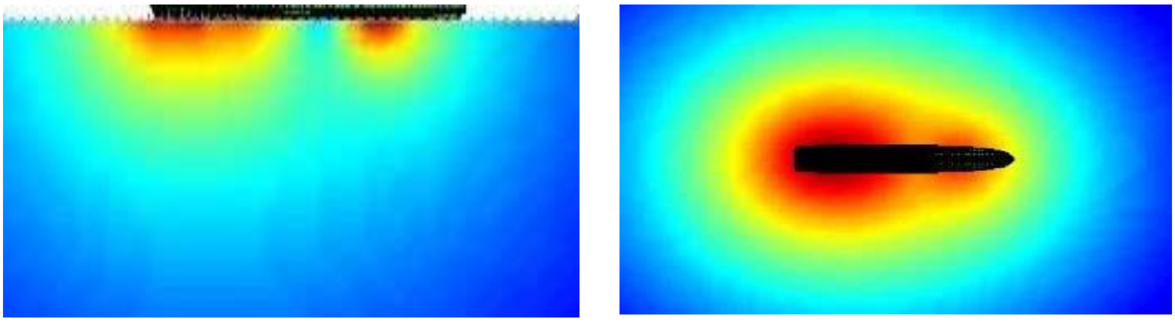

Fig.13. Underwater noise radiation prediction due to structure-borne noise excitation of the vessel; side view (left) and top view (right)

4. DYNAMIC MODELLING AND SIMULATION OF MACHINERY

4.1. Overview of energy flow simulations

The stringent existing and upcoming environmental and current market conditions lead the shipping industry towards the adoption of new technologies, solutions and alternative fuels, for increased energy efficiency and environmental performance. Sophistication and complexity of marine energy systems increase in the process. Emerging and future powering components (e.g. fuel cells, batteries, renewable auxiliary sources) will result in even more complexity. In response to these challenges, new simulation approaches emerge for energy systems analyses.

Energy and mass flow simulation is a relatively new addition to the suite of simulations used in design and operation of ships. However, this technology has spread rapidly over the last few years. The technology is so young that a common terminology has yet to evolve. So we find “dynamic simulation of machinery operation”, “ship energy modelling”, “energy system modelling” or “energy process modelling”, describing the same class of simulations. In essence, the simulation model considers energy converters (= main engine and generator sets) and energy consumers (propeller, pumps, heat exchangers, ventilators, cargo handling gear, etc.) in a graphical network, Fig.14, *Dimopoulos and Kakalis (2010)*. Ambient conditions and operational profile are input dynamically (i.e. changing over time) and the simulation reveals energy flows and utilization rates (with bottlenecks and idle over-capacity). The detailed insight can be used to improve systems or operational procedures.

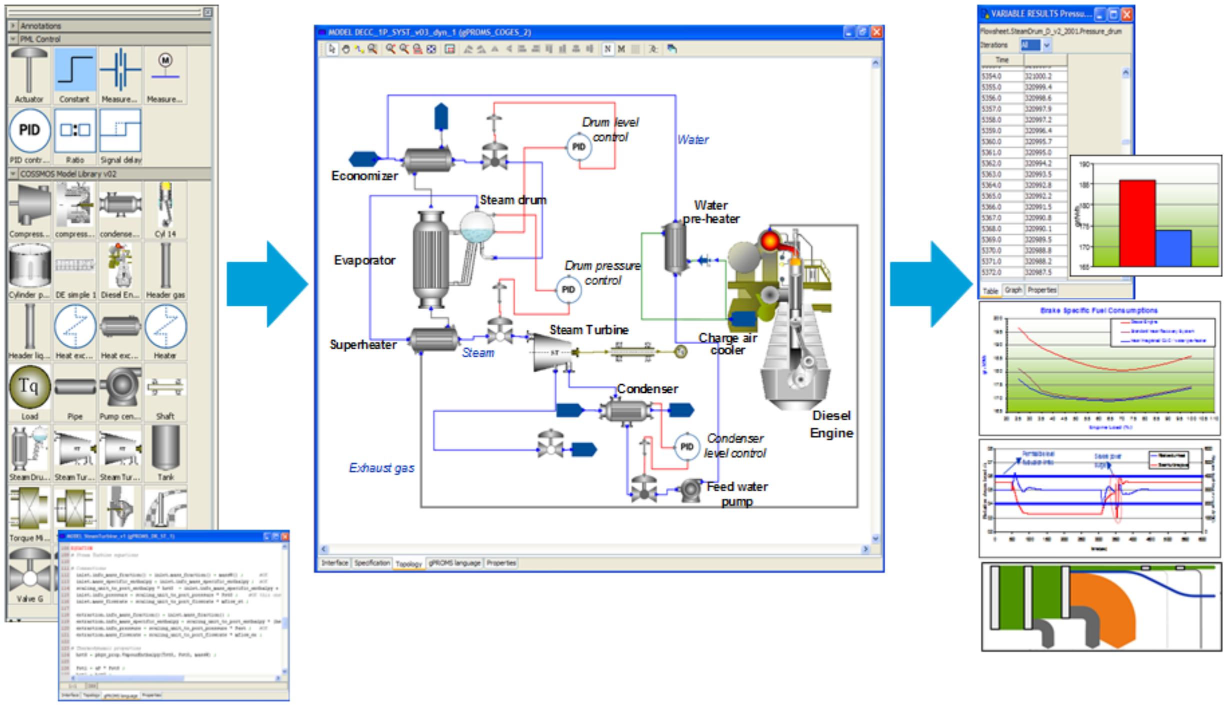

Fig.14. Energy flow simulation model with graphical network and typical output

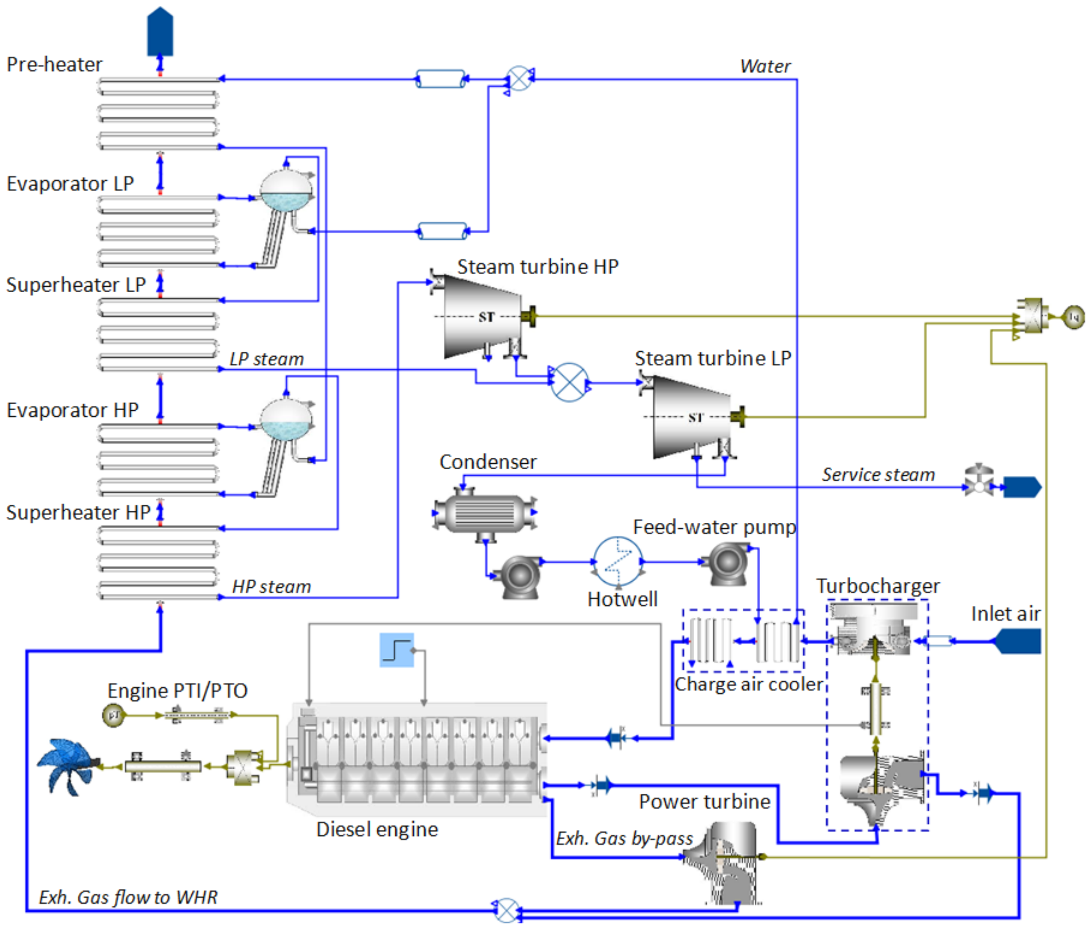

Fig. 15. COSSMOS model of a dual pressure WHR (waste heat recovery) configuration

For complex systems, energy flow simulations often reveal interesting potential problems as well as saving potential, especially for off-design conditions. It is expected that this simulation technology will continue to develop dynamically and become a standard technique in design of high-performance marine vessels over the next decade.

4.2. COSSMOS approach

DNV GL has developed its own model-based systems engineering methodology for simulating complex marine energy systems, *Dimopoulos and Kakalis (2010), Dimopoulos et al. (2011)*. This work has resulted in a process modelling framework for:

- design of on-board machinery with respect to energy efficiency, emissions, safety and cost effectiveness;
- performance evaluation, diagnostics and optimisation under real-service conditions for the entire mission envelope of existing systems; and
- assessment of the potential, operational capabilities, and safety of innovative designs.

The associated computer implementation of this framework is called COSSMOS. COSSMOS (Complex Ship Systems Modelling and Simulation) is based on the mathematical modelling of the steady-state and dynamic thermo-fluid behaviour of marine energy system components, Fig.14. The component process models are generic, reconfigurable, suitable for different types of studies and valid for a wide range of operating conditions. The models employ a library from which systems can be created from component models, Fig.15.

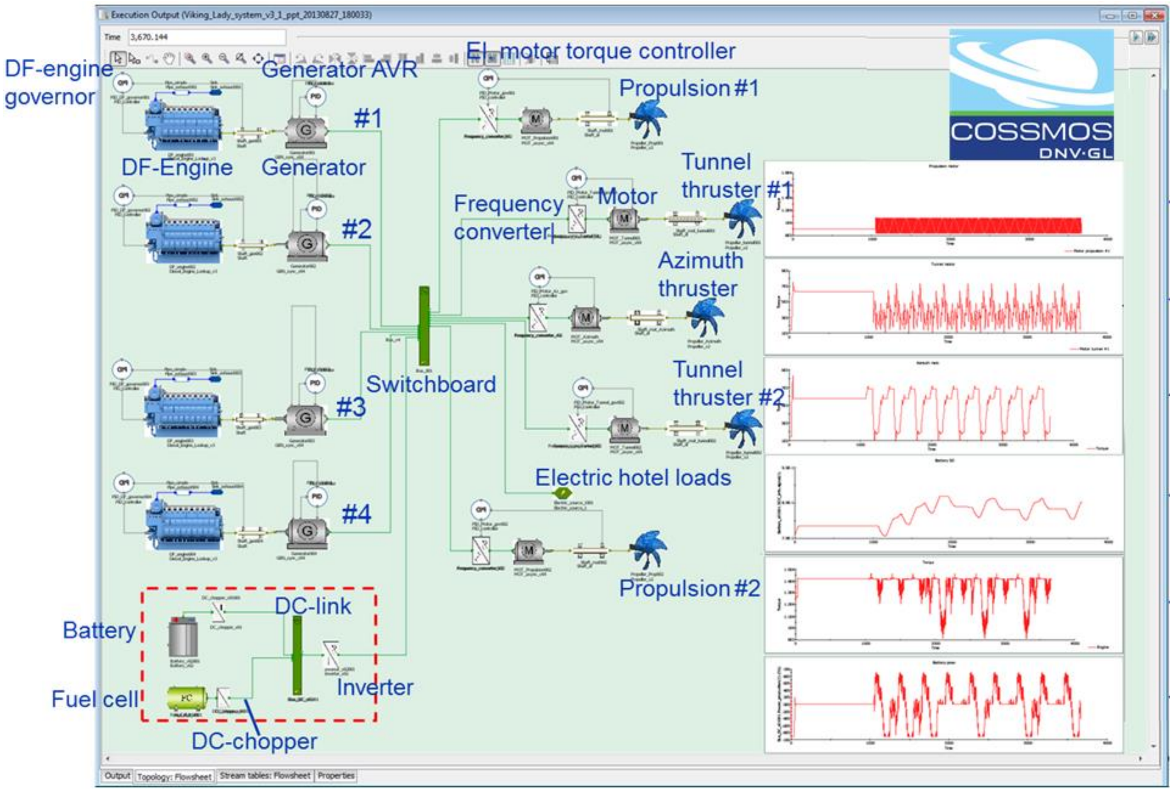

Fig. 16. COSSMOS hybrid-electric propulsion system model

4.3. Application to hybrid-electric vessels

Electric propulsion has been utilised in the design of various ship types, including megayachts, ferries, tugs, and offshore supply vessels. The main benefits over conventional mechanical propulsion are better overall efficiency and operational flexibility. A typical electric propulsion arrangement consists of several generators producing the required power for all the on-board power demands. Hybrid-electric propulsion adds energy storage devices, e.g. batteries. We consider the dynamic modelling and simulation of a hybrid-electric propulsion arrangement for an OSV (offshore supply vessel). The complete hybrid-electric system was modelled in COSSMOS, Fig. 16, *Kakalis et al. (2014)*. The model was calibrated using data from manufacturers' manuals and validated from commissioning tests during the vessel's delivery. The model is able to capture the dynamic behaviour of the system in order to simulate the actual operational strategies that will be used on-board the vessel.

Energy flow simulations are particularly attractive for vessels with large variations and sharp peaks in power demand, e.g. megayachts, OSVs or navy vessels.

4. CONCLUSIONS

The technological progress is rapid, both for hardware and software. Simulations aid decisions in design for high-performance vessels, sometimes 'just' for qualitative ranking of solutions, sometimes for quantitative 'optimization'. Engineering is more than ever the art of modelling, finding the right balance between level of detail and resources (time, man-power). This modelling often requires intelligence and considerable experience.

References

ABT, C. and HARRIES, S. (2007), *A new approach to integration of CAD and CFD for naval architects*, 6th Conf. Computer and IT Applications in the Maritime Industries (COMPIT), Cortona, pp.467-479

BERTRAM, V. and COUSER, P. (2014), *Computational methods for seakeeping and added resistance in waves,* 13th Conf. Computer and IT Applications in the Maritime Industries (COMPIT), Redworth, pp.8-16

BERTRAM, V.; HOFFMEISTER, H.; MÜLLER, S. and MOLTSCHANIWSKYJ, A. (2010), *Technological challenges for construction and classification "Tûranor PlanetSolar",* 7th Int. Conf. on High-Performance Marine Vehicles (HIPER), Melbourne, pp.76-85

CIORTAN, C. and BERTRAM, V. (2014), *RANSE simulations for the effect of welds on ship resistance*, 17th Numerical Towing Tank Symp. (NuTTS), Marstrand

DIMOPOULOS, G.G. and KAKALIS, N.M.P. (2010), *An integrated modelling framework for the design, operation and control of marine energy systems,* 26th CIMAC World Congress, Bergen

DIMOPOULOS, G.G., GEORGOPOULOU, C.A. and KAKALIS, N.M.P. (2011), *Modelling and optimisation of an integrated marine combined cycle system,* 24th Int. Conf. Energy, Cost, Optimization, Simulation and Environmental Impact of Energy Systems (ECOS), Novi-Sad

EL MOCTAR, O.M. and BERTRAM, V. (2002), *Computation of viscous flow around fast ship super-structures,* 24th Symp. Naval Hydrodynamics, Fukuoka

HARRIES, S. and VESTING, F. (2010), *Aerodynamic Optimization of Superstructures and Components,* 9th Int. Conf. Computer and IT Applications in the Maritime Industries, Gubbio, pp.335-347

HOCHKIRCH, K. and BERTRAM, V. (2012a), *Hull optimization for fuel efficiency – Past, present, future*, 11th Int. Conf. Computer and IT Applications in the Maritime Industries (COMPIT), Liège, pp.39-49

KAKALIS, N.; DIMOPOULOS, G. and STEFANATOS, I. (2014), *A novel framework for dynamic modelling of integrated machinery systems*, 13th Conf. Computer and IT Applications in the Maritime Industries (COMPIT), Redworth, pp.137-149

MENZEL, W.; EL MOCTAR, O.M. and MUMM, H. (2008), *Advanced thinking on tricky excitations*, The Naval Architect, March, pp.64-69

OOSSANEN, P. van; HEIMANN, J.; HENRICHS, J. and HOCHKIRCH, K. (2009), *Motor yacht hull form design for the displacement to semi-displacement speed range*, 10th Int. Conf. Fast Sea Transportation (FAST), Athens

Efficient propeller Designs based on Full scale CFD simulations

N.W.H. Bulten, P.W. Stoltenkamp, J.J.A Van Hooijdonk

Wärtsilä Propulsion, R&D-Hydrodynamics, Lipsstraat 52, 5151 RP Drunen, The Netherlands

ABSTRACT

In order to be able to further enhance the performance of ship propellers, the possibilities of full scale numerical flow simulations have been investigated. The aim is to get a full understanding of the occurring flow phenomena on the actual ship. With this knowledge the optimum propeller design can be made. During the validation process a critical review of the model scale measurements methods has been made. The validity of some of the commonly used procedures has been evaluated. The use of full scale CFD simulations provide direct full scale data on the hull wake field and the propeller performance. It has been shown that the commonly used extrapolation methods predict different answers. Decomposition of the forces acting on the hull, the propeller and the rudder is being used to get a proper insight in the flow field at full scale. In the end the design features which contribute to efficiency increase, and thus fuel consumption reduction, can be isolated, based on the results from detailed flow simulations.

1. INTRODUCTION

Though the design process of fixed pitch and controllable pitch propellers are based on a long history, there is still a desire to further improve the efficiency of the propellers. In order to come to even better designs, it is important to evaluate the available knowledge and the research tools. The majority of the current knowledge on ship resistance, propeller performance and propeller-hull interaction has been derived from model scale measurements. During the last two decades the developments of numerical flow simulations have made such progress, that the use of Computational Fluid Dynamics (CFD) has become within reach in maritime industry. The required costs to get the simulations up and running and the achievable accuracy of the simulations are nowadays at a level that it can compete with experiments in model basins.

The insights obtained from numerical flow simulations have led to a close review of the methods applied in model testing. It is acknowledged that there have been made decisions in the past to follow a certain approach in model testing. Nevertheless, some constraints from experimental side, might not be present in numerical simulations, and therefore the approach can be revised in some cases. This point can only be reached after an extensive validation process of the numerical methods however.

In the following section the historical method for performance prediction based on model scale testing will be reviewed. This will give the background of the ideas where numerical flow simulations may have benefits. In section 3 the development of the numerical methods will be reviewed. Some results of the extensive validation process will be shown to give an impression of the achievable accuracy of the methods. Most validation work is based on model scale dimensions in order to be able to make a fair comparison with experimental data. Although full scale performance data is scarce, it is the authors opinion that the step to full scale numerical simulations should be made. Analysis of the differences in results from both model scale and full scale simulations can provide valuable information on the occurring Reynolds scaling effects. In such way an indirect evidence of the validity of the full scale results can be obtained.

Once the confidence in the full scale numerical flow simulations has been established, all kind of design variations can be analysed. Typical examples of cases studies can be propeller diameter variations to determine the effects on both open water efficiency and propeller-hull interaction losses, or implementation of energy saving devices like rudder bulbs or propeller boss cap fins. Results from some of these cases will be discussed in detail in section 4. The conclusions from the full scale numerical flow simulations will be drawn in the last section.

2. HISTORICAL PERFORMANCE DETERMINATION

For a very long time model scale experiments were the only way to collect data on the propulsive performance of the vessels. The extrapolation of the measured model scale data to the actual full scale performance of the vessel is partly based on an empirical approach. This process has been tuned by the different model basins over the years to come to quite accurate full scale performance predictions.

In order to get more insight in the overall vessel performance, there have been introduced three interaction factors. The background of these factors will be discussed in the following subsection.

2.1 Propeller-hull interaction factors

The coupling between hull resistance and propeller performance is based on the so-called interaction factors: wake fraction, thrust deduction, relative rotative efficiency. The conventional method of performance determination is based on a set of measurements:

- bare hull resistance
- propeller open water performance
- self-propulsion (combination of hull and propeller)

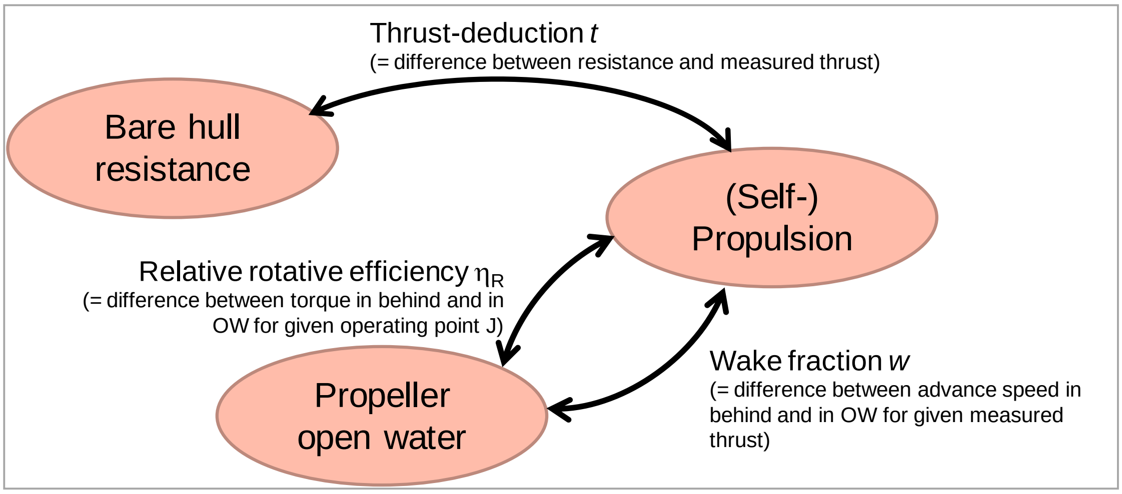

Fig. 1. Relations between model tests and interaction factors

It is known that the hull resistance in the self-propulsion test increases due to the working propeller, which creates a low pressure just upstream of the propeller. This increase in resistance is expressed as thrust-deduction factor t. The thrust-deduction couples the measured bare hull resistance with the measured thrust in the self-propulsion case. The inflow velocity to the propeller in behind the vessel is lower, due to the development of a boundary layer along the hull and the presence of shafts, skegs and brackets in front of the propeller. This velocity deficit is denoted with the wake fraction w. This wake fraction couples the measured thrust in the open water set-up with the measured thrust in the in behind condition. In order to get the bookkeeping closed there is one additional factor required, which gives the ratio between the power absorption in behind and in open water. This is the relative rotative efficiency η_R, which is for open propellers often close to 1.00.

2.2 Interpretation of interaction factors

Though the methods to calculate the interaction factors seems straight forward, significant differences in interaction factors can be found between different model basins. Given the method of data analysis and the impact of relative small deviations in the measurements, the interpretation of the interaction coefficients should be done with care. Nevertheless, over the years some rules of thumb have been derived to get rough indications of the interaction values. As a consequence the interaction factors have gained quite an important position in the performance prediction of ships.

With the introduction of integrated rudders, energy saving devices and ducted propellers, the use of interaction factors has continued, though this has led to non physical interpretation of interaction parameters in many cases. So, for more modern propulsion concepts and energy saving devices, the conventional approach of the interaction factors has been stretched over the limits of its validity. In those cases the possible gains in fuel consumption might end up in non physical interaction factors and as a consequence the phenomena might be discarded based on the motivation of measurement inaccuracies.

2.3 Review of open water performance test set-up

According to the commonly accepted procedures a propeller is driven from the downstream side in an open water performance test. In this way the inflow to the propeller is as uniform as possible. In case the propeller has to be driven from upstream side, the drive mechanism will create a flow disturbance which is undesirable. The choice to put the drive shaft downstream has had the consequence that the impact of the hub cap design has not been taken into account in the propeller performance measurement for decades. This is shown in fig. 2.

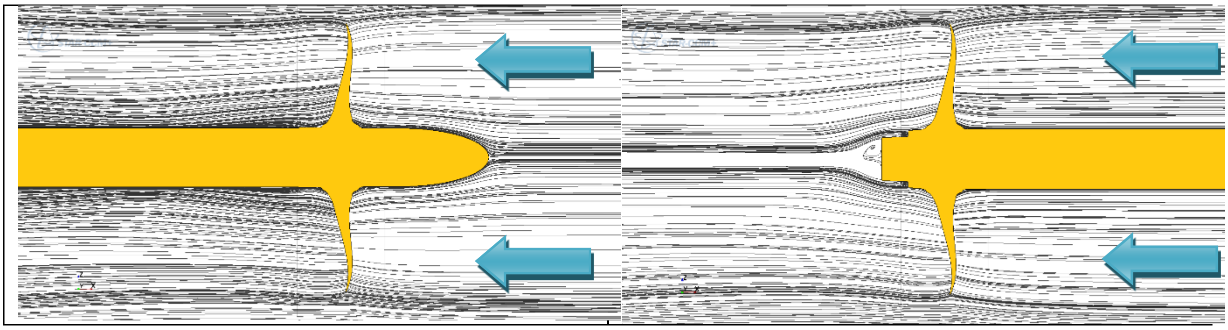

Fig. 2. Comparison of open water test set-up configuration and set-up in self-propulsion in behind ship

In the self-propulsion measurements, where the actual hub cap shape is modelled properly, possible gains or losses are part of the overall performance measurement. Any possible impact of the performance of the hub cap will therefore end up in one or more of the interaction or correction factors. The unavoidable inconsistency in the open water testing method will not reveal the true performance of the applied hub cap shape. The flow simulations for the example case as shown in fig. 2 revealed an efficiency drop of about 2%. In the conventional model testing approach, these effects will end up in the various interaction factors, and become untraceable in that way. Moreover the development of energy saving devices like propeller boss cap fins has suffered from this test methodology. With numerical flow simulations the potential benefits of boss cap fins can be determined properly, both on model scale and full scale (Kawamura 2013).

3. DEVELOPMENT OF NUMERICAL METHODS

In the following subsection the current status of the viscous flow simulations will be described. This should give a good impression of what can be expected as state-of-art methodologies nowadays. An important aspect of the implementation is the validation of the numerical methods. This will be discussed in the subsequent subsection, where some results of the extensive implementation and validation process will be discussed. In subsection 3.3 an evaluation will be made of the added value of full scale simulations. Typical phenomena which are occurring in model scale testing might be avoided with aid of numerical simulations. Examples are among others the Reynolds scaling effect on wake fields and ducted propeller performance and the sensitivity analysis of hull roughness on resistance and performance.

3.1 Current status of numerical simulations

The development of numerical methods is a continuous process. Significant steps forward are being made both on the hardware side and on the commercial software side. In general these developments are globally driven. It is therefore expected that the developments will continue further in the coming years. Based on this assumption, it is worthwhile to start working on method development of numerical flow simulations, which might at this point in time not yet be suitable for daily commercial use. However, by the time the methodologies have reached a certain maturity level, which means sufficiently validated, and captured well in process descriptions and procedures, the lead times and costs have reduced enough for commercial applications.

Nowadays the effects of viscous flow can be taken into account, which means that accurate bare hull resistance predictions are feasible. Based on current technology the viscous flow simulations (also denoted as RANS (Reynolds-Averaged Navier-Stokes)) can take the effects of the free surface (VOF) and the dynamic sinkage and trim into account. And the accuracy of the calculations can compete with the accuracy of the model scale measurements.

Moreover, there will be differences in the results when model scale and full scale geometries are compared. Due to the proper calculation of the full scale viscous flow effects the need for the semi-empirical extrapolation methods, as used in the model tests, will diminish.

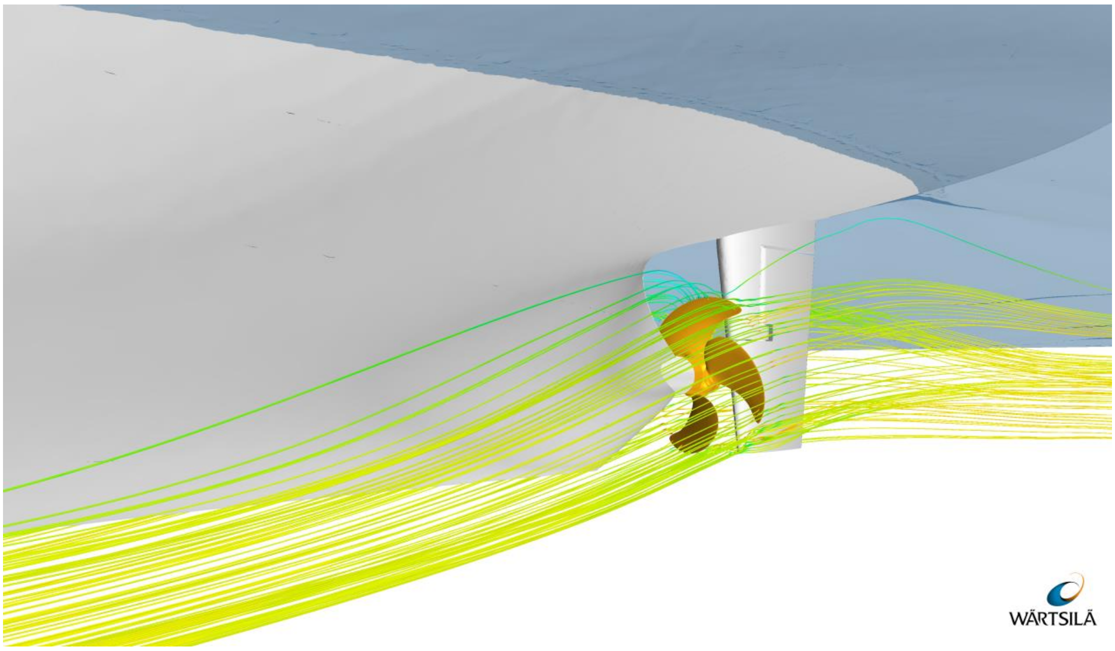

Fig. 3. Numerical flow simulation of hull and propeller, including free surface effects

The following step in the development of the numerical simulations is the propulsion calculation, where the ship and the propeller are analyzed together. The propeller performance is then derived from fully transient moving mesh simulations with sliding interfaces. In these simulations, the propeller position is adjusted every time step, which gives the time dependent solution of the flow. The propeller thrust and torque are calculated for each time step in this approach.

The added value of the numerical simulations is found in the extensive options of flow visualization (see for example fig. 3) and post-processing. With these other means of data analysis it is possible to get new insights on the actual occurring flow phenomena, like the interaction phenomena. It is also possible to determine the drag contribution of different components and appendages on the hull to get an indication of the contribution to the total resistance.

3.2 Implementation and validation of numerical methods

Numerical flow simulations in maritime industry have gained maturity during the last years. One of the important issues in this process is the quality assurance of the simulations. This covers not only the level of achieved accuracy, but also the processes and procedures to reach the repeatability of the results. The target should be that proper implemented numerical methodologies are independent of the expert who is carrying out the simulations. The methodology should also be robust enough to handle different ship and propeller designs. This target can be achieved with parametric mesh topology definitions in general.

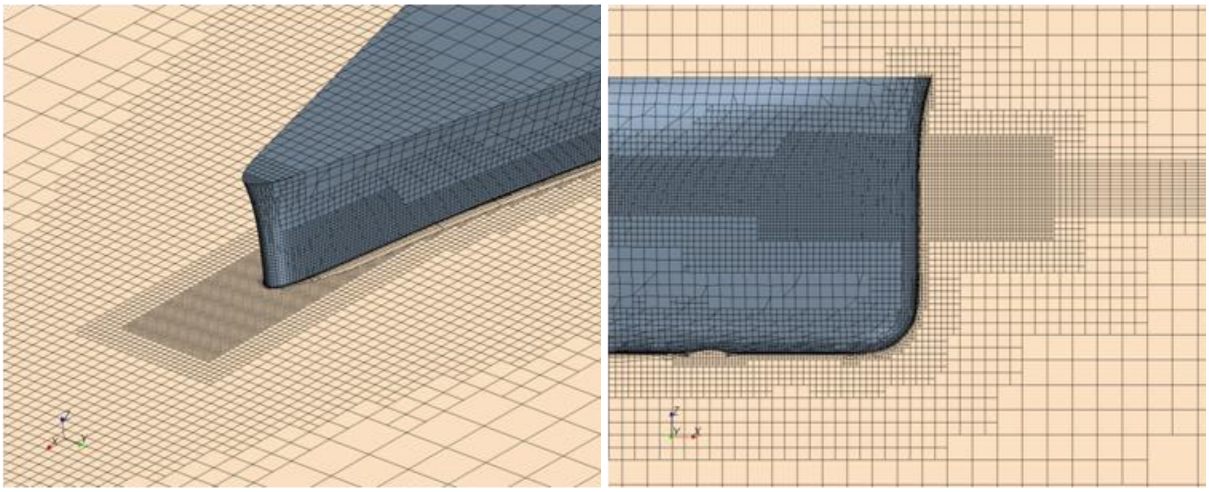

Fig. 4. Mesh near bow with local refinements to capture free surface effects

An example of the mesh topology around the bow of the hull is shown in fig. 4. In order to get a good balance between total cell count and required mesh density, local mesh refinement near the free surface is implemented. The actual free surface is based on the solution of the Volume of Fraction (VOF) of the water and air mixture. The final meshing approach has been the deliverable of the implementation and validation process.

The outcome of a bare hull resistance calculation with free surface is shown in fig. 5, where the model scale resistance is shown for different vessel speeds. The agreement between the measured and the calculated values is good over the complete range of ship speeds. Similar results have been found for other vessels, which indicate the robustness of the method.

Besides an accurate calculation of the bare hull resistance it is also required to implement a proper propeller performance methodology. The quality of such method can be verified with open water model scale performance measurements. In the marine industry, the critical success factors for propeller performance calculations are regarded to be the ability to model the blade geometry with sufficient detail (meshing), proper implementation of the rotation of the propeller and selection of the turbulence model. Fig. 6 shows the open water performance curves for a selected open propeller. For this propeller two well-known turbulence models, k-ε and k-ω-SST, have been used to calculate the open water performance on model scale. The figure shows that comparable results can be obtained with both turbulence models. At low advance ratios a slightly different trend can be observed, which may be attributed to a small pitch effect due to differences in boundary layer development along the blade. However, the overall performance comparison indicates that both models can be used in the numerical simulations. Comparison of the numerical results with the model scale measurements learns that the overall trends of thrust and torque are captured well over the whole range of advance speeds. Though there is a difference between the measurements and the calculations near the top efficiency. This is a result of the fairly subtle differences in the thrust and torque values, which might be a result of some laminar flow effects or not properly reported hub cap correction factors in the experiments in the end. Near the design point of the propeller, which is around J=0.65, the agreement between measurements and calculations is better.

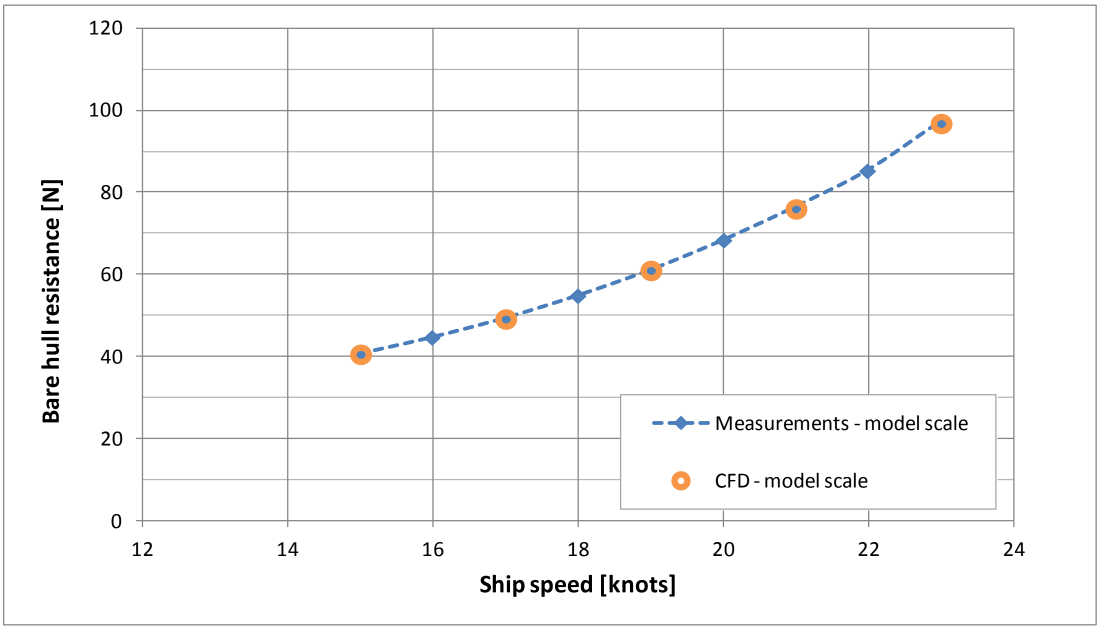

Fig. 5. Comparison of bare hull resistance measurements and calculations

Implementation of the propeller rotation in the numerical simulations can be either based on the quasi-steady Multiple-Frame-of-Reference (MFR) approach or the full transient moving mesh (MM) approach. In the MFR method the mesh remains fixed in a frozen position and the additional terms due to centrifugal and Coriolis forces are implemented in a spin domain. In this approach the steady solvers can be used leading to relatively short calculation times. In case the fully transient moving mesh option is used, a specified domain around the propeller is rotated every time step, resulting in a fully transient solution of the flow. The MFR approach works well for propeller open water calculations, where a uniform inflow is present and no flow disturbances are present behind the propeller. Apart from the propeller blade geometry an axi-symmetrical flow problem is being solved.

For propulsion calculations initially the MFR method has been applied. This gave results which looked plausible, but were wrong. The concept of averaging several MFR calculations, with different blade positions, is not recommended by the authors either. Therefore the fully transient moving mesh approach is regarded to be the only valid alternative for propulsion calculations, though it will be most computational intensive.

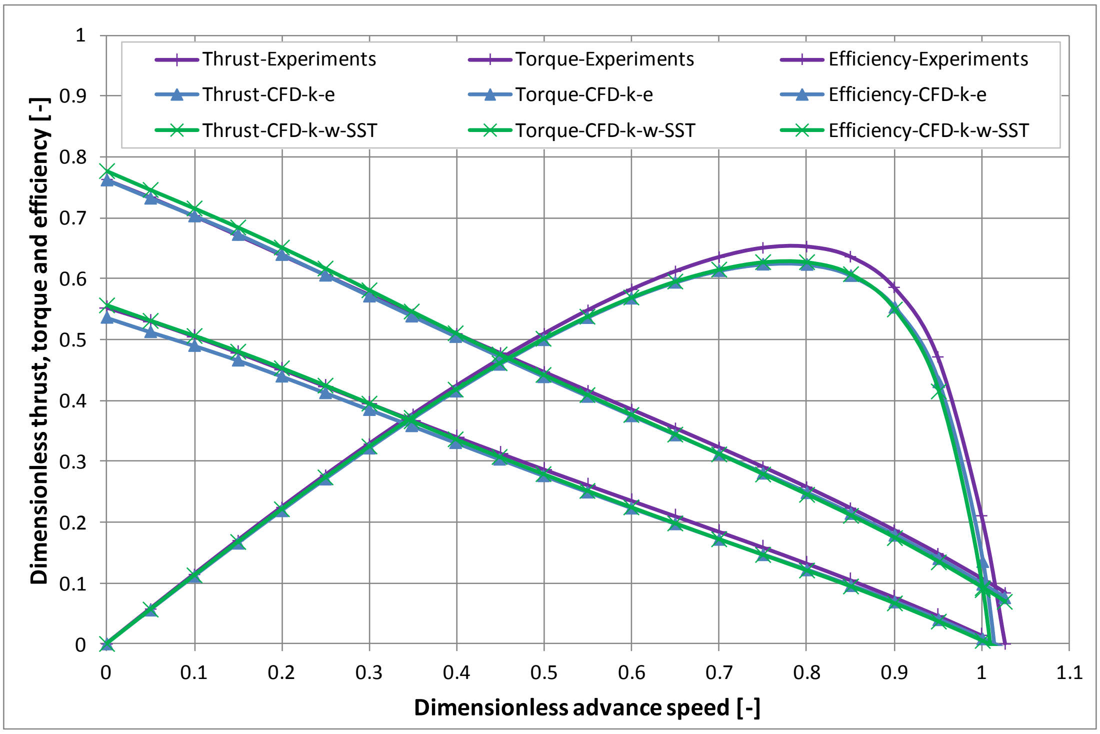

Fig. 6. Comparison of open water performance curves for open propeller based on model scale measurements and numerical simulations with k-ε and k-ω-SST turbulence models

3.3 Added value of full scale numerical simulations

Even though there are still differences between model scale measurements and numerical simulations, it is interesting to investigate further steps on the side of the simulations. Calculations made for the actual full scale can provide knowledge and understanding of the occurring Reynolds scaling effects. It is also known for long time that some typical phenomena suffer from the Reynolds scaling effects, like the friction along the hull (ITTC 1957 friction line) and the propeller performance effects (ITTC 1978 ΔKt and ΔKq), which are addressed in several ITTC-conferences (ITTC 2011). Also the differences between model scale and full scale wake fields and the consequences for the propeller loading have been acknowledged (Ligtelijn 2004).

Another issue from model testing, which can be investigated easily with numerical simulations, is the location of the drive shaft, either upstream or downstream. In the simulations the drive shaft can be modelled in various ways, since it has no actual functionality. In this way a sensitivity analysis can be carried out. Such sensitivity analyses may also help in understanding the working principles of various energy saving devices, like propeller boss cap fins and rudder bulbs.

The use of full scale propeller performance data has an impact on the selection of optimum propeller diameter. The common approach is to use B-series data, derived from the published polynomials (Oosterveld 1974). With a performance polynomial of full scale B-series, a comparison can be made on the selection of the optimum diameter, based on model and full scale performance. Once this point has been reached, the true value of the capabilities of the numerical simulations comes to the surface.

The added value of the simulations do not limit to the design phase of the vessel and propeller. Once the vessel is in service, it is of interest to get a good indication of the effects of increasing roughness of the hull and the propeller on the fuel consumption. At certain point in time there will be a trade off between the cost of cleaning and the gains in fuel costs during operation. Numerical simulations with various grades of hull roughness can be of help in such evaluation.

4. RESULTS FROM FULL SCALE CFD PERFORMANCE SIMULATIONS

In this section the aforementioned topics will be analysed in more detail, based on the results from the flow simulations. First the wake scaling effects will be shown and afterwards the effects of Reynolds scaling effects on propeller open water performance and the impact on the propeller diameter selection. Finally, results from the work on energy saving devices will be shown.

4.1 Wake scaling

The wake field of a vessel is one of the key input parameters for the propeller design process. Once the bare hull design is available and resistance measurements are carried out, often the wake field is measured as well. It has been recognized that the model scale wake field will differ from the actual full scale wake field (Benedek 1968), due to Reynolds scaling effects. The boundary layer development along the hull causes not only a difference in hull friction, but also in the velocity distribution at the aft part of the vessel, where the propeller will be located. For the propeller designer two factors in the wake field are of importance in the propeller design process: the depth of the wake peek in the top position and the gradients of the velocity along a circular path. These parameters determine how and to which extent the blade load fluctuates during a revolution. A comparison of two calculated wake fields is shown in fig. 7 for a single screw vessel. The wake field, as calculated for model scale, shows a deeper wake peek compared to the full scale wake field. Moreover, the overall wake fraction *w* will be larger for model scale compared to full scale.

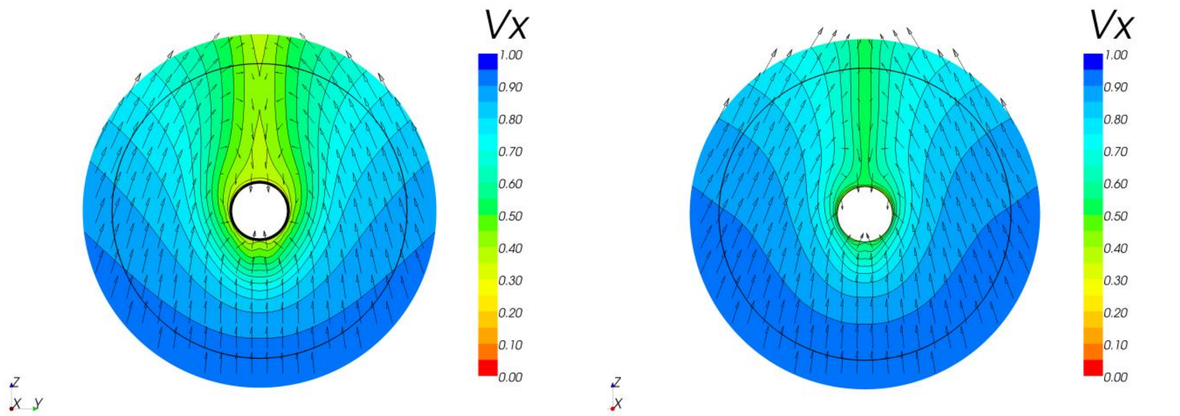

Fig. 7. Comparison of calculated wake field on model scale (left) and full scale

4.2 Propeller open water performance

For the scaling of propeller open water performance ITTC has made a procedure back in 1978 (ITTC 1978). This scaling method introduces an offset on the non-dimensional thrust and torque values Kt and Kq. Due to reduction of blade friction, it is expected that the thrust increases slightly and the torque decreases at the same time. More recent CFD studies have shown that such a trend could be observed for certain families of propeller designs. However, there were also indications that for other families of propellers, for example with more skew, other phenomena played a role. For skewed propellers, there seems to be a pitch effect on the blades, which results in a shift of both thrust and torque in the same direction (Minguito 2005).

The Reynolds scaling effect on propeller performance is presented in fig. 8, where the calculated open water curves for model scale and full scale are shown, together with the experimental data. This diagram shows a quite significant difference between the model scale and full scale calculations. The torque at full scale is reduced and the thrust is increased slightly, which is in line with the expectations. The averaged ΔKt and ΔKq have been derived from the CFD results and compared with the values from the ITTC’78 method. The values are shown in table 1. Significant differences are found between the two methods. As a consequence the full scale performance prediction based on the ITTC’78 method will differ significantly from the calculated full scale curves.

Table 1. Comparison of ΔKt and ΔKq

	Δ Kt	10Δ Kq
ITTC'78	0.0003	-0.0029
CFD	0.0015	-0.0194

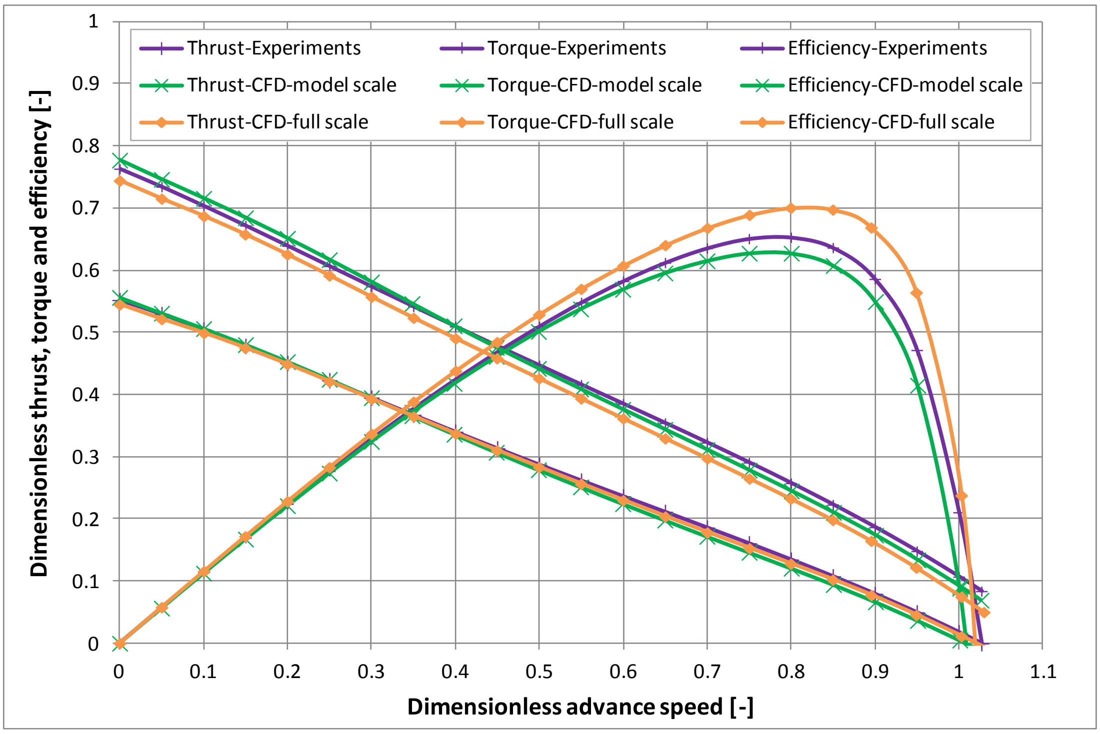

Fig. 8. Open water performance for calculated model scale and full scale and measured data

The differences in open water performance, due to Reynolds scaling effects, do have an impact on the selection of the optimum diameter for a given application. Based on the overall propeller powering characteristics, like power, RPM, ship speed, an optimum propeller diameter can be selected. This process is often based on the available Wageningen B-series polynomials, which have been derived from the model scale experimental data.

Recently, a similar polynomial has been generated for full scale geometries based on CFD. With these results it has become possible to carry out the propeller diameter selection process based on both model scale and full scale data. The results are shown in fig. 9 and the outcome is quite remarkable. Based on the full scale open water data a 7% larger propeller diameter would have been selected.

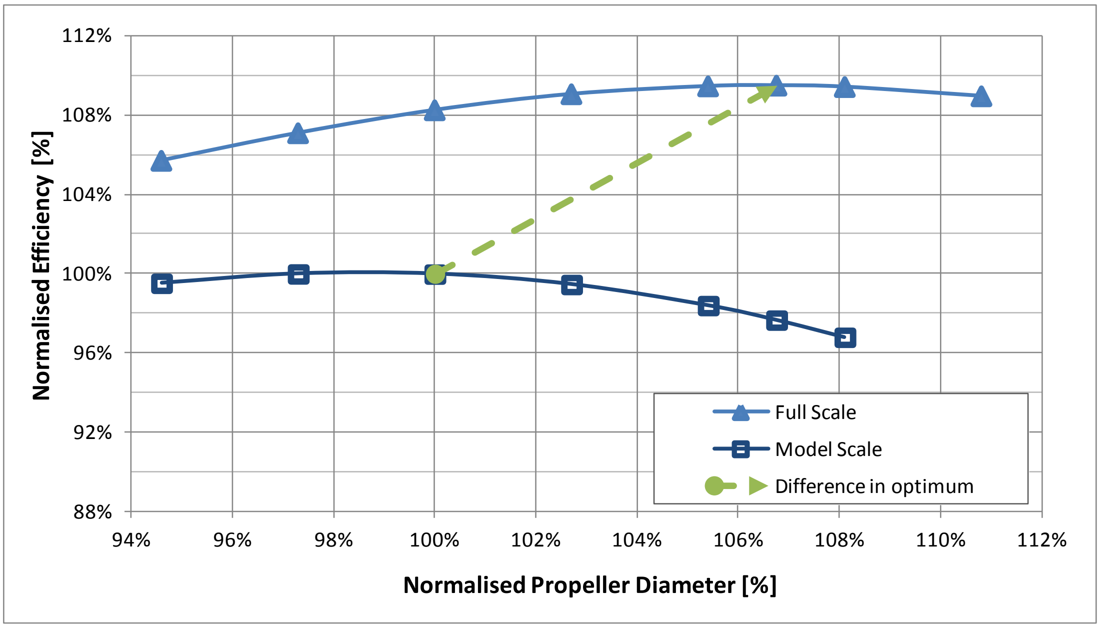

Fig. 9. Comparison of propeller diameter selection based on B-series model scale and full scale

4.3 Energy saving devices

The energy saving devices (ESD), like propeller boss cap fins and rudder bulbs, have attracted quite some attention in the last years. Though these concepts differ a lot in geometry, they have in common that the flow near the propeller hub is influenced mostly by these devices. In order to be able to give a proper evaluation of the effectiveness of these ESDs, it is important to understand the occurring flow phenomena near the hub and to minimize the impact of laminar flow and Reynolds scaling effects. Full scale numerical flow simulations of the hull, propeller and rudder can potentially provide the proper information to reach this goal.

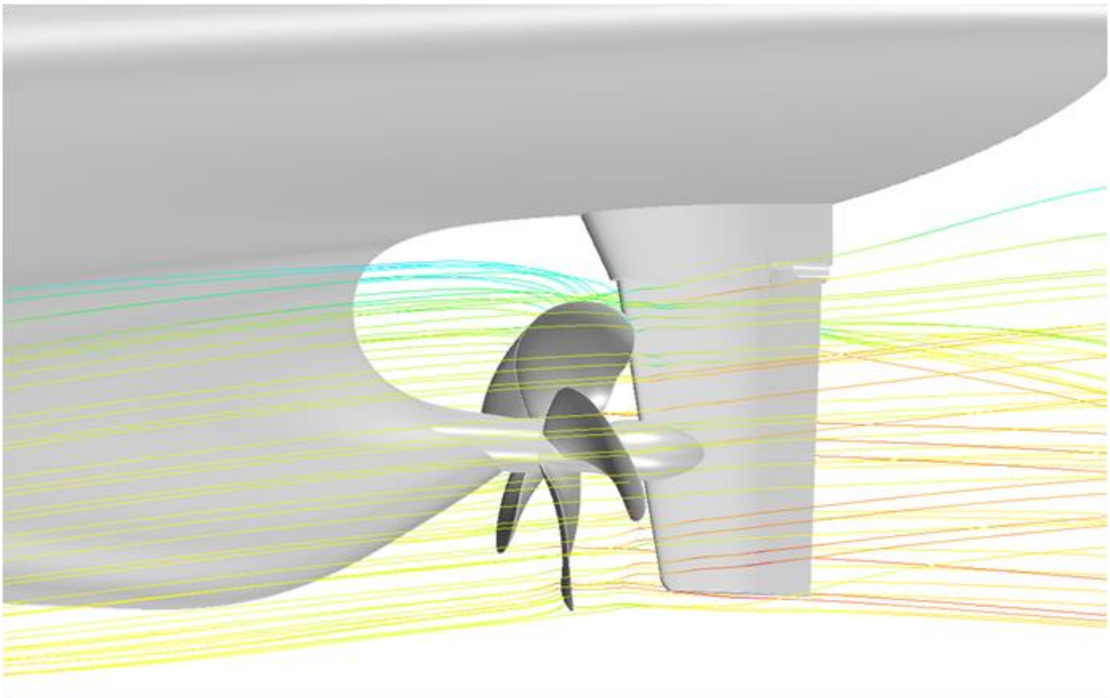

Fig. 10. Numerical flow simulation of hull, propeller and rudder with rudder bulb

CFD calculations of a vessel with and without rudder bulb have been made to investigate the differences in performance (see fig. 10). The major part of the hull resistance will not change and therefore differences in overall efficiency of a few percent are found. Nevertheless the components which are responsible for the performance gains can be isolated. Based on this analysis the coupling between efficiency gains, occurring flow phenomena and actual physical principles can be made.

5. INCORPORATION IN DESIGN PROCESS

In this paper various aspects of both model scale testing and full scale numerical flow simulations have been discussed. Though there are still steps to be made on the development of numerical simulations, the added value can be utilized in the design process of propellers. Fig. 11 shows a process description of a propeller design process. The conventional process, based on model scale experimental data, is described in the top half. In the lower half the possibilities of full scale numerical flow simulations are incorporated. On the input side of the propeller design process a full scale wake field and propeller diameter can be used. Once the design is available, either open water and self-propulsion performance evaluations can be made based on full scale simulations, or on the conventional model scale measurements.

6. CONCLUSIONS

In order to be able to further enhance the performance of ship propellers it is necessary to have a full understanding of the occurring flow phenomena on the actual ship. In the past the majority of research and development in this field was based on model scale experiments. Nowadays it has become possible to get more detailed insights in the flow field when numerical flow simulations are carried out. Proper understanding of the propeller open water efficiency and propeller-hull interaction factors can be achieved with CFD simulations.

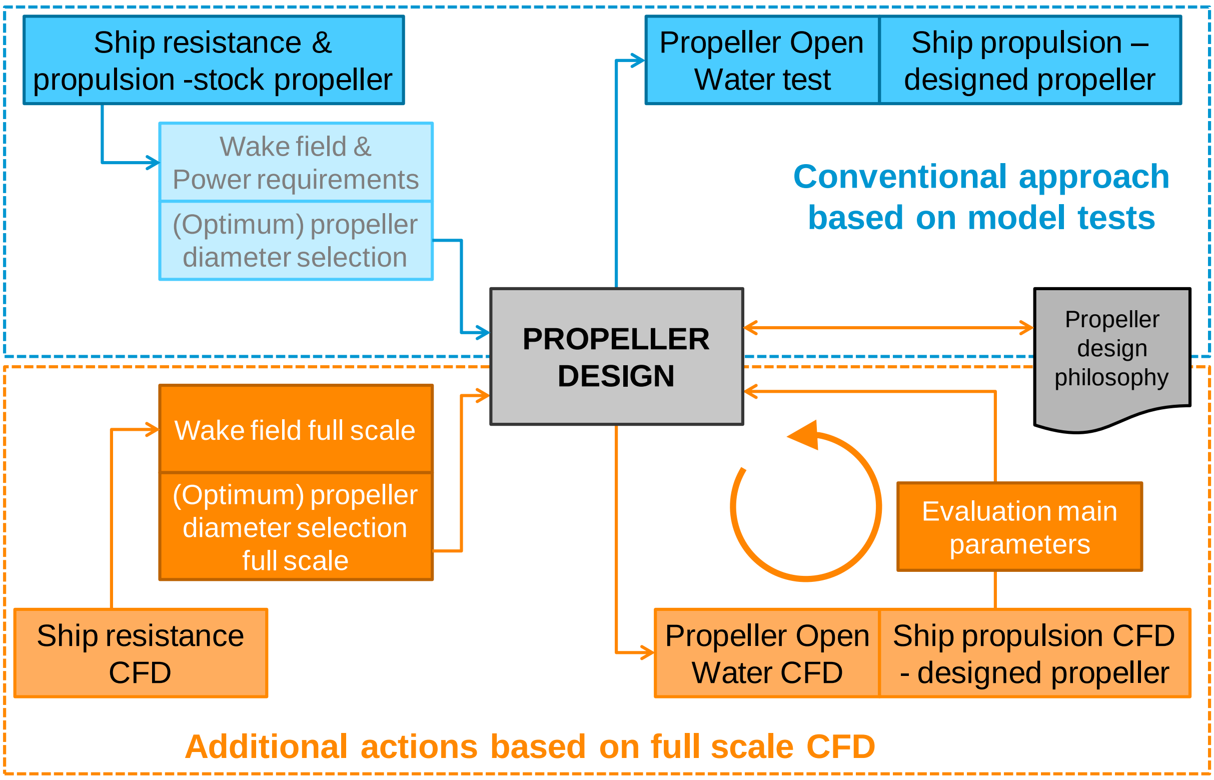

Fig. 11. Flow chart of implementation of full scale flow simulations in design process

Whilst gaining more knowledge and understanding on the flow effects, also some commonly used procedures in model scale testing can be revised. In the end the design features which contribute to efficiency increase, and thus fuel consumption reduction, can be isolated and further improved, based on the results from detailed flow simulations.

ACKNOWLEDGEMENTS
The authors would like to thank the CFD-experts from Wärtsilä Business Line Propulsion for distributing the results from their simulations.

References

Benedek, Z and Balogh B., “The scale effect on nominal wake fraction of single-screw ships”, Periodica Polytechnica, Vol 12, No 1, 1968

ITTC, “1978 ITTC performance prediction method”, Section 7.5-02-03-01.4, 1978

ITTC, proceedings of 26th ITTC, Rio de Janeiro, 2011

Kawamura, T., Ouchi, K., Takeuchi, S., “Model and full scale CFD analysis of propeller boss cap fins (PBCF)”, Proc. of Third International Symposium on Marine Propulsors, pp 486- Launceston, Australia, 2013

Ligtelijn, J.T., Van Wijngaarden, H.C.J., Moulijn, J.C., Verkuyl, J.B., “Correlation of Cavitation: Comparison of Full-Scale Data with Results of Model Tests and Computations”, SNAME Maritime Technology conference, Washington, USA, 2004

Minguito, E., “Assessment of scale effects on propeller performance”, Dissimination workshop EU-project Leading Edge, Copenhagen, Denmark, 2005

Oosterveld, M.W.C. and Van Oosanen, P., “Further Computer-Analysed Data of the Wageningen B-screw Series”, IV International Symposium on Ship Automation, Genova, Italy, 1974

Investigating the feasibility of Green Ships with electric propulsion

E. Sofras and J. Prousalidis
National technical University of Athens, School of Naval Architecture & Marine Engineering
Division of Marine Engineering, 9 Heroon Politechniou Str., 15773 Athens, Greece

Abstract

In this paper a methodology on how to design the energy system of a vessel with diesel electric propulsion, which is considered as an appealing alternative towards green shipping, is outlined. The method takes into account several particular parameters of such ship configurations that are not often considered in other vessels. Further, it is showcased in the case study of a small passenger ferry. Thus, it is shown that the electric propulsion can be an appealing solution, but only in certain operating conditions, such as when the fuel is Natural Gas.

Key words: Diesel Electric propulsion, All Electric Ship, ship electric energy systems.

1. Introduction

Worldwide concern about air quality, greenhouse gas emissions, and oil supplies has led to stricter emissions regulations and fuel economy standards, as well as to exploration of alternative propulsion systems. Amongst certain alternatives, the electric propulsion can be proven under certain circumstances, a means towards greener shipping. Extending the electric propulsion concept, the modern concept of All Electric Ship (AES) includes the incorporation of multiple independent sources of power generation, as well as extensive electrification of main and auxiliary energy consuming systems (propulsion subsystem, oil/water/ballast/cargo pumps, ventilation fans, oil/cargo heaters, distillers, purifiers, navigation subsystems, general ship loads, hotel/lighting loads, etc.). The AES concept exemplifies the rapidly increasing trend in the marine industry to move from mechanical to electrical systems resulting to an clean, safe and efficient vessel.. This is motivated by the additional flexibility that such systems offer. More specifically, propulsion systems comprise electric motors driven by associated power electronic converters, acting as their gear boxes. This combination results in several advantages as increased maneuverability, precise and smooth speed control, reduced machinery space, and low noise and pollutant emission levels. Furthermore, AES results in savings in running and maintenance costs.

It is well accepted that every ship for which the application of diesel electric propulsion is under consideration should be treated as a special and separate case. The lack of technical evidence and data from existing ships, which could be evaluated during the study, especially when dealing with ships where the diesel electric propulsion has rather pure applications (i.e. typical bulk carriers, tankers, small passenger vessels e.t.c.) makes the evaluation of the diesel electric propulsion not easy. For that reason the diesel electric propulsion should be selected after very careful consideration and evaluation of many technical and economic parameters.

In this paper a new methodology on how to design the energy system of a vessel with diesel electric propulsion is presented. Due to the extensive electrification, it is shown that certain studies not often performed at the ship design stage such as analytical weight estimation, power quality analysis, balance of reactive power have to be included As a case study, the method is applied to a special ship type, namely a small passenger ferry. By performing the detailed techno-economical analysis, it is shown that the electric propulsion can be an appealing solution, but only in certain operating conditions, such as when the fuel is Natural Gas.

2. Background

2.1 Typical diesel-electric propulsion plants configurations

The selection of the Diesel-electric propulsion plant mainly depends on the type of vessel from which are originated the specifications related to dynamic positioning, high redundancy, safety and comfort on navigation, high reliability etc. To this end, the main configuration types are categorized according to the type of vessel as follows **[3]**, **[4], [5]**:

2.1.1 LNG carriers

A typical Diesel-electric propulsion configuration of LNG vessels, (Fig. 1), consists of two high speed electrical motors of about 600 or 720 rpm and a reduction gearbox with two input terminals and one output, whereas the rated power of the installed alternator is around 40MW. The main requirement for such a vessel is the high redundancy, and the equipment for that configuration is a VSI (*voltage source inverter*) converter with 24-pulse PWM (*pulse width modulated*), a supply transformer and an electric propulsion motor.

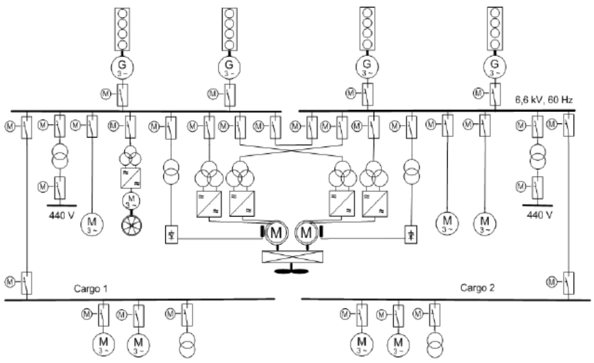

Fig. 1: Diesel-electric configuration of an LNG vessel **[5]**

2.1.2 Offshore support vessels

Platform Supply Vessels (PSV), Anchor Handling/Tug/Supply (AHTS), Offshore Construction Vessel (OCV), Diving Support Vessel (DSV), Multipurpose Vessel etc. are included in the broad category of offshore support vessels. The main requirements of dynamic positioning and station keeping capability impose the exploitation of Diesel-electric propulsion plant along with variable speed motor drives and fixed pitch propellers.

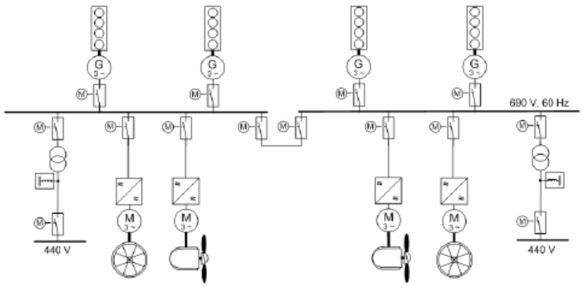

Fig. 2: Diesel-electric configuration of a PSV **[5]**

In modern applications, (Fig. 2), frequency converters with an active front end are used, which give specific benefits in the space consumption of the electric plant, as it is possible to eliminate the heavy and bulky supply transformers. The electric motor is an induction (asynchronous) motor which is stiff, simple design and cost competitive and ensures, in most cases, a long lifetime with a minimum of breakdown and maintenance.

2.1.3 Cruise vessels

High reliability and redundancy are the main requirements of a propulsion system intended for cruise vessels, as well as that onboard comfort is a high priority allowing only low levels of noise and vibration from the ship machinery.

A typical Diesel-electric propulsion configuration for cruise vessels, (Fig. 3), consists of VSI type converter with 24-pulse PWM technology, supply transformers and a synchronous slow speed electric motor of about 150 rpm.

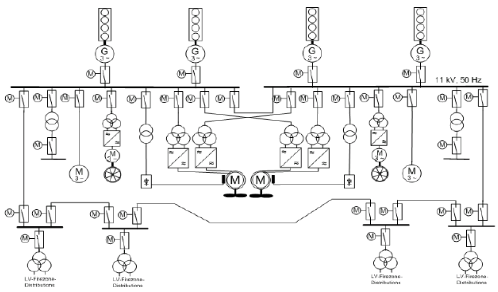

Fig. 3: Diesel-electric configuration of a cruise vessel **[5]**

2.1.4 RoPax vessels

The requirements for a cruise liner are also valid for a RoPax. A representative configuration, (Fig. 4), consists of high speed electric motors (900 or 1200 rpm), geared transmission, frequency converters of VSI type with 12-pulse PWM technology, supply transformers with two secondary windings and an induction motor for propulsion motor.

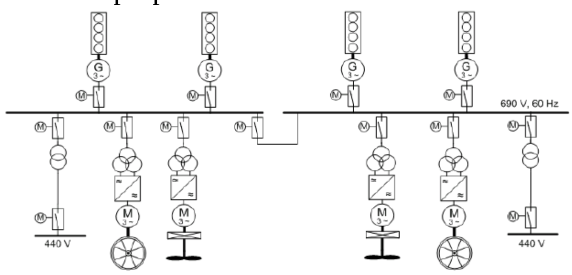

Fig. 4: Diesel-electric configuration of a RoPax vessel **[5]**

2.1.5 RoRo vessels

In this case, (Fig. 5), an electric propulsion motor running on two constant speed levels (medium and high, respectively) along with a controllable pitch propeller (CPP) provides a high reliable and compact solution with low electrical plant losses. The main equipment for this plant is a power electronic converter and an induction motor with no supply transformer.

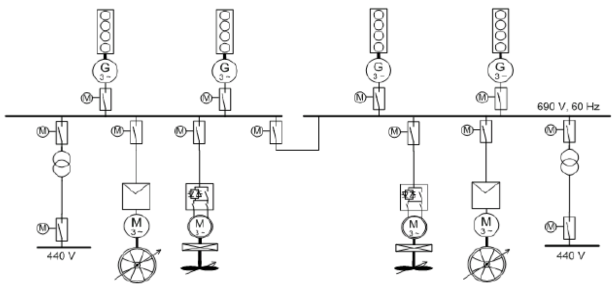

Fig. 5: Diesel-electric configuration of a RoRo vessel **[5]**

3. **Case study**

The developed methodolgy on how to design the energy system of a vessel with diesel electric propulsion **[1], [2]** has been applied to a small passenger ferry with carrying capacity 150 pax. Via this method the feasibility of the Diesel-electric propulsion from both technical and economical point of view is investigated. As well as a comparative analysis between the conventional and the diesel electric propulsion applied to the same vessel has been elaborated.

For the given vessel the following two propulsion systems configurations have been evaluated in order to detect which type of propulsion is more suitable for the vessel.

For the comparison and evaluation of the two types of propulsion the following critical parameters have been examined:

1) Weight of basic electromechanical equipment
2) Electric power factor (cosφ) of the network

3) Loading of generators for every operational profile
4) Energy Efficiency Design Index
5) Operational expenditure
6) Capital expenditure

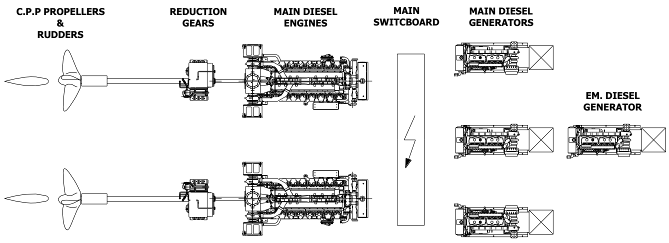

Fig. 6: Conventional Propulsion configuration

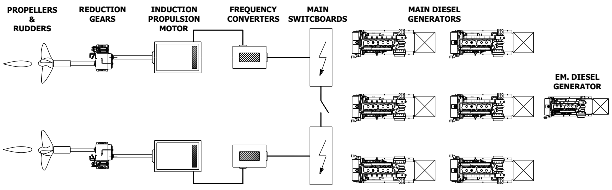

Fig. 7: Diesel-electric Propulsion configuration

3.1 Main Technical Characteristics

The main particulars of the under study vessel **[1]** are shown in the table 1 here below.

Table 1: Main Particulars of the under study vessel

Length over all:	55,00 m
Length between	47,88 m
Breadth mld:	9,00 m
Depth mld:	3,50 m
Design draught mld:	2,80 m

The residual resistance **[6]** has been derived from the average of the resistance given from De Groot **[7]** and NPL **[8]** systematic series and the frictional resistance has been derived using the ITTC line of 1957 **[9]**. The results of the Total resistance as well as the EHP function to the speed of the vessel are given in table 2.

Table 2: Summarizing table of R_T and EHP

V (knots)	R_T (kp)	$1,15xR_T$ (kp)	EHP (PS)	EHP (HP)	EHP (Kw)
13	5404,07	6214,68	554,12	561,82	407,56
15	8009,96	9211,45	947,67	960,85	697,02
18	16859,02	19387,87	2393,55	2426,82	1760,48
20	23677,34	27228,94	3735,08	3787,00	2747,19
22	31082,74	35745,15	5393,61	5468,58	3967,05

The SHP and BHP for the range of velocities as calculated in the conventional propulsion are summarized in Table 3.

Table 3: Summarizing table of SHP and BHP

V (knots)	EHP (kW)	SHP (kW)	BHP (kW)
13	407,56	582,23	727,79
15	697,02	995,74	1244,68
18	1760,48	2514,97	3143,71
20	2747,19	3924,56	4905,70
22	3967,05	5667,21	7084,02

3.2 Energy demand for diesel electric propulsion

A typical diesel electric propulsion system power flow **[3]** is illustrated in Fig 8, where a prime mover rotates the electric generator's shaft and the electricity produced, distributed through the main switchboard, the transformer and the frequency converter to the electric propulsion motor. The shaft of the electric motor is connected directly or sometimes through gearbox (depending on the electric motor rounds) to the propeller shaft of the vessel and the required thrust for sailing is achieved from the propellers.

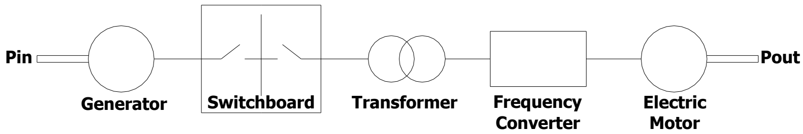

Fig. 8: Power flow in a simplified diesel electric system **[3]**

The power lost in the components between the prime movers shaft and the electric motor shaft is both mechanical and electrical losses giving heat and temperature increase in equipment and ambient. The overall electrical efficiency of the system could be derived from the following formula:

$$\eta = \frac{P_{out}}{P_{in}} \quad \textbf{(Eq. 1)}$$

where P_{in} can be expressed as a function of P_{out} and P_{losses} according to the formula

$$P_{in} = P_{out} + P_{losses} \quad \textbf{(Eq. 2)}$$

For each of the components the electrical efficiency can be calculated and typical values at full rated power are given here below:

Generator: η=0,95 – 0,97
Switchboard: η = 0,999
Transformer: η = 0,99 – 0,995
Frequency converter: η = 0,98 – 0,99
Electric motor: η = 0,95 – 0,97

Hence the overall efficiency of a diesel electric system from diesel engine shaft to electric propulsion motor shaft is normally 0,875 – 0,926 at full load and depends on the loading of the system.

The required shaft power (P_{out}) for the under study vessel taken from table 3 at the speed 20 knots is 3924,56 kW, therefore using the overall efficiency for the diesel electric system the intake power (P_{in}) will be

$$P_{in} = \frac{P_{out}}{\eta} = \frac{3924,56}{0,926} \sim 4240\text{kW}$$

This intake power has been used at the electrical balance analysis in order to determine the total energy demand including the electrical power used for propulsion.

3.3 Electrical load analysis

The summarizing tables of the electric load analysis as well as the selected diesel generators with the loading in every operational condition are presented in tables 4 and 5 here below.

Table 4: Electrical balance analysis for the vessel with the conventional propulsion

CONDITION	SEA GOING	REST IN PORT	MANEUVERING
TOTAL REQUIRED POWER (kW)	217	59	237
DIESEL GENERATORS (2 x 238 ekW + 1 x 76 ekW)	1 x 238	1 x 76	1 x 238 + 1 x 76
GENERATOR TOTAL CAPACITY (kW)	238	76	314
AVAILABLE LOAD PERCENTUAL (%)	91,1	77,7	75,6

Table 5: Electrical balance analysis for the vessel with the diesel electric propulsion

CONDITION	SEA GOING	REST IN PORT	MANEUVERING
TOTAL REQUIRED POWER (kW)	4221	81	1597
DIESEL GENERATORS AVAILABLE (5x1014kW + 1x99kW)	5 x 1014	1 x 99	2 x 1014
GENERATOR'S TOTAL CAPACITY (kW)	5070	99	2028
AVAILABLE LOAD PERCENTUAL (%)	83,3	81,8	78,7

4. Comparative analysis

4.1 Weight of basic electromechanical equipment

The weight of the basic electromechanical equipment has been calculated taking into consideration the following factors:

1) Main propulsion engines
2) Reduction gears
3) Low Voltage Diesel generators
4) Medium Voltage Diesel Generators
5) Emergency Diesel Generator
6) Propulsion Motors
7) Frequency converters
8) Cabling

The results are presented in Figure 9 where we can notice that the weight of the basic electromechanical equipment in case of diesel electric propulsion is significant higher than the corresponding of conventional propulsion.

Furthermore if we isolate the cabling weight we can see that (see fig. 10) in diesel electric propulsion it is twice compared to the conventional propulsion and this is because of the presence of medium voltage cables in the diesel electric propulsion.

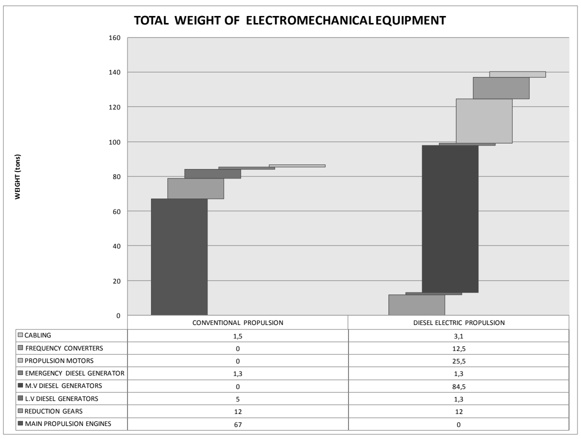

Fig. 9: Total basic electromechanical equipment weight for the two types of propulsion

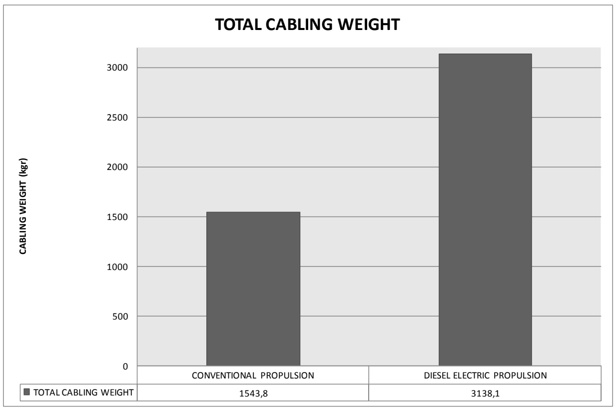

Fig. 10: Total cabling weight for the two types of propulsion

4.2 Energy Efficiency Design Index (E.E.D.I)

The Energy Efficiency Design Index has been calculated for the conventional propulsion using the guidelines of IMO in MEPC.1/Circ.681 **[12]**. The fuels that have been utilized are both liquid fuels (H.F.O, L.F.O, M.D.O, and M.G.O) and gas fuels (L.N.G)

Furthermore the calculation of the Energy Efficiency Design Index for the diesel electric vessel has been elaborated using both the latest IMO guidelines (MEP 65/22) adopted on 17 May 2013 and a methodology which has been proposed by the "Centre for Maritime Technology and Innovation" on Nr.3075 **[14]** report.

It is worth noting here that in the IMO guidelines for the calculation of EEDI the carbon emission factor is constant for all engines, including engines for diesel electric and hybrid propulsion cruise passenger ships. For that reason only one index has been calculated corresponding to all type of fuels which can be utilized to the engines. In order to make a comparison graph between the EEDI of the conventional propulsion and the EEDI of the diesel electric propulsion the average of the values of the liquid fuels in the conventional propulsion has been calculated. The results are presented in figures 11, 12 and 13.

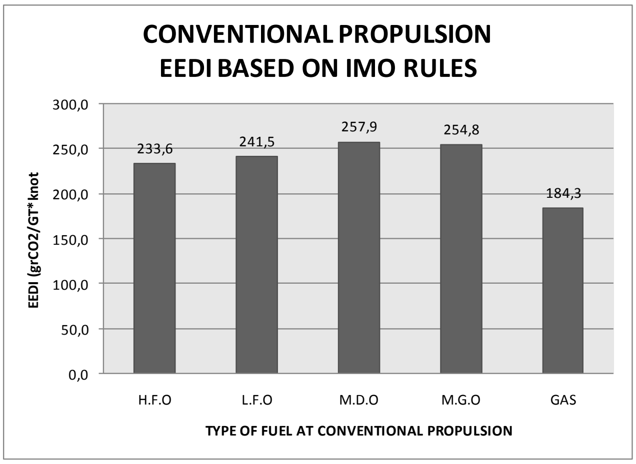

Fig. 11: Conventional propulsion E.E.D.I for various types of fuels based on IMO rules

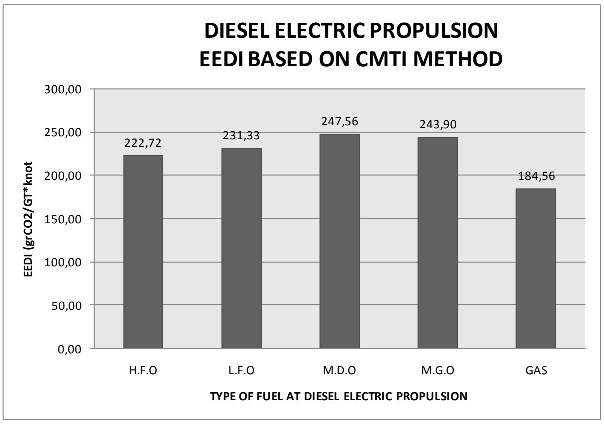

Fig. 12: Diesel electric propulsion E.E.D.I for various types of fuels based on CMTI method.

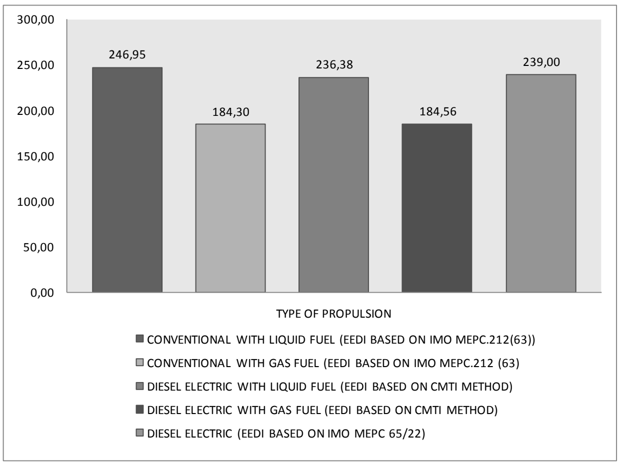

Fig. 13: Comparison diagram of EEDI for both types of propulsions and different fuels

From the above graphs the following comments can be made:
1) The best solution concerning the E.E.D.I. is to use gas as fuel for both types of propulsion. The value of E.E.D.I. is significantly smaller than that with the next highest price corresponding to HFO.
2) The E.E.D.I. of the Diesel-electric propulsion when using liquid fuels is slightly better (about 10 grCO_2/GT*Knot less) than that of the conventional propulsion, except when using LNG as fuel, where the two indexes are exactly the same.
3) The E.E.D.I for both types of propulsion for the under study vessel are significantly higher compared with E.E.D.I. of other types of vessels. The only type of vessel with similar E.E.D.I. is that of yachts. The main reasons for this high differentiation are mentioned here below:
3.1) the under study vessel (like yachts) has very low capacity, a parameter which is at the denominator of the E.E.D.I calculation formula and, hence, increase dramatically the index.
3.2) the under study vessel has very high installed power - in relation to her size - for the propulsion in order to achieve high speed. The installed power of main and auxiliary engines is presented at the numerator of the E.E.D.I. formula and increases the index.
4) As a final result, it can be argued that the under study vessel with either type of propulsion is a rather polluting ship due to her high service speed and low transport work.

4.3 Techno-economic analysis

In order to evaluate which one of the two propulsion systems are more profitable **[15], [16]** for the under study vessel, a techno-economic analysis has been performed. The NPV, IRR, DPB, and PWC have been calculated for both types of propulsion using as variable parameter the type of the fuel and the cost of:
In addition, the CAPEX (CAPital EXpenditure) and OPEX (OPerational EXpenditure) indices have been calculated for both types of propulsion, (see Fig 14 and 15).

The criterion of economic performance in the techno-economic analysis, is the difference in Net Present Value (NPV) of the investment between that of the conventional propelled vessel ($NPV_{conventional}$) and that of the Diesel-electric propelled vessel ($NPV_{\text{Diesel-electric}}$) **[15]**.

Where $\Delta(NPV)>0$, then the conventional propulsion is considered to be more profitable than the Diesel-electric propulsion (see fig.16).

4.3.1 Techno-economic scenario

For the under study vessel the following Techno economic scenario has been considered **[1]**, **[2]**.

➢ The total investment cost is assumed to be the cost for the delivery of the vessel. This cost is divided in two categories.

- The first category is the cost for the construction and acquisition of the hull and any other relative equipment and is assumed equal to ***2.500.000 €*** (This price has been derived from a vessel with similar dimensions and type). This cost will be covered with own funds and it is assumed to be constant for both types of propulsion (conventional and Diesel electric).
- The second category is the cost of the acquisition and construction of the electromechanical and propulsion systems. This cost has been analyzed thoroughly for both types of propulsion operating either in Diesel or in gas mode. This cost will be covered exclusively by a loan of ***20 years*** duration.

➢ The initial annual incomes are derived from the passengers carried on board, assuming ***300 days trading per year***, ***6 trips per day*** and ***75% average booking capacity***. The net ticket price per passenger after deducting any taxation has been assumed to be ***15 €***.

➢ The annual costs assumed to be the cost of the fuel and lubricating oil plus the cost of the machinery maintenance plus the crew pay roll.

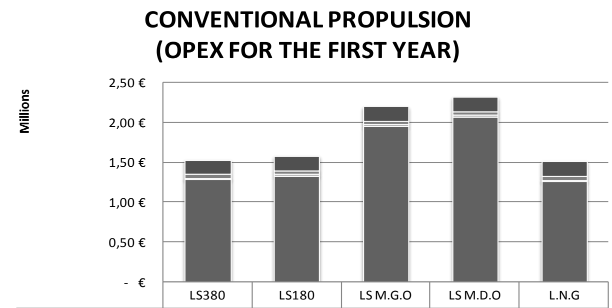

	LS380	LS180	LS M.G.O	LS M.D.O	L.N.G
CREW PAY ROLL	180.000	180.000	180.000	180.000	180.000
LUB OIL COST	46.662	46.662	46.662	46.662	46.662
MAINTENANCE COST	19.246	19.246	19.246	20.589	20.589
FUEL OIL COST	1.289.696	1.334.070	1.960.908	2.076.313	1.264.819

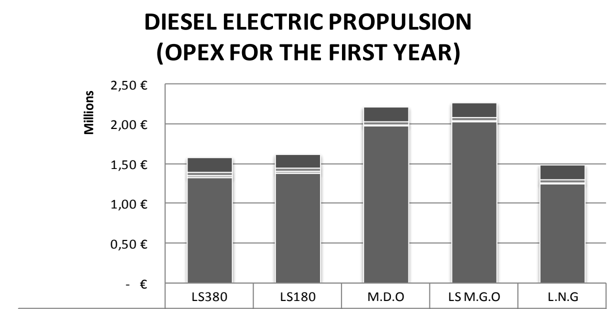

	LS380	LS180	M.D.O	LS M.G.O	L.N.G
CREW PAYROLL	180000	180000	180000	180000	180000
MAINTENANCE COST	43242,6	43242,6	43242,6	43242,6	43242,6
LUB OIL COST	18967,08	18967,08	18996,912	18967,08	18996,912
FUEL OIL COST	1337179,14	1386608,5	1975694,365	2028902,8	1247416,098

Fig. 14: OPEX for the conventional and Diesel electric propulsion

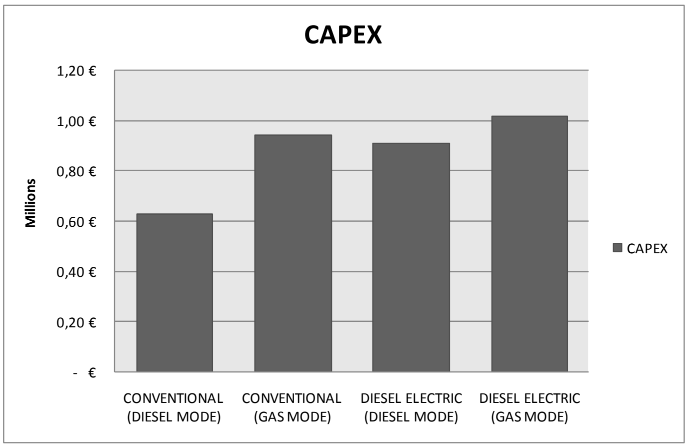

Fig. 15: CAPEX comparison diagram

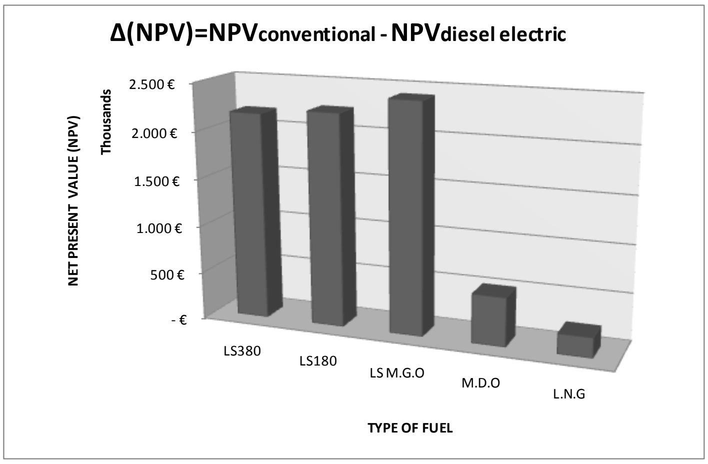

Fig. 16: Δ(NPV) comparison diagram

5. **Summary of results – Discussion**

The results of both types of propulsion are tabulated in Table 6 so that critical factors such as weight, emissions, cost etc can be easily compared.

Thus, the electric propulsion for the small passenger vessel considered, seems to be less technically and economically competitive than the conventional propulsion for the following reasons:

- The cabling weight at the Diesel-electric propulsion is about twice the cabling weight at the conventional propulsion. Furthermore, it is noted that in the Diesel-electric propulsion case, there are five (5) Diesel Generators operating at medium voltage, while in the conventional propulsion case there are two (2) Diesel Generator of low voltage. This implies and proved here that the Diesel-electric propulsion require heavier electromechanical equipment. This fact is against to the payload of the vessel as well as to the effort, especially at high speed vessels to reduce the lightship.
- The power factor of the electric grid for both types of propulsion is at good level (around 0.8 inductive), and taking into consideration the total electric load at all operating conditions, it can be argued that the generators are to operate in a rather efficient manner.
- Regarding the E.E.D.I, taking into consideration the value of the base line which has been calculated for the conventional propulsion ($E.E.D.I_{base\ line}$ = 113,52 $grCO_2/GT \cdot Knot$) and for the diesel electric propulsion ($E.E.D.I_{base\ line}$ = 45 $grCO_2/GT \cdot Knot$) it can be concluded that the under study vessel using either conventional propulsion or Diesel-electric propulsion is a rather polluting vessel due to high service speed and low transport work. The best solution concerning the E.E.D.I is to use gas as fuel for both types of propulsion. The value of E.E.D.I is significantly smaller than the option of HFO as fuel (which is the next highest price). In addition, in this gas fuel case, the E.E.D.I at the Diesel-

electric propulsion (as calculated with the CMTI method) is in the same level from the corresponding conventional propulsion.

➢ The lowest capital expenditure is in the case of conventional propulsion using liquid fuel. The capital expenditure for both types of propulsion using gas fuel is higher from the corresponding using liquid fuel due to higher acquisition cost of the required LNG equipment.

The lowest operational expenditure is when gas is used at the engines due to the low cost of the LNG. The next lowest OPEX value corresponds to the use of HFO. As a result, the conventional propulsion is more profitable for the investor, especially, when burning HFO at the engines.

Table 6: Summarizing table

		CONVENTIONAL PROPULSION	**DIESEL-ELECTRIC PROPULSION**
CABLING WEIGHT		1543,8 kgr	3138,1 kgr
EL/MECH. EQUIP. WEIGHT		86,8 tons	140,2 tons
ELECTRIC POWER FACTOR	SEA GOING	0,819	0,801
	IN PORT	0,847	0,824
	MANEUVERING	0,831	0,803
LOADING OF GENERATORS	SEA GOING	91%	83%
	IN PORT	78%	82%
	MANEUVERING	76%	79%
E.E.D.I	H.F.O	233,6	222,72
	L.F.O	241,5	231,33
	M.G.O	254,8	243,9
	M.D.O	257,9	247,56
	L.N.G	184,26	184,56
CAPEX	DIESEL MODE	632.660 €	912.086 €
	GAS MODE	943.931 €	1.020.059 €
OPEX (for the first year)	L.S 380	1.535.604 €	1.579.389 €
	L.S 180	1.579.978 €	1.628.818 €
	L.S M.G.O	2.206.816 €	2.271.112 €
	L.S M.D.O	2.323.564 €	2.217.934 €
	L.N.G	1.512.071 €	1.489.656 €

6. Conclusions

In this paper a new methodology on how to design the energy system of a vessel with diesel electric propulsion is outlined. The method takes into consideration certain particular and critical characteristics of ships with extensive electrification while ii is showcased in the case study of a small passenger ferry.

Via a detailed techno-economical analysis and evaluation of special parameters, it is shown that the electric propulsion can be an appealing solution, but only in certain operating conditions, such as when the fuel is Natural Gas.

ACKNOWLEDGMENT

The work presented in this paper has been financially supported within the framework of the "DC-Ship" project (ARISTEIA-EXCELLENCE-I contract No 987/2012 of the General Secretariat Research and Technology of the Hellenic Government) co-financed by the European Union (European Social Fund – ESF) and Greek National funds through the Operational Program "Education and Lifelong Learning" of the National Strategic Reference Framework (NSRF) - Research Funding Program "ARISTEIA" (EXCELLENCE).

7. References

[1] E. Sofras, PhD Dissertation "Contribution to the development of a design methodology of a power system of a ship with electric propulsion, with emphasis on the investigation of related power supply quality problems", N.T.U.A School of Naval Architecture & Marine Engineering Athens 2014.

[2] E. Sofras, J. Prousalidis, "Developing a New Methodology for Evaluating Diesel - Electric Propulsion" paper to be published in the autumn issue of the Journal of Marine Engineering Technology (JMET), IMarEST.

[3] A. Adnanes, "Maritime electrical installations and Diesel-electric propulsion," ABB AS, Oslo, Apr. 2003.

[4] A. Harsema - Mensonides, "Dual Fuel Electric Propulsion Systems in LNG shipping." MPT Consultancy.

[5] "Diesel-electric propulsion plants - A brief guideline how to design a Diesel-electric propulsion plant." MAN.

[6] P. Van Oossanen, *Resistance prediction of small high - speed displacement vessels - State of the art*, vol. 27. International Shipbuilding Progress, 1980.

[7] D. d. Groot, *Weerstand en voorstuwing van motorboten Schip en Werf, 1951*, vol. 2,No6. Published in English in International Shipbuilding Progress, 1955.

[8] D. Bailey, *The NPL high speed round-bilge displacement hull series*, vol. No4. Royal Institution of Naval Architects, Maritime Technology Monograph, 1976.

[9] 1957 International Towing Tank Conference

[10] M. Islam, *Handbook to IEEE standard 45: A guide to electrical installations on shipboard*. Standard Information Network IEEE press, 2004.

[11] MARPOL 73/78 ANNEX VI, *Prevention of Air Pollution from ships entered into force on 19 May 2005*.

[12] IMO.2009, "Interim Guidelines on the Method of Calculation of the Energy Efficiency Design Index for New Ships. MEPC.1/Circ.681."

[13] IMO.2013, "Interim 2013 Guidelines for calculation of reference lines for use with the energy efficiency design index (EEDI) for cruise passenger ships having non-conventional propulsion" MEPC 65/22 Annex17 adopted on 17 May 2013

[14] D. Anink and M. Krikke, "Energy efficiency of small ships and non conventional propelled ships," Centre for Maritime Technology and Innovation, 3075, Jan. 2010.

[15] S. Gertsos, J. Prousalidis, and C. Frangopoulos, "Electric Propulsion: from Infancy to Adolescence," presented at the 8th International Marine Design Conference,, Athens (Greece), 2003, vol. II, pp. 529–540.

[16] C. Frangopoulos, Analysis and Optimization of Energy Systems *(in Greek)*. NTUA publications, 2003.

FLAPPING WING SYSTEMS FOR AUGMENTING SHIP PROPULSION IN WAVES BY EMPLOYING SYSTEMATIC DATA, ACTIVE CONTROL AND EXPLOITING HYDROELASTIC EFFECTS

V.Tsarsitalidis[1],G.K. Politis[2], K.A.Belibassakis[3]
[1] Naval Architect and Marine Engineer, Ph.D. candidate, NTUA Athens, Greece, vtsars@central.ntua.gr
[2] Professor, NTUA, Athens Greece, polit@central.ntua.gr
[3] Associate professor, NTUA, Athens Greece, kbel@fluid.mech.ntua.gr

ABSTRACT

The urge for increased efficiency and also for added safety, lead to serious consideration of unconventional systems. Biomimetic systems (i.e. flapping -pitching and heaving- foils), have been long studied and acknowledged as highly efficient, but disregarded as difficult to design and operate, as the number of parameters for the motion of such system is larger, compared to conventional. After the development of a systematic series (Politis & Tsarsitalidis 2014), it is possible to design prescribed motion propulsors, but also to produce an active control system (by analysing the data for system identification), for the pitching motion, so that it is capable of adapting to wave induced motions. In this paper, the concept of a system that is capable of harvesting the energy of wave induced motions and converting it directly to thrust, thus working as an energy saving system and a seakeeping device, is presented and analysed. The system may be an active Propulsor (mechanically induced heaving foil motion), or an energy saving system (heaving from the ship's motions), while the pitching motion is determined either by a simple control method like "pitch control parameter" (Politis and Politis 2012), (Belibassakis and Politis 2013). The potential of all methods is evaluated and designs that will lead to proof of concept experiments are presented, as well as concept designs of the final system.

1. INTRODUCTION

Demand for low costs, regulations on emissions, and unstable markets, make an ever growing demand for lower consumptions, which lead to a serious decrease in powering of vessels. On the other hand, the increased demand on safety and the rougher seas observed lately, dictate an increase of installed power and improvement of seakeeping characteristics. As it was already expressed by Rozhdestvensky (2003), it is evident that the interest in biomimetic devices is justified because such systems:

- can be viewed as ‘‘ecologically’’ pure,
- are relatively low-frequency systems,
- possess sufficiently high efficiency,
- are multi-functional in the sense of being capable of operating in different regimes of motion,
- can combine the function of propulsor, control device and stabilizer,
- can provide static thrust,
- can provide high maneuverability,
- possess more acceptable cavitation characteristics than conventional propellers,
- have relatively low drag in the ‘‘switched-off’’ position,
- allow the use of modern controls, MEMS, piezoelectric, reciprocating chemical muscles (RCM), and other technologies.

From the identified characteristics, it is understandable, that Biomimetic systems have the potential of surpassing the aforementioned stalemate.

The modern history of biomimetics starts in 1935 with Gray's paradox, and theoretical developments start with the works of Sir James Lighthill (1969) and (1973) and T.Y. Wu (1971). A thorough review of those theories can be found in Sparenberg (2002). Extensive reviews of computational and experimental work in biomimetics can be found in the papers of Shyy (2010) regarding aerodynamics and aeroelasticity; of M. Triantafyllou (1991, 2004) regarding experimental developments and of Rozhdestvensky (2003) regarding all types of applications, even full scale, with additional care given to the work done by eastern scientists (i.e. Russians and Japanese). Interesting information is also included in the books by. (Shyy,

Aono et al. 2010) and Taylor et al. (2011). Marine biomimetic propulsors are also discussed in the book of Bose (2010).
The idea of employing the characteristics of an oscillating wing for the production as an energy saving device, is far from new. As also reported in the extended review by Rozhdestvensky & Ryzhov (2003), the Norwegian Fishing Industry Institute of Technology carried out full-scale tests of a passive propulsor, comprising two wings with elastic links, installed at the bow of a 180ton research fishing ship. The tests showed that the efficiency of such a propulsor reached up to 95% and it was demonstrated that it could be combined with a conventional screw propeller. At a speed of 15kn in waves up to 3m height, a significant part (25%) of the thrust was provided by the wing propulsors. Using only the wing propulsor the ship was able to travel at speed up to 8kn. Furthermore, full-scale tests of a 174ton Russian research fishing vessel equipped with a wing device for extracting sea wave energy (see, e.g., (Nikolaev, Savitskiy et al. 1995)), showed that such a device could increase the engine power up to 50-80% and reduce the ship motions by at least a factor of 2. Also, Japanese researchers used a suspended engine to oscillate a flapping wing system, (Isshiki 1994). Two different arrangements of the wing elements of the flapping propulsor have been considered. The first consists of two vertically mounted wings, operating in opposite phase, and the second of a horizontal wing, operating below a stationary plate. This engine-propulsor system was tested and the measured data show that it provides the same efficiency as a screw propeller, for an extended range of operating conditions. The above full-scale experiments confirm that the flapping wing, in some modes of operation, could be found to be equally effective as the typical marine propeller. However, operating at lower frequency it has the advantages to excite less noise and vibration. Apparently, there is already strong evidence about the good performance and capabilities of the proposed system, permitting the development of tools for technological design and innovation..

The scope of the present work is: (a) to show the potential of biomimetic (flapping wing) systems both as a propulsor and as an energy saving system (b) to propose a concept design for the application of such systems on ships. To this end, data from the systematic series which have been produced, using the code UBEM (Unsteady Boundary Element Modeling), and have been presented in (Politis and Tsarsitalidis 2014), were extracted to provide useful insight in the behavior of such systems. The code UBEM has also been coupled with a 1DOF hydroelastic model for the pitching motion, but also with an active pitch control algorithm, in order to evaluate their effectiveness both in simple and more complex motions. In (Politis and Tsarsitalidis 2014) systematic were presented in the form of charts, along with a design method, that employs the produced charts. This method was used to calculate the powering performance of three different ships equipped with wing propulsors (virtual paradigms). Powering performance calculations were also made for the same ships equipped with conventional propellers and the comparison showed flapping wing propulsors can produce high efficiencies superior to those obtained from conventional propellers. Another important remark, was that the power required for pitching motions, was significantly (orders of magnitude) smaller than the total power. The question remained about the performance of such systems in a wavy environment, where it could also be used as an energy saving system, by means of passive or active pitch control. Working in this direction, the authors proceeded some further steps. The prescribed pitching setup was substituted by an active pitching control, using a proper control mechanism and a pitch setup algorithm, on the basis of the (known) random motion history of the wing, (Politis and Politis 2012). Additionally, theoretical/numerical tools were developed, capable of analyzing in detail and support the design of ships equipped with such biomimetic wing propulsors, (Belibassakis and Politis 2013), (Filippas and Belibassakis 2014).

More specifically, ongoing research work by the authors is focused on the hydrodynamic analysis of flapping wings located beneath the ship's hull, operating in random motion; see Fig.1. The wing(s) undergo a combined transverse and rotational oscillatory motion, while the ship is steadily advances in the presence of waves. The present system is investigated as an unsteady thrust production mechanism, augmenting the overall propulsion system of the ship. In the first arrangement (Fig1a), the horizontal wing undergoes a combined vertical and angular (pitching) oscillatory motion, while travelling at constant forward speed. The vertical motion is induced by the random motion of the ship in waves, essentially due to ship heave and pitch, at the station where the flapping wing is located. Wing pitching motion is controlled as a proper function of wing vertical motion and it is imposed by an external mechanism. A second arrangement of a vertical oscillating wing-keel located beneath the ship's hull is also considered (Fig1b). The transverse motion is induced by ship rolling and swaying motion in waves, respectively. The angular motion of the wing about its pivot axis, is again properly controlled on the basis of the ship rolling motion in order to produce thrust, with simultaneous generation of significant antirolling moment for ship stabilization. The proposed method is based on coupling the seakeeping operators associated with the longitudinal and transverse ship motions with the hydrodynamic forces and moments produced by the flapping lifting surfaces, using unsteady lifting line theory and non-linear 3D panel methods (Politis 2011). In this paper, the main focus is on the characteristics and behaviour of the horizontal wing, decoupled from the total problem (i.e. when ship motions are given)

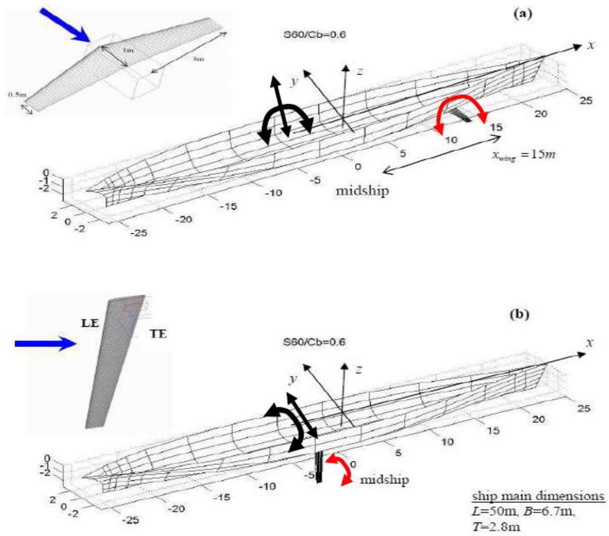

Fig. 1 Initial concept of wave propulsors. (a) Ship hull equipped with a flapping wing located below the keel, at a forward station. (b) Same hull with a vertical flapping wing located below the keel, at the midship section. Geometrical details of the flapping wings are included in the upper subplots. The main flow direction relative to the flapping wings is indicated by using an arrow. Black arrows indicate ship-hull oscillatory motion and red ones the actively controlled (pitching) motion of the wing about its pivot axis, for which only a quite small amount of energy is provided. First numerical results presented in Belibassakis & Politis (2013) Filippas & Belibassakis (2014) indicate that high levels of efficiency are obtained in sea conditions of moderate and higher severity, under optimal control settings.

2. Wing geometry, motion and panel generation.

For the case of a flapping wing configuration, the independent variables which define the state of the system can be decomposed in two groups. Group A contains the geometric variables and group B contains the motion related variables.

Group A: Wing geometries, which are thoroughly described in (Politis and Tsarsitalidis 2014) and the outline and meshing is presented in **Fig. 2**. The main parameters are span length s, chord length c and the wing section profiles, which are NACA0012 throughout the span for all cases.

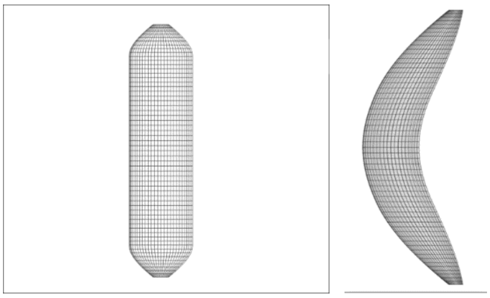

Fig. 2 Geometry of a straight and a 30° swept wing of s/c=4.0

Group B: Wing motion is defined by: (a) the amplitude h_0 of a sinusoidal heaving motion normal to the velocity of advance U, (b) the frequency f for heaving motions.

Thus the state of the system is completely defined by the variables: (U, f, h_0). Contrary to previous works, the pitching motion is not prescribed (i.e. given by a harmonic function), but determined either by the dynamics of a spring loaded axis, or by an active pitch control law.

With the previous parameters known, along with the calculated pitch angle $\theta(\mathrm{t})$, define the instantaneous angle of attack $a(t)$ of each wing with respect to the undisturbed flow through the equation:

$$a(t) = \theta(t) - \tan^{-1}\left(\frac{h_0 2\pi f \cdot \cos(2\pi f \cdot t)}{U}\right) \tag{1}$$

or in non-dimensional form:

$$a(t) = \theta(t) - \tan^{-1}(\pi \cdot Str \cdot \cos(2\pi f \cdot t)) \tag{2}$$

where Str denotes the Strouhal number defined by:

$$St = \frac{f \cdot h}{U}, h = 2h_0 \tag{3}$$

and h denotes the heave height.

Additionally, as in previous works the Thrust coefficient is

$$C_T = \frac{T}{0.5\rho U^2 S} \tag{4}$$

where T the calculated mean thrust and S the swept area covered by the wing in motion, given by $s \cdot 2h$.

3. Initial assumptions

In order to proceed with the simulations, initial assumptions/decisions have to be made regarding the properties of the wing (shape, mass, moment of inertia) and the spring-damper system, along with the position of the pitching axis. For the properties of the wing, an initial simple geometry is chosen and conventional materials were assumed. For the spring and damper, choices have been made through knowledge of the dynamics of a harmonic oscillator and the position of the pitching axis was selected by employing knowledge gained from prescribed motions simulations as explained below.

4. Wing properties

For the wing, an initial geometry is selected to be that of a straight foil of s/c=4.0 and a mass distribution resembling that of solid wood or an aluminium shell of the same shape was assumed. Then, the mass, centre of mass and moment of inertia can be calculated by employing a CAD software, numerical integrations or empirical rules (found in textbooks) for simple geometries. **Fig. 2**, shows the selected wing. For such a wing of c=1.0m (s=4.0m) the calculated useful data are:

- Surface area= $7.5818m^2$
- Volume = $0.2823m^3$
- Center of volume at 0.4188m from le
- Volume moment of inertia about centroid Iz=$0.0151326m^5$

(it is reminded that mass moment of inertia is taken by multiplying the volume moment of inertia with density, when density is constant and should not be confused with the second moments used for analysis of sections)

5. Spring – Damper system

As it is known from the dynamics of harmonic oscillators,

$$\zeta = \frac{c}{2\sqrt{Ik}} \qquad (5)$$

is called the 'damping ratio'.

The value of the damping ratio ζ critically determines the behaviour of the system. A damped harmonic oscillator can be *Overdamped* (ζ>1, *Critically damped* (ζ=1) or *Underdamped* (ζ<1). It is desirable that the system is not allowed to resonate with the excitation, but also that it does not delay to respond. Thus, *ζ=1* was chosen as a parameter for the initial explorations. From a known ζ, the corresponding damping factor c can be calculated for each setting of k, which will be chosen to vary for the systematic simulations.

6. Selection of Pitching Axis Position

For the selection of the pitching axis position, the decision was made that it should be at a position in front (closer to the leading edge) of the center of pressure of the wing throughout the duration of motion, in order to have a stable case. Thus, this decision depends on the determination of the hydrodynamic center of the wing.

The hydrodynamic center of the wing, is the axis around which the total moment is zero. At any other point, the moment will be $M_z = F_y \cdot d$, where d is the distance between the center and the different point. Solving for d , gives $d = M_z / F_y$. Then, by analysing the results from existing (prescribed motion) simulations and applying $d(\mathrm{t}) = M_z(\mathrm{t}) / F_y(t)$ for each selected simulation, the position of the hydrodynamic center is estimated at each instant. In **Fig. 3** and **Fig.** , results of these calculations are shown for whole packages of prescribed motion simulations, as taken from previous works (one linetype for each simulation) for the pitching axis positioned at 0.3c and 0.2c from the leading edge. The peaks of the lines should be disregarded, as they are result of the very small F_y at the upper and lower points of the oscillation. From the main part of the curves, it can be concluded that the hydrodynamic center resides slightly ahead of 0.3c from le for most of the time for all cases, while the position of the pitching axis has a secondary effect on its position. After this analysis, the starting point for simulations of spring loaded wings is to have the pitching axis at 0.25c from le, or closer to the leading edge, while for controlled, it will be at 0.25c from leading edge, for minimization of moments. It should be noted that a position much closer to the le, could mean large moments, which could lead to strong responses and instabilities, difficult to solve, if all parameters are not set correctly.

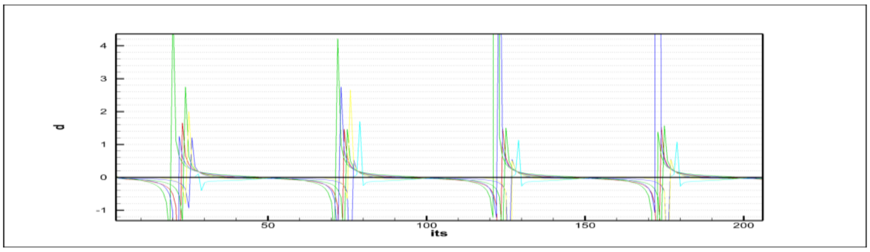

Fig. 3 Histories of position of the hydrodynamic center, relative to the pitching axis, for pitch axis at 0.3c from le. (negative is for forward)

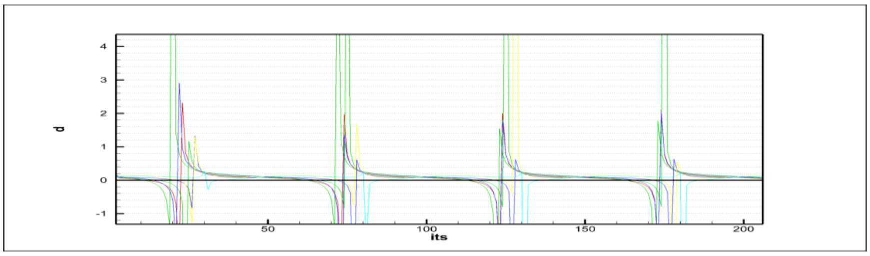

Fig. 4 Histories of position of the hydrodynamic center, relative to the pitching axis, for pitch axis at 0.2c from le. (negative is for forward)

7. Spring loaded wing simulations

The problem of a spring loaded wing in unsteady heaving motion, is in essence a one degree of freedom hydroelasticity problem and can be handled in the same manner, as aeroelastic problems are. A wealth of literature can be found in the aerospace engineering sector, most of which are also based on structural dynamics. Most notable sources are, (Hodges and Pierce 2002) , Wright and Cooper (Wright and Cooper 2007) and Geradin and Rixen (Geradin and Rixen 1994). However, aerospace applications have the primary objective of minimizing instabilities and resonances, rather than operating at their limit. Thus, there are little or no experimental data on the specific case. This means that the models produced can be verified in parts and/ or for simpler cases, as it will be discussed in the sequel. The underlying dynamics have also been a point of interest for structural mechanics and analysts (Chopra 2007) from which most models have been originally investigated.

In order to find the pitching angle at each moment, the following differential equation has to be solved for $\theta(t)$

$$M_{ext}(t) = I_a\ddot{\theta}(t) + C\dot{\theta}(t) + K\theta(t) \qquad (6)$$

Where M_{ext} is the external moment (in the specific case, the hydrodynamic moment).

The solution of the coupled problem is done in an explicit scheme, where the hydrodynamic forces calculated in each step are used as $M_{ext}(t)$ in order to find the deflections for the next. As long as the timestep is small enough and deflections are also small, this scheme is expected to be robust and accurate, as long as time integrations (solution of (6) for constant $M_{ext}(t)$ and given timestep) are made correctly. For the time integration of (6) a Newmark -β scheme is applied.

Fig. presents the calculated response histories for a straight wing for varying K and the same Strouhal number. It is reminded that C is calculated by enforcing ζ=1. The dashed line is the history of heaving motion. As expected, the increase of stiffness produces decreased responses.

A small difference of the phase of the responses is also observed. Systematic simulations for Str ranging from 0.2 to 0.7 and K from 1 to 20 Nm/rad, are used to produce the chart of **Fig.** in the same way systematic charts were made for (Politis and Tsarsitalidis 2014). The chart produced for the same wing under fully prescribed motion, is given in **Fig. 7** for comparison. Substantiall thrust is produced, but the maximum efficiency is smaller and for a narrower area of parameters. It should be noted, that although the propulsive efficiency is simple to comprehend for an actuated (motion given by user) system (and the system in hand looks unfavorable for a propulsor compared to the prescribed motion), it has a different meaning when motion is taken from the ship. In the case of the energy saving system, the calculated efficiency is the factor of conversion of energy taken from motions to thrust. Even in this context, high efficiency is still a goal, as it will mean larger thrust for the same motions, while a lower efficiency, might mean that it operates mostly as a seakeeping device. The effect of parameters such as pitching axis position, damper settings, different wing shapes and possible non- linear springs and dampers have to be investigated, but the existing knowledge, that spring loaded wings operate well in limited conditions, is confirmed.

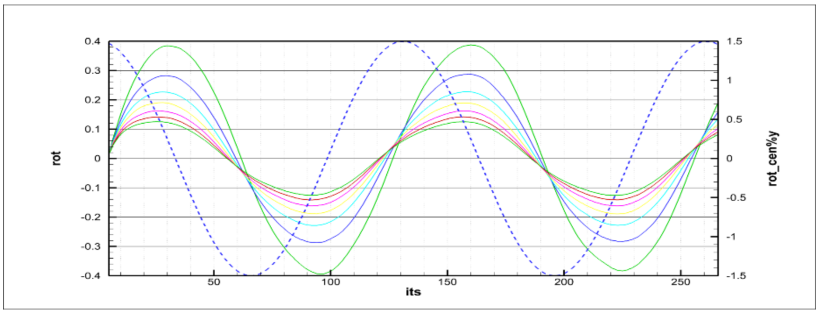

Fig. 5 Responses (rot) in radians, for varying K(1-20Nm/rad) for straight wing s/c=4 at Str=0.3 h/c=1.5 Dashed line is for the y position of the rotation center (pitching axis)

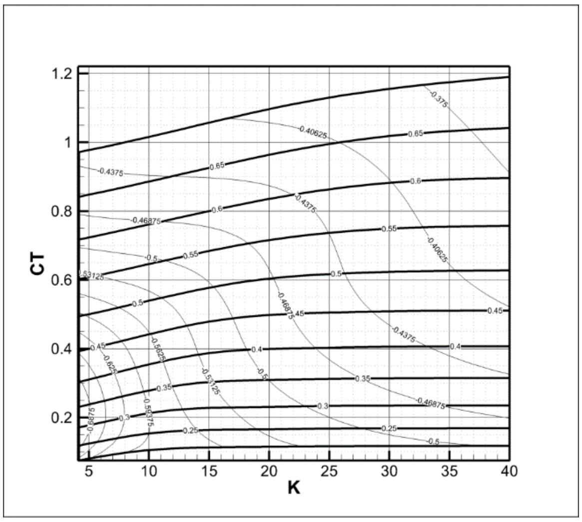

Fig. 6 Ct-K chart for a strainght wing s/c=4, h/c=1.5, under simple harmonic motion. Thicker lines are for Strouhal number and thinner, are for efficiency.

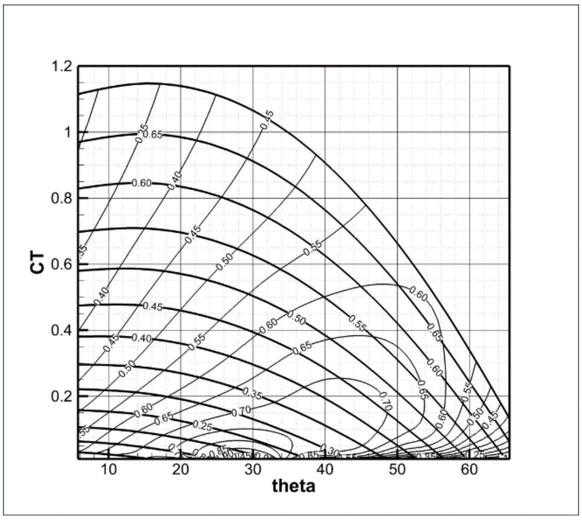

Fig. 7 Ct-θ_0 chart for a straight wing of s/c=4, h/c=1.5. Thin contour lines are for Efficiency and thick ones are for Strouhal Number

8. Active pitch control

Knowing from the literature that spring loaded wings operate well in a narrow area of conditions, it was deemed necessary to develop an active pitch control algorithm. For the specific application, the simple open loop algorithm presented by (Politis and Politis 2012), (Belibassakis and Politis 2013) is employed and evolved as follows.
From the original of (Politis and Politis 2012), the pitch angle at each step is defined as:

$$\theta(t) = w \tan^{-1}(dh/dt/U) \quad (7)$$

Where w, a control parameter ranging from zero to one that is set beforehand. Knowing the expected heave amplitude, frequency and speed of advance, and knowing that:

$$a(t) = (1-w)\tan^{-1}(dh/dt/U) \quad (8)$$

the parameter w can be set to a number that the maximum angle of attack does not exceed a defined value.
Closer examination of (8), leads to the realization that $\tan^{-1}(dh/dt/U)$ gives the angle of the undisturbed flow and that decrease in the value of w, increases the angle of attack. If the constant parameter w is substituted with a variable $w(t)$ and keeping in mind the objective of keeping the angle of attack below a given value, a new law for obtained for $w(t)$, by finding the solution for $w(t)$ of

$$A \ge (1-w(t))\tan^{-1}(dh/dt/U), A = given \quad (9)$$

while keeping the lowest allowed value. The value found, is then substituted in (7), to give the pitching angle. This gives at a minimal addition of computational cost, a different, non-harmonic profile of pitching motion, where the angle of attack is kept below the given value, but also equal to it for a longer time. It should be noted, that when the angle of the undisturbed flow is smaller than the desired angle of attack (and when it changes from the positive to negative –one side of foil to the other-) it is better to keep the foil at a zero pitch angle, something that this algorithm follows very well. As shown below, the angle profiles can be very different to the known patterns so far, producing interesting results. Figures **Fig. 8** **Fig. 2**, show time series for selected cases, while **Fig. 3** thru **Fig. 5**, are the Ct-Target A_{max} diagrams equivalent to the previous, but with the user defined Target A_{max} as a second varying parameter (along with Str). For the preudo-random case, a time series of elevations taken from a ship's response to a random wave of sea state 4 (Belibassakis & Filippas 2014) was added to the harmonic heave motion produced systematically for each Strouhal number. The last two charts are for a swept wing with 30^{o} skewback. High thrust coefficients are observed, accompanied with high efficiencies for the harmonic cases. Performance is satisfactory for the pseudo-random case as well.

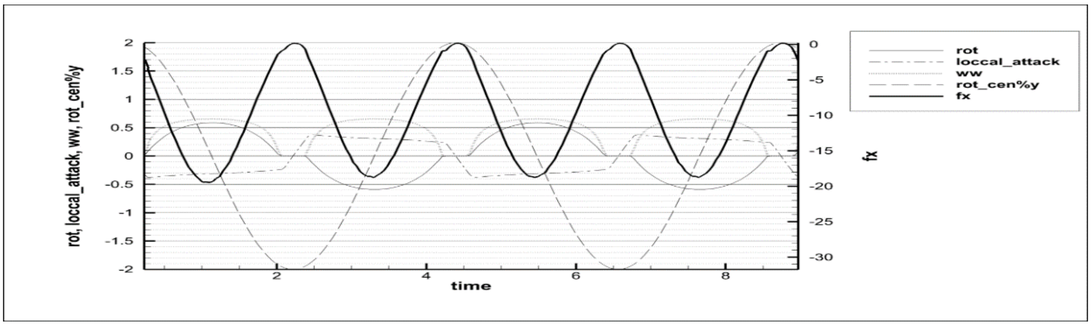

Fig. 8 Time series of simulation of a Controlled foil of S/c=4 at Str=0.4 and Target A_{max}=17^{o}. Thin solid: selected pitch of foil (rad), Dash dot: instantaneous ngle of atack (rad), Dotted: selected instantaneous w factor, Dashed: heave motion of the foil, Thich solid: Instantaneous Fx/ρ (negative is thrust)

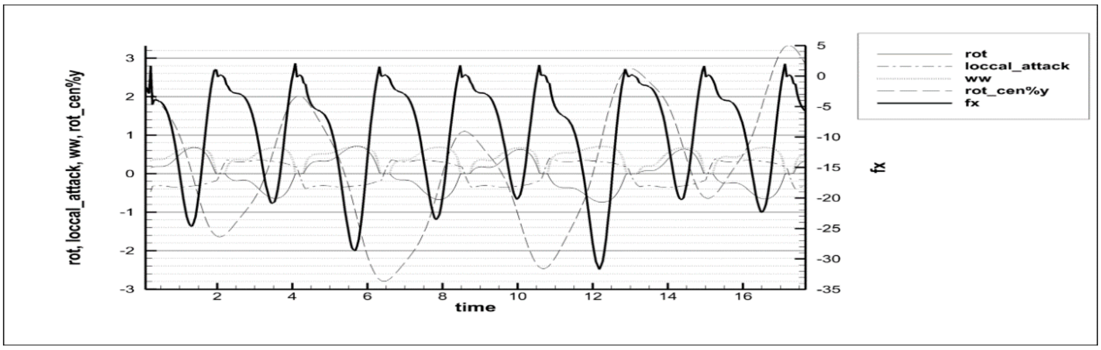

Fig. 2 Time series of simulation of a Controlled foil of S/c=4 at Str=0.4 plus pseudo-random motion and Target A_{max}=17^{o}. Thin solid: selected pitch of foil (rad), Dash dot: instantaneous ngle of atack (rad), Dotted: selected instantaneous w factor, Dashed: heave motion of the foil, Thich solid: Instantaneous Fx/ρ (negative is thrust)

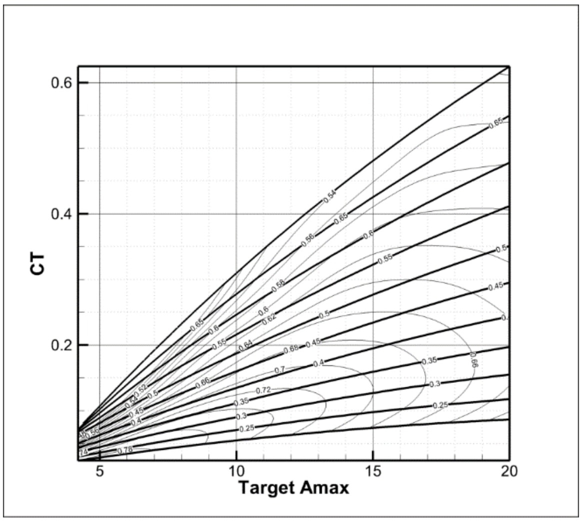

Fig. 3 Ct-Target A_{max} chart for a straight foil s/c=4, h_0/c=2, under simple harmonic motion. Thicker lines are for Strouhal number and thinner, are for efficiency.

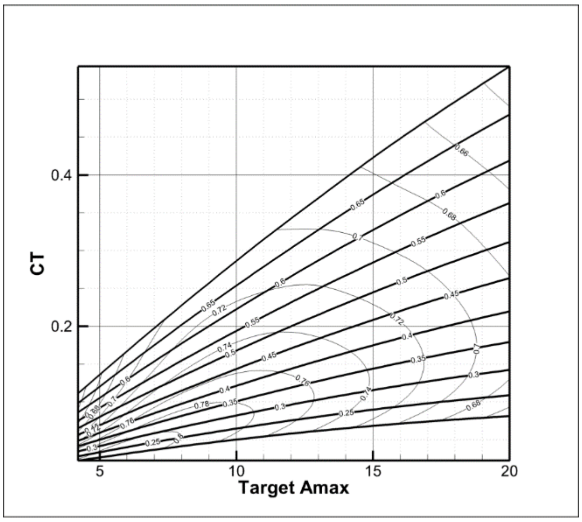

Fig. 4 Ct-Target A_{max} chart for a 30° swept foil, S/c=4, h_0/c=2, under simple harmonic motion. Thicker lines are for Strouhal number and thinner, are for efficiency.

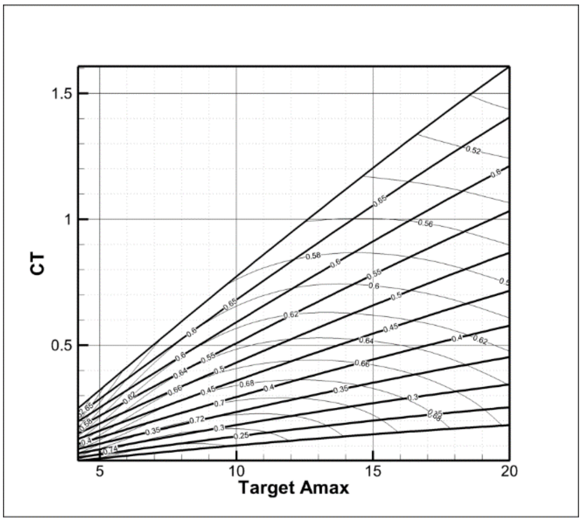

Fig. 5 Ct-Target A_{max} chart for a 30° swept foil S/c=4, h_0/c=2, under pseudo-random motion. Thicker lines are for Strouhal number and thinner, are for efficiency.

9. Conclusions – Future work

An initial exploration of the potential of wings with passive (spring loaded) and active pitch control has been presented. Both systems seem promising, with the actively controlled being more adaptable, but with the spring loaded independent of electronics and mostly predictable. Before any verdict is made, further investigations have to be made. For the case of spring loaded wings, a wider systematic variation of parameters is needed, while also investigating the effect of the pitch axis position and the damping factor. The effects of different shapes are another big issue, while the use of springs of nonlinear stiffness may show a great potential. Almost the same apply for the case of actively controlled wings. Variation of the position of pitching axis is to be investigated, but also it is interesting to see its performance for different wing shapes. Different methods of control need to be applied, as well as more sophisticated systems that would use the data from the existing simulations for system recognition that would lead to the creation of a state-space controller for thrust production in random motions.

After these, an introduction of the updated concept design is in order. **Fig. 6** presents a conventional ship, equipped with (passive) wings, acting as energy saving systems. Horizontal wings fore and aft, are for energy extraction from heaving and pitching motions, while the vertical is for extraction of energy from rolling motions. The horizontal wings are located as close to the baseline as possible and the longitudinal position has to be investigated in order to maximize effects, while minimizing the risk of damage from slamming. From the mechanical engineering part, the ability to make the systems retractable is necessary as well as sizing, positioning and fixing actuator motors. Last but not least, experimental setups, similar to this concept are being constructed, in order to proceed with a detailed feasibility study of the best designs produced by the aforementioned extended investigations.

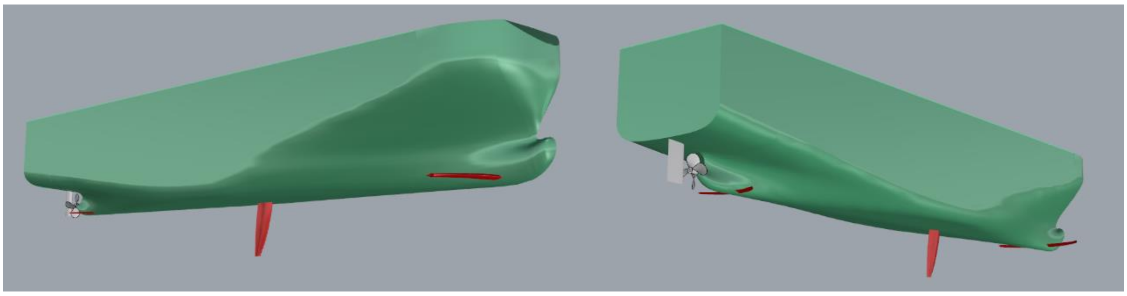

Fig. 6 Conventional ship equipped with foils working as energy saving systems

ACKNOWLEDGEMENT

This research has been co-financed by the European Union (European Social Fund – ESF) and Greek national funds through the Operational Program "Education and Lifelong Learning" of the National Strategic Reference Framework (NSRF) 2007-2013: Research Funding Program ARISTEIA - project BIO-PROPSHIP: «Augmenting ship propulsion in rough sea by biomimetic-wing system»..

References

Belibassakis, K. A. and G. K. Politis (2013). "Hydrodynamic performance of flapping wings for augmenting ship propulsion in waves." Ocean Engineering **72**: 227-240.

Belibassakis, K. A. and Filippas, E. S. (2014). "A method for the analysis and design of flapping-foil thrusters for augmenting ship propulsion in waves." MARTECH 2014

Chopra, A. K. (2007). Structural Dynamics.

Filippas, E. S. and K. A. Belibassakis (2014). "Hydrodynamic analysis of flapping-foil thrusters operating beneath the free surface and in waves." Engineering Analysis with Boundary Elements **41**: 47-59.

Geradin, M. and D. Rixen (1994). "Mechanical vibrations. Theory and application to structural dynamics." Mechanical Vibrations: Theory and Application to Structural Dynamics.

Hodges, D. H. and G. A. Pierce (2002). "Introduction to structural dynamics and aeroelasticity." Introduction to Structural Dynamics and Aeroelasticity.

Isshiki, H. (1994). Wave energy utilization into ship propulsion by fins attached to a ship. Proceedings of the International Offshore and Polar Engineering Conference.

Lighthill, J. (1973). "AQUATIC ANIMAL LOCOMOTION." 1973.

Nikolaev, M. N., A. I. Savitskiy and Y. U. F. Senkin (1995). "Basics of calculation of the efficiency of a ship was propulsor of the wing type." Sudostroenie **4**: 7-10.

Politis, G. and K. Politis (2012). "Biomimetic propulsion under random heaving conditions, using active pitch control." Journal of Fluids and Structures.

Politis, G. K. (2011). "Application of a BEM time stepping algorithm in understanding complex unsteady propulsion hydrodynamic phenomena." Ocean Engineering **38**(4): 699-711.

Politis, G. K. and V. T. Tsarsitalidis (2014). "Flapping wing propulsor design: An approach based on systematic 3D-BEM simulations." Ocean Engineering **84**(0): 98-123.

Politis, G. K. and V. T. Tsarsitalidis (2014). "Flapping wing propulsor design: An approach based on systematic 3D-BEM simulations." Ocean Engineering **84**: 98-123.

Rozhdestvensky, K. V. and V. A. Ryzhov (2003). "Aerohydrodynamics of flapping-wing propulsors." Progress in Aerospace Sciences **39**(8): 585-633.

Shyy, W., H. Aono, S. K. Chimakurthi, P. Trizila, C. K. Kang, C. E. S. Cesnik and H. Liu (2010). "Recent progress in flapping wing aerodynamics and aeroelasticity." Progress in Aerospace Sciences **46**(7): 284-327.

Sparenberg, J. A. (2002). "Survey of the mathematical theory of fish locomotion." Journal of Engineering Mathematics **44**(4): 395-448.

Triantafyllou, M. S., A. H. Techet and F. S. Hover (2004). "Review of experimental work in biomimetic foils." IEEE Journal of Oceanic Engineering **29**(3): 585-594.

Triantafyllou, M. S., G. S. Triantafyllou and R. Gopalkrishnan (1991). "Wake mechanics for thrust generation in oscillating foils." Physics of Fluids A **3**(12): 2835-2837.

Wen, L., Z. Fan, T. Wang and J. Liang (2010). "Fuzzy control of biomimetic propulsion using flapping foil." Jiqiren/Robot **32**(3): 306-313.

Wright, J. R. and J. E. Cooper (2007). "Introduction to Aircraft Aeroelasticity and Loads." Introduction to Aircraft Aeroelasticity and Loads.

Wu, T. Y. (1971). "Hydromechanics of swimming propulsion. Part 1. Swimming of a two-dimensional flexible plate at variable forward speeds in an inviscid fluid." J. of Fluid Mechanics **46**: 337–355.

Zhu, Q. (2011). "Optimal frequency for flow energy harvesting of a flapping foil." Journal of Fluid Mechanics **675**: 495-517.

DEVELOPMENT OF COMMERCIAL WIG CRAFT IN CHINA

Ye Yonglin, Yang Youning, Xing Fu, You Guohong

China ship scientific research center, 222 Shanshui East Road, Wuxi City, Jiangsu, 214082, China

ABSTRACT

Wing-In-Ground craft is a new type of high performance vessel with wings flying over the water. Several countries have established or been establishing their WIG craft developing plans. To boost and standardize WIG craft, many rules and guidelines have been proposed by IMO and other organs. In China, there are more than 40 years research history of WIG craft, and more than 10 WIG crafts have been built. Each craft is small, and whose total weight is less than 10 tons. The craft's developing process is from mechanism study to model test validation, and then to practical craft with the hull made by GRP, antirust aluminum alloy or high strength composite material. They cruise in the rivers, lakes and South Sea in China to stand the test of rough sea. In the paper, the achievements and new commercial WIG craft are presented during the WIG craft commercialization process in China. Some practical problems for the rules are also proposed.

1. INTRODUCTION

To boost and standardize WIG craft, '*Interim Guidelines for Wing-in-ground (WIG) Craft'* has been proposed by IMO in 2002, where WIG craft was defined as a new type of dynamic supporting ship. Except for China and Russia, several countries including Germen, Korea and Singapore, have established or been establishing their WIG craft development plans. Some other countries have been greatly interested in and made their great efforts to WIG craft. For example, Lloyd's Register in U.K. has proposed the Regulations for the Classification of Wing in Ground Effect Craft.

In China, there are more than 40 years history of WIG craft's research, and more than 10 WIG crafts have been built. Each craft is small, and whose total weight is less than 10 tons. The craft's development process is from mechanism study to model test validation, and then to practical craft. And they are made of GRP, antirust aluminum alloy or high strength compound material. They cruise in the rivers, lakes and South Sea in China to stand the test of rough sea.

In the paper, it will be presented with an example of the newly developed commercial WIG craft that technical achievements and legal problems during the WIG craft commercialization process in China, which includes the longitudinal stability, seakeeping performance and structural design technology. The legal problems, like the practical problem of the existing laws, standards and guidelines suitable for the WIG craft, and water area and airspace controlling problem.

2. WIG's CHARACTERISTICS AND COMMERICAL USE

Wing-In-Ground craft is a new type of high performance vessel with wings, which can fly in high speed on the water by the Wing-in-ground effect of the wings. The Wing-in-ground effect is that the L/D ratio will greatly rise when WIG craft fly on the water for that its lift increases but the induced resistance debases. The navigation speed of WIG craft is between that of normal ship and aircraft, and the outstanding characteristics from the aircraft are that it can steadily fly over the water/ground.

The main performance characteristics of WIG craft are the following:

- High speed: Its speed can be up to 100-300kn, is 7-20 times of that of the normal speed, and corresponds to the normal propeller-driven aircraft.
- Well seakeeping: WIG craft can fly on the wave without being limited by the wave conditions. In the same sea condition and for the same total takeoff weight, the seakeeping of the WIG craft can be at least a high sea scale than that of the seaplane.

• Good economy: For the high lift-drag ratio (L/D), it has the characteristic of low fuel consumption, great loads and well cruising ability. In addition, the low work and maintenance costs for the complex Facilities and the runway at the airport required by airplanes are not required.
• Well safety, reliability, comfort: comparing with the airplane, it can safely land on the water which provides very smooth cushion for the craft's landing by Wing-in-ground effect. On the other hand, comparing with the normal ship, it has the best comfort as that of the airplane.
• Amphibious and Climbing ability: It can launch out and get to land by power augmentation, hydroskis and beaching gears. And Class B, C of WIG crafts can climb to overcome obstacles.
Based on above technology characteristics, for the outstanding application value of tour and sightseeing, rapid transportation, official duty, environmental protection, search and succor, and so on, WIG craft is worth to develop as the commercial product.

3. KEY TECHNOLOGY RESEACH OF WIG CRAFTS IN CHINA

By the research and develop for more than 40 years, based on the model tests and real boats development, some key technologies of WIG craft in China have been broken through, as the following:

• Design of aerodynamic layout and shape optimization
• Hydrodynamic assembly design
• Longitudinal and transverse stability analysis
• Power augmentation technique
• External loads prediction method
• Structure analysis and calculation method
• Model wind tunnel test technique
• Model tank test technology
• Remote-control ship model test technique

Based on the deep study of the longitudinal stability, several series of aerodynamic layout crafts are achieved, shown as Fig.1.
The control method of longitudinal stability can be described by static stability and dynamic stability, shown as the following:
If the flying craft is in longitudinal static stability, there is the following condition:

$$\begin{cases} \overline{X}_T < \overline{X}_{F\vartheta} \\ \overline{X}_{FH} < \overline{X}_{F\vartheta} \end{cases} \tag{1}$$

$\overline{X}_T = X_T / C$ ——Dimensionless position of C.g. on mean aerodynamic chord.

$\overline{X}_{FH} = \overline{X}_T - m_Z^{\overline{H}} / C_y^{\overline{H}}$ ——Dimensionless position of the focus for flying height on mean aerodynamic chord.

$\overline{X}_{F\vartheta} = \overline{X}_T - m_Z^{\vartheta} / C_y^{\vartheta}$ ——Dimensionless position of the focus for pitch angle on mean aerodynamic chord.

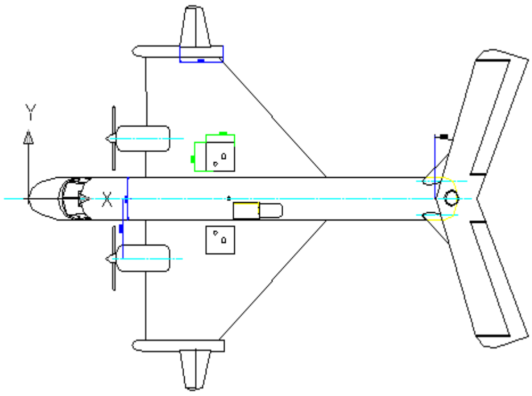

a. Lippisch type

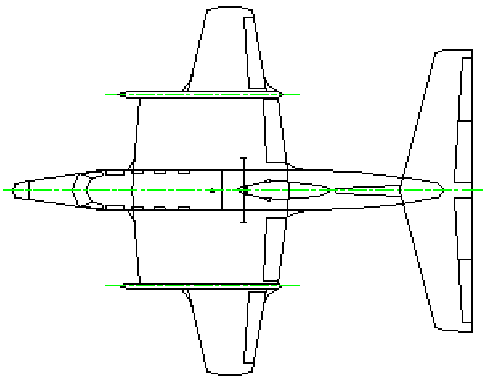

b. combination wings type

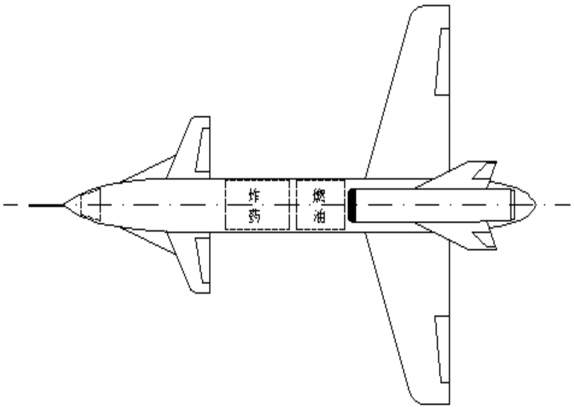

c. canard wing type

Fig.1 aerodynamic layouts of WIG crafts

For there is 5 orders of dimensionless linear differential equation to describe the longitudinal motion of WIG craft, the corresponding characteristic equation is the 5 orders of algebraic equation as following:

$$\lambda^5 + A_1\lambda^4 + A_2\lambda^3 + A_3\lambda^2 + A_4\lambda + A_5 = 0$$

The coefficients $A_i (i = 1,2,3,4,5)$ of characteristic equation are constant real numbers, and obtained by the aerodynamic parameters and structure parameters. The necessary and sufficient conditions that the real of all the solutions of above algebraic equation are nonzero negative are that all the coefficients should be satisfied with the following inequations:

$$\begin{cases} A_i > 0 \quad (i = 1,2,3,4,5) \\ A_1A_2 - A_3 > 0 \\ (A_1A_2 - A_3)(A_3A_4 - A_2A_5) - (A_1A_4 - A_5)^2 > 0 \end{cases} \tag{2}$$

The general solution of the linear differential equation are the linear combination $\sum_i C_i e^{\lambda it}$ of $e^{\lambda it}$. When A_i satisfies with all the inequalities of condition (2), $\mathrm{R_e}\,\lambda_i < 0$, thus there is $e^{\lambda it} \xrightarrow[t\to\infty]{} 0$. It means that the craft is stable for that it can return to its original state by eliminating the disturbance by itself when its motion parameters have any small disturbance. While A_i does not satisfy with the condition (2), λ will has zero or positive real part. It means

that the craft is unstable for that the solution of the motion equation is divergent, at least not convergent.
Then condition (2) is the stability criterion of longitudinal motion of WIG craft.

4. WIG CRAFTS IN CHINA

Based on mechanism study and model tests, several series of layout designs of WIG craft are finished in China. Some crafts already have the function of commercial products. Fig.2 shows the model test of new combination wings type of WIG craft.

Fig.2 combination wigs type of WIG craft

Fig.3 'Xiangzhou 1' craft

Table 1 shows the dimensions and main parameter of some typical WIG crafts including 'Xiangzhou 1' craft, which is a commercial craft built lately in China, shown in Fig.3. It takes off stably and rapidly on the water, flies agilely over the water. It has well flying stability and manoeuvreability, which can satisfy with the requirements of WIG flying on the complex water zone.

Table 1. main WIG crafts in China

model	961	902	XTW-1	XTW-2	XTW-3	XTW-4	XTW-5	Xiangzhou 1
first flight	1968	1983	1988	1993	1997	1999	2003	2013
Max. weight (kg)	720	400k	950	3600	4000	6000	4200	2500
Person	1	1	4	15	12	20	8	7
material	Aluminium alloy	GRP	GRP	GRP	Aluminium alloy	Aluminium alloy	Aluminium alloy	composite material
Loa (m)	7.3	9.5	12.6	18.5	17.9	21.7		12.7
Breadth (m)	5.8	5.8	8.2	12.7	11.8	14.5		11.5
speed (km/h)	110	110~120	110~130	130~150	140	150~180		140~160
Cruising height (m)	0~0.3	0~0.5	0~1	0~1.5	0~2	0~2	0~2	0-2
Max. height (m)	5	10	20	20	20	20	20	60
Curding Range (km)	—	—	400	900	≥400	500		400

The craft adapts combination wings type of aerodynamic layouts with single engine and elevated thrust propellers. There are water-tight cabins in the hull, 4 rows of seats for 7 passengers, and two doors for the person alleyway and getting away in emergency. It is convenient to train the drivers by the paratactic double steers and linked manipulation system.
The hull is made of advanced foam sandwich composite materials, with neat and clear surface, well structural strength and stiffness, especially good heat-insulation and sound-insulation performance. There are home-grown integrated displays and ventilation system in cabin, and special trolley and rails to launch the craft or landing.
The craft has successfully finished the first flying over the water on 1 May, 2013. The test results illustrates that it has well performance of taking off, fly over the water, and manoeuvrability. Then it has been awarded the inspection certificate, and finishes the classification of registration by China classification society (CCS) after the trial on South China Sea in April 2014. It starts the commercial use of WIG crafts in China.

5. INTERNATIONAL RULES OF WIG CRAFT

By now, several rules of law or classifications of WIG craft in the world have been released by the classification societies or the state maritime administrative organs, such as by CCS and Russia early in 1998. In 2002, IMO issued the "*Interim Guidelines for Wing-in-ground (WIG) Craft"*, whose details are discussed recently by the researchers from China, Russia, Korea, and so on. In recent years, the correlative law and rules are issued by Lloyd's Register of shipping(LR), IMO and CCS after more practical study are carried out about the classification, use and train. It points out the direction of commercial production development of WIG crafts. Main rules show as the following:

- Russia ship register department, Classification and building rules of Class A WIG craft, 1998
- IMO, Interim Guidelines for Wing-in-ground (WIG) Craft, 2002
- LR, Regulations for the Classification of Wing in Ground Effect Craft, 2005
- IMO, General principles and recommendations for knowledge, sills and training for officers on Wing-In-Ground (WIG) craft operating in both displacement and ground effect modes, 2005
- Russia ship register department, Interim guidelines of Classification and building of WIG crafts, 2008
- CCS, Guidelines for Survey of Wing-In-Ground craft, 2008

6. PROBLEM OF THE FULES IN PRACTICAL USE

6.1 Rule integrality

The requirements of above law and rules should be satisfied with by the Chinese commercial WIG craft in the development process. As a whole, all kinds of safety requirements of commercial craft are presented by above law and rules, including:

- For main systems and safety safeguard, there are specific regulations in the rules, such as the requirements of buoyancy and stability, manipulation and stabilization system of hydrodynamic and aerodynamic design.
- For the structural strength and construct, there are the inspection requirements of the structure, material and building craftwork.
- For the power unit, there are inspection requirements of turbine and auxiliary system, etc.
- For the electrical system, there are requirements of the craft's electricity safety and environmental protection, and specific inspection requirements of signal units, navigation devices, radio-communication devices and lifesaving equipments.
- For the outfit system, there are some requirements such as the equipments disposal and safety measures for the cabin layout.

• For the mooring system, there are some requirements of anchors, pulling, safe securing and landing devices.
• For the fire fighting and lifesaving system, there are special requirements of fire fighting and telecontrol, alarm and safety system.
• For the control system, there are inspection requirements of control and stability system.
• For the landing wheel system or hydro-ski system of some special WIG crafts, there are special inspection requirements in the rules in Russia.
In addition, there is the requirement that the first built WIG craft should be assessed for the safety, which can further enhance the safety of the craft.

6.2 Existing problem

Although there are many requirements, some detail requirements in the rules are still difficult to adapt to the exact craft production. For example, there are some problems in the new commercial craft, shown as the following:
• For the practical use of the WIG craft, the requirements are still deficient in each country. For example, there is not any formal law to manage the WIG craft's use by Chinese marine organ, or special requirement in the law or regulation of low altitude aviation.
• There are still details needed to discuss in the *Interim Guidelines for Wing-in-ground (WIG) Craft* by IMO, such as:

- In unit 3.2.2 of part A, WIG cargo crafts with 5 tons of full load displacement should be excluded, which ensures that the small cargo craft does not need to equip too many devices.
- According to the *guidelines*, all the WIG crafts for international navigation should satisfy with the requirements of the *guidelines*. While it is too rigorous to satisfy with for the small WIG craft, especially for the lifesaving and mooring device.

• For the rules, the example WIG crafts are not enough to check up and perfect the applicability of the regulations. For example, in the *Guidelines for Survey of Wing-In-Ground craft(2008)* by CCS, there are some requirements from the steel boat, but not suitable to the WIG craft.

7. CONCLUSIONS

Based on mechanism research, model test and trial craft development, WIG crafts have been used preliminary commercially by the development for more than 40 years in China. At present, the long-term applied WIG crafts are seldom for that in the commercial process, there are some technique, rule and law problems needed to develop and perfect, which needs the hard works of the researchers, classification societies and commercial organizations of WIG craft in the world.

ACKNOWLEDGEMENTS

The authors gratefully acknowledge the colleagues of the WIG craft group in CSSRC, such as Prof. Yuan Changhua, Mr. Si Yajun, for their high quality work, especially for Xiangzhou 1 craft's development. The supports from Prof. Cai Daming and Prof. Gu Jianming are greatly appreciated.

References

1. Ye Yonglin, "Conceptual design of WIG craft", Wuxi:Ship mechanics, Vol 6, pp.95-103, Oct 2002
2. Zhang Guofeng, "The development and supervision of WIG craft", Tianjing: Tianjin navigation, pp.62-64, Mar 2010
3. Li Yulong, Yang Wei, Yang Zhigang, Numerical study on longitudinal static stability f a canard WIG craft, FLIGHT DYNAMICS, Vol.28, pp.9-12, Feb 2010

4. Yuan changhua,Zhou Qian, Xu Xingfa, A practical design method of Wing-In-Ground-Effect-Ship form, Journal of Ship Mechanics, Vol.12, pp.59-62, Feb 2008
5. Yuan Changhua, etc. design of Xiangzhou 1 craft. Wuxi: report of China Ship Scientific Research Center, 2013

A COMPARISON OF TWO PLANING MODELS FOR A CYLINDRICAL HULL ON A CIRCULAR FREE SURFACE

John Dzielski[1]

[1]Davidson Laboratory, Stevens Institute of Technology, 711 Hudson St., Hoboken, NJ, 07030, USA.

ABSTRACT

This paper presents a comparison of two models for estimating the normal force on a non-prismatic cylindrical hull planing on a cylindrical surface. One model is analytical in origin and the second is empirically derived from experimental data. Both models relate the immersion and orientation of a cross-section to the force coefficient per unit length on the hull. Integrating or summing the forces on the immersed sections yields a net normal force. The comparisons presented are both qualitative and quantitative. The qualitative comparison discusses the different shapes and features of the force distributions. The qualitative comparison compares the normal forces predicted by the two models for different keel immersions, planing angles, and the relative size of the gap between the hull and surface. The comparisons emphasize the model predictions for small and large gaps. For very small gaps, the analytical model appears to over-predict the distributed force by a significant margin and yields results that are not physically reasonable. Because the source of the gap correction used in the empirical model does not contain data with very small gaps, there is a possibility that the correction under-predicts the force for narrow gaps. Both yield similar results for larger gaps and the experimental data is probably more reliable, especially with regard to the location of the force centre.

1. INTRODUCTION

Being able to model the force on a cylindrical hull on a curved surface is important to modelling the dynamics of a submerged body running in a cavity. Because non-prismatic hulls tend to have higher lift-to-drag ratios than prismatic hulls and because they do not have hydrostatic stability, they are not particularly useful for surface craft. As a result, there have not been a lot of investigations into their characteristics. The work [1] describes an extensive series of experiments measuring the lift, drag, and moment on a series of cylinders on flat and curved surfaces. Some of the data was measured on a flat or curved free surface where the curvature was created by a scoop on a flow channel. Most of the data was taken in vaporous or lightly ventilated gas cavities in a tunnel. Much of the data is taken at submergences and angles of attack that are large when compared with what might be expected for a body in a cavity operating at a high Froude number.

The references [2,3] describe an empirical model for a cylinder impacting a curved surface. The approach attempts to model the momentum of the fluid displaced by the impact of a circular cross-section into a circular free surface. The approach is analogous to that of [4,5] except that calculating the free-surface rise is considerably more complicated. The second model is derived from the data used to develop the model presented in [6]. In [7], that data is reprocessed so that the lift and drag are rotated into a body fixed frame where the forces are tangent to and normal to the keel. The contribution of the tangent force to the pitching moment is modelled and subtracted from the moment. Finally, the fit uses both the force and moment data to compute the fit.

In the next section, the two planing models are described and documented sufficiently to allow them to be used. The following section presents a comparison of the results predicted by the two models. The models are first compared qualitatively based on the shapes of the force distributions on the hulls. The comparison looks first at the narrow gap condition where the radii of curvature of the hull and fluid surface are similar and then the case where the gap is large. The models are then compared quantitatively based on the total normal force. Again, both the small and large gap conditions are examined separately. In the last section, conclusions and recommendations about the use of the models are made.

2. PLANING MODELS

In this section, two models for the planing of a cylindrical hull section on a cylindrical surface are presented. Both the free surface and the hull are cylindrical with no longitudinal curvature. The models are formulated to yield the force normal to the hull as opposed to the lift force that is normally defined normal to the surface. This formulation is more useful when the result is going to be applied in a dynamics model for the body. The functional form of the model used here is

$$N=\frac{1}{2}\rho D^2V^2\int_0^{L_k}C_N\left(\tau,\lambda,D_c/D\right)d\lambda \tag{1}$$

where N is the force normal to the hull, t is the trim angle between the hull and the surface, l is the distance from the transom to a hull cross-section normalized by the beam D, D_c is the diameter of the fluid surface, and L_k is the beam normalized length of the wetted hull. The function $C_N\left(\tau,\lambda,D_c/D\right)$ represents the non-dimensional lift per unit length on the hull as a function of wetted-keel length. Since the diameter normalized immersion h is related to l by

$$h\left(\lambda\right)=\left(L_k-\lambda\right)\tan\tau \tag{2}$$

C_N can also be expressed as a function of immersion depth. The remaining terms in (1) correspond to the dynamic pressure.

2.1 Analytical planing model

The papers [2,3] present similar discussions about the derivation of the formula for the variation in wetted beam width as a function of immersion. The formula is based on a flow similarity between a circular hull immersing in a circular surface and the immersion of an expanding circular arc with angular extent $2B$. The papers reduce the problem to solving the integral equation

$$2h'-z(e'+h')=\frac{2}{\pi}\int_0^z\frac{1-\sqrt{1-(e'+h')^2f(2-f)}}{\sqrt{f(z-f)}}df \tag{3}$$

for z. In the above equation e',h' are the normalized gap $(R-r)/r$ and immersion h/r where R and r are the fluid surface and body radii. This equation differs from the one in the references in that both sides have been divided by r. The length of the circular arc is obtained from the formula $B=\arccos(1-z)$. The papers give the formula

$$m\left(h\right)=\pi\rho R^2\left(1-\cos^4\left(\frac{B}{2}\right)\right) \tag{4}$$

for the mass of the fluid displaced by the immersing section.

Reference [2] contains a solution to (3) for the case of an asymptotically small gap and reference [3] presents a solution for asymptotically large gap. Since equation (3) is relatively straightforward to solve numerically, a numerical solution is used for the results presented here. For a given gap, the algorithm solves (3) for a range of normalized immersions starting from zero. The solution procedure stops when $B>\pi/2$. The solution procedure yields a list of values for $z\left(h\right)$ and the trigonometric identity $\cos\left(B/2\right)=1-z/2$ is used to compute

$$C_N^P\left(\tau,h,D_c/D\right)=2\pi\left[\frac{d}{dh}\left(1-\cos^4\frac{B}{2}\right)\right]\sin^2\tau\left(\frac{0.5D_c}{D}\right)^2 \tag{5}$$

A numerical method computes the derivative indicated in (5).

2.2 Empirical planing model

The empirical planing model described here is based on experimental data collected in the towing tank at the Davidson Laboratory at Stevens Institute of Technology. The tank is 100m long and the carriage can be operated at speeds in excess of 30 m/s; although, practically, speeds in excess of 15 m/s are rarely used. The data set used to parameterize the planing model is the same as that used in the paper [6]. The paper [7] transforms the data in to a reference frame with axes parallel to and normal to the keel and applies a model for the location of the centre of pressure to remove the contribution of the parallel force to the pitch moment. The data is reduced to a similar parametric form, but the force is modelled as a force distributed along the wetted hull and both the force and moment data are used to compute the fit. The resulting model is

$$C_N^S\left(\tau,h,D_c/D\right)=\tau^{1.47}\left[0.615\lambda^{-0.465}\tan^{-1}\left(20\lambda\right)\frac{2}{\pi}\right]\left(1+\left(1.63-0.0774h'-5.25\tau\right)\frac{D}{D_c}\right) \quad (6)$$

The model in [7] includes a term in the square brackets that when dimensionalized is independent of speed and corresponds to a buoyancy effect. At high Froude numbers, this term is negligible and since (5) has no buoyancy term it is not included here. The terms on the right are a curvature correction derived from data in [1].

3. RESULTS AND DISCUSSION

This section presents a comparison of the two models. The next section shows a comparison of the distribution of force coefficient along the wetted hull predicted by the two models. The results examine the predictions for small gap clearance and large gap clearance at similar conditions of trim and wetted keel length. Gap is the difference between the diameters of the cavity and body. The emphasis of the next section is on the features of the distribution curves and is qualitative in nature. The subsequent section compares the predicted force coefficients. Again, the comparison is between similar conditions of trim and immersion, but for small and large gap clearances. The emphasis of this section is on a quantitative comparison of the results.

3.1 Qualitative comparison of the models

The plots in Figure 1-Figure 3 show the calculated distribution of normal force coefficient C_N^P on the left and C_N^S on the right for trim angles of [2,4,6] degrees, respectively. Each plot shows four curves corresponding to fluid surface to body diameter ratios of [1.1, 1.25, 1.5, 2]. These correspond to gaps between the fluid surface and body of 10%, 25%, 50%, and 100% of the body diameter when. For all cases, the transom immersion is 10% of the diameter. The two models predict similar results for gap ratios exceeding 50%. The Paryshev model predicts that the normal force coefficient increases rapidly as the gap begins to approach 20%, and the peak value of the coefficient for the Paryshev model exceeds that predicted by the Stevens model by a factor of about four. The Stevens model does not predict a similar rapid increase in normal coefficient with decreasing gap. A possible reason for this is that the data from which the curvature correction was calculated has gap only ratios down to 1.67. This is not that close to the value of 0.25 where the Paryshev model predicts rapid variation with the gap. The Paryshev model also predicts that the force distribution coefficient goes to zero at some point. This corresponds to the point where the wave-rise associated with the immersion reaches the beam and the model predicts no further change in mass. This is the same condition as the "chines wet" case for prismatic hulls. Physically, since there is mass transport off the beam or chine, the force should not drop to zero and the Stevens model predicts that it does not. The Paryshev model's peak value for the 6 degree trim approaches 0.4 which is 80% of the value of 0.5 that would be expected for a cylinder normal to the flow at zero cavitation number [8]. Also, the Paryshev model predicts that as the gap approaches zero the normal force coefficient will grow without bound and will significantly exceeding the expected experimentally measured limit of 0.5.

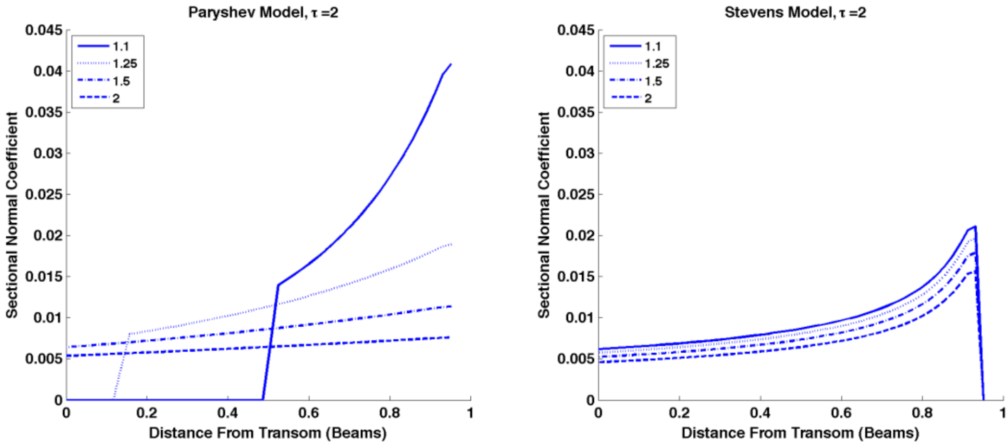

Figure 1. Distribution of force coefficient for trim 2 deg. and Dc of 1.1D, 1.25D, 1.5D, and 2D.

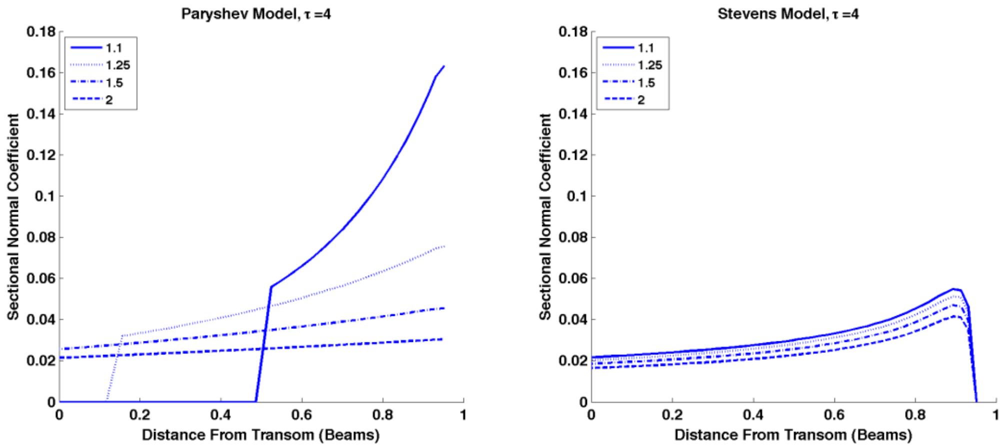

Figure 2. Distribution of force coefficient for trim 4 deg. and Dc of 1.1D, 1.25D, 1.5D, and 2D.

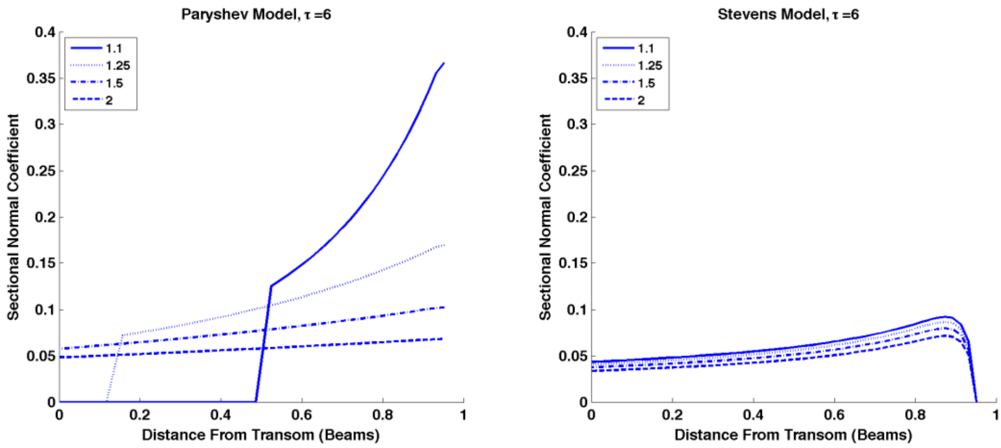

Figure 3. Distribution of force coefficient for trim 6 deg. and Dc of 1.1D, 1.25D, 1.5D, and 2D.

The same set of cases was re-run for larger gap clearances. Figure 4-**Error! Reference source not found.**Figure 6 show results for fluid surface diameters of of 2D, 5D, 10D, and 20D. The Paryshev model predicts an essentially linear variation in force distribution while the Stevens model predicts a peak near the leading edge of the wetted surface. This is consistent with physical measurements and the observation that there is expected to be a stagnation point near this location. Qualitatively, the Paryshev model seems to be under-predicting the normal force distribution, especially at shallower trim angles. The Paryshev model will also predict a centre of pressure aft of where the Stevens model predicts it is. Note that as the planing surface flattens, the Stevens model approaches the values expected from direct physical measurements.

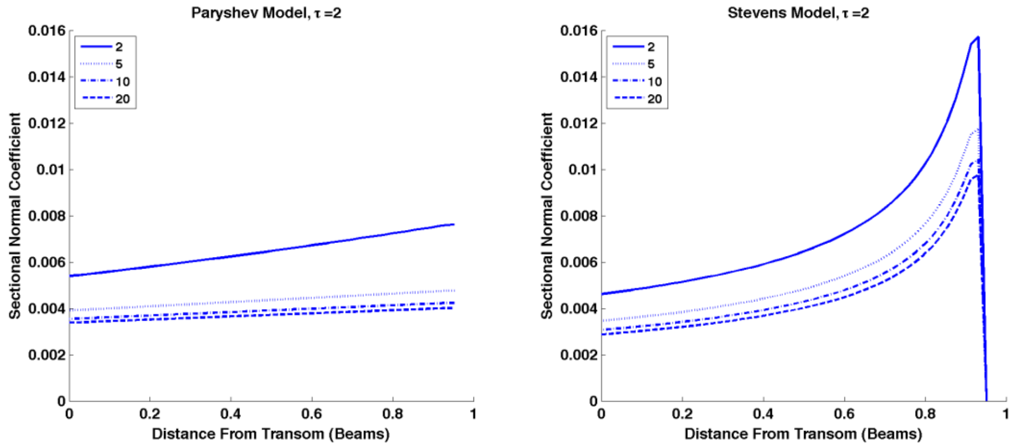

Figure 4. Distribution of force coefficient for trim 2 deg. and Dc of 2D, 5D, 10D, and 20D.

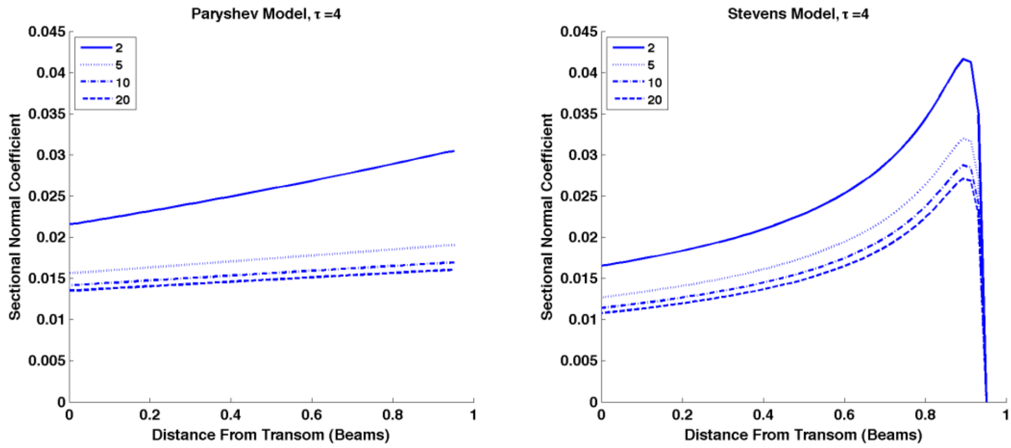

Figure 5. Distribution of force coefficient for trim 4 deg. and Dc of 2D, 5D, 10D, and 20D.

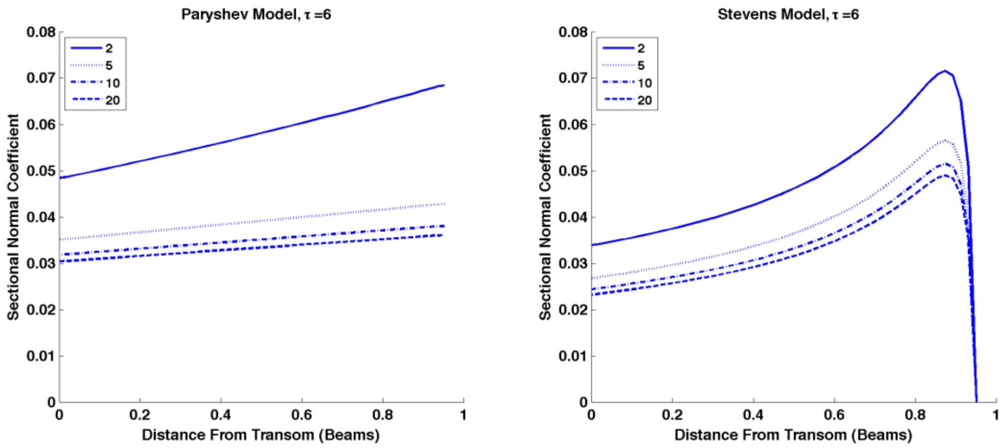

Figure 6. Distribution of force coefficient for trim 6 deg. and Dc of 2D, 5D, 10D, and 20D.

3.2 Quantitative comparison of the models

For the same set of small gaps considered in the previous section (10, 25, 50, 100) per cent of the hull diameter, the data in Figure 7- Figure 9 shows the calculated normal coefficient for trim angles of (1,2,3) degrees, respectively. For the two largest gap clearances, 50 and 100 per cent, the data are similar between the Paryshev and Stevens models. The coefficients calculated using the Paryshev formulation show unusual behaviour for the two smaller gaps in that the curves are flat. This situation appears to occur for the 50 per cent gap with the two points of deepest immersion. The fact that the model predicts that the lift force should remain about constant with decreasing immersion is not physically reasonable. The reason that the model predicts this behaviour can be seen in Figure 10. The left plot shows the distribution of force coefficient associated with the four data points of the top curve of the left-hand side in Figure 7 corresponding to the 10% gap. The force distribution is identical for each of the curves at different immersions but shifted along the keel. Because the distributions are the same the integrated total force coefficient is the same. The normal force coefficient predicted by the Paryshev model is identical until the beam separation point reaches the transom. For comparison, the right plot in Figure 10 shows the distribution of force coefficient associated with the bottom curve in of the right-hand plot in Figure 7 corresponding to the 100% gap.

Figure 11-Figure 13 show the normal force coefficients corresponding to the four larger gaps with fluid surface diameters of [2,5,10,20] times the hull diameter. All of the cases show similar results predicted using the Paryshev and Stevens models with the Stevens model tending to predict slightly higher force coefficients. While the results are not presented here, the locations of the centres-of-pressure predicted by the two models are very similar for these larger-gap cases. Both models predict a linear shift forward of the centre-of-pressure proportional to the immersion at the transom with the Stevens model tending to predict the location more forward of the transom. Note that for a transom immersion of 0.2D and Dc/D=2, the Paryshev model predicts a flow separation at the beam forward of the transom. In all other cases, the wetted width is predicted to be less than the beam.

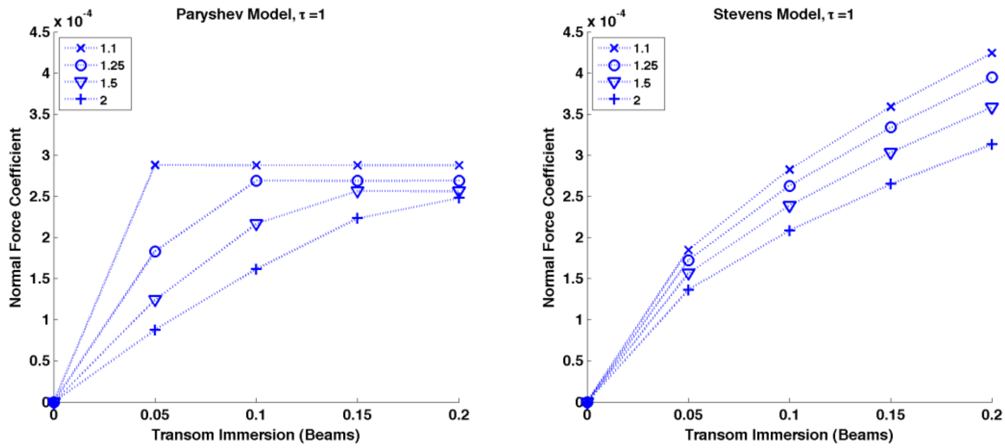

Figure 7. Normal force coefficients for trim 1 deg. and Dc of 1.1D, 1.25D, 1.5D, and 2D.

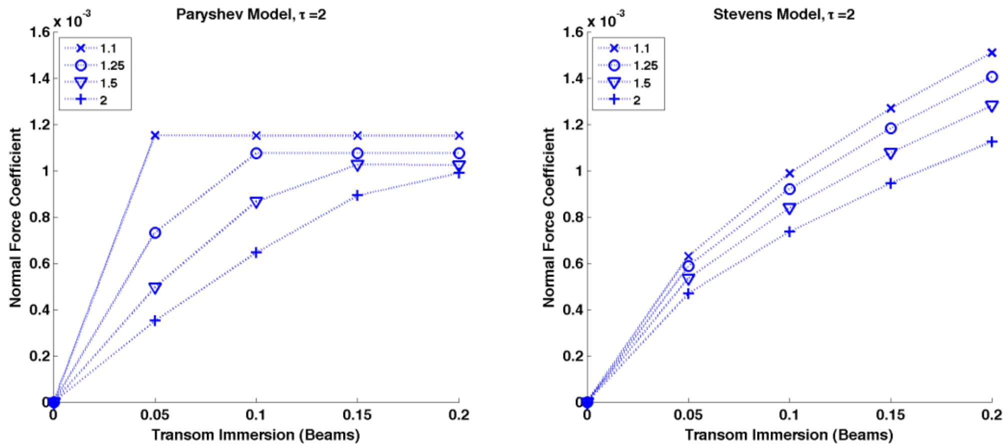

Figure 8. Normal force coefficients for trim 2 deg. and Dc of 1.1D, 1.25D, 1.5D, and 2D.

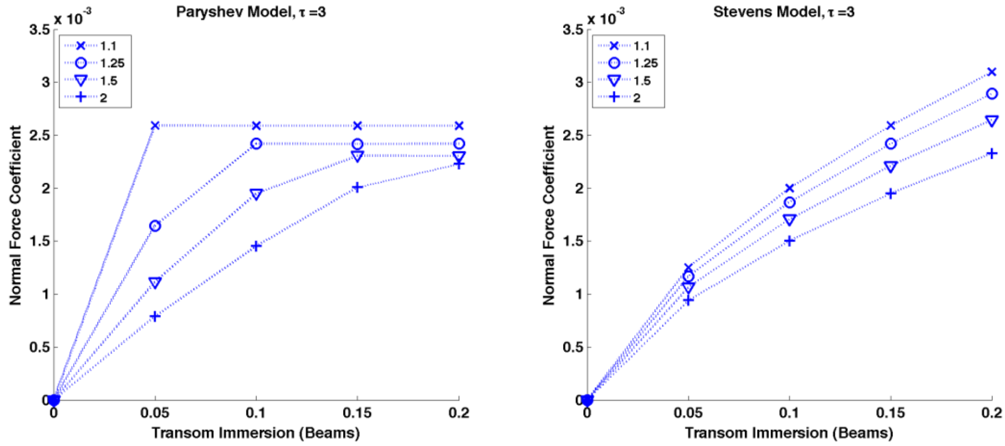

Figure 9. Normal force coefficients for trim 3 deg. and Dc of 1.1D, 1.25D, 1.5D, and 2D.

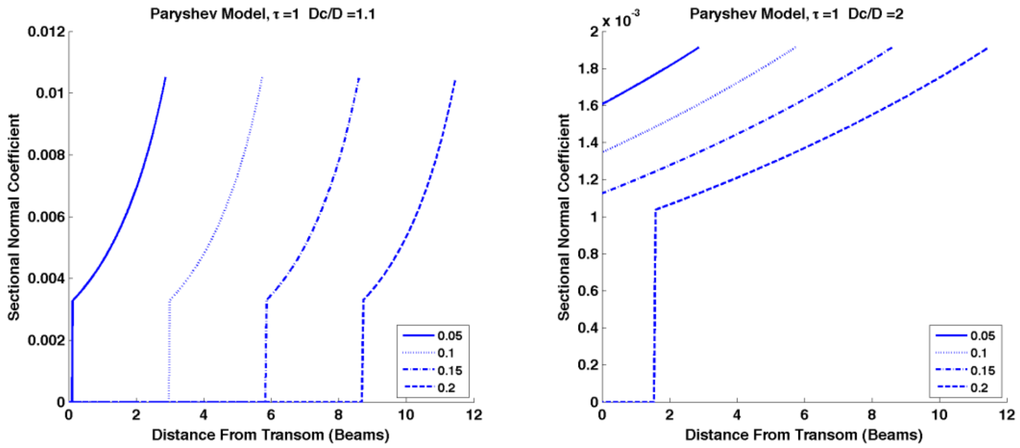

Figure 10. Distribution of force coefficients for trim 1 deg. and transom immersions of [5,10,15,20] per cent.

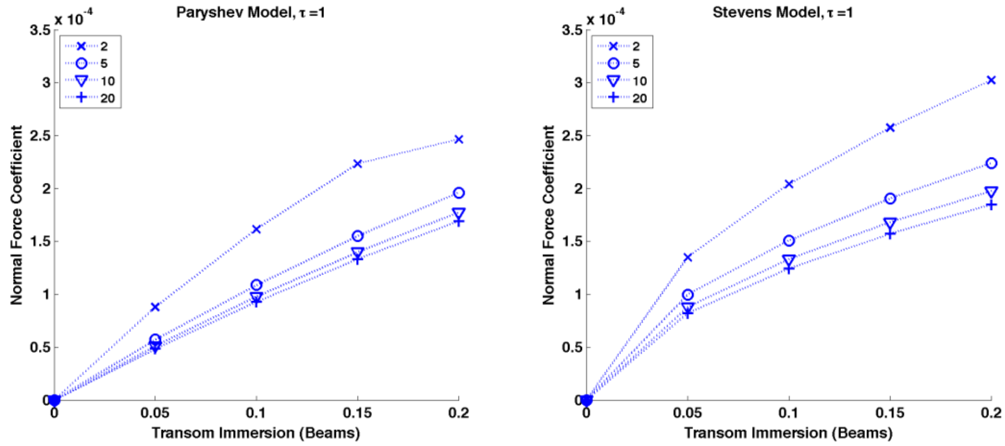

Figure 11. Normal force coefficients for trim 1 deg. and Dc of 2D, 5D, 10D, and 20D.

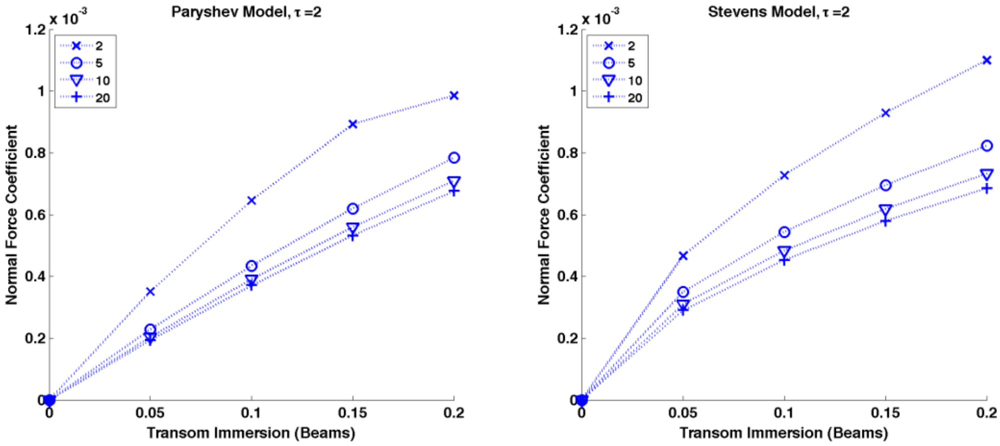

Figure 12. Normal force coefficients for trim 2 deg. and Dc of 2D, 5D, 10D, and 20D.

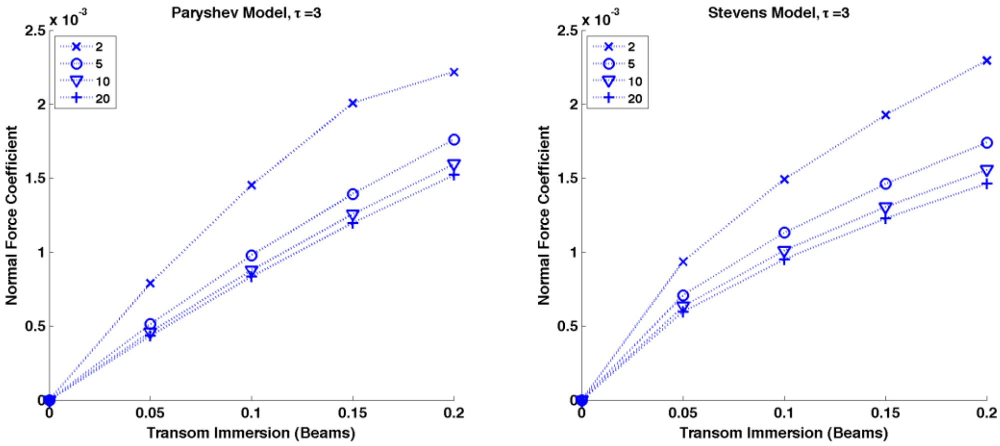

Figure 13. Normal force coefficients for trim 3 deg. and Dc of 2D, 5D, 10D, and 20D.

4. CONCLUSIONS

The paper described two models for predicting the lift on a circular hull planing inside a circular fluid annulus. The paper described differences in the shape of the force distributions predicted by the two models and compared the predicted net forces. The primary focus was on comparing results for small and large gaps between the boundary of the hull and the annulus at similar trim and immersions. When the annulus diameter exceeds twice the hull diameter and the trim angles and immersions are small enough that the Paryshev model does not predict a flow separation at the beam, both models yield similar results. Because the Stevens model is derived from experimental data, the conclusion is that the analytical Paryshev model is in fact capturing the relevant physics for these conditions. For conditions where the fluid annulus diameter is less than 1.25 times the hull diameter, the Paryshev model yields results that deviate significantly from what is physically reasonable. Because the diameter of a cavity associated with a cavity-running body is related to the drag that creates it, it is expected that a cavity-running body will have small gap clearances and the usefulness of the Paryshev model in this application is questionable. There is also a question about the Stevens model possibly under predicting the rise in the normal force coefficient with narrowing gap. The data from [1] used to compute the curvature correction used values for surface to body diameter ratios of 3.3 and 1.7. The Paryshev model predicts that there might be a substantial variation in the forces when the ratio approaches 0.3 and smaller.

ACKNOWLEDGEMENTS
This work has been sponsored by the Office of Naval Research under grant number N00014-14-1-0085, under the direction of Dr. Ronald Joslin, Code 332.

References

1. Waid, R. and Kermeen, R., "Forces on cylinders planing on flat and curved surfaces in cavitating and non-cavitating flow," *California Institute of Technology Report No. E73.5,1957*.
2. Paryshev E., "The plane problem of immersion of an expanding cylinder through a cylindrical free surface of variable radius," *International Summer School on High Speed Hydrodynamics*, Cheboksary, Russia, 2002.
3. Vasin, A. and Paryshev, E., "Immersion of a Cylinder in a Fluid Through a Cylindrical Free Surface," Fluid Dynamics, **36**/2 (2001), 169-177.
4. Von Karman, T., The Impact of Seaplane Floats During Landing, NACA TN 321, 1929.
5. Wagner, H., Landing of Seaplanes, NACA TN 622, 1931.
6. Yen, T., et al., "*Investigation of cylinder planing on a flat free surface,*" Proceedings of 11th International Conference on Fast Sea Transportation, Honolulu, Hawaii, USA, 2011.
7. Dzielski, J., "Modeling the planing dynamics of a cavity-running body", unpublished manuscript.
8. May, A., "Water Entry and the Cavity-Running Behaviour of Missiles," *NAVSEA Hydroballistics Advisory Committee,* Report TR 75-2, 1975.

NUMERICAL SIMULATION OF SELF-PROPULSION TESTS OF A PRUDUCT-CARRIER AT VARIOUS CONDITIONS

George D. Tzabiras and Kyriakos G. Psaras

Laboratory for Ship and Marine Hydrodynamics (LSMH)
School of N.A.M.E., National Technical University of Athens, 9 Heroon Polytechniou Av., Zografos, 15773, Greece

ABSTRACT

The proposed work is concerned with the numerical calculation of the resistance and self-propulsion parameters of a Chemical/Product Carrier 20000 DWT by applying CFD tools that have been developed at LSMH of NTUA. The basic method solves the RANS equations by applying the finite volume approach in a restricted computational domain underneath a prescribed free-surface which is determined through the potential flow solution. The propeller is simulated as an actuator disk exerting body forces in the axial momentum. Numerical tests have been performed to compute the horsepower requirements of the ship at various loading and trim conditions. They are compared to the estimations based on the sea-trials and useful conclusions are drawn with respect to its possible hydrodynamic performance

1. INTRODUCTION

The proper engine and propeller selection required to attain the desired speed of a ship is certified in sea trials. The ideal case should be to perform these tests at the real full load condition of the ship. However, due to technical reasons, it is many times impossible to achieve this situation and sea trials are performed in lower displacements and, according to regulations, at zero trim. Then, the shipbuilders have to prove that applying extrapolation procedures based on the measured in situ quantities the established horsepower will produce the design speed of the ship without any problems. Especially for new designs, the usual way to make safe predictions is to perform towing tank tests at several conditions. Nevertheless, these tests present always a degree of uncertainty (owing to scale effects) which is associated to both the extrapolation of resistance as well as the propeller performance. Therefore, it is not sure that will lead on the safe side and the ship may operate at a lower speed. To improve such predictions CFD may be used as an alternative valuable tool. The aim of the present study is to show the possible benefits of such applications in order to avoid the undesired problems. The numerical method which is used has been developed at the LSMH of NTUA and it is hybrid, in the sense that solves the RANS equations underneath a free-surface calculated by the potential flow solution. Computations have been performed for the case of a product carrier which could not fulfil the contractual obligations. In this respect, the influence of the change of displacement and trim are examined at two load conditions: full load and heavy ballast. In addition, an attempt is made to calculate the engine horsepower at a low speed in order to investigate the efficiency of a “low steaming” case.

2. THEORETICAL BACKGROUND

The present method solves the RANS under a fixe free-surface by adopting a block arrangement that permits the application of very fine grid resolutions in order to obtain as far as possible accurate results. If the examined hull has a bulbous bow (the case under consideration) a C-type grid is generated and defines the domain of Block *I*, as shown schematically in Fig. 1. Otherwise, Block (I) consists of a sequence of parallel transverse sections (H-O type). If there is a transom stern, two more blocks are introduced covering respectively the stern and the wake part of the computational domain. These H-O type Blocks are characterised as *II* and *III* in Fig.2. In any case, the mesh generation is based on the conformal mapping of simple or doubly connected regions as described by Tzabiras & Kontogiannis (2011).

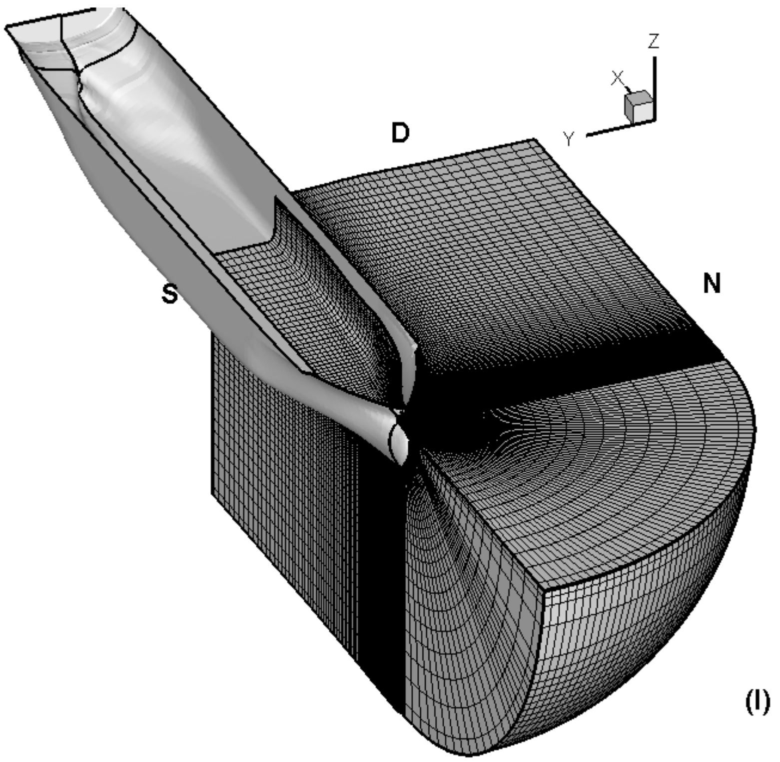

Fig. 1. C-type grid formation about a bulbous bow (Block I).

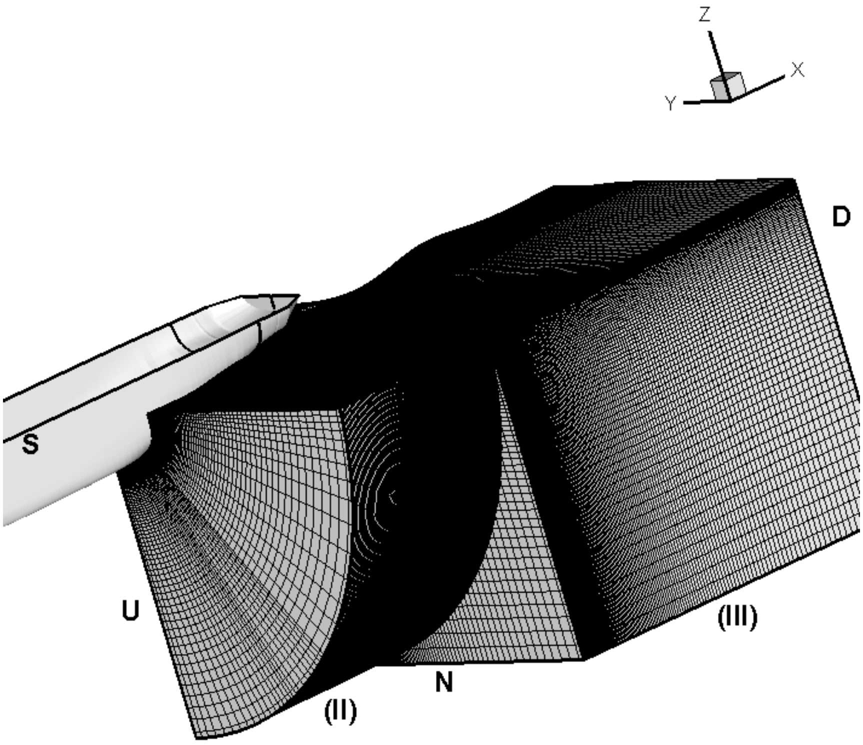

Fig. 2. H-O type grid in blocks *II* and *III*.

The RANS equations are solved using an orthogonal curvilinear system (x_i, x_j, x_l) with metrics (h_i, h_j, h_l) and velocity components (u_i, u_j, u_l). In this system the u_i-momentum equation reads:

$$\begin{aligned} C(u_i) = & -\frac{1}{h_i}\frac{\partial p}{\partial x_i} + \rho u_j^2 K_{ji} + \rho u_l^2 K_{li} - \rho u_i u_j K_{ij} - \rho u_i u_l K_{il} + \left(\sigma_{ii} - \sigma_{jj}\right) K_{ji} + \left(\sigma_{ii} - \sigma_{ll}\right) K_{li} \\ & + \sigma_{ij}\left(2K_{ij} + K_{lj}\right) + \sigma_{il}\left(2K_{il} + K_{jl}\right) + \frac{1}{h_i}\frac{\partial \sigma_{ii}}{\partial x_i} + \frac{1}{h_j}\frac{\partial \sigma_{ij}}{\partial x_j} + \frac{1}{h_l}\frac{\partial \sigma_{il}}{\partial x_l} \end{aligned} \quad (1)$$

In Eq.1 K_{ij} stands for the curvature, ρ for the fluid density, p for the pressure and σ_{ij} are the stress tensor components. The other two momentum equations are derived by cyclic permutation of indices (i, j, l). The convective part on the l.h.s. of Eq. 1 is written for any scalar variable Φ as:

$$C(\Phi) = \frac{\rho}{h_i h_j h_l}\left[\frac{\partial\left(h_j h_l u_i \Phi\right)}{\partial x_i} + \frac{\partial\left(h_i h_l u_j \Phi\right)}{\partial x_j} + \frac{\partial\left(h_i h_j u_l \Phi\right)}{\partial x_l}\right] \quad (2)$$

The stress tensor components are computed by adopting the eddy viscosity concept as:

$$\begin{aligned} \sigma_{ii} &= 2\mu_e e_{ii} = 2\mu_e\left[\frac{1}{h_i}\frac{\partial u_i}{\partial x_i} + u_j K_{ij} + u_l K_{il}\right] \\ \sigma_{ij} &= \mu_e e_{ij} = \mu_e\left[\frac{h_j}{h_i}\frac{\partial}{\partial x_i}\left(\frac{u_j}{h_j}\right) + \frac{h_i}{h_j}\frac{\partial}{\partial x_j}\left(\frac{u_i}{h_i}\right)\right] \end{aligned} \quad (3)$$

In Eq. 3 the effective viscosity μ_e is calculated according to the SST-k-ω turbulence model of Menter (1993) by solving two more differential equations, the one for the kinetic energy of turbulence k and the other for the specific dissipation rate ω:

$$\begin{aligned} & C(k) = \\ & \frac{1}{h_i h_j h_l}\left[\frac{\partial}{\partial x_i}\left(\sigma_k \mu_t \frac{h_j h_l}{h_i}\frac{\partial k}{\partial x_i}\right) + \frac{\partial}{\partial x_j}\left(\sigma_k \mu_t \frac{h_i h_l}{h_j}\frac{\partial k}{\partial x_j}\right) + \frac{\partial}{\partial x_l}\left(\sigma_k \mu_t \frac{h_i h_j}{h_l}\frac{\partial k}{\partial x_l}\right)\right] \\ & + G - \beta^* \rho \omega k \end{aligned} \quad (4a)$$

$$\begin{aligned} & C(\omega) = \\ & \frac{1}{h_i h_j h_l}\left[\frac{\partial}{\partial x_i}\left(\sigma_\omega \mu_t \frac{h_j h_l}{h_i}\frac{\partial \omega}{\partial x_i}\right) + \frac{\partial}{\partial x_j}\left(\sigma_\omega \mu_t \frac{h_i h_l}{h_j}\frac{\partial \omega}{\partial x_j}\right) + \frac{\partial}{\partial x_l}\left(\sigma_\omega \mu_t \frac{h_i h_j}{h_l}\frac{\partial \omega}{\partial x_l}\right)\right] \\ & + \frac{\gamma}{v_t} G - \beta \rho \omega^2 + 2\rho(1 - F_1)\frac{\sigma_\omega}{\omega}\frac{1}{h_j^2}\frac{\partial k}{\partial x_j}\frac{\partial \omega}{\partial x_j} \end{aligned} \quad (4b)$$

The generation term G of turbulence in Eqs. 4a, 4b is defined as:

$$G=2\mu_t\left[e_{ii}^2+e_{jj}^2+e_{ll}^2+\tfrac{1}{2}\left(e_{ij}^2+e_{il}^2+e_{jl}^2\right)\right] \tag{5}$$

The eddy viscosity μ_t as a function of k and ω as well as the constants and the blending function F_1 appearing on the r.h.s. of Eq. 4 and 5 are defined in the original paper of Menter (1993)

The numerical method to solve equations (1) and (4) is based on the control volume approach by adopting a staggered grid system (Tzabiras & Kontogiannis 2011). Second order approximation is applied for diffusion and spatial derivatives, while convection terms are modeled by the upstream second order scheme in conjunction to the min-mod limiter. A SIMPLE-type algorithm is applied to solve the pressure field. In all examined problems the numerical solution is completed by performing several sweeps of the domain until convergence is achieved. The wall function approach has been adopted to model the flow just above solid boundaries, while Neumann-type conditions are applied on the flow-symmetry planes. Since the free-surface is treated as a fixed boundary, the kinematic condition is applied for the velocity components and the pressure is determined through the Neumann condition normal to it. Dirichlet conditions are applied on the external boundary N (Figs 1 and 2) by calculating the velocity components and the pressure from the potential flow solution around the hull and beneath the specified free-surface. Open-type conditions are applied at the downstream plane D of block *III* (Tzabiras 2004), whereas in the three-block arrangement of Figs. 1 and 2 the variables on the matching planes of blocks *II* and *III* are calculated by linear interpolations. The solution is completed firstly in block *I* while blocks *II* and *III* are solved simultaneously. Self-propulsion simulations are performed regarding the propeller as an actuator disk with a sinusoidal circulation distribution along the blades. Body forces are taken into account only in the axial flow momentum equation and their longitudinal variation follows the exact propeller geometry as described by Tzabiras (1997), (2004). The prediction of the propeller performance is based on a theoretical open water test and the employment of *Wageningen B-Series* (Tzabiras 1996).

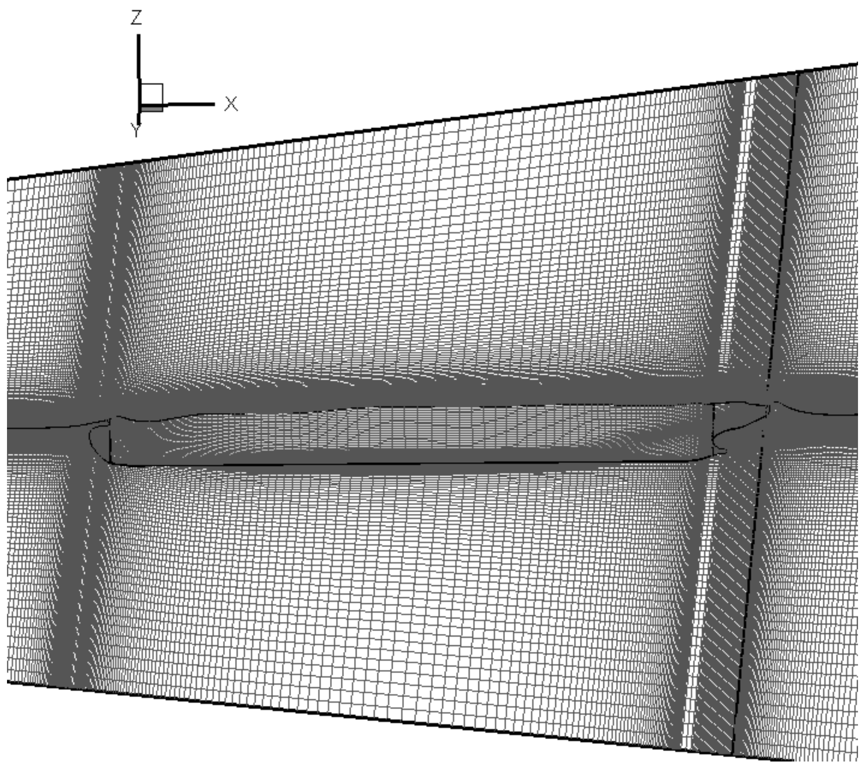

Fig. 3. Panel arrangement on the hull and free-surface for performing potential flow calculations.

The computation of the free-surface by the potential flow solution is made by applying the non-linear panel method of Tzabiras (2008). The Laplace problem is solved by the standard Hess & Smith (1968) method, distributing quadrilateral panels on the real surface and the ship hull. A typical example of panel arrangement is shown in Fig. 3. An iterative Lagrangian-Eulerian algorithm is performed to calculate the final free boundary and the procedure stops when both the dynamic and kinematic conditions hold. The code can calculate variable dynamic trim and sinkage conditions past conventional and catamaran vessels.

3. TEST CASES

The described method has been applied to calculate the resistance and propulsion characteristics of a real Chemical/Product Carrier (IMO type 2) 20,000 DWT. The main characteristics of the ship are: L_{OA}=150m, Breadth=23.20m and Depth=13m. A controllable pitch (CPP) propeller with diameter D=4.250 m was selected to move the ship at the service speed pf 14 Knots. Computations were performed for five typical loading conditions FL1, FL2, FL3, BL1 and BL2 a shown in Table 1. Condition FL1 corresponds to the full load departure, FL2 to the sea trials, FL2 as FL1 to investigate the effect of trim, while BL1 and BL2 refer to heavy ballast departure with and without trim. The displacement and static trim angles give trough the hydrostatic curves the longitudinal position of the centre of gravity (LCG), which was introduced in the free-surface calculations in order to determine the dynamic trim in Table 1. The Froude number at the speed of 14 knots is equal to 0.187.

Table 1. Conditions of test cases at Vs=14knots.

	FL1	FL2	FL3	BL1	BL2
Disoplacement (KN)	25,980	23,105	25,980	15,982	15,982
Static trim angle (deg.)	0.584	0.080	0.080	1.413	0.080
Dynamic trim (deg)	0.601	0.043	-.119	1.433	0.004
(+ : trim by stern)					

In the potential flow computations performed to determine the free-surface geometry, about 43000 panels (depending on the case) have been used, where 3000 of them cover the hull and 40,000 the free boundary. In any case, the upstream boundary of the solution domain was placed at a distance of 0.7L_{OA} ahead the bow, the exit at 1.7 L_{OA} after stern, while the corresponding distances of the external line from the centre line (CL) were equal 1.2 L_{OA} and 2.75L_{OA}, respectively. A typical example of the calculated free-surface geometry about the hull is given in Figs. 4 and 5, corresponding to the full load condition FL3. In all cases the transom was treated as dry.

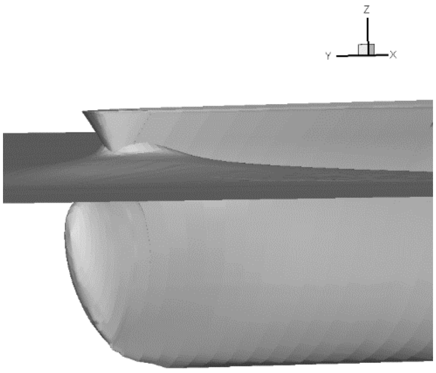

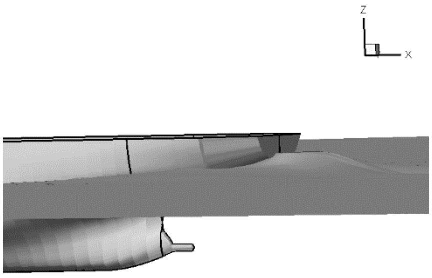

Fig. 4. Computed free-surface about the bow (left) and stern (right) in FL3.

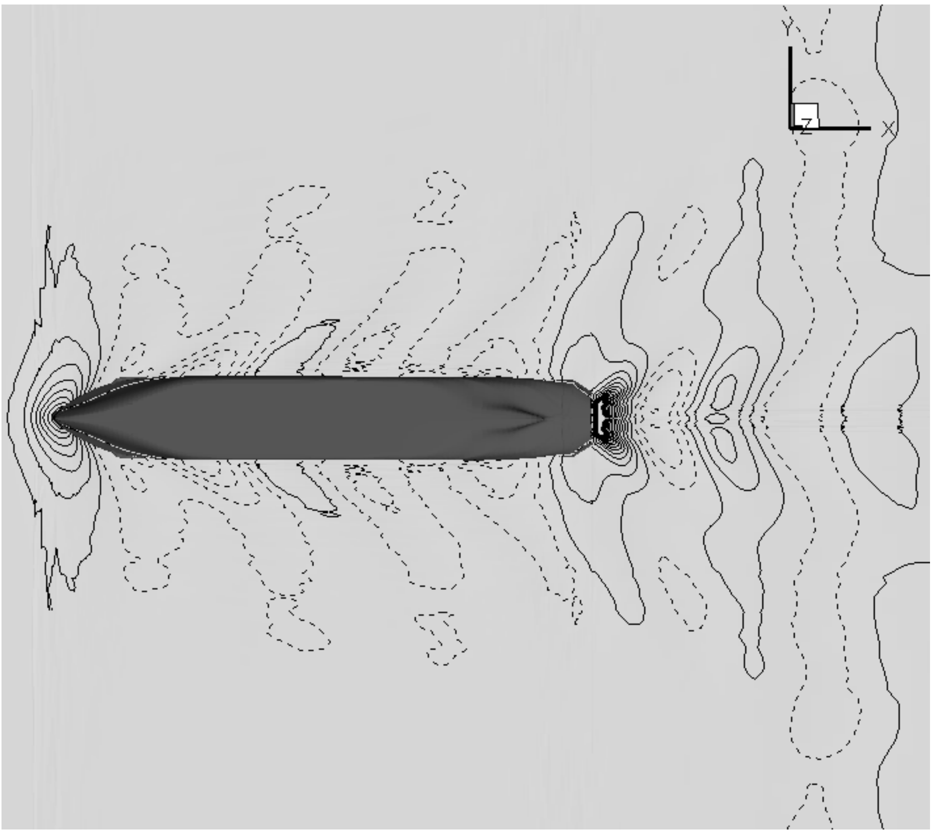

Fig. 5. Free-surface contours of condition FL3.

The same grid density and domain boundaries have been applied in all RANS computations under the specified free-surface geometries. The external boundary *N* in Figs.1 and 2 was placed at a distance of 0.4 L_{OA} from the *CL*. Block *I* extended up to 0.53L_{OA}, the upstream boundary of block *II* was located at 0.46 L_{OA} and of block *III* at 0.95 L_{OA}, while the distance of exit plane *D* of *III* from the stern of the ship was equal to 0.4 L_{OA}. In Table 2 the results from grid dependence tests are presented separately for the bow and stern regions. The grid densities are defined by three numbers, where the first stands for “transverse” sections the second for points around a section and the third for points in the normal direction. As observed, the differences of the calculated total resistance coefficients differ by 3-4% between the two finer grid resolutions. This degree of convergence was assumed as satisfactory for the purpose of the present comparative study and the finer grid consisting of 5.46M, nodes was employed in all evaluations. The non-dimensional resistance coefficients are derived through the integrated skin friction and pressure forces (*F* and *P*) according to:

$$C_F = \frac{F}{1/2\rho S v_S^2}, \; C_P = \frac{P}{1/2\rho S v_S^2}, \; C_T = C_F + C_P$$

In the above relations, *S* denotes the wetted surface of the hull which depends on the tested condition. The non-dimensional y^+ values at points adjacent to the wall where in the range 200-600. Numerical experiments have shown that this range is acceptable in the wall function approach when high Reynolds numbers are examined. In the particular case the Reynolds number based on L_{OA} was equal to $8.63x10^8$.

Table 2. Grid dependence tests for case FL3.

Nodes in BLOK(I)	$C_{TB}x10^3$	Nodes in BLOCKS (II)+(III)	$C_{TS}x10^3$
102x15x50	7.102	101x15x50+43x25x50	4.927
204x30x100	4.884	201x30x100+86x50x100	3.486
306x45x150	4.697	291x45x150+127x75x150	3.339

The resistance and propulsion characteristics for the three conditions FL1, FL2, and FL3 are depicted in Tables 3 and 4, respectively. In order to calculate the engine horsepower and RPM the propeller performance was modelled according to the *Wageningen B-Series* with an expanded area ratio of 0.7, while the optimum pitch was calculated in each test. The measured SHP in sea trials was equal to 5328 KW. According to extrapolations of towing tank experiments and in order to have an adequate margin to face the real situation FL1 as well as rough weather conditions, the selected engine could produce a maximum of 5850 KW at 173 RPM. Evidently, the recorded situation during the sea trials has shown that this was a rather low margin (about 10%). By comparing the computed EHP values between FL1 and FL2 in Table 3 it is apparent that an increase in resistance of almost 15% would probably result to SHP higher than the established. This is verified in Table 4 by comparing the corresponding DHP values. It is, at first, noticeable that computations give a DHP about 2% lower than the measured, indicating that realistic results can be acquired with the applied method. Then, according to the numerical DHP results (6,117 KW) the engine horsepower should be increased at least by 5% implying that, otherwise, it is impossible to achieve the desired speed at full load. Unfortunately, this drawback was verified in reality after the delivery of the ship.

Between FL1 and FL2, different values for the nominal wake fraction w_N, the effective wake fraction w_E and thrust deduction t are found. On the other hand, the propeller characteristics P/D, K_T, K_Q and η_P do not show substantial variations. Condition FL3 was examined theoretically in order to study the influence of the trim on resistance and propulsion parameters at full load. Due to the different wave formation around the ship, a slight difference in the wetted surface is observed. The friction and pressure coefficients are higher in the trimmed condition, resulting to a slightly higher EHP by 1.6%. However, this situation changes in self-propulsion where practically equal DHP values are predicted. Although these results lie probably within the range of the numerical uncertainty, a slight change of the thrust deduction factor due to the differences between the stern flow-fields seems to be responsible for this effect. Anyhow, the computed results show that there are no essential differences between the trimmed and zero-trim conditions which is in accordance to the ITTC regulations that require the sea trials to be performed at even keel.

Table 3. Resistance characteristics at full load, Vs=14knpots.

	FL1	FL2	FL3
C_Tx10^3	3.408	3,155	3.339
C_Fx10^3	1.552	1.534	1.530
C_Px10^3	1.856	1.622	1.809
$1-w_N$	0.673	0.657	0.673
R(KN)	4,880	4,270	4,800
EHP(KW)	3,511	3,070	3,454
S wetted (m**2)	5,394	5,095	5,416

Table 4. Self-propulsion characteristics at full load, Vs=14knpots.

	FL1	FL2	FL3
$C_T x10^3$	4.066	3.816	4.059
$C_F x10^3$	1.558	1.545	1.542
$C_P x10^3$	2.508	2.271	2.517
1-t	0.838	0.826	0.823
$1\text{-}w_E$	0.719	0.698	0.716
T(KN)	5,820	5,159	5,834
DHP(KW)	6,117	5,171	6,125
RPM	172	162	172
P/D	0.820	0.830	0.820
K_T	0.212	0.212	0.213
$10K_Q$	0.291	0.294	0.292
η_P	0.493	0.501	0.491
J	0.425	0.437	0.423

Trim effects are more pronounced when the heavy ballast conditions BL1 and BL2 are examined. The free-surface formation is substantially different at the bow and stern regions as shown in Figs. 6 and 7. As expected, the bow wave is higher at the bow in BL2 (zero trim) and lower at the stern region. In the trimmed condition BL1, the bow wave intersects the bulb.

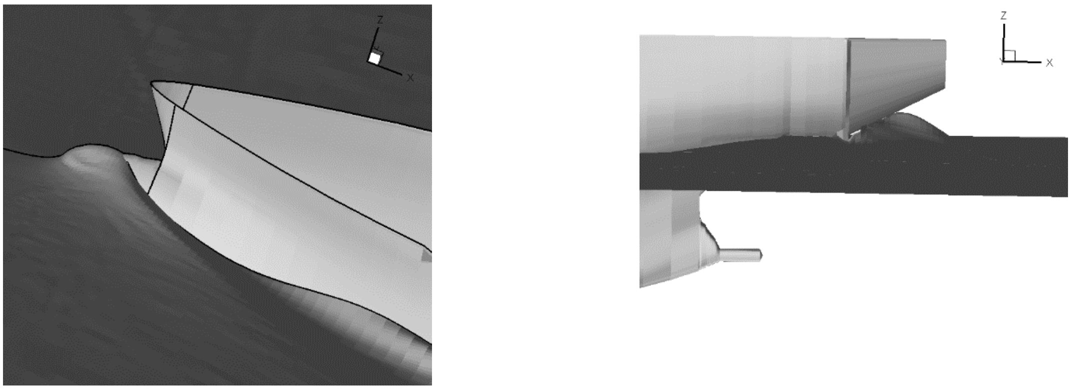

Fig. 6. Computed free-surface about the bow (left) and stern (right) in BL2 (zero trim).

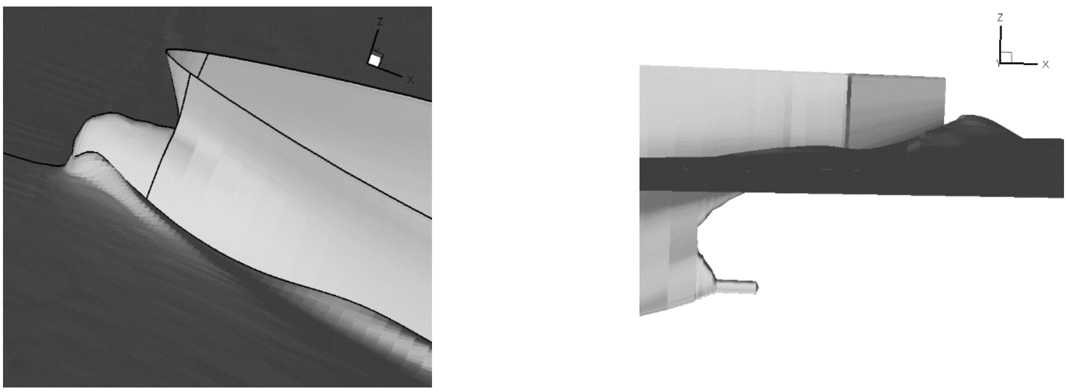

Fig. 7. Computed free-surface about the bow (left) and stern (right) in BL1 (trimmed).

Owing to the above free-surface differences the resistance and self-propulsion characteristics exhibit also substantial variations. Table 5 shows that the computed EHP with trim is almost 7% lower than the zero-trim condition BL2. This is mainly due to the lower pressure coefficient C_P which is influenced considerably by the wave formation at low drafts. In addition, a significant reduction of the nominal wake fraction $1\text{-}w_N$ is observed in BL2 showing a strong effect of the stern drafts. The propulsive parameters in Table 6 show that an opposite behaviour is observed for the propeller thrust and DHP. The thrust deduction is favourable in BL2 and consequently the thrust is almost equal in the two cases. However, a significant decrease of DHP of about 5% is observed in the zero trim condition. This performance leads to the remarkable conclusion that the simple towing-resistance and self-propelled conditions may present quite different trends.

Table 5. Resistance characteristics at ballast condition, Vs=14knpots.

	BL1	BL2
$C_T x10^3$	3.068	3.260
$C_F x10^3$	1.542	1.532
$C_P x10^3$	1.525	1.730
$1\text{-}w_N$	0.673	0.575
R(KN)	3,471	3,730
EHP(KW)	2,498	2,633
S wetted (m**2)	4,263	4,229

Table 6. Self-propulsion characteristics at ballast codition, Vs=14knpots.

	BL1	BL2
$C_T x10^3$	3.659	3.687
$C_F x10^3$	1.553	1.539
$C_P x10^3$	2.106	2.149
1-t	0.838	0.884
$1\text{-}w_E$	0.715	0.645
T(KN)	4,140	4,139
DHP(KW)	3,953	3,765
RPM	143	146
P/D	0.900	0.835
K_T	0.217	0.209
$10K_Q$	0.325	0.293
η_P	0.539	0.510
J	0.507	0.450

The last case which has been examined is concerned with the prediction of horsepower demands at the low service speed of 10 Knots. The full load condition FL1 has been examined and the calculated results for the resistance and self-propulsion characteristics are presented in Tables 7 and 8. The free-surface has been calculated again in this condition since the Froude number changes to 0.134 and the dynamic sinkage to .615 deg.. By comparing Tables 3 and 7, it is obvious that a significant reduction of EHP is apparent at the low speed, which is of the order of 70%. As expected, the pressure coefficient is lower at 10 Knots due to the reduction of the wave-making resistance, while the friction coefficient increases due to the Reynolds effect. The influence on the thrust deduction and effective wake parameters is less significant and as a consequence, the ratio of DHP values between Tables 4 and 8 is nearly equal to the ratio of EHP. Therefore, the energy saving from 14 to 10 knots can be approximated by comparing directly the resistance curves derived by towing tank experiments. Naturally this trend refers to the particular ship form.

Table 7. Resistance characteristics at full load, Vs=10knpots.

	FL1
$C_T x10^3$	2.965
$C_F x10^3$	1.603
$C_P x10^3$	1.362
$1\text{-}w_N$	0.669
R(KN)	2,157
EHP(KW)	1,108
S wetted (m**2)	5,372

Table 8. Self-propulsion characteristics at full load, Vs=10knpots.

	FL1
$C_T x10^3$	3.636
$C_F x10^3$	1.616
$C_P x10^3$	2.019
1-t	0.815
$1\text{-}w_E$	0.708
T(KN)	2,645
DHP(KW)	1,908
RPM	116
P/D	0.830
K_T	0.210
$10K_Q$	0.292
η_P	0.505
J	0.441

4. CONCLUSIONS

The performed numerical experiments about the particular product-carrier show that CFD may provide valuable information with regard to the variation of propulsive parameters at various load conditions. The predicted horsepower at the design speed is essentially unaffected by small trim changes at full load. This is not the case in ballast conditions where the EHP and DHP changes show remarkably opposite trends. In addition, the reduction of DHP at low speeds and full load can be predicted by the ratio of the corresponding EHP values, implying that the expected benefit can be calculated through the simple resistance curve. As far as the exact predictions are concerned, the computed propulsive parameters may be used as a guide to avoid undesirable situations, such as an unsuccessful engine selection.

References

1. Hess, J.L. & Smith, A.M.O., “Calculation of arbitrary flow about arbitrary bodies”, Prog. in Aeron. Sci. **8** (1968), 1-138.
2. Menter, F., “Zonal two equation turbulence models for aerodynamic flows”, 24th Fluid Dynamics Conference, AIAA, paper no 93-2906, Orlando, Florida, 1993.
3. Tzabiras, G.D., 1992, “ A numerical investigation of Reynolds scale effect on the resistance of bodies of revolution”, Ship Technology Res., **39** (1992), 28-44.
5. Tzabiras, G.D., “A numerical study of actuator disk parameters affecting the self-propulsion of a tanker”, Int. Shipbuiding Progress, **1** (1996), 55-47.
6. Tzabiras, G.D., “A numerical study of additive bulb effects on the resistance and propulsion characteristics of a full ship form”, Ship Technology Res., **44** (1997), 98-108.
7. Tzabiras, G.D., “Resistance and self-propulsion simulations for a Series-60, c_B=0.6 hull at model and full scale”, Ship Technology Res.,**51** (2004), 21-34.
6. Tzabiras, G.D., “A method of predicting the influence of an additive bulb on ship resistance”, 8th International Conference on Hydrodynamics, pp. 51-65, Nantes, 2008.
7. Tzabiras, G.D. and Kontogiannis, K., “An integrated method for predicting the hydrodynamic performance of low c_B ships”, Computer Aided Design Journal, **4** (2010), 985-1000.

ASSESSMENT OF STRAIGHT AHEAD AND MANEUVERING FOR SURFACE COMBATANT 5415 VIA VISCOUS FLOW CODES

Irene S. Kefallinou and Gregory J. Grigoropoulos

National Technical University of Athens (NTUA), 9 Heroon Polytechniou str., 15773 Zografou, Greece

ABSTRACT

This paper presents the results obtained using a commercial viscous flow code to solve the flow around the surface combatant denoted as DTMB 5415, in straight ahead and 20 degree static drift conditions. The numerical calculations referred to the model sailing at a speed corresponding to a Froude of No 0.28,in calm water and they simulated the respective experimental arrangement in the towing tank. The estimated hydrodynamic components of X-force, Y-force and N-moment are compared with the respective quantities derived via model tests. An unstructured, trimmed, hexahedral mesh is employed in the discretization of the fluid domain, while the model is constrained in all degrees of freedom. The numerical approach uses the Reynolds-Averaged Navier-Stokes equations and employs the Volume-Of-Fluid (VOF) solver to properly describe the free surface. The effect of k-ε and k-ω turbulence models as well as grid size on the predicted values is presented and discussed.

Keywords: viscous flow, manoeuvring, 5415 DTMB, resistance estimation

1. INTRODUCTION

The accurate numerical prediction of the flow characteristics around the ship's hull has been a common issue in the marine hydrodynamics over the past decades with a number of different codes having been developed to address this issue.

Potential flow codes that estimate the wave-making resistance of a floating body have been widely used with much success and represent a valuable tool in predicting the wave resistance in different ship speeds. The most representative example lies in the parametric optimization process, where the small computational time addresses the successive estimation of the pressure forces for multiple geometries in very short time leading in the derivation of the best geometry with respect to the wave-making resistance.

But the lack of numerically estimating the viscous effects that form a major component of resistance especially in low Froude numbers and the need to observe and deepen the knowledge of the chaotic flow behaviour, has led in the development of viscous computational fluid dynamics codes (viscous CFD codes) that numerically solve the Navier-Stokes equations through approximate solutions. Thus, in macroscopic scale an estimation of the forces acting on the ship can be derived, similarly to the experiment, while in microscopic, if detailed enough, the formation of the boundary layer and of the vortices can be observed.

The flow characteristics are directly dependent on Reynolds number (Re) that represents the ratio of the inertial forces to the viscous forces. In high Reynolds numbers that are of practical use in marine hydrodynamics, the flow is turbulent. Turbulence is characterized by the superposition of a highly irregular and oscillatory velocity pattern upon an otherwise "smooth" flow (Newman,1977). These fluctuations result in a significant distortion of the mean flow field values (a term more used in RANS approach) – that is velocity and pressure, thus the proper evaluation of the flow characteristics relies heavily on the estimation of these fluctuations. The higher the Reynolds number the larger the size of the turbulent structures that are created in the flow regime. Under the viscous effects, these structures dissipate into smaller ones, resulting in the parallel existence of various scale turbulent structures at the same time within the flow. The higher the Reynolds number the greater the number of different scales. Furthermore, each structure imposes oscillation on the otherwise "smooth" velocity and pressure field that is higher as the structures grow in size.(Viola et al., 2013)

To be able to accurately describe the flow, each of these vortices must be captured by the grid size, so the spatial resolution must be high enough, meaning that the cell size must be smaller than the smallest turbulent structure, a length that depends on the flow characteristics. Similarly, to capture the smallest oscillations of the field, the time discretization must ensure a small enough time step. This problem could be approached with Direct Numerical Simulation (DNS) where the Navier-Stokes equations are directly solved on each node in the fluid regime. The drawback of this method is the extremely high computational cost even for low Reynolds numbers that makes this approach prohibited for the marine hydrodynamic problems.

Since the direct computation of the field is out of reach, modelling of the flow is the next step. The basic modelling approaches are based on, either the filtering of the turbulent structures by a physical length that represents the smaller, allowable by the grid, turbulent structure size and modelling the ones smaller than that by subgrid models – Large Eddy Simulation (LES) approach, or by time averaging the flow field and solve for the mean velocity and pressure field the so-called Reynolds-Average-Navier-Stokes approach (RANS), or by combining the above mentioned to the hybrid Detached Eddy Simulation (DES) approach. The most widely used due to the reasonable amount of computational cost and accuracy is the RANS approach and it is the one that is used in this paper.

To obtain the RANS equations, the Navier-Stokes equations for the instantaneous velocity and pressure field are decomposed in a mean value and a fluctuating component. To provide closure for the problem semi-empirical methods are introduced the so-called turbulence models. In the present study we investigate the effect of the two most widely used, the k-ε and the k-ω SST model with more results presented for the k-ε model.

2. STATE OF THE ART

A variety of different viscous CFD codes are in use today each based more or less on the above mentioned methods or improved versions of them. Presented here, are some of the most contemporary, with basic information regarding each of them.

IIHR, a department of the University of Iowa College of engineering, has developed a general-purpose viscous-flow CFD code. This code is a finite-difference solver, that solves the unsteady Reynolds averaged Navier-Stokes (URANS)/detached eddy simulation (DES) equations for semi-coupled two-phase flow. The turbulence modeling is achieved by blended k-ω/k-ε (BKW) or anisotropic Reynolds stress (ARS) models, and includes their DES (Xing et al., 2007) and wall-functions (Bhushan et al., 2009) options. A multi-block dynamic overset grid approach is used to allow relative motions between the grids for six degrees of freedom ship motions. The governing equations are discretized using node-centered finite difference schemes.

The Maritime Research Institute Netherlands (MARIN) has developed a viscous-flow CFD code that solves multiphase (unsteady) incompressible flows with the RANS equations, complemented with turbulence models, cavitation models and volume-fraction transport equations for different phases. The code is a finite volume solver and is currently being developed, verified and validated at MARIN (in the Netherlands) in collaboration with IST (Lisbon, Portugal), USPTPN (University of São Paulo, Brazil), Delft University of Technology, University of Groningen and recently University of Southampton. The code is targeted, optimized and highly validated for hydrodynamic applications, in particular for obtaining current, wind and maneuvering coefficients of ships, submersibles and semi-submersibles (Toxopeus et al., 2012).

Ecole Centrale de Nantes and CNRS have developed another solver available as a part of the FINETM/Marine computing suite, which is an incompressible unsteady Reynolds-averaged Navier-Stokes (URANS) method mainly devoted to marine hydrodynamics. This finite volume solver features several sophisticated turbulence models, apart from the classical two-equation k-ε and k-ω models, the anisotropic two-equation Explicit Algebraic Stress Model (EASM), as well as Reynolds Stress Transport Models, are available with or without rotation corrections. Wall-functions or low-Reynolds near wall formulations can be used. Hybrid LES turbulence models based on Detached Eddy Simulation (DES) are also implemented along with several cavitation models that are available in the code. The solver is based on the finite volume method to build the spatial discretization of the transport equations.(IIHR Report,2014)

Naval Surface Warfare Center Carderock Division has developed a solver built around OpenFOAM, an open-source, general-purpose CFD software tool-kit written in C++ and offers an extensive suite of RANS equations turbulence models including two-equation, isotropic (linear) and nonlinear eddy-viscosity models based on k-ε and k-ω families, and Reynolds-stress transport models. In the improved, developed version of this finite volume solver, a number of more contemporary RANS turbulence models is added such as the modified Wilcox' k-ω model, k-ω-based explicit algebraic Reynolds-stress models, and a Reynolds-stress transport model (RSTM) based on ω equation, along with a newer version of Menter's k-ω model. The solver employs a cell-centered finite-volume spatial discretization method that permits use of arbitrarily unstructured polyhedral meshes. (IIHR Report,2014)
STAR-CCM+, a commercial finite volume solver developed by CD-Adapco, is a general purpose viscous-flow CFD code that employs a number of tools for marine hydrodynamics. The code supports unstructured grids (face to face) and uses the finite volume method for the discretization of the integral form of the equations. The turbulence models available in STAR CCM+ are the Reynolds-Averaged-Navier-Stokes equations (RANS), Large Eddy Simulation (LES) and Detached Eddy Simulation (DES)-the hybrid RANS/LES modeling approach. Wall functions and low-Reynolds models are available. Turbulence modeling includes the standard Spalart-Allmaras, k-ε, k-ω turbulence models and variations of them, Reynolds Stress Transport and Smagorinsky Subgrid Scale Turbulence models. The code supports unstructured grids (face to face), overset meshing, and adaptive grid refinement among others.

3. GEOMETRY/MODEL SETUP

Model 5415 was conceived as a preliminary design for a Navy surface combatant ca. 1980. The hull geometry includes both a sonar dome and transom stern. The experiments were conducted in the towing tank facility at IIHR. The hull form used was the DTMB 5512, a 1:46.6 scale, 3.048 m long, fiber-reinforced Plexiglas hull, manufactured by the Naval Surface Warfare Center. This model is a geosym of the DTMB 5415, a 1:24.8 scale, 5.72 m model. The full-scale hull form is a preliminary design for the 5415 surface combatant for the US Navy. The model is un-appended except for bilge-keels, i.e., not equipped with skeg, shafts, struts, propellers, nor rudders.
The model is first assembled rigidly, constrained in all degrees of freedom and ballasted to the dynamic sinkage ($\sigma = 0.192 \times 10^{-2}L$) and trim ($\tau = -0.136^{0}$; bow down) corresponding to a straight-ahead towing at Fr = 0.28. The ship model was tested at static drift angle $\beta = 0°$ and 20° in calm-water condition. The Froude number 0.28 corresponds to the full-scale cruising speed of the vessel at 20 knots, meaning 1.531m/s in model scale. The corresponding model scale is Re $= 5.13 \times 10^{6}$, based on water temperature of 20° (NATO AVT-183, 2011).
The main particulars are listed on the next table.

Table 1. Main particulars

	Full-scale	DTMB 5415	DTMB 5512
Scale	1:1	1:24.83	1:46.6
L_{PP} (m)	142.0	5.72	3.048
L_{WL} (m)	142.18	5.7273	3.052
B_{WL} (m)	19.10	0.769	0.410
T_m (m)	6.16	0.248	0.132
∇ (m^3)	8472.0	0.5540	0.0086
C_B	0.506	0.506	0.506

Figure 1. Photographs of DTMB model 5512. The top view highlights the bilge keels. (NATO AVT-183,2011)

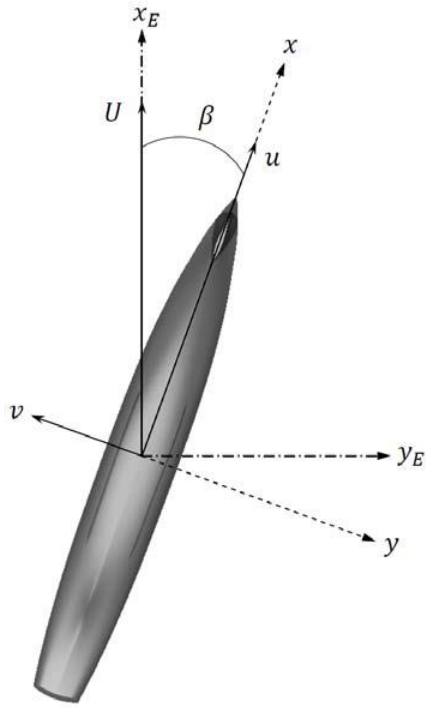

Figure 2. Static drift maneuver and coordinate system (NATO AVT-183,2011)

$x_E y_E$: Earth-fixed, inertial reference frame
xy: Ship-fixed, non-inertial reference frame moving relative to $x_E y_E$
Ship advance speed, $U = \sqrt{(u^2 + v^2)}$
Surge velocity, $u = U\cos\beta$
Sway velocity, $v = -U\sin\beta$
Drift angle, $\beta = -tan^{-1}\left(\frac{v}{u}\right)$

After having imported the geometry in STAR-CCM+ from an .iges file, the surface remesher tool is applied in order to optimize the quality of the imported surface and prepare it for the volume mesh. The unstructured grid is formed with the use of the trimmer model, where hexahedral cells are created on the previously retriangulated surface and are refined/ trimmed on the hull surface. This provides higher accuracy of the solution and at the same time reduces the computational cost by minimizing the required number of cells far from the body. To obtain a higher resolution of the boundary layer/near wall region, the prism layer model is implemented,where orthogonal prismatic cells are generated next to wall boundaries. This allows the control of the y wall distance that was taken as 7.0×10^{-4} m resulting in y+ between 30~40 for the most of the hull, apart from the stagnation and the separation points especially in the bow and the bilge keels. Volumetric controls are assigned within the region to control the size of the cells especially in the vicinity of the bow and the bilge keels to accurately capture the flow around their surface. As for the physics model, the implicit-unsteady scheme is employed along with the segregated flow model for the Dynamic-Fluid-Body-Interaction (DFBI). The coupling of the pressure and velocity equations is achieved by using a Rhie-and-Chow-type coupling combined with a SIMPLE-type algorithm. With the Volume Of Fluid (VOF) model – in use with the Eulerian Multiphase mixture for incompressible flow- each cell near the contact area of the water-air mixture consists of a volume fraction of both phases. This spatial distribution of the phases in any given time introduces the free surface in the simulation.

For the straight ahead static drift condition only the half of the geometry is modeled. The computational domain extends from 2.5Lpp aft of the stern, 1.5Lpp forward of the bow, 1.5Lpp from the centerline and 1.0Lpp from the baseline in both directions. The boundary in front of the ship, the side, top and bottom boundaries are assigned as velocity inlets, while the boundary behind the ship is a pressure outlet and symmetry plane the boundary that lies on the centerplane.

Figure 3. On the left the computational domain for the symmetrical problem

For the 20° static drift condition the computational domain has the same dimensions only that now the whole region is simulated due to the non-symmetry condition. Thus, the domain extends 1.5Lpp from the centerline in both directions. In order to avoid possible reflections from the boundaries and maintain the domain dimensions within limits, it was decided to keep the hull in 0° and have the flow entering the region with 20° angle in accordance with the instructions. With this configuration, the boundaries in front of the ship and on the starboard side are assigned as velocity inlets- the same applies for the top and bottom boundary- while the boundary behind the ship and on the portside, where the fluid leaves the region, are pressure outlets. The 5512 hull and bilge keels are simulated according to the experimental conditions and the ship is set in the fixed sinkage and trim in the earth-fixed coordinate system.

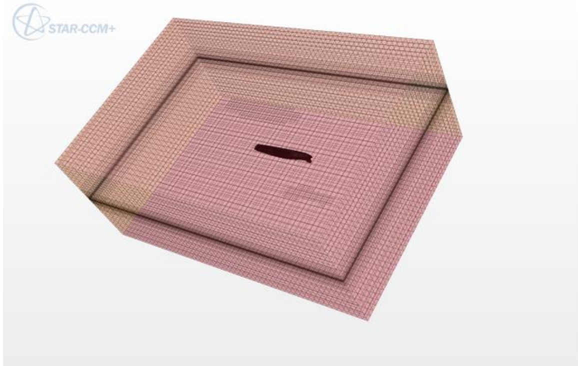

Figure 4. On the right the computational domain for the 20° condition.

A number of different grids were used to examine the behavior of the solution with the more representative of them being presented here. Time-step, number of iterations, order of temporal discretization, prism layer thickness and number of prism layers changed but had no significant effect on the solution only to the level of convergence, but regardless the choice of the models all simulations converged around a steady value. The results of four different grids for the straight ahead condition and of three different grids for the 20° static drift condition are presented.

For the straight ahead condition four different grids are generated. The dimension of the cells surrounding the hull is reduced by a step of 50% in each refinement with the rest of the domain far from the body slowly following the changes. The majority of the cells are located around the free surface and the bilge keels to capture as effectively as possible the fluid motion. The use of the symmetry plane allows the modeling of the half of the domain. The resulted grids consist of 2.5M – 3.0M – 3.5M - 4.4M cells.

The same grid configuration is used for the static drift 20° condition. The grid is refined by cutting down the size of cells by 50% in the area close to the hull, and placing the majority of the cells close to the free surface and bilge keels. Here, are presented the results from three different grids with 4.6M-5.7M-7.0M cells.

The slight change in the number of cells in each refinement is explained by the fact that most of the cells are already placed around the bilge keels and the free surface. The simulations run until the residuals were normalized and the computed forces were oscillating around a steady value.

The simulations were performed on two Dell Alienware systems -i7 at 3.2Gz- with 6-core hyper-threading INTEL processors of 6GB and 12GB RAM respectively. The simulation time varied from 40 to 120sec, with respect to the grid size. The k-ε simulations run mostly with 2nd order temporal discretization scheme and the k-ω with 1st order since time was a major parameter. Overall, the computational time varied from 2 up to 9 days.

4. NUMERICAL RESULTS

The calculated values for X-force,Y-force and N-moment (resistance in x-axis, resistance in y-axis and moment around z-axis) were non-dimensionalized as shown below. The comparison error is derived as the percent of the difference between CFD result and experimental data divided by the experimental value.

$$X = \frac{X_{hydro}}{\frac{1}{2}\rho U^2 LT} \qquad Y = \frac{Y_{hydro}}{\frac{1}{2}\rho U^2 LT} \qquad N = \frac{N_{hydro}}{\frac{1}{2}\rho U^2 L^2 T}$$

$$E(\%D) = \frac{S - D}{D} \times 100,$$

where D = EFD data and S = CFD simulation.

At first the simulations were performed with the k-ε turbulence model and the results are presented in the following tables.

Table 2. Straight ahead condition
Non-dimensionalized estimated X-Force.

*CFD Scheme/ EFD Test **k-ε***	*X*	
	×10^-3	*E%D*
EFD Data		
	-16.63	*-*
RANS (2.5M grid)	*-15.69*	*-5.7*
RANS (3.0M grid)	*-15.59*	*-6.2*
RANS (3.5M grid)	*-15.49*	*-6.8*
RANS (4.4M grid)	*-15.89*	*-4.5*

Table 3. Static drift 20° condition
Non-dimensionalized estimated Forces and Moments

*CFD Scheme/ EFD Test **k-ε***	*X*		*Y*		*N*	
	×10^{-3}	*E%D*	*×10^{-3}*	*E%D*	*×10^{-3}*	*E%D*
EFD Data						
	-28.57	*-*	*153.57*	*-*	*59.86*	*-*
RANS (4.6M grid)	*-28.43*	*-0.6*	*161.5*	*4.1*	*57.3*	*-4.3*
RANS (5.7M grid)	*-28.17*	*-1.4*	*154.09*	*0.3*	*57.44*	*-4.0*
RANS (7.0M grid)	*-28.3*	*-0.9*	*154.62*	*0.7*	*57.23*	*-4.4*

Regarding the straight ahead condition as seen from the results, the comparison error fluctuates between -4.5% and -6.8%. All results predict lower X-Force from the experimental values, nevertheless it is difficult to assume convergence since the results maybe around the same values but these values seem to be be grid dependent.

For the static drift 20° condition, results show a different behaviour. From the coarser grid(4.6M cells) the comparison error seems to be within acceptable limits (<5%) and with grid refinement values are confined within specific values. X-Force converges fast followed by Y-Force, while N-moment retains an error around 4%. Due to the peculiarity of the specific condition simulated, small fluctuations of the calculated results are assumed acceptable and that grid independence is achieved.

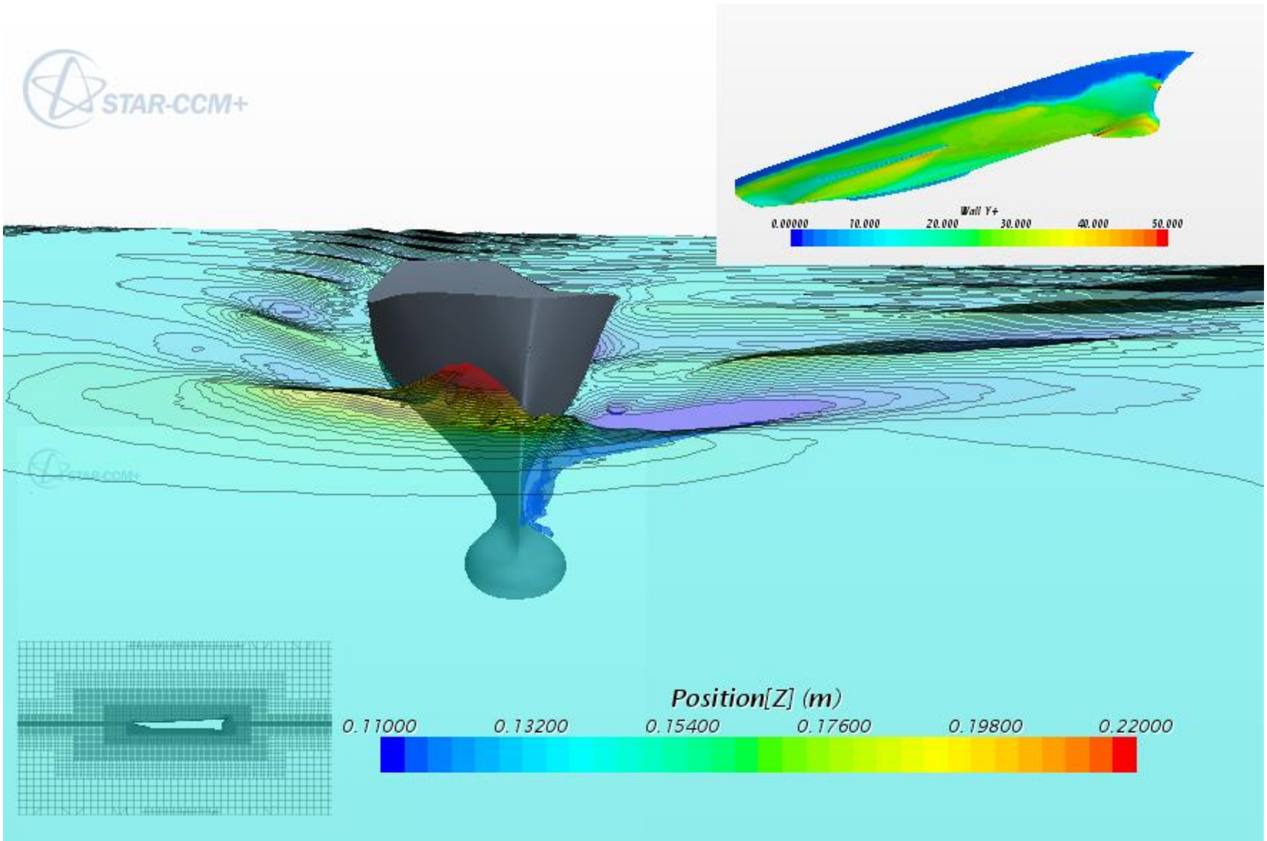

Figure 5. Scalar scene for the 20° static drift condition. On the top right wall y+ distance and on the bottom left mesh scene. All scenes refer to the 7M grid.

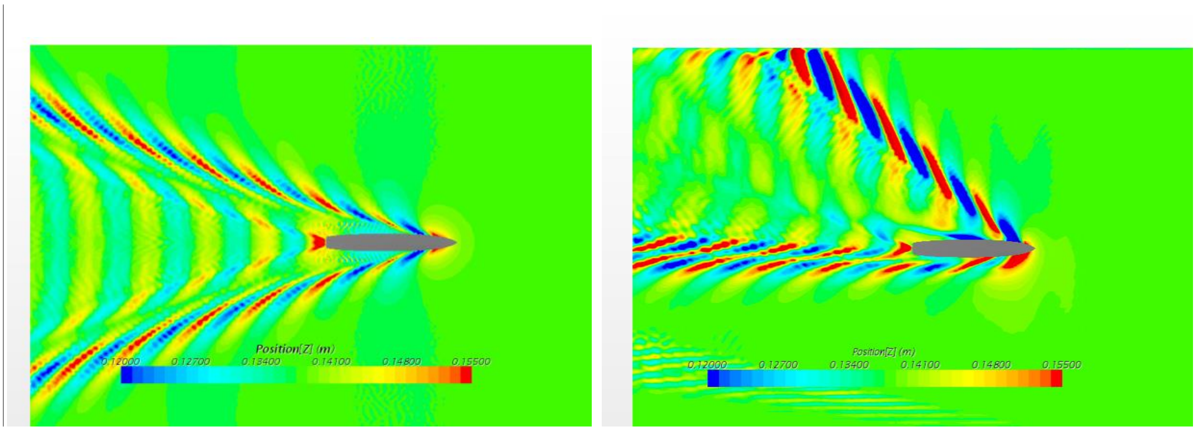

Figure 6. On the left free surface elevation for the straight ahead condition and on the right similarly for the 20°.

The fail of convergence in the straight ahead condition led to a further investigation of the phenomenon. Thus, the k-ω SST model, as the second more popular turbulence model was employed, in an attempt to obtain results that could be different from the ones derived with the k-ε model. The mesh remained the same in every test case so as the physics conditions. The only difference was at the turbulence model and the temporal discretization scheme (1st order from 2nd) that affected the time step (twice the initial value) and the number of iterations (more iterations than in previous case) in order to provide the appropriate conditions for convergence within reasonable limits in terms of computational time.
For the straight ahead condition all four cases were reproduced and the results are summarized in the next table.

Table 4. Straight ahead condition
Non-dimensionalized estimated X-Force.

*CFD Scheme/ EFD Test **k-ω***	*X*	
	×10^{-3}	*E%D*
EFD Data		
	-16.63	-
RANS (2.5M grid)	*-17.16*	*3.2*
RANS (3.0M grid)	*-16.8*	*1.0*
RANS (3.5M grid)	*-16.7*	*0.4*
RANS (4.4M grid)	*-16.73*	*0.5*

As it can be seen, the effect of the k-ω SST model produces significant changes in the estimated values. Convergence is achieved and the results are within desirable levels even for the coarser grid as it happened previously in the static drift 20° condition.
Due to the lack of time similar investigation did not come to fruition for the 20° condition. From the three meshes only one was simulated and that is the 5.7M cells grid. The results are presented in the next table.

Table 5. Static drift 20° condition
Non-dimensionalized estimated Forces and Moments

CFD Scheme/ EFD Test ***k-ω***	*X*		*Y*		*N*	
	×10⁻³	*E%D*	*×10⁻³*	*E%D*	*×10⁻³*	*E%D*
EFD Data						
	-28.57	*-*	*153.57*	*-*	*59.86*	*-*
RANS (5.7M grid)	*-29.87*	*4.5*	*144.2*	*-6.1*	*57.97*	*-3.16*

It seems that the k-ω model failed to provide similar accurate results as in the k-ε case. X-Force is over-predicted while Y-Force is predicted smaller than the experiment. The error for N-Moment however is smaller than in the previous cases. Though we cannot draw any definite conclusions, it seems that the k-ε model achieved good results for the 20° condition but failed to converge in 0°. With the k-ω model at least for the current geometry and conditions the results are reversed and convergence occurs in 0° but most probably not in the 20°.

The next images provide an overview of the flow behavior as it is captured by STAR CCM+ for the static drift 20° condition with the k-ε model. Ten axial velocity contour plots are presented from the 7M cells grid for x/LPP =0.06, 0.1, 0.12, 0.2, 0.3, 0.4, 0.6, 0.8, 0.935 and 1.0. The plots are from the left to right for each position.
At x/LPP =0.06 the separation in the leeward side and the formation of the sonar dome tip vortex on the top of the sonar dome is shown. The sonar dome vortex moves near the symmetry plane and then starts to move away from the hull to the leeward side. At x/LPP = 0.4 the position of the vortex is slightly shifted further from the hull while the formation of the windward fore-body keel vortex is observed.

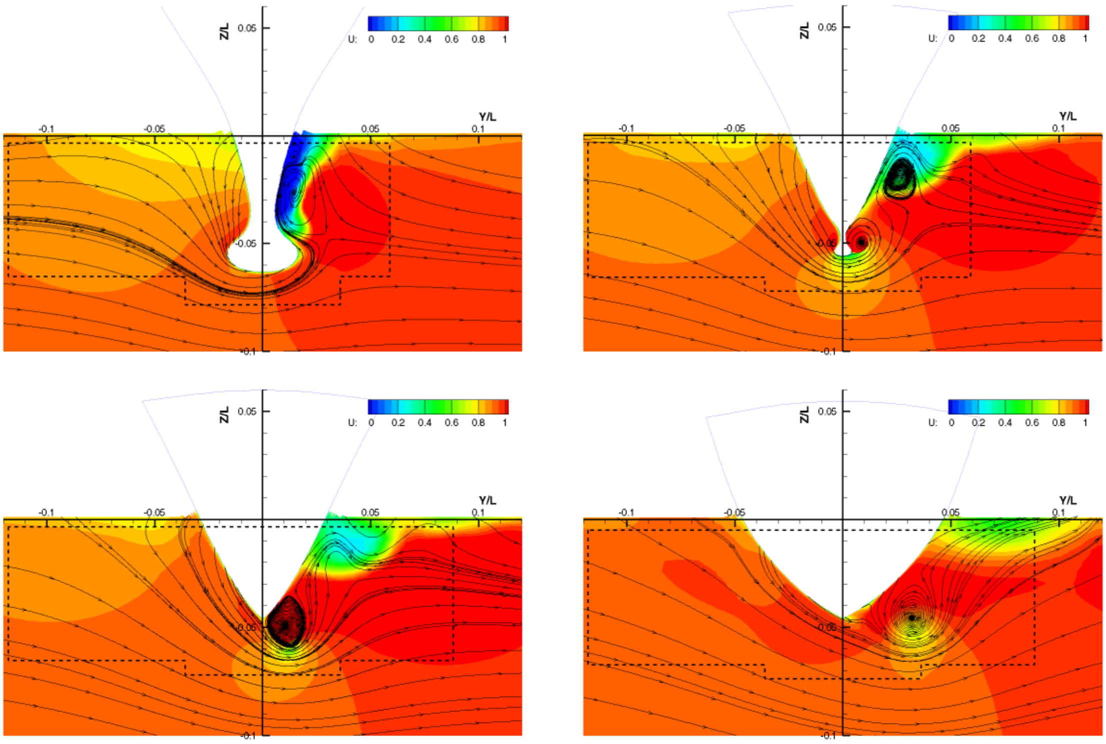

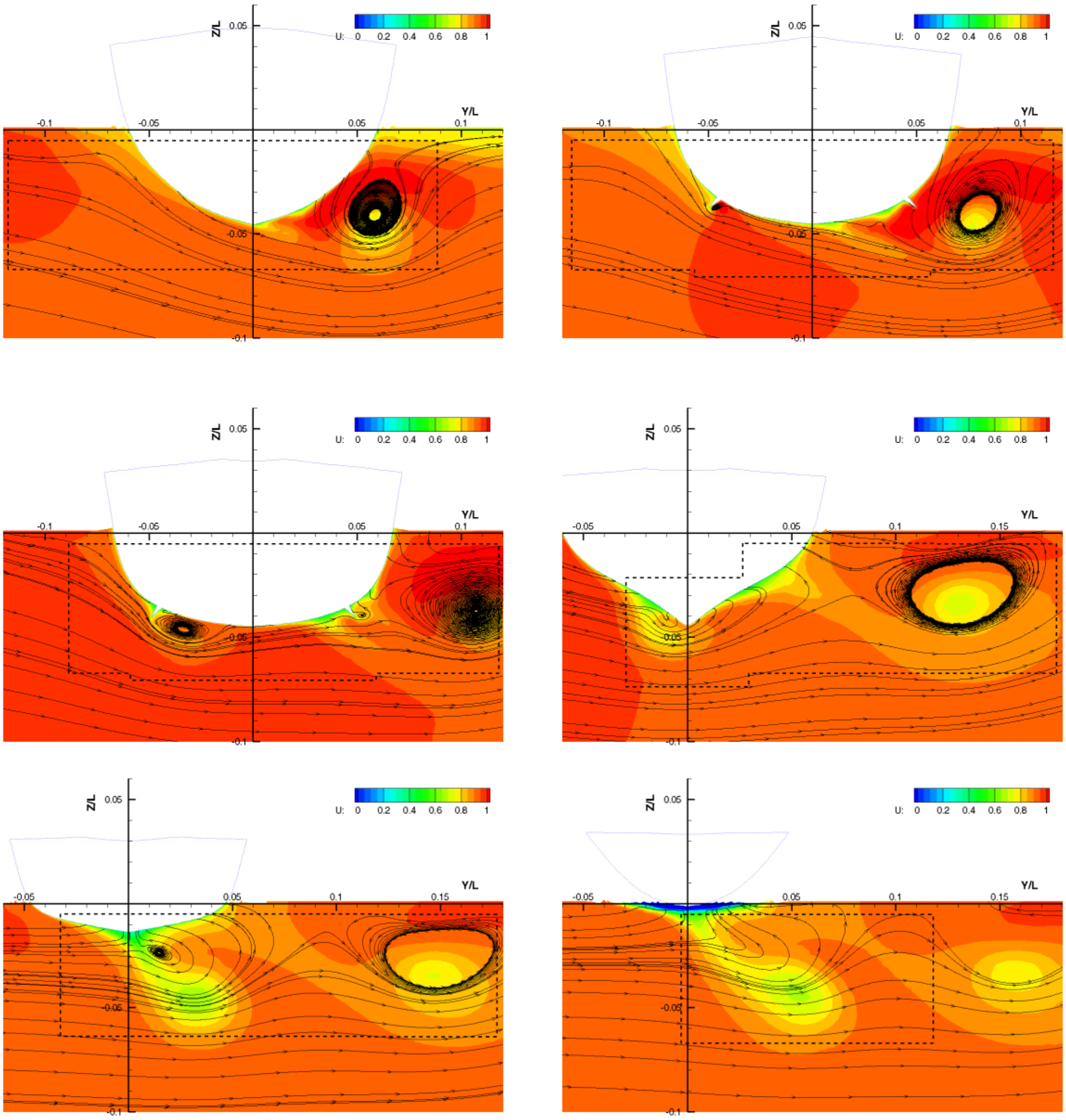

At x/LPP =0.6 both bilge keels have generated vortices that are not further noticed in the subsequent plots. The sonar dome vortex is still visible and the after body keel vortex is shown at x/LPP =0.935.

The results generally are in good agreement with the experimental results that are not presented here, since the purpose was to give a general idea of the code capabilities. The 5.7M cells grid overestimates the axial velocity when compared with the 7M cells grid, but the size and location of the vortices remain the same. The 3D analysis of the vortices however is not achievable by this grid size due to the low number of cells, so the fluid behavior is analyzed in a qualitative level by providing a general but accurate description of the flow.

5. DISCUSSION AND CONCLUSIONS

As mentioned above the choice of the turbulence model had a different effect in the straight ahead and the 20° static drift condition. The results converge in the 20° condition with the k-ε turbulence model but that does not occur in the straight ahead condition. Reversibly, the results converge in the straight-ahead condition with the k-ω model, but fail to do the same in the 20°. Simulations performed for similar geometries with the k-ε model in straight-ahead conditions did not result in the same behavior. Convergence occurred and grid independence was evident. The greater difference between these arrangements was the y-rotation and z-translation degrees of freedom (here the model is fixed in all degrees of freedom) and the existence of the bilge keels. Since the k-ω SST model is accepted as more appropriate for flows with separation (Wilcox, 1993) one could point that the bilge keels may be the reason for the non-convergence in 0°. Of course, the 20° condition also includes bilge keels and k-ω SST should also predict more accurate results but it is assumed that the peculiarity of the flow in this condition may be the reason for the diverse estimations with the two turbulence models.

As a tool for predicting calm-water resistance, it can be said that STAR CCM+ overall showed accurate results already from the coarser grids by providing error of less than 1.5% for the X-Force in both cases and below 4-5% for the Y-Force and N-Moment. The instability of the computed values in the straight ahead condition with the k-ε model seemed to be key factor of verifying the accuracy of a simulation. Since the result was unaffected by any change in grid and prism layer setup, time-step and number of iterations,changing the turbulence model was the next step.

Regarding the predicted flow characteristics, the formation, size and location of the vortices is computed accurately enough in a qualitative level. Bearing in mind the complexity of the flow and the low grid resolution, it can be said that the code provides an adequate analysis of the flow characteristics with relatively low computational cost and accurate resistance calculations, but in a quantitative level the flow is not resolved enough to provide an deeper view of the flow behavior.

ACKNOWLEDGEMENTS

The authors would like to acknowledge the partners of NATO STO AVT-183 Research Technical Group. The fruitful discussions with them stimulated our endeavor to derive reliable results using the available computational tools.

References

1. Newman, J.,N., Marine Hydrodynamics, The MIT Press,Cambridge,Massachusetts,1977
2. Viola, M., Bartesaghi, S., Della Rosa, S. and Cutolo, S., "On the use of CFD for the design of yacht hulls", Trans RINA, Vol 155,Part B2,Intl J Small Craft Tech, Jul-Dec 2013
3. Xing, T., Kandasamy, M., and Stern, F., "Unsteady Free-Surface Wave-Induced Separation: Analysis of Turbulent Structures using Detached Eddy Simulation and Single-Phase Level Set," Journal of Turbulence, Vol. 8, No. 44, pp. 1–35, 2007.
4. Bhushan, S., Xing, T., Carrica, P., Stern, F., "Model- and Full-scale URANS Simulations for Athena Resistance, Powering, and Seakeeping, and 5415 Maneuvering," Journal of Ship Research, Vol. 53 No. 4, pp. 179–198, 2009.
5. Toxopeus, S. L., Atsavapranee, P., Wolf, E., Daum, S., Pattenden, R. J., Widjaja, R., Zhang, J. T. and Gerber, A. G. "Collaborative CFD Exercise for a Submarine in a Steady Turn", 31st International Conference on Ocean, Offshore and Arctic Engineering (OMAE), Rio de Janeiro, Brazil, July, 2012
6. S. Bhushan , H. Yoon , F. Stern, E. Guilmineau, M. Visonneau , S. Toxopeus ,C. Simonsen, S. Aram, S-E Kim , G. Grigoropoulos, K. Petterson and C. Fureby, "IIHR Report 2014"
7. STAR CCM+ User Guide 9.04,CD-ADAPCO, 2014
8. IIHR-Hydroscience & Engineering, The University of Iowa, "DTMB model 5415(5512) Static drift Test at β=20°", 2011
9. Patankar, S.,V., Numerical Heat Transfer and Fluid Flow, Hemisphere Publishing Corporation, New York, 1980
10. Wilcox, C.,D., Turbulence Modelling for CFD, DCW Industries, Canada,1993

PREDICTION OF ADDED POWER IN SEAWAY BY NUMERICAL SIMULATION

Vladimir Shigunov[1] and Volker Bertram[2]

[1] DNV GL, Brooktorkai 18, D-20457 Hamburg, Germany, Vladimir.Shigunov@dnvgl.com
[2] DNV GL, Brooktorkai 18, D-20457 Hamburg, Germany, Volker.Bertram@dnvgl.com

ABSTRACT

The paper describes a numerical approach to predict added power requirements in waves. An introduction describes the importance of this keystone technology for energy efficiency, addressing correct definition of operating point and sea margin, routing optimization, and hull performance monitoring. Added resistance, drift forces and moments due to waves are key input parameters for added power requirements. The 3d Rankine singularity method to compute them is described in detail. The method solves the problem in the frequency domain, linearizing wave-induced solution around the fully nonlinear steady flow. The added power software combines added resistance and drift forces and moments due to waves with wind forces and moments, calm-water manoeuvring forces and moments, rudder and propeller forces, propulsion and engine model and computes associated resistance and power as well as changes in ship propulsion in waves. The approach is demonstrated for a containership where predictions and full-scale data are compared.

1. INTRODUCTION

1.1.Why do we need computations of added power in waves?

Ships are traditionally designed (and optimised) for calm-water performance. For example, the "total resistance" according to ITTC (International Towing Tank Conference) procedures is the total calm-water resistance. However, in real life, ships operate most of the time in moderate seaways which reduce speed or increase power. Traditionally, seakeeping has been considered as (too) complicated for most design and operational purposes and the effect of seaways has been covered by employing global margins.

Seakeeping calculations have progressed over time and a variety of more or less sophisticated, more or less specialised methods is used today in industry, *Bertram (2012)*, *Bertram and Couser (2014)*. These methods are mostly applied for studies concerning safety (extreme loads, motions and accelerations) and comfort (motion sickness). More recently, there has been increased interest in added resistance (better: added power requirements) in waves in the context of energy efficiency:

- Performance monitoring – Hull and propeller performance monitoring systems for ships in service require corrections (a.k.a. normalization) of in-service conditions to reference conditions, *Bertram and Lampropoulos (2014)*. One of these corrections concerns converting the recorded condition to calm-water condition. Good correction schemes will lead to less scatter in performance monitoring and faster insight.

- Routing – Route optimization considers weather forecasts and added power requirements as function of seaway, speed and course. The usefulness of routing advice depends on the accuracy of the predicted seaways and the accuracy of the ship response (added power requirement as function of given seaway and operational parameters). Savings of "up to 8%" as given by some vendors appear doubtful if seakeeping methods are employed which have much higher margins of errors for added power in waves that the purported savings.

- Power margins and operability – Many textbooks give "sea margins" of 15% which are added to calm-water power requirements to select suitable propeller and engine in the design stage. Such power margins should depend at least on ship length, but are generally taken as universal "one-size-fits-them-all" values. Selecting power margins based on (simulated) seakeeping performance could avoid inefficient power excess as well as potential problems with operability for too low margins. Similarly, advance knowledge of added power requirements for given seaways could support a better selection of operating point, propeller and engine.

- Hull form optimisation – In their survey paper on ship hull optimization, *Hochkirch and Bertram (2012)* foresee: "More sophisticated seakeeping models, especially for added resistance in waves… Such computations, coupled with meta-modelling and initially using coarse meshes, may drift gradually into industry applications over the next decade." A recent case study indicates the potential for further fuel savings if performance in waves is considered in hull design, especially for bulk carriers and tankers. Two hull variants of a Handymax bulk carrier were investigated: one with a conventional bulbous bow, one with a rather straight bow profile. The assessment considered a typical trade and a simplified operational profile with two load conditions (fully loaded and in ballast) and two speeds (service speed and slow steaming). The design with the straight bow contour reduced average fuel consumption by 3%.

The aim of this paper is to describe some of the difficulties associated with the accurate prediction of added power requirements in seaways, raise awareness of important uncertainties and which of these uncertainties may be controlled or reduced by using advanced computational procedures.

1.2. Added resistance in waves – A simpler problem and yet unsolved

Added power in waves should consider more than just added resistance in waves (the time-average longitudinal force due to waves), namely added resistance due to manoeuvring forces compensating drift forces and yaw moment due to waves, as well as changes in propeller and engine efficiencies due to added resistance. However, added resistance in waves, particularly in shorter waves, is already a difficult problem in its own right.

The longitudinal force on the ship in a seaway is, at first order, a harmonically oscillating quantity. The time-average of the first-order force is zero. A non-zero second-order added resistance can be estimated using linear theory. Two main contributions appear:

Contributions due to the waves generated as a consequence of the ship's motions ("radiation")
Contributions due to reflection and distortion of the incident wave field ("diffraction")

Some methods omit contributions coming from diffraction. Other methods neglect contributions from ship motions, *Bertram and Couser (2014)*. Omission of terms can be justified for certain subsets of problems, e.g. very large ships in short waves, or slender ships in head seas. However, such approaches, derived for specific problems, are frequently used beyond their realm of applicability. Therefore we advocate using generalised methods which are applicable to a broad range of problems, for example, 3D numerical methods.

Various formulations of added resistance are used. Some formulations try to manipulate the basic formula to an analytically equivalent form, but one that is less sensitive to the numerical scheme employed. Others omit or curb terms that are known to be computed with large errors. The accuracy of computed added resistance depends on the accuracy of the (first-order) quantities used as input for the added resistance formulae employed (motions, wetted surface, etc.).

There are no simple design formulas to predict ship motions. However, analytical and semi-empirical formulas to estimate added resistance in waves have been proposed, e.g. *Faltinsen et al. (1980)*, *Kuroda et al. (2008)*, *Tsujimoto et al. (2008)*, *Alexandersson (2009)*, *IMO (2013)*. One of the oldest of these simple approaches dates back to *Kreitner (1939),* as employed by *ITTC (2005), Hansen (2011).* The temptation to use such simple approaches is understandable: with very little effort the desired quantity is obtained. However, the old adage applies: If something sounds too good to be true, it probably is. *Nabergoj and Prpić-Oršić (2007)* compared five of these simple approaches for a ro-ro vessel, with large scatter of obtained added resistance (factor of four between lowest estimate and highest estimate). *Perez Arribas (2006)* discusses various semi-analytical approaches and compares three against model tests for a ship in head waves. Added resistance results scatter by a factor 3. *Boom et al. (2008,2013)* compare a different set of empirical wave correction methods coming to the same conclusion: "The results were shockingly different". We tested the Kreitner formula for a containership comparing against computational simulations, finding differences of 20-110%.

2. NUMERICAL METHOD FOR ADDED POWER IN NATURAL SEAWAYS

2.1. Coordinate Systems and Motion Equations

The ship is assumed to sail in the direction north with the speed v_s; its heading deviates from the course by the drift angle β (positive clockwise). The main wave and wind directions are specified by angles β_e and β_w, respectively (0° for the waves and wind from the north, 90° from the east and 180° from the south).
The coordinate system is fixed to the ship with origin O amidship at the water plane and x-, y- and z-axes pointing towards bow, starboard and downwards, respectively (positive rotations and moments around the z-axis are clockwise). Rudder angle δ is positive to port.
Projecting the forces on the x- and y-axes and moments on the z-axis leads to the following equilibrium equations:

$$X_s + X_w + X_d + X_R + (1-t)T = 0, \tag{1}$$

$$Y_s + Y_w + Y_d + Y_R = 0, \tag{2}$$

$$N_s + N_w + N_d + N_R = 0, \tag{3}$$

X and Y denote force projections on the x- and y-axes, respectively. N denotes moments with respect to the z-axis. Indices s, w, d and R denote steady still-water hydrodynamic reactions, wind loads, drift loads due to waves and forces and moment due to the rudder; T is the propeller thrust and t is the thrust deduction factor. For the prediction of required power, the total average longitudinal force $X_s+X_w+X_d+X_R$ is relevant.

2.2. Still-Water Hydrodynamic Forces and Moment

The still-water hydrodynamic forces X_s, Y_s and moment N_s are calculated as

$$X_s = X'_s(\beta)\frac{\rho}{2}v_s^2 L_{pp} T_m,\quad Y_s = Y'_s(\beta)\frac{\rho}{2}v_s^2 L_{pp} T_m,\quad N_s = N'_s(\beta)\frac{\rho}{2}v_s^2 L_{pp}^2 T_m \tag{4}$$

The prime indicates a nondimensional coefficient. ρ is the water density, L_{pp} the length between perpendiculars and T_m is the draught amidship. The nondimensional coefficients were derived from steady CFD (computational fluid dynamics) computations; alternatively, steady-drift or planar-motion model tests can be used.

2.3. Wind Forces and Moment

Forces and moment due to wind are expressed as:

$$X_{\mathrm{w}} = X'_{\mathrm{w}}(\varepsilon)\frac{\rho_{\mathrm{a}}}{2}v_{\mathrm{w}}^2 A_{\mathrm{F}}, \quad Y_{\mathrm{w}} = Y'_{\mathrm{w}}(\varepsilon)\frac{\rho_{\mathrm{a}}}{2}v_{\mathrm{w}}^2 A_{\mathrm{L}}, \quad N_{\mathrm{w}} = N'_{\mathrm{w}}(\varepsilon)\frac{\rho_{\mathrm{a}}}{2}v_{\mathrm{w}}^2 A_{\mathrm{L}} L_{\mathrm{oa}}, \tag{5}$$

The prime indicates again a nondimensional coefficient. ε denotes the apparent wind angle of attack (measured from the ship centre plane, positive when wind is coming from port). ρ_a is the air density, v_w the apparent wind speed, A_F the forward projected area above the water plane, A_L the lateral plane area and L_{oa} the overall length of the ship. Aerodynamic coefficients $X'_{\mathrm{w}}(\varepsilon)$, $Y'_{\mathrm{w}}(\varepsilon)$ and $N'_{\mathrm{w}}(\varepsilon)$ were defined in model experiments; alternatively, CFD simulations or empirical data can be used.

2.4. Drift Wave Forces and Moment

The time-averaged wave drift forces X_d, Y_d and moment N_d in irregular waves are calculated using the spectral method, i.e. as

$$X_{\mathrm{d}} = 2\int_0^{\infty}\int_0^{2\pi} \frac{X_{\mathrm{d}}(u_{\mathrm{s}},\mu,\omega)}{\zeta_{\mathrm{a}}^2} S_{\zeta\zeta}(\omega) D(\mu)\,\mathrm{d}\omega\,\mathrm{d}\mu \tag{6}$$

(similarly for Y_{d} and N_{d}), where $X_{\mathrm{d}}(u_{\mathrm{s}},\mu,\omega)/\zeta_{\mathrm{a}}^2$ is the quadratic transfer function of the mean longitudinal drift force, assumed to depend on the longitudinal ship speed u_{s}, mean wave direction with respect to the ship centre plane $\mu = \beta_{\mathrm{e}} - \beta$ and wave frequency ω. ζ_a is the wave amplitude, $S_{\zeta\zeta}$ the wave spectrum and D the spreading function. The quadratic transfer functions $X_{\mathrm{d}}(u_{\mathrm{s}},\mu,\omega)/\zeta_{\mathrm{a}}^2$, $Y_{\mathrm{d}}(u_{\mathrm{s}},\mu,\omega)/\zeta_{\mathrm{a}}^2$ and $N_{\mathrm{d}}(u_{\mathrm{s}},\mu,\omega)/\zeta_{\mathrm{a}}^2$ were computed with the linear Rankine singularity method GL Rankine, *Söding et al. (2014)*. Alternatively, model tests can be used to compute quadratic transfer functions of wave drift forces.

2.5. Steering and Propulsion Models

The forces on the rudder are calculated as

$$X_{\mathrm{R}} = -L\sin(\alpha-\delta) - D\cos(\alpha-\delta), \tag{7}$$

$$Y_{\mathrm{R}} = L\cos(\alpha-\delta) - D\sin(\alpha-\delta), \tag{8}$$

L and D are lift and drag forces on the rudder, respectively. α is the angle of attack with respect to the surrounding flow. The moment around z-axis from the rudder is calculated as $N_R = -Y_R l_R$, where l_R is the lever of the rudder side force, measured from the main section.
The lift and drag on the rudder are calculated, respectively, as

$$L = C_{\mathrm{L}}(\alpha)\frac{\rho}{2}v_{\mathrm{R}}^2 A_{\mathrm{R}}, \quad D = C_{\mathrm{D}}(\alpha)\frac{\rho}{2}v_{\mathrm{R}}^2 A_{\mathrm{R}}, \tag{9}$$

A_R is the submerged projected rudder area, v_R the average inflow speed to the rudder. Rudder forces behind a working propeller were defined with a semi-empirical method from *Brix (1993)*; alternatively, model tests of CFD simulations can be used to compute lift and drag.
Propeller thrust is found from equilibrium in the x-direction, Eq.(1), and thrust deduction factor t; with known thrust, J is found from $T = \rho u_{\mathrm{a}}^2 D_{\mathrm{P}}^2 K_{\mathrm{T}}(J)/J^2$ using the usually known open-water propeller curve $K_T(J)$ and wake fraction w. For found J, K_Q is found from the open-water propeller curve $K_Q(J)$. Then the propeller rpm is found from $n = u_{\mathrm{a}}/(JD_{\mathrm{P}})$ and the required delivered power on the propeller is calculated as $P_{\mathrm{D}} = 2\pi nQ = 2\pi\rho n^3 D_{\mathrm{P}}^5 K_{\mathrm{Q}}(J)$. The open-water propeller curves were taken from model experiments; alternatively, CFD simulations or empirical data can be used.
An engine model is used to find available delivered power $P_{\mathrm{D}}^{\max}$ and compare it with the required delivered power P_D. For diesel engines, $P_{\mathrm{D}}^{\max}$ is a function of rotation speed n due to torque-speed limitations. If the exact torque-speed limitation dependency is unknown, the following approximation is used:

$$P_{\mathrm{D}}^{\max}(n) = P_{\mathrm{DM}}(n/n_{\mathrm{M}})^2, \tag{10}$$

P_{DM} and n_M are the installed MCR and the corresponding rotation speed, respectively.

2.6. Verification

For the assessment of fuel consumption in long-term operation, the following data are required: loading profile, speed profile, statistics of wind speed and directions, directional scatter tables of wind sea and swell, frequency spectra and angular distribution of wind sea energy and current speed and directions. Some of these factors are known, some can be assumed with sufficient accuracy, and some are rarely known. In the rather typical examples below, loading condition and forward speed (over ground) are known, wind speed and direction are based on observations, as well as the height and direction of wind sea and swell. Current speed and direction are unknown, as well as periods of wind sea and swell and wind sea spectra.

Fig. 14 compares measured added power for two sister post-panamax container vessels (▲ and ■) at design draught in bow-quartering waves with numerical computations by the described method (shown with lines). The range of computational results for each wave height corresponds to the variation of the periods of wind sea and swell, as well as their angular direction within the uncertainty of visual observations. Pierson-Moskowitz frequency spectra with $\cos^2$-angular distribution of wave energy were assumed for wind sea. Fig. 2 and Fig. 15 show corresponding results for beam and stern-quartering seaway, respectively.

The dispersion of observations and their deviations from numerical results can be explained by the influence of unknown current, uncertainty of wind speed and direction, height and direction of wind sea and swell, as well as deviations of the actual wave energy spectra from the assumed one.

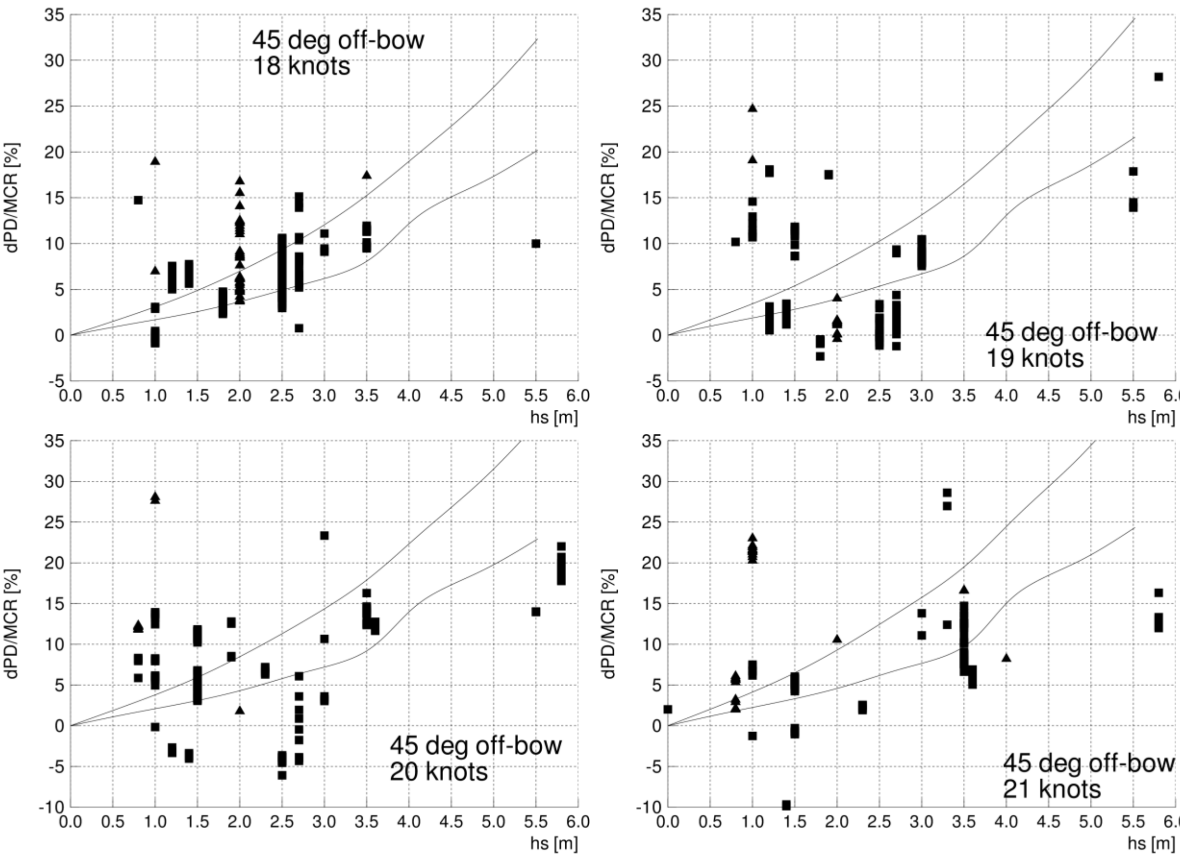

Fig. 14. Measured added power for two sister post-panamax container vessels (▲ and ■) vs. computations (lines) in bow-quartering seaway depending on significant wave height

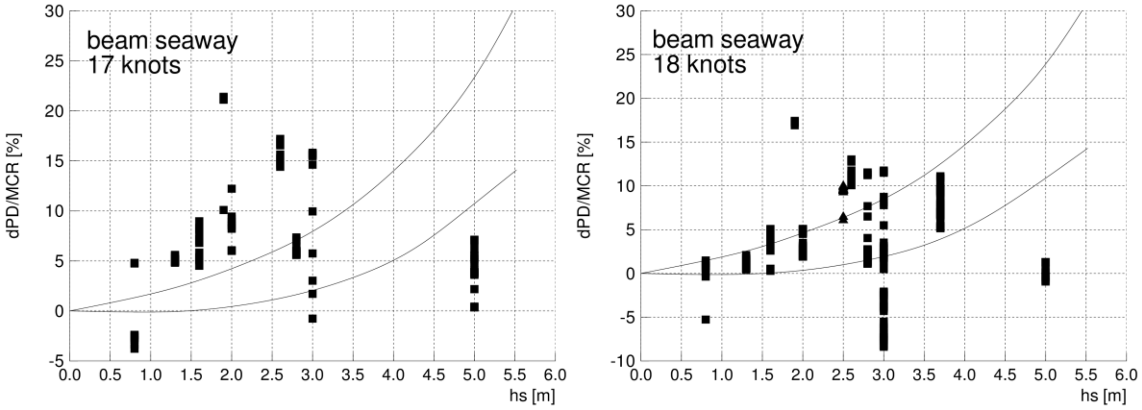

Fig. 2. As in Fig. 14, but for beam seaway

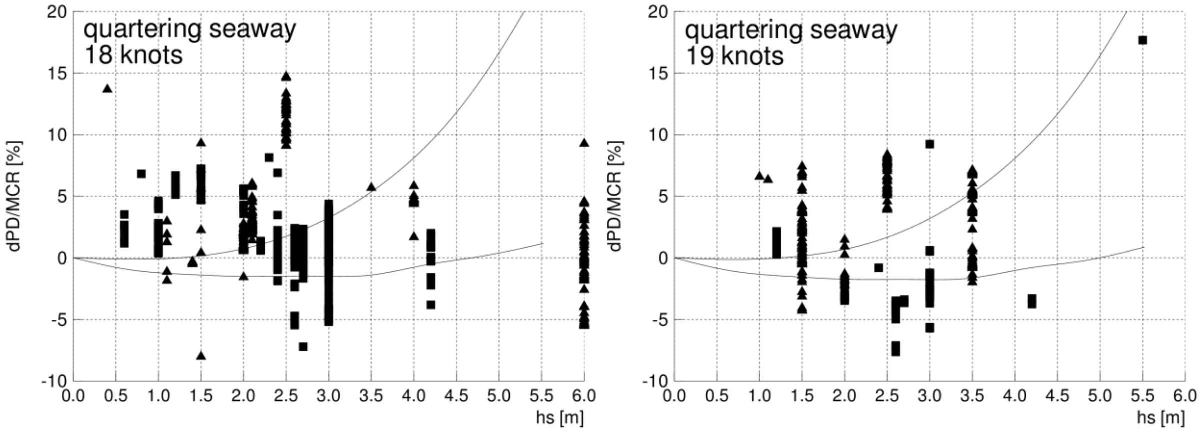

Fig. 15. As in Fig. 14, but for stern-quartering seaway

3. SELECTED RESULTS

Added resistance in waves depends significantly on wave period, Fig. 16. Therefore, average added resistance over all possible wave periods for a given significant wave height was used, with weighting factors corresponding to the frequency of occurrence of the seaway in the Pacific-Atlantic-crossings (GL PAX) scatter table, *GL (2014)*. Fig. 5 compares so obtained average added resistance with added resistance obtained in another wave climate, North-Atlantic winter scatter table, *IACS (2001)*. In all examples throughout this paper, the Pierson-Moskowitz seaway spectrum was used for frequency energy spectrum and $\cos^2$ distribution of wave energy with respect to the main wave direction was used as spreading function.

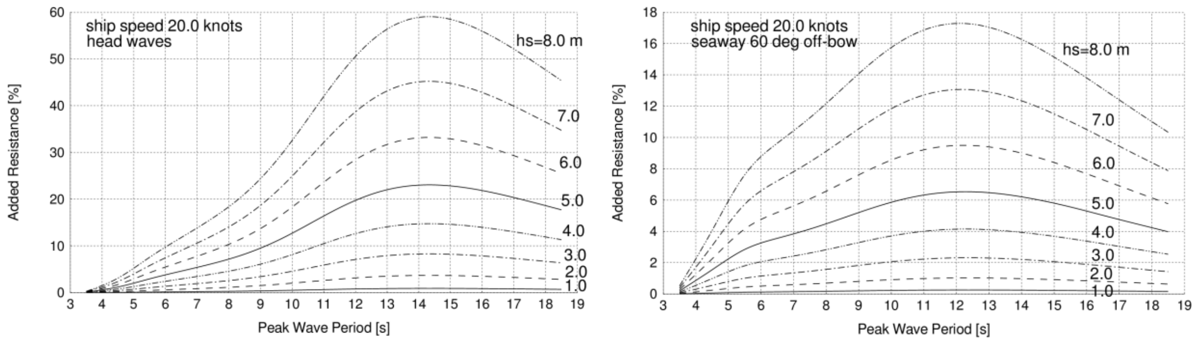

Fig. 16. Added resistance for a post-panamax container vessel (as percentage of calm-water resistance at design speed) vs. peak wave period and significant wave height in head waves (left) and waves 60° off-bow (right)

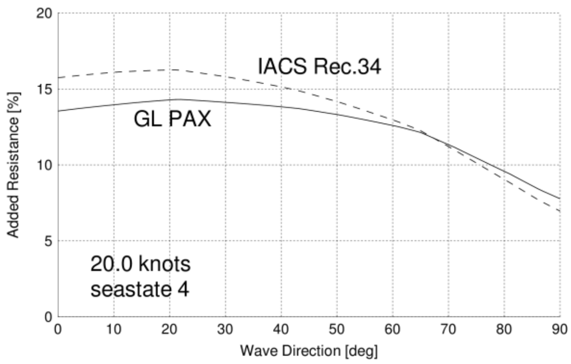

Fig. 5. Added resistance as percentage of calm-water resistance at design speed of a post-panamax container vessel at forward speed 20 knots in sea state 4, average over all wave periods in Nord-Atlantics winter wave climate (- - -), *IACS (2001)*, and in GL PAX wave climate (—), *GL (2014)*

Another assumption, required for long-term assessment, is the correlation between wave height and wind speed. For a fully developed seaway, significant wave height is equal to $h_s = 0.21 u_c^2 / g$, whereas according to ITTC recommendation, the dependency of significant wave height h_s [m] on wind speed v_w [m/s] can be approximated as

$$h_s = 0.115 v_w^{1.41}; \tag{11}$$

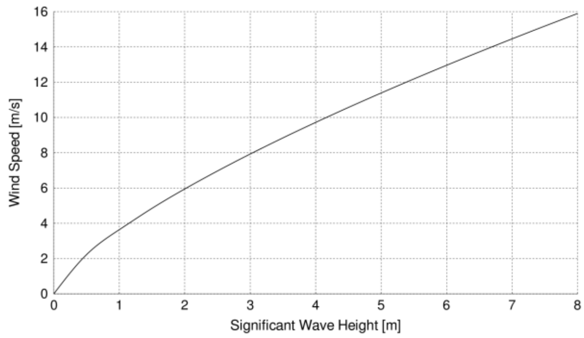

Fig. 17. Wind speed vs. significant wave height according to Eq.(11)

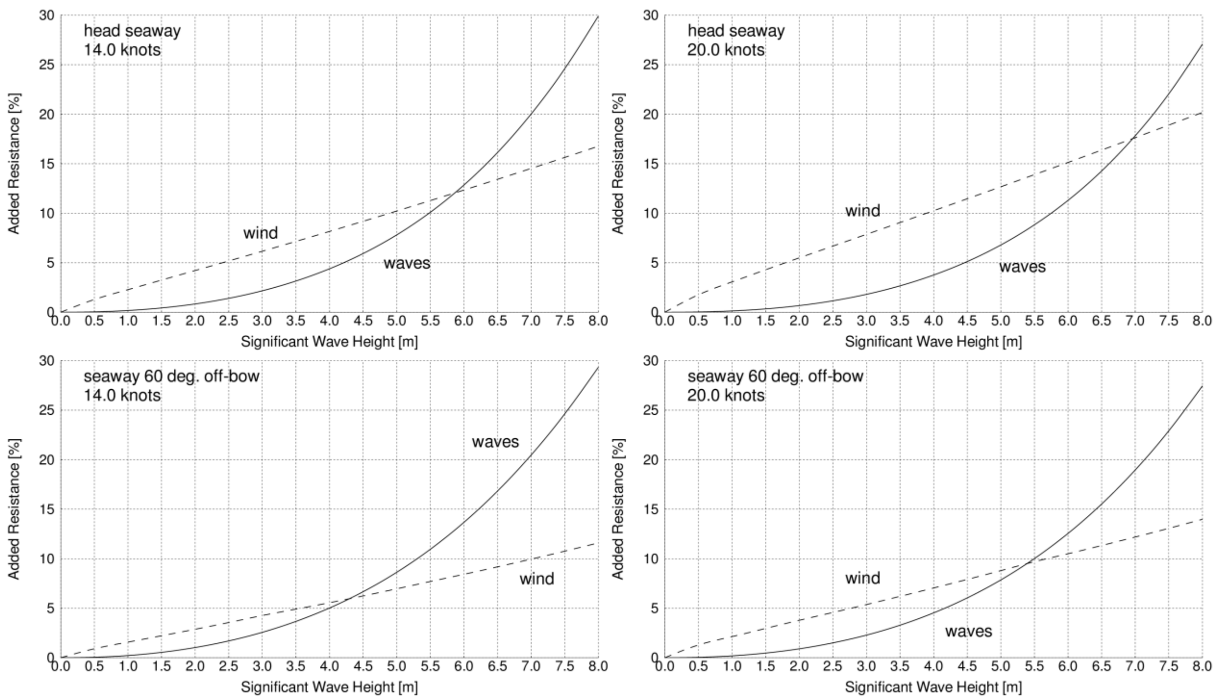

Fig. 18. Added resistance components as percentage of calm-water resistance at design speed for a post-panamax container vessel vs. significant wave height when wind speed is given by Eq.(11)

Eq.(11) was used in this paper, Fig. 6. Because wave drift forces are proportional to h_s^2 when spectral method, Eq.(6), is used, and wind forces are proportional to v_w^2, i.e. increase with significant wave height as $h_s^{1.42}$, added resistance due to waves increases quicker than added resistance due to wind with increasing wave height. This is illustrated in Fig. 18, which shows that wind resistance dominates in moderate sea states. Note that the dominating part of the wind resistance is the term proportional to the ship forward speed, $2v_w v_s$, which is large when the ship forward speed is large, Fig. 8.

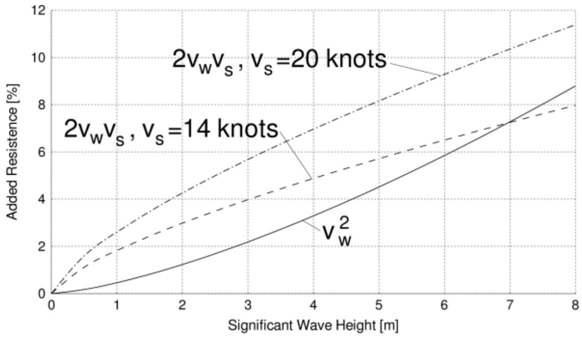

Fig. 8. Components of added resistance due to wind as percentage of calm-water resistance at design speed: terms proportional to v_w^2 (—) and $2v_w v_s$ (- - - and - · - · -)

Fig. 19 and Fig. 200 show contour plot of added resistance due to wind and waves, respectively, as function of significant wave height (radial coordinate) and mean wave direction (circumferential coordinate). Added resistance is shown as percentage of calm-water resistance at design speed, at two forward speeds, 14.0 (left) and 20.0 (right) knots. The dependencies on the wave direction are qualitatively different for the added resistance values due to wind and due to waves.

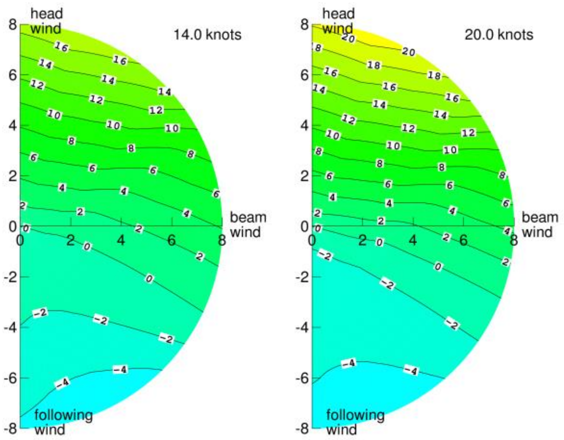

Fig. 19. Wind resistance as percentage of calm-water resistance at design speed

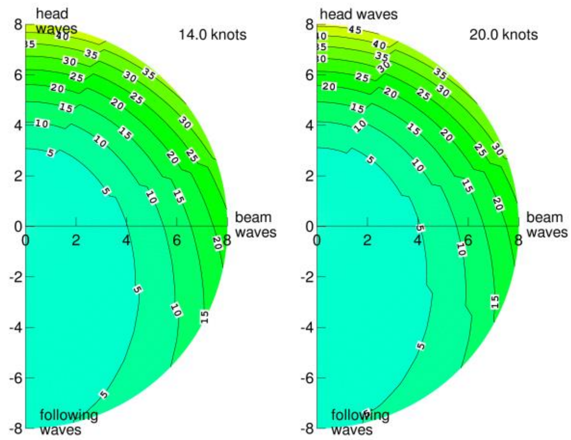

Fig. 200. Added resistance due to waves as percentage of calm-water resistance at design speed

Directional alignment of waves and wind is another uncertainty: whereas directions of wind waves deviate from wind direction due to Coriolis forces, addition of swell makes this alignment even more complex. Fig.11 illustrates that the shift between wind and wave directions is important for the added resistance, because it significantly influences the wind component of added resistance.

Fig. 122 shows rudder contribution to the total resistance, and Fig. 23 shows total resistance.

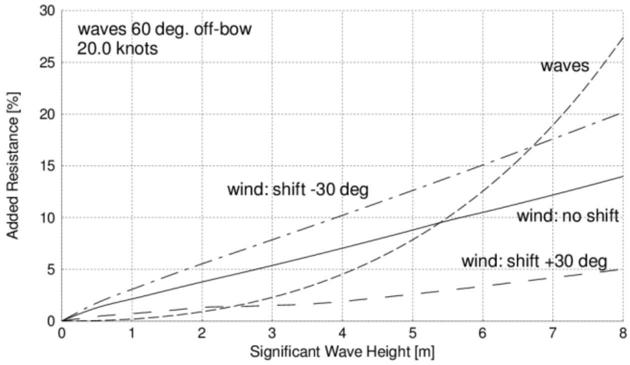

Fig. 21. Added resistance for a post-panamax container vessel vs. significant wave height taking into account shift of wind direction from wave direction

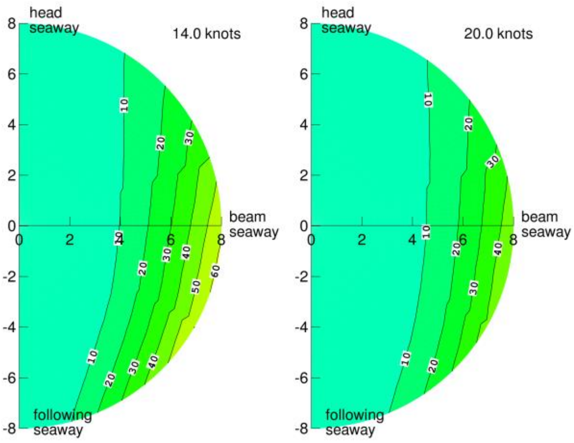

Fig. 122. Rudder resistance as percentage of calm-water resistance at design speed

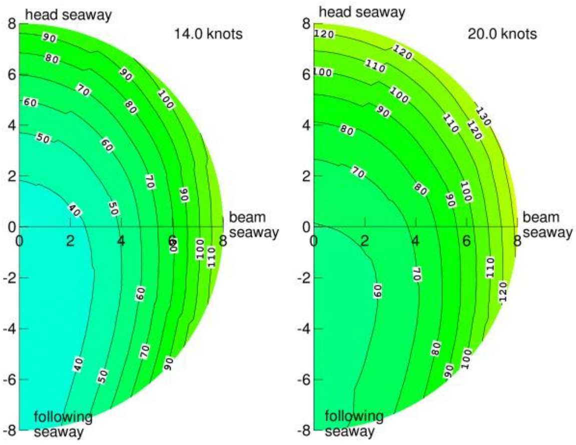

Fig. 23. Total resistance (calm-water, wind, waves and rudder) as percentage of calm-water resistance at design speed

For added power in seaway, not only resistance increase but also change of propulsion efficiency is important. Propulsion efficiency changes due to the change of propulsion point, propeller pitching and change of hull-propeller interaction in waves. Propeller pitching is relevant only in heavy sea, when fuel consumption is of lower priority. Change of hull-propeller interaction factors (thrust deduction and wake fraction) in waves has not been sufficiently studied to provide practical recommendations; thus hull efficiency is assumed in seaway the same as in calm water. Fig. 24 shows propeller efficiency η_0 as a function of seaway direction and wave height; Fig. 25 shows the corresponding variation of the required delivered power P_D.

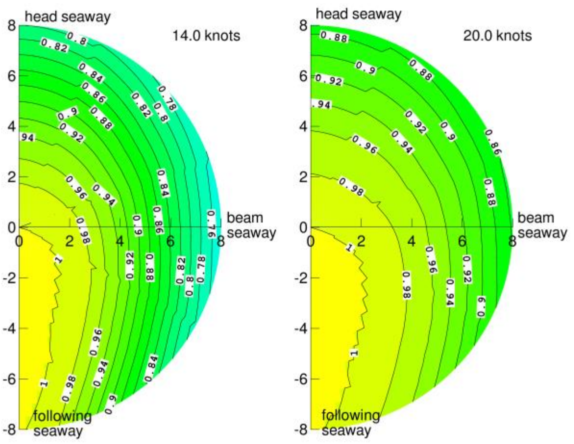

Fig. 24. Propeller efficiency η_0 in seaway as fraction of propeller efficiency in calm water

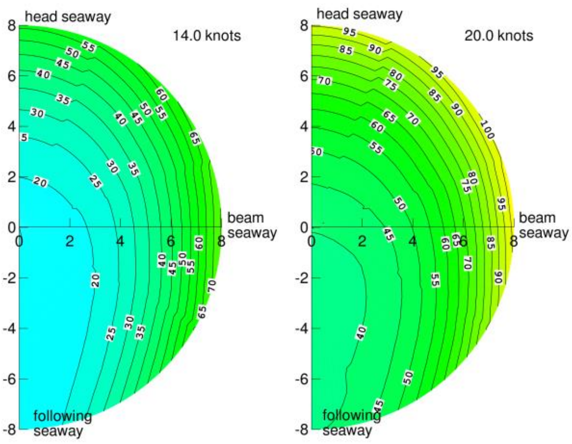

Fig. 25. Delivered power in seaway as % MCR

Finally, the influence of free drift was studied: the system of equations (1)-(3) was solved, for comparison, with restrained heading (denoted "fixed drift"), and compared with the usual solution with unrestrained heading (denoted "free drift"). Results show a minor increase in added resistance both due to waves and due to wind when heading is considered unrestrained. Note that free drift (and thus steering) increases added resistance also due to increased rudder resistance, Fig. 122.

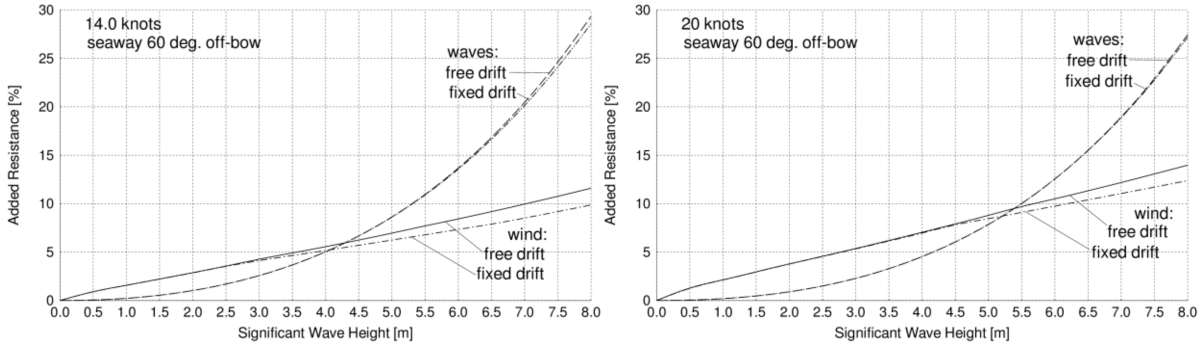

Fig. 26. Added resistance components of a post-panamax container vessel as fraction of calm-water resistance at design speed vs. significant wave height from solutions with free and restrained drift

4. LESSON LEARNT

The main conclusions so far are:

- Wind contributes more than waves to added resistance for low to moderate sea states.
- Ships encounter maximum resistance going against oblique waves and wind.

The quantification of the various contributions to added power requirements in waves is expected to be very useful in the future, both for qualitative understanding of the mechanisms and in support of better ship design and operation.

References

ALEXANDERSSON, M. (2009), *A study of methods to predict added resistance in waves*, Master Thesis, KTH, Stockholm
http://www.kth.se/polopoly_fs/1.151543!/Menu/general/column-content/attachment/Alexandersson.pdf

BERTRAM, V. (2012), *Practical Ship Hydrodynamics*, Butterworth & Heinemann, Oxford

BERTRAM, V.; COUSER, P. (2014), *Computational methods for seakeeping and added resistance in waves*, 13th Conf. Computer and IT Applications in the Maritime Industries (COMPIT), Redworth, pp.8-16
http://www.ssi.tu-harburg.de/doc/webseiten_dokumente/compit/dokumente/compit2014_redworth.pdf

BERTRAM, V.; LAMPROPOULOS, V., *A hull performance monitoring model for energy efficient operation*, 6th European Conf. Production technologies in Shipbuilding (ECPTS), Hamburg

BOOM, H.v.d.; HOUT, I.E. v.d.; FLIKKEMA, M. (2008), *Speed-power performance of ships during trials and in service*, SNAME http://www.marin.nl/web/Publications/Papers/SpeedPower-Performance-of-Ships-during-Trials-and-in-Service.htm

BOOM, H.v.d.; HUISMAN, H.; MENNEN, F. (2013), *New guidelines for speed/power trials level playing field established for IMO EEDI*, Hansa 150/4
http://www.hansa-online.de/sta-jip.pdf

BRIX, J. E. (1993) *Manoeuvring Technical Manual*. Seehafen Verlag, Hamburg

FALTINSEN, O. M.; MINSAAS, K. J.; LIAPIS, N.; SKJØRDAL, S. O. (1980), *Prediction of resistance and propulsion of a ship in a seaway*, 13th Symp. Naval Hydrodyn., Tokyo

GL (2014) *Guidelines to assess high-frequency hull girder response of container ships*, GL Rules for Classification and Construction. 1. Hull Structural Design Analyses. V. Analysis Techniques, DNV GL, Hamburg

HANSEN, S.V. (2011), *Performance monitoring of ships*, PhD Thesis, Danish TU, Lyngby
http://www.fam.web.mek.dtu.dk/dcamm05/DCAMM_report_S142.pdf

HOCHKIRCH, K.; BERTRAM, V. (2012), *Hull optimization for fuel efficiency – Past, present and future*, 11th Conf. Computer and IT Applications in the Maritime Industries (COMPIT), Liege, pp.39-49
http://www.ssi.tu-harburg.de/doc/webseiten_dokumente/compit/dokumente/compit2012_liege.pdf

IACS (2001) *Standard wave data*, Rec. No. 34, Int. Association of Classification Societies

IMO (2013) *Additional information on revision of ISO 15016:2002*, International Maritime Organisation, London, paper MEPC 66/INF.7

ITTC (2005), *Full scale measurements – Speed and power trials – Analysis of speed/power trial data*, Recommendations of the 24th Int. Towing Tank Conf., Edinburgh

KREITNER, J. (1939), *Heave, pitch and resistance of ships in a seaway*, Trans. Institution of Naval Architects 81

KURODA, M.; TSUJIMOTO, M.; FUJIWARA, T.; OHMATSU, S.; TAKAGI, K. (2008), *Investigation on components of added resistance in short waves*, J. Japan Soc. Naval Arch. and Ocean Eng. 8

NABERGOJ, R.; PRPIĆ-ORŠIĆ, J. (2007), *A comparison of different methods for added resistance prediction*, 22nd Int. Workshop Water Waves and Floating Bodies, Plitvice
http://www.iwwwfb.org/Abstracts/iwwwfb22/iwwwfb22_38.pdf

PEREZ ARRIBAS, F. (2007), *Some methods to obtain the added resistance of a ship advancing in waves*, Ocean Eng. 34/7, pp.946-955

SÖDING, H.; GRAEFE, A.v.; EL MOCTAR, O.; SHIGUNOV, V. (2012a), *Rankine source method for seakeeping predictions*, 31st Int. Conf. Ocean, Offshore and Arctic Eng. (OMAE), Rio de Janeiro

SÖDING, H.; SHIGUNOV, V.; SCHELLIN, T.E.; EL MOCTAR, O.; WALTER, S. (2012b), *Computing added resistance in waves – Rankine panel method vs RANSE method*, 15th Numerical Towing Tank Symp. (NuTTS), Cortona
http://www.uni-due.de/imperia/md/content/ist/nutts_15_2012_cortona.pdf

SÖDING, H.; SHIGUNOV, V.; SCHELLIN, T. E.; EL MOCTAR, O. (2014), *A Rankine panel method for added resistance of ships in waves,* J. Offshore Mech. Arct. Eng. **136**(3), 031601·1-031601·7

TSUJIMOTO, M.; SHIBATA, K.; KURODA, M.; TAKAGI, K. (2008) *A practical correction method for added resistance in waves*, J. Japan Soc. Naval Arch. and Ocean Eng. **8,** 177-184

SEAKEEPING AND ADDED RESISTANCE OF A FAST SEMI-SWATH SHIP

Ageno Emanuela, Vernengo Giuliano, Bruzzone Dario

Department of Naval Engineering, University of Genoa, Via Montallegro 1, Genoa, 16145, Italy

ABSTRACT

Multi-hull vessels, including SWATH vehicles, are interesting design solutions for a number of marine applications, from coastal ferries to workboats. Some hybrid and unconventional configurations, able to combine good quality of more classic designs, appear to be also attractive. This is the case of Semi-SWATHs, that merge the stern shapes of high speed catamarans with the bow shapes of conventional SWATHs.

The aim of the proposed work is to go deeper into its seakeeping behavior also evaluating the added resistance. The analysis is carried out by means of a three dimensional Boundary Element Method (BEM), that makes use of a Rankine source distribution over the hull and the free surface. Incoming head waves only are considered in this study. Both the response amplitude operators of heave and pitch motions and the added resistance of the high speed catamaran are compared with available experimental data. The same analysis is carried out on the proposed Semi-SWATH vessel and results are critically discussed.

1. INTRODUCTION

Multi-hull ships are particularly suitable for high speed passenger ferry applications due to their inherent efficiency in terms of wide transportation capability at the cost of a relatively small power increase with respect to an equivalent mono-hull design. Several numerical methods have been developed to analyze the problem of twin hull catamaran. Among them, Shelling and Rathje (1995) used a three dimensional method based on high frequency oscillating sources, Kring and Sclavounos (1995) analyze the time domain problem, Van't Veer (1997), Bruzzone (2003) developed three dimensional Rankine sources based methods for motions analysis. More recently Castiglione et al. (2011) successfully applied 3D viscous methods to find the motions and added resistance of a fast catamaran.

Beyond the classic high speed catamaran design, there is a variety of other possible different configurations. Small Waterplane Area Twin Hulls (SWATH) for example are generally used when seakeeping performance are of relevant importance in the overall design economy. Despite their good qualities with respect to motions, they often show worse resistance performance compared to mono-hulls or catamarans. To overcome this drawback Papanikolaou et al. (1991) modified the shape of the submerged hull. Brizzolara and Vernengo (2011) performed hydrodynamic shape optimization coupled with a fully parametric model to find an unconventional shape of the submerged body of a double strut fast SWATH.

A hybrid solution is represented by the so called Semi-SWATH craft. This kind of vessel is fairly used as fast multi hull passenger ferries for high speed applications. However, very few other studies are available on this unconventional type of hull form. A first study on Semi-SWATH designs used for high speed passenger ferries has been proposed by Shack (1995) where the *SeaJet* project has been described. Another successful high speed ferry design that has been used by many international shipyards (such as Austal) is the *Stena HSS*. Holloway (1998) studied the seakeeping behaviours of both SWATH and Semi-SWATH vessels by a time domain strip-theory approach for high Froude numbers. Armstrong and Clarke (2009) performed resistance towing tank model tests on several Semi-SWATH crafts (showing both V-shaped and U-shaped sections) and they also studied their seakeeping qualities with a strip-theory based approach, aiming at giving some practical information about hull shape influence on overall performance. Recently Vernengo et al. (2014) proposed an application of hydrodynamic shape optimization based design of such a vessel type.

The validation of the method proposed by Bruzzone (2003) on a fast catamaran tested by Molland et al. (2000) is showed. The seakeeping performance of a Semi-SWATH design are analyzed and response amplitude operators of heave and pitch motions as well as the added resistance is shown. The added resistance of both the catamaran and the Semi-SWATH are computed based on a near field method proposed for example in Faltinsen et al.(1980), Kim and Kim (2011), Joncquez et al. (2012) and recently applied to mono hull ships in Ageno et al. (2014).

2. NUMERICAL METHOD FOR THE PREDICTION OF MOTIONS AND ADDED RESISTANCE

A ship oscillating in regular waves advancing with forward speed is considered. A right handed Cartesian reference system fixed with the ship is used. The still water plane is represented by the xy geometric plane; the x axis is positive to stern and the xz plane identifies the symmetry plane; z axis is normal to the water plane and is positive upwards. To determine the hydrodynamic forces, necessary to compute ship motions a set of three-dimensional boundary value problems must be formulated.

The water is considered inviscid and incompressible, the flow irrotational and a total potential Φ_T at a position $\vec{x} = (x, y, z)$ is assumed as:

$$\Phi_T(\vec{x},t) = \Phi_S(\vec{x}) + [\phi_o(\vec{x}) + \phi_7(\vec{x}) + \sum_{k=1}^{6} \phi_j(\vec{x})\varsigma_j]e^{i\omega_e t} \tag{1}$$

In which: $\Phi_S(\vec{x})$ is a steady potential due to the uniform motion at the ship speed U, $\phi_o(\vec{x})$ is the potential due to the incident ambient waves, $\phi_j(\vec{x})$, (j=1,...6) are the complex amplitudes of the radiation potentials for each mode of motion of unitary amplitude and $\phi_7(\vec{x})$ is the complex amplitude of the diffraction potential.

Potentials $\phi_j(\vec{x})$ are determined by solving a set of six radiation and one diffraction problem. Considering the wave encounter frequency, ω_e, the normal terms, $\vec{n}$, and the classical formulation of the *m*-terms, the following body boundary conditions are enforced on the mean hull surface S_H:

$$\frac{\partial \phi_j}{\partial n} = i\omega_e n_j + m_j \tag{2}$$

For the radiation problems and for the diffraction problem:

$$\frac{\partial \phi_0}{\partial n} + \frac{\partial \phi_7}{\partial n} = 0 \tag{3}$$

For each of the identified problems, a linearized formulation of the coupled dynamic and kinematic free surface boundary condition is fulfilled at $z = 0$.

From the solution of the complete BVP the pressure field acting on the hull surface due to each of the mentioned problem is computed. Also, the added mass and damping coefficients are calculated as well as the resulting exciting forces. Accounting for the classical equation of motions, the ship response amplitude operators (RAOs) can be derived.

In the present study, a near field method for the computation of the added resistance is used.

Assuming the added resistance in regular waves as the time average value of the longitudinal component of the second order forces, it results to be proportional to the squared wave amplitude. This observation is confirmed by the experimental results of Strom-Tiesen (1973).

Using Bernoulli's equation and Taylor's expansion, the second order pressure can be evaluated, and the second-order force is provided by integrating the second-order pressure on the body surface. It can be shown that non null time averaged values of the second order forces are those obtained by cross multiplying first order effects and by considering first order variations of the mean hull surface. Then there is no need to solve the second-order boundary value problem. In the present work, only the added resistance due to vertical motion in head sea is considered composed by two terms: R_{aw1} and R_{aw2}. The first, derived from the difference between the average and the instantaneous wetted surface of the hull, is given as the mean value of the following integral over the waterline:

$$R_{aw_1} = \overline{\int_{WL} \frac{1}{2}\rho g \varsigma_r n_1 dl} \tag{4}$$

Considering the wave elevations relative to the various boundary value problems, ς_j, and the vertical displacement a point on the waterline, ς_3, the first-order difference between average (steady) and instantaneous wave profile on the hull, ς_r, is calculated as:

$$\varsigma_r = \sum_j \varsigma_j(l) - \varsigma_3(l) \tag{5}$$

The second contribution to the added resistance is the pressure integral over the average wetted surface of the hull; considering that only the second-order terms of the integrand are retained, it can be written as the mean value of the following integral:

$$\begin{aligned} R_{aw_2} = \; & \rho \overline{\int_S \frac{1}{2} \nabla\phi_1 \cdot \nabla\phi_1 n_1 dS} \; + \\ + \; & \rho \overline{\int_S \nabla\left[\left(\frac{\partial \phi_1}{\partial t}\right) + \left(\nabla\Phi_S \nabla\phi_1\right)\varsigma_p\right] n_1 dS} \; + \\ + \; & \rho \overline{\int_S \left[\frac{\partial \phi_1}{\partial t} + \nabla\Phi_S \nabla\phi_1 + g\varsigma_p\right] n_1 dS} \end{aligned} \tag{6}$$

where ς_P is the vector which expresses the motion at a point P on the hull surface and ϕ_1 are first order radiation and diffraction potentials.

3. VALIDATION OF THE METHOD FOR MULTI-HULL VESSELS

Before performing the seakeeping and added resistance analysis on the proposed Semi-SWATH design, the numerical method described above has been validated in the case of a fast catamaran whose experimental data are available in literature. Results of this preliminary validation are showed in the next chapter.

3.1 Fast Catamaran Motions

The main characteristic of the high speed multi-hull vessel are listed in Table 1. Each of the two twin demi-hulls of the catamaran is derived from the round bildge transom stern hull of the NPL series. The perspective view of the discretized boundary surfaces of the used catamaran is shown in Fig. 1.

Table 1. Particulars of the Fast Catamaran (Model scale).

Displacement (kg)	13.44
L_{OA} (m)	1.6
L_{WL} (m)	1.6
X_G aft of F_{PP} (m)	-6.4%
ρ_{YY}/ L_{OA}	0.26
s/ L_{WL}	0.4

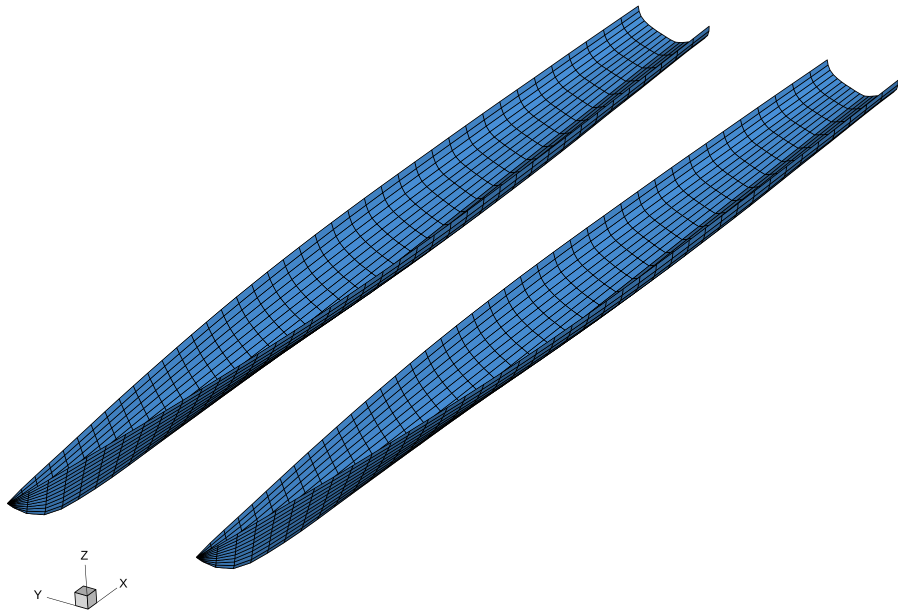

Fig. 27. Perspective view of the Catamaran showing the panel mesh used for seakeeping computations.

The computations have been performed with the separation ratio, s/L, equal to 0.4 and Froude number of 0.5. Comparisons with experimental values for the vertical motions are shown in Fig. 2 and Fig.3. Numerical results show a very good agreement with the experimental ones for the pitch motion while the heave response is overestimated. This can be primarily due to the formulation of the method itself, that inherently neglect viscosity, responsible of a damping effect on the motion responses. This influence of the viscosity on the seakeeping has been recently analyzed by Brizzolara et al. (2013) for SWATH crafts and it can be also enhanced in the case of the Semi-SWATHs.

The last validation has been done on the added resistance. Such comparison is shown in Fig. 4 again for s/L=0.4 at Fn=0.5. There is a little difference in the range of short wave lengths and a more evident higher predicted peak value than the experimental one. This is a direct consequence of the previously highlighted mismatch of the heave peak response prediction. The agreement of the numerical prediction with the experimental data for the added resistance is instead better in the range of the higher wave length.

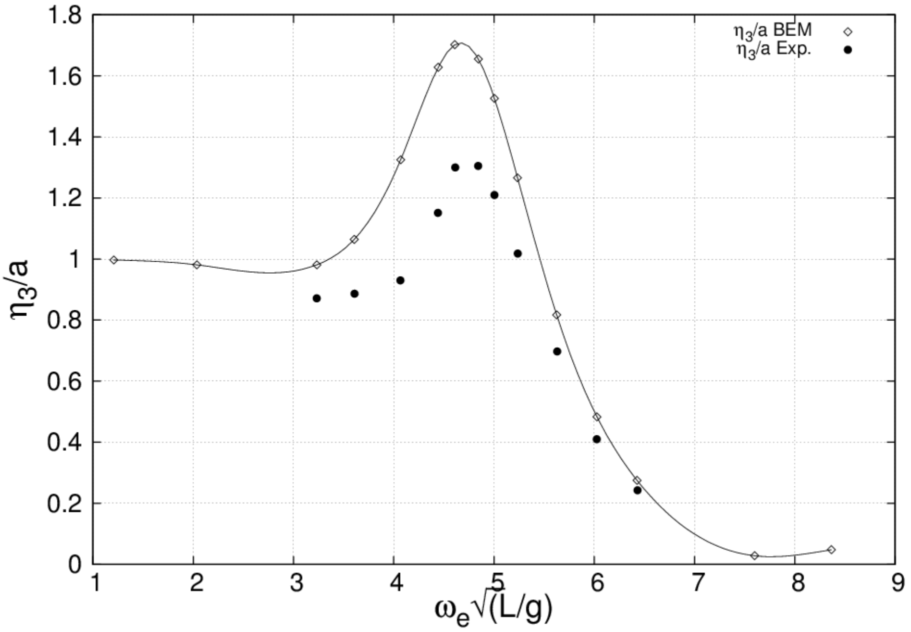

Fig. 28. Numerical vs experimental non dimensional RAO of heave motion for the fast catamaran (s/L=0.4)

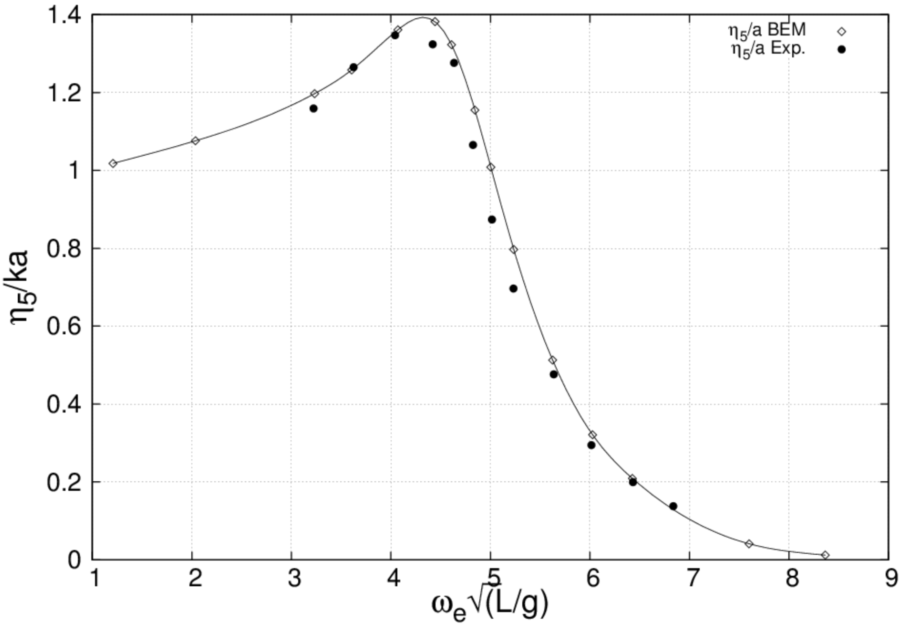

Fig. 29. Numerical vs experimental non dimensional RAO of pitch motion for the fast catamaran (s/L=0.4)

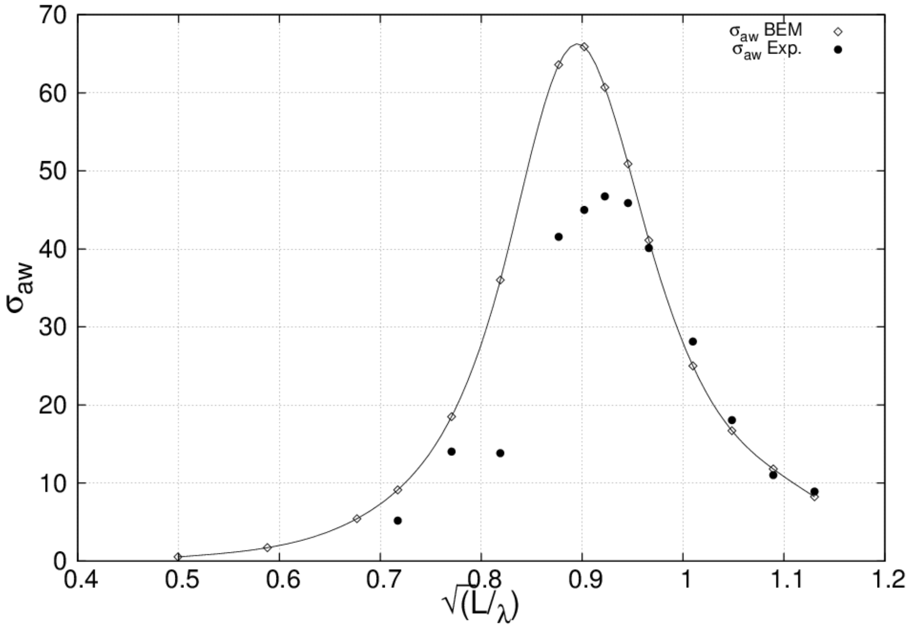

Fig. 30. Numerical vs experimental added resistance for the fast catamaran (s/L=0.4)

3. RESULTS OF THE SEMI-SWATH SEAKEEPING PERFORMANCE AND CROSS COMPARISON OF THE PROPOSED DESIGNS

As previously mentioned, a Semi-SWATH represents a kind of hybrid craft that merges the stern shape of a fast catamaran together with the bow shape of a classic SWATH. The resulting vessel hence maintains some of the specific characteristics of the two parent hull types. The shape of the aft body is more full to accommodate water-jet propellers. The bow of the hull shows a bulb that is intended to produce at least two positive effects: it will reduce the hull motions by creating a damping effect and it allows the entrance angle of the design waterline to be as narrow as possible, reducing the wave making resistance. Hence the design waterline assumes a wedge-like shape, having the maximum breadth in the aft part and a very tight shape moving forward. A perspective view of the proposed Semi-SWATH design is shown in Figure 5; the hull in the picture is represented with the panel mesh used for the seakeeping computation. Main particulars of the hull are listed in Table 2.

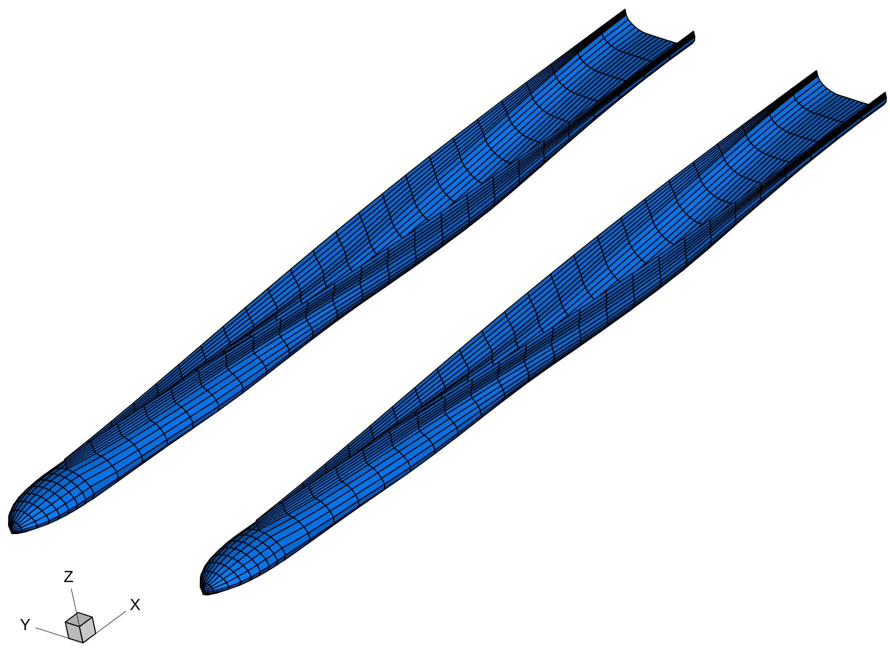

Fig. 31. Perspective view of the proposed Semi-SWATH showing the panel mesh used for seakeeping computations.

Table 2. Particulars of the Semi-SWATH craft (Full scale).

Displacement (tons)	~50
L_{OA} (m)	26
L_{WL} (m)	24
T (m)	1.5
s/ L_{WL}	0.3

The comparison of the RAOs of heave and pitch due to incoming regular head waves between the proposed Semi-SWATH craft and the previously described catamaran are shown in Fig. 6 to Fig. 8 with respect to the non-dimensional wave length over ship length ratio, λ/L. The comparison have been performed at the same volumetric Froude number, Fn_{∇}, in order to account for the difference in the volume of the two hulls. The heave response of the Semi-SWATH vessel shows a first peak very close to $\lambda/L = 1$ that is higher than the corresponding one of the catamaran except for the faster test for which the two peaks are almost equivalent. The second peak appears at $\lambda/L \cong 2$; this peak, that should recall the double peak more typical of a SWATH response, is not present in the catamaran RAO. On the other hand the pitch is generally damped out by the Semi-SWATH, resulting in a lower response with respect to the catamaran. The added resistance of the Semi-SWATH is shown in Fig. 9 for the previously used three volumetric Froude numbers. Its trend reflects that of the motion responses, in particular the one of the heave RAO; there is a higher peak in correspondence of the medium speed (probably due to resonance effects) that is then lowered at the higher Froude number.

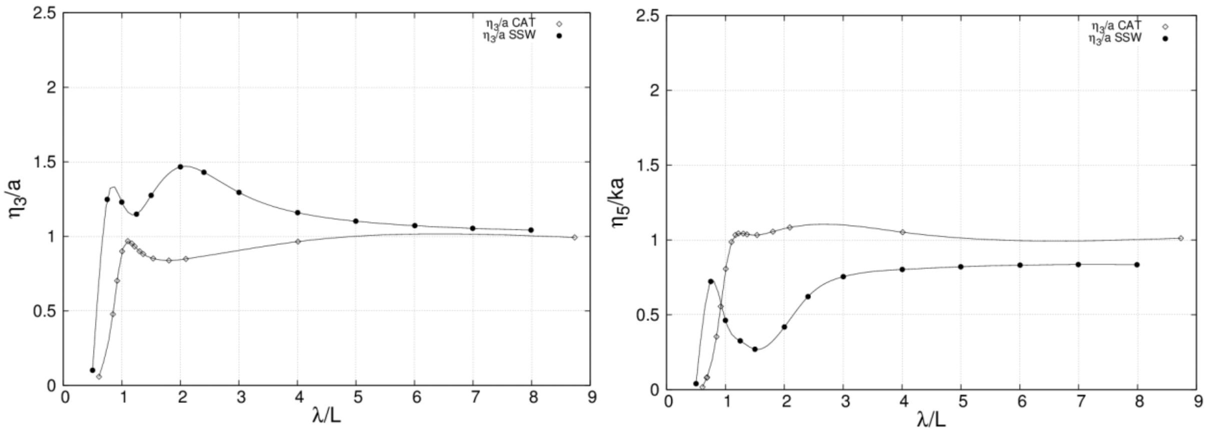

Fig. 32. Heave and Pitch RAOs of the Semi-SWATH (SSW) against those of the Catamaran (CAT) at $\boldsymbol{Fn_{\nabla} = 0.91}$

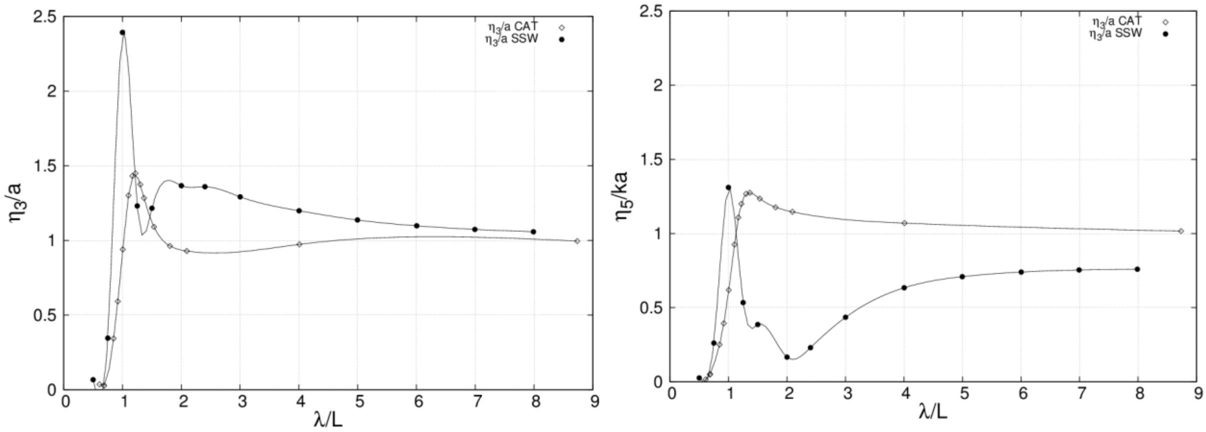

Fig. 33. Heave and Pitch RAOs of the Semi-SWATH (SSW) against those of the Catamaran (CAT) at $\boldsymbol{Fn_{\nabla} = 1.14}$

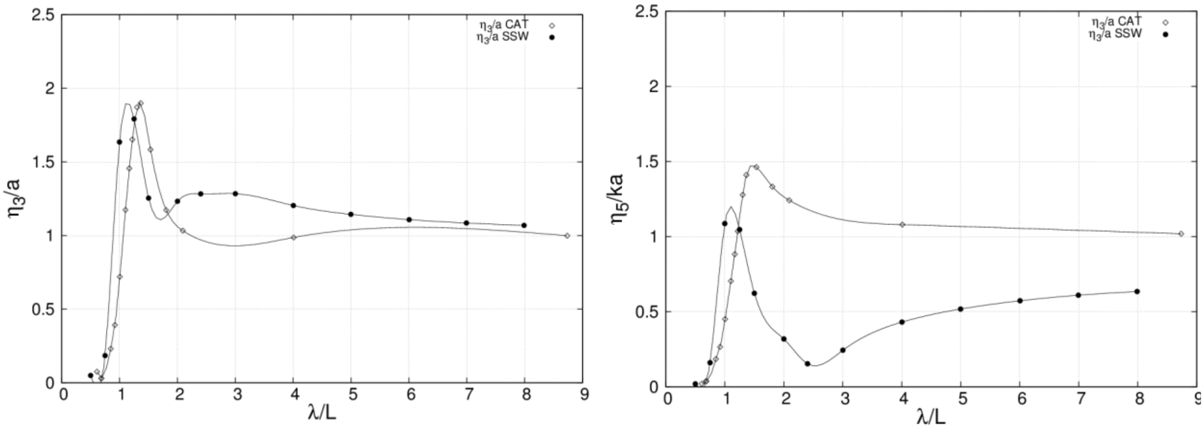

Fig.8. Heave and Pitch RAOs of the Semi-SWATH (SSW) against those of the Catamaran (CAT) at $\boldsymbol{Fn_{\nabla} = 1.37}$

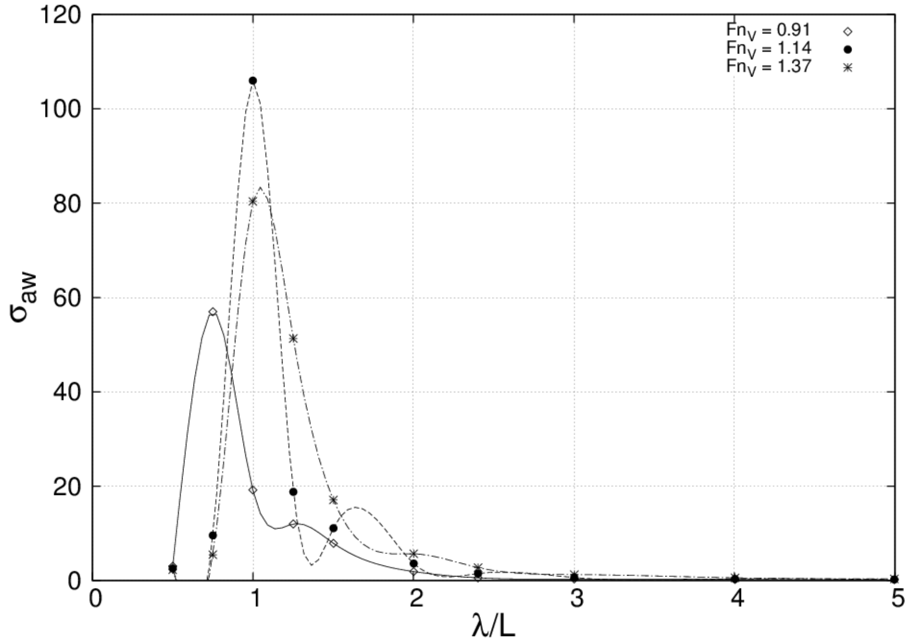

Fig. 34. Added resistance for the Semi-SWATH vessel at different volumetric Froude numbers

4. CONCLUSIONS

The analysis of the seakeeping behaviours of a Semi-SWATH vessel designed for relatively high speeds has been performed. The motion responses have been computed by means of a three dimensional boundary element method in the frequency domain that has been preliminarily validated for a fast multi-hull catamaran whose experimental data are available in literature. The seakeeping responses of the fast Semi-SWATH design at different speeds have been then compared with the one of the high speed catamaran. From this cross comparison seems that the heave response of the proposed Semi-SWATH design is generally higher than the one of the catamaran, especially in the peak range of wave length. On the contrary the pitch response is much lower than the one of the catamaran in all the wave length range. The added resistance has been computed by a near field approach based on motion responses. For this reason it reflects the attitude of motion RAOs, particularly the one of the heave motion. There is a trend to reach lower peaks of the heave response, hence of the added resistance for higher speeds.

In conclusion, this unconventional type of vessel can have promising performance in some sea states with respect to other types of multi-hull crafts, especially if the hull is properly modified to damp out the peak of the responses. In this respect it is important to note that there are more possibilities of changing the shape of the hull in order to reach better performances (for example acting on the bulbous bow) if compared to other conventional multi-hulls like catamarans. A better understanding of the seakeeping behaviours of such an unconventional vessel will be reached if viscous effects, here inherently neglected, will be evaluated.

ACKNOWLEDGEMENTS
This work has been done in the context of a research grant fund by Regione Liguria (*PO CRO Fondo Sociale Europeo Regione Liguria 2007-2013 Asse IV "Capitale Umano" ob. specifico I/6*), whose financial support is gratefully acknowledged.

References

1. Ageno E., Bruzzone D., Villa D. "Numerical simulation of Added Resistance in Head waves: a RANSE and BEM approach" 2th International Conference on Maritime Technology and Engineering, 15th-17th October, 2014.
2. Armstrong, T, Clarke, T. "On the effect of hull shape on the performance of some existing high-speed ferries", 10th International Conference on Fast Sea Transportation, FAST09, Athens, Greece, 5th – 8th October, 2009.
3. Brizzolara S., Bonfiglio L., Seixas de Medeiros, J. "Influence of viscous effects on numerical prediction of motions of SWATH vessels in waves", Ocean Systems Engineering, Vol. 3, No. 3 (2013) 219-236.
4. Brizzolara, S, Vernengo, G. "Automatic Optimization Computational Method for Unconventional S.W.A.T.H. Ships Resistance". International Journal of Mathematical Models and Methods in Applied Sciences, Issue 5, Volume 5, pp. 882-889, 2011.
5. Bruzzone, D. (2003). "Application of a Rankine source method to the evaluation of motions of high speed marine vehicles", Proceedings of the 8th International Marine Design Conference, Athens, May 2003, Vol. II, pp. 69-79.
6. Castiglione, T., Stern, F., Bova, S. and Kandasamy, M. "Numerical Investigation of the Seakeeping Behavior of a Catamaran Advancing in Regular Head Waves". Ocean Engineering, Elsevier, 2010.
7. Faltinsen, O.M., Minsaas, K.J., Liapis, N., Skjordal, S.O. "Predictions of resistance and propulsion of a ship in sea wave". Proceedings of the 13th Naval Hydrodynamics Symposyum, Tokyo, pp. 505-529, 1980.
8. Holloway, D.S. "A High Froude Number Time Domain Strip Theory Applied to the Seakeeping of Semi-SWATHs", PhD Thesis, University of Tasmania, 1998.
9. Joncquez S.A., Andersen P., Bingham H.B. "A Comparison of Methods for Computing the Added resistance", Journal of Ship Research, Vol.56, No.2, pp. 106-119, 2012.
10. Kallio, J.A. "Seaworthiness Characteristics of a 2900 tons Small Waterplane Area Twin Hull (SWATH)", David W. Taylor Naval Ship Research and Development Center, Ship Performance Department, SPD-620-03, Maryland, 1976.
11. Kim, K-H., Kim Y. "Numerical study on added resistance of ships by using a time-domain Rankine panel method", Ocean Engineering, 38, pp. 1357-1367, 2011.
12. Kring, D., Sclavounos, P.D. "Numerical stability analysis for time-domain ship motion simulations", Journal of Ship Research, 39 (4), pp. 313-320, 1995.
13. Molland A. F., Wellicome J. F., Temarel P., Cic J. and Taunton D. J. "Experimental Investigation of the Seakeeping Characteristics of Fast Displacement Catamarans in Head And Oblique Seas", Transactions RINA, vol. 142, 2000.
14. Shack, C. "Research on Semi-SWATH hull form", 3rd International Conference on Fast Sea Transportation, FAST95, Lübeck-Travemünde, Germany, September 25th – 27th, 1995. Editor C.F.L. Kruppa, TUB, Berlin, vol.1, pp.527-538.

15. Shelling T.E. and Rathje H. "A panel method applied to hydrodynamic analysis of twin-hull ships", 3rd International Conference on Fast Ship Transportation, Lubeck-Travemunde, September 1995.
16. Strom-Tejsen J, Yeh H.Y.H., Moran D.D. "Added Resistance in Waves", Transaction SNAME, vol. 81, pp.109-143, 1973.
17. Papanikolaou, A, Zaraphonitis, G, Androulakakis, M. “Preliminary Design of a High-Speed SWATH Passenger/Car Ferry”, Marine Technology, Vol. 28, no.3, May 1991, pp. 129-141, 1991.
18. Van’t Veer, R. "Catamaran seakeeping predictions", International Workshop on Water Waves and Floating Bodies (IWWWFB12), 16–19 March 1997, Carry le Rouet, France.
19. Vernengo G., Brizzolara S., Bruzzone D. “Hydrodynamic Design of a Fast Semi-SWATH Passenger Ship for Littoral Applications: An Automatic Parametric Optimization Approach”, The 24th International Ocean and Polar Engineering Conference, June 2014, Busan, Korea.

DESIGN OF MODERN FERRIES WITH OPTIMIZED PERFORMANCE IN A VARIETY OF SEA CONDITIONS

Dimitrios A. Makris and Gregory J. Grigoropoulos

National Technical University of Athens (NTUA), 9 Heroon Polytechniou str., 15773, Zografou, Greece

ABSTRACT

This paper deals with the optimization of a fast displacement ferry for both, the wave resistance in calm and the dynamic responses in rough waters. To this end, the geometry of an existing design was parameterized respectfully to the initial form, using an optimized fitting of B-Splines on various curves of the parent hull. The outcome consists of parametric curves defined by a few control points, which can be varied in a smooth manner. This design technique combined with modeling tools provided by a parametric design software, can be used in the representation of any geometry, accommodating a set of design features and permits the definition of the desired design variables. The interpolation code was developed in Visual C++, and it was integrated with CAESES – Friendship Framework in a bi-directional way within the optimization scheme.

Parametric design of the hull was also performed within CAESES Friendship Framework. Using this software, variant geometries are generated to feed a multi-objective genetic algorithm. Their performance in potential flow was evaluated using a 3D Rankine source panel code as well as a strip theory code, in calm water and in head seaways, respectively. Finally, the parent and the optimized hull forms found on the Pareto front of the optimization scheme were evaluated using a commercial viscous flow RANS solver (STAR CCM+), to investigate the validity of the optimization results.

1. INTRODUCTION

Ship design is a complicated and demanding process in which various modeling aspects and many times contradictive parameters should be considered by the designer, under specific constraints and ship owner's specification. One of the important aspects of ship design is the optimization of the efficiency in both calm and rough water. Especially after the recent regulations established by the IMO for EEDI, the aforementioned optimization became an indispensable phase of ship design and the tools used to support it are constantly improved.

Nowadays, the evolution of Computer Aided Design (CAD), Computational Fluid Dynamics (CFD) codes and optimization tools, as well as the rapidly growing CPU power, led to the integration of conventional ship design techniques with the so called Simulation Based Design (SBD). Regarding the performance of a vessel, the SBD technique encompasses the integration of parametric modeling, the evaluation of ship performance characteristics and a powerful optimization scheme to derive variant hull forms with superior operational characteristics on the basis of an initial hull. Campana et al [1] describe some important aspects of single and multi-objective optimization framework that should be taken into account in SBD such as the importance of considering the basis of both global and local design variables that affect the vessel's performance in terms of the optimization criteria chosen.

This paper presents the SBD framework of a fast displacement ferry in terms of its wave making resistance and seakeeping performance. The whole process is fully automated and integrates hull variation, CFD simulation and genetic algorithms in a unified multi-objective, single stage optimization process. The optimization of various hull forms, using one or more objectives as well as one or more stages was initiated in early eighties. A review of the pertinent research activity is presented by the second author of the paper (Grigoropoulos [2]).

In this work, a custom parametric design of an existing conventional hull form was developed using CAESES Friendship Framework (CAESES FFW) [3], a powerful commercial software that can interact with other utility software. Variant hull forms were generated automatically by varying specific design variables which were selected according to their effect on the objective functions. In addition, a procedure has been produced to optimize the fitting of the parametric geometry to the parent hull form, using 3rd degree B-Spline curves.

As for the calm water performance evaluation of the ship sail, the SWAN 1 [4] potential code solver was used, in order to estimate its wave resistance. However, potential flow solvers neglect viscous phenomena prevailing in the stern region, resulting in over-prediction of the resistance. On the other hand, they predict more accurately the profiles of the waves generated by a ship underway. Based on that fact, Heimann [6] presented an alternative method where the wave pattern characteristics of hull forms are optimized instead of their wave resistance. This is considered as a reasonable choice whose reliability is investigated in this paper. To this end, two different optimization processes were performed by altering the objective function related to the calm water performance of the ship. This objective function was set as the wave pattern's maximum height at a constant distance athwartship for the first and as the wave resistance for the second. The simulations were performed at the service speed of the fast ferry (Fr = 0.348), where the wave resistance constitutes a major percentage of the total one.

Regarding the performance in rough water, seakeeping qualities were estimated by the strip theory based evaluation code SPP-86 [7], developed at the Laboratory for Ship and Marine Hydrodynamics of the National Technical University of Athens. Instead of the statistical values of the responses in a seaway, the optimization is based on the peak values of the unimodal Response Amplitude Operator (RAO) curves of the absolute vertical acceleration at the forepeak. Grigoropoulos [8] demonstrated that within the optimization space the modal frequencies of these bell-shaped RAO curves do not shift significantly and that the minimization of their peak values, results in improving the statistical responses in the practical range of seaways encountered. This concept reduces significantly the computational work and eliminates the dependency of the results on the operating scenario. In addition, the added resistance curves, obtained by the SPP-86 code, of the initial and optimized geometries were compared to each other.

Finally, the calm water performance of the initial and optimized hull forms were evaluated by estimating their total resistance using the Reynolds-Averaged Navier-Stokes (RANS) solver STAR CCM+ [9] provided by CD-ADAPCO. The simulation was performed with a multiphase (air and water) free surface flow with the same constant speed used in the potential flow simulations. The fluid flow is modeled as turbulent and the mesh generation is based on a gradually fining strategy for the flow field away from the hull as well as on local refinements in volume regions with significant changes in pressure and velocity fields. The viscous flow simulations were performed in order to verify the obtained results, as well as to assess the relative merit of the two alternative objectives used in the optimization procedure.

2. STATE-OF-THE-ART REVIEW

In recent years, hull form optimization for calm water resistance has been reported using potential and viscous solvers as well a combination of them. In most of them, genetic algorithms or evolutionary strategies are used as optimization tools. Some of these reports are reviewed in the sequel.

Grigoropoulos et al. [10] have implemented an optimization scheme for a fast displacement ferry, based on Genetic Algorithms (GA) and integrated with the modeFRONTIER environment using potential solvers to minimize the hull's wave resistance. Abt et al. [11] presented an application of hull form optimization, where parametric modeling using FRIENDSHIP-Modeler in conjunction with SHIPFLOW for CFD calculations is used. In order to minimize the computational cost, SHIPFLOW uses a potential solver forward of amidships and a RANS solver for the stern region where viscous effects are dominant. Recently, Peri et al. [12] have demonstrated a remarkable optimization process of a water-jet propelled Catamaran, regarding its total resistance and propulsive efficiency. This is a multi-stage, single and multi-objective SBD research using both potential (WARP) and URANS (CFDSHIP) solvers stabilizing for each stage the computational demands and accuracy of the generated results which were also verified experimentally. Quite recently, Li, Zhao and Ni [13], performed a multi-objective optimization of a bulk carrier using solely RANS solvers for minimizing its total resistance and improve the quality of the propeller's disk wake field.

Grigoropoulos and Chalkias [14] implemented a fully automatic multi-objective optimization scheme for the parent hull of NTUA double-chine high-speed series in calm and rough water in a single stage. At the same work a single objective dual stage optimization was performed for a fast displacement ferry by varying its global and local form parameters in order to reduce the wave making resistance by minimizing the wash waves pattern maximum height at a predefined distance athwartships. Both of these computational processes have been incorporated Friendship-Modeler as a parametric hull production tool, the EASY optimization software and also the SWAN 1 and the NTUA SPP-86 strip theory code for the evaluation of the calm and rough water hull performance, respectively.

Finally viscous codes were also used in order to locally improve the propulsive efficiency of the optimized hull form. Similar work was presented recently by Pellegrini et al. [15], for multi-objective optimization of a high speed Catamaran in terms of its seakeeping qualities and total resistance. Calm water performance was evaluated by URANS solvers, meta-models and uncertainty quantification methods, while the seakeeping performance has been examined with simulation of the ship sail in real ocean environment. This was achieved by modeling sea states and speed with stochastic methods.

3. THE PROPOSED METHOD FOR SHIP PERFORMANCE OPTIMIZATION

3.1 General Description of the method

The main purpose of a performance optimization of a ship, is improving its calm and rough water sailing efficiency, by minimizing its resistance and improving its seakeeping qualities. To this end, model tests and CFD calculations are used.

Calm water resistance minimization of the hull usually refers to its total resistance at service speed, as it is directly related to its fuel consumption. Since for most vessels the fuel cost is the prime component of the daily cost, its reduction directly affects the total operational cost. Total resistance estimations can be performed by simulating the ship sail, with RANS solvers. However, these solvers are still too time-consuming and cumbersome to be incorporated in an automatic optimization process where hundreds or even thousands of variants are evaluated via a conventional computer cluster. At present, repetitive viscous CFD evaluations using coarse grids are proposed by only a few researchers, with access to large computational facilities.

In contrast, potential solvers are much faster and can easily be embedded in an automated process, but they can only estimate the wave resistance as they are unable to simulate flow phenomena affected by viscosity. However, wave resistance is significant at high speeds and hence, an optimization with respect to this part of the total resistance is reasonable especially for high-speed displacement ships, as the one examined in this work.

On the other hand, the seakeeping performance isn't a dominant parameter in traditional design process. However, the incorporation of superior seakeeping qualities in a new ship design is obviously desirable. The minimization of the vertical motions and accelerations onboard a ship in head seas and the associated increase of resistance affect the comfort of its passengers and the fuel consumption, respectively. Seakeeping qualities can be efficiently estimated by potential flow codes for all degrees of freedom except for roll motion, while RANS solvers haven't yet managed to produce reliable results.

Since seakeeping optimization is known to lead to a slightly increased calm water resistance, both criteria should be taken into account in a balanced multi-objective scheme. In this scheme a large number of variants specified by a set of design variables are evaluated. Therefore, the reduction of these evaluations is of significant importance. To this end, genetic algorithms contribute by improving the efficiency of the optimization process.

Finally, the automatic derivation of the variants in the optimization process necessitates the use of parametric modeling techniques. RANS solvers and/or model tests in the towing tank may be used to validate a posteriori the initial and the finally derived hull forms.

The methodology described above constitutes an improved answer to the real problem of the designer of assuring good propulsion and resistance characteristics both in calm water and in waves, with the minimum possible resources.

3.2 Hull form modeling and variation

CAESES FFW has been used for the entire process of parametric modeling of a fast ferry's hull. This software is the evolution of FRIENDSHIP-Modeler which can only provide specific hull types and their variation is affected by a limited number of design variables. In contrast, inside the environment of CAESES FFW, any geometry can be constructed as the user is able to implement a totally custom design process, in which he is responsible of creating the design variables.

In custom parametric design, a vessel's hull form can be created in various different ways using numerous techniques, CAD tools and functions provided by CAESES FFW. The design process highly depends on whether the designer seeks to create a new geometry, or to which extent approximate an existing initial non-parametric hull. Close fitting of an initial geometry by its parametric representation, could be desired in an optimization process for various reasons such as maintaining displacement and position of the center of buoyancy between the variants and the initial hull, or keeping the general form of specific regions due to structural, hydrodynamic or arrangement constraints.

In case that initial lines are provided, the quality of their approximation is usually related to the design variables chosen and also how these variables affect specific hull regions. Most of the times, close fitting of curves and surfaces limits the variation range of the respective hull's part. In contrast, using simple parametric design tools can permit a significant hull modification range, but also reduces the approximation quality of the initial hull form. An efficient parametric design strategy consists of evaluating whether a close fit or a wide variation is preferred for each hull region and implement the most suitable technique. In many cases combining simple tools with close fitting curves such as NURBS and B-Splines can prove to be quite useful.

In every parametric design process the objective functions and the related design variables have to be predefined as they directly affect the design process flow. Design variables should not depend on any other parameters and can be incorporated in many design features such as coordinates, angles and sectional areas. These design features affect curves and surfaces of the final hull form and thus lead to global or local form variation possibilities. In this work, where the wave resistance is set as one of the objective functions, special consideration should be given to the bulb surface parameterization in order to assure a wide variation range.

The geometry representation is mainly based on B-Splines that are widely used, easy to handle curves whose form is not affected by affine transformations. Since they are defined by limited number of control points, they can be proved to be useful in parametric modeling. A B-Spline curve possesses the following main properties:

- $P_0, P_1, P_2, \dots, P_n$, $n+1$ control points
- $p = k - 1$ the degree of the curve and k its order where $k \leq n + 1$
- $U = \{u_0, u_1, u_2, \dots, u_m\}, 0 < u_i < 1$, the knot vector where $m = n + k$

Then, the B-Spline is provided by equation (1), while the basis functions $N_{i,p}(u)$ are given by equations (2).

$$\boldsymbol{C}(u) = \sum_{i=0}^{n} N_{i,p}(u)\boldsymbol{P}_i \,, \qquad 0 < u < 1 \tag{1}$$

$$N_{i,0}(u) = \begin{cases} 1\,, & u_i < u < u_{i+1} \\ 0\,, & elsewere \end{cases}$$
$$N_{i,p}(u) = \frac{u-u_i}{u_{i+p}-u_i} N_{i,p-1}(u) + \frac{u_{i+p+1}-u}{u_{i+p+1}-u_{i+1}} N_{i+1,p-1}(u) \quad (2)$$

Regarding the way these curves can be used to interpolate a given set of 3D points, there is an extensive research by Piegl and Tiller [16].

Specifically for interpolating a set of Q_i points with B-Splines, the NxN linear equations system (3) should be solved. This is a quite straightforward process that gives a unique solution. The output is the P_i control points, and a knot vector defining a B-Spline curve that interpolates all of the Q_i points which may lie on a curve. However there is no consideration about the rest of this curve and how closely it is approximated. Curves in ship design many times have local extremes that cannot be part of a B-Spline obtained by this method except if an interpolation point is set there. That issue was addressed by extending this method and integrating it with evolutionary algorithms in order to optimize the fitting of a curve in a fully automated process. The method is described in the upcoming publication "Optimization of Fitting Curves with B-Splines".

$$\begin{bmatrix} 1 & 0 & \dots & 0 & 0 \\ N_{0,p} & N_{1,p} & \dots & 0 & 0 \\ \vdots & \vdots & \ddots & \vdots & \vdots \\ 0 & 0 & \dots & N_{k-1,p} & N_{k,p} \\ 0 & 0 & \dots & 0 & 1 \end{bmatrix} \cdot \begin{bmatrix} P_0 \\ P_1 \\ \vdots \\ P_{n-1} \\ P_n \end{bmatrix} = \begin{bmatrix} Q_0 \\ Q_1 \\ \vdots \\ Q_{n-1} \\ Q_n \end{bmatrix} \quad (3)$$

As a brief description, the optimization consists of minimizing the distance between the initial and final curve by varying the interpolation points' positions. Based on the fact that different methods, like chord length and centripetal, can be implemented affecting the knots distribution, an additional design variable was created in order to search amongst infinite different such methods. The interpolation code was built in Visual C++ and is able to construct B-Splines of any degree with the additional option to also define the tangent vectors' direction and norm at their endpoints, which assures continuity between the interpolation curves and other curves and surfaces, to which they are adjacent. The code was integrated with CAESES FFW in order to implement an optimization scheme in which input and results files are exchanged. Interpolation of two adjacent curves with tangent vector (C^1) and curvature (C^2) continuity at their joint point is an additional capability of the code.

The aforementioned technique, was used in conjunction with FSplines (i.e. B-Spline curves defined by limited parameters) which are provided inside the CAESES FFW environment, in order to parameterize sections and the forward part of the waterline. This resulted in creating design variables affecting the forward part of the hull, such as the entrance angle and the waterplane's area fullness in that region, while maintaining at the same time the initial hull shape for specific values of the relevant design variables (i.e. initial design variables' values). In addition, the produced surfaces remain smooth for every possible value of these design variables, within a predefined range.

An optimization of fitting B-Splines was also implemented for the aft sections between the FOS and the skeg's baseline. These sections are depended on the skeg's maximum breadth which was set as a design variable. However, due to the fact that optimization should be performed with potential flow solvers, a modification of the aft region was necessary in order to eliminate multiple intersections with the waterplane. This modification should cause the minimum change possible in the hydrostatics of the hull and so another optimization was performed.

Each aft section was modified by being represented with two adjacent FSpline curves with their joint point lying on the initial section. These curves depend on two principal parameters which are the position of their common point and their end tangent vector angle at that point which has obviously the same value for both of them. In the most forward section modified, this angle was kept constant and equal to that of the initial section's at the same point (whose position is a parameter), as it has no local maximum or minimum. That gives two design variables for the position of the common point in the first and last section and one design variable for the tangent vector's angle on the transom section. In order to maintain fairness of the surface that is to be created by these curves, the values of the position and angle should change gradually along the x coordinate. The way chosen to assure this, was to define their values at each longitudinal position by smooth curves with endpoints on the first and last section modified. These curves are also FSplines defined by design variables which were used in the optimization process. These design variables are their tangent vectors' angles at their endpoints, which were variated within a predefined range like the ones aforementioned. Table (1) presents the variables used in this process.

Table 1. Design variables' values for optimizing the aft sections' modification process

Design Variable	Units	Lower Limit	Upper Limit	Final Value
Common Point Y Coord. Aft	(m)	1.5	7	3.562
Common Point Y Coord. Fwd	(m)	8	12	11.237
Angle at common point Aft	(deg)	0.5	25	0.73
Position Crv Angle Aft	(deg)	0	60	11.462
Position Crv Angle Fwd	(deg)	0	60	18.876
Angle Crv Angle Aft	(deg)	0	60	1.514
Angle Crv Angle Fwd	(deg)	0	60	25.253

The objective function chosen is actually a demand to minimize both volume and its centroid position difference, which is simply expressed as minimizing the difference in the sectional area with the y axis, between each set of initial and final sections, as shown next:

$$\sum_{i=1}^{n}(A_{Ii} - A_{Fi})^2$$

The minimization of the above objective function resulted in a set of new aft sections that only slightly affect the overall hydrostatics of the obtained hull form. Specifically the displacement of the modified hull is 0.42 % greater that the initial while its longitudinal position of the centre of buoyancy is 0.49 % aft of the respective value of the initial.

The implemented parameterization with B-Splines mentioned earlier, is not applicable on sections with endpoints that have equal values for one of their coordinates that belong on the plane to which they lie on, since internal control points are made depended on these endpoints. In addition, the form variation range and the extent to which the bulb surface would be affected were of major importance compared to the close fit of its initial surface. This was based on the fact that an approximation of the bulb only slightly affects the overall hydrostatics, but a wide variation of its surface may significantly affect the hydrodynamic performance of the ship.

The bulb is separated in two parts by a 3-dimensional curve defining its maximum breadth that starts from the middle of the lower part of the FP section and ends in the bow tip. In this case only the upper profile of the bulb was interpolated to fit its initial shape (i.e. the intersection of the upper half of the bulb with the centre plane) which is actually the only one with sharp turns. The curve that separates the two halves is a 3-dimensional FSpline whose end angles on xy and xz planes are set as design variables. This curve is the one to which two more FSpline curves meet in order to define the bulb's sections in each longitudinal position. The angles of these two curves at their intersections with the centre plane and on the yz plane, are also set as design variables. The last two design variables for the bulb region are the x and z coordinate of the tip. The bulb's surface is created by a curve engine function that takes into account the values of the parameters in each longitudinal position.

Having fully defined the parametric hull form, an optimization scheme can be implemented regarding the two selected objective functions. The design variables used in this process are listed below:

- Skeg breadth at base plane
- Draft at the transom section's endpoint lying on the centre plane
- Fullness of the forward part of the waterline
- Entrance angle
- Bulb length
- Bulb's tip (the most forward point of bulbous bow profile) elevation
- Bulb's max breadth curve end angle (at tip) on the xz plane
- Bulb's max breadth curve end angle (at tip) on the xy plane
- Bulb's aft section's (at FP) lower angle on the yz plane
- Bulb's aft section's (at FP) upper angle on the yz plane
- Bulb's forward section's (at tip) lower angle on the yz plane
- Bulb's forward section's (at tip) upper angle on the yz plane

The range of each parameter is selected so that its variation, with the rest of the parameters kept constant, leads to realistic hull forms. This does not mean that any combination of the parameters within their respective range produces smooth hull forms. In fact, not all geometries generated acceptable results as in about 10 % of the cases, potential codes crashed.

The above approach, compared to the traditional modeling methods, offers a flexible way to generate variant hull shapes with modified local and some global parameters. In order to maintain the principal particulars of the initial hull, a constraint has been set regarding the displacement of geometries produced, demanding not to differentiate more than 1.5 %.

3.3 Hydrodynamic tools

The 3-D panel code SWAN1 described in detail by Sclavounos [5] is used to assess the wake wash of the hull forms. A suitable interface to automatic prepare the detailed description of the hull form, fed to that code, has been devised. Although this code could also be used for seakeeping calculations, it is quite time-consuming in that case, while for some variants with shallow transom the code failed to provide the dynamic responses. This difficulty is directly related to the detailed input necessary for the panel method and by no means depreciates the value of the code. Thus, the simple, robust and reliable strip theory code was promoted for the seakeeping runs. Furthermore, in the execution of SWAN1 an iterative procedure was added to converge to the actual dynamic draft and trim of the vessel.

The seakeeping qualities of the variant hull forms can be assessed using either two-dimensional (2-D) strip theory or three-dimensional (3-D) panel methods. The SPP-86 code the standard software of the Laboratory for Ship and Marine Hydrodynamics of the National Technical University of Athens (NTUA) has been used for the strip theory calculations. It uses the modified strip theory of Salvesen, Tuck and Faltinsen [17], disregarding the transom stern terms, coupled with the close-fit hull form representation proposed by Frank [18]. As is well known, strip theory remains a solid basis for seakeeping calculations and competes successfully with newer and more rigorous methods (Bailey et al [19], Grigoropoulos et al. [20]), even at high speeds, when compared with experimental (Blok and Beukelman, [21]) and full-scale results (Grossi and Dogliani [22]). Furthermore, strip theory predicts quite well the shape of the RAO curve around its resonance for the vertical ship responses (Bruzzone et al [23]), which is essential for the proposed seakeeping optimization merit criterion.

In order to verify the wave resistance optimization results gained by the potential code SWAN 1, the initial and both optimized hulls were evaluated in terms of their total resistance by simulating the viscous flow phenomenon of ship sail in calm water. The simulation was performed with the commercial viscous flow RANS solver STAR CCM+. The physical model consists of a multiphase (air and water) fluid flow with a free surface that flows with constant speed around the hull. The fluid flow is viscous and turbulence is defined by the k-ε model. Since a 3 dimensional mesh is needed for the solution of the flow field, and in order to minimize the computational load, there are various mesh control volumes that define specific mesh generation and refinement strategies, in order to produce a more coarse mesh in regions where significant changes in pressure and velocity fields occur. The whole process has been automated by creating java macros in which the principal particulars of the ship as well as some key values regarding specific hull regions, the velocity of the flow field and the mesh cells size, are set as parameters. By this way the simulation setup time was minimized. This automated process can be implemented for various different hull shapes with bulbous bow as well as for every possible scale.

3.4 Optimization algorithms

Contrary to classic optimization methods, which process and improve only a single solution at a time, evolutionary algorithms maintain a population of several candidate solutions simultaneously and determine their relative merit. Populations evolve according to the principles of natural selection and the survival of the fittest concept. In this concept fittest individuals increase their presence in successive generations, so that the most promising parts of the search space are explored by exploiting knowledge gained during previous explorations and the optimal solution is finally located.

The theory of evolution and the survival of the fittest concept gave rise to the so-called Evolutionary Algorithms (EA). Genetic Algorithms (GA) and Evolution Strategies (ES) are the two most widely used EA for a wide range of problems. EA work with generations of individuals, which are formed by breeding the fittest individuals of the previous ones together using operators borrowed from natural genetics and the probabilistic processes which are implicit to them. Further to their robustness, EA can:

- escape from local optima and to locate the global optimal solution
- accommodate any analysis software
- handle multi-objective and multi-disciplinary optimization problems
- locate feasible optimal solutions, in optimization problems with constraints

In multi-objective optimization problems, an optimal performance according to one objective often implies unacceptably low performance in one or more of the other objectives, calling for a compromise between them. A family of non-inferior, alternative solutions, known as the Pareto optimal front, characterizes multi-objective problems. An unlimited number of objectives may be handled in this way, providing a multi-dimensional Pareto front of optimal solutions as well as post-processing tools for getting answers and making critical decisions. Furthermore, they may handle any kind and number of constraints by penalizing unfeasible solutions that emerge during the evolution process by reducing their fitness value in proportion to the degree of constraint violation and thus gradually eliminating them.

Basic EA phases are the formation of the initial starting population by random sampling in the search space, the objective function used to judge the quality of the population members as well as the process for creating offspring. Individuals are selected according to their fitness to produce offspring, through recombination. In the GA the whole parent population is replaced by their offspring and their cost value is computed, while in ES this happens partly only. EA can provide a number of potential solutions to a given problem leaving the final choice to the user. For this paper MOSA (Multi-Objective Simulation Annealing) and NSGA-II (Non

Dominated Genetic Algorithm II) algorithms were used. Both of them are provided inside the CAESES FFW interface and support single and multi-objective optimizations.

The MOSA algorithm is the extended version of the single objective Simulation Annealing algorithm, whose principles are based on the slow cooling process of metals in order to get to lower energy states. The number of epochs and each epoch's duration should be defined, which are the number of different states and the sample population of each state, respectively. In every state there is only one design variable perturbed that leads to different population members. This process is repeated for each epoch with different design variables perturbation. Each design variable is selected randomly and is perturbed by means of Laplacian distribution. The attribute sigma is another value to be defined and represents the magnitude of the perturbation. This algorithm was used in the optimization process that took place in order to best fit the initial hull's curves and was integrated with the Visual C++ interpolation code in order to exchange input and result files with CAESES FFW. Although NSGA-II was also tested for that process, MOSA proved to be more efficient for this process. For this case, 400 different curves were adequate to gain an almost perfect fit to the initial curve. The epoch and epoch duration values were both set to 20, while the sigma factor was set to 0.25.

NSGA-II is the extended version of NSGA and implements the non-dominated sorting evolution strategy. The values that need to be defined are the generations' number, the population of each generation as well as the mutation and crossover probabilities. Each generation is a group of members which are sorted in terms of their performance and produce off-springs that tend to form a new generation with better characteristics. The mutation probability describes how often the parents are mutated before they produce children while the crossover probability defines how often an offspring will be generated by one or two parents. This algorithm was used in the rest of the optimization processes. The first case was the optimization performed in order to modify the aft sections of the hull to prevent them from having multiple intersections with the waterplane. For this, 20 generations of 32 members were created which was proved to be adequate in order to gain a good result. The crossover and mutation probabilities were set to 0.9 and 0.01 respectively. As for the wave resistance and seakeeping optimization, the number of generations was set to 50 with 32 members each, while the crossover and mutation probabilities were set the same values with the previous process. As this is obviously an optimization with two objective functions, the optimized hull form was selected amongst geometries located in a Pareto front of the total population scatter.

4. RESULTS

Two dual-objective, single stage optimization processes were implemented in order to improve the hydrodynamic performance of a fast displacement ferry. Their difference was on the objective function used to quantify the performance in calm water; either the wave resistance or the height of the wave wash were used. In each of them 1600 variants were evaluated. The parent and the optimized hull forms were further validated by a RANS solver. All hydrodynamic calculations were performed at the ship's service speed (Fr = 0.348). Table (2) presents the main particulars of the parent hull whose form was optimized.

Table 2. Principal Particulars of parent hull

Property	Value
Length WL (m)	174.8
Beam (m)	25
Draft (m)	6.39
Displacement (tn)	17.272
Service Speed (kn)	29.03

The flow chart of the optimization process is presented in Fig. 1. As it is shown in this figure, the NSGA-II algorithm is responsible for producing 50 generations. Each generation is produced after the implementation of a process of sorting and selection of the most efficient, amongst the previous generation's members on the basis of the objective functions. The members that perform better are used to produce off-springs according to their probabilities to mutate and crossover. The parents together with their children produce the next generation with a population size of 32 members. After the definition of the values of design variables, CAESES FFW produces variants, which are then exported to be simulated.

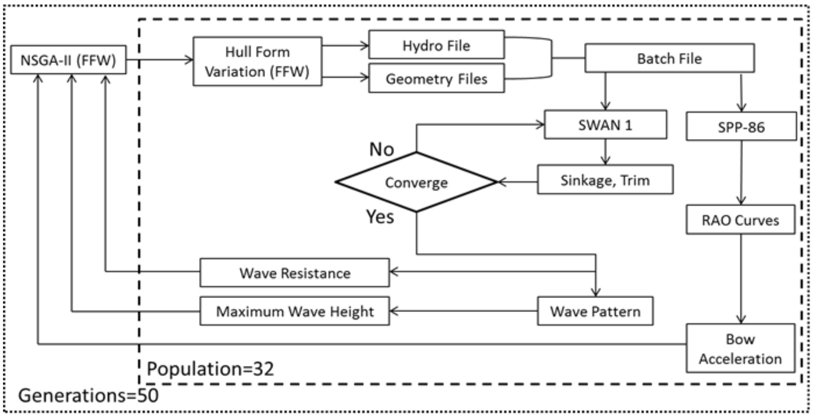

Fig. 1. Optimization process flow

The potential flow solver SWAN 1 runs iteratively until a convergence has been reached regarding both the trim and sinkage of each ship. The output contains both the wave resistance and the wave pattern from which the maximum wave height at a distance athwartship is obtained. Then, the SPP-86 code calculates the RAO curves referring to the motions, velocities and accelerations induced at various positions of the ship, for a range of wave frequencies. The peak value of the RAO curve of the acceleration at bow is then defined. The results obtained by the SWAN 1 and SPP-86 codes are fed back to the CAESES-FFW as single values to be used in the context of the NSAG-II algorithm. All programs running externally to CAESES FFW are manipulated by a single batch file. The chart presented in Fig.1 is simplified as the process flow requires the execution of some additional Fortran codes manipulating the input and result files.

The optimization process was performed in two different cases in order to investigate the most reliable technique for wave resistance minimization. The first objective function was set as the maximum wave height of the wave pattern for the first optimization (Optimization 1) and as the wave resistance itself for the second (Optimization 2). Although only one of the calm water criteria was considered in each optimization process, both of them are calculated and thus presented in a scatter figure. In both cases the second objective function was set as the peak value of the RAO curve referring to the induced acceleration at the bow of the ship.

The produced geometries database is presented in Fig. 2 and Fig. 3. The variants obtained by optimizations 1 and 2, are shown in the scatter diagrams presented in Fig 2, distributed in respect of their wash wave height and seakeeping quality. Fig 3 presents the same databases of geometries but they are distributed according to their wave resistance and seakeeping performance. In all presented diagrams the initial geometry is marked in red color. The diagrams whose axes do not refer to objective functions are presented for evaluation purposes of the whole process.

As shown in all diagrams of Fig. 2 and Fig. 3, there is a clear Pareto front defined by a set of optimum geometries. Each one of these hull forms has no other to be definitely better i.e. that has lesser values in both objective functions at the same time. A variant was selected from each optimization case in order to represent the respective optimized geometry. The selection was obviously made from the diagram that represents both objective functions implemented for that case. Since, regarding the calm water performance, the main goal is to minimize the wave resistance, this value was additionally considered even in the case that it was not set as objective function. The main selection parameters taken into account were the relevance of objective functions values, as well as the displacement's difference compared to the initial hull. Since comparing the two optimization processes is subject of investigation, the selected optimized geometries were picked in order to have similar seakeeping qualities (i.e. that have close acceleration at the bow values).

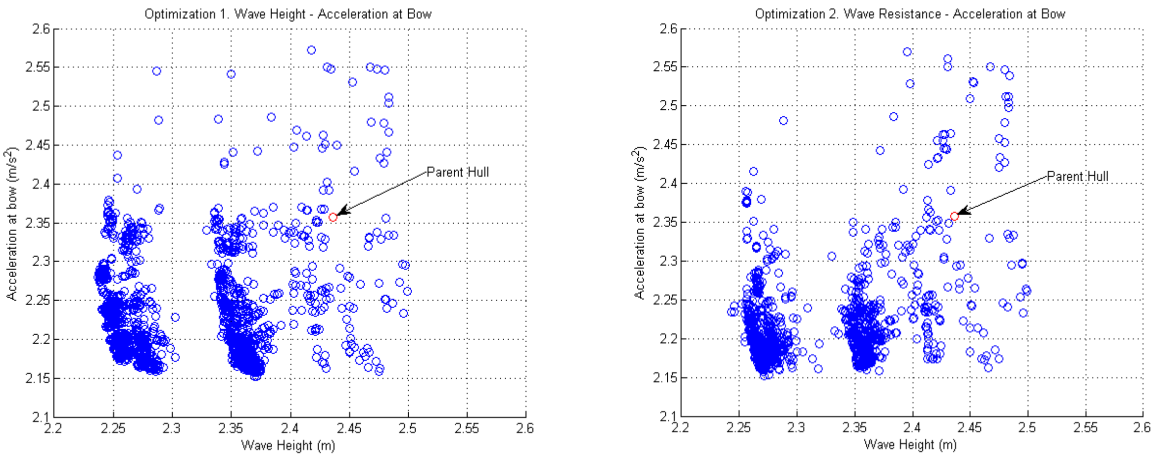

Fig. 2. Database population members of Optimizations 1 and 2, in respect of their wave height and acceleration at bow values

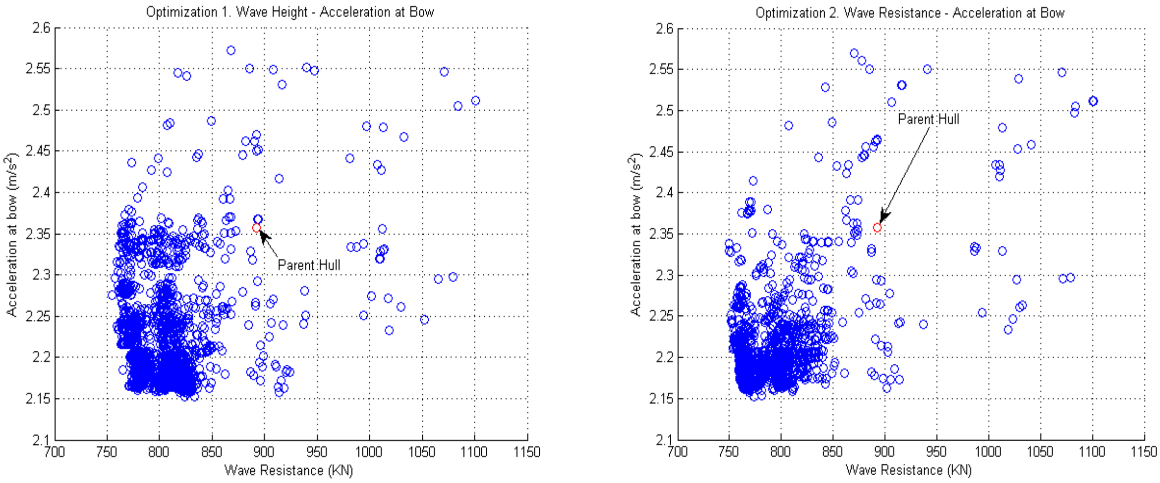

Fig. 3. Database population members of Optimizations 1 and 2, in respect of their wave resistance and acceleration at bow values

The initial and final values as well as the variation range of all design variables are presented in Table 3. The lower and upper limits were set to the most extensive range within which the variables produced fair hull surfaces. As shown in this table, the optimized geometries do not have similar final values for every design variable. It is interesting to note that this fact is quite significant for the bulb length. This has to be considered in conjunction with the rest of the bulb related values, since the two optimized bulb shapes are depended on 8 different variables. The efficiency of both hull and bulb shapes is further investigated by the RANS solver simulation.

Table 3. Design variables for the initial and the optimized hull forms.

Design Variable	Units	Initial Value	Lower Limit	Upper Limit	Opt 1	Opt 2
Skeg Breadth	(m)	1.37	0.7	2.2	0.9	0.91
Transom Height from BL	(m)	6.05	5.95	6.15	5.97	6.15
Waterline Fwd fullness	(%)	0	-6.82	6.99	6.02	5.53
Entrance Angle	(deg)	12.5	10	16	15.94	15.99
Bulb Length	(m)	7.6	6.8	8.4	6.9	7.49
Bulb Tip Z Position	(m)	6	5.2	6.4	5.28	5.36
Bulb Mid Crv End Angle Z	(deg)	0	0	60	13.28	44.18
Bulb Mid Crv End Angle Y	(deg)	90	60	90	87.43	60.69
Bulb Sec Aft Low Angle	(deg)	32	20	50	20.31	20.54
Bulb Sec Aft Up Angle	(deg)	153	140	170	167.43	168.8
Bulb Sec Fwd Low Angle	(deg)	25	15	35	23.94	15.26
Bulb Sec Fwd Up Angle	(deg)	145	135	155	138.91	154.61

Table 4 presents the results derived from both optimization schemes in terms of the objective functions determined, as well as the displacement constraint. The results refer to the selected geometries and also the geometries with the best performance in terms of one objective function for each (i.e. the optima obtained from both optimization processes). As shown in this table all criteria considered were improved compared to the initial geometry. The selected variants are both located in the Pareto front and were considered of adequate quality in terms of both criteria. The final choice was made amongst numerous geometries of similar quality that were also located on the Pareto front, by evaluating the values of objective functions as well as their relevance to each other. During this process the wave resistance reduction was of slightly higher priority than the acceleration at bow. That was based on the fact that wave resistance is only part of the total and hence, the latter's improvement would be of lesser percentage.

Table 4. Optimization results for calm and rough water at constant speed

	Wave Resistance		Acceleration at Bow		Wash Wave Height		Displ. Variation
	(KN)	(%)	(m/s^2)	(%)	(m)	(%)	(%)
Initial Geometry	892.5	0	2.3573	0	2.4363	0	0
Optimization 1	782.9	-12.28	2.1868	-7.23	2.2503	-7.63	1.29
Optimization 2	758.8	-14.98	2.1862	-7.26	2.264	-7.07	1.21
Wave Resistance Optim.(Opt 2)	749.5	-16.02	2.3291	-1.20	2.2571	-7.36	-0.59
Seakeeping Optimum (Opt 2)	773.3	-13.36	2.1519	-8.71	2.2718	-6.75	1.63
Wave Height Optim.(Opt 1)	760.9	-14.75	2.2794	-3.30	2.2373	-8.17	0.1

Fig. 4 presents the wave pattern of the initial geometry compared to both the optimized. These wave patterns are an output of the SWAN 1 potential solver. In both cases a significant reduction in the wave pattern's wave heights, is obtained. As expected the maximum reduction is noticed in the optimized variant for which the wave height was set as objective function.

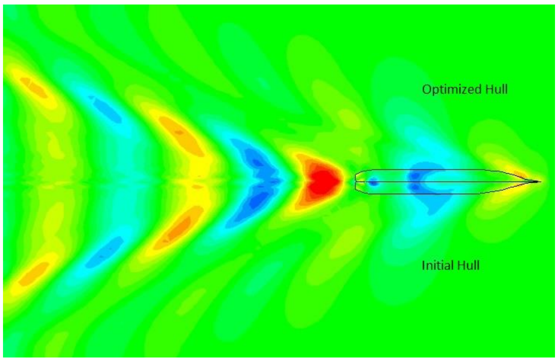

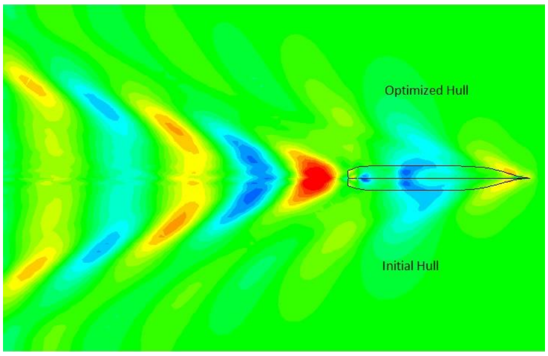

Fig. 4. Wave pattern of initial and optimized hulls from optimizations 1 (left) and 2 (right).

The RAO curves representing the acceleration at bow and added resistance for each wave frequency are presented in Fig. 6. Since the optimized geometries have similar maximum acceleration reductions, their curves are almost identical and thus cannot be visually distinguished. On the other hand, the two optimized geometries have contradicting trends for the added resistance, compared to the respective response of the parent hull. This implies that added resistance could be included in a multi-objective optimization scheme.

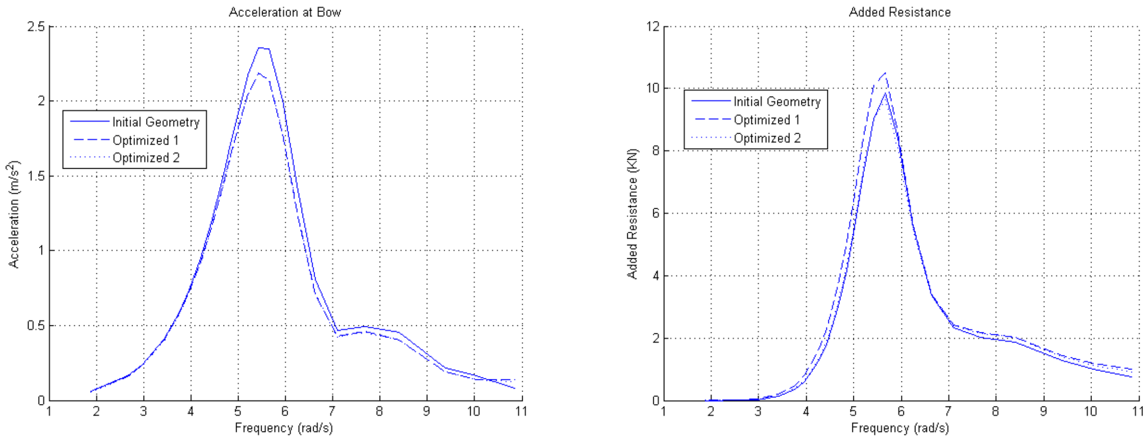

Fig. 6. RAO curves of absolute vertical acceleration at bow and added resistance of initial and optimized geometries from both optimization processes.

The lines plans of the two optimized geometries are compared to the initial and presented in Fig. 7. The optimized are represented in dashed while the initial in continuous lines. In both cases the design variables alteration has an obvious effect on every part of the hull region. Regarding the bulb, a significant shape variation can be noticed for its sections for the hull obtained by optimization 2.

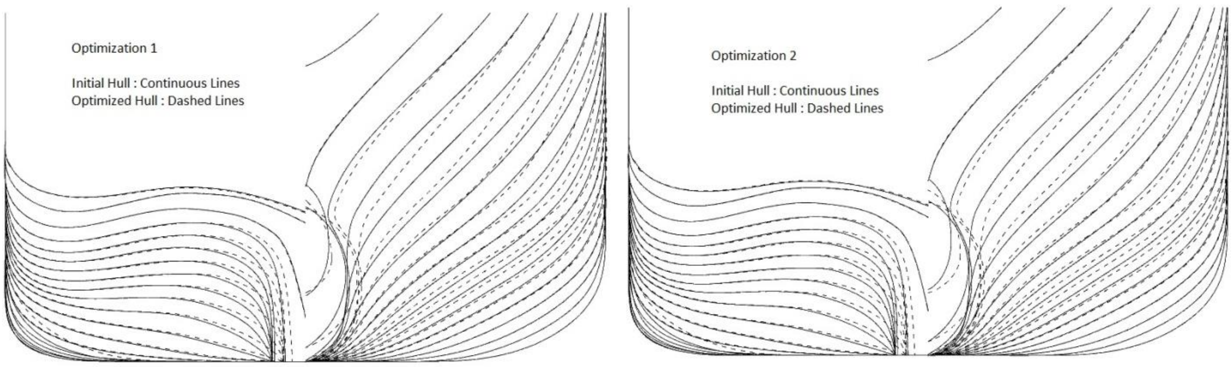

Fig. 7. Lines Plan of initial and optimized geometries.

The results derived from the RANS solver simulation of the two optimized hull forms according to their total resistance, confirmed the conclusions obtained by the potential flow solver simulations. Specifically, compared to the parent hull, the obtained reduction in total resistance is 5.74 % for the optimized hull form of optimization 1 while the respective value obtained from optimization 2 was 7.27 %. Consequently the wave resistance proved to be more reliable to be set as an objective function than the wave pattern's maximum height. In addition, although the design variables of the optimized variants differ, both hull forms are of adequate quality.

The wave patterns produced by STAR CCM+ of the optimized variants are presented in Fig. 8. Despite the fact that the optimized hull forms have similar total resistance values, an improved wave pattern can be noticed for the variant obtained by optimization 2.

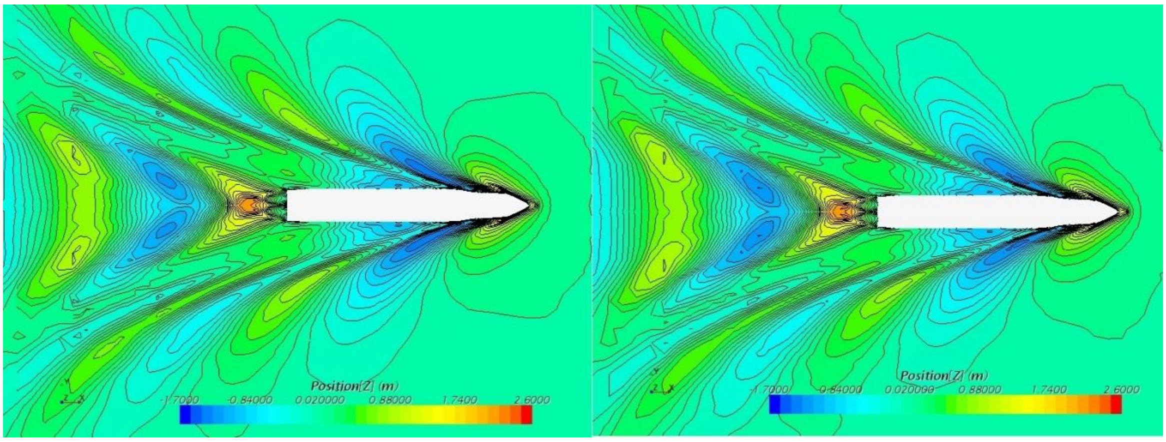

Fig. 8. Wave pattern of optimized geometries obtained by optimization 1 (left) and optimization 2 (right), simulated in the RANS solver STAR CCM+.

5. CONCLUSIONS

In this paper two optimization processes were performed in order to improve the sailing performance of a fast displacement ferry in both calm and rough water. In both processes the acceleration at bow was set as objective function, while the other was set as the maximum wave height for the first case (Optimization 1) and the wave resistance for the second (Optimization 2). These two optimizations were single stage, multi-objective and fully automated within an efficient Simulation Based Design scheme.

The hull representation was performed by implementing a fully custom parametric design process including optimization of fitting of existing hull curves as well as using design tools and functions provided by CAESES Friendship Framework. The evaluation of the calm water performance of the produced hull forms was performed using the potential flow solver SWAN 1, while their seakeeping qualities were estimated by the strip theory based evaluation code SPP-86, produced by the Laboratory for Ship and Marine Hydrodynamics of the National Technical University of Athens. In each optimization process, 1600 variants were generated and their quality was evaluated by the NSGA-II genetic algorithm. The initial and the two optimized hulls were further evaluated in terms of their calm water total resistance by simulating a constant speed ship sail using the RANS solver STAR CCM+.

The optimization results showed that improvements can be achieved in respect to both criteria chosen, as the average reduction gained by the two optimization processes was 13.6 % and 7.25 % for the wave resistance and acceleration at bow, respectively. In addition, the viscous flow simulation software STAR CCM+ confirmed the results obtained by the potential calm water evaluation as both of optimized hull forms proved to have improved calm water performances. Specifically, the reduction of the total resistance was found to be 5.74 % for Optimization 1 and 7.27 % for Optimization 2, and thus the wave resistance is slightly more reliable than wave height to be set as an objective function in calm water optimization. The total resistance reduction is not significant but it should also be considered that the parent hull is an already well-shaped geometry, as it belongs to an existing fast displacement ferry. Regarding the obtained results the following conclusions are drawn:

1. The Simulation Based Design process can be quite efficient in optimizing an existing hull form in terms of specific criteria. In each part of this process, though, the reasonable choice of the parametric modeling technique, the CFD evaluation tools as well as the algorithms

that manipulate the population produced, are of major importance for the efficiency of this unified strategy.
2. Genetic algorithms are capable of concluding to a Pareto front of optimized hull forms after a reasonable number of variants have been evaluated, especially in multi-objective schemes. The final results are quite superior compared to the parent design.
3. Potential flow solvers constitute an efficient and fast tool for the evaluation of the hydrodynamic behavior of large number of ship variants. On the other hand, viscous codes can provide a more accurate simulation tool which should be used for only limited evaluations.
4. Although both the maximum wave height and the wave resistance can be used as objective functions for calm water performance optimization, the wave resistance led to a hull form with slightly better performance than the height of the wash wave, as it was demonstrated by viscous flow simulation.
5. The proposed multi-objective optimization process using potential flow codes should always be validated a posteriori via CFD or experimental investigation in the towing tank.

References

1. Campana, E., Peri, D., Tahara, Y., Kandasamy, M., Stern, F., (2009), Numerical Optimization Methods for Ship Hydrodynamic Design
2. Grigoropoulos, G.J., (2004), Hull Form optimization for hydrodynamic performance, *Marine Technology, Vol. 41, No. 4*, October
3. https://www.caeses.com/
4. SWAN1 (1999), User Manual Vs.3.1: Ship Flow Simulation in Calm Water and in Waves, *Boston Marine Consulting Inc.*, Boston MA 02116, USA.
5. Sclavounos, P.D. (1996), Computation of Wave Ship Interactions, *Advances in Marine Hydrodynamics*, ed. by M. Qhkusu, Computational Mechanics Publ.
6. Heimann, J. (2006), CFD-based Optimization of the Wave-Making Characteristics of Ship Hulls, Jahrbuch der Schifbautechnischen Gesellschaft e.V. , **101**, pp. 234-249.
7. SPP-86 (1994), User's Manual, *Report No: NAL-114-F-94*, Lab. Ships and Marine Hydrodynamics, National Technical Univ. of Athens.
8. Grigoropoulos G.J. (1989), Hull Form Optimization with Respect to Seakeeping, PhD Thesis, NTUA, Dept. of Naval Arch. and Marine Eng., Athens, Greece, May.
9. http://www.cd-adapco.com/products/star-ccm
10. Grigoropoulos, G.J., Chalkias, D.S., Tikkos, C. (2004), Multi-Objective Hull Form Optimization of High-Speed Vessels, *Intl. Conf. HIPER 2004*, Rome, 27-29 September.
11. Abt, C.; Harries, S., Heimann, J., Winter, H., (2003), From Redesign to Optimal Hull Lines by means of Parametric Modelling, *2nd Intl. Conf. Computer Applications and Information Technology in the Maritime Industries, COMPIT 2003*, Hamburg.
12. Peri, D., Kandasamy, M., Tahara, Y., Wilson, W., Miozzi, M., Campana, E., Stern, F., (2012) Simulation Based Design with Variable Physics Modeling and Experimental Verification of a waterjet propelled Catamaran, *29th Symposium on Naval Hydrodynamics, Gothenburg, Sweden, August.*
13. Li, S.,Z., Zhao, F., Ni, Q.,J., (2014) Bow and Stern Shape Integrated Optimization for A Full Ship by a Simulation Based Design Technique, *Journal of Ship Research, Vol. 58, N^{o}2, June.*
14. Grigoropoulos, G.J., Chalkias, (2010), Hull-Form Optimization in Calm and Rough Water, Computer Aided Design 42, pp. 977-984.
15. Pellegrini, R., Campana, E., Diez, M., Serani, A., et al. (2014), Application of Derivative Free Multi-Objective Algorithms to Reliability-Based Robust Design Optimization of a High Speed Catamaran in Real Ocean Environment, *29th Symposium on Naval Hydrodynamics, Gothenburg, Sweden, August.*

16. Piegl, L., Tiller, W., (1997), The NURBS Book, 2nd edition, Chapter 9.
17. Salvesen N., Tuck E.O., Faltinsen O. (1970), Ship Motions and Sea Loads, *Trans. SNAME*, **78**, pp. 250-287.
18. Frank, W. (1967), Oscillation of Cylinders in or Below the Free Surface of Deep Fluids, *NSRDC, Rep. No. 2375*, Washington, D.C.
19. Bailey, P.A., Hudson, D.A., Price, W.G., Temarel, P. (2000), Comparisons between Theory and Experiment in a Seakeeping Validation Study, *Trans. RINA*, **142**, pp. 44-77.
20. Grigoropoulos, G., Harries, S., Damala, D., Birk, L., Heimann, J. (2003), Seakeeping assessment for high-speed monohulls – A comparative study, *8th Intl. Marine Design Conf.*, Athens, 5-8 May.
21. Blok, J.J., Beukelman, W. (1984), The High-Speed Displacement Ship Systematic Series Hull Forms – Seakeeping Characteristics, *Trans. SNAME*, **92**, pp. 125-150.
22. Grossi, L., Dogliani, M. (2000), Load and Seakeeping Assessment of HSC Based on Full-Scale Monitoring, *Intl. Conf. On Ship and Shipping Research NAV 2000*, Paper 2.8, Venice, Sept. 19-22.
23. Bruzzone, D., Gualeni, P., Sebastiani, L. (2000), Application of Green's Function Methods to the Seakeeping Computations for High-Speed Vehicles, *Intl. Conf. Ship and Shipping Research NAV 2000*, Paper 9.1, Venice, September 19-22.

COMPARISON BETWEEN RANS SIMULATIONS WITH LOW NUMBER OF CELLS AND BEM ANALYSIS FOR A HIGH SPEED TRIMARAN HULL

Andrea Agrusta[1], Dario Bruzzone[1], Cuono Esposito[2] and Igor Zotti[3]

[1]University of Genoa,
[2]Sanlorenzo Spa
[3]University of Trieste

ABSTRACT

The use of RANS viscous CFD simulations to evaluate the resistance of ships is well established. These methods, however, often require a high number of calculation cells with consequent substantial hardware requirements. BEM analysis can be performed in a short time and with modest hardware resources, but returned more qualitative results without the viscous part, even if proven and reliable. The objective is to achieve good RANS simulations in a short time so as to make them competitive with panel methods especially in the evaluation phase of different design alternatives. The aim of this work is to study and standardize the operating modes to do viscous simulations with low number of cells, for carrying out more rapidly the calculations, without any necessity of super-computers. The foregoing methods are applied to study high speed trimaran hulls. For the RANS method a system of localized mesh-sizing of the computational grid is evaluated to get a good simulation in the shortest time possible. Results for resistance and trim from RANS 3-DOF simulations are compared with experimental towing tank tests and with BEM analysis also using transverse and longitudinal wave-cuts.

1. INTRODUCTION

Computational Fluid Dynamics (CFD) used in hull design phase is necessary when there is the need to perform predictions and analysis of a high number of cases; then CFD is extremely advantageous in the analysis of a given design: it allows different initial configurations to be considered in a relatively simple way compared to the experimental investigation and allows to eliminate or reduce the necessity of numerous physical models to be experimentally studied.
The numerical analysis can be performed through panel methods called BEM, which are based on the potential flow theory, or through the use of viscous methods called RANS, solving the averaged Navier-Stokes equations.
BEM methods are efficient and rapid; they allow the evaluation of different design solutions in a short time with the aid of modest computing resources. However, the results obtained are approximate and the absence of analysis of the viscous fluid prevents the possibility to assess the resistance in a complete way.
RANS (or RANSE) methods are able to reach more accurate results in absolute terms, so delivering to a designer much more information regarding the analyzed physical phenomenon. These methods require computational domains with a high number of cells and therefore enormous amounts of data to be processed, involving higher computation time as well as considerable hardware resources.
The objective of this work, in the study of high speed trimaran hulls, was minimizing the number of computational cells in order to reduce both time and cost of simulations, preserving adequate results in each case. In this way viscous RANS simulations will be more attractive in comparison to BEM potential methods even from computing time point of view.

2. THEORETICAL BACKGROUND

2.1 BEM method

The numerical method employed for the analysis of the steady waves and for the evaluation of the steady wave resistance and for the evaluation of the wave resistance is based on Rankine sources and can deal also with some types of high speed vehicles, including round bilge and hard chine mono-hulls, catamarans and trimarans [1],[2],[3],[4].

The governing equations for a ship advancing with a given speed U is based on boundary conditions written for a total velocity potential. The hull boundary condition requires that no flow passes through the wetted hull and can be written as:

$$\nabla\Phi \cdot \vec{n} = 0$$

where $\vec{n}$ is the unit outward normal vector. The free surface condition, linearized about the double model potential is:

$$\begin{gathered} g\frac{\partial\Phi'}{\delta z} + \nabla\,\Phi_D * \nabla\,(\nabla\Phi_D \cdot \nabla\Phi') + \frac{1}{2}\nabla\Phi'. \\ \nabla\,(\nabla\Phi_D \cdot \nabla\Phi_D\,) = \nabla\Phi_D \cdot \nabla\,(\nabla\Phi_D \cdot \nabla\Phi_D) + \\ -\nabla\Phi_D \cdot \nabla\,\left(\frac{\partial\Phi_D}{\partial x}\cdot U\right) - \frac{1}{2}U\vec{\imath}\; \cdot \nabla\,(\nabla\Phi_D \cdot \nabla\Phi_D) \end{gathered} \qquad (1)$$

where Φ_D is the double model potential and $\Phi = Ux + \Phi'$.

The resulting boundary value problem is numerically solved using quadrilateral panels distributed over the hull and over a portion of the undisturbed free surface. On each panel a uniform source density is considered. The panels are formed according a number of structured grids. On the hull they allow to define different surface patches depending on the number of hulls and on their form; on the free surface the structured grids considered are involved by the number of hulls and by the presence or not of transom wakes. The second order derivatives of the relevant velocity potentials are evaluated by using longitudinal and transverse four point finite difference operators.

Finally, a linear system of equations is obtained in the unknown source densities relative to each panel. Then, after the solution of this system and the computation of the velocities on each panel, the application of the Bernoulli equation allows to determine the pressure forces on the hull and, consequently, the wave resistance, the running trim and sinkage and the wave elevation on the free surface portion considered. The generated wave pattern may be analyzed using transversal and longitudinal cuts.

2.2 RANS method

Viscous calculation codes solve the equations of mass and momentum conservation within an accuracy that depends on the characteristics of the model and the computing resources. In our problem, given the presence of two fluids, it is necessary to insert an additional equation ("multi-phase" model). An enormous number of specialized literature about the subject exists (see for inst. [5]); The present work shows only an essential outline.

The governing equations expressing mass and momentum conservation for incompressible fluids are given by the following relationships:

$$\frac{\partial u_i}{\partial x_i} = 0 \qquad (2)$$

which represents the continuity equation, and:

$$\rho\frac{\partial u_i}{\partial t} + \rho\frac{\partial(u_i u_j)}{\partial x_j} = \mu\nabla^2 u_i - \frac{\partial p}{\partial x_i} + F_i \qquad (3)$$

representing the conservation of momentum; ρ is the fluid density, μ the viscosity, u_i are the components of the velocity, p the pressure, and F_i are the forces of volume.

If more fluid phases are involved, by solving further equations you can determine their boundary and their distribution into the calculation domain by using a multiphase method.
You may also evaluate the surface interface between two homogeneous zones. In this specific case the waves generated by a marine vehicle advancing at a given speed will be calculated as "ripples" in the interface zone, between air and water. So, by considering this interaction, also the contribution due to waves, the wave resistance, will be included in its resistance.
A powerful model meeting the needs of the calculation in question is the VOF ("Volume of fluid") [6].
The VOF can model two or more immiscible fluids by solving a single set of conservation of momentum equations and subsequently plotting the volume fraction of each of the two fluids through the entire domain.
If α_l is the volume fraction of each phase, the transport equations takes the following form:

$$\frac{\partial \alpha_l}{\partial t} + v_i \frac{\partial \alpha_l}{\partial x_i} = \frac{S_{\alpha_l}}{\rho_l} \tag{4}$$

S_{α_l} is a source term that in our study assumes the value of zero.
The properties in the transport equations are determined by the presence of the component phases in each control volume. In a two-phase system, named 1 and 2, in terms of the volume fraction of α_1, the density in each cell is given by:

$$\rho = \alpha_1 \rho_1 + \ +(1 - \alpha_1)\rho_2 \tag{5}$$

Finally, in this paper the *k-ε* model was used for the computations. It is very well known and widely used, for simulations of turbulent flows, especially in the industrial field. It is characterized by two differential equations: one for the turbulent kinetic energy k and the other for the turbulent dissipation rate ε.

3. RANS ADOPTED APPROACH

3.1 Surface and volume mesh

For the hull surface mesh, a different grid density is used for each area in order to maintain an adequate resolution of the involved geometries with accurate geometric details representation, though minimizing the number of elements, where possible, for instance in flat surfaces or where the curvature is large.
It was decided to use a coarse basic volume-mesh thickening through appropriate volumetric-controls only in areas of interest. In particular, volumetric-controls of mesh thickness were created around the hull, around the upper portion of the hull and near the free surface, in order to capture the wave pattern with adequate resolution.
As far as the free surface concerned, a first volumetric control has been created around the entire surface, with a higher anisotropic condensation along the z axis, in order to evaluate wave pattern geometry without increasing the number of cells too much; a second volumetric control has been created in the triangular area where we expect the wake (fig. 1).

3.2 Type of hulls

In the development of the method three different hull families have been considered to outline the meshing procedure: 1) round bilge displacement hulls; 2) semi-planing hulls with round bilge or with chine; 3) Hard chine planing hulls, both for monohull and multihulls. [7]
Each of these families is characterized by a similar geometry and by the same Froude number range. So a different type of grid is optimized to identify the peculiarities of the particular flow behavior typical of each family.

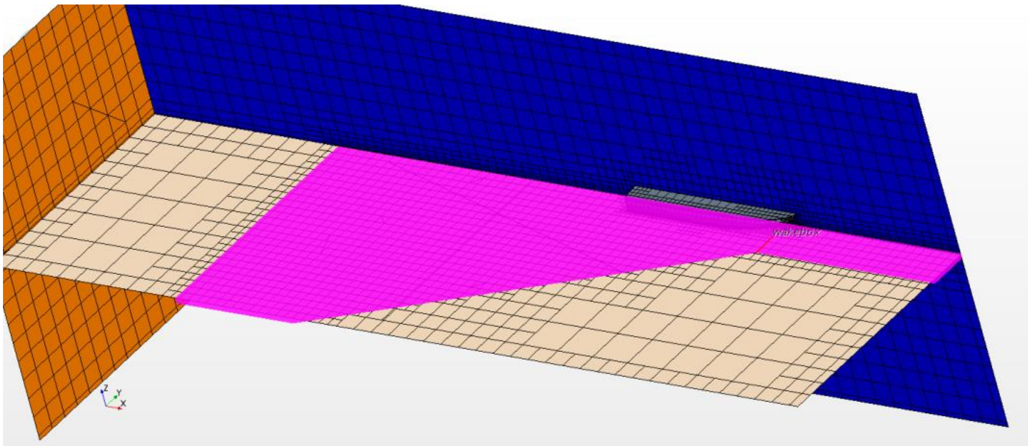

Fig.1. Volume mesh: triangular volumetric control for wake analysis

3.3 Domain and conditions

Computational models with domain of about 2 million cells are typically required in order to evaluate the resistance of a semi-displacement multihull, to analyze the pressure field on the bottom and to assess the generated wave pattern. By testing grid convergence, the methodology applied in this study shows that domains of approximately 450,000 cells may be already adequate. The calculations are carried out in three degrees of freedom to consider the ship advancing free to sink along the z axis and to assume trim rotations about the y axis.
The resistance and the dynamic trim are evaluated during the phase of uniform rectilinear motion of the hull.
The method used is implicit unsteady and then there is the possibility to use the so called "fast transient" method. This allows the possibility of working with Courant numbers between 1 and 10, rather than smaller than 1. In this way, the computation time is strongly reduced.
The convergence is tested using analysis of residual diagrams stationarity (see fig.2) and it is achieved by means of degrees of freedom gradual release of trim and sink in order to allow the simulation settling even with low numbers of cells.

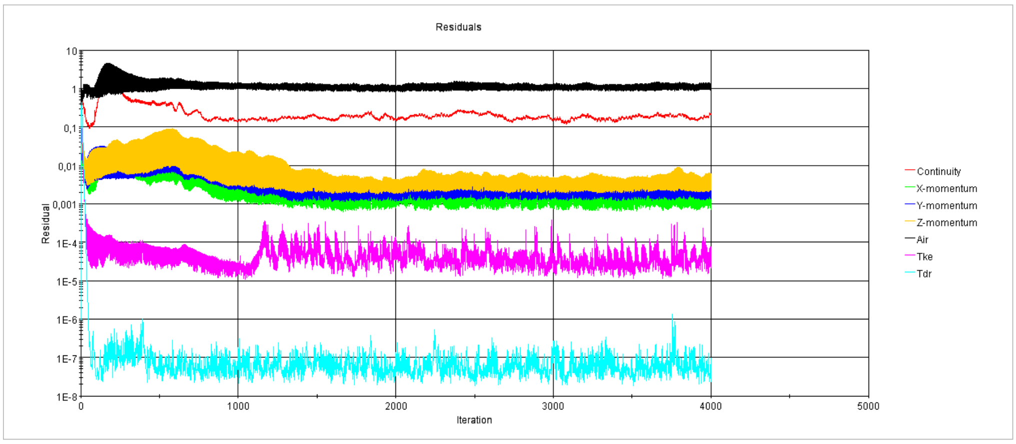

Fig. 2. Residual analysis

3.4 Improvement of method

The method of standardization of simulations at a low number of cells has been developed and validated through numerous simulations performed on hulls both slow and fast, round bilge and hard chine (see the work of Agrusta and others, [7]), by comparing the results obtained from tank tests.

4. RESULTS AND DISCUSSION

For comparison, a particular trimaran hull called Monotricat was used in two different version: the first with thinner outriggers and flat bottom central hull, the second with wider outrigger and stern of the central hull with more deadrise angles (see fig. 3, 4 and 5)

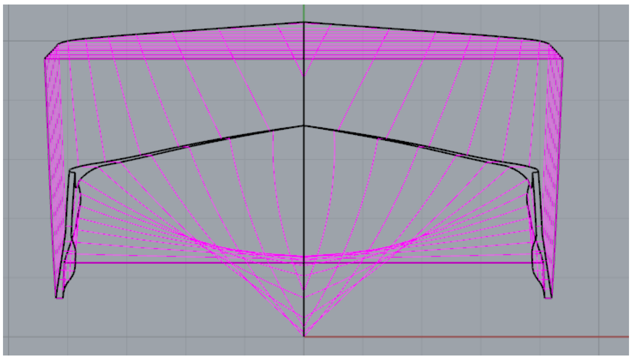

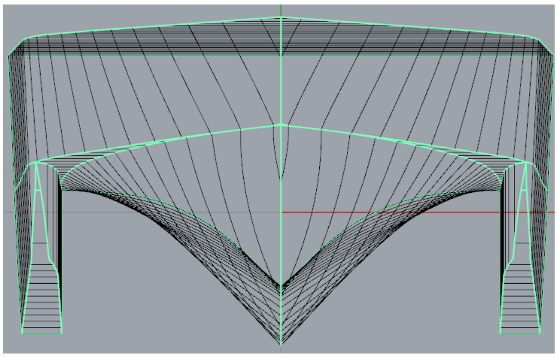

Fig.3 e Fig.4. Transversal section of the Monotricat v1 (fig.3) e v2 (fig.4)

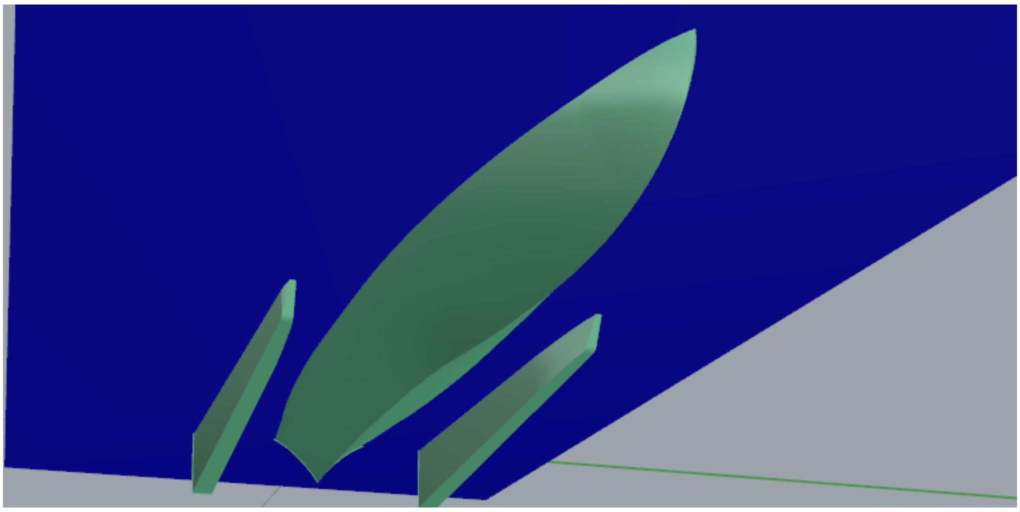

Fig.5. Underwater view of monotricat v2

4.1 Comparison of the resistance measurement between RANS calculation and tank test

Simulations with viscous method were carried out to replicate tests performed in the towing tank. The calculations were performed on a scale model (λ=8.5) in order to directly compare the results without any scale. Some graphical extrapolation of the results can be seen in Figure 6 and 7.

As can be noted in figure 8, the resistance trend line measured in CFD is fully validated, although worked with a coarse grid and then having lost some resolution on the absolute value of resistance (average error abt. 6.9%).

Table 1. Comparison between RANS CFD and tank results.

Vm	Vs kn	Fn	FnV	Rtm CFD v1	Rtm CFD v2	Rtm tank v1	v1/tank
[m/s]	[kn]	[-]	[-]	[N]	[N]	[N]	[-]
1.412	8.00	0.27	0.65	19.15	17.93	18.24	5.0%
2.117	12.00	0.41	0.97	68.83	60.82	64.73	6.3%
2.823	16.00	0.55	1.30	104.75	116.53	97.29	7.7%
3.529	20.00	0.69	1.63	124.40	146.77	115.33	7.9%
4.235	24.00	0.82	1.95	155.24	221.78	144.56	7.4%

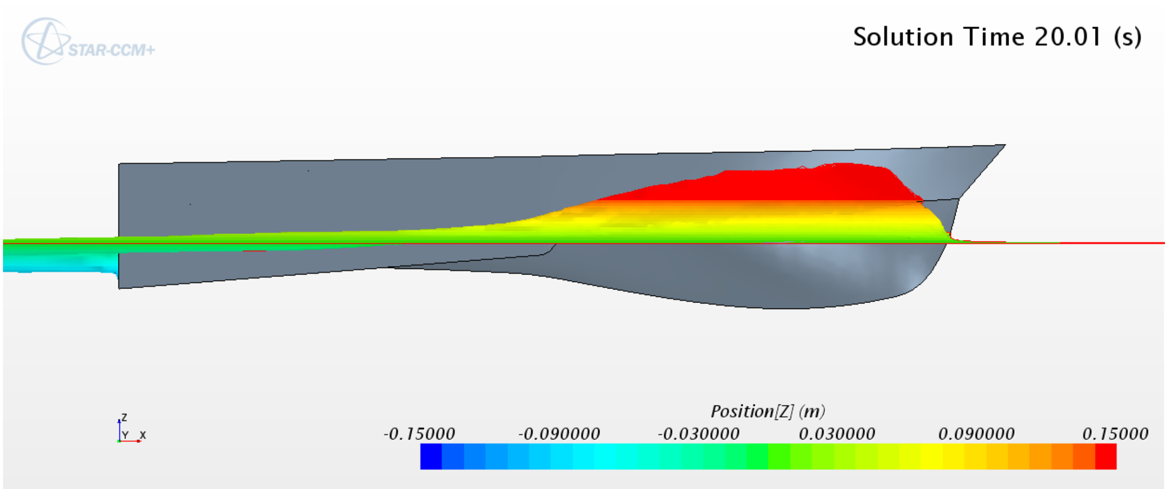

Fig. 6. Wake profile of hull v1 at 24Kn

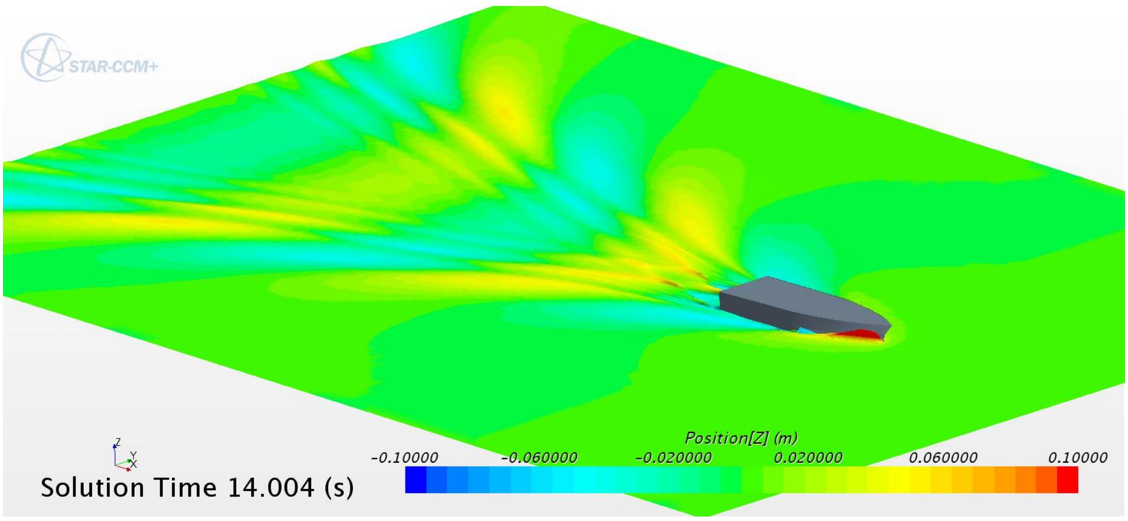

Fig. 7. Perspective view of wake of v2 at Fn 0.55

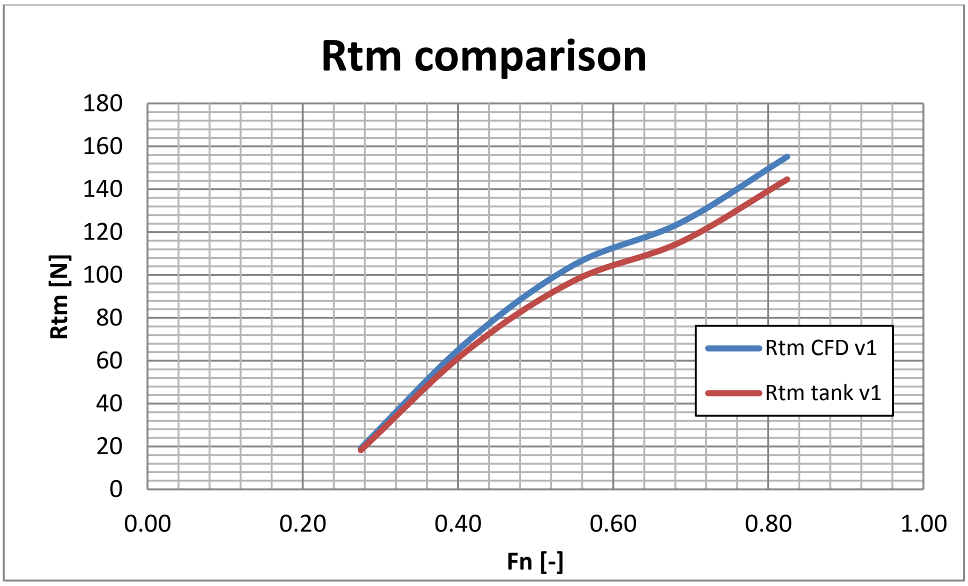

Fig.8. Comparison between CFD and tank total resistance curves

4.2 Comparison of wake calculation between RANS and BEM methods

Despite having worked with a coarse grid, standardizing the volume mesh through the method RANS (see fig.9) we tried to densify the mesh thickness in the free surface area in order to capture with a good approximation also the waves generated by there hull, thus to compare them with those calculated with BEM method.

For Monotricat v2 hull, some simulations were performed in the same conditions of immersion and trim, at relative speeds of Fn = 0.41, Fn = 0.55 and Fn = 0.69, in order to measure three entities of the wake quite different from each other since at these speeds the hull comes into transition from displacement to planing.

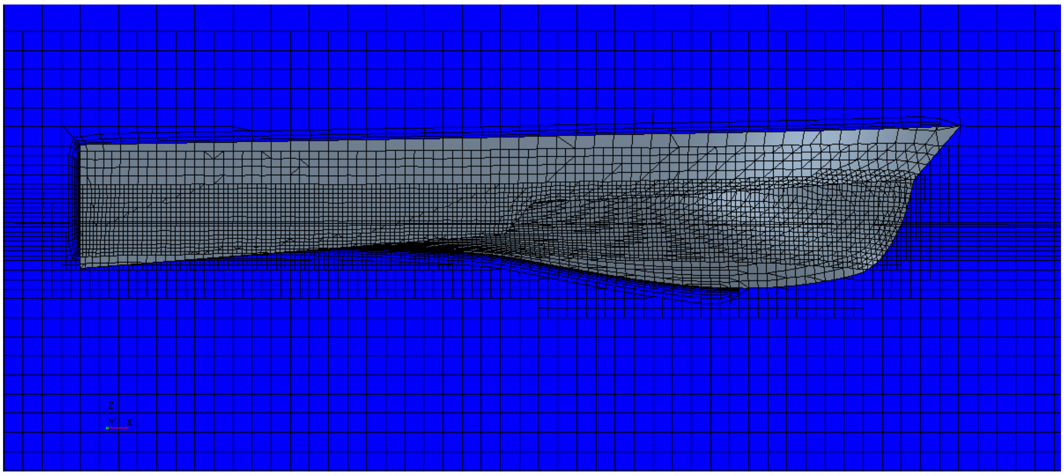

Fig. 9. volume mesh

The results obtained have been evaluated initially by visual assessment comparing the wave formation and the contour lines (see fig. 10, 11 and 12).

Then several wavelength cuts have been carried out for both methodologies (see Fig. 13) and, in particular, for each of the three speeds tested: one longitudinal cut at y = 0.3L from the center line and three transverse cuts, respectively at x = 0, that is in correspondence of transom , x = -0.5L and finally at x = -L.

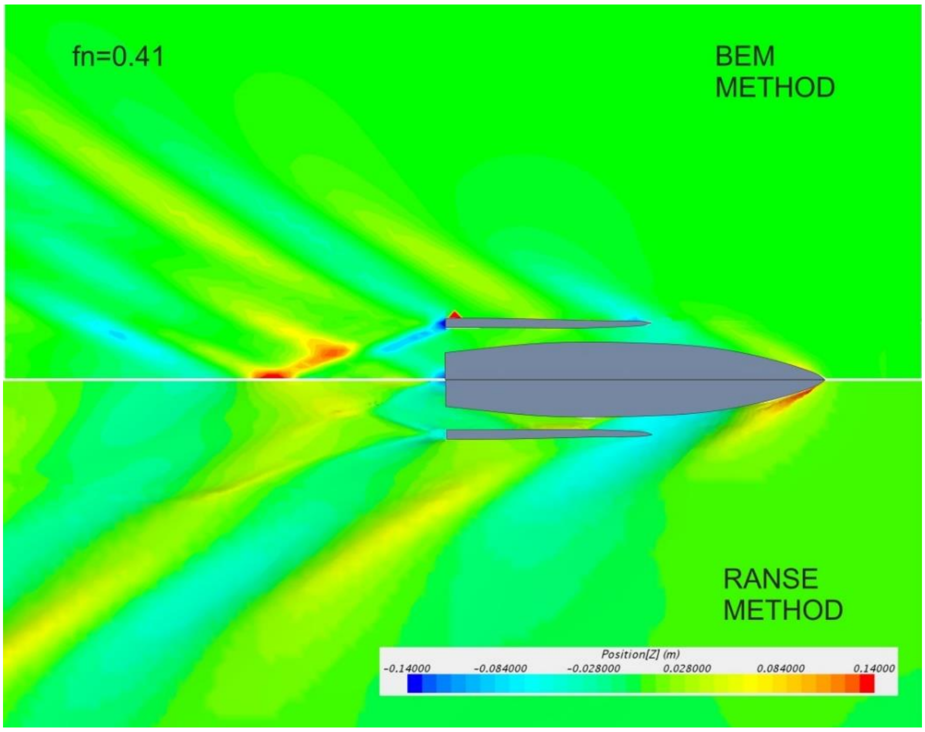

Fig. 10. Wave pattern: Comparison between BEM and RANS methods at Fn=0.41

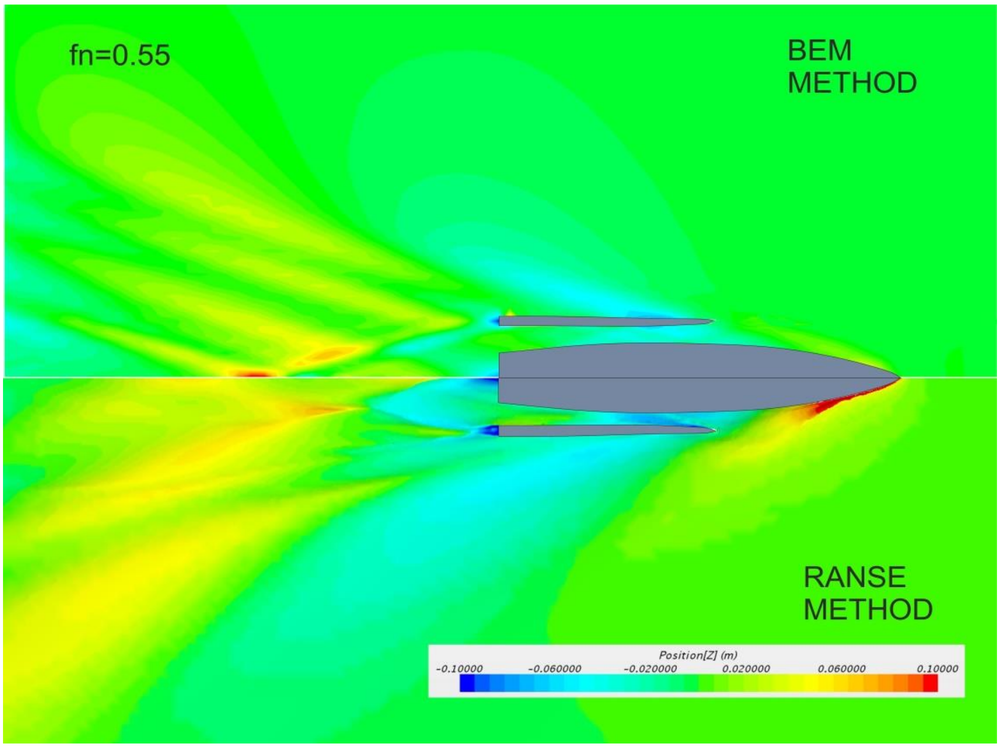

Fig. 11. Wave pattern: Comparison between BEM and RANS methods at Fn=0.55

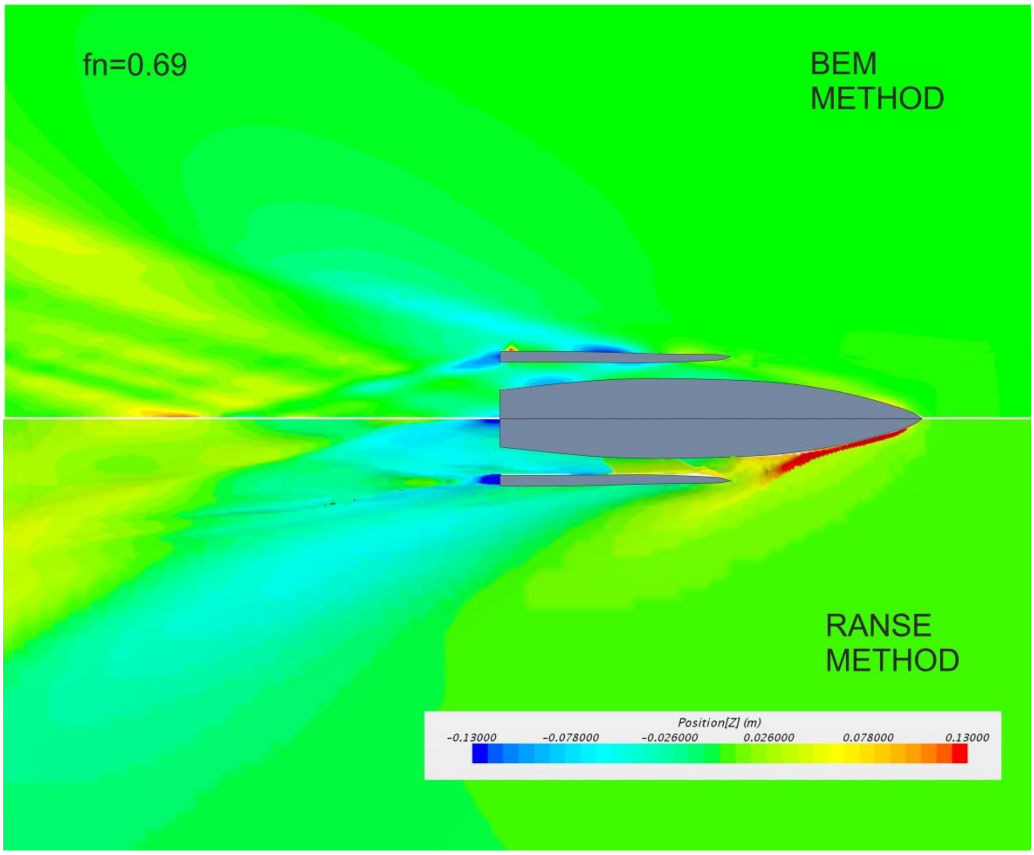

Fig. 12. Wave pattern: Comparison between BEM and RANS methods at Fn=0.69

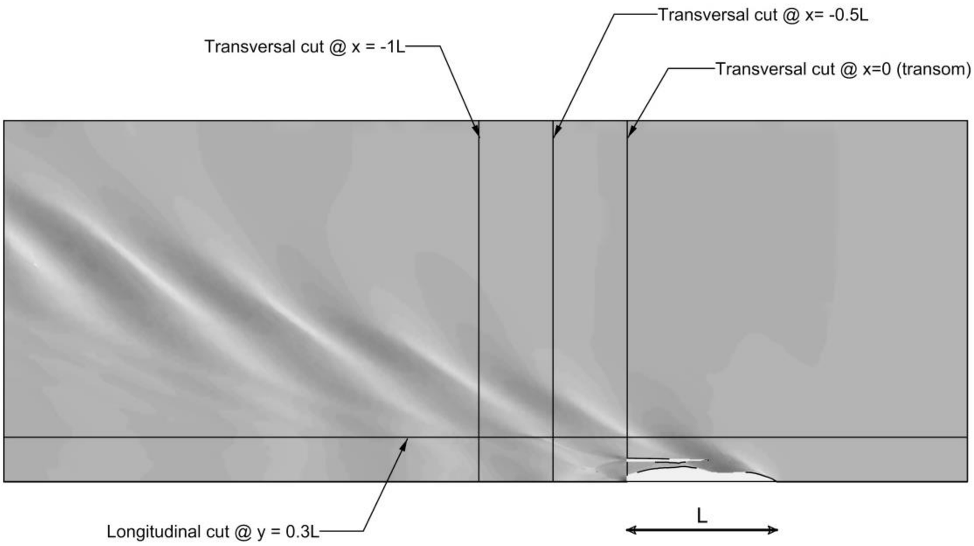

Fig. 13. Transverse and longitudinal wave cuts position

From the accurate comparison obtained between the different wavelength cuts, it can be seen that the two methods, although based on completely different techniques and in spite of the different coarse grid adopted to significantly reduce the computation time in the RANS method, the wavelength cuts' geometry appear similar and the comparison results therefore succeed (for transverse wave cuts see fig. 14, 15 and 16 for Fn = 0.41; fig. 17, 18 and 19 for Fn = 0.55; fig. 20, 21 and 22 for Fn = 0.69; for longitudinal wave cuts instead see fig. 23, 24 and 25).

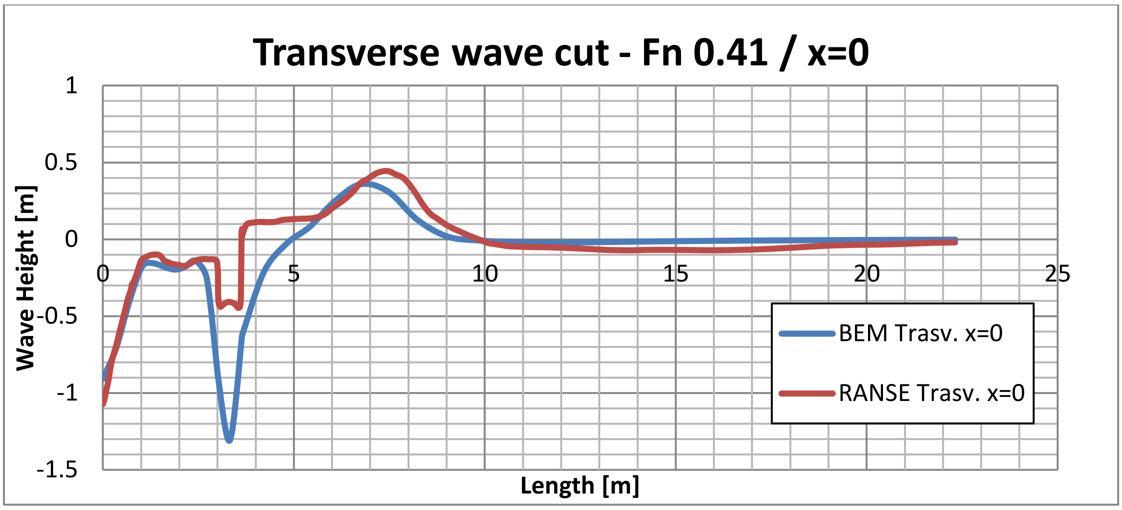

Fig. 14. Transverse wave cut at Fn 0.41, x= 0.0 L

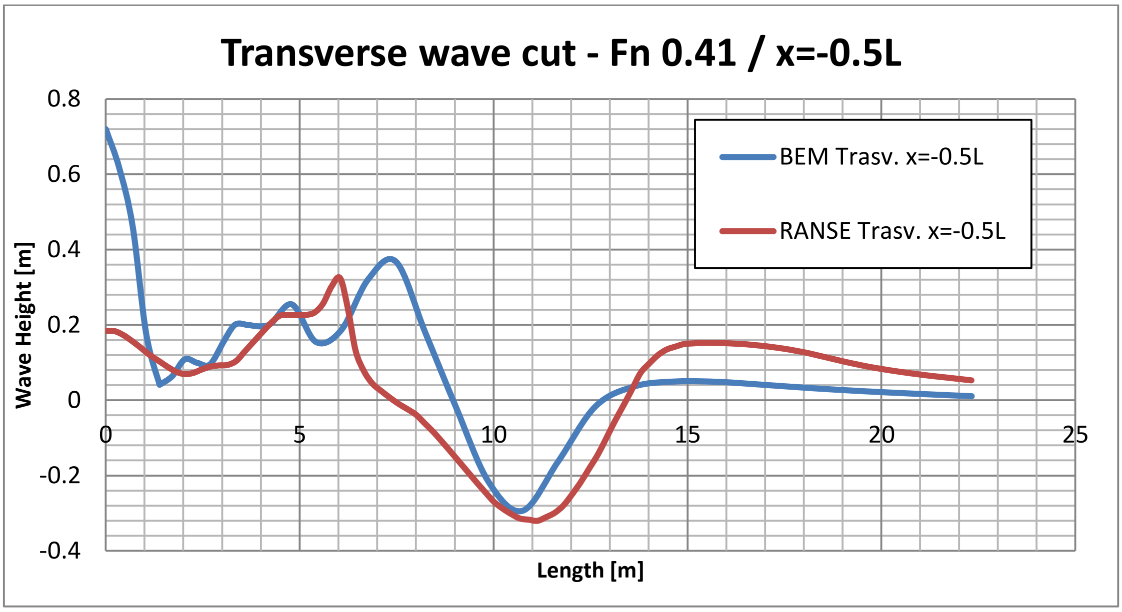

Fig. 15. Transverse wave cut at Fn 0.41, x= -0.5 L

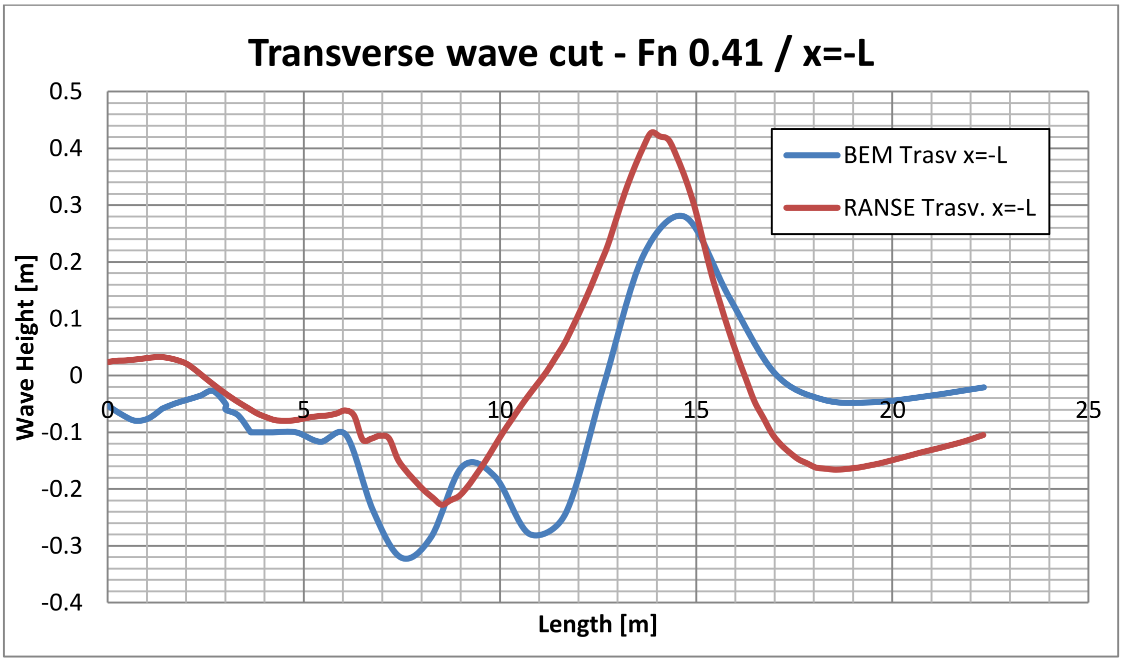

Fig. 16. Transverse wave cut at Fn 0.41, x= -L

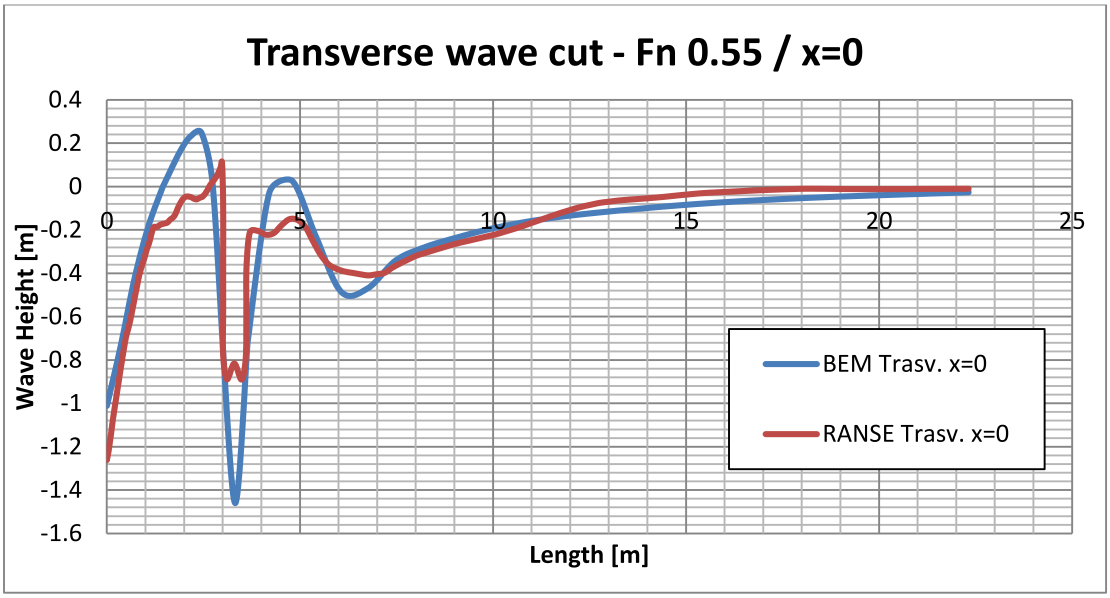

Fig. 17. Transverse wave cut at Fn 0.55, x= 0.0 L

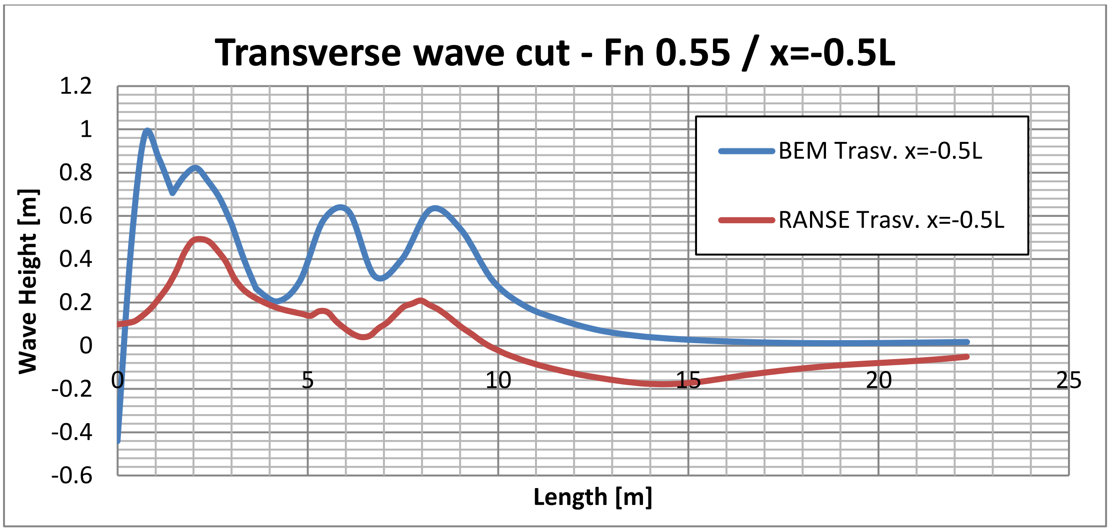

Fig. 18. Transverse wave cut at Fn 0.55, x= -0.5 L

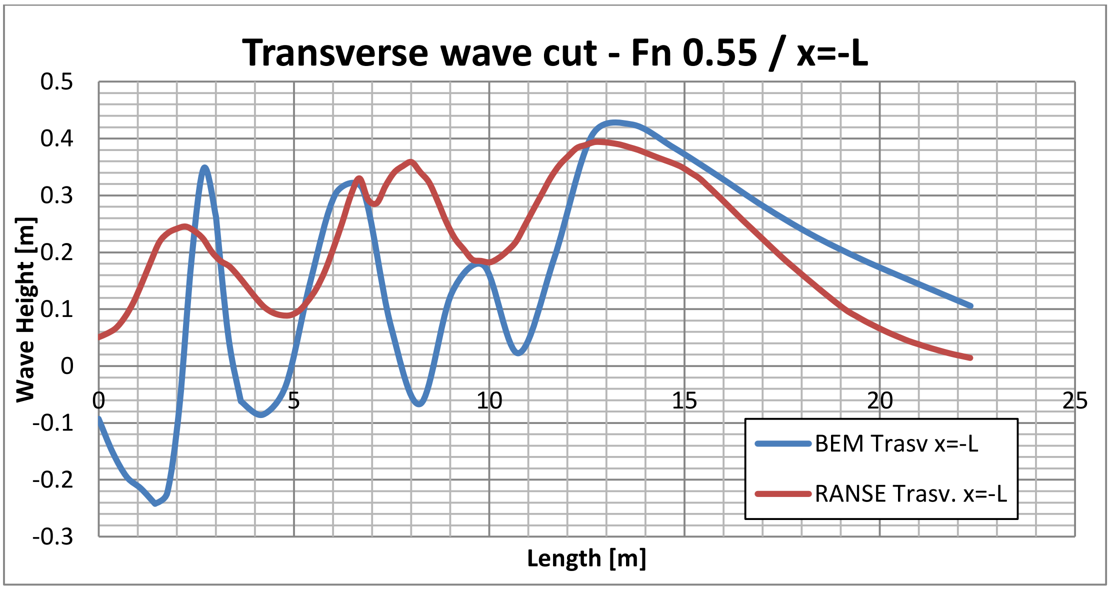

Fig. 19. Transverse wave cut at Fn 0.55, x= -L

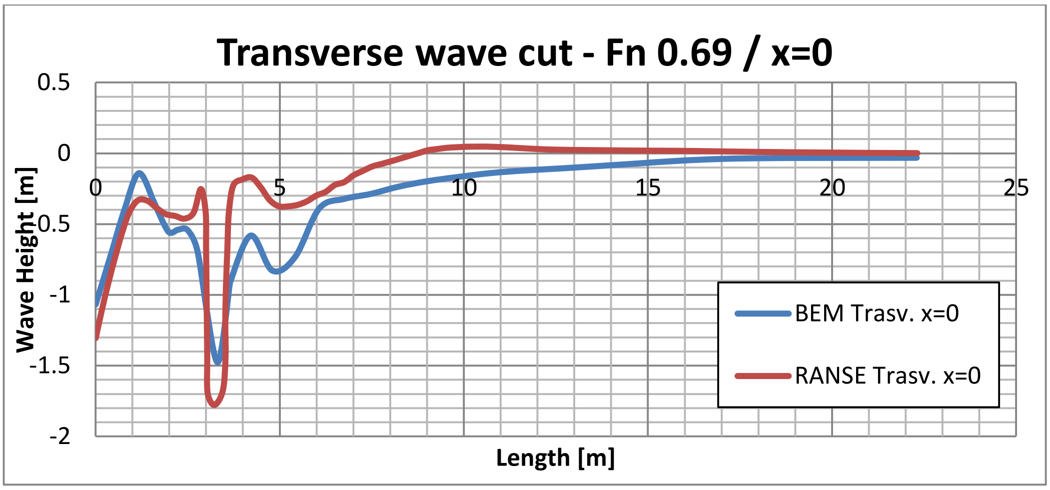

Fig. 20. Transverse wave cut at Fn 0.69, x= 0

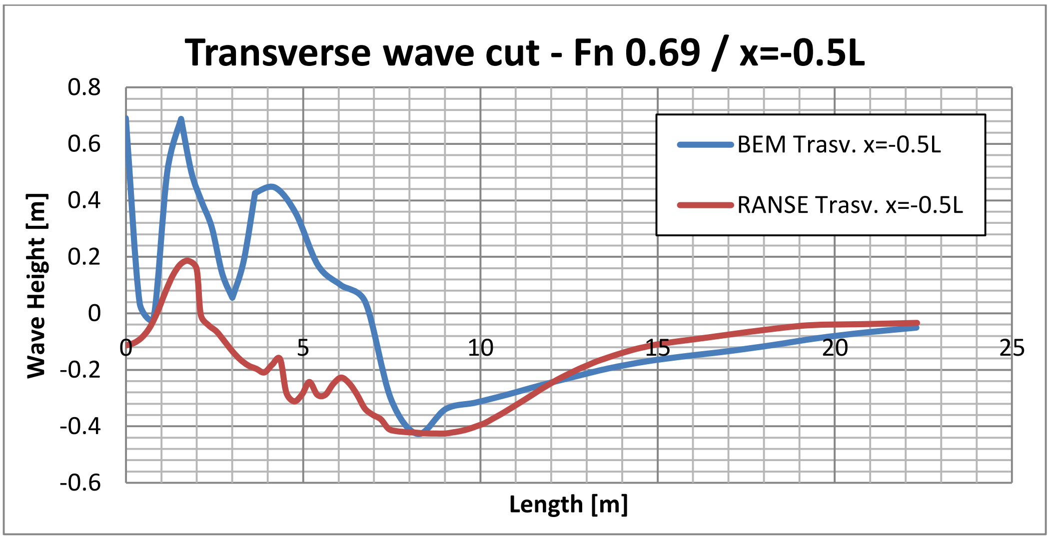

Fig. 21. Transverse wave cut at Fn 0.69, x= -0.5 L

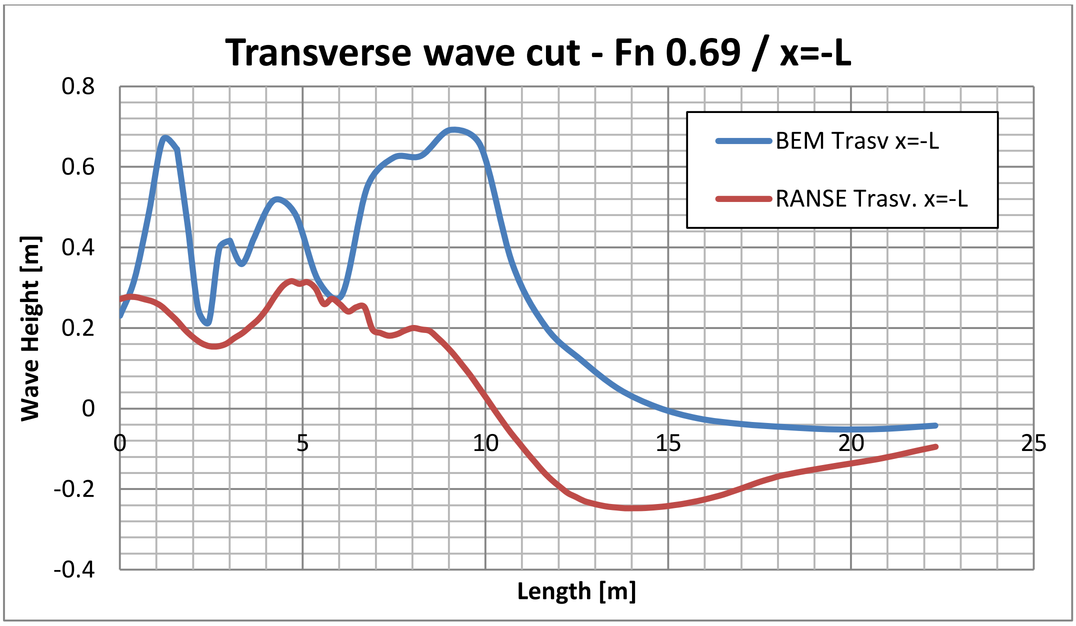

Fig. 22. Transverse wave cut at Fn 0.69, x= -L

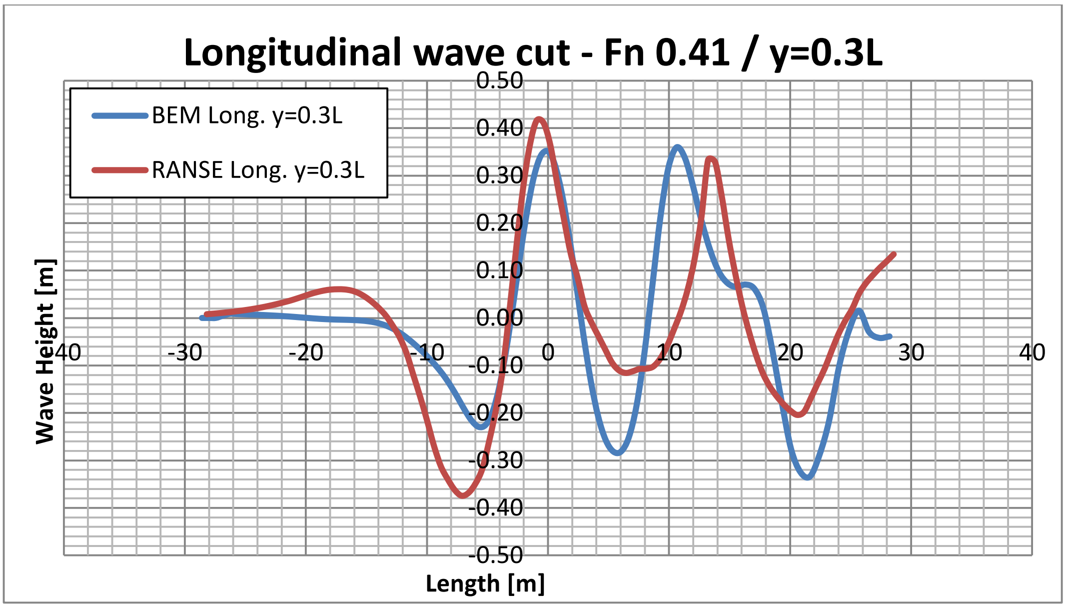

Fig. 23. Longitudinal wave cut at Fn 0.41, y= 0.3L

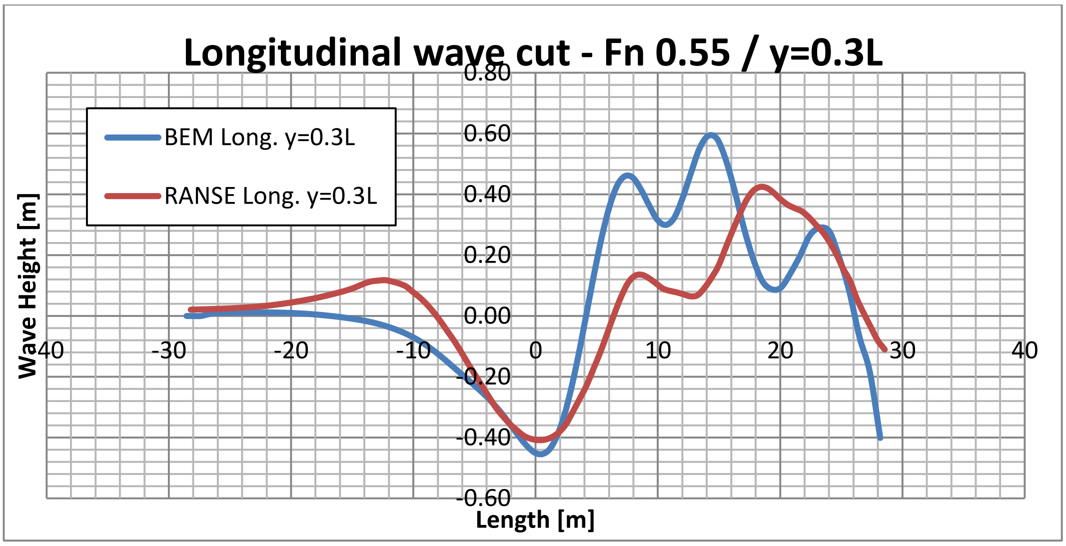

Fig. 24. Longitudinal wave cut at Fn 0.55, y= 0.3L

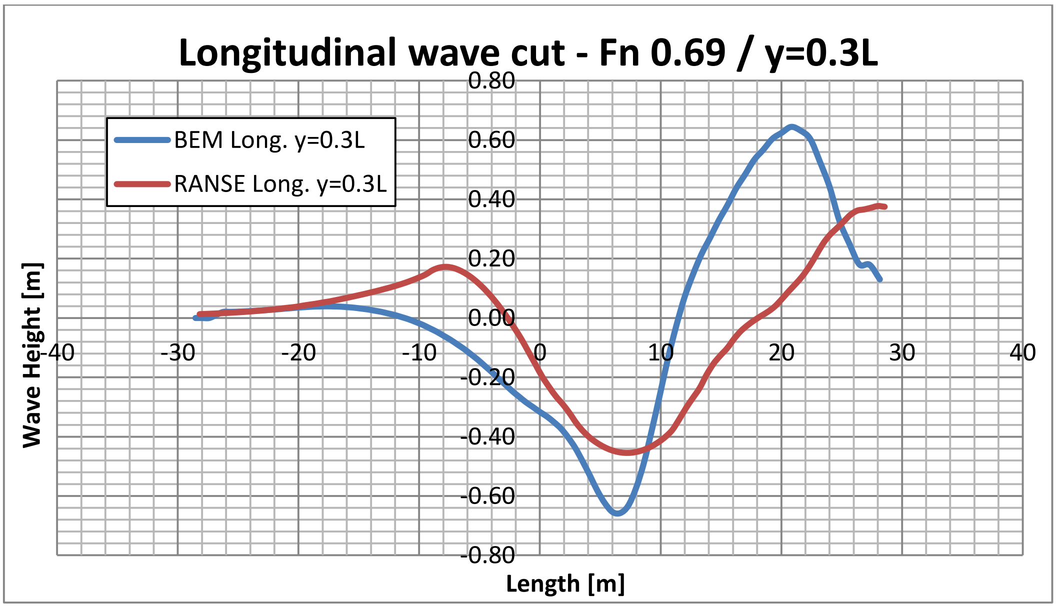

Fig. 25. Longitudinal wave cut at Fn 0.69, y= 0.3L

5. CONCLUSIONS

This study confirms that it is possible using RANS methods even in the preliminary phase of design achieving physically realistic simulations using viscous methods with low number of cells, both for resistance and for trim analysis.

Normally in the first phase of survey, BEM methods were used, considered reliable and useful to compare wave resistance between different design alternatives. Only later, at an advanced stage of the design, RANS methods were used in order to have access to more and more detailed information. Using this RANS method at low number of cells allows to use viscous simulations from the beginning, spending more time than BEM simulations but also obtaining equally reliable results and a multitude of additional information such as the total resistance and friction, streamlines and any other physical information necessary in the design phase.

The lower number of cells allows a significant part of computing time and resources, as well as computer costs, to be saved. In addition, valuable design information may be obtained in shorter times employing a computing power readily available. This study aims to show that the reduction of cells may be parameterized and rationally defined *a priori* depending on the type of hull to be tested.

ACKNOWLEDGEMENTS

Dr. Luigi Mascellaro, Monotricat designer, who made available hull geometry is acknowledged. The financial support of Regione Liguria with a research grant to Andrea Agrusta within "Progetti di alta formazione relativi al finanziamento di assegni di ricerca sul PO CRO Fondo Sociale Europeo Regione Liguria 2007-2013" is aknowledged.

References

1. Begovic, E., Bertorello, C., Bruzzone, D., Cassella, P., Zotti, I., "High Speed Trimarans Validations on Numerical Results by Geosim Tests", Proc. Of the 6th International Conference on Fast Sea Transportation FAST 2001, vol II, pp.285-294, Southapthon, 2001.
2. Bruzzone, D., Cassella, P., Pensa, C., Scamardella, A., Zotti, I., "On the Hydrodynamic Characteristics of a High Speed Catamaran with Round Bilge Hull: Wave Resistance and Wave Pattern Experimental Tests and Numerical Calculations", Proc. of FAST '97, Sidney Australia, 1997.
3. Brizzolara, S., Bruzzone, D., Cassella, P., Scamardella, A., Zotti, I., "Wave Resistance and Wave Patterns for High Speed Crafts. Validation of Numerical Results by Model Tests", Proc. of 22nd Symposium of Naval Hydrodynamics, pp.69-83, Washington D.C,1998.
4. Bruzzone, D., Cassella, P., Coppola, C., Russo, Krauss, G., Zotti, I., "Power Prediction for High-Speed Catamarans from Analysis of Geosim Tests and from Numerical Results", Proc. of the 5th International conference on Fast Sea Trasportation, Seattle Wa, 1999.
5. Ferziger, J.H., Peric, M., Computational Methods for Fluid Dynamics, 3rd Edition , Springer, New York, 2002.
6. Hirt, C.W., Nichols, B.D., "Volume of Fluid (VOF) Method for the Dynamics of Free Boundaries", Journal Of Computational Physics, **39** (1981), 201-225.
7. Agrusta, A., Bruzzone, D., Esposito, C., Zotti, I., "CFD simulations to evaluate the ships resistance: development of a systematic method with use of low number of cells", Proc. of SORTA 2014, Rijeka, Croatia, October 2014

CONTROLLING THE RIDE HEIGHT OF HYDRO-FOILING BOATS IN RANSE CFD

F.M.J. Bergsma[1], K.S. Zaaijer[1], N. Moerke[1]

[1] Van Oossanen Naval Architects, Costerweg 1b, 670AA, Wageningen, Netherlands

ABSTRACT

High performance crafts include hydro foiling crafts. In many types of design the high performance nature and the fuel efficiency of foiling marine vehicles is employed to develop state of the art designs. One example is the Solar Challenge, a biannual race between solar powered boats. By obtaining a stable foiling mode top speeds and efficiency can be improved. By controlling the pitch of the foils, the stability of the foiling mode can be improved and therefore foils control strategies should be developed. These control strategies are to find a balance between the attitude and velocity of the vessel at one side, and the dynamically generated forces on the other side. A target ride height and attitude is to be achieved in a stable way. This paper presents a method to perform simulations of the transition of a vessel from displacement mode to a target ride height. The pitch of all foils of the vessel is controlled using a proportional controller implemented via an user defined code in a commercially available RANSE CFD package. Computational issues concerning the rotation of the foils and the large vertical movement of the vessel are addressed as well in this paper. The results for two control strategies are presented.

NOMENCLATURE

AGR	Adaptive Grid Refinement
CFD	Computational Fluid Dynamics
COG	Centre of Gravity
e_{Ry0}	error in trim of vessel
e_{Tz0}	error in rise of vessel
$K_{i_{aft}}$	integral gain for aft foil
$K_{i_{fwd}}$	integral gain for forward foil
$K_{p_{aft}}$	proportional gain for aft foil
$K_{p_{fwd}}$	proportional gain for forward foil
RANSE	Reynolds Averaged Navier-Stokes Equations
Rn_{aft}	pitch angle of aft foil
$Rn_{aft_{max}}$	upper bound of pitch angle of aft foil
$Rn_{aft_{min}}$	lower bound of pitch angle of aft foil
Rn_{fwd}	pitch angle of forward foil
$Rn_{fwd_{max}}$	upper bound of pitch angle of forward foil
$Rn_{fwd_{min}}$	lower bound of pitch angle of forward foil
$Ry0$	trim angle of vessel
$Ry0_{target}$	target trim angle
$Tz0$	Rise of vessel
$Tz0_{target}$	target translation in z-direction (ride height)
$\vec{g}$	gravitational acceleration
$\bar{\bar{I}}$	Unit tensor
K	turbulence kinetic energy
$\vec{n}$	outward bound normal vector
p	pressure field
S	control volume surface
$\bar{\bar{S}}$	mean strain rate tensor
$\vec{U}$	velocity field

$\vec{U}_d$	velocity of surface S
$\overrightarrow{u'}$	flow velocity fluctuation
V	control volume
μ_t	turbulent viscosity
ρ	density
$\bar{\bar{\tau}}$	stress tensor
$\bar{\bar{\tau}}_l$	viscous stress tensor
$\bar{\bar{\tau}}_t$	Reynolds stress tensor

1. INTRODUCTION

1.1 Hydro-foiling Boats

For over a century mankind has the possibility to rise out of the water using hydro-foiling boats. First efforts were made by Enrico Forlanini and John Thornycroft around the beginning of the 20^{th} century. With development efforts by, among others, Alexander Graham Bell knowledge on the hydro-foiling boats increased. It was only after the 2^{nd} World war that hydro-foiling boats were used in commercial and military applications.

The peak of the popularity of hydro foils in commercial and military applications was in the 1960s and 1970s. Since that moment the popularity has decreased. One of the reasons is the technical complexity of hydro-foiling boats. Advanced ride control is required for hydro-foiling boats with fully submerged foils. Currently the application of hydro foils has an increasing popularity in racing and high performance competitive environments.

1.2 Solar Boat Challenge

The hydro-foiling boat analysed in the current paper is a design for the DONG Energy Solar Challenge. This is the largest race for solar powered boats worldwide. The race is a 200 km long course in the province of Friesland in The Netherlands and the competition is between dozens of international teams that design and build their own solar powered boat particularly designed for this race (Dong Energy Solar Challenge, 2014a). Since hydrofoils were first used in the Solar challenge of 2010, more and more competitors are using foils to increase top speed and efficiency (Dong Energy Solar Challenge, 2014b)

1.3 Geometry

The studied hydro-foiling solar boat has an overall length of 7 meters and a width of 1.6 meters. The foil configuration consists of one fully submerged foil forward on two struts, and one foil aft on a single strut. Nacelles are placed at the intersection of the struts and foils to house hinging mechanisms. The majority of the load is carried by the forward foil. Each foil section is able to pivot independently in order to control ride height, dynamic trim and roll independently.

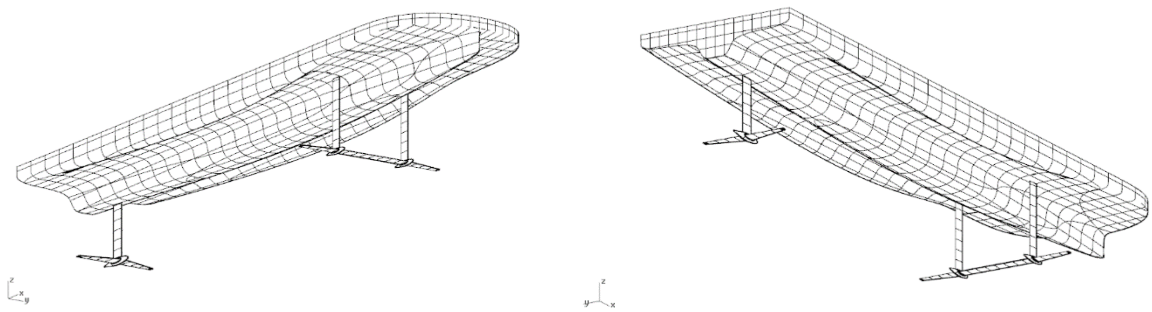

Fig. 1. Wire frame of the studied geometry.

The present study is aimed at introducing a method to study the control of the so called ride height and the trim of hydro-foiling vessels. Dynamic behaviour is simulated using established Computational Fluid Dynamics (CFD) methods. Pitch angles of the foils are adjusted during the simulation, using dynamic libraries that use the dynamic position of the vessel to adjust the foils orientations. First the employed method is described. Then the results obtained with the presented method for two control strategies are presented. In the final chapter the results are discussed and the conclusions are presented.

2. METHOD

This chapter provides the description of the methods applied for simulating a controlled ride height using a Computational Fluid Dynamics method. In section 2.1 details of the employed CFD method are given. In section 2.2 the control strategy is detailed.

2.1 Computational Fluid Dynamics Method

In this section a description is given of the CFD method used to determine the flow characteristics. The commercially available package FINE/Marine is used for generating the unstructured hexahedral mesh and solving the unsteady flow. In section 2.1.1 the governing equations are given. To enable the rotation of the foils of the hydro-foiling craft, a custom domain was generated. This is described in section 2.1.2. From this domain a mesh was generated. This is discussed in section 2.1.3. Adaptive refinement of the mesh is used to capture the water surface properly. The refinement of the water surface is discussed in section 2.1.4.

2.1.1. Governing equations

The modelling of the viscous flow is based on Reynolds Averaged Navier Stokes equations (RANSE) for incompressible unsteady flow. The equation for mass conservation is given in integral conservation form by:

$$\frac{\partial}{\partial t}\int_V \rho dV + \int_S \rho\left(\vec{U} - \vec{U}_d\right)\cdot \vec{n} dS = 0 \tag{1}$$

The equation of conservation of momentum is given by:

$$\frac{\partial}{\partial t}\int_V \rho \vec{U} dV + \int_S \rho \vec{U}\left[\left(\vec{U} - \vec{U}_d\right)\cdot \vec{n}\right] dS = \int_S\left(\bar{\bar{\tau}} - p\cdot \bar{\bar{I}}\right)\cdot \vec{n} dS + \int_V \rho \vec{g} dV \tag{2}$$

Closure of this set of equations is obtained by defining the stress tensor:

$$\bar{\bar{\tau}} = \bar{\bar{\tau_t}} + \bar{\bar{\tau_l}} \tag{3}$$

Here $\bar{\bar{\tau_t}}$ is the Reynolds stress tensor and $\bar{\bar{\tau_l}}$ the viscous stress tensor. The viscous stress tensor is defined as:

$$\bar{\bar{\tau_l}} = 2\mu\left(\bar{\bar{S}} - \frac{1}{3}\bar{\bar{I}}\,\vec{\nabla}\cdot\vec{U}\right) \tag{4}$$

The Reynolds stress tensor is given by:

$$\bar{\bar{\tau_t}} = -\rho\overline{\vec{u'}\cdot\vec{u'}} \tag{5}$$

A closure of this term is required to solve the set of equations. Turbulence viscosity models are used for this closure. These models are based on the Boussinesq approximation. This commonly used approximation gives the Reynolds stress as follows:

$$\bar{\bar{\tau}}_t = -\rho\overline{\vec{u'} \cdot \vec{u'}} = 2\mu_t\left(\bar{\bar{S}} - \frac{1}{3}\bar{\bar{I}}\,\vec{\nabla} \cdot \vec{U}\right) - \frac{2}{3}\rho K\bar{\bar{I}} \tag{6}$$

The near wall low Reynolds SST k-ω model of Menter (1993) was used. This is the recommended turbulence model for these kinds of computations (Numeca International, 2011).

2.1.2 Domain and Boundary Conditions

The domain around the hull is constructed such that the boundaries are far enough away to not influence the results. Using the symmetry from the centre-line, only half of the vessel was modelled. The dimensions of the computational domain around the hull are given in table 1. These are given relative to the reference point, which is at the intersection of the centreline, transom and water plane in hydrostatic condition.

Table 1. Domain size in meters relative to the reference point.

Direction	Minimum (m)	Maximum (m)
X (longitudinal)	-21.0	14.0
Y (beam)	0.0	14.0
Z (height)	-14.0	3.5

All hull surfaces had a no-slip boundary condition using wall functions to capture the boundary layer. In the symmetry plane a mirror boundary condition was applied and on the top and bottom of the domain the pressure was prescribed. All remaining domain faces have external/free-flow boundary conditions with a prescribed flow speed of v = 0 m/s.

The domain around each of the foils is constructed such that the foils can rotate around their span wise axis. Cylinder shaped domains are formed around the foils and all cylinders had a radius of 0.22 m. Their centreline was parallel to the y-axis and was collocated with the axis of rotation of the foil. In figure 2 the cylindrical domain around the foil is given as generated inside the domain around the hull.

All surfaces of the foils had a no-slip boundary condition using wall functions to capture the boundary layer. In the symmetry plane a mirror boundary condition was applied. All other surfaces of the cylinder are coupled with the box shaped domain by means of sliding grids.

The box shaped domain around the hull (as described earlier) has cylinder-shaped recesses at the locations of the cylindrical domains around the foils. The surfaces that form the recess are coupled with the cylinders by means of sliding grids. This method to connect the domains, allow the foils to pitch, within the main domain while keeping a coupling between the domains. The sliding grid approach was validated using submerged propellers (Queutey et al, 2011a) (Queutey et al, 2011b) and a self-propulsion computation with a rotating propeller (Visonneau et al, 2011).

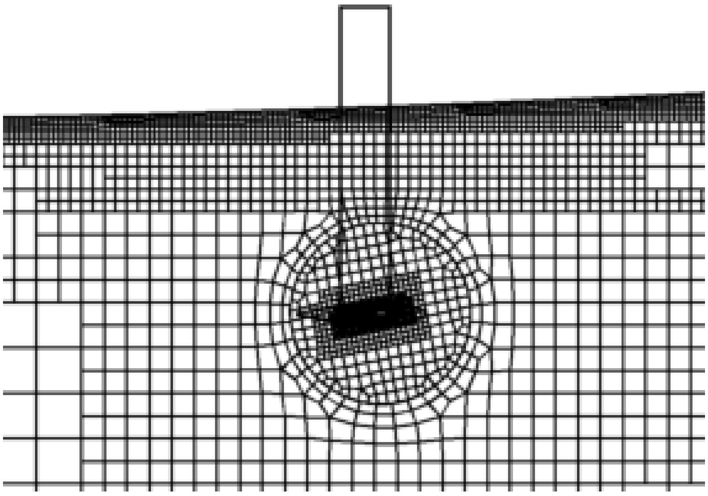

Fig. 2. Cylindrical mesh around the foil.

2.1.3 Computational Mesh

In this paragraph details of the unstructured mesh on the surface of the geometry are given. The domain volume is divided into small cells to generate the mesh. The largest cells on the hull are approximately $\Delta(X,Y,Z) \approx 0.0275$ m in size. In areas with large curvature and detailed flow phenomena, cells as small as $\Delta(X,Y,Z) \approx 0.00085$ m were used to ensure that flow features have a good resolution. The first cell near the wall was set to have a size of approximately 0.00033 m, such that its non-dimensional distance (y+) to the wall was approximately 29.6.

In order to have the best possible data transfer between the cylindrical domains around the foils and the cubic domain around the vessel via the sliding grid method, the mesh density (i.e. the cell size) was refined to be similar at both sides of the domain interface of the sliding grid. This leads to a mesh with approximately 4.3 million cells.

2.1.4 Refinement of mesh at free surface

Cells near the air-water interface were refined to have a size of 0.017 m in z-direction. These refinements are not included in the mesh a priori but are updated during the computation via Adaptive Grid Refinement (AGR). The cells that intersect with the free surface are further refined to the criterion mentioned above. Cells that do not intersect with the free surface anymore are de-refined (Wackers et al, 2012).

Initially the free surface is not refined at all. Therefore a very aggressive AGR strategy is used in the first 6 iterations in order to capture the free surface properly. Every time step the AGR method is called to make sure the mesh is sufficiently detailed to capture the free surface when the boat is accelerating.

The AGR method is used in order to allow a large rise of the vessel. Non-adaptive meshing strategies for capturing the free surface would move with the rising vessel causing the mesh to deform strongly. This negatively influences the stability of the computation. In addition the free surface refinement would not be at the location of the actual free surface. This would decrease the accuracy of capturing the free surface. Figure 3 and 4 show the adaption of the mesh to the water surface, while the vessel is rising.

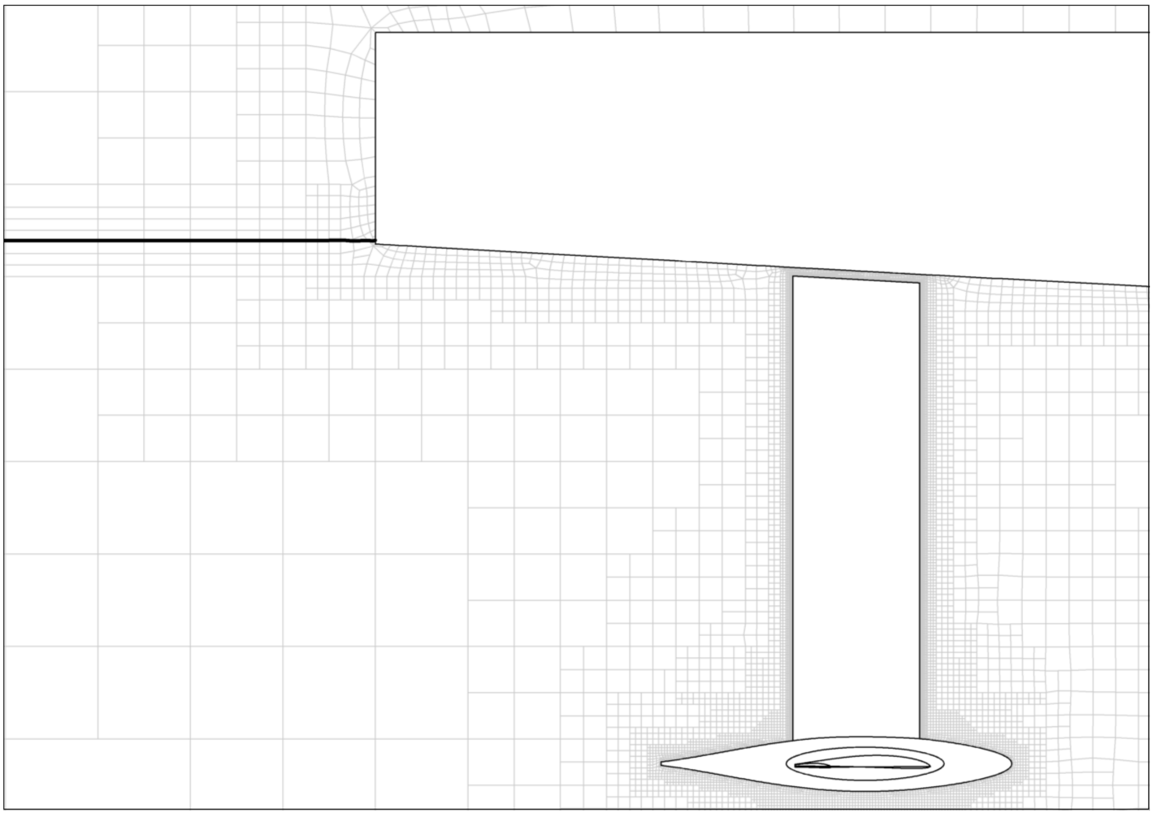

Fig. 3. The mesh at the free surface with the vessel in displacement mode.

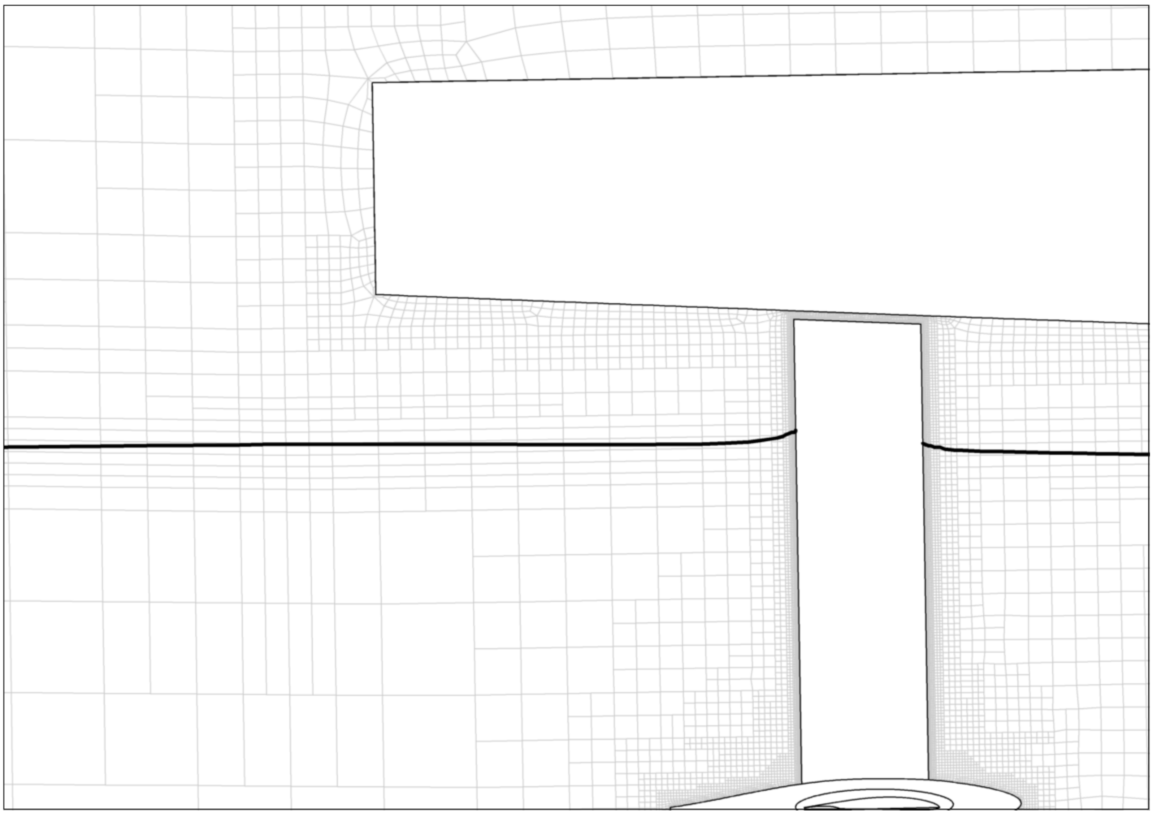

Fig. 4. The mesh at the free surface with the vessel in foiling mode.

2.2 Control strategy

The motion of each foil is controlled via so called 'dynamic libraries'. These control the motion of the foils as a function of variables resulting from the CFD computation. For each time step the pitch angle of the foils are computed and updated. The pitch angle is based on the trim and rise of the vessel.

The pitch angle of the forward foils is given by:

$$Rn_{fwd} = K_{p_{fwd}}\, e_{Tz0}(t) + K_{i_{fwd}} \int_0^t e_{Tz0}(t) dt \tag{7}$$

This means that the pitch angle of the forward foils is influenced by the sum of the proportional term and the integral term. The proportional term produces an output that is proportional to the magnitude of the current error. The integral term produces an output that is proportional to both the magnitude and the duration of the error. This takes in account the accumulated error over the past time. The error in the rise e_{Tz0} is given by:

$$e_{Tz0} = Tz0_{target} - Tz0 + Ry0 * 3.50 \tag{8}$$

Here $Tz0_{target}$ is the target rise at the location of the bow. The actual rise (at the bow of the vessel) is equal to $Tz0 - Ry0 * 3.50$ (bow-up trim is negative). Here the first term is the rise in the centre of gravity, and the second term is the trim multiplied by the distance between the centre of gravity (COG) of the vessel and the bow of the vessel. This accounts for the additional rise at the bow due to the dynamic trim of the vessel.

The pitch angle of the aft foils is given by:

$$Rn_{aft} = K_{p_{aft}}\, e_{Ry0}(t) + K_{i_{aft}} \int_0^t e_{Ry0}(t) dt \tag{9}$$

This means that the pitch angle of the aft foils is influenced by the sum of the proportional term and the integral term. The proportional term produces an output that is proportional to the magnitude of the current error. The integral term produces an output that is proportional to both the magnitude and the duration of the error. This takes in account the accumulated error over the past time. The error in the trim e_{Ry0} is given by:

$$e_{Ry0} = Ry0_{target} - Ry0 \tag{10}$$

Here the trim is set to a target value of $Ry0_{target}$. The actual trim is equal to $Ry0$. (bow-up trim is negative).

Both values for Rn_{fwd} and Rn_{aft} are limited to a range. These are bound by $Rn_{fwd_{min}}$ and $Rn_{fwd_{max}}$ for the forward foil and by $Rn_{aft_{min}}$ and $Rn_{aft_{max}}$ for the aft foil. If the calculated value exceeds these limits, the value will be set to this limit. This is to prevent excessively large pitch angles of the foils.

3. RESULTS AND DISCUSSION

This chapter provides the results of the analyses that were performed using the method described in chapter 2. In section 3.1 an overview of the employed control configurations is given followed by the results of these strategies. In section 3.3 the results are discussed.

3.1. Control configurations

The employed control strategies are based on the control strategy as described in section 2.2. An overview is given in table 2.

Table 2. Overview of employed control configurations

Parameter	Unit	configuration 1	configuration 2
$Tz0_{target}$	[m]	0.27	0.27
$K_{p_{fwd}}$	[-]	-45.0	-20.0
$K_{i_{fwd}}$	[-]	0.0	-5.0
$Rn_{fwd_{min}}$	[deg]	-8.0	-8.0
$Rn_{fwd_{max}}$	[deg]	3.0	3.0
$Ry0_{target}$	[deg]	0.0	0.0
$K_{p_{aft}}$	[-]	-2.5	-2.5
$K_{i_{aft}}$	[-]	0	-1.0
$Rn_{aft_{min}}$	[deg]	-8.0	-8.0
$Rn_{aft_{max}}$	[deg]	3	3

As can be observed from table 2, the first control configuration has proportional gain. The integration gain is equal to zero, therefore this is equal to a P-controller. The second control configuration has both proportional and integral gain, i.e. a PI-controller. To compensate for the contribution from the integrative action, the value for $K_{p_{fwd}}$ was lowered.

Both control configurations have the upper and lower bound for the foils set to 3 and -8 degrees respectively. This is done to prevent separation at the foils due to excessive pitch angles. It should be noted that a negative values for Rn_{aft} and Rn_{fwd} correspond to an increasing angle of attack.

In all analyses, the hydro-foiling vessel was accelerated in 10 seconds from a speed of 0 m/s to 8 m/s via an imposed acceleration profile.

3.2 Results

In the first part of this section the results are given for control configuration 1. In the second part of this section the results are given for control configuration 2.

3.1.1. Results for control configuration 1

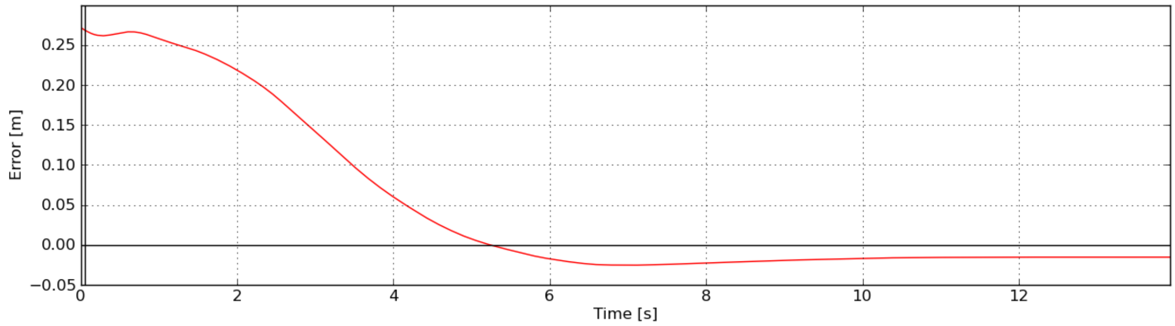

Fig. 5. e_{Tz0} as a function of time for the hydro-foiling vessel.

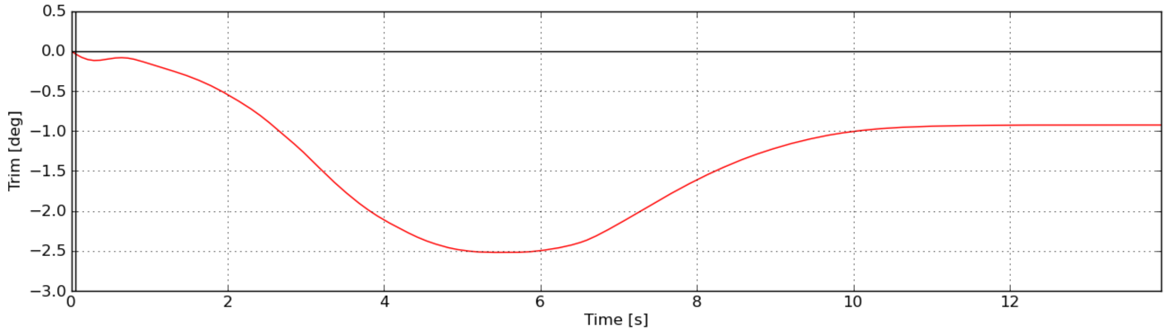

Fig. 6. $Ry0$ as a function of time for the hydro-foiling vessel.

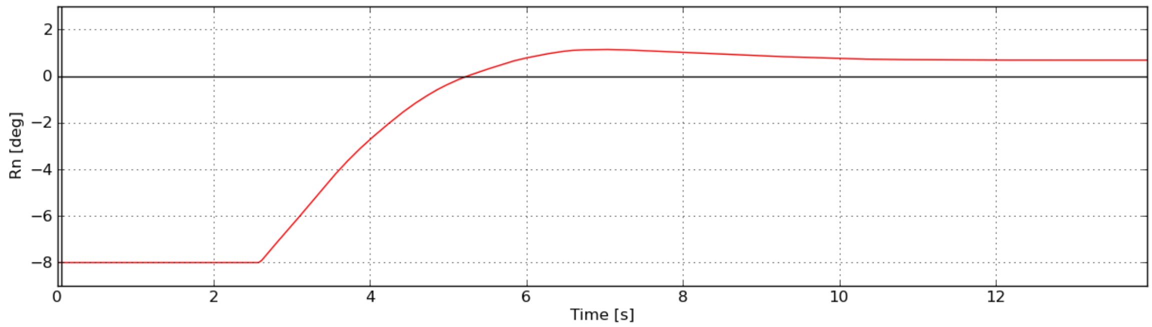

Fig. 7. Rn_{fwd} as a function of time for the hydro-foiling vessel.

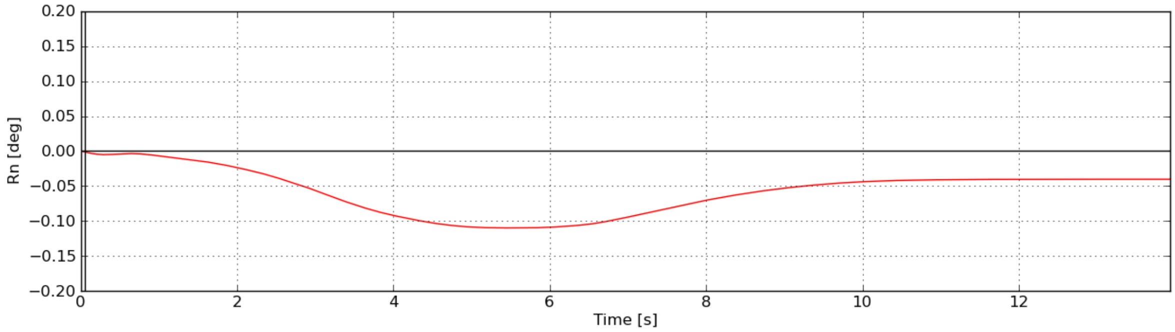

Fig. 8. Rn_{aft} as a function of time for the hydro-foiling vessel.

Figure 5 to 8 show the error in rise e_{Tz0}, the trim of the vessel (which is by definition -e_{Ry0}) and the pitch of the foils respectively. The vessel has reached its top speed after 10 seconds. After settling, the rise $Tz0$ has a value of 0.23 m. the trim has a value of -0.92°. This leads to an error e_{Tz0} of 0.015 m.

3.1.2. Results for control configuration 2

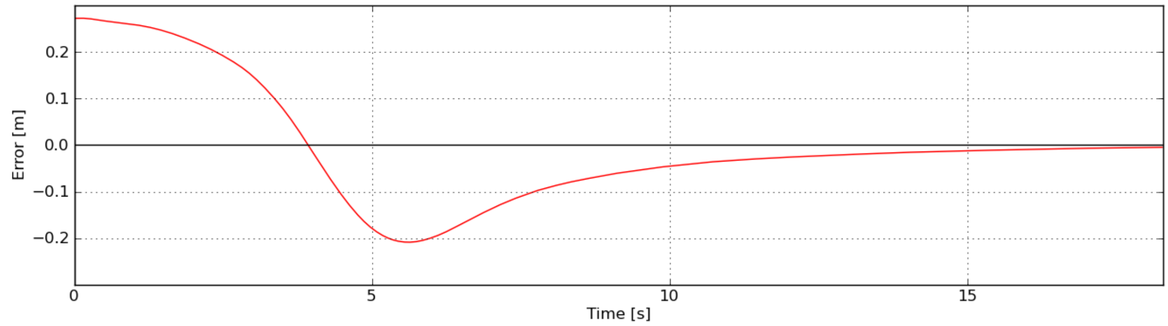

Fig. 9. e_{Tz0} as function of time for the hydro-foiling vessel.

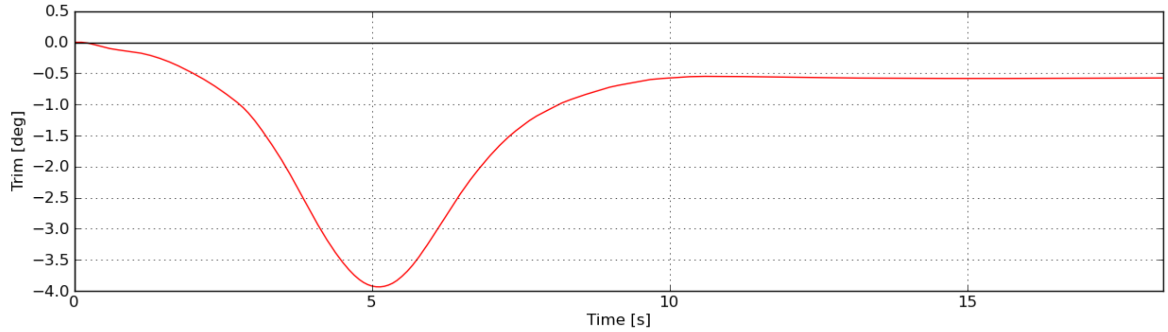

Fig. 10. $Ry0$ as a function of time for the hydro-foiling vessel.

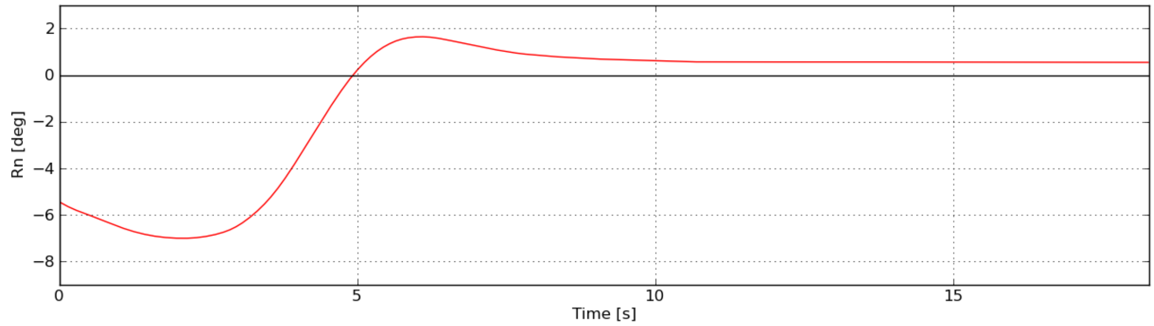

Fig. 11. Rn_{fwd} as a function of time for the hydro-foiling vessel.

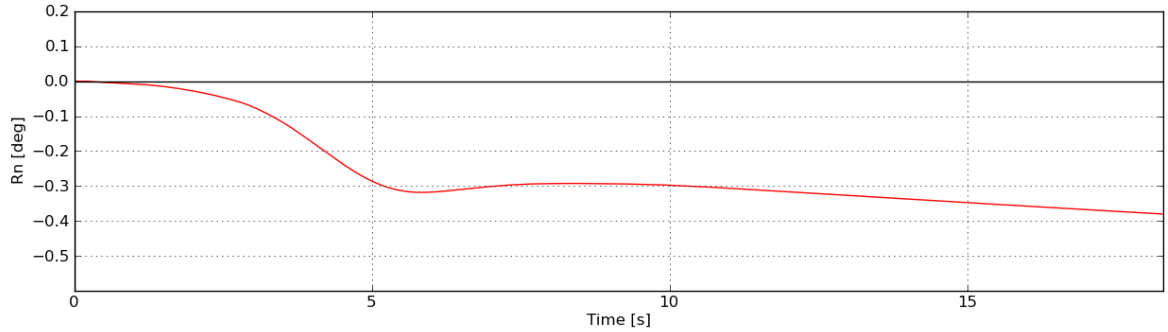

Fig. 12. Rn_{aft} as a function of time for the hydro-foiling vessel.

Figure 9 to 12 show the error in rise e_{Tz0}, the trim of the vessel (which is by definition -e_{Ry0}) and the pitch of the foils respectively. The vessel has reached its top speed after 10 seconds. After settling, the rise $Tz0$ has a value of 0.24 m. the trim has a value of -0.57°. This leads to an error e_{Tz0} of 0.005 m.

3.1.3. Discussion of the results

As can be seen the hydro-foiling vessel rises out of the water as intended for both control strategies. The results show a successful simulation of the transition from displacement mode to foiling mode for the present vessel where the vessel reacts as expected to the different control strategies.

For the control configuration 1 with the P-controller the following can be observed:

- An error is obtained of -0.015 meters.
- A constant e_{Tz0} error is obtained as shown in in figure 5. This is called droop, and is common for proportional controllers.
- For the first 2.5 seconds the forward foil has a constant pitch angle of -8 degrees. This can be observed in figure 7. The constant pitch is caused by the large error during this time frame in combination the large proportional gain $K_{p_{fwd}}$ This leads to a large pitch angle which is limited by the lower bound of pitch angle of the foil $Rn_{fwd_{min}}$.

For the control configuration 2 with the PI-controller the following can be observed:

- An error e_{Tz0} is obtained of -0.005 meters.
- The error e_{Tz0} goes to 0 asymptotically as shown in in figure 9. This behaviour is achieved by the integrative action of the PI-controller. The integrative action prevents the droop that is observed for control configuration 1.
- Due to the lower value for $K_{p_{fwd}}$ in control configuration 2 the lower bound for the forward foil pitch angle $Rn_{fwd_{min}}$ is not achieved.
- Overshoot can be observed in figure 9 and 10. This is caused by the integrative action and the slow response of the hydro-foiling vessel.
- From figure 12 it can be observed that the value for Rn_{aft} has not fully settled. This is caused by the still present error in the trim of the vessel. The integrative action of the PI-controller builds up the pitch angle of the aft foil until the error in the trim has asymptotically reached zero.

4. CONCLUSIONS

This paper demonstrates a method to study the control of the ride height and the trim of hydro-foiling vessels in RANSE based CFD computations. Using FINE/Marine the dynamic behaviour of the vessel was simulated. By using sliding grids pitch motion of the foils relative to the vessel was enabled. The changing free surface location, due to the large vertical translations of the vessel, was accurately resolved using Adaptive Grid Refinement (AGR).

Trim and rise of the vessel were controlled by adapting the pitch of the foils. Two control strategies, both based on a PID-controller as presented in section 2.2, were developed. The numerical method proved able to simulate the described control strategies.

The described method can be used for simulating and analysing complex ride height problems for a range of vessel. The future objective is to validate the method against test results from the vessel, and to improve the performance of the currently analysed solar boat.

ACKNOWLEDGEMENTS

The authors would like to thank J. Blom from the NHL Solarboat racing team for kindly providing the geometry for the presented analysis.

References

1. Menter F., “Zonal two-equations k-ω turbulence models for aerodynamic flows”. AIAA paper 93-2906, 1993
2. Numeca International, User Manual FINE/Marine v3 (including ISIS-CFD), Numeca International, Brussels, Belgium, 2014
3. Queutey, P., Deng G., Wackers, J. and M. Visonneau, M., “Ventilated propeller simulation with a ranse solver”, The 7th International Workshop on Ship Hydrodynamics, IWSH’2011, Shanghai, China,19 September 2011.
4. Queutey, P., Deng G., Wackers, J. “Coupled sliding grids and adaptive grid refinement for rans simulation of ship-propeller interaction,” 14th Numerical Towing Tank Symposium, NUTTS’2011, Poole, United Kingdom, October, 2011.
5. Visonneau, M., Queutey, P., Deng, G., Guilmineau, E., Leroyer, A., and Mallol, B., “Computation of free surface viscous flows around self-propelled ship with the help of sliding grids,” 11th International Conference on Computer Applications and Information Technology in the Maritime Industries, COMPIT’2011, Liege, Belgium, April, 2011.
6. Wackers, J., Deng, G., Leroyer, A., Queutey, P. and Visonneau, M., “Adaptive grid refinement for hydrodynamic flows”, Computers & Fluids **55** (2012), 85-100
7. Dong Energy Solar Challenge, “Information folder”, as retrieved from: http://www.dongenergysolarchallenge.com/uploads/Persdocumenten/Informationfolder%20DSC14-24June2014-lr.pdf, on 09th of September 2014
8. Dong Energy Solar Challenge, “History”, as retrieved from: http://www.dongenergysolarchallenge.com/information/history, on 09th of September 2014

NEW STANDARD OF SPEED AND POWER PERFORMANCE BY ANALYSIS OF SPEED TRIAL DATA

Taichi TANAKA[1], Eriko NISHIMURA[2], Kazuyoshi HIROTA[3], Kotaku YAMAMOTO[4], and Ken TAKAGI[5]

[1] Ship & Ocean Engineering Department, Shipbuilding & Ocean Development Division, MITSUBISHI HEAVY INDUSTRIES, LTD. 16-5, Konan 2-Chome, Minato-ku, Tokyo 108-8215, Japan
[2] Regulation Unit, Japan Ship Technology Research Association (JSTRA). 10-9, Akasaka 2-Chome, Minato-ku, Tokyo 107-0052, Japan
[3] Hydrodynamic Design Group, Planning & Development Department, Ship & Offshore Division, Japan Marine United Corporation 20th Floor, Mita Bellju Bldg., 36-7, Shiba 5-Chome, Minato-ku, Tokyo 108-0014, Japan
[4]Basic Design Department, Ship & Ocean Project Headquaters, MITSUI ENGINEERING & SHIPBUILDING CO., LTD. 1-50, Tsutsujigaoka 1-chome, Akishima-shi, Tokyo 196-0012, Japan
[5] Department of Ocean Technology, Policy, and Environment, Graduate School of Frontier Sciences, The University of Tokyo, 5-1-5 Kashiwanoha, Kashiwa-shi, Chiba 277-8563, Japan

ABSTRACT

Concerns over global environment problems have been increasing, and stricter emission requirements started to come into force. At the same time, the development of innovative technologies to reduce CO_2 emissions from vessels is being accelerated. Therefore, to develop a concrete method of speed power analysis at sea trial is greatly desired by the shipping industry. This paper describes the background, technical challenges, principal theory, practical application and the overview of the new sea trial analysis, which ISO expert group has been developing. Especially this paper will focus on the 'Iterative' method newly introduced and developed by the authors for current correction.

1. INTRODUCTION

Regulations on CO_2 emissions in international maritime transportation (Energy Efficiency Design Index: EEDI regulations) require the energy efficiency design index of a ship (EEDI value) to be determined in speed trials. Some attendees to Marine Environment Protection Committee (MEPC) in the International Maritime Organization (IMO) began to argue for the use of a procedure for implementation and analysis of speed trials that the International Towing Tank Conference (ITTC) formulated in 2012, and not the conventional procedure followed by many shipyards, that is, ISO 15016:2002 "Ships and marine technology -- Guidelines for the assessment of speed and power performance by analysis of speed trial data" (Janse et al 2012). Then, a debate over procedures for implementation and analysis of speed trials has come to the surface.

2. BACKGROUND ON NEW SPEED TRIAL ANALYSIS (UP TO MEPC64 IN OCTOBER 2012)

2.1 Relationship between EEDI and the method of analysis of speed trials

For all ships of 400 gross tonnages and above that engage in international voyages and whose building contract is placed on or after 1 January 2013, the attained EEDI shall be calculated and shall be verified by the Administration. In principle, survey and certification of the EEDI should be conducted on the following two stages.

- Calculation of a preliminary EEDI value resulting from a tank test and a planned value at the design stage, as well as an survey and certification; and
- Calculation of a final EEDI value based on the results of full-scale tests such as a weight assessment test, a determination of the main engine's fuel consumption at shop and a speed trial conducted after construction of the ship, as well as survey and certification.

EEDI is the index of transportation efficiency of a ship at calm with no wind, no waves, and no current. However, this condition rarely applies to speed trials. Therefore, accurately evaluating the numerical values obtained in speed trials requires elimination of the effects of external environment factors (e.g. waves, winds, and currents). Many shipyards used ISO 15016:2002 until the discussion on EEDI began with regard to a procedure for analysing results of speed trials and eliminating external environment factors (method of speed trial analysis). This led the IMO guidelines on survey and certification of the EEDI to require results of speed trials to be calibrated in accordance with ISO 15016:2002 or the equivalent.

2.2 Remarks from IMO (up to July 2011)

However, several countries in IMO were anxious to see that the sea trial assessment methods, being the core element in verifying the EEDI. They pointed out the following problems in the ISO 15016:2002.

- Complicated and confusing procedures;
- Several different results due to various correction methods; and
- Possibility of arbitrary operation;

The IMO convention had not required speed trials until the introduction of the EEDI regulations. Speed trials have been conducted to confirm the guarantee speed of a singed ship building contact. ISO 15016:2002 was oriented toward more flexible international standards so that the parties concerned with the contract could easily agree to it. Ironically, however, this flexibility was attributed to a problem connected to the introduction of the new EEDI regulations. In other words, it was feared that the flexibility might help open a loophole in the regulations (choosing and arbitrarily using an analysis method that would provide the best EEDI can improve the apparent EEDI value).

2.3 Amendment work at ITTC PSS committee (July 2011 – July 2012)

In 2011, ITTC set up a specialist committee on PSS (Performance of Ship in Service) and discussed procedures for analysis and implementation of speed trials requested by IMO. The ITTC PSS discussed which would be more appropriate for the basis of new ITTC method, the STA method (Boom et al 2008) or the conventional ISO 15016:2002. The former was created by the Sea Trial Analysis Group (hereinafter "the STA-Group") and led by the Maritime Research Institute Netherlands (MARIN). It was decided that a method based on improvement of the STA method would be selected as the basis. The decision was reported at the MEPC64 meeting held in October 2012.

As a supplementary note, the STA-Group was set up as a joint industry project with ship owners, research institutes, and classification societies, as well as some shipyards. They advocated establishing transparent and accurate procedures for implementing and analysing speed trials for the purpose of developing the STA method.

2.4 Disapproval of ISO Draft PAS (April 2012 – December 2012)

At first, ISO barely modified ISO 15016 and formulated a plan for amending only the methods for correcting the effects of winds and waves in which multiple procedures were written. In September 2012, Japan and South Korea, only two countries that had virtually participated in the discussion, formulated a provisional draft for amendment to ISO 15016 (ISO 15016 Draft PAS).

However, as a result of the voting on the provisional ISO draft at the end of 2012, five countries voted for the draft whereas eight countries voted against it. The draft was vetoed.

2.5 Next action taken by ISO

This led ISO to change its strategy. The authors tried to solve problems that had been pointed out in relation to ISO 15016:2002, and to analyse actual problems with the ITTC method.

3. THE ITTC METHOD

It is considered that no concession would be acceptable for ISO, in other words, an amendment was needed, with regards to the following issues in the ITTC method.

3.1 Questionable accuracy despite the burden of current correction

In the past, the current correction method with the ITTC method only required 1 Double Run at one power setting to correct current effects as well as ISO 15016:2002. Presently, the 'mean of means' (MoM) method requiring 2 Double Runs is introduced to be used in the new ITTC method 2012. As this MoM method was also described in the Principles of Naval Architecture (1967 edition), in fact, it is a classical approach for current correction and has been used since before World War II. The advantage of the MoM method is that the calculation is very simple. However, it was considered that accuracy was not enough in the case of longer time periods between the runs since the MoM method could make corrections only if a current velocity is varying parabolically with time. In fact, the run interval is very long in VLCCs or other large ships which have been built recently, which acts negatively in making effective corrections. In this way, regardless that the burden is even greater, the requirement of the ITTC method on current correction procedures also poses a question in terms of accuracy.

As an aside, the following describes the Taniguchi-Tamura method which was designed to solve challenges of the MoM method, a classical method, and has been adopted in the ISO 15016:2002. Being correctable in accordance with current changes by the periodic function affected by lunar cycles, etc., the method could be satisfactorily applicable to recent VLCCs or other large ships. The method was adopted by ISO 15016:2002 and was used by many shipyards around the world. In this method, an analyst is required to manually draw current curves when correcting the current. The problem is that this involves arbitrariness and results may vary among different analysts. This was pointed out along with the discussion of EEDI.

Taking this into consideration, STA-Group decided to go back to the classic MoM method. On the other hand, the authors developed an innovative method for the current correction, called 'Iterative' method. This method retains the advantage of the Taniguchi-Tamura method to obtain accurate results with fewer runs even if the run interval is very long, while this method surpasses the weaknesses of the Taniguchi-Tamura method in respect of arbitrariness and ambiguity, since the method would completely eliminate arbitrariness, namely the act of requiring manual drawings.

3.2 Lack of transparency in fundamental analysis methods

ITTC insisted that the development of the ITTC method had focused on three points: (1) making it analysable by everyone, (2) ensuring any analysts the same result for the same speed trial, and (3) high accuracy. However, it could be considered for the authors that the procedure issued by ITTC failed to facilitate understanding about details of the Direct Power Method (hereinafter "DPM"), a fundamental method of analysis in speed trials. Assessing the basic performance of a ship would be unacceptable as long as the black box remains.

4. A NEW DRAFT OF THE AMENDMENT TO ISO 15016

4.1 Principles of the international standard

In order for a fresh start, the authors decided to restructure the draft of amendment to ISO 15016:2002 by satisfying the three principles based on the same awareness of problems as that of ITTC, instead of trying to minimize amendments to ISO 15016:2002 as much as possible.

4.2 Outline of new proposal for an amendment

Two ISO standards conventionally apply. ISO 15016:2002 specified a method for speed trial analysis, while ISO 19019 specified a method for trial preparation and conducting of sea trials. Since both of these could be flexibly addressed for the reasons given above, it was found that ISO 19019, a method that would significantly affect the results of speed trial analysis, would also need to be amended. ISO 19019 covers not only speed tests but also sea trials overall. Instead of amending the two ISO standards, it was decided that the amendment would incorporate the implementation procedure into ISO 15016.

It was decided that the ITTC method would be incorporated into the implementation procedure and the analysis method as much as possible. Detailed improvements were repeated in terms of issues that were deemed to need improvements from a practical perspective and a perspective of accuracy improvement.

Among the analysis methods, current correction is particularly different from the ITTC method. As a counter proposal to the MoM method and based on a recommendation by Professor Toki of Ehime University, the authors decided to propose a method that eliminates the arbitrariness of ISO 15016:2002 and minimizes the burden on speed trials . For this method, the following formula that represents current changes as a function of lunar periodicity + linear term of time + constant term, in order to eliminate to manually draw current curve (data shaping using analysis results) was introduced as shown in Eq.1.

$$V_{\mathrm{C}} = V_{\mathrm{C,C}} \cos\left(\frac{2\pi}{T_{\mathrm{C}}} t\right) + V_{\mathrm{C,S}} \sin\left(\frac{2\pi}{T_{\mathrm{C}}} t\right) + V_{\mathrm{C,T}} t + V_{\mathrm{C,0}} \tag{1}$$

By applying a method that has been used by the British Ship Research Association (BSRA), the authors developed a calculation method for unambiguously obtaining answers from measurements in speed trials and named it the ‘Iterative’ method. This also involved choosing the above formula of current expression from multiple candidates, a shift from a method to solve simultaneous equations proposed by Professor Toki to an iteration-based method recommended by BSRA, and choosing a regression equation that would represent the speed and power necessary for solving the ’Iterative’ method among others. The method was intensively discussed among the authors and concerned persons.

The method eliminated the conventional shortcomings of ISO 15016 and made it possible to ensure the absence of arbitrariness and the standardization in analyses of speed trials at shipyards around the world. The number of runs would be less than that in the MoM method, and improvements in analytic accuracy would be expected with slow-speed large ships which typically involve longer intervals of runs.

5. INTERNATIONAL DEBATES FOR ACCEPTING NEW PROPOSAL AND ITS CHALLENGE

5.1 The 2nd ISO expert meeting (February 2013)

The 2nd ISO expert meeting was held in London for two days in February, 2013. Attendees included the representative of ITTC, researchers who took the lead in the development of the ITTC method, representatives from ship owners' organizations, IACS and other interested parties.

Since ISO recognized the problem of ISO 15016:2002 and changed the policy for the amendment to ISO 15016, the direction of discussion was changed from "confrontation" to "harmonization". This is one of the significant outcomes of the meeting.

5.2 Aiming at harmonization with the ITTC method (May to September 2013)

In order to solve the lack of transparency of DPM, the authors formulated a draft with a step-by-step description based on their understanding and estimation. In August 2013, ITTC and the authors had a meeting. ITTC was interviewed on details of DPM and cooperated in creating and reviewing the draft overall. The draft of ISO amendment formulated by the authors was based on the ITTC method but underwent improvements such as inclusion of a current correction method that was more practical and more accurate than that in the ITTC method. ITTC supported the draft and regarded it as an analysis method that would also be applicable to EEDI certification. The harmonization between ISO and ITTC decided the outline of a draft of the amendment to ISO 15016.

5.3 The 3rd ISO expert meeting (September 2013)

MEPC65, held in May 2013, welcomed the cooperation between ISO and ITTC regarding the amendment work.

The 3rd ISO expert meeting was held in London for two days in September 2013. Attendees included the representative of ITTC, researchers who took the lead in the development of the ITTC method, representatives from ship owners' organizations, IACS and many other concerned persons including the chairman of the STA-Group. The meeting had a total of 22 attendees.

A heated discussion went on for two days. As a result, all attendees including those from ITTC and the STA-Group consented to the draft of amendment to ISO 15016 which had been formulated by the authors. They also consented to conducting a vote on the draft. The following explains major discussions by topic.

5.3.1 Preparation and conducting of sea trials

The ITTC method describes some unrealistic requirements such as forward draught requirements in a trim state (±0.1 m from the state of tank test). Because of this and with consideration of the feasibility of speed trials, the attendees consented to adding a clause that would ease the requirements provided that three parties, namely the Shipbuilder, the Owner and the Verifier, consented. The clause allowed for changes in draught restriction, measurement time, trial direction and other conditions depending on the reality of the situation that the three parties consented to.

5.3.2 Direct Power Method (DPM)

Concerning the DPM, it was supported by presenting a plan for describing an analysis procedure step-by-step. The extended power method proposed by the authors is recognized to be useful to deepen the technological knowledge, since this calculation is based on the full-scale wake fraction. The advantage led to a decision to add the extended power method as an Informative Annex.

5.3.3 Current correction and run number

In terms of run number, some members pointed out that “3 Double Runs at three different power settings” with the ’Iterative’ method would be inferior to “5 Double Runs at three different power settings” with the MoM method in the accuracy of disturbance correction and sensitivity to measurement errors. As a result, they settled for a compromise in which, even if the ’Iterative’ method is to be used, 2 Double Runs are required at the EEDI power only for the first ship, which means total 4 Double Runs.

5.3.4 Water temperature/density correction

The EEDI survey and certification guideline of IMO did not allow water temperature or density correction when this discussion was held. On the assumption of this, a member explained an occurrence of phenomena that would not agree with the theory, based on the results of speed trials of a series of ships of a same type, which had been sorted by water temperature. However, almost all attendees against sparing water temperature/density correction since the resistance would theoretically depend on the water temperature and/or density. This led to a decision to include water temperature/density correction in the amendment to ISO draft.

5.3.5 Effect of shallow water

The ITTC method specified a formula that showed an area in which a trial operation would not be allowed due to effects of shallow water. The authors proposed that the formula should be treated as the upper limit in the amount of correction of the effects of shallow water. The proposal was accepted.

5.4 The first DIS voting resulted in a rejection (January – April 2014)

Based on an agreement reached at the 3rd ISO expert meeting, a voting on DIS (Draft International Standard) was conducted from January to April 2014. Seven countries voted for it whereas five countries voted against it. The agenda was not approved. Passing DIS required two different requirements to be satisfied: (1) affirmative votes from two thirds or more of the P-members (Participating members) who voted, and (2) negative votes from one fourth or fewer of the total number of voters. Neither of the requirements was satisfied.

537 comments were submitted during the voting, but most of these were editorial. Technically, the largest reason of opposition was an absence of a third party’s validation of the ’Iterative’ method newly proposed for the ISO method.

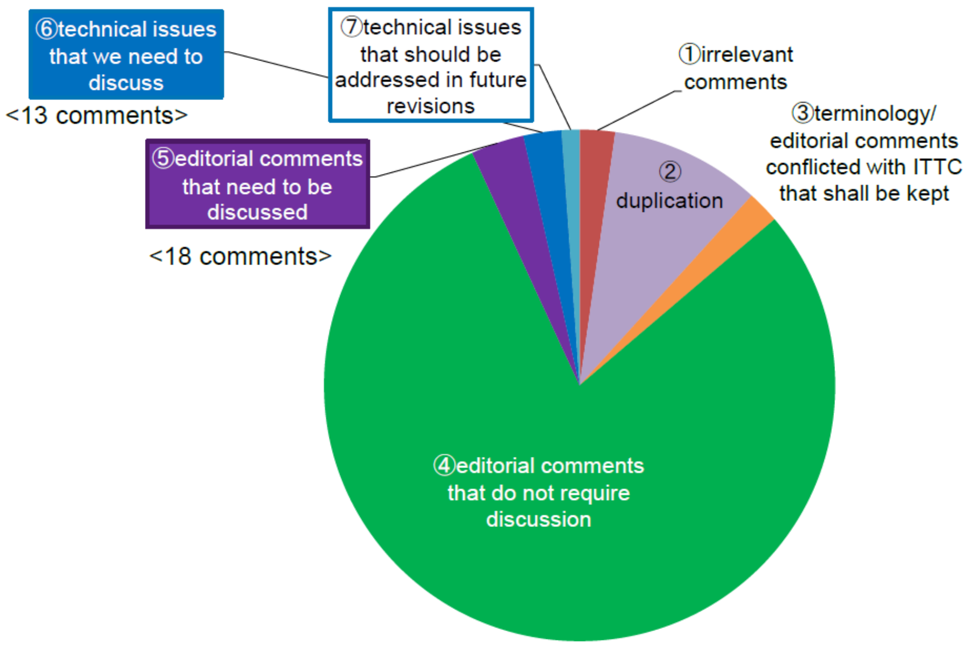

Fig. 1. Categorisation of the comments during the voting

5.5 The 4th ISO expert meeting (June 2014)

The 4th ISO expert meeting was held in London for three days in June, 2014. As in the previous meeting, the representative ITTC/AC, the ITTC-related researchers from major ship model basins who had been involved in the validation of the ’Iterative’ method , major IACS-members, representatives of ship owners’ organizations and other concerned persons including the chairman of the STA-Group. The total number of attendees was 22.

It was pointed out that three days would be too short to read and sort out the 537 comments gathered during the first DIS voting and that it would be impossible to complete the validation of the ’Iterative’ method by the end of June. Despite this, the attendees consented to the draft of the amendment to ISO 15016 which included the ’Iterative’ method. They also consented to conducting the 2nd DIS voting. The following describes results of major discussions by topics. (ISO and ITTC 2014)

5.5.1 Validation of current correction method

In the ITTC validation method, the current correction methods (the MoM method and the ’Iterative’ method) and two power correction methods (DPM and extended power method) were evaluated, with the assumption that added resistance is known. A difference of 0.1 knot or smaller in comparison with the true answers on the ship speed would be judged as an acceptable accuracy. Six ship types of LNG, small and large container ships, small and large tankers and cruise liners and five types of current profiles taken at various locations in Asia/Europe were prepared. Multiple cases of intervals between runs were set, depending on the type of ship. Variation in time between runs, gaps in disturbance between runs, and errors in model test results were taken into consideration to include assumable factors for fluctuation and the two current correction methods were statistically compared with each other in terms of accuracy and robustness.

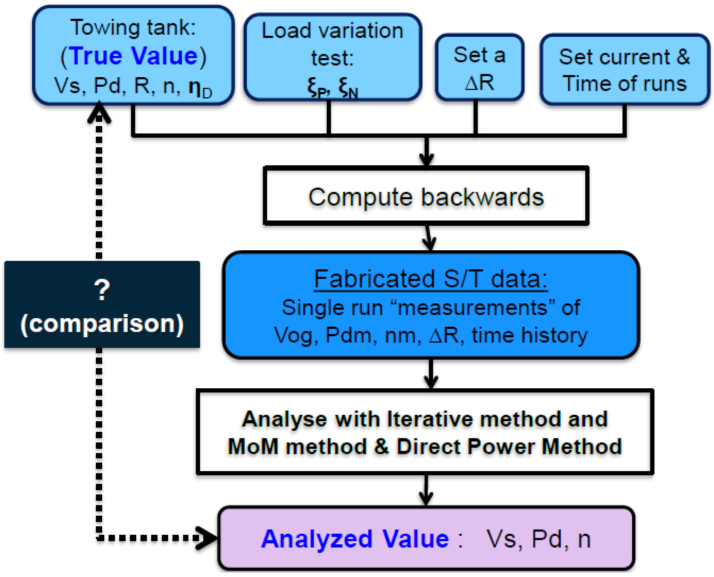

Fig. 2. Validation method implemented by ITTC

The following are results of validation implemented by ITTC (Strasser et al 2014).
- In general the 'Iterative' method leads to less errors in average of the tested cases when (1+2+2 Double Runs) are used in the MoM method.
- Using the MoM method for each power setting, 2 Double Runs should be made (2+2+2 Double Runs).
- In the case of shorter time periods between the runs (up to 60 minutes) the methods are equally adequate.
- In specific cases, the MoM method has advantages over the 'Iterative' method: In cases where the speed-power curve deviates significantly from the assumed power function (a+bV^q), e.g. in case of a large speed range and/or humps and hollows occur within the power curve.
- In case of current time history deviating from the assumed parabolic/sinusoidal trend and the change of the current within the timespan of two Double Runs is very high, neither of the methods is applicable. These areas, when known, should be avoided.
- The 'Iterative' method is fully compatible with the simple Direct Power Method (DPM described in the ITTC method). (This is a supplementary explanation to correct the prevalent misunderstanding that the 'Iterative' method can only be used in combination with extended power method proposed by the authors, which is described in the annex of the ISO draft.)

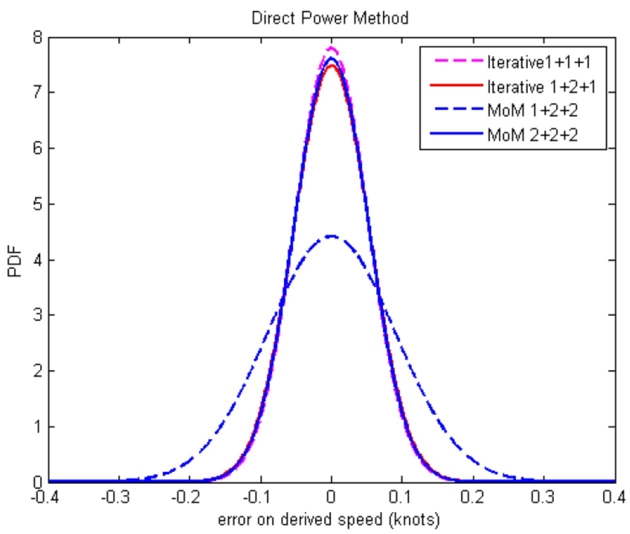

Fig. 3. ITTC’s Statistical distribution: both methods are adequate if for the MoM method at each power setting 2 Double Runs are performed (dotted blue line represents MoM with 1+2+2 Double Runs)

Bureau Veritas (BV) also gave a presentation regarding the results of a study in which the class society used 16,320 simulations to compare both the ’Iterative’ and MoM method and concluded that, the ’Iterative’ method (1+2+1 Double Runs) leads to fewer errors around EEDI power range, but the MoM method (1+2+2 Double Runs) performed better at maximum power output (de Hauteclocque 2014).

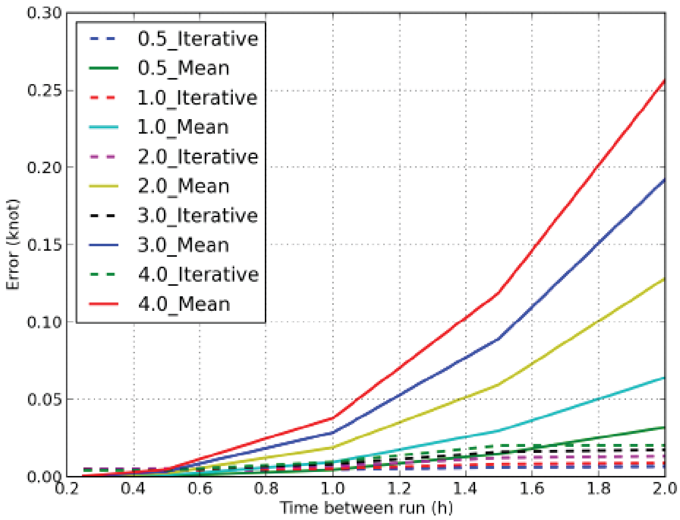

Fig. 4. Example result of BV’s validation at EEDI power: The relationship between “Time between run (h)” and “Error (knot)” is shown in a graph form in accordance with changes of current velocity. The illustration shows that the error in the ’Iterative’ method is smaller than that in the MoM method.

Based on the validation work performed by ITTC and others, the 4th ISO expert meeting agreed that the ’Iterative’ method was fully validated and confirmed to be accurate enough to be used as a current correction method in the ISO draft.

5.6.2 Number of runs

It was agreed to follow the ITTC’s recommendation of the run numbers of the ’Iterative’ method and the MoM method in order to achieve equivalent accuracy as follows:

<’Iterative’ method>
- 1+2+1Double Runs for the first ship
- 1+1+1 Double Runs for sister ships

<MoM method>
- 2+2+2 Double Runs for the first ship
- 1+1+1 Double Runs for sister ships
- For sister ships, when a current variation of above 0.2 knots within 1 Double Run is observed, 1 additional Double Run is needed for that power setting.

5.6.3 Procedure for creation of a speed/power curve

It was shared the understanding about the fact that the trend of the speed/power curve in the result of the model test did not always correspond to that of a real ship. They also discussed the accuracy of a model test and the measurement accuracy of a full-scale ship test. As a result, they agreed to improve the description of processing the result more accurately as follows:

- Use the speed/power curve from the model tests for the specific ship design at the trial draught. Shift this curve along the power axis to find the best fit with all corrected speed/power points according to the least squares method. When more than three(3) power settings are obtained, it is allowed to find the best fit with all corrected speed/power points using the ‘least squares’ method.

5.6.4 Modulus of rigidity (G-Modulus)

It was decided that a certain default value should be made available for the use of a shaft torque measurement devices to determine the power of the main engine during a speed trial, for the purpose of preventing G-Modulus from being arbitrarily set. The STA-Group and others argued that setting a numerical value as conservatively as possible would provide an incentive for actual measurement of material property.

According to past research project conducted in Japan, it was reported that the number of G-Modulus obtained by actual size shafts was about 1~3% lower than that obtained by small test pieces. Therefore, it was supported to use not the conservative number but the reference number. Then, the expert meeting finally decided to adopt the default value of 82,400N/mm^2 proposed by Italy, unless the Shipbuilder can prove another value based on an actual shaft torsional test.

5.7 Informal resolution meeting, etc. (September 2014)

After the 4th ISO expert meeting, several minor editorial issues to be solved were found. Therefore, the informal resolution meeting was held in September 2014, and some member countries which submitted comments after the 4th ISO expert meeting, ITTC and STA-Group joined this meeting. The following items of sea trial preparations, conditions, and procedures and analysis were defined for clarity and to avoid arbitrary applications;

- Speed/power curve
- Definition of sister ships
- Draught measurement prior to sea trials
- Limitation of shallow water correction
- Measured parameters
- Sea trial area
- Run numbers
- Power settings
- Ship’s profiles for dataset for of wind correction
- Standard water temperature
- Appropriate restrictions for the theoretical method with simplified tank test of added resistance due to waves

Furthermore, the intensive and comprehensive discussions have brought the amended ISO draft nearer to a high degree of perfection.

6. FUTURE SCHEDULE

The 2nd DIS vote on the amended ISO draft has been being conducted from 6 October to 6 December, 2014.

After enactment, the amended ISO draft will be reviewed three years later. Discussions of specifics such as water temperature/density correction, shallow water correction and wave correction will continue.

7. IN CLOSING

Discussions with interested parties continued during this period and understanding was developed with classification societies and the STA-Group, as well as with ITTC, with which a cooperative relationship had already been established with ISO. The result of validation of the 'Iterative' method was highly regarded. Fortunately the standard was made more convincing and reached a greater level of completeness.

This international debate almost symbolized the importance of communication based on technology, while identifying the trend of international opinion. The fact that DPM had been a "black box" for the authors until it turned out to be almost the same as the author's conventional method was a typical example.

With three years before the review, ISO experts will engage in continuous activities for improvement in accuracy, practice and applicability in accordance with technological progress.

Discussions on international regulations have been gathering momentum with each year. As a consequence, industry-academia-government cooperative action and the use of methods for speed trials will continue, because leading the development of a mechanism to utilize the technological strength as intellectual property should indirectly contribute to the profits of the industries.

ACKNOWLEDGEMENTS

References

1. Boom, Henk van den, Hout, Ivo van der, Flikkema, Maarten: Speed-Power Performance of Ships during Trials and in Service, SNAME, 2008.
2. ISO (de Hauteclocque et al): Validation work of the "Iterative" method in the revised ISO15016 by several organizations, IMO MEPC 67/INF.16, 2014.
3. ISO and ITTC: Work progress on revision of ISO standard 15016:2002, IMO MEPC 67/4/8, 2014.
4. ITTC (Strasser, Gerhard et al): Information on the validation of the current correction methods in ISO 15016, IMO MEPC 67/4/7, 2014.
5. Norway (Janse, G.H. et al): Verification of the EEDI and Comments on ISO 15016:2002 and the equivalent methods for performing sea trials, IMO MEPC 62/4/8, 2011.

ON THE ENERGY EFFICIENCY DESIGN INDEX (EEDI) OF RO-RO PASSENGER AND RO-RO CARGO SHIPS

Aimilia G. Alisafaki[1] and Apostolos D. Papanikolaou[1]

[1] National Technical University of Athens - Ship Design Laboratory,
School of Naval Architecture and Marine Engineering
9, Heroon Polytechniou, 15773 Athens-Zografou, Greece

ABSTRACT

This paper proposes alternative formulations of the correction factor f_{jRoRo} pertaining to Ro-Ro Cargo and Ro-Ro Passenger ships, as defined in the Energy Efficiency Design Index (EEDI) equation according to IMO Resolution MEPC 245(66) on the "2014 Guidelines on the method of calculation of the attained Energy Efficiency Design Index (EEDI)". The alternative formulations were derived by studying a large sample of Ro-Ro Cargo ships and Ro-Ro Passenger ships, built in the period 1990-2012. The estimation of ships' resistance and powering was conducted by use of Holtrop's method. Obtained formula's exponent values were compared with corresponding ones from latest IMO studies on EEDI and they appear to better represent and fit to the energy efficiency and environmental impact of the operating fleet of Ro-Ro Cargo and Ro-Ro Passenger ships.

1. INTRODUCTION

The 67th session of the IMO Marine Environment Protection Committee (MEPC 67, October 2014) recently confirmed a very optimistic prediction of the 3rd edition of the IMO study on the greenhouse gas (GHG) emissions for the international shipping sector in the period 2007-2012; namely the fact that the global shipping industry GHG emissions were reduced from 2.8% of the world's total GHG emissions in year 2007 to 2.2% in year 2012 (IMO MEPC 67/6/INF.3), which corresponds to *a decrease of 20% of the shipping GHG emissions within a five years period*! This is a remarkable reduction that was made possible with the introduction of operational efficiency measures in the existing and newly introduced fleet worldwide.

Ro-Ro Cargo and Ro-Ro Passenger ships dispose in general wide diversity in mission profile, as well as in terms of design and operational conditions. Their relatively high-installed power, in combination with the enhanced service speed being an integral part of their service to the society, lead to a wide EEDI scatter. This, in turn, required the introduction of suitable correction factors in order to get a proper EEDI reference line for this type of ships. This was the reason why these ship types were excluded from the implementation of the required EEDI in the first phase. It was not until April 2014 when the method to include the Ro-Ro Cargo and Ro-Ro Passenger ship types into the IMO energy efficiency regulatory framework was finally adopted by the Resolution MEPC 245(66).

The impetus for conducting the research described in the present paper was triggered by the IMO studies submitted by Denmark and Japan, MEPC 65/4/18, focusing on "Comments on the method to include the Ro-Ro Cargo and Ro-Ro Passenger ship types into the IMO energy efficiency regulatory framework as proposed in MEPC 64/4/14 and MEPC 65/4/4", which both were submitted by Germany, Sweden, Community of European Shipyard Associations (CESA) and INTERFERRY.

In the present paper, we propose alternative formulations and values for the exponents of the f_j correction factor for Ro-Ro Cargo ships and Ro-Ro Passenger ships, namely $f_{jRo\text{-}Ro}$, which resulted from a regression analysis of a large number of vessels, built between 1990-2012 (source of original data: IHS Fairplay database). The prediction of resistance and powering was conducted by Holtrop's method (1984); the obtained exponent values were compared with corresponding data of Kristensen (2012). Derived values are compared with the latest IMO developments concerning EEDI and despite their difference they appear to rather better represent the energy efficiency and environmental impact of the operating fleet of Ro-Ro Cargo and Ro-Ro Passenger ships.

2. THEORETICAL BACKGROUND

The attained new ship Energy Efficiency Design Index (EEDI) is a measure of ships' energy efficiency [g/t nm] and is calculated by the following formula (MEPC 245(66), Annex 5):

$$EEDI_{att}\left[\frac{g}{t \cdot nm}\right] = \frac{\left(\prod_{j=1}^{n} f_j\right)\left(\sum_{i=1}^{nME} P_{ME(i)} C_{FME\,(i)}\, SFC_{ME(i)}\right) + \left(P_{AE}\, C_{FAE} SFC_{AE}\right) + \left(\left(\prod_{j=1}^{n} f_j \cdot \sum_{i=1}^{nPTI} P_{PTI(i)} - \sum_{i=1}^{n_{eff}} f_{eff\,(i)} \cdot P_{AEeff\,(i)}\right) C_{AE} SFC_{AE}\right) - \left(\sum_{i=1}^{n_{eff}} f_{eff\,(i)} \cdot P_{eff\,(i)} C_{FME} SFC_{ME}\right)}{f_i \cdot f_c \cdot f_l \cdot Capacity \cdot f_w \cdot V_{ref}} \quad (1)$$

In the above Eq. (1), the subscripts $(\,)_{ME(i)}$ and $(\,)_{AE(i)}$ refer to the main and auxiliary engine(s) respectively. In the numerator, the P corresponds to the power of the main and auxiliary engines, measured in [kW]. The $P_{ME(i)}$ is 75% of the rated installed power (MCR) for each main engine $(\,)_{(i)}$. The P_{AE} is the required auxiliary engine power to supply normal maximum sea load including necessary power for propulsion machinery/systems and accommodation, at the reference speed V_{ref} [kn]. In case shaft motor(s) are installed, the $P_{PTI(i)}$ is 75% of the rated power consumption of each shaft motor divided by the weighted average efficiency of the generator(s). The $P_{eff(i)}$ is the output of the innovative mechanical energy efficient technology for propulsion at 75% main engine power. The $P_{AEeff\,(i)}$ is the auxiliary power reduction due to innovative electrical energy efficient technology measured at $P_{ME(i)}$. The C_F is a non-dimensional conversion factor between fuel consumption measured in [g] and CO_2 emission also measured in [g] based on carbon content. The SFC stands for the certified specific fuel consumption, measured in [g/kWh], of the engines. The Capacity is defined as the deadweight for Ro-Ro Cargo and Ro-Ro Passenger ships. The $f_{eff(i)}$ is the availability factor of each innovative energy efficiency technology. The f_i is the capacity factor for any technical/regulatory limitation on capacity and equals to 1.0 (one) for Ro-Ro Cargo and Ro-Ro Passenger ships. The f_l is the factor for general cargo ships equipped with cranes and other cargo-related gear. The f_w is a non-dimensional coefficient indicating the decrease of speed in *representative* sea conditions of wave height, wave frequency and wind speed (factor accounting for the added resistance and increased powering of the ship operating in realistic environmental conditions).

2.1 Correction factors for Ro-Ro Cargo and Ro-Ro Passenger ships

In order to adjust the introduction of the Ro-Ro Cargo and Ro-Ro Passenger ships into the EEDI framework, the capacity correction factor f_{cRoPax} for Ro-Ro Passenger ships and the ship design correction factor f_{jRoRo} for both Ro-Ro Cargo and Ro-Ro Passenger ships were introduced in MEPC 64/4/14. Noting that in Eq.(1), f_c is the cubic capacity correction factor and should be assumed equal to one (=1.0) if no necessity of this factor exists. Ro-Ro Passenger ships designed for large passenger accommodation capacity and associated spaces are, compared to cargo ships, adjusted by the introduction of the cubic capacity correction factor f_{cRoPax}. This cubic capacity correction factor f_{cRoPax} is applicable only to Ro-Ro Passenger ships exhibiting a (DWT/GT)-ratio of less than the fleet average, which was found to be approximately 0.25; it is defined as follows (MEPC 245(66):

$$f_{CRoPax} = \left(\frac{\left(\frac{DWT}{GT}\right)}{0.25}\right)^{-0.8} \quad (2),$$

where GT is the gross tonnage in accordance with the International Convention of Tonnage Measurement of Ships 1969, annex I, regulation 3.

Finally, the f_j is a correction factor that accounts for ship specific design elements. For both Ro-Ro Cargo and Ro-Ro Passenger ships, this correction factor f_{jRoRo} is calculated as follows (MEPC 245(66)):

$$f_{jRoRo} = \frac{1}{\left(F_{nL}^{\alpha} \times \left(\frac{L_{PP}}{B}\right)^{\beta} \times \left(\frac{B}{T}\right)^{\gamma} \times \left(\frac{L_{PP}}{\nabla^{\frac{1}{3}}}\right)^{\delta}\right)} \tag{3}$$

where L_{pp} is the ship's length between perpendiculars [m], B is the ship's breadth [m], T is the ship's draught [m], ∇ is the ship's volumetric displacement [m^3] and F_{nL} is the Froude number defined as

$$F_{nL} = \frac{0{,}5144 \times V_S}{\sqrt{g \times L_{PP}}} \tag{4}$$

where g is the gravitational acceleration [= 9.81m/sec^2] and V_{ref} is the ship' s reference speed [kn].

If $f_{jRoRo} > 1$, then $f_{jRoRo} = 1$. It is noted that both correction factors f_{cRoPax} and f_{jRoRo} are used in the calculation of the attained EEDI, as well as for the development of the EEDI reference line.

2.2 Ship Design Variable (SDV)

The denominator of the fraction in Eq. (3) is defined as a Ship Design Variable SDV (MEPC 64/4/14). That is:

$$SDV = F_{nL}^{\alpha} \times \left(\frac{L_{PP}}{B}\right)^{\beta} \times \left(\frac{B}{T}\right)^{\gamma} \times \left(\frac{L_{PP}}{\nabla^{\frac{1}{3}}}\right)^{\delta} \tag{5}$$

so the Eq. (3) can be also written as follows:

$$f_{jRoRo} = \frac{1}{\left(F_{nL}^{\alpha} \times \left(\frac{L_{PP}}{B}\right)^{\beta} \times \left(\frac{B}{T}\right)^{\gamma} \times \left(\frac{L_{PP}}{\nabla^{\frac{1}{3}}}\right)^{\delta}\right)} = \frac{1}{SDV}$$

The Ship Design Variable (SDV) is the product of $(F_{nL})^{\alpha}$ and the non-dimensional ratios, all of which have a significant influence on the ship-power performance.

2.3 Estimated EEDI Index Value

The Estimated EEDI Index Value for each *Ro-Ro Cargo* sample ship is calculated as follows (MEPC 231(65)):

$$Estimated\ EEDI\ Index\ Value = \frac{3.1144 \cdot (f_{jRoRo} \cdot 190 \cdot \sum P_{MEi} + 215 \cdot P_{AE})}{Capacity \cdot V_{ref}} \tag{6}$$

Likewise, the Estimated Index Value for each *Ro-Ro Passenger* sample ship is calculated as follows (MEPC 231(65)):

$$Estimated\ EEDI\ Index\ Value = \frac{3.1144 \cdot (f_{jRoRo} \cdot 190 \cdot \sum P_{MEi} + 215 \cdot P_{AE})}{f_{cRoPax} \cdot Capacity \cdot V_{ref}} \tag{7}$$

The auxiliary power P_{AE} for *Ro-Ro Cargo* ships with a total installed propulsion power of 10,000kW and above is calculated as follows (MEPC 231(65)):

$$P_{AE} = \left(0.025 \cdot \left(\sum_{i=1}^{nME} MCR_{ME(i)} + \frac{\sum_{i=1}^{nPTI} P_{PTI(i)}}{0.75}\right)\right) + 250 \tag{8}$$

For *Ro-Ro Cargo* ships with a total propulsion power below 10,000kW the formula is modified as follows (MEPC 231(65)):

$$P_{AE} = \left(0.05 \cdot \left(\sum_{i=1}^{nME} MCR_{ME(i)} + \frac{\sum_{i=1}^{nPTI} P_{PTI(i)}}{0.75}\right)\right) \tag{9}$$

The auxiliary power P_{AE} for *Ro-Ro Passenger* ships is calculated as follows (MEPC 231(65)):

$$P_{AE} = 0.866 \cdot GT^{0.732} \tag{10}$$

2.4 P_{ME} as a function of SDV and ∇

The required EEDI is expressed as (MARPOL 73/78, Annex VI, Regulation 21):

$$Required\ EEDI \leq a \quad \cdot (Capacity)^{-c} \tag{11}$$

Hence, when applying to the left hand side of the above Eq. (11) the estimated EEDI value from the Eq. (6), the correction factor f_{jRoRo} as described in the Eq. (3), and noting that the largest influence on the emitted CO_2 on their numerator is by far coming from P_{ME}, and based on the assumption that the capacity (DWT for these ship types) is linearly proportional to ship's displacement volume, then the Eq. (11) is reformulated to the following expression for P_{ME}:

$$P_{ME} \leq Const. \ \cdot L_{PP}{}^{\frac{1}{2}} \cdot F_{nL}^{(a+1)} \cdot \left(\frac{L_{PP}}{B}\right)^{\beta} \cdot \left(\frac{B}{T}\right)^{\gamma} \cdot \left(\frac{L_{PP}}{\nabla^{\frac{1}{3}}}\right)^{\delta} \cdot \nabla^{\varepsilon} \tag{12}$$

The relation between the main engine power P_{ME} (=75% MCR) and the relevant ship particulars, as expressed on the right hand side in the Eq. (12) is investigated. The right hand side of the Eq. (12) is introduced as the Main Engine Power Ship Design Variable SDV_{PME}:

$$\mathrm{SDV_{PME}} = \mathrm{L_{PP}}^{\frac{1}{2}} \cdot \mathrm{F_{nL}^{(a+1)}} \cdot \left(\frac{\mathrm{L_{PP}}}{\mathrm{B}}\right)^{\beta} \cdot \left(\frac{\mathrm{B}}{\mathrm{T}}\right)^{\gamma} \cdot \left(\frac{\mathrm{L_{PP}}}{\nabla^{\frac{1}{3}}}\right)^{\delta} \cdot \nabla^{\varepsilon} \tag{13}$$

3. METHODOLOGICAL APPROACH

The aim of the present study is the calculation of suitable values for the exponents $\alpha, \beta, \gamma, \delta$ and ε of the Ship Design Variables SDV (Eq. 5) and SDV_{PME} (Eq. 13). The study was conducted by using Holtrop's method (1984) for the estimation of the powering of the sample ships and Normand's relational method (Papanikolaou, 2014) for the calculation of suitable values for the exponents α, β, γ, δ and ε. Normand's relational method leads in general to estimations of ship's displacement for small variations of ship's dimensions and speed with respect to a basis (reference) ship; it can only be applied when the deviations from the values of the parent ship are relatively small (in the range of 10%). The parent ship for each investigated ship type is assumed corresponding to the average ship of the relative sample (relevant operating fleet) and her main characteristics are presented in Table 1:

Table 1. Reference parent ship for each ship type

Average Parent ship($_{\text{Index }0}$)	Ro-Ro Cargo	Ro-Ro Passenger
L_{PP0} [m]	148.54	132.80
B_0 [m]	23.40	23.29
T_0 [m]	6.85	5.34
V_0 [kn]	18.33	19.79
C_{B0}	0.640	0.576
∇_0 [m^3]	15238.00	9519.91
Δ_0 [ton]	15618.95	9757.90

According to IMO MEPC 64/4/14, for both ship types under study, the main engine power P_{ME} was linearly proportional to Ship Design Variable SDV_{PME}.

$$P_{ME} = Const. \times L_{PP}^{\frac{1}{2}} \times F_{nL}^{(\alpha+1)} \times \left(\frac{L_{PP}}{B}\right)^{\beta} \times \left(\frac{B}{T}\right)^{\gamma} \times \left(\frac{L_{PP}}{\nabla^{\frac{1}{3}}}\right)^{\delta} \times \nabla^{\varepsilon} \tag{14}$$

The above Eq. (14) can be further analyzed after some mathematical arrangements to the following:

$$P_{ME} = Const. \times V^{(\alpha+1)} \times L_{PP}^{-\frac{\alpha}{2}+\beta+\delta} \times B^{-\beta+\gamma} \times T^{-\gamma} \times \nabla^{-\frac{\delta}{3}+\varepsilon} \tag{15}$$

By keeping constant the four out of the five ship parameters of Eq. (15), and applying differential calculus to the each selected parameter, the exponents were calculated as follows:

$$(\alpha+1) = P'_{ME} \times \frac{V_0}{P_{ME\,0}} = \frac{\Delta P_{ME}}{\Delta V} \times \frac{V_0}{P_{ME\,0}} \qquad for \frac{\Delta V}{V} \ll 1.0 \tag{16}$$

$$\left(-\frac{\alpha}{2}+\beta+\delta\right) = P'_{ME} \times \frac{L_{PP\,0}}{P_{ME_0}} = \frac{\Delta P_{ME}}{\Delta L_{PP}} \times \frac{L_{PP\,0}}{P_{ME\,0}} \qquad for \frac{\Delta Lpp}{Lpp} \ll 1.0 \tag{17}$$

$$(-\beta+\gamma) = P'_{ME} \times \frac{B_0}{P_{ME\,0}} = \frac{\Delta P_{ME}}{\Delta B} \times \frac{B_0}{P_{ME\,0}} \qquad for \frac{\Delta B}{B} \ll 1.0 \tag{18}$$

$$-\gamma = P'_{ME} \times \frac{T_0}{P_{ME_0}} = \frac{\Delta P_{ME}}{\Delta T} \times \frac{T_0}{P_{ME_0}} \qquad for \frac{\Delta T}{T} \ll 1.0 \tag{19}$$

$$\left(-\frac{\delta}{3}+\varepsilon\right) = P'_{ME} \times \frac{\nabla_0}{P_{ME_0}} = \frac{\Delta P_{ME}}{\Delta \nabla} \times \frac{\nabla_0}{P_{ME_0}} \qquad for \frac{\Delta \nabla}{\nabla} \ll 1.0 \tag{20}$$

Further details can be found in Alisafaki (2013).

3.1 Sample Presentation

The ship types under study are defined in regulations 2.34 and 2.35 in Annex VI of Chapter 1 of MARPOL 73/78. The statistical sample was generated for the relevant ship types, namely for Ro-Ro cargo and Ro-Ro passenger ships, built between 1990 – 2012, by use of the IHS Fairplay (IHSF) World Shipping Encyclopaedia version 12.01 database. Data relating to existing ships of 400GT and above were used. The noted IHSF database service speed is used as reference speed V_{ref} and likewise the IHSF database field giving ship's total installed main power is used for the identification of $MCR_{ME(i)}$ respectively.

The Ro-Ro Cargo ships sample consists of 154 ships (81 ships built between 1990-1999 and 73 ships built between 2000-2012) of the following ship subtypes:

- Ro-Ro Cargo Ship, Statcode-5 A35A2RR: Ro-Ro Cargo Ship
- Ro-Ro Cargo Ship, Statcode-5 A35A2RT: Rail Vehicles Carrier

The following Figs. 1, 2 and 3 represent the main Ro-Ro Cargo ships sample characteristics.

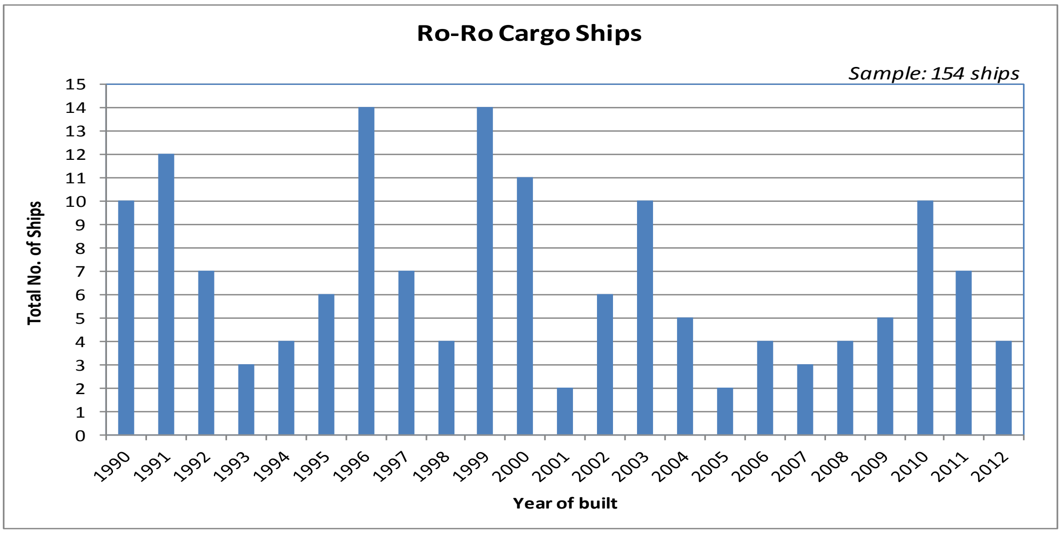

Fig. 1. Ro-Ro Cargo ships under study: Year of Built.

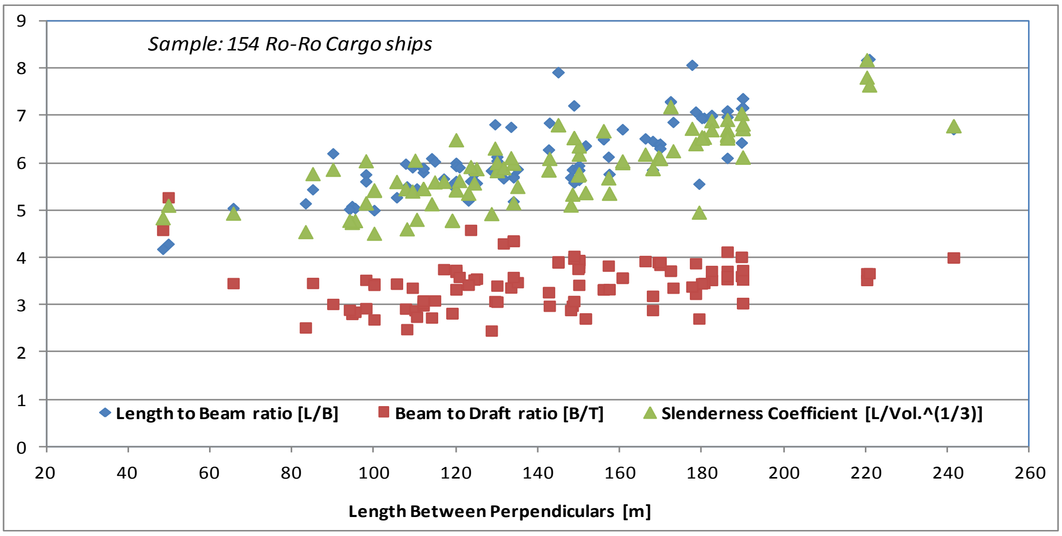

Fig. 2. Ro-Ro Cargo ships under study: L/B, B/T & L/Vol.$^{\wedge(1/3)}$.

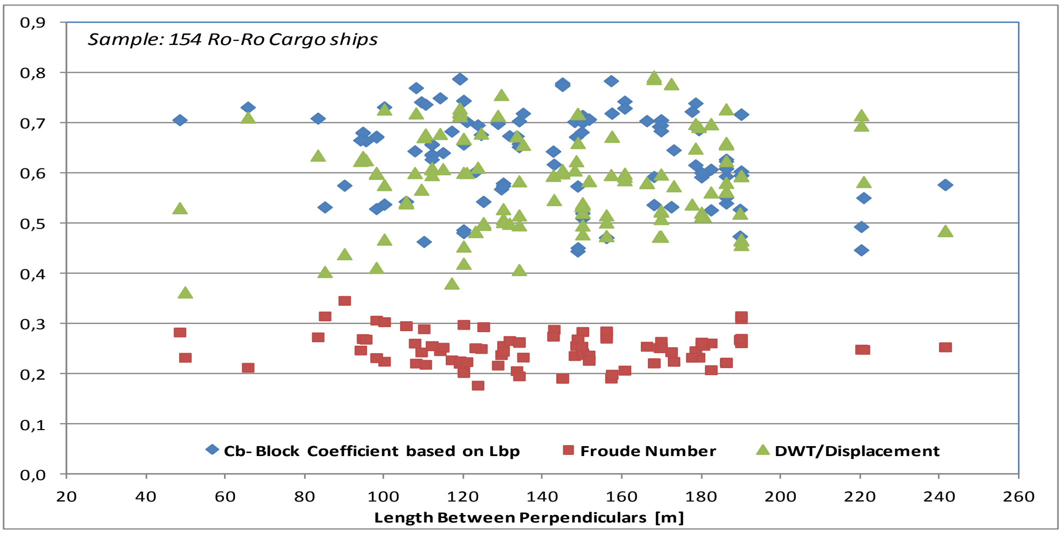

Fig. 3. Ro-Ro Cargo ships under study: c_b , Fn & DWT/Displacement.

The Ro-Ro Passenger ships sample consists of 181 ships (112 ships built between 1990-1999 and 69 ships built between 2000-2012) of the following ship subtypes:

— Passenger / Ro-Ro Cargo Ship (vehicles) Statcode-5 A36A2PR

— Passenger / Ro-Ro Cargo Ship (vehicles/rail), Statcode-5 A36A2PR

The following Figs. 4, 5 and 6 represent the main Ro-Ro Passenger ships sample characteristics.

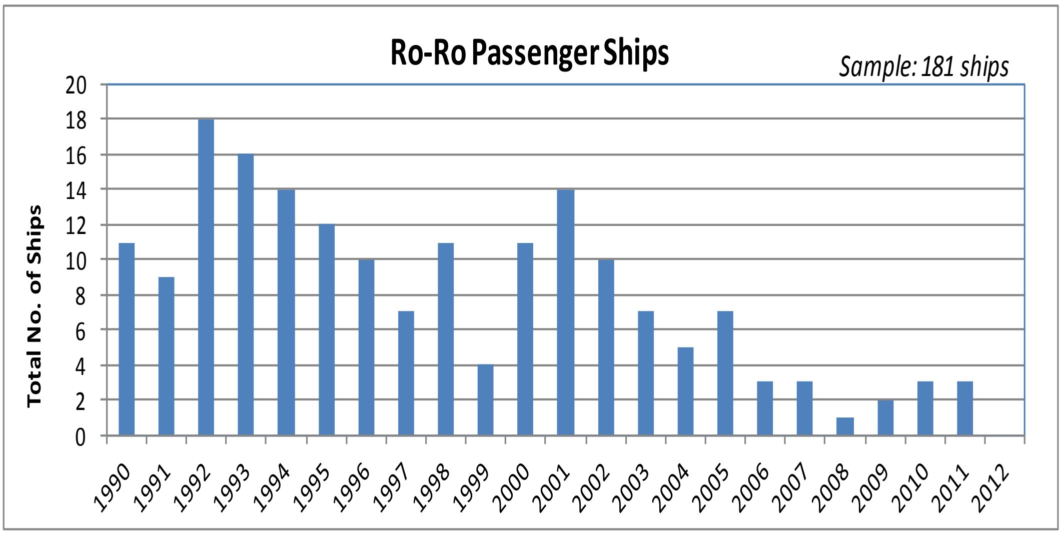

Fig. 4. Ro-Ro Passenger ships under study: Year of Built.

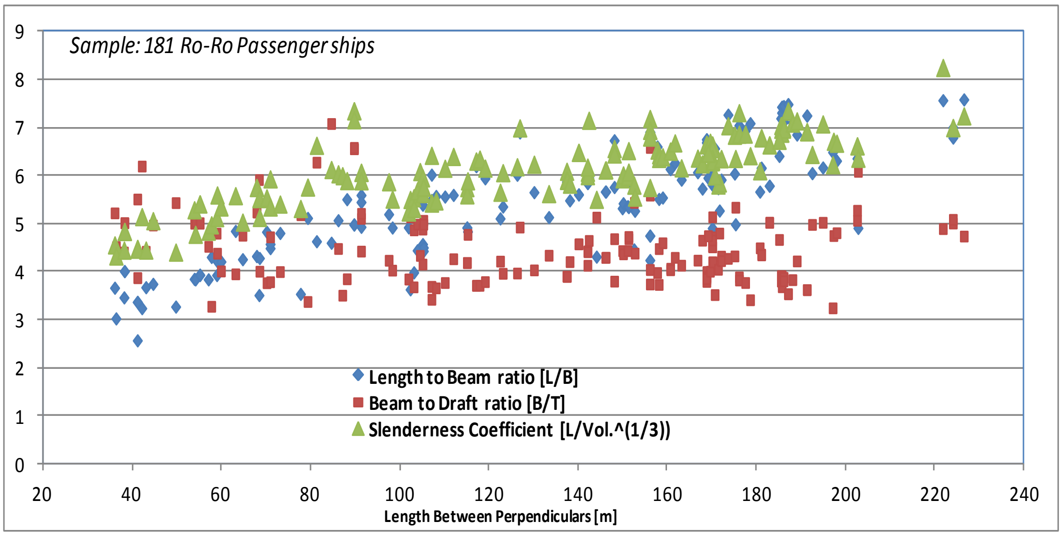

Fig. 5. Ro-Ro Passenger ships under study: L/B, B/T & L/Vol$^{\wedge(1/3)}$.

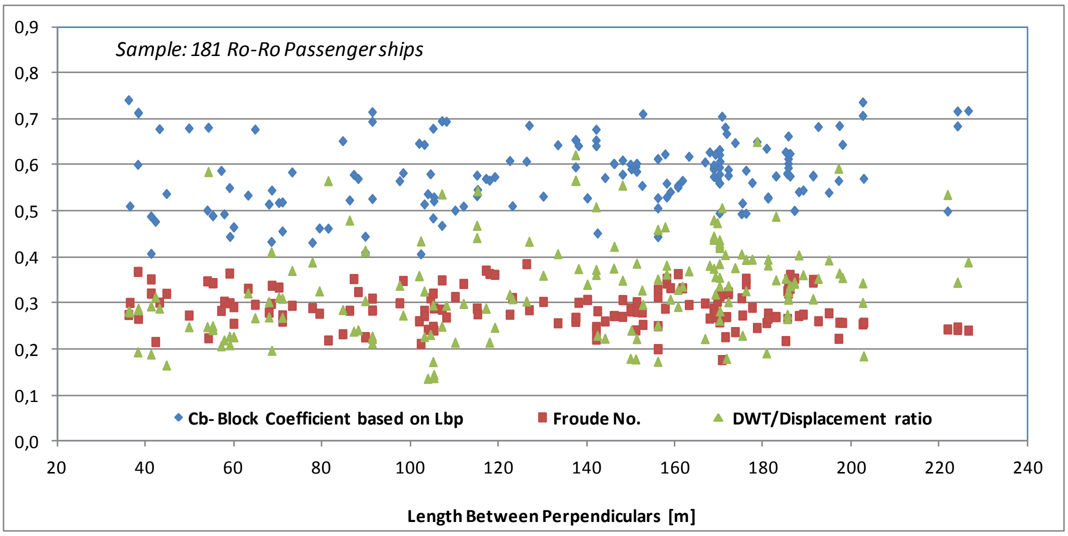

Fig. 6. Ro-Ro Passenger ships under study: c_b , Fn & DWT/Displacement.

4. ANALYSIS OF RESULTS AND DISCUSSION

The herein obtained exponent values for Eq. (5) and Eq. (13) vary significantly from the exponent values that have been adopted by IMO. At first, we recall the definition of the EEDI reference/boundary line, which should be not exceeded (Resolution MEPC 231(65)):

$$Max\ (EEDI):\ Reference\ line\ value = a \cdot (100\%\ Deadweight)^{-c} \tag{21}$$

It is noted that in MEPC 64/4/14 it was supposed that there is a proportional function between P_{ME} and the mathematical expression in the right on the Eq.(14). Therefore, in our study, we calculated the sought exponent values for the case *of linearity b*etween P_{ME} and SDV_{PME}, as well as in case of a *non-linear* modeling. The results of both approaches (*Non-Linear approach* and *Linear approach*) are presented in Table 2 (for Ro-Ro Cargo ships) and Table 3 (for Ro-Ro Passenger ships). Also, the adopted *IMO values* are listed in the first column, which *are based on a linear relationship* between P_{ME} and SDV_{PME}. It is noted that in both Tables 2 and 3, the values according to IMO of the exponent ε of the ship's volumetric displacement follow the MEPC 64/4/14, while the IMO for the exponents α, β, γ and δ follow the Resolution MEPC 245(66).

Table 2 Exponent values for Ro-Ro Cargo ships.

Exponent Values	acc. to IMO	present study Non-Linear approach	present study Linear approach
α	2.00	2.80	2.00
β	0.50	1.89	2.00
γ	0.75	1.26	1.50
δ	1.00	-1.84	-1.00
ε	0.503	0.93	0.503

Table 3 Exponent values for Ro-Ro Passenger ships.

Exponent Values	acc. to IMO	present study Non-Linear approach	present study Linear approach
α	2.50	2.79	2.00
β	0.75	1.97	2.00
γ	0.75	1.40	1.50
δ	1.00	-2.07	-1.00
ε	0.567	0.93	0.567

Both our approaches resulted in an opposite sign for the values of the exponent δ of the slenderness coefficient, compared to the corresponding IMO value. Our study concluded that this value is negative, which is also in agreement with the physics of the problem in hand, namely that a high slenderness coefficient leads to a reduction of the intensity of the generated ship-bound waves, and consequently of ship's wave resistance and of associated powering, which is a significant part of the overall powering for Ro-Ro ships, operating at relatively high Froude number (Papanikolaou, 2014).

The derived common exponent values α, β, γ & δ for Ro-Ro Cargo and Ro-Ro Passenger ships for the linear approach in our study lead to an efficient way for calculations in practice, since the correction factor f_{jRoRo} remains the same for both shiptypes.

Fig. 7 for Ro-Ro Cargo ships and Fig. 8 for Ro-Ro Passenger ships clearly show that the correlation factor of the herein derived formulas is higher (though in the range of 1-2%) than the corresponding one of the IMO adopted values, when applied to the same sample under study, thus much better represent the properties of the currently operating Ro-Ro Cargo and Ro-Ro Passenger fleet.

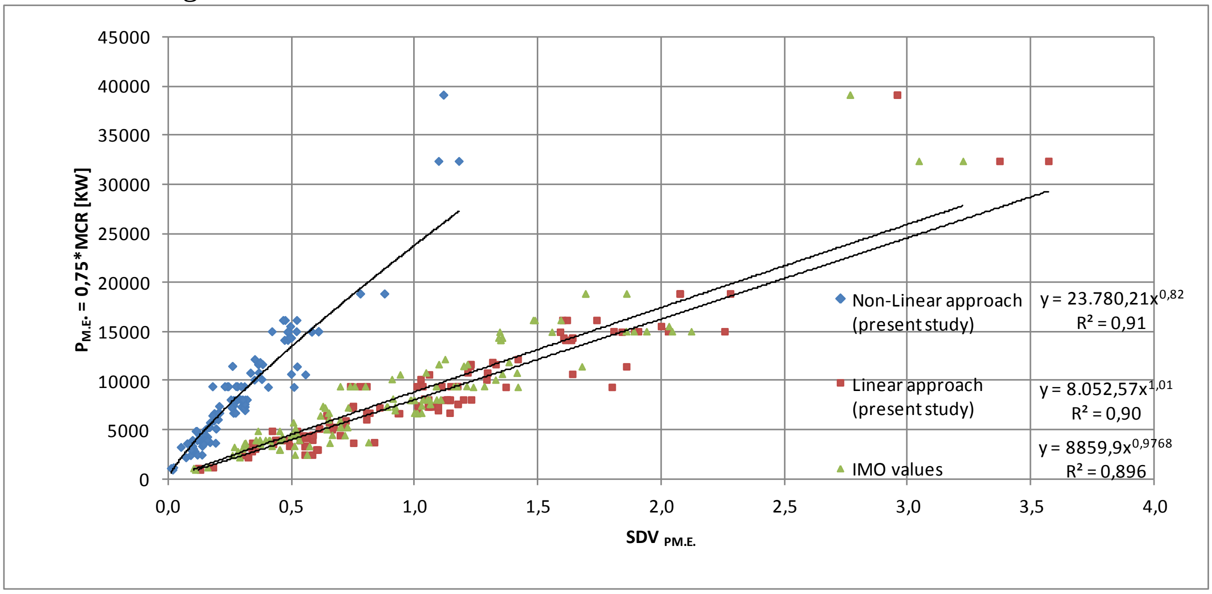

Fig. 7. Ro-Ro Cargo ships under study: P_{ME} as a function of SDV_{PME}.

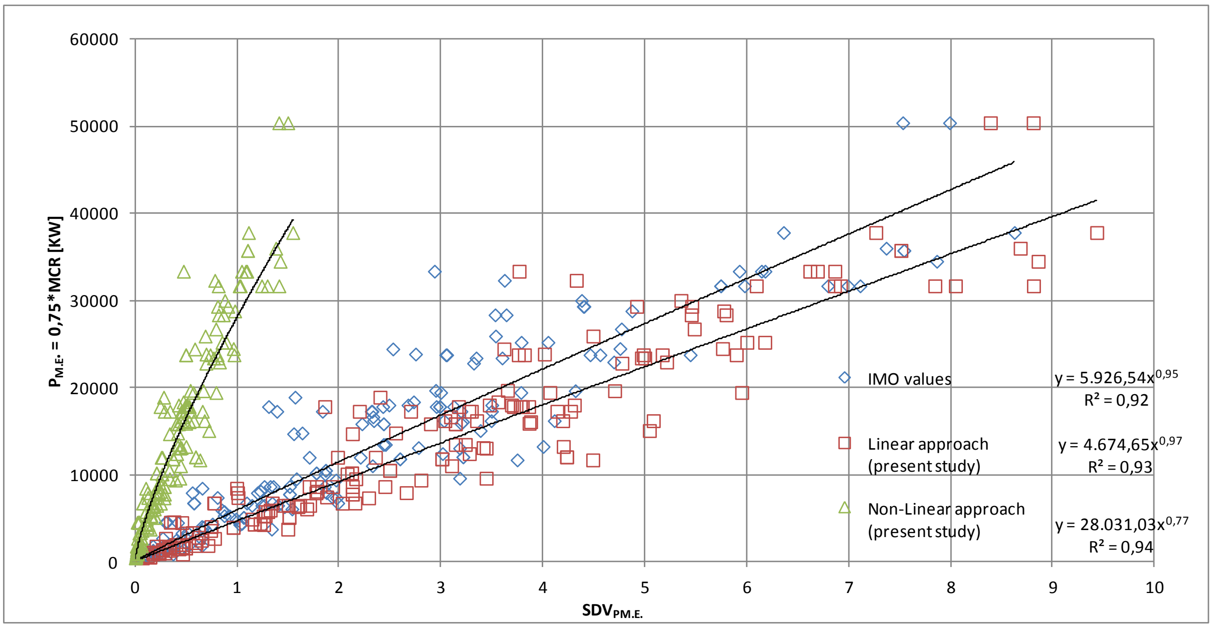

Fig. 8. Ro-Ro Passenger ships under study: P_{ME} as a function of SDV_{PME}.

The following Figs. 9 & 10 show an improved fitting in the proposed reference line according to the present linear approach of our study for both ship types. In both figures the curve of EEDI original (meaning without the correction factor f_{jRoRo}) is also plotted. The correction factor f_{jRoRo} reduces the EEDI value and simultaneously the scatter of the estimated index values.

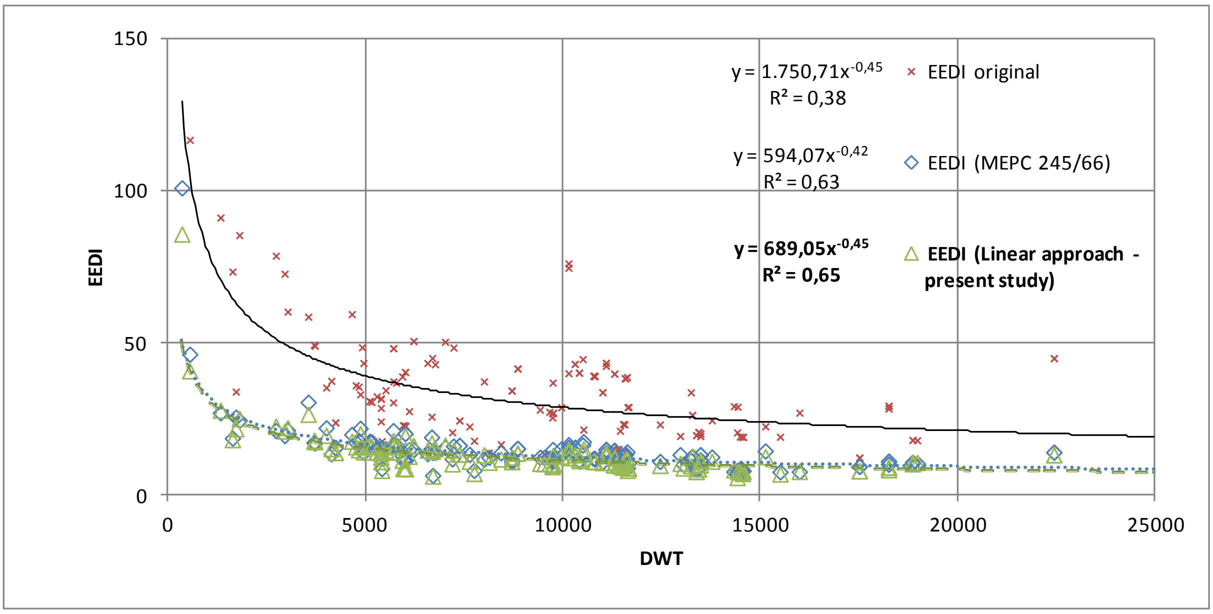

Fig. 9. EEDI reference lines for Ro-Ro Cargo ships under study.

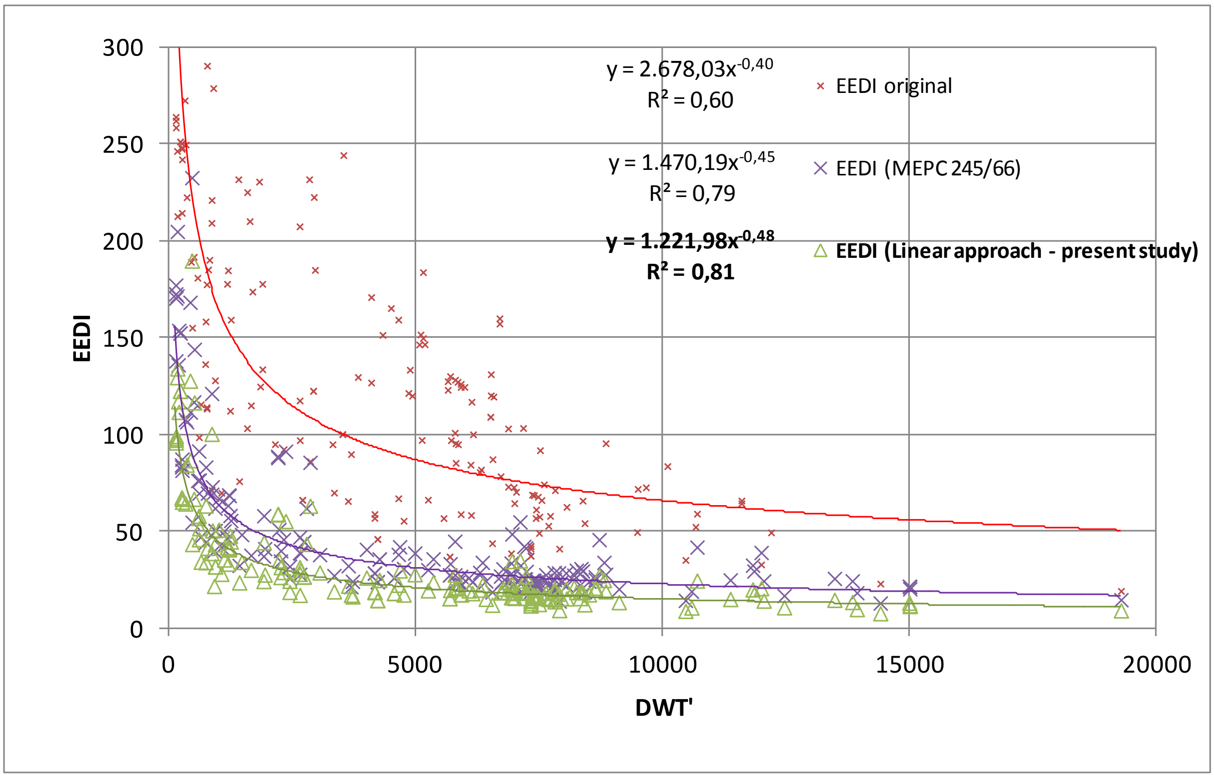

Fig. 10. EEDI reference lines for Ro-Ro Passenger ships under study.

5. CONCLUSIONS

The paper presents alternative values for the exponents of the correction factor f_{jRoRo} pertaining to Ro-Ro cargo and Ro-Ro passenger ships in the EEDI calculation. For both ship types under study, a non-linear relationship between P_{ME} and Ship Design Variable SDV_{PME} proved superior to others and of a higher correlation coefficient with respect to the representativeness of the employed ship sample. The linear approach, also developed in parallel in the present study, led also to a higher (even marginally) correlation coefficient, when calculating the EEDI reference line for a large sample of ships, compared to the corresponding one adopted by IMO(MEPC 245(66)). This diversity in the quality of fitting and the variation of the exponent values raises some justified questions regarding the maturity of EEDI reference lines adopted so far by IMO. Obtained parametric relationships between the powering of Ro-Ro cargo and Ro-Ro passenger ships and basic ship design parameters can be generally exploited in parametric ship design optimization procedures in the frame of holistic ship design optimization (Papanikolaou, 2010).

References

1. Papanikolaou, A.D. (2014). Ship Design: Methodologies of Preliminary Design, SPRINGER, ISBN 978-94-017-8751-2, September 2014.
2. Alissafaki, A. (2013) "Research on Alternative Equation Formulations in Estimating the Energy Efficiency Design Index (EEDI) for Ro-Ro Cargo Ships & Ro-Ro/ Passenger Ships", MSc thesis, Ship Design Laboratory, National Technical University of Athens. (http://dspace.lib.ntua.gr/handle/123456789/8528?mode=full)
3. Holtrop, J. (1984) "A Statistical Re-Analysis of Resistance and Propulsion Data", International Shipbuilding Progress, Vol. **31**, pp.272–276.
4. International Maritime Organization, MARPOL 73/78, Consolidated Edition 2013.
5. International Maritime Organization, "Third IMO GHG Study 2014", MEPC 67/6/INF.3, Executive Summary and Final Report, June 2014.
6. International Maritime Organization, Resolution MEPC 245(66), "2014 Guidelines on the Method of Calculation of the Attained Energy Efficiency Design Index (EEDI) for New Ships", MEPC 66/21/Add.1, Annex 5, 2014.
7. International Maritime Organization, Resolution MEPC 231(65), Annex 14, "2013 Guidelines For Calculation of Reference Lines For Use With The Energy Efficiency Design Index (EEDI)", MEPC 65/22, Annex 14, May 2013.
8. International Maritime Organization, "Comments on the Method to Include the Ro-Ro Cargo and Ro-Ro Passenger Ship Types into the IMO Energy Efficiency Regulatory Framework as Proposed in MEPC 64/4/14 and MEPC 65/4/4", MEPC 65/4/18, submitted by Denmark and Japan, 8th March 2013.
9. International Maritime Organization, "Revised Proposal for the Inclusion of the Ro-Ro Cargo and Ro-Ro Passenger Ship Types into the IMO Energy Efficiency Regulatory Framework", ,MEPC 65/4/4, submitted by Germany, Sweden, Community of European Shipyards Associations (CESA) and INTERFERRY, 8th February 2013.
10. International Maritime Organization, "Comments on the Method to Include the Ro-Ro Cargo and Ro-Ro Passenger Ship Types into the IMO Energy Efficiency Regulatory Framework as Proposed in MEPC 64/4/14 and MEPC 65/4/4", MEPC 65/4/18, Submitted by Denmark and Japan, 8th March 2013.
11. International Maritime Organization, "Proposal for the Inclusion of the Ro-Ro Cargo and Ro-Ro Passenger Ship types into the Energy Efficiency Regulatory Framework", MEPC 64/4/14, submitted by Germany, Sweden and the Community of European Shipyards' Association (CESA), 29th December 2012.
12. International Maritime Organization, International Convention of Tonnage Measurement of Ships 1969.
13. Kristensen, H. O. (2012) "Analysis of a new proposal (MEPC 64/4/14) to include the Ro-Ro cargo and Ro-Ro passenger ship types in the energy efficiency regulation framework", DTU Mechanical Engineering Report, Technical University of Denmark, November 2012.
14. World Shipping Encyclopaedia version 12.01, IHS Fairplay Eds.
15. Papanikolaou, A. (2010) "Holistic ship design optimization". Journal Computer-Aided Design, Elsevier, Vol. 42, Issue 11, pp. 1028-1044.

Appendix Benchmarking of Exponent Values

According to IMO MEPC 64/4/14, for both ship types under study, the main engine power P_{ME} was linearly related to Ship Design Variable SDV_{PME}.

$$P_{ME} = Const. \times L_{PP}^{\frac{1}{2}} \times F_{nL}^{(a+1)} \times \left(\frac{L_{PP}}{B}\right)^{\beta} \times \left(\frac{B}{T}\right)^{\gamma} \times \left(\frac{L_{PP}}{\nabla^{\frac{1}{3}}}\right)^{\delta} \times \nabla^{\varepsilon} \tag{14}$$

We benchmarked the obtained exponents *β* & *γ* for three different ship lengths (namely for Ro-Ro Cargo ships: 120 meters, 150 meters and 180 meters, and for Ro-Ro Passenger ships: 100 meters, 140 meters and 180 meters) and for typical main dimensions and block coefficients of the sample under study. The powering calculation was performed for three different Froude numbers (0.24, 0.26 and 0.28) by using the Holtrop method (1984). The resultant values were compared to the corresponding ones calculated by Kristensen (2012), as presented in the following Tables 4 - 7.

Table 4 Exponent values for –*β*- for Ro-Ro Cargo ships
(L/B= 6.10-6.50 , B/T=3.5, L/V $^{1/3}$=6.0 C_B = 0.603-0.685).

L [m]	***β*** *(present study)*	***β*** *(acc. to Kristensen)*	**Fn**
120	1,94	*2,47*	0,24
120	1,96	*3,62*	0,26
120	2,38	*5,62*	0,28
150	1,99	*2,52*	0,24
150	2,00	*3,70*	0,26
150	2,43	*5,77*	0,28
180	2,02	*2,55*	0,24
180	2,03	*3,77*	0,26
180	2,47	*5,87*	0,28

Table 5 Exponent values for –γ- for Ro-Ro Cargo ships
(L/B= 6.3 , B/T: 3.3-3.7 , L/V $^{1/3}$=6.0, C_B= 0.606-0.680).

L [m]	**γ** *(present study)*	***γ*** *(acc. to Kristensen)*	**Fn**
120	1,30	*1,86*	0,24
120	1,32	*2,44*	0,26
120	1,57	*3,46*	0,28
150	1,31	*1,88*	0,24
150	1,32	*2,48*	0,26
150	1,58	*3,52*	0,28
180	1,33	*1,90*	0,24
180	1,34	*2,52*	0,26
180	1,60	*3,58*	0,28

Table 6 Exponent values for –β- for Ro-Ro Passenger ships (B/T = 4.0).

L [m]	***β*** ***(present study)***	***β*** **(acc. to *Kristensen)***	**L/B**	**C_B**	**L/V ^ $^{1/3}$**	**Fn**
100	0.92	*1.37*	5.3-5.7	0.520-0.602	6.0	0.24
100	1.12	*1.82*	5.3-5.7	0.520-0.602	6.0	0.26
100	1.61	*2.75*	5.3-5.7	0.520-0.602	6.0	0.28
140	2.58	*3.04*	5.8-6.2	0.623-0.712	6.0	0.24
140	2.66	*4.41*	5.8-6.2	0.623-0.712	6.0	0.26
140	2.82	*6.69*	5.8-6.2	0.623-0.712	6.0	0.28
180	0.89	*1.29*	6.7-7.1	0.523-0.588	7.0	0.24
180	1.12	*1.64*	6.7-7.1	0.523-0.588	7.0	0.26
180	1.43	*2.37*	6.7-7.1	0.523-0.588	7.0	0.28

Table 7 Exponent values for –γ- for Ro-Ro Passenger ships (B/T: 3.8-4.2).

L [m]	L/B	γ (acc. to Holtrop method)	*γ (acc. to Kristensen)*	C_B	L/V $^{1/3}$	Fn
100	5.50	0.77	*1.30*	0.532-0.588	6.0	0.24
100	5.50	0.88	*1.54*	0.532-0.588	6.0	0.26
100	5.50	1.15	*2.01*	0.532-0.588	6.0	0.28
140	6.00	1.70	*2.24*	0.633-0.700	6.0	0.24
140	6.00	1.74	*2.92*	0.633-0.700	6.0	0.26
140	6.00	1.85	*4.07*	0.633-0.700	6.0	0.28
180	6.50	1.47	*1.97*	0.612-0.677	6.4	0.24
180	6.50	1.48	*2.56*	0.612-0.677	6.4	0.26
180	6.50	1.75	*3.58*	0.612-0.677	6.4	0.28

The values for the exponent β according to our study vary from 1.94 to 2.47 for Ro-Ro Cargo ships and from 0.89 to 2.82 for Ro-Ro Passenger ships, while the corresponding values according to Kristensen (2012) varies from 2.47 to 5.87 for Ro-Ro Cargo ships and from 1.29 to 6.69 for Ro-Ro Passenger ships.
The values for the exponent γ according to our study vary from 1.30 to 1.60 for Ro-Ro Cargo ships and from 0.77 to 1.85 for Ro-Ro Passenger ships, while the corresponding values according to Kristensen (2012) vary from 1.86 to 3.58 for Ro-Ro Cargo ships and from 1.30 to 4.07 for Ro-Ro Passenger ships.
All-in-all, the calculated values by Holtrop method are lower than the relevant values according to Kristensen (2012), who used for the estimation of the powering the FORMDATA method of Guldhammer. But in all cases, obtained exponents strongly depend on the Froude number, thus on the ship's relative speed, and they undisputedly differ from the IMO adopted values, as pointed out by Kristensen (2012) and is stressed in the submission of Denmark and Japan to IMO in 2013(MEPC 65/4/18).

INTRODUCING HIGH-END CAE PRE- AND POST-PROCESSING SOLUTIONS IN MARITIME AND OFFSHORE DESIGN

George Korbetis [1]

[1] BETA CAE Systems S.A., Thessaloniki, Greece

ABSTRACT

In our days, the CAD and CAE models in maritime and offshore products development are becoming increasingly complex. Same time, more analyses are necessary before a new design is ready for construction. Additionally to the standard assessments, extensive calculations are often needed to ensure the product's performance characteristics, and minimize the failure risk, through its lifetime since such structures are often of large scale, making a full model physical test impossible.

For the fast employment of such analyses with CAE simulation tools, the use of high efficient pre- and post-processing software becomes essential. Moreover, the tight collaboration of the pre-processor with the solvers and the CAD systems ensures adequate feedback from the calculations to the design department at the early design stages of the product. This can affect considerably the quality and performance characteristics of the final product. This presentation focuses on the capabilities of the ANSA / μETA pre- and post- processing suite of BETA CAE Systems S.A. ANSA is an advanced multidisciplinary CAE pre-processing tool that provides all the necessary functionality for full-model build up, from CAD data to ready-to-run solver input file, while μETA is a sophisticated multi-purpose post-processor, famous for its high performance and its automation capabilities.

1. INTRODUCTION

Three case studies are demonstrated for the scope of this work as typical problems in the maritime and offshore design. The FE models are set-up for structural and CFD analysis in order to investigate the strength and improve the design and operation efficiency.

2. STRUCTURAL ANALYSIS OF A CARGO SHIP

At the first case study a handysize class double skin bulk carrier is analysed. The simulation consists of a static analysis in sagging condition with the effect of an 8 meter height ocean wave, with length identical to the ship's length (figure 1). The ship is considered fully loaded as all holds are filled. Buoyancy is applied as hydrostatic pressure in the elements bellow waterline and varies linearly with water depth. The target of this analysis is the determination of the maximum stresses on critical areas of the vessel.

The process of the FE model set-up begins by handling CAD in order to clean-up and simplify the geometrical model. The process continues with automatic assembly of all parts and meshing according to specified parameters and quality criteria. Finally, special tools of ANSA are used for the wave definition, mass balance and buoyancy application in order to complete the FE model set-up. The NASTRAN solver has been used for this analysis.

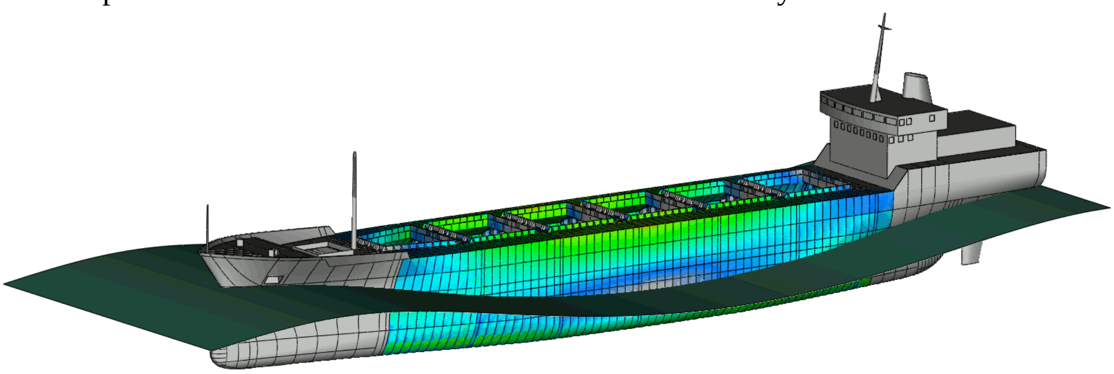

Fig. 1. Structural analysis of a cargo ship.

3. CONTACT ANALYSIS OF A RISER'S FLEXIBLE JOINT

At the second case study, a flexible joint of a riser is analysed (figure 2). In this example, it is of great importance to ensure that the moving parts of the flexible joint will stay always in contact in any loading condition avoiding any fluid leakage. A static analysis is performed using the ABAQUS solver for different loads of the riser line. The flexible joint is meshed with full hexa mesh of approximately 200 thousands hexas using the ANSA's HEXA BLOCK tool. The connecting bolts are automatically defined as FE representation consisted of BEAMs and rigid body elements and a pre-tension model is applied on them. Pre-tension is also applied on the elastomeric part of the joint. μETA Post-Processor's special tool investigates the contact pressure between the moving parts.

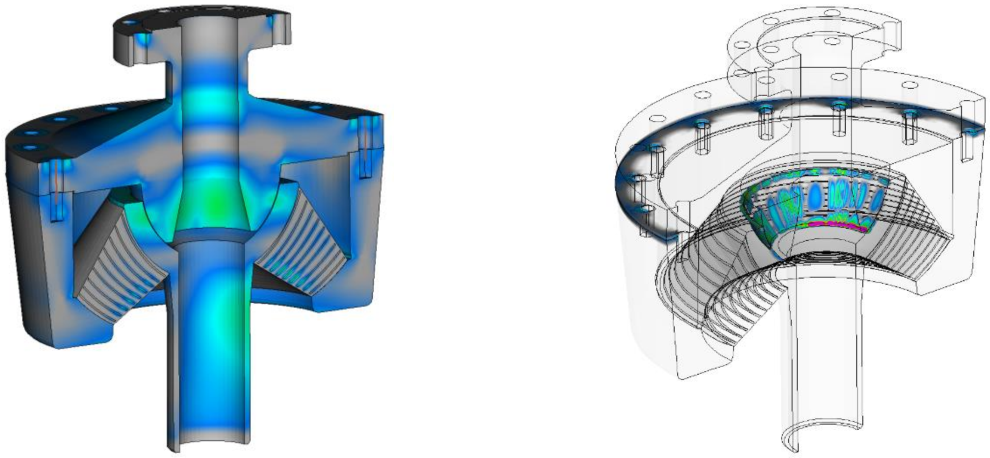

Fig. 2. Contact analysis on a riser's flex-joint.

4. MULTI OBJECTIVE DESIGN OPTIMIZATION OF A RUDDER.

The next case study demonstrates the suggested process of the definition of a strength analysis and the application of the multi objective optimization during the design process on a ship's rudder. A CFD analysis calculates the maximum force applied on the rudder's surface. The calculated force is taken as the loading condition for the rudder's structural analysis. The static analysis is set up using automated processes like the results mapping, the contact pair definition and the batch meshing which are provided by ANSA. Model shape parameterization is performed by the ANSA Morphing Tool and the Optimization Task and different design variables are defined to control the model.

To investigate the model behaviour, the structural analysis is coupled with an optimization process. The first step of this process identifies the variables that have big influence to the model's strength, while a second step performs a multi objective optimization to find the optimum combination of the input variables.

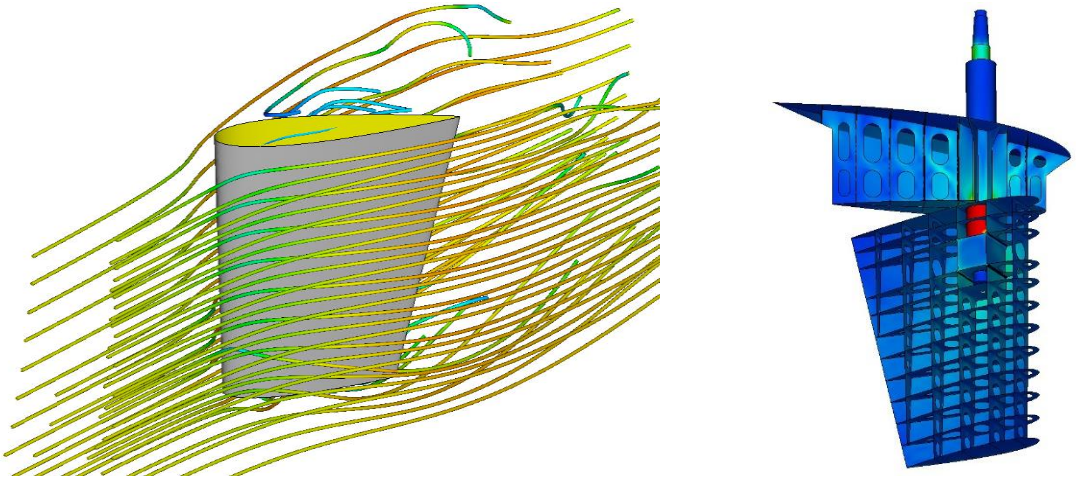

Fig. 3. Multi objective design optimization of a rudder.

5. COMPOSITE MATERIAL OPTIMIZATION OF A WINDSURFING BOARD FIN.

A composite material multi objective optimization is performed on a windsurfing slalom board fin. The fin is the most important component of a windsurfing board which affects considerably the performance of the board. Thus, carbon and glass fabrics are used for the fin construction aiming to achieve the desired behaviour in the sea. The optimization problem focuses on the construction of the fin by finding the best solution for the laminate layout. An initial CFD analysis determinates the pressure that develops on the fin at a speed of 30 knots. A structural analysis determinates the deflection and torsion of the composite FE model of the fin. Deflection, torsion and weight have to be minimized by finding the best orientation and thickness of each composite layer. The Laminate tool of ANSA is used to define and control the composite model.

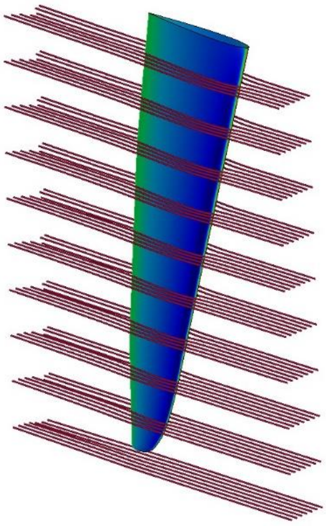

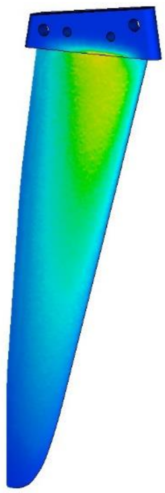

Fig. 3. Composite optimization of a windsurfing fin.

6. CONCLUSIONS

ANSA pre- processor and μETA and post-processor were successfully and efficiently used for the definition of several CAE analyses scenarios for structural and CFD disciplines. The needs in CAE set-up for the offshore structures design are covered by special tools. Applications like wave creation, mass balance, vessel balance waves and buoyancy calculation can be automated using the above mentioned tools.

References

1. O.B. Sertã, Petrobras S.A.; M.M. Mourelle, Petrobras S.A.; F.W. Grealish, MCS International; S.J. Harbert, Oil States Industries; L.F.A. Souza, Oil States Industries "Steel Catenary Riser for the Marlim Field FPS P-XVIII", OTC, 1996
2. Ben C. Gerwick, Jr.; "Construction of Marine and Offshore Structures", CRC Press, 2007
3. K J RAWNSON and E C TUPPER, B.P. (1997), Basic Ship, pp.555-563
4. GL RULES and GUIDELINES (2011), Rudder and Manoeuvring Arrangement
5. GL RULES and GUIDELINES (2011), Steel Plates, Strips, Sections and Bars
6. GIASSI, A.; MAISONNEUVE, J.; BENNIS, F.; (2003), Multidisciplinary Optimization and Robust Design Approaches Applied to the Concurrent Design, COMPIT 2003

A NUMERICAL WAVE RESISTANCE PREDICTION METHOD FOR HIGH-SPEED ROUND BILGE HULL FORMS

Steven S Meyer[1] and Prasanta K Sahoo[2]

[1] MS student in Ocean Engineering at Florida Institute of Technology, USA, e_mail: smeyer2009@my.fit.edu
[2]Assoc.Professor, Dept.of Marine & Environm. Systems, Florida Inst. of Technology,USA, e_mail: psahoo@fit.edu

ABSTRACT

Resistance prediction is one of the several important aspects of hydrodynamics of surface vessels of any type. It has been the endeavor of numerous researchers in the area of hydrodynamics to predict as accurately as possible the total resistance of marine vehicles. Since the last two decades high-speed craft have been in service around the world for rapid movement of goods, passengers and troop deployment to areas of conflict and disaster zones. As these types of marine vehicles are expected to operate with the highest efficiency, it has become imperative that their resistance be estimated with a high degree of accuracy in the design stage itself. Evaluating the wave making resistance of a ship is very important in order to predict the overall resistance of a ship. Prediction of wave making resistance can prove to be a difficult task in the absence of any experimental data. Errors in calculating the wave making resistance of a ship can impose severe penalty over the life of the ship by several millions of dollars. This paper attempts to revisit the numerical and other analytical methods that can be used to predict the wave making resistance of high-speed round bilge monohull vessels with a sufficient degree of accuracy so as to be used in the preliminary design stage.

In this paper a numerical method based on Michell's Integral as postulated by Tuck (1987) and simulations using ANSYS FLUENT in the computational fluid dynamics domain have been investigated. The results thus obtained from the above methods and procedures will be used to validate against experimental results conducted on high-speed round bilge hull forms of AMECRC systematic series, which h have extensive towing tank test results available in published articles.

The results of this investigation show that Michell's' thin ship theory with all its limitations are very encouraging and is able to predict with a high degree of accuracy the wave resistance of high-speed hull forms. It is also apparent that Computational Fluid Dynamics (although computationally intensive) offers a quick and reliable prediction procedure over a range of Froude numbers. It is envisaged that further study needs to be carried out, analyzing a larger spectrum of ship types and using other CFD codes such as the open source program Open FOAM.

1. INTRODUCTION

In this paper an attempt has been made to utilize the mathematical formulation of Michell's Integral (1898) as postulated by Tuck (1987) to determine the wave resistance of high-speed round bilge displacement monohull forms. ANSYS FLUENT which is a CFD program has also been used for comparative analysis of the wave resistance of the models. The hull forms included are based on 14 systematic series hull forms developed by the Australian Maritime Engineering Cooperative Research Center (AMECRC) and tested at the Australian Maritime College Ship Hydrodynamics Centre.

Over the past several years CFD has become more popular due to the increase in computing power and advanced algorithms to handle complex fluid flows. Using ANSYS FLUENT CFD it is possible to determine the resistance characteristics of any hull form with a reasonable degree of accuracy at a lower cost than model testing.

2. NOMENCLATURE

B	Breadth of Ship	R_F	Frictional Resistance
C_B	Block Coefficient	R_T	Total Resistance
C_F	ITTC 1957 ship-model correlation line	R_R	Residuary Resistance

C_P	Prismatic Coefficient	R_W	Wave Resistance
C_R	Residuary Resistance Coefficient	S	Wetted Surface Area
C_T	Total Resistance Coefficient	T	Draft of Ship
C_V	Viscous Resistance Coefficient	R_n	Reynolds Number
C_W	Wave Making Resistance Coefficient	u	Velocity of Water
Fn	Froude Number	V	Velocity of ship
g	Gravitational constant	Δ	Displacement
H	Wave Height	∇	Volumetric Displacement
1+k	Form Factor	ρ	Density of Water
L	Length of Ship	ν	Kinematic Viscosity

3. ABBREVIATIONS

CFD Computational Fluid Dynamics
ITTC International Towing Tank Conference

4. KEYWORDS

Resistance, Wave resistance, Michell's Integral, Slender Body Theory, CFD

5. HIGH-SPEED ROUND BILGE HULL FORMS

As described in Bailey (1976), semi-displacement hulls have a characteristic underwater shape distinguished by curvature between the bottom and sides, known as round bilge or soft chine. They have straight entrance waterlines, straight buttock lines and a transom stern. Their application is in the workboat, launch, frigate and corvette field. The extremes of the range are the heavy displacement, low speed workboat and the light displacement, fast patrol boat. The same author suggests that for Fn below 1.05 this type of hull form consistently offers a better performance in calm water than hard chine vessels. More detailed recommendation regarding this comparison could be found in Blount (1995). However, in naval and many other applications, the well proven high-speed round bilge monohull vessels still dominate, as stated by Lahtiharju et al. (1991). The major interest of the maritime community for round-bilge hull forms is exemplified by the impressive growth in the number of high-speed ferries, and special purpose marine vehicles which utilize these hull forms. The resistance per unit weight of these craft is significantly less than for planing hulls, and they have substantially larger useful load fractions.

6. AMECRC SYSTEMATIC SERIES

Over a ten-year period, starting in 1979, a major research project on combatant-vessel design was conducted at the Maritime Research Institute Netherlands (MARIN). This program was initiated as an outcome of the growing belief that a significant improvement in the performance of transom stern, round-bilge monohulls could be obtained, especially with regard to their calm water resistance and seakeeping characteristics. The project was jointly sponsored by the Royal Netherlands Navy, the United States Navy, the Royal Australian Navy and MARIN.

Extensive testing in calm water and waves was carried out on a systematic series of high-speed displacement hull forms (HSDHF), as described by Blok and Beukelman (1984), Van Oosanen and Pieffers (1985), MARIN Report 30 (1987) and Robson (1988). The test data for 40 models were analysed and included in a powerful computer system. However, except for the parent hull, the results of the tests and the analysis were not published.

The AMECRC systematic series is based on the HSDHF systematic series. The work on this project started in 1992, as described by Rikard-Bell (1992). The parent model is very similar to that of the HSDHF series and has the following parameters: L/B = 8.0, B/T = 4.0 and C_B = 0.396 and shown in Figure 1. The series transformation procedure is based on the variation of L/B, B/T and C_B and range of parameters for all models are shown in Table 1, as follows:

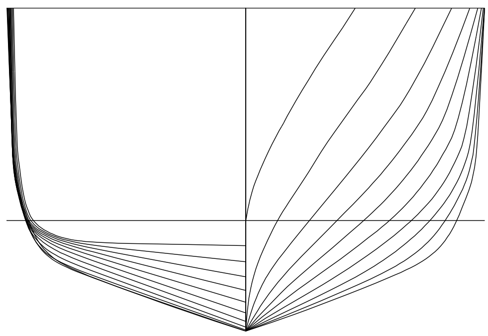

Figure 1: Parent hull of AMECRC systematic series

Table 1: Ranges of varied parameters for HSDHF and AMECRC Systematic Series.

	HSDHF	AMECRC
L/B	4 - 12	4 - 8
B/T	2.5 - 5.5	2.5 - 4.0
C_B	0.35 - 0.55	0.396 - 0.50

This 'parameter space' or series 'cube' is shown in Figure 2. The parameters of each of the 14 models can be identified from Table 2. All models have the same length of 1.6 m during tow tank tests.

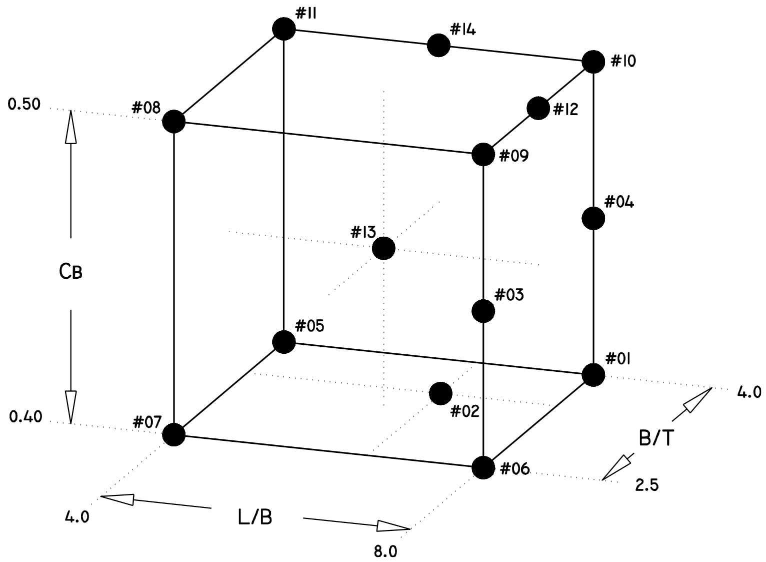

Figure 2: AMECRC Systematic Series [Bojovic and Sahoo (1998)]

Table 2: Systematic Series Parameter Range

Model	L/B	B/T	C_B	Model Disp.(kg)	$L/\nabla^{1/3}$	WSA (m^2)
1	8	4	0.396	6.321	8.653	0.3149
2	6.512	3.51	0.395	11.455	7.098	0.3849
3	8	2.5	0.447	11.454	7.098	0.3626
4	8	4	0.447	7.158	8.302	0.3064
5	4	4	0.395	25.344	5.447	0.6087
6	8	2.5	0.395	10.123	7.396	0.3566
7	4	2.5	0.396	40.523	4.658	0.7175
8	4	2.5	0.5	51.197	4.308	0.7552
9	8	2.5	0.5	12.804	6.839	0.3747
10	8	4	0.5	8.002	7.998	0.3145
11	4	4	0.5	32.006	5.039	0.6318
12	8	3.25	0.497	9.846	7.464	0.3366
13	6	3.25	0.45	15.784	6.379	0.4384
14	6	4	0.5	14.204	6.606	0.4193

7. MICHELL'S INTEGRAL

Michell's thin-ship theory as postulated by Tuck (1987) states that the wave resistance of a single hull can be obtained using three separate integrals. The first integral is shown below in equation 7. F(x, θ) integrates in the vertical z-direction from the lowest point of the section to the waterline. Y(x,z) represents the half breadth of waterline for all stations along the depth up to the load waterline.

$$F(x,\theta) = \int Y(x,z)\exp\left(kzsec^2(\theta)\right) dz \qquad (7)$$

Where $k = \frac{g}{V^2}$ (8)

And $F(x,\theta) = \sum_{j=0}^{N_z} \omega_j Y\left(x, z_j\right) \exp(kz_j \sec^2\theta)\Delta z$ (9)

The integral in equation 7 must be evaluated for each station from x_0 to x_n, where x_0 is at the bow of the ship and x_n represents each of the stations with n ranging from 1 to the total number of stations. Equation 7 must also be evaluated for all θ from 0 to π/2 where θ_0 is the forward direction of the vessel and θ = π/2 is perpendicular to θ_0. The last operation is to integrate across each waterline from z_o to z_n, where z_0 is at the lowest point of section of the ship and z_n represents each of the waterlines with n ranging from 1 to the total number of waterlines terminating at the load waterline. The next integral uses the results from 9 and is shown below in equation 10. P(θ) describes the even component of the bow induced disturbance.

$$P(\theta) = \int F(x,\theta)\cos(kxsec\theta)\, dx \qquad (10)$$

P(θ) can be approximated to form the equation 11.

$$P(\theta)\approx\sum_{i=1}^{N_x-1}\omega_i F(x_i,\theta)\cos(kx_i sec\theta)\Delta x \tag{11}$$

for i being even

$$\omega_{2i} = \frac{3K+Kcos(2K)-2\sin 2K}{K^3} \tag{12}$$

for i being odd

$$\omega_{2i+1} = \frac{4(sinK-KcosK)}{K^3} \tag{13}$$

Where

$$K = ksec\theta\Delta x \tag{14}$$

Similar to P(θ), Q(θ) can be determined from the equation (15) where in it describes the odd component of the bow induced disturbance.

$$Q(\theta) = \int F(x,\theta)\sin(kxsec\theta)\, dx \tag{15}$$

Equation 15 can be approximated from the following expression:

$$Q(\theta)\approx\sum_{i=1}^{N_x-1}\omega_i F(x_i,\theta)\sin(kx_i sec\theta)\Delta x \tag{16}$$

Using the results obtained from P(θ) and Q(θ), the total wave resistance can be determined from the following equation 17.

$$R_W = c\int_0^{\pi/2}(P^2+Q^2)\sec^5\theta d\theta \tag{17}$$

Where

$$c = \frac{4\rho g^4}{\pi V^6} \tag{18}$$

The algorithm based on the above theory was implemented in MATLAB for carrying out the computations. In order to verify the accuracy a Wigley hull was modelled and tested against experimental data. The data used for validation has been taken from the paper by Chen and Noblesse (1983). The Wigley hull form can be defined by a simple expression as shown in equation 19.

$$\frac{y}{b} = \frac{1}{2}\left[1-\left(\frac{2x}{L}\right)^2\right]\left[1-\left(\frac{z}{T}\right)^2\right] \tag{19}$$

Where y is the half breadth of the waterline, b is the maximum breadth at midships, x is the position of section along length and z is the location of half breadth measured from keel. It can be seen from Figure 5 that the data of Chen and Nobleesse (1983) shows good correlation when compared with Michell’s Integral.

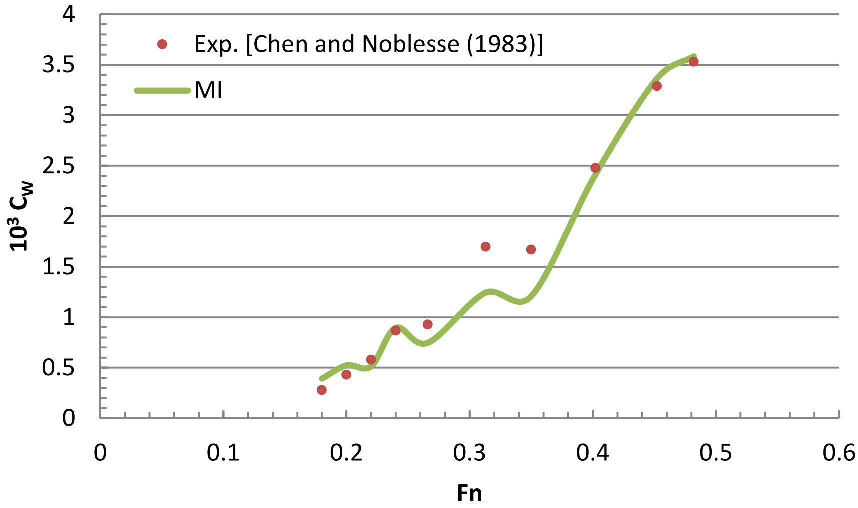

Figure 5: Wave Resistance coefficient Validation with Michell's Integral for Wigley Hull Form

From Figure 6 it can be seen that Michell's Integral predicts reasonably well against experimental wave resistance values of AMECRC model #1. However this is not the case with other models. Except for models 13 and 14 Michell's Integral under predicts the wave resistance of all other models. Two extreme examples of experimental wave resistance results against Michell's Integral for models 8 and 14 are shown in Figures 7 and 8.

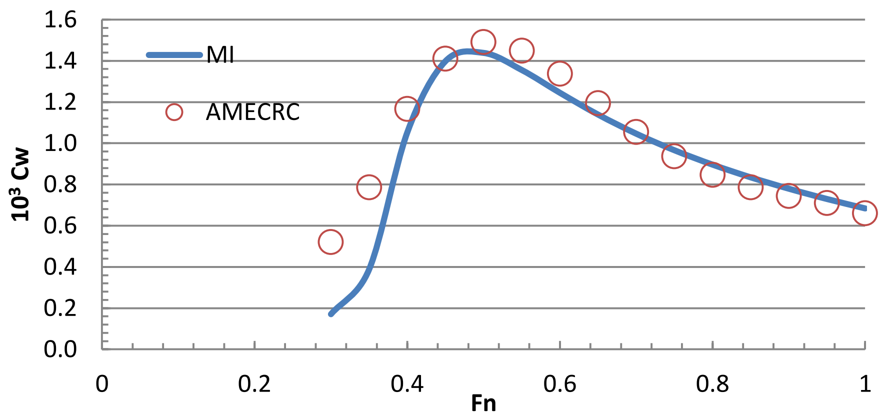

Figure 6: Comparison of Experimental data against Michells Integral for AMECRC Model #1

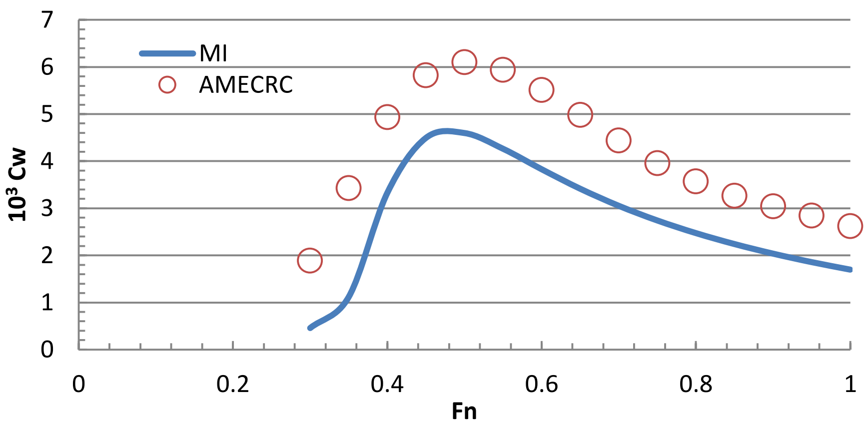

Figure 7: Comparison of Experimental data against Michell's Integral for AMECRC Model #8

8. MODELLING WITH ANSYS FLUENT

The hull is transformed into a solid before it is imported into the ANSYS geometry. Two methods exist for constructing the geometry. The first method is to replicate the depth and width of the towing tank with two ship lengths aft of the model and one ship length forward of the model. The other method is to use one ship length as the depth, one ship length port and starboard, two ship lengths aft and one ship length forward. The model is then cut from the solid body leaving a void where the ships initial geometry was located. Due to the symmetric nature of a ship in calm water the solid is then sliced along the central longitudinal axis. To satisfy the mesh requirements a smaller domain was used.

In the ANSYS CFD Mesh program the explicit option comes with the best meshing options to model fluid. The solver preferences include ANSYS FLUENT, ANSYS CFX and ANSYS Polyflow and in this investigation FLUENT option has been used. ANSYS academic version limits the number of cells elements to 512,000. This number is suitable for mechanical simulations but is not appropriate for modeling the flow around a ship where a free surface exists. When modeling a ship the number of elements usually ranges from 1.5 to 18 million cells. The meshing methods for ANSYS FLUENT options include cut cell elements and tetrahedrons. Tetrahedrons are square based pyramidal elements that allow for more precise computations. The cut cell meshing method was used as it allows for a greater mesh quality with the element limitations of ANSYS academic version.

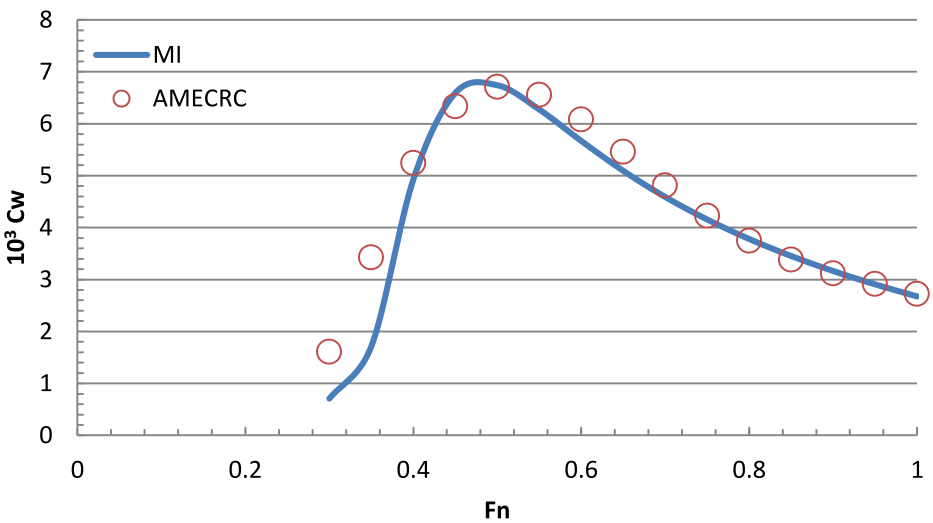

Figure 8: Comparison of Experimental data against Michell's Integral for AMECRC Model #14

The mesh orthogonal quality can range from 0 to 1, with zero representing a mesh of no quality and 1 representing a very fine mesh. In this study the mesh orthogonal quality was 0.163 due to limitations of the ANSYS academic version. This mesh is far below the standard or 0.27, a mesh quality that should be achieved for fluid flow computation. Two approaches exist to modeling fluid flows including the Eulerian and Lagrangian approaches. The Lagrangian approach follows the individual fluid particles through time. The Eulerian approach focuses on a spatial location and the changes that occur at that individual point [Kundu, Cohen and Dowling (2012)]. The Volume of Fluids Method (VOF) is similar to the Eulerian method but solves only a single set of momentum equation for the entire domain. This method works best for modeling free surface flows such as ship motion through open water, filling of a tank and sloshing [DSTO (2013)].

For the VOF method an implicit or explicit scheme can be used. The implicit scheme can be used for both transient and steady state calculations [ANSYS FLUENT (a) (2014)]. Implicit methods are iterative and solve equations for the current state while solving the next state. Explicit methods solve for properties at a later time based off the current time. When the open channel selection is selected ANSYS FLUENT automatically selects the implicit time scheme to allow for greater precision and larger time steps [ANSYS FLUENT (b) (2014)]. Many different solution methods exist for calculating the pressure and viscous forces on free surface ship flow. The combination found to be most successful included are shown in Table 3 below.

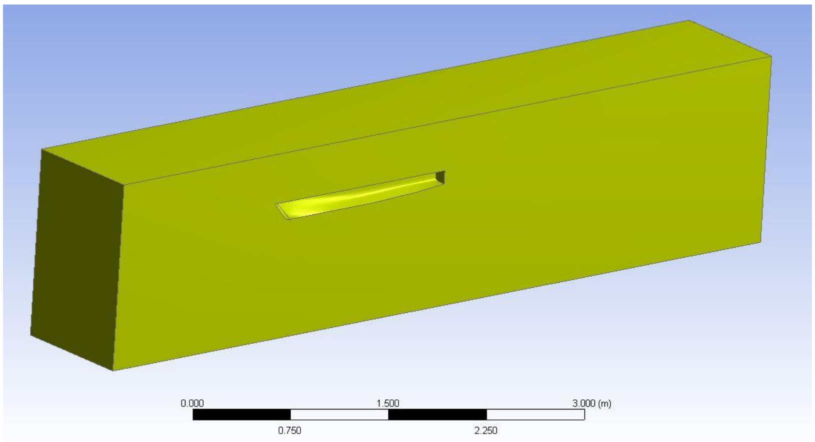

Figure 9: Geometry of model in ANSYS

Table 3: Solution Methods

Scheme	Simple
Gradient	Least Squares Cell Based
Pressure	Body Force Weighted
Momentum	Second Order Upwind
Volume Fraction	First Order Upwind
Turbulent Kinetic Energy	Second Order Upwind

9. RESULTS FROM ANSYS FLUENT

The wave resistance of AMECRC model #1 obtained from experimental results of towing tank was validated against ANSYS FLUENT and has been shown in Figure 10. It is apparent from the figure that within the limitations of the academic version of ANSYS reasonably good correlation exists between the experimental and wave resistance computed by ANSYS FLUENT.

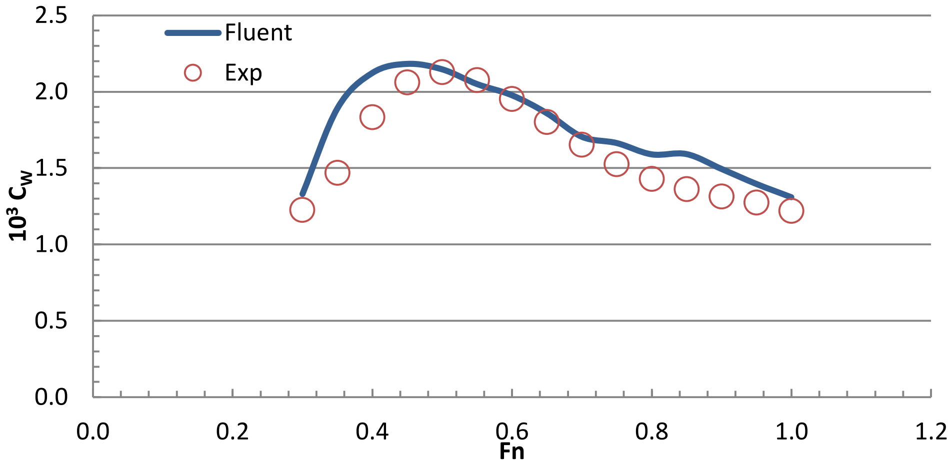

Figure 10: Experimental Wave Resistance Coefficient comparison against FLUENT for AMECRC Model#1

The percent errors shown above were calculated from the average percent difference across the different models and speeds. Equation 24 shown below was used to calculate the percent difference and Table 4 presents the average difference across all models for various components of resistance.

$$\%diff = \frac{theoretical - \text{experimental}}{\text{theoretical}} \qquad (20)$$

Table 4: Percent Error from ANSYS FLUENT

Component	**Average Percent Difference**
Total Resistance	4.985%
Frictional Resistance	10.035%
Residuary Resistance	8.986%
Total Resistance Coefficient	5.355%
Residuary Resistance Coefficient	9.031%

ANSYS FLUENT produced results that were typical with results found in other studies. In a study conducted by the Defense, Science and Technology Organization (DSTO) on a model designed by the US David Taylor Model Basin [DTSO (2013)] found results similar to this study using ANSYS FLUENT. The total resistance coefficient was off by 4.5% and the residuary resistance coefficient was off by a factor of 12.4% [DSTO (2013)]. Another study conducted at the University of Leeds, UK analyzed Series 60 hulls and found that ANSYS FLUENT results were off by 8.56 % [Pranzitelli, Nicola & Miranda (2011)].

Given that the results were off by a similar margin it may be suitable to multiply the total resistance coefficient by a factor of 10% in order to obtain results that would be close to experimental values. The results obtained from ANSYS FLUENT appear to be very promising. The resistance values that were predicted would be acceptable for preliminary designs.

10. CONCLUSIONS

The wave making resistance of a ship is very important in order to predict the overall resistance of a ship because it can account for over 50% of the total resistance. Under predicting the wave making resistance of a ship can result in a vessel that has a lower maximum speed than designed for, has a lesser range than designed for and costs millions of dollars more in operational costs. Though a considerable amount of research has been carried out there still remains a large degree of uncertainty in this area. This paper attempts to revisit numerical and other analytical methods that can be used to predict the wave making resistance of high-speed round-bilge monohull vessels.

Empirical techniques offer a low cost method that is not computationally intense to find the resistance characteristics but do not offer the accuracy achieved by other methods. Michell's Integral (1898) as postulated by Tuck (1987) offered results that were reasonably accurate for the AMECRC hull forms.

Computational Fluid Dynamics (CFD) has become more reliable over the past two decades. CFD offers a method where hull forms can be rapidly changed and tested at an economical advantage when compared to model testing. ANSYS FLUENT produced results that could be considered accurate and replace model testing. Using CFD a Naval Architect could prototype multiple ship designs to determine which one will have the best wave making resistance characteristics. This process offers a simple and convenient method where upstream data can be rapidly changed and tested. Out of all of the methods examined in this report it is clear that using CFD is the most accurate and reliable way of predicting the resistance of high-speed round bilge hull forms.

• ACKNOWLEDGEMENTS

The authors would like to express their sincere gratitude to Florida Institute of Technology, Melbourne, USA for their support, and encouragement throughout the course of this research work.

• REFERENCES

ANSYS FLUENT (a). 23.3.1 (2014): Overview and Limitations of the VOF Model

ANSYS FLUENT (b). 25.3.2. (2014): Modeling Open Channel Flows

Bailey, D., 1976, "The NPL High Speed Round Bilge Displacement Hull Series", RINA, Maritime Technology Monograph No.4

Blount D.L., 1995, "Factors Influencing the Selection of a Hard Chine or Round-Bilge Hull for High Froude Numbers", *Proc. Of the Third International Conference on Fast Sea Transportation (FAST '95),* Schiffbautechnische Gesellschaft, Vol. 1

Blok, J.J. and Beukelman, W. 1984, "The High-Speed Displacement Ship Systematic Series Hull Forms - Seakeeping Characteristics", *Transactions, Society of Naval Architects and Marine Engineers*, Vol. 92:125-150.

Bojovic, P. and Sahoo, P.K. 1998, "A Study on Motion Analysis of High Speed Displacement Hull Forms", *Proc. Seventh International Symposium on Practical Design of Ships and Mobile Units*, The Hague, The Netherlands: 545-553.

Chen, C. Y. and Noblesse, F. 1983, “Preliminary Numerical Study of a New Slender Ship Theory of Wave Resistance”, *Journal of Ship Research,* Vol. 27, No 3, pp 172-186

DSTO-TR-2465, 2013, Defense Science and Technology Organization

Kundu, P., Cohen, I. and Dowling, D. 2012, Fluid Mechanics, Fifth Edition, Waltham, MA

Lahtiharju, E., Karppinen, T., Hellevaara, M., Aitta, T., 1991, “Resistance And Seakeeping Characteristics Of Fast Transom Stern Hulls With Systematically Varied Form”, *Tran. Of Society of Naval Architects and Marine Engineers (SNAME)*, Vol. 99, pp 85-118

Maritime Research Institute Netherlands, 1987, "MARIN High Speed Displacement Hull Form Designs", MARIN Report 30.

Rikard-Bell, M. 1992 "Report of Research - October/November 1992", AMECRC IR 92/1 : 1-28.

Robson, B.L. 1988, "Systematic Series Of High Speed Displacement Hull Forms For Naval Combatants", *Tran. Royal Institution of Naval Architects*, Vol. 130, pp 241-252.

Van Oossanen, P. and Pieffers, J.B.M. 1985, "NSMB-Systematic Series Of High-Speed Displacement Forms", *Workshop on Developments in Hull Form Design*, Wageningen : 16.

Tuck, E. 1987, “Wave Resistance of Thin Ships and Catamarans”, Report. No. T8701, Applied Mathematics Department, The University of Adelaide

Bailey, D. and Marwood, W. (1969): Design Data for high-speed displacement hulls of round-bilge form. British National Physics Laboratory, Ship Division, Report No. 99

ANTIFOULING –
HIGH-TECH STRATEGIES FOR AN ANCIENT PROBLEM

Volker Bertram[1]

[1] DNV GL, Brooktorkai 18, D-20457 Hamburg, Germany, Volker.Bertram@dnvgl.com

ABSTRACT

This article discusses antifouling strategies for ships, giving an introduction in layman's terms. Currently popular copper-based coatings are under scrutiny by environmentalists who demand a general ban on biocide coatings. Various alternatives start to emerge, frequently reconsidering previously suggested approaches in view of present technological progress. Discussed approaches include: low-surface energy coatings, nano-coatings, surface treated coating combined with robotic cleaning, electro-conductive coatings, sheeting and riblet coating. The article briefly describes history and recent developments for the options, along with strength and shortcomings.

1. FOULING

Fouling, i.e. marine growth on ship hulls and propellers, progresses in stages, Fig.1:

1. Slime: Within hours after a ship is immersed in seawater, the hull accumulates a microbial biofilm, consisting of bacteria and single-cells organisms. This microscopic slime already reduces the ship's performance by several percent points. It is widely considered as inevitable.
2. Biofilm: Slime enables the settling of other organisms, such as algae and marine fungi. This biofilm is already visible to the human eye.
3. Soft fouling: Green weed can grow up to 15cm long in a band a few meters wide at the waterline. It grows rapidly and scrubbing it off triggers an even more vigorous growth within a few weeks.
4. Shell fouling (a.k.a. "calcareous fouling" from calcium in the shells) may consist of barnacles, mussels, tubeworms, etc. This hard fouling may penetrate coatings and destroy them. It is also hard to remove, requiring forceful cleaning that may also damage coatings.

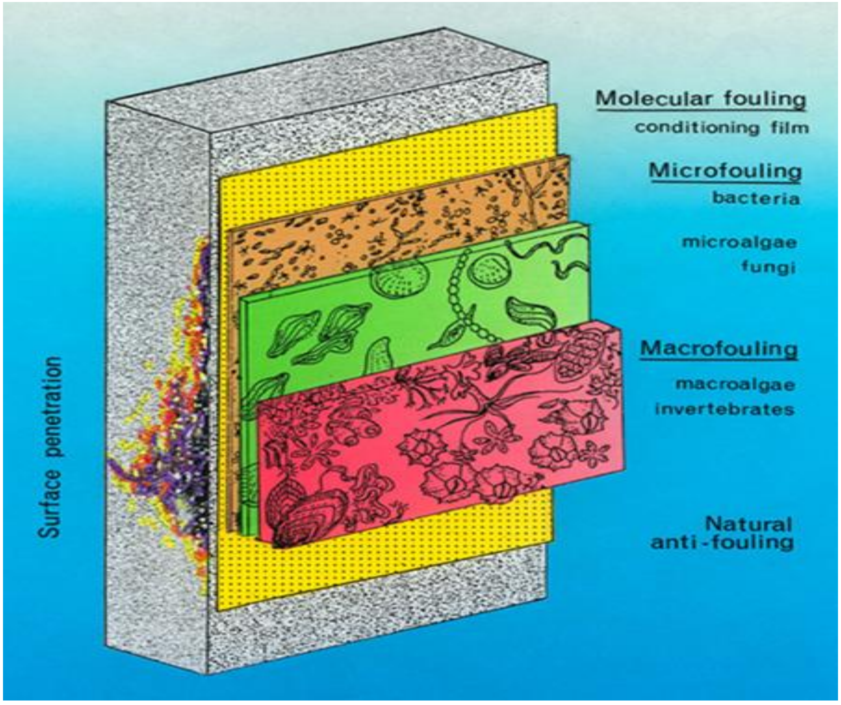

Fig.1. Stages of fouling (source unknown)

The US Navy uses a simple system to rate hull fouling, *NN (2006)*. Via an image catalogue, fouling severity and coverage is rated from 0 to 100, in steps of 10, Fig.2. This allows quick qualitative monitoring of fouling. But how does fouling translate into fuel penalties?

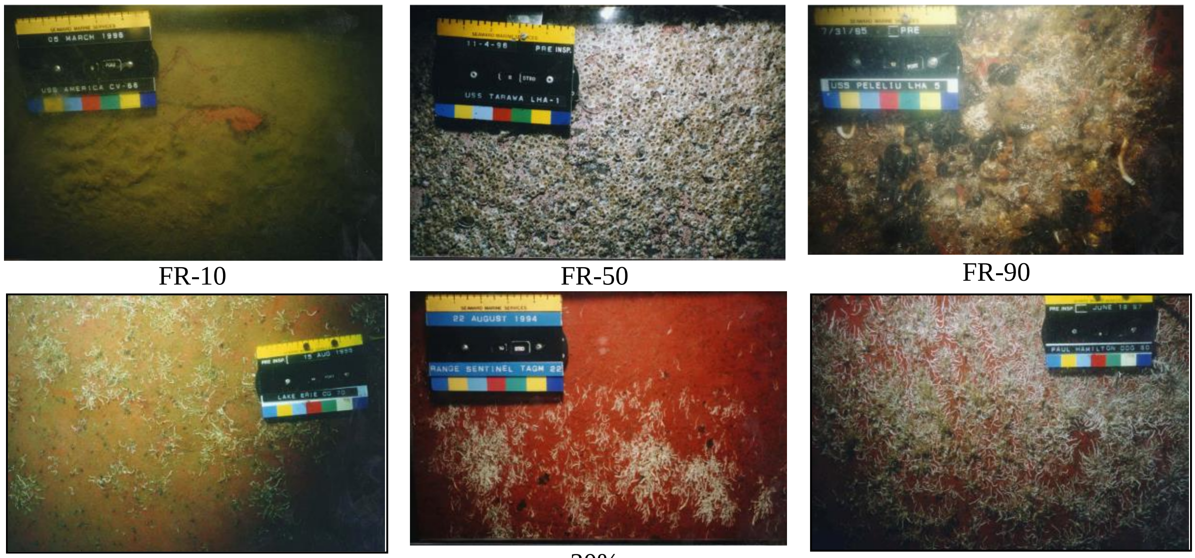

FR-10 FR-50 FR-90

20% 30% 90%

Fig.2. US Navy rating scale examples. fouling severity (top) and coverage (bottom), *NN (2006)*

Weed and shell fouling decrease the ship's performance sometimes drastically with typical values in the range of 30-50% more fuel consumption (and associated emissions) compared to a smooth hull. For comparison, many energy saving devices target 3-5% fuel savings. Antifouling, the prevention of marine growth on ships, is thus both an economic and ecological necessity for shipping.

The importance of antifouling measures is widely known in shipping circles. But attempts to improve antifouling strategies stop often after the first encounter with jargon of coating experts: “low surface energy coatings”, “self-polishing copolymers”, “surface treated coatings”. You may have heard the terms, but who wants to admit not understanding the jargon of the coating industry? Generally, neither naval architects (in ship yards), ship engineers (in superintendent positions) nor ship masters receive any training in the basics of ship coatings – except global statements on the importance of good hull surface husbandry. The following shall give a simple introduction to commonly used and more recently proposed coating approaches.

2. A PROBLEM SOLVED – OR SO WE THOUGHT

Fouling has been a headache for shipping since ancient times. Some of the oldest testimonies are Greek texts dating 300 BC describing the use of tar and wax to protect ships.

By 1850, antifouling paints had become the predominant way prevent marine growth on ship hulls. The basic principle was the same as in most of today's antifouling paints: In contact with seawater, antifouling paint releases biocides (= poison) which form a toxic boundary layer preventing marine growth. A certain concentration of these toxicants has to be maintained for effective protection. As toxicants are washed as the ship moves through water, the paint has to re-supply the protective boundary layer with new toxicants. The poison enters the water through contact and shear forces created while the ship moves through water. The leaching rate depends then on ship speed.

The earlier antifouling paints were so-called contact paints. Here seawater penetrates the paint film as the toxicants dissolve, leaving a honeycomb structure. This increases surface roughness and thus resistance. It also yields an exponentially decaying leaching rate, releasing far more poison than necessary in the beginning and dropping below the minimum effective level long before all poison in the paint has been released. After about one year, ship performance usually dropped drastically making a dry-dock interval necessary for re-painting.

The solution came with self-polishing copolymers, i.e. a coating matrix that also dissolved slowly in water. Self-polishing paints dissolve slowly in seawater exposing toxicant particles. As the hosting matrix film (the “co-polymer” in self-polishing copolymers) dissolves, the surface remains smooth (=self-polishing) and an almost constant leaching rate is obtained. Various self-polishing paints have been developed tailored to ship types, speed, and operation area. According to this leaching mechanism, a self-polishing paint may be classified as depletion type, hydration type, or hydrolysis type.

The most popular toxicant was TBT (tributyltin), a member of the organotin chemicals. This tin compound was highly toxic. Hence small quantities sufficed to protect the hull from fouling. TBT provided up to 5 years fouling-free performance, kept the hull smooth and low-resistant, and was easy to apply. The antifouling problem seemed to be solved at last. However, in the early 1980s it became clear that organotin (TBT) not only killed fouling organisms. Its slow release into the water had toxic effects on a wide range of other marine species, particularly mollusks such as whelks and oysters. Environmental concerns grew as poisoning of marine organisms including fish had risen to alarming levels. These concerns prompted world-wide regulations restricting the use of TBT coatings, first for pleasure boats, then for commercial shipping. Since 2008, TBT coatings have been banned by IMO for all ships.

3. THE WRITING ON THE WALL FOR COPPER-BASED COATINGS

The short-term solution for the shipping industry was copper-based antifouling paint. As TBT was 10 – 20 times more effective (toxic) than copper compounds, copper-based paints require much higher leaching rates than TBT paints. Therefore, usually more paint is required, and even then the paints are not 100% effective. Various herbicides and fungicides are added to address plant fouling that is not affected by copper-compounds. These additional toxicants are somewhat misleadingly dubbed “boosters” in marketing jargon.

While being more expensive and less effective than TBT paints, copper-based coatings were rapidly embraced by the industry after the TBT ban. An estimated 90% of the world fleet used these in 2010. However, there is reason for concern:

- Some organisms have developed a copper resistance. These “gladiator” species cause increasing concern, particularly with respect to the spreading of invasive species.
- Marine biologists publish concerns about the long-term effect of copper-based coatings. Already some states (Washington and California in the USA, the Netherlands, Sweden and Denmark for the Baltic Sea) have banned copper-based coatings for recreational craft. The ban on TBT started the same way.
- The “precautionary approach” is a legal sword of Damocles in this respect. In layman terms, the precautionary approach puts the burden of proof on the industry (suppliers, but possibly also ship owners and operators) that a substance or procedure does not damage the environment. The EU has already made the precautionary approach a statutory requirement. It is expected that the precautionary approach will also guide future IMO antifouling legislation.
- Many ports do not permit hull cleaning, partly to reduce problems with invasive species, partly because the additional leaching of toxicants contaminates the port

waterbeds. Disposal of the contaminated soil after dredging will become increasingly costly.

One can only speculate about a global ban on the currently so popular copper-based antifouling paints. A US wide ban of these paints is expected to swing IMO opinion. But convincing alternatives must be in place before such a ban could enter into force.

4. ALTERNATIVES – MANY IDEAS, NO DOMINANT CHALLENGER

Many alternatives to antifouling paints have been proposed and patented in the course of time. Ideas which were at the time of invention unpractical are now being reviewed in the light of new technologies, for example:

- Low-surface energy (LSE) paints
  Fouling may be prevented basically by making adhesion of slime mechanically difficult, Fig.3. All marine fouling organisms use adhesive secretions for attachment. The lower the surface energy of the hull, the weaker the adhesion. Hull coatings with sufficiently low surface energy should prevent fouling because organisms would not be able to adhere to it. The principle is similar to that of a Teflon surface. Even if fouling is not completely prevented, such "non-stick" coatings make the surfaces easier to clean, e.g. by wiping or low-pressure rinsing. On fast moving boats, they can be self-cleaning, but on slower ships cleaning is necessary, especially in niches with low water speed (such as bow thruster tunnels and sea chests). The LSE coatings developed so far are mostly based on fluorinated silicone elastomeric, chemical cousins to Teflon. LSE coatings contain no biocides and remain active as long as the coating remains undamaged. However, like Teflon, these coatings are mechanically sensitive and fouling starts rapidly after the coating has been scratched. Consequently, performance of the LSE coatings degrades over time significantly, Fig.4.

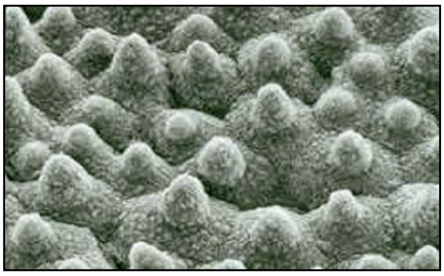

Fig.3. LSE surface under the microscope

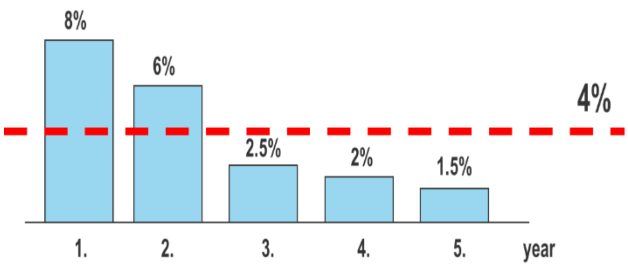

Fig.4. LSE performance for large tanker

- Mechanical cleaning / grooming
  In 1862 mechanical patents proposed scrubbing of the hull by rotating knives. This proposal can be seen as a forefather to present ideas using robot technology for mechanical cleaning of hulls. Cleaning strategies should depend on coating used. Copper-based antifouling paints release toxicants under shear forces. Thus any brushing or wiping will release more toxicants and each cleaning will deplete more toxicants leading to premature degradation of the coating. LSE coatings are damaged by hard cleaning, and require more frequent soft grooming. Hard coatings are suited for frequent cleaning. Surface Treated Composite (STC) coatings embed tiny glass or platelets to achieve a ceramic-like hard surface, Fig.5. In itself, this surface offers no fouling protection, but allows frequent cleaning. "Frequent" may mean every two weeks, to give an idea. While the coating technology is in place, more work is needed to develop cheap, fast and widely available cleaning. Recent developments on robotic cleaning are very interesting in this respect, Fig.6, *Darling (2014)*.

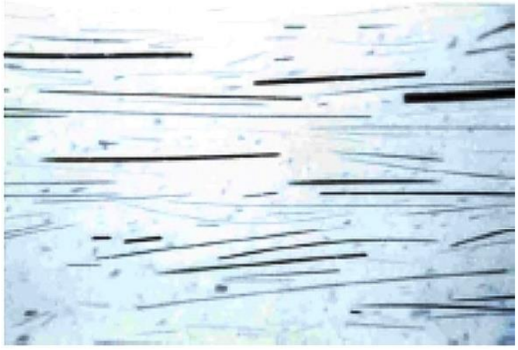

Fig.5. STC coating with embedded glass plates

Fig.6. HullBug cleaning robot, *Darling (2014)*

- Biologically inspired surfaces
  Surface structure of e.g. shark skin or lotus leaves makes adhesion difficult for organisms. There are assorted efforts to recreate these effects industrially for ship coatings. "Nanocoatings" are water-repellent, dirt-repellent paints known as "anti-graffiti" coatings for houses. Nano-coatings are increasingly popular also for ships. A major marine coating supplier gave the performance as not yet superior to LSE coatings in personal communication. The German Fraunhofer institute developed a riblet varnish that mimics shark skin, Fig.7. Open problems with this approach include long-term deterioration, re-application of coating and application is high-curvature areas.

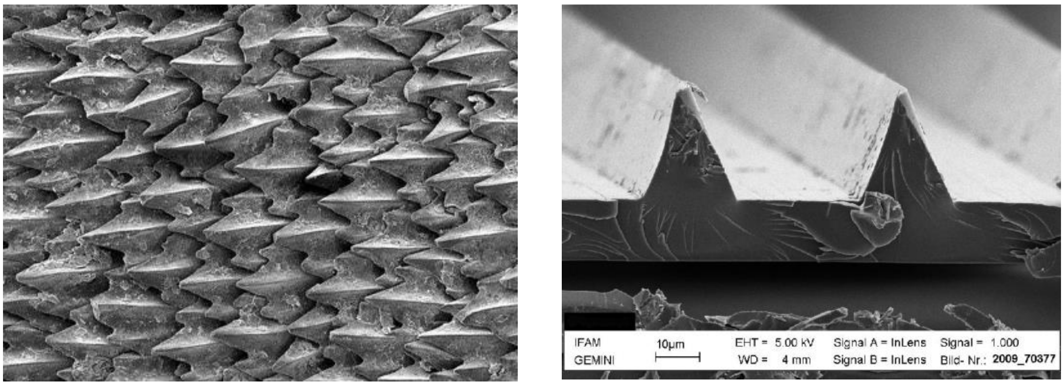

Fig.7. Microscopic view of shark skin (left) and riblets (right)

Fig.8. Historic **c**opper sheeting on 'Cutty Sark'

Fig.9. Modern copper-beryllium sheeting

- Metal sheeting
  The history of metallic sheeting for fouling protections dates back to ancient times. Copper sheeting was used by navies and expensive ships such as tea clippers in the 19th century, Fig.8. However, copper and iron in contact lead to galvanic corrosion. The rapidly increasing demand for steel ships in the second half of the 19th century ended

the era of metallic sheeting and the era of antifouling paints started. The 1980s saw a renaissance of research for the sheeting approach. Researchers in Japan and the USA found copper alloys that gave at least satisfactory antifouling performance. For most sheeting systems, the complete hull must be immersed in a bed of the sheeting alloy, Fig.9. Installation costs, both for material and application process, make sheeting unattractive.

- Air or gas carpets
In the 20th century, some patents proposed (chlorous or other) gas insertion at the keel. Also the use of steam from steam engines was proposed as antifouling measure. More recently, air lubrication has been proposed to reduce ship resistance. It is yet unclear how air lubrication may affect fouling of the ship bottom, but in any case it is unpractical for the vertical walls where the buoyancy of the bubbles prevents stable coverage.

- Electric protection
In 1891 Edison patented his ideas for an electric antifouling system. In 1907 a US patent was granted for electric protection of the ship hull by forming a boundary layer of antifoulant gases through electrolysis. In the 1960s, these ideas were revived in Japan. Since the early 1990s, Mitsubishi Heavy Industries commercialized an electrical antifouling system named MAGPET. Using electric hydrolysis, sea water is decomposed forming hypochlorite ions (ClO^-), a well-known antifouling agent. The water contact surface of the hull shell plating is coated with an electro-conductive paint film. A small current is passed through the paint film attracting the hypochlorite ions. This prevents adhesion of marine growth such as micro-organisms, algae, and seashells. The ions react again to sea water when detached from the hull avoiding long-term contamination. As a limitation, the system requires sea water and does not work in fresh water. Possibly due to high installation costs, it was not accepted by the market.

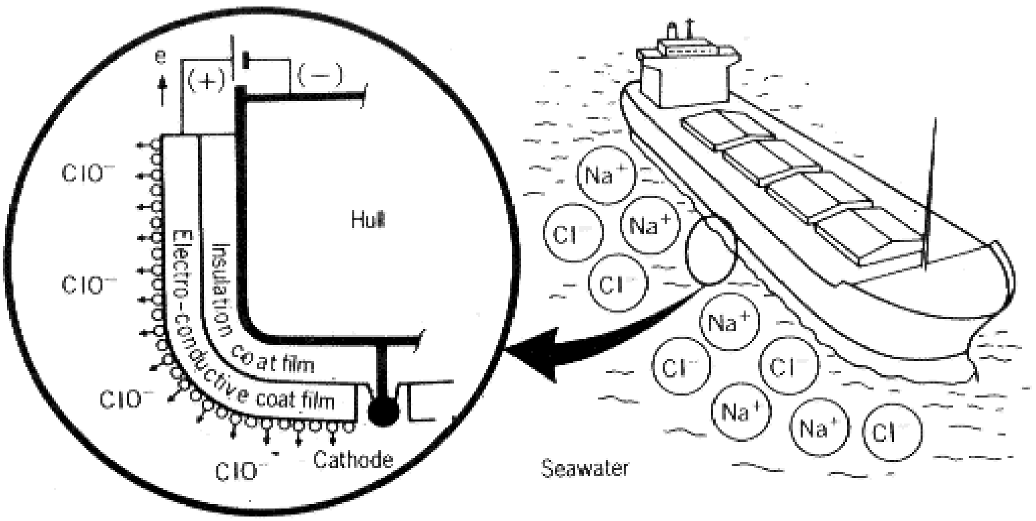

Fig.10. MAGPET principle for electric protection of hull against fouling

- Ultrasonic solution
In the 1960s, ultrasonic antifouling methods were investigated in Norway, England, and Japan. Ultrasonic vibrations cause very high accelerations which destroy cell structures of algae and weed. However, ultrasonic antifouling requires many oscillators over the hull and constant energy supply. Ultrasonic antifouling systems have been successfully applied to yachts, where oscillators are spaced typically at intervals of 6 m. For large

cargo vessels, this would lead to many oscillators which will require a network of electrical supply and will be difficult to maintain or replace in case of failures.

- Bio-Paints
  Many sea creatures repel marine organisms without causing widespread harm. Research on the actual mechanisms of repulsion and chemical agents used by repelling plants and animals is active, but at an early stage. Bio-paints are still a long way away from being a practical alternative. World-wide, over 400 marine organisms are important in causing fouling problems. The biological compounds found so far deter only a fraction of these. And a natural poison is still a poison. Natural compounds must be mass produced, either by chemical engineering or farming. And compounds must stay active for several years for application in shipping. This makes biological paints at present rather impractical as an alternative.

4. CONCLUSION

Antifouling methods for ships date back to ancient times, but still we are striving for a solution that satisfies all aspects of easy application, durability, effectiveness, and minimum ecological impact. Creativity, interdisciplinary co-operation, and a lot more research will be required before we might be able to find this 'final answer' to the ship fouling dilemma. It is encouraging to see both a growing awareness of the problem and first steps which could lead eventually towards the desired goal.

ACKNOWLEDGEMENTS

I gratefully acknowledge the support of Hydrex, Jotun and International Paint in supplying material and in patiently answering my many questions. The statement in this paper neither represent their opinion nor that of DNV GL as a company, but are my personal view of the fascinating world of antifouling.

References

BERTRAM, V. (2000), *Past, present and prospects of antifouling*, 32nd WEGEMT School on Marine Coatings, Plymouth, pp.87-97

DARLING, D. (2014), *HullBUG – Hull grooming crawler robot with fluorometric fouling recognition*, 13th Conf. Computer and IT Applications in the Maritime Industries, Redworth (late paper, not in proceedings)

NN (2006), *Waterborne underwater hull cleaning of navy ships*, Naval Ships Technical Manual 081, US Navy, http://www.hnsa.org/doc/nstm/ch081.pdf

NN (2014), *Detecting the sound of a CleanShip*, The Naval Architect, February, pp.22-25

AN UPDATE ON THE DEVELOPMENT OF THE HULL VANE®

K. Uithof[1], P. van Oossanen[1,2], N. Moerke[1,2], P.G. van Oossanen[1,2], and K.S. Zaaijer[2]

[1] Hull Vane B.V., Costerweg 1b, 6702 AA, Wageningen, Netherlands
[2] Van Oossanen Naval Architects B.V., Costerweg 1b, 6702 AA, Wageningen, Netherlands

ABSTRACT

Although the early beginnings of the Hull Vane® can be traced back to its application on a catamaran in 1992, the research has gathered pace since the first patent was applied for in 2002. The Hull Vane® is a fixed foil located below the waterline, near the stern of the vessel. The lift it creates can be decomposed into a force in x-direction, reducing the total resistance of the vessel, and in z-direction, influencing the trim and thus the total resistance. Additionally, the Hull Vane® reduces the generation of waves and the vessel's motions in waves. Resistance reductions of up to 26.5% have been found with the use of CFD computations, model tests and sea trials. For commercial applications, resistance reductions between 5 and 10% are common. The Hull Vane® is especially applicable on ships sailing at moderate to high non-planing speeds, with Froude numbers between 0.2 and 0.7. In this paper, the development process, the working principles, and the achieved results up to now are discussed.

NOMENCLATURE

A	Planform area	[m²]
α	Hull Vane® inflow angle	[rad]
β	Hull Vane® angle	[rad]
C_D	Drag coefficient	[-]
C_L	Lift coefficient	[-]
D	Drag force	[N]
Δ	Displacement	[m³]
ΔR_T	Change in total resistance	[%]
F	Force	[N]
Fn	Froude number	[-]
g	gravitational constant	[kg*m/s²]
GM_L	Longitudinal metacentric high	[m]
H_W	Wave height	[m]
L	Lift force	[N]
R_T	Total resistance	[N]
ρ	Density	[kg/m³]
T_W	Wave period	[s]
θ	Trim angle	[rad]
V	Hull Vane® inflow velocity	[m/s]
x, z	Inertial coordinate system	
x', z'	body-fixed coordinate system	

Subscripts

HV	Hull Vane®
x	x-direction (forward)
z	z-direction (up)

1. INTRODUCTION

The ongoing quest for fuel efficiency of ships is divided into four areas of research: engine efficiency, propulsion efficiency, alternative sustainable sources of power, and the lowering of the resistance of the hull.

As naval architects, Van Oossanen Naval Architects mainly focuses on the latter. Within this category they have developed the patented Fast Displacement Hull Form, and the Hull Vane®: a fixed, resistance-reducing foil situated below the waterline near the stern of the ship. Since Peter van Oossanen's invention of the Hull Vane® in 1992, and the first patent application in 2002, a significant amount of research has been performed aimed at the optimization of the concept. Throughout the following years various applications of the Hull Vane® have been analysed by means of model tests, Computational Fluid Dynamics (CFD), and full-scale trials. These include sailing yachts, motor yachts, various merchant ships, naval vessels, cruise ships, and more. Fuel reductions in excess of 20% were found for displacement motor yachts, while for other types of ships reductions of 5 to 10% were found to be common. Various examples are given in this paper.

Now that the first two vessels fitted with a Hull Vane®, a 42 m motor yacht and a 55 m supply vessel, have been launched it is appropriate to review the results that have been obtained. This paper provides an update on past, current and future developments in this respect.

2. THE DEVELOPMENT PROCESS

The early beginnings of the Hull Vane® can be traced back to 1992. The first full-scale application of the Hull Vane® was on a catamaran vessel not reaching its required speed due to excessive trim and wave generation. Placing a foil in the steepest part of the interacting wave system aft of the midship of the catamaran proved to reduce the bow-up trim and the resistance significantly. This result led to an increased interest in the device and the associated hydrodynamics, and more research would follow.

The next application of the Hull Vane® was on *Le Defi Areva*, the French challenger for the 2003 America's Cup (figure 1). During model tests a resistance reduction of 5% was found at model scale for a full-scale speed of 10 knots. Unfortunately, the application of the Hull Vane® during the races was disallowed by the America's Cup regulations as an appendage that would give an unfair advantage.

Fig. 1. The second application of the Hull Vane®, on the 2003 IACC yacht *Le Defi Areva*.

After these first applications, focus has been on further research of the working principles of the Hull Vane®. Numerous applications have been tested, mainly with the use of CFD computations. The models that have been tested range from sailing yachts and motor yachts to more commercial applications, such as supply vessels, containerships, cruise ships and Ro-Ro vessels. The found influence of from the Hull Vane® on the total resistance have varied between a resistance decrease of -26.5% and a resistance increase of +9.5%, showing that the fuel saving device is not suitable to all cases. A number of these results will be further discussed in section 4.

In 2014, two Hull Vane®-equipped ships were launched. Shipyard De Hoop in the Netherlands built the 55 metre supply vessel *Karina*, which saw its required engine power during sea trials reduced by 15% after a Hull Vane® was retrofitted to the transom. More on these sea trials can be found in section 4.

The second vessel that was launched with a Hull Vane® this year is a 42 metre displacement yacht, built by the Dutch yacht builder Heesen Yachts. For this vessel, the Hull Vane® was incorporated during the design phase, which allowed for resistance reductions of up to 23%.

3. WORKING PRINCIPLES

This section will elaborate on the working principles of the Hull Vane®. Four interrelated effects of the Hull Vane® can be found: a thrust force, a trim correction, the reduction of waves, and the reduction of motions in waves. These effects will be discussed below. After this, the influence of the location of the Hull Vane® and the influence of ship speed and hull shape are discussed. A discussion of the effectiveness of the Hull Vane® will conclude this section.

3.1 Thrust force

The first effect of the Hull Vane® is based on basic foil theory. In figure 2, a schematic overview of the forces on the Hull Vane® is given. In this figure, α is defined as the Hull Vane® inflow angle (the angle between the inflow and the chord line), β is defined as the Hull Vane® angle (the angle between the chord line and the body-fixed x'-axis). The vessel in the figure is displayed at zero trim.

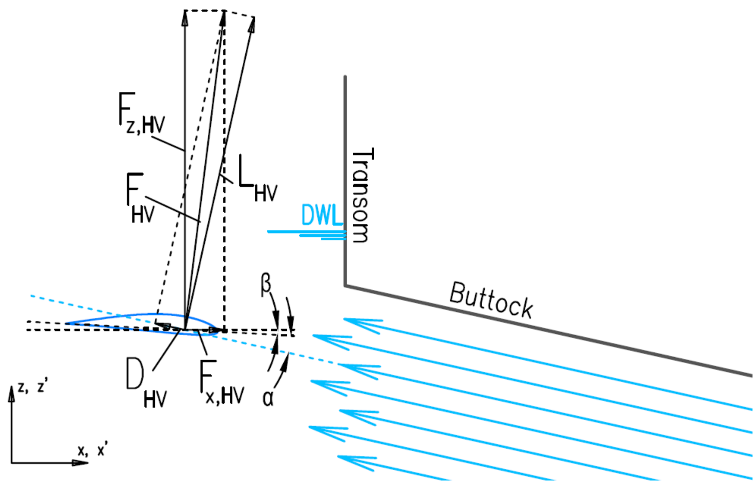

Fig. 2. Schematic overview of the forces on the Hull Vane® in a section view of the aft ship.

The foil creates a lift force vector $\vec{L}_{HV}$ which is by definition perpendicular to the direction of the flow of water, and a drag force vector $\vec{D}_{HV}$ in the direction of the flow. The sum of these vectors $\vec{F}_{HV}$ can be decomposed into an x-component and a z-component:

$$\vec{L}_{HV} + \vec{D}_{HV} = \vec{F}_{HV} = \vec{F}_{x,HV} + \vec{F}_{z,HV} \tag{1}$$

If the x-component of the lift vector is larger than the x-component of the drag vector, the resulting force in x-direction provides a thrust force. The lift and drag forces can be estimated by equation 2 and 3. In these formulae, C_L and C_D are not only dependent on the shape of the Hull Vane®, but also on other factors, such as the vicinity of the free surface.

$$L_{HV} = C_L * \frac{1}{2}\rho V^2 A \tag{2}$$

$$D_{HV} = C_D * \frac{1}{2}\rho V^2 A \tag{3}$$

If θ is defined as the trim angle (the angle between the body-fixed x'-axis and the inertial x-axis), the thrust force that is generated by the Hull Vane® can be derived by equation 4.

$$F_{x,HV} = \sin(\alpha + \beta + \theta) * L_{HV} - \cos(\alpha + \beta + \theta) * D_{HV} \tag{4}$$

3.2 Trim correction

It must be noted that not only the resulting force in x-direction has an influence on the performance of the vessel. The force in z-direction affects the trim, and especially at higher speeds, this trim reduction proves to have a large influence on the total resistance of the vessel. This effect can also be achieved with interceptors, trim tabs, trim wedges or ballasting. Similarly to the force in x-direction, the force in z-direction can be estimated by equation 5:

$$F_{z,HV} = \cos(\alpha + \beta + \theta) * L_{HV} + \sin(\alpha + \beta + \theta) * D_{HV} \tag{5}$$

With this, the influence of the Hull Vane® on the running trim can be derived with equation 6:

$$\delta\theta = \frac{trimming\ moment}{righting\ moment\ per\ degree\ of\ trim} \approx \frac{\mathrm{F_z}*arm}{GM_L*\Delta*g*\sin(1°)} \tag{6}$$

Not only the trim reduction itself has a positive influence on the hull's performance, but the trim also affects the angle of attack of the water flow on the Hull Vane®. In equation 4 it can be seen that this has an important influence on the thrust force generated by the Hull Vane®.

3.3 Reduction of waves

The third effect of the Hull Vane® is related to the reduction of the wave system of the ship. The flow along the Hull Vane® creates a low pressure region on the top surface of the Hull Vane®. This low pressure region interferes favourably with the transom wave, resulting in a significantly lower wave profile. This result can be seen in figure 3, in which the wave pattern of the 55 metre supply vessel with Hull Vane® (bottom figure) is compared to the same vessel without Hull Vane® (top figure), at 20 knots.

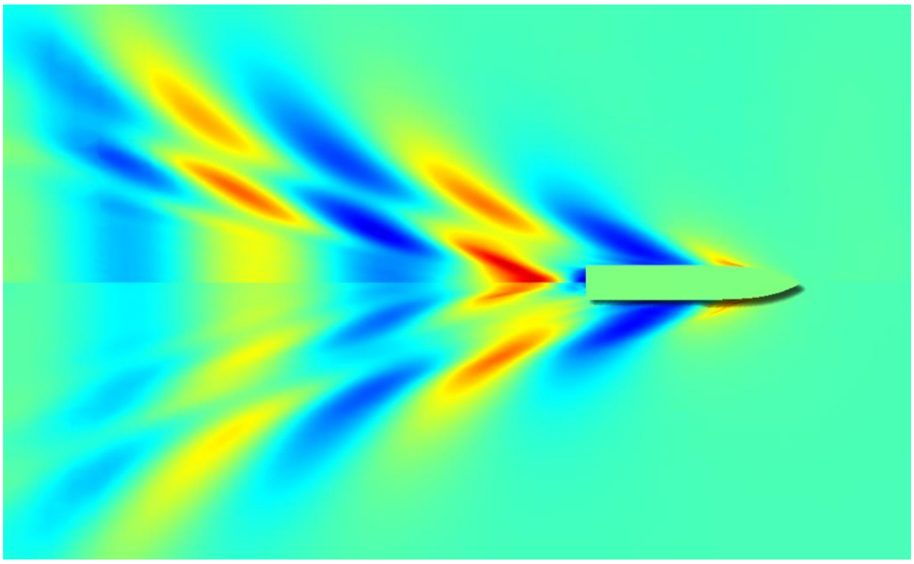

Fig. 3. Wave pattern on the 55 metre supply vessel without Hull Vane® (top) and with Hull Vane® (bottom) at 20 knots, as seen from above, from CFD computations (blue portrays a wave trough and red a wave crest).

The wave reduction is so significant, that it can be observed by eye. In figure 4, photographs of the wave pattern of the same supply vessel during sea trials are shown. Both photographs were taken at a ship speed of 13 knots. The wake is clearly reduced with the attachment of the Hull Vane®, pictured on the right.

Fig. 4. Comparison of the wave profile of the 55 metre supply vessel without Hull Vane® (left) and with Hull Vane® (right) at 13 knots, as seen from the aft deck during sea trials.

The reduction of waves not only leads to a more beneficial resistance, it also leads to less noise on the aft deck, and to a lower wake. The first is mainly beneficial for yachts, the latter is important for inland shipping, where wake restrictions limit ship speeds in ports or other enclosed areas.

3.4 Reduction of motions in waves

The final effect the Hull Vane® produces is that it dampens the heave and pitch motions of the vessel. When the vessel is pitching bow-down the stern of the vessel is lifted and the vertical lift on the Hull Vane® is reduced by the reduced angle of attack of the flow. This counteracts the pitching motion. Similarly, during the part of the pitching motion in which the stern is depressed into the water, the vertical lift on the Hull Vane® is increased. This again counteracts the pitching motions. Similar reasoning exists for the heave motions.

The reduction of the motions reduces the added resistance due to waves, which makes the Hull Vane® even more effective in waves then it is in calm water. For instance, on the 169 metre container ship *Rijnborg*, model tests showed that the required propulsion power at 21 knots can be reduced by 10.2% in calm water and by 11.2% in waves.

The second benefit of the reduced motions is that it increases comfort, safety and the range of operability. For the 55 metre supply vessel, a CFD analysis showed that the root mean square of the vertical motions on the foredeck was reduced by approximately 10%, while that at the aft deck was reduced by approximately 20% in typical wave conditions ($H_W = 1.0$ m, $T_W = 5.7$ s).

3.5 Influence of Hull Vane® location

During the last years, much of the research has been focused on the optimal position of the Hull Vane® relative to the ship's hull. One of the main considerations was found by Moerke. His CFD analysis showed that if the Hull Vane® is fitted too close to the hull, it might be positioned in the boundary layer reducing the lift it creates. Additionally, the low pressure region on the upper side of the Hull Vane® is reflected on to the hull, creating an additional pressure resistance on the hull. Because of this 'pressure reflection', the resistance of the combination hull and Hull Vane® is increased when the Hull Vane® is situated fully below the hull. Moerke investigated various modifications with the aim to reduce the pressure reflection, but was unable to fully solve this problem with the Hull Vane® underneath the hull. Only by placing the Hull Vane® behind the transom of the vessel can the pressure reflection problem be solved, with a slight reduction in Hull Vane® thrust as a consequence.

The second consideration in the positioning of the Hull Vane® is the angle of the water flow near the stern of the vessel. When not changing the orientation of the Hull Vane® itself, the largest angle of attack can be achieved by placing the Hull Vane® in the steepest part of the transom wave. Unfortunately, especially at higher speeds, this location is too far aft of the hull which creates difficulties for the attachment of the Hull Vane® to the hull. An additional complication is that this optimal location is very dependent on wave length, and thus on ship speed. In vertical direction, a higher angle of attack can be achieved by placing the Hull Vane® closer to the hull. This is however limited by the free surface effect on Hull Vane® lift, and possibly by slamming in waves and the pitching motions if the Hull Vane® is placed too close to the water surface.

3.6 Influence of ship speed and hull shape

In his research, Moerke also noted that the results of the Hull Vane® improve with increasing speed. This was confirmed a few years later during model tests carried out at MARIN. A 169m container vessel was equipped with a Hull Vane®, and power reductions of 3.3% at 17 knots (Fn 0.21) up to 10.2% at 21 knots (Fn 0.27) were achieved on model scale.

Higher savings can be achieved at higher Froude numbers. During tank tests for a 42 metre motor yacht, maximum resistance reductions of 23% were found at Fn 0.44. The dependency of the resistance reduction on Froude number for this particular yacht is shown in figure 5, alongside the results of a 55 metre yacht from tank tests, the results of a 47 metre motor yacht from CFD computations, and the results for a 300 metre container vessel from CFD computations. The Hull Vane® seems to be most favourable at moderate to high Froude numbers in the non-planing region, approximately between 0.2 and 0.7.

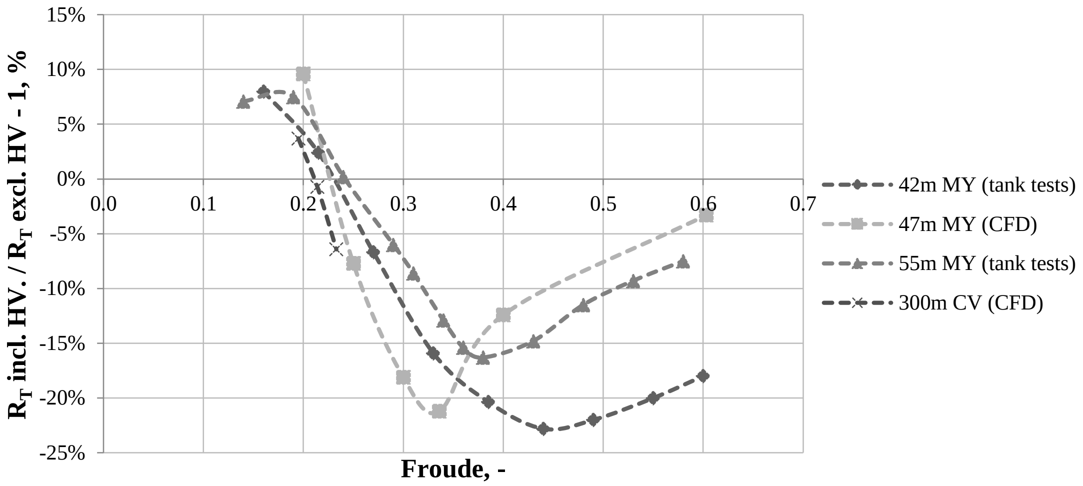

Fig. 5. Measured resistance reduction for a 42m, a 47m and a 55m motor yacht and a 300m container vessel, fitted with a Hull Vane® compared to the same vessels without a Hull Vane®, as functions of Froude number.

These results can be explained by the dominance of frictional resistance below Froude numbers of 0.2. The addition of a Hull Vane® to a vessel adds to the wetted surface area. Therefore, the frictional resistance is increased compared to the vessel without Hull Vane®. Above Froude numbers of 0.2, the pressure resistance becomes a more dominant resistance component. As the Hull Vane® decreases pressure resistance, most gains are found in the region of Froude numbers between 0.2 and 0.7. At higher Froude numbers, the force generated by the Hull Vane® creates an unbeneficial bow-down trim.

The Hull Vane® can be specifically designed for the cruising speed or maximum speed of a vessel, or for its operating profile. In most cases the operating profile is such that a loss in the low Froude number region is acceptable since these speeds are only sailed while manoeuvring. In absolute terms, a resistance increase at the low Froude numbers is negligible compared to the potential fuel savings at higher speeds.

In 2009, Zaaijer and Moerke performed a systematic study into the performance of the Hull Vane®. They found that buttock angle and transom submergence are key factors. The influence of the buttock angle is clear when looking at figure 2: If the buttock angle is increased, the angle of attack of the flow to the Hull Vane® is increased, and the lift vector is directed more forward, increasing the resulting decomposed force in x-direction. If the water column near the transom is maintained as much as possible, and the effect of pressure reflection on the hull is minimized, the overall resistance is reduced most. The horizontal buoyancy force on the Hull Vane® contributes to the overall performance as well: the leading edge region of the Hull Vane® experiences a lower hydrostatic pressure than the trailing edge region when the Hull Vane® is positioned below the front of the transom wave.

Additionally, the shape of the stern of the ship is important. Flat buttocks, ensuring a uniform flow to the Hull Vane® are ideal. Trawler-type fishing vessels are suboptimal for this reason, and significant gains from Hull Vane® application are more difficult to obtain for this kind of ship types.

3.7 Effectiveness

The fact that the results are dependent on ship speed and hull shape makes it clear that not every ship type is suitable for fitting a Hull Vane®. For bulk carriers and crude oil carriers the Hull Vane® will not bring much gain. Not only is their speed too low, but the difference in draft between loaded and ballast condition makes it nearly impossible to achieve gains in both conditions. For small vessels (below 30 metre) the investment costs are often too high relatively to the fuel savings to recoup these costs.

The ideal candidates for Hull Vane® application are medium and large-sized vessels operating at moderate or high non-planing speeds. Examples are ferries, supply vessels, cruise ships, patrol and naval vessels, motor yachts, reefer ships, Ro-Ro vessels, car carriers, and container vessels.

4. RESULTS AND DISCUSSION

As can be expected, 12 years of research and development into the performance of the Hull Vane® has generated a vast amount of data. Some interesting results will be presented below. This section is divided into three parts. In the first part, results from CFD computations will be discussed. Some of the model tests will be discussed in 4.2. The last part of this section is devoted to the results of the first systematically performed sea trials on a Hull Vane® equipped vessel: a 55 metre supply vessel.

4.1 CFD computations

Van Oossanen Naval Architects has built up a vast experience in hydrodynamic consultancy in CFD. It is therefore no surprise that a majority of the research into Hull Vane® performance has been carried out with the use of CFD. For this, the FINE/Marine CFD package is used, developed by École Centrale de Nantes and NUMECA International, specifically for hydrodynamic application in ship design. Throughout the years this research has produced detailed insight in how the Hull Vane® works, and how it can be optimized for various applications.

The first systematic series of CFD computations were performed by Moerke. He tested the Hull Vane® in several positions under the stern of a full-block dredger, in 2D. He found that in the configuration as pictured in figure 6, the Hull Vane® caused an increase of pressure resistance on the hull. The increase in pressure resistance on the hull was a slightly larger component than the thrust force generated by the Hull Vane®, and therefore an increase of the total resistance was found. In figure 6, the dynamic pressure on the stern is shown. It can be observed that the low-pressure region above the Hull Vane® is indeed reflected on to the hull. The benefit from the lift force created by the Hull Vane® is thus undone by the increased resistance of the hull.

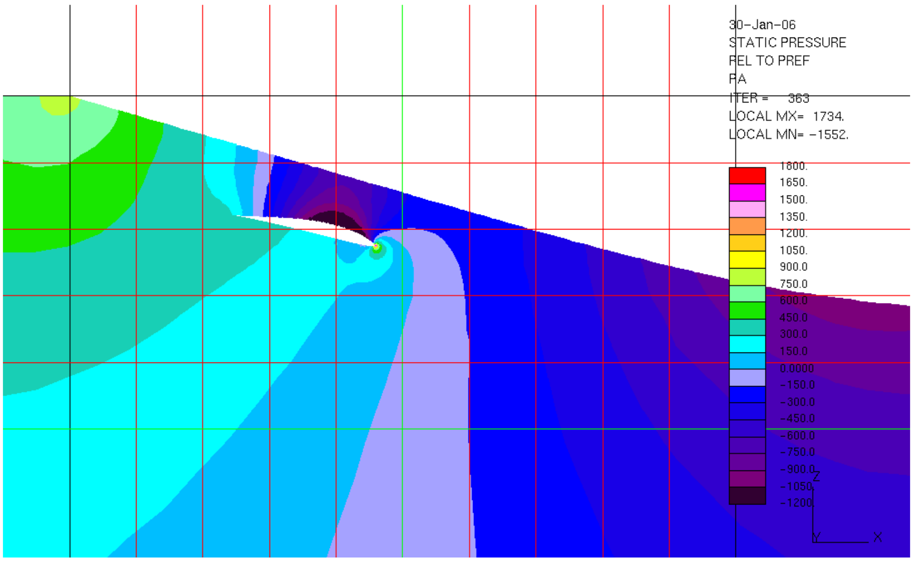

Fig. 6. Dynamic pressure around the stern of a full-block dredger equipped with a Hull Vane®.

Many variations of hull shape, Hull Vane® profile and Hull Vane® location were tested, but the increase in pressure resistance associated with the reflection of the low-pressure region on the hull always remained. Only by positioning the Hull Vane® aft of the transom can this phenomenon be sufficiently reduced. This was confirmed in the 2009 systematic 2D study by Zaaijer and Moerke, who found that the total resistance is reduced when the Hull Vane® is placed aft of the transom and not too close to the free surface.

After these 2D studies, a range of different ship types have been analysed. Most of these have been tested at different speeds, with different positions, and different shapes for the Hull Vane®. An (incomplete) overview of ship types, lengths, tested speeds and achieved resistance reductions is displayed in table 1. It can be seen that the Hull Vane® offers resistance reductions on a wide range of vessels, but is unfortunately unable to offer this for all ships. Additionally it shows that the gains are dependent on ship speed. Those ships in table 1 for which no resistance reduction was achieved, had either a speed near or below the critical level (Fn 0.2), or a complex (e.g. trawler) hull shape, involving reverse flow around the aft-end of the vessel.

Table 1. Resistance reductions achieved, from CFD computations.

Ship type	Tested speeds	ΔR_T
47m motor yacht	7.7 kn / Fn 0.20	+9.6%
	13 kn / Fn 0.34	-21.2%
	23.3kn / Fn 0.60	-3.3%
169m container vessel	17 kn / Fn 0.21	-4.1%
	21 kn / Fn 0.27	-15.5%
152m container vessel	15.5 kn / Fn 0.21	+1.2%
179m ro-ro vessel	18 kn / Fn 0.22	-2.7%
176m paper carrier	17 kn / Fn 0.21	+6.6%
285m container vessel	20 kn / Fn 0.19	+3.7%
	22 kn / Fn 0.21	-0.7%
	24 kn / Fn 0.23	-6.4%
64m motor yacht	15.9 kn / Fn 0.33	-26.5%
350m container vessel	24 kn / Fn 0.21	-7.2%
55m supply vessel	20 kn / Fn 0.46	-6.5%
142m navy vessel	18 kn / Fn 0.25	-6.7%
	24 kn / Fn 0.33	-7.5%
	30 kn / Fn 0.41	-6.2%
126m cruise liner	15 kn / Fn 0.22	-9.6%
33m fishing trawler	11 kn / Fn 0.31	+1.3%

4.2 Model tests

The first two sets of model tests have been performed on an America's Cup sailing yacht and a dredger. The sailing yacht was tested over a range of speeds in excess of 6 knots, for Froude number values higher than 0.22. For the dredger the longitudinal position of the Hull Vane® was varied. These tests revealed that the optimal longitudinal position of the Hull Vane® is one where a positive interaction between the hull's wave system and that of the Hull Vane® can be realized.

This first research also looked into the vertical positioning of the Hull Vane®, and it was found that the Hull Vane® should not be placed too close to the hull. On the other hand, it should not be placed too far below the hull, as the angle of attack from the water flow is then decreased. Additionally, this research showed that the hull shape of the tested vessel has a major impact on the performance of the Hull Vane®: The vicinity of the Hull Vane® below the steep buttocks of the dredger creates a pressure reflection cancelling the benefits of the Hull Vane® itself. The Hull Vane® only had a beneficial contribution to the system when placed behind the transom.

After the model tests for the sailing yacht and the dredger, two container vessels (137 and 169 metre) from Wagenborg were tested in the towing tank for Hull Vane® suitability (figure 7). These tests have provided further insight into the performance of the Hull Vane®, as these tests included dynamometers fitted to the Hull Vane®. With these dynamometers, it became possible to measure the F_x and F_z forces that are generated by the Hull Vane®. Again, the Hull Vane® was tested for different positions relative to the hull, for different angles, and different ship speeds. This again confirmed the working principles of the Hull Vane®, and showed that the Hull Vane® is able to provide resistance reduction if positioned and designed well. Additionally, the performance in waves was determined, and this showed that the Hull Vane® provides heave and pitch motion damping, leading to a lower added resistance in waves.

Fig 7. One of three Hull Vanes® as tested on a model of a 169 metre container vessel.

The reduced motions in waves and the subsequent reduction of the added wave resistance was later confirmed in tests on a 42 metre motor yacht which was tested at different speeds in different wave conditions. The effects on model scale in this case were relatively small however, and full-scale simulations in CFD have provided a clearer difference.

4.3 Full-scale sea trials

At this time, four full-scale applications of the Hull Vane® have been tested. The first two applications were described in section 2; the third one will be discussed below. The fourth full-scale application of the Hull Vane®, on a 42 metre motor yacht, was tested in October 2014, and the results were not available at the time of writing this paper.

The *Karina* was launched during the summer of 2014. She is a 55 metre Fast Supply Intervention Vessel (FSIV) built by Shipyard De Hoop in the Netherlands. During sea trials, she was retrofitted with the Hull Vane®, so that it was possible to compare the performance with and without Hull Vane®. As she left port, the lower stern wave system was readily visible (figure 4). Measurements were taken by a third party of shaft power, speed and manoeuvrability. The results are corrected for water depth and are displayed in figure 8.

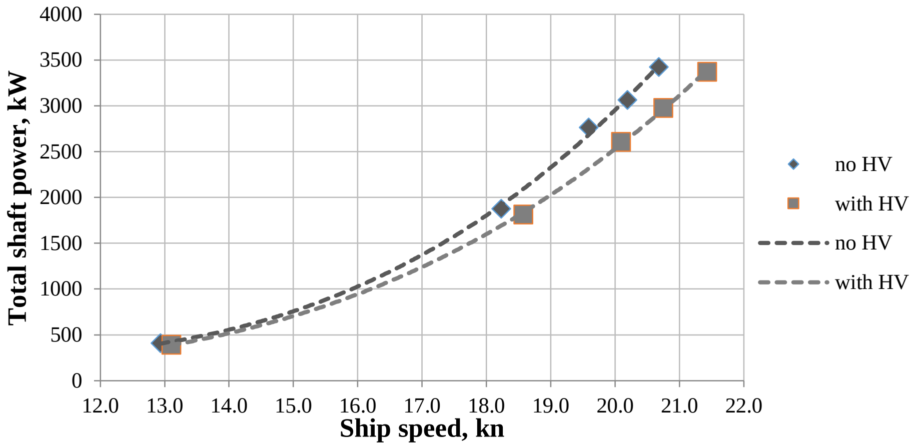

Fig. 8. The results from sea trials of a 55m FSIV, equipped without and with a Hull Vane®.

The manoeuvrability tests show that the turning circle was slightly increased due to the increased directional stability created by the struts that connect the Hull Vane® to the hull. This gain in directional stability reduces the chance of broaching in stern-quartering waves.

The newest application of the Hull Vane®, on a 42 metre motor yacht, is pictured in figure 9. Unfortunately the results of the sea trials of this vessel were not available at the time of preparing this paper.

Fig. 11. The latest application of the Hull Vane®: a 42 metre motor yacht.

5. CONCLUSION AND FUTURE RESEARCH

While most fuel saving devices focus on a reduction of the frictional resistance (e.g. air lubrication) or propulsive efficiency (e.g. Mevis ducts, propeller boss cap fins), the Hull Vane® is one of the few fuel saving devices (along with the bulbous bow) that aim to lower the pressure resistance, which is the dominant component of the resistance at higher speeds. Therefore the Hull Vane® proves to be one of the most promising fuel saving devices available today. CFD computations, model tests and sea trials have shown potential resistance reductions of more than 20% depending on ship speed and hull shape. On merchant ships, potential resistance reductions between 5% and 10% are common. The Hull Vane® is especially interesting for vessels that operate at a moderate to high non-planing speed (Froude numbers between 0.2 and 0.7), such as ferries, supply vessels, cruise ships, patrol- and naval vessels, motor yachts, reefer ships, Ro-Ro vessels, car carriers, and container vessels.

Now that the first commercial applications have been launched it is not the time to sit back and relax. To improve the concept and to further explore the possibilities of the Hull Vane®, more research is needed. Such research has commenced with the investigation of a 50 metre trimaran platform concept, in which the Hull Vane® is attached to the outriggers, which are positioned partly aft of the main hull. The first results have been promising, outperforming equivalent monohulls in resistance, comfort and deck space.

ACKNOWLEDGEMENTS

The authors would like to thank everyone that has been involved with the development of the Hull Vane® through the last 22 years.

Leading Energy Efficient Cargo Ship Solutions – Innovation in Practice

Konstantinos Fakiolas, Naval Architect & Marine Engineer, National Technical University of Athens, MSc, MBA, Deltamarin Ltd, Turku/Finland, konstantinos.fakiolas@deltamarin.com

ABSTRACT

This paper describes a holistic approach of energy and fuel efficiency optimization techniques applied in cargo vessels with low Froude numbers.
The improvement of energy efficiency is achieved by upgrading the hull hydrodynamic performance, the propeller efficiency and rudder design, through applying state-of-the-art CFD tools, while maintaining the vessel's operational efficiency, cargo capacity increase and enhanced manoeuvrability.
Two examples of B.Delta bulk carrier ships are presented and analysed, compared to conventional and modern designs, while results from Model tests and Sea trials are demonstrated, to show that the optimization approach is feasible and proven.

1. INTRODUCTION

Even before year 2008, IMO had started proposing and developing the Energy Efficiency Design Index, primarily applicable to new ships, as a tool for control of CO2 emissions from ships, and in an effort to improve energy efficiency via mandatory implementation during design and construction stage.

After the worldwide financial crisis that started in September 2008, the continuously high fuel costs, and the consequent huge impact in worldwide trade, it became necessary for new ships to be built under a design philosophy targeting to achieving reduced fuel consumptions, increased operational efficiency and conforming to the forthcoming air emission regulations.

Since the introduction and implementation of EEDI phasing out, which became applicable since 1st January 2013, under chapter 4 of MARPOL Annex VI, the design of cargo ships had to be optimized in ways such as to use energy efficient main engines, auxiliary machinery, energy saving technologies, so that CO2 emissions are reduced over a given transportation work.

Deltamarin has developed since 2006 an innovative, quantum leap ship design optimization technique for cargo vessels, starting with applications on bulk carriers, by delivering the first proven energy efficient designs, fully conforming with EEDI rules, while combining fuel efficiency with operational superiority over conventional methods.

2. THEORETICAL BACKGROUND

The scope of a modern cargo vessel design, with a view to complying with EEDI regulations, is to ensure higher cargo carrying capacity under the same main dimensions restrictions as occasionally dictated by ship trading routes and Ports, while having an as much as possible lower fuel consumption in the most frequent operational drafts (i.e. scantling, design or ballast draft), on a certain speed range.
Towards this effort, the main dimension ratios have been considerably changed, to satisfy above operational needs:

- The L/B ratio has decreased even below 5
- The B/T ratio has increased, to ensure shallow draft operation and multiple operational utilization of the ships, a fact which is by principle detrimental to total resistance and powering efficiency

- Length has to remain restricted due to shipbuilding costs, as well as harbour and route limitations
- The Cb has been increased (even close to 0.90 in some cases), which is also unfavourable for powering efficiency.
- A shift of LCB aftwards which enables a smoother forward shoulders and lower waterline entrance angle, thus decreased resistance, with typical figures today varying between -1,8%.... +1.0% of LCB, aft or fwd of Lpp/2. Design waterline angle can be reduced at same time with 1.5…..2.5 degrees.

Designwise, the energy and fuel efficiency optimization of a cargo vessel should be implemented through working on below aspects:

- Reducing total resistance of the hull, especially the added wave & form resistance.
- Improving propulsive efficiency
- Optimizing appendage resistance (i.e. rudders, etc)
- Introducing energy saving devices, when and where appropriate, to recover rotational and axial wake losses.
- Optimize main propulsion, through selecting new Main Engine and propulsion systems technologies (i.e. electronically controlled engines, properly tuned, etc)

In the below sub-sections, it will be demonstrated how these design tasks are contributing towards an improved energy efficiency of the ship, and how these elements were implemented successfully in the B.Delta energy efficient Bulk Carrier designs.

2.1 Hull total resistance

Through the use of extensive and advanced CFD analysis tools, the hydrodynamic properties of the cargo vessel's hull are re-defined, both in studying potential and viscous flow

The hull form, including the propeller/rudder arrangement has been designed with special regard for minimum resistance and maximum propulsion efficiency, good sea keeping and maneuverability, taking into account the special requirements for this type of vessel, such as space reservations for engine room layout and cargo holds, thus maintaining a high block coefficient, suitable for the service speeds, which are ranging from 13 – 15 kn.

The main effort, which defines the hull form, is done such as to ensure:

- Improved waterline entrance angles
- Reduced pressure gradients variations from bow to middle body
- Streamlined flow from bow to stern
- Uniform pressure field from aft shoulders to stern
- Smooth transition over bilge
- Reduced dynamic sinkage and trim

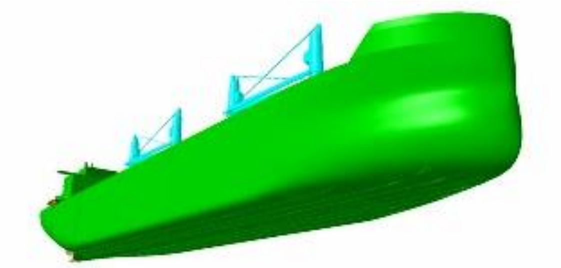

Image 1: B.Delta hull

During the potential flow CFD analysis[5], the goal is to determine the performance of the hull form at different draughts ensuring low bare hull resistance and high propulsion efficiency.
Special attention has been paid for the stem wave height, wave troughs around the fore and the aft shoulder, stern wave height (also behind the stern), water flow to the propeller and the pressure distribution in the bow and around the aft shoulder.
During the viscous flow CFD analysis[5], specific hull variants are selected, which seem optimal from the potential flow calculations, for estimating the real full scale performance of the hull form. The pressure distribution along the hull, wave profile, friction coefficient and the non-dimensional wake field at propeller disc are analyzed.

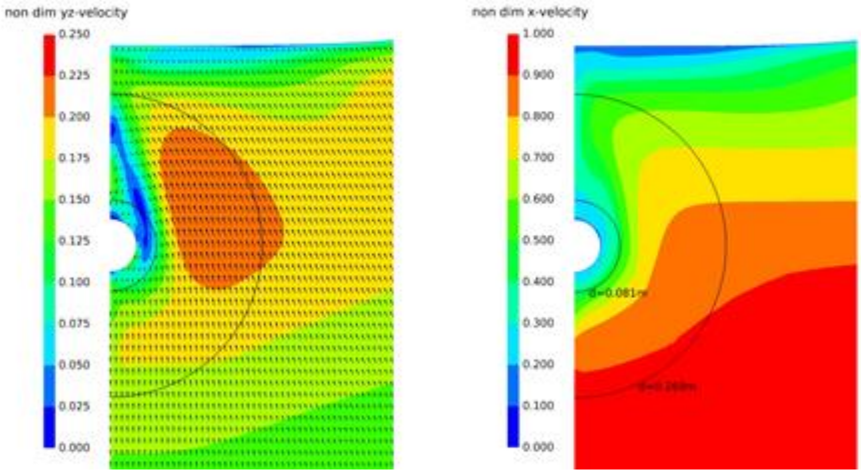

Figure 3: Non dimensional velocities at propeller disc[5]

The wake analysis of the propeller disk is shown in Figure 3, where it can be noted that the wake is expected to be at good level, with normally expected axial velocities losses on the upper part of the propeller.
All of the CFD run cases are made for the design, scantling and ballast draughts, optimized per trim and for various operational speeds of the vessel.
It can be noted, that for such low Froude numbers, in the range of 0.33-0.34, a bow configuration without bulb and a vertical stem can be effectively implemented, through ensuring proper waterline angles.

2.2 Propulsive efficiency

Once ensuring a streamlined flow over the hull, and an optimized aft hull lines, such worked as to reduce rotational losses and boundary layer separation, especially across the aft buttocks, the propeller can operate in a more favourable wake field.
In addition, the propeller is specifically designed such as to work effectively under the given hull wake inflow properties, as it can be seen in Figure 4, thus maximizing propulsion efficiency, even above 0.8, while conventional designs and even other modern designs are performing well below 0.75.

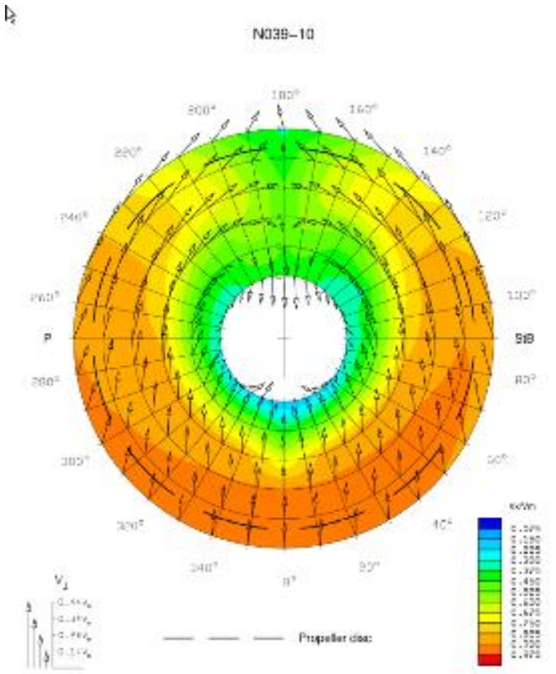

Figure 4: Optimized axial and tangential wake field in front of propeller disk

During the design of the propeller, special care is taken for ensuring a low as possible cavitation and therefore induced vibrations, through further minimizing pressure pulses on the hull.
In the B.Delta37 design, the 40.000 dwt bulk carrier, the measured forces[3] induced to the hull are of magnitude of 17kN, quite small for the case, while, comparatively for a passenger vessel, the permissible level for high passenger comfort is at 50kN.

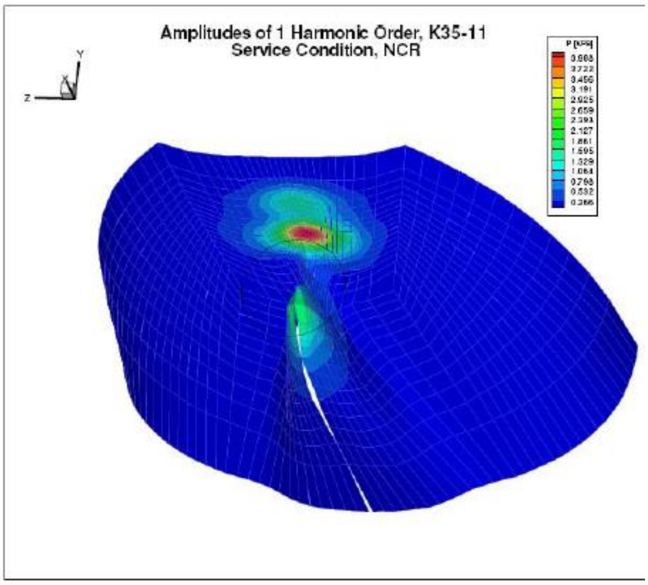

Figure 5: Distribution of propeller induced pressure field on B.Delta hull[3]

In Figure 5, this fact can be observed through the measurement of propeller induced forces distribution, which is extremely small comparative to conventional designs of such ship classes and types.
The propeller optimization also ensures no axial vibration excitations occur and that an improved propeller performance during low engine RPM and loads is to be expected.

2.3 Optimized appendages

In line with the hull-propeller-rudder optimization sequence, the rudder is selected at such a type and size as having reduced added resistance and further promoting enhanced manoeuvrability.

For this reason, a semi-balanced NACA 6 slender form horn rudder is selected, with higher area, and with closer clearances to the propeller hub and aft stern form, than conventional rudders used in cargo vessels.

Specific end-plates are installed to reduce tip vortices from trailing edge, while a rudder bulb is selected so that rotational losses from propeller hub are retrieved on the best possible way.

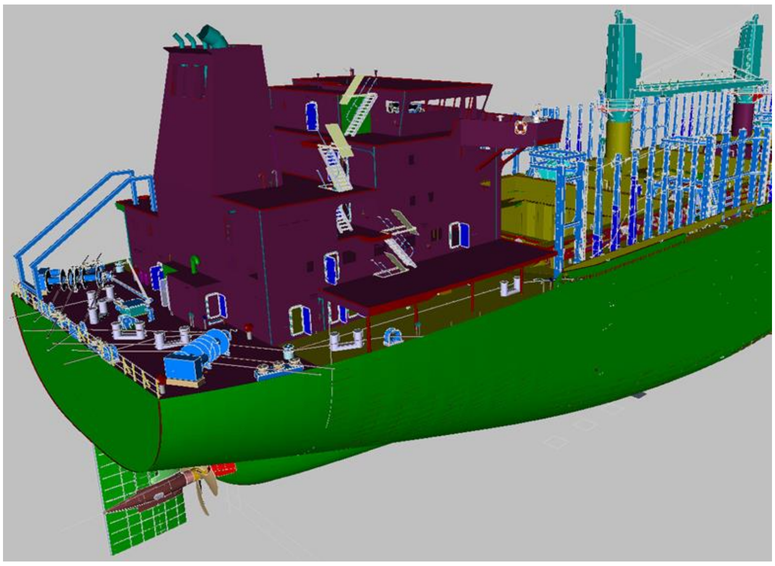

Image 2: Optimized propeller-rudder

The higher rudder area, combined with optimized incoming flow from the propeller is offering an improved manoeuvrability both in head and quarter seas, while, due to the optimized hull, a lower drift angle is experienced in currents.

The Model Tests of B.Delta bulk carrier[4] designs have shown an improved manoeuvrability, well below the IMO MSC.137(76) manoeuvrability criteria, which are effected from the aforementioned optimization sequence.

	This vessel	Permissible according to IMO resolution
10°/10° 1st overshoot angle	19.4 °	20.0 °
10°/10° 2nd overshoot angle	28.0 °	40.1 °
20°/20° 1st overshoot angle	19.0 °	25.0°
Travelled ship lengths required for 10°change of heading with 10° rudder angle	1.56 L_{pp}	2.50 L_{pp}
Tactical diameter (35° rudder angle)	2.25 L_{pp}	5.0 L_{pp}
Advance at 90° change of heading (35° rudder angle)	2.78 L_{pp}	4.5 L_{pp}

Figure 6: Manoeuvring parameters for B.Delta64, 64.000 dwt Ultramax bulk carrier[4]

As shown in figure 6, the application of rudder optimization is making B.Delta64 ultramax bulk carrier fully compliant with IMO MSC. 137(76) manoeuvrability criteria[6], while the turning circles are proven to be very small, with the tactical diameter being less than half as large as the limit.

2.4 Optimization of main propulsion

The modern propulsion technologies are offering the possibility to use 2-stroke electronically controlled main engines with much longer strokes (super or ultra-long stroke), enabling lower specific fuel consumption on the MCR point with lower RPM, and the use of a larger, more efficient propeller.

The main engine is selected optimally as close as possible to the L4 layout diagram, for achieving a design point as close as possible to the optimum SFOC, while also selecting a more suitable tuning for the intended operation (part load, or low load tuning).

Due to the optimized low vibration induced propeller design, there is no need for extra torsional vibration damper for the Main engine, despite the fact that five cylinders engines can also be mainly selected, which is considered as a non-favourable factor.

2.5 Extensive Model tank testing

Further the meticulous CFD analysis performed, for the step-by-step optimization prediction of hull-propeller-rudder, the B.Delta designs are passing extensive model tests in reputable basins, such as Hamburg's HVSA, comprising of:

- Streamline paint tests
- Resistance tests at design, scantling and ballast drafts
- Self-propulsion tests at design, scantling and ballast drafts with 4 bladed stock propeller and with final propeller
- 3D Wake measurement
- Trim tests
- Self-propulsion tests in rough seas
- Manoeuvring tests
- Propeller cavitation and pressure pulse measurements with final propeller

As it can be seen from the Image 2, the B.Delta designs – hereby shown the B.Delta210, a 210.000 dwt Newcastlemax bulk carrier[8], is having a very steamlined flow along the waterline length, while the first bow induced wave is of low height and fast amortized, while no divergent waves are observed in the fore and aft shoulders between the middle body and the aft/bow part of the ship.

$V = 14.70$ kts / $F_N = 0.1394$

Image 2: Model test of B.Delta210 at design speed of 14.7kn, design draft of 16.40m[8]

2.6 Fuel efficiency

The B.Delta optimized hull-propeller-rudder combination is offering an energy efficient ship having below properties against conventional bulk carrier designs:

- at least 10% lower fuel consumption
- at least 10% higher cargo carrying capacity

Indicatively, comparing B.Delta37 with Imabari38, the benchmark of handysize bulk carrier designs for many years until 2008, we can notice below figures:

	Imabari 38	**B.Delta37**
Length overall (m)	180.00	179.99
Breadth (max) (m)	29.80	30.00
Depth (m)	15.00	15.00
Draft, moulded design (m)	10.00	9.50
Draft, moulded scantling (m)	10.55	10.5
DWT, design (mt)	35.000	34.600
DWT scantling (mt)	37.500	40.000
Cargo capacity (m3)	47.000	50.000
Main Engine	MAN B&W 6S46MC-C07	MAN B&W 5S50 ME
MCR (kW)	7.330	6.050
NCR (kW)	5.450	4.560
Service Speed (kn)	14	14
DFOC (mt/day)*	22.6	17.60

**ISO conditions, incl 15% Sea Margin, excluding engine tolerance*

Table 1: Comparison between B.Delta37 and Imabari 38 handysize bulk carriers

As it can be seen in Table 1, B.Delta37 presents 7.4% more deadweight, 6.4% more cargo cubic capacity, 16% less propulsion power, 18% less installed power and 25% less DFOC than the best conventional design of 38.000 Handysize segment.
Up-to-date, B.Delta bulk carrier designs are having improved performance figures in all bulk carrier sizes, indicatively shown in the Table 2, for the same design draft:

B.Delta design type	**DWT class (max) mt**	**DFOC (mt/day) B.Delta***	**DFOC* (mt/day), Best modern energy efficient designs**	**Service Speed (kn)**
B.Delta37	40.000	17.6	17.7	14
B.Delta43	43.000	17.8	18.3	14
B.Delta64	64.000	23.2	23.8	14.5
B.Delta82	82.000	26.7	26.8	14.5
B.Delta180	180.000	41.5	45.1	14.5
B.Delta210	210.000	45.0	47.2	14.5

**at design draft, ISO conditions, incl 15% Sea Margin, excluding engine tolerance*

Table 2: B.Delta design series compared to other modern eco-designs

It can be observed from the Table 2 that B.Delta series are offering the lowest fuel consumption, while maintaining optimized cargo spaces, enhanced manoeuvrability and course keeping properties.

3. PROVEN RESULTS

3.1 Sea Trials of first B.Delta energy efficient ships

The results of two different types and sizes of B.Delta energy efficient bulk carriers are presented for further review:

- B.Delta SUL Panamax, a 72.000 dwt Self-Unloading Bulk Carrier[9]
- B.Delta37, a 40.000 dwt Handysize bulk carrier[2,1]

Both above ships were launched in Chinese Shipyards during 2012-2013, having successful sea trials.

The B.Delta SUL Panamax vessel is a 72.000 dwt bulk carrier ship with a bow thruster opening, higher draft than usual Panamax bulk carriers, at 13,5m, due to the heavy Self-unloading outfitting throughout the cargo holds, with shaft generators and without any energy efficient devices installed, fully optimized on the principle of Deltamarin hull-propeller-rudder design methodology as presented in above Chapters.

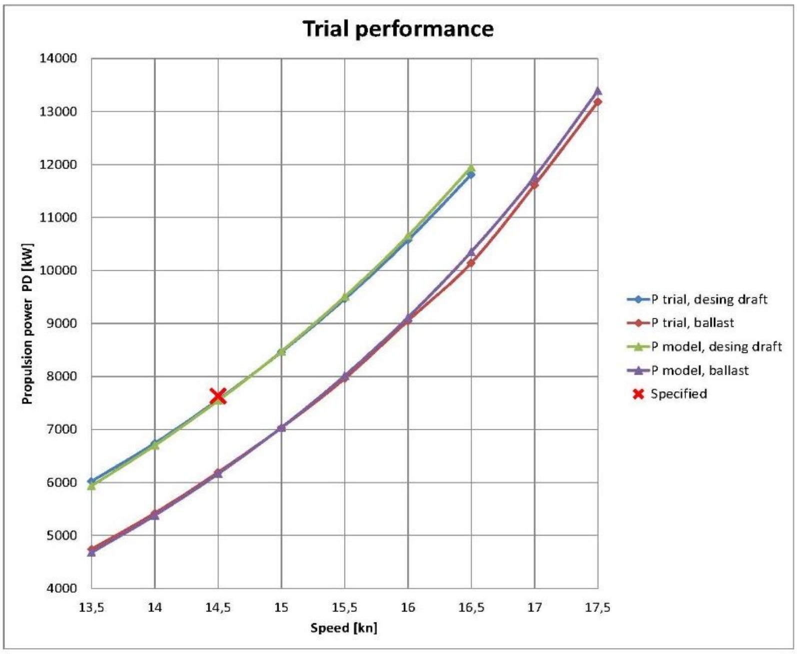

Figure 7: Sea Trial/Model test curves – B.Delta SUL Panamax[9]

In Figure 7, both Sea Trial and Model test curves are shown, superimposed, as confirmed by HSVA model basin[9], to observe the excellent matching in both ballast and design drafts.

The B.Delta37 is a 40.000 dwt geared handysize bulk carrier, with 5 cargo holds, without bow thruster or shaft generators, fully optimized as per Deltamarin hull-propeller-rudder methodology and techniques for fuel efficiency.

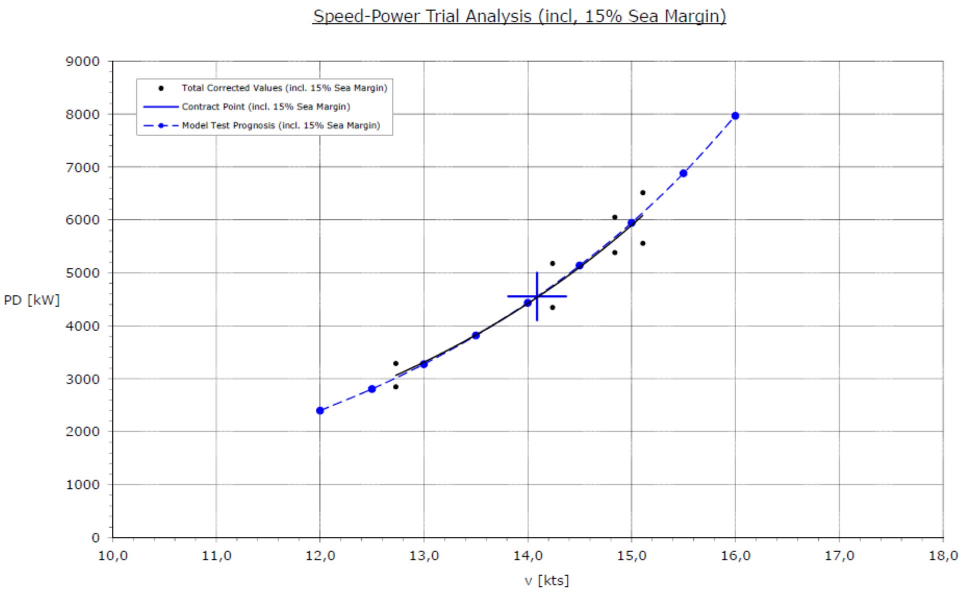

Figure 8: Sea Trial / Model Test curves – B.Delta37 bulk carrier[2,1]

In Figure 8, the same superposition is shown, as confirmed by HSVA model basin[2,1], which proves again an excellent matching in design draft conditions.
The above figures show that the techniques of hydrodynamic and propulsion optimization, as developed and predicted through CFD analysis, is fully feasible and proven, with a very high level of accuracy, despite the uncertainties incurred.

3.2 Enhanced manoeuvrability

During the Sea Trials of B.Delta delivered ships, it was noticed that the ships were also performing in an excellent way in manoeuvrability tests[4], proving the predictions of relevant model tests.

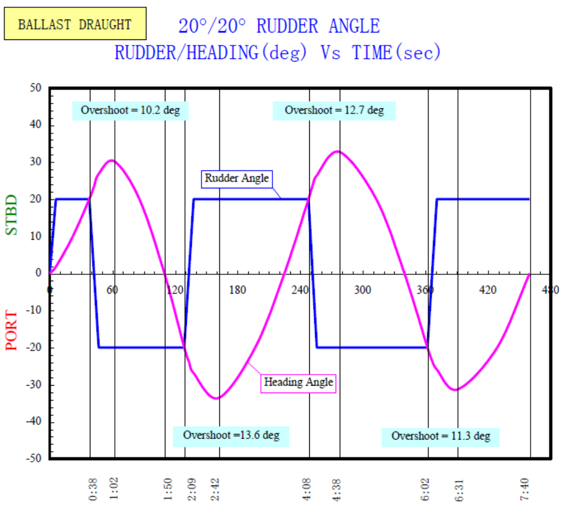

Figure 9: B.Delta37 manoeuvrability Sea Trials, 20/20 deg zig-zag tests[4]

As it can be seen from Figure 9, the ship is following the rudder order in a quite disciplined way, during zig-zag tests, without excessive overshooting, and with a very fast response on the cross-rudder order, revealing a highly manoeuvrable and obedient ship, despite the high block coefficient.

The maximum overshoot angle achieved in the Sea Trials are of magnitude of 13.6 deg, for 20/20 degrees rudder deflection, far lower than IMO MSC.137(76) permissible limits, which are:

- $20^{o}/20^{o}$: 25.0^{o}
- $10^{o}/10^{o}$: 19.1^{o} / 38.7^{o}

4. CONCLUSIONS

Deltamarin has studied and developed since 2006 the concept of a wholly-optimized energy & fuel efficient cargo vessel design, implementing an in-house theory of hydrodynamic and propulsion optimization, applied first on a Panamax and Handysize Bulk Carrier design.
The methods used were based on advanced CFD analysis, which introduced changes in the way of developing hulls for cargo trades, in an effort to maximize cargo carrying capacity and minimized fuel consumption, a contradicting combination based on conventional ship theory, effected through revolutionary considerations in hull form, propulsion arrangements and appendage design.
Up-to-date, having already 23 successfully sea trialled B.Delta ships of various sizes and types, the design is proven, fully complying with EEDI Phase 2 & 3, offering 25% better fuel consumption and 10% higher cargo carrying capacity than conventional bulk carrier designs, while it is still ahead of modern design proposals in performance.

References

1. HSVA Model test report, 40.000 dwt Bulk Carrier, 2009
2. HSVA, Evaluation of Speed Trials, CX0341, November 2013
3. HSVA, Report K 61-11, Determination of propeller induced hull forces for the Deltamarin B.Delta37 bulk carrier, November 2011
4. HSVA, Report Man 255/08, Model tests on the Manoeuvring and Course keeping performance of a Handymax Bulk Carrier, Sept 2008.
5. B.Delta64 CFD analysis report for project 410, RANS CFD Analysis and Powering Prediction, Deltamarin
6. International Maritime Organization: Resolution MSC.137(76), Standards for ship manoeuvrability, December 2002
7. MEPC.1 / Circ. 681, ‘Interim guideline on the method of calculation of the energy efficiency design index for new ships’, Aug 2009.
8. HSVA, Model Test report, 210.000 dwt Bulk Carrier, June 2013
9. HSVA, Speed Trials evaluation of SUL Panamax, 2012

COMPACT ELECTRIC ENERGY STORAGE FOR MARINE VEHICLES USING ON-BOARD HYDROGEN PRODUCTION

Alon Gany[1], Shani Elitzur[2] and Valery Rosenband[3]

Faculty of Aerospace Engineering, Technion – Israel Institute of Technology, Haifa 3200003, Israel

ABSTRACT

The use of electric energy in marine vessels has been increasing in recent years. In general, it is motivated by the low ecological impact. However, in the case of underwater vehicles it is functionally essential. The objective of this study is to demonstrate the advantage of electric power generation and storage based on on-board hydrogen generation via the reaction between activated aluminium and water and application of the hydrogen in a proton exchange membrane (PEM) fuel cell. The original activation process enabling a spontaneous reaction with water to produce hydrogen as well as a parametric study of hydrogen generation rate and yield are briefly described. The potential increase in specific energy (energy per unit mass) and energy density (energy per unit volume) vs. batteries and other means of hydrogen storage is presented. It is shown that the use of the present technology may result in a substantial increase of specific electric energy along with a reduction in volume or an increase in operating time for the same overall energy storage and generation system.

1. INTRODUCTION

Electric energy and power are required for variety of applications in modern marine vessels. Electric power for the main vehicle propulsion is essential for submarines in underwater operations as well as for surface and underwater unmanned vehicles (UUVs) or autonomous underwater vehicles (AUVs). UUVs and AUVs have shown increasing application for monitoring of sea water properties, pollutants, undersea flora and fauna, detection of oil spillage or operating problems around nautical oil rigs, as well as for military missions. Carreiro and Burke [1] present a variety of UUVs operated by the US Navy. Auxiliary and emergency electric power may be needed routinely in all kinds of vessels. Electricity can provide quiet and ecologically clean operation. However, electric energy storage (typically by means of batteries) is characterized by a fundamental problem of low energy density (energy per unit volume) and specific energy (energy per unit mass).

1.1 Electric energy storage - batteries

As has been stated before, most commonly electric energy is stored in batteries. Batteries are divided into two categories: primary batteries (non-rechargeable) and secondary batteries (rechargeable). The energy density of primary batteries is typically higher than that of secondary (rechargeable batteries). However, the latter may be recharged and used tens and hundreds of times. Good primary batteries may yield specific energy storage of about 300 Wh/kg. Some of them, e.g., Zn/air and $Li/SOCl_2$ (specific energy of 290-300 Wh/kg) can provide only limited power output which is adequate for small devices but not for high power operations. The Li/SO_2 primary battery with a typical specific energy of 260-280 Wh/kg may be a good choice for higher power, military or industrial applications [2, 3]. It is however a high cost device. Primary batteries may suit one-way or one-time missions. Usually, for multiple applications secondary, rechargeable batteries are preferred. Table 1 presents some commonly used rechargeable batteries and their characteristics. Note that good rechargeable batteries such as lithium/ion or lithium/polymer give electric energy density as high as 150 Wh/kg and even 200Wh/kg. Nevertheless, special high performance rechargeable batteries with specific energy

[1] Professor Emeritus, Head, Sylvia and David IA Fine Rocket Propulsion Center, Fellow RINA; +972-4-8292554, gany@tx.technion.ac.il

[2] PhD Student; +972-4-8294964, elitzur.shani@gmail.com

[3] Dr.Sc. Senior Research Fellow; +972-4-8294966, aervaro@tx.technion.ac.il

similar to that of primary batteries may be available. However, they are very expensive and would typically be used for special missions.

Table 1. Specific energy and characteristics of some commonly used secondary (rechargeable) batteries.

Type	Specific Energy [Wh/kg]	Characteristics	Applications
Lead-acid	35-40	Popular. Low cost. Low energy density. Moderate specific energy. Available in various sizes and shapes.	Automotive, golf carts, lawn mowers, tractors, aircraft, marine, industrial trucks, portable electronics, emergency power
NiMH	75-80	Maintenance free.	Portable electronics, electric and hybrid vehicles.
NiCd	35-55	High cost. Good low temperature and high rate performance. Excellent life cycle. Maintenance free. Environmental not friendly - strongly regulated.	Biomedical, aircraft.
Li-ion	120-150	Moderate cost. High specific energy. High energy density. Low life cycle. Long shelf life.	Portable electronic equipment, electric vehicles, space applications.

1.2 Hydrogen storage and fuel cells

Hydrogen is considered an ultimate fuel due to its extremely high heat of reaction (low heating value of 120.9 MJ/kg and high heating value of 142.9 MJ/kg, about three times higher than that of hydrocarbon fuels) and due to his minimal ecological impact, as its reaction products are only water (in liquid or vapour state). Hydrogen is also an ideal fuel for application in fuel cells which convert directly chemical energy into electric energy at a relatively high efficiency (typically 50% and more). As will be shown later, the use of hydrogen in a fuel cell may yield much higher specific energy compared to batteries. The most convenient fuel cell type for electricity generation is the proton exchange membrane (PEM) fuel cell, using hydrogen (fed from certain means of storage) and oxygen (typically from the ambient air) and operating at low temperatures (typically between room temperature and 100°C). Both batteries and fuel cells convert chemical energy into electric energy. The difference between those options for energy storage is the location of the active material (fuel and oxidant). In batteries the fuel and oxidant are part of the device, whereas in fuel cells they are supplied externally. This difference leads to several advantages of fuel cells over batteries: fast recharging, longer continuous run-time (approximately two to ten times longer), constant voltage and lack of power decrease during operation, greater durability in outdoor environment under a wide temperature range, and less maintenance [4]. Additionally, fuel cells are characterized by a quiet operation. A schematic illustration of a PEM fuel cell is presented in Fig. 1.

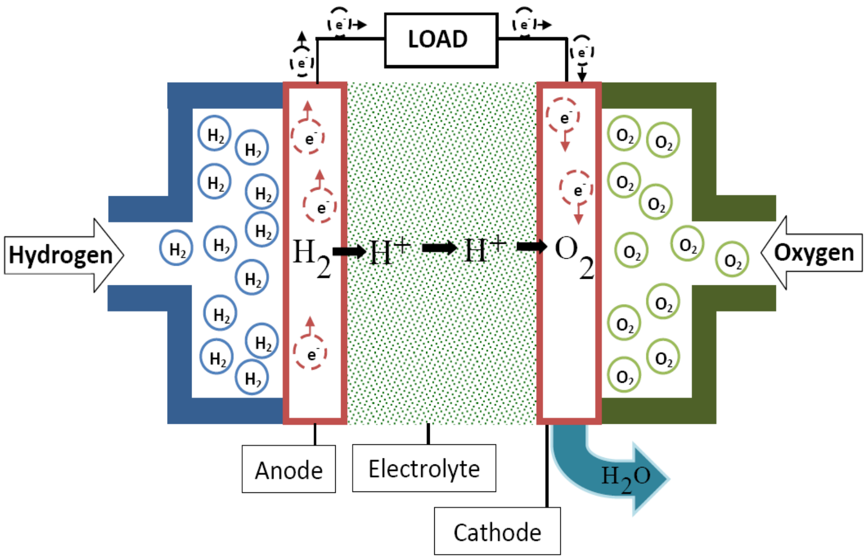

Fig. 1. Schematic illustration of a PEM fuel cell.

Despite its outstanding properties, hydrogen poses difficult handling, storage, and transportation problems due to its extremely low density, 0.089 kg/m^3 (gas), about 14 times less than air, and 71 kg/m^3 (liquid), 14 times less than water, and its high flammability and explosion hazards. In addition, its cost is higher than that of conventional fuels. For many applications hydrogen is stored as gas in high pressure (200-700 bar) tanks. The common use of steel tanks yields a relatively low overall hydrogen mass fraction, typically 2-4%, though for special applications composite light weight tanks may be used, yielding a higher hydrogen mass percentage. Liquid hydrogen gives a much better mass fraction. However, the overall hydrogen density in all those arrangements is very low and does not exceed about 60 kg/m^3. Liquid hydrogen (stored at about 20K) is difficult for handling, and its refrigeration requires substantial amount of energy. Hydrogen storage challenges have been the subject of many publications, e.g., [5-9].

In order to increase the overall hydrogen density as well as to reduce the risks involved in storing high pressure hydrogen gas, solid materials that can store hydrogen and release it in a controlled and convenient manner have been sought. The most common materials for a compact storage of hydrogen are metal hydrides, which are chemical compounds of metals or metal alloys with hydrogen. There are many metal hydrides with mass fractions of hydrogen ranging from about 1% to over 20%. However, only few of them can release hydrogen upon mild heating and are practically used. Table 2 presents a number of practically used metal hydrides and the content of hydrogen. As one can see, practical metal hydrides such as $LaNi_5H_6$ or $FeTiH_2$ contain only 1-1.5wt% of usable hydrogen (hydrogen may be released only to a certain extent and not in full). It means that 1 ton of hydride can store only 10-15 kg of hydrogen. However, due to the high density of the these hydrides, the overall density of the contained hydrogen is about 115 kg/m^3 for the former and about 100 kg/m^3 for the latter [11-12], higher than for liquid or high pressure gaseous hydrogen. This is an advantage for volume limited systems besides the improved safety. Additional information is included in [13, 14].

Table 2. Selected practical metal hydrides used for hydrogen storage.

Metal/Alloy	Hydride	Hydrogen Capacity (wt%)	Hydrogen Density (kg/m^3)	T for 1 bar (°C)
$LaNi_5$	$LaNi_5H_6$	1.37	115	12
$CaNi_3$	$CaNi_3H_{4.4}$	1.8		25
FeTi	$FeTiH_2$	1.89	100	-8

2. ALUMINUM-WATER REACTION FOR HYDROGEN PRODUCTION

Potentially, the chemical reaction between aluminium and water can yield very high (11%) mass of hydrogen compared to the aluminium mass, presenting a substantially higher hydrogen storage capacity and overall hydrogen density than liquid or gaseous hydrogen and a much better mass fraction than in practical metal hydrides. Equation 1 presents the reaction:

$$Al + 3H_2O \rightarrow Al(OH)_3 + \frac{3}{2}H_2 \quad (1)$$

However, aluminium is naturally covered with a thin oxide film that practically prevents further chemical interaction with oxidizing species (air, water). Many researchers have tried different activation and catalytic methods as well as operating conditions to promote the reaction. Vlaskin et al. [15] and Yavor et al. [16] showed good reaction rate and hydrogen production yield when reacting aluminum powder (in the micron size range) with high-temperature water (typically 150-300°C) at elevated pressure. Ball milling [17, 18] and mechanical cutting [19] have also been investigated for enhancing the reaction between aluminum and water. The latter related the research to power generation. The use of gallium and other alloying elements with aluminum have been studied as well [20]. Reaction of aluminum in alkali solution [21] could also yield hydrogen.

The present research has proposed, studied, and patented an original method of a thero-chemical treatment of aluminum particles with a small amount (typically 1-2.5%) of lithium based activator, enabling the aluminum to react spontaneously with water at room temperature and produce hydrogen [22-24]. The activator diffuses into the aluminium lattice and helps modifying the oxide layer around the particles to become non-protective. This method of aluminium activation seems ideal for hydrogen production and storage. It is safe, easy to handle, does not need additives in the water, and gives high yield of hydrogen production (about 90% and more). A brief summary of a parametric study of the activated aluminum reaction with water is given below. Figure 2 shows the effect of water/aluminum mass ratio on the hydrogen production rate vs. time. One can see that the reaction rate is higher for a lower mass ratio. The main reason is the faster temperature increase during the (exothermic) reaction and its substantial effect on the reaction rate. The stoichiometric water-aluminum mass ratio is 2. However, when reacting in an open vessel the water boils and partially evaporates. Hence, excess water was used in the experiments. One can see that the reaction comes to completion in a few minutes.

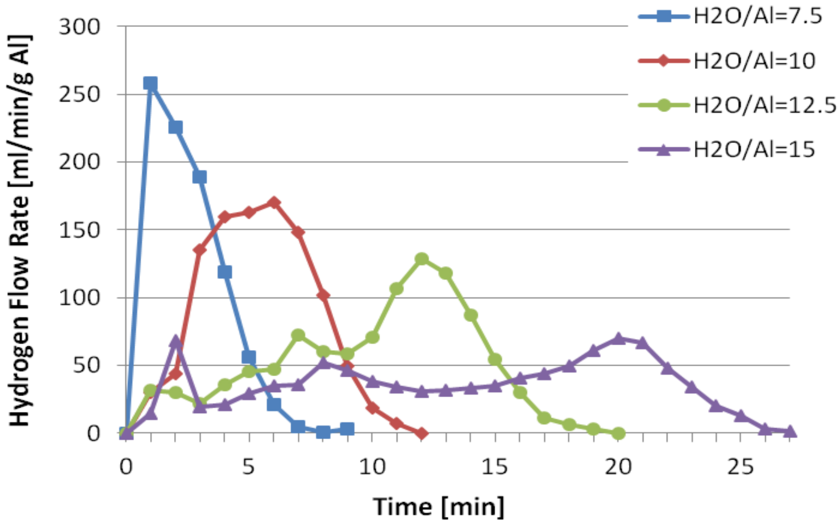

Fig. 2. Effect of water/aluminum mass ratio on the hydrogen production rate vs. time. Activator fraction 2.5%.

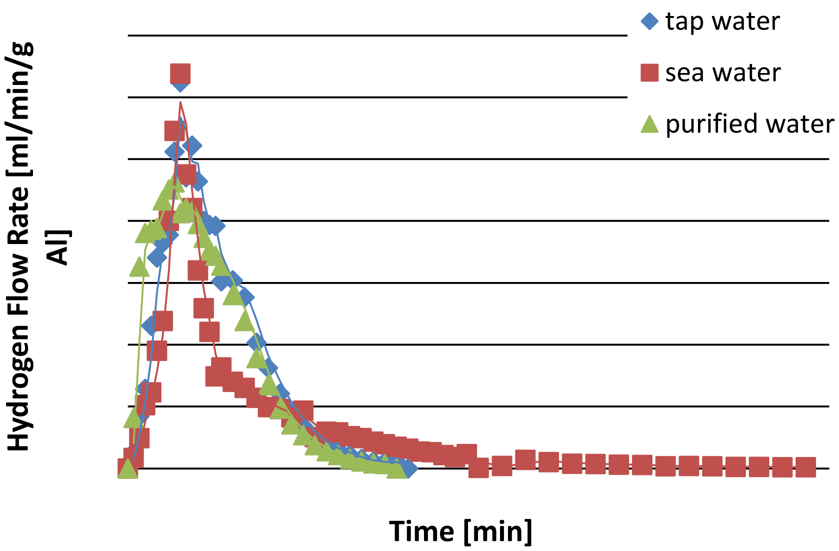

Fig. 3. Hydrogen production rate vs. time. Effect of water type. Activator fraction 2.5%.

It is most interesting to learn that the activated aluminum reacts in a similar manner with any type of water (Fig. 3). The fact that sea water may be used is very significant for marine applications, as water can be pumped directly from the sea and should not be carried along.

3. COMBINED HYDROGEN AND ELECTRIC ENERGY PRODUCTION AND STORAGE

3.1 Performance and specific electric energy

As was stated before, the aluminum-water reaction may be considered as compact hydrogen storage. Channelling the hydrogen produced to a fuel cell can generate electricity on-board and on-demand safely and conveniently, as the hydrogen gas is used upon its production and should not be accumulated. One can show that the application of this technology for electric marine propulsion can yield very high specific electric energy storage. In surface vessels both the water needed for the reaction with aluminum and the air required for the fuel cell are acquired from the surrounding. In underwater application water is available from the ambience whereas oxygen has to be stored in some form for the fuel cell operation. The specific electric energy storage when using a PEM fuel cell with 50% efficiency is 2200 Wh/kgAl, greater by an order of magnitude than the storage by batteries. Indeed, when considering the overall specific energy one should take into account also other components including the fuel cell system and controls, the hydrogen reactor, and the oxygen storage in case of underwater vehicles (submarines often carry liquid oxygen for undersea operation). A conservative estimate of the system mass (fuel cell and reactor) is about 10 kg per kW of electric power capacity (scaled with the power). The longer the operating time the higher the specific energy, as the fixed mass of the fuel cell and reactor represents a smaller fraction of the overall mass, and the fuel component becomes dominant. Table 3 presents the specific electric energy for different marine operation scenarios and mission duration with regard to the present Al-water-fuel cell technology in comparison to other storage means. Some of the data also appeared in the work by Elitzur et al. [25] which assessed the technology for surface and aeronautical applications as well.

Considering that batteries can store between 100 and 300 Wh/kg (independent of the mission duration), one concludes that for missions of the order of one hour duration, batteries are superior to the present Al-water-fuel cell technology with regard to specific electric energy storage. However, for longer missions of 10 hours and more, the present technology reveals substantial advantage. At very long missions (1000 hours) one extracts almost the entire specific energy potential of the aluminum-water reaction.

Referring to metal hydride energy storage: their maximum potential of specific electric energy (when using the hydrogen released in a PEM fuel cell) is about 300 Wh/kg (assuming 1.5% usable hydrogen mass fraction). Nevertheless, for underwater operation oxygen has to be carried along, reducing the maximum specific energy to about 267 Wh/kg (assuming the use of liquid oxygen). For long underwater missions hydride/fuel cell technology exhibits almost twice the specific energy compared to the commonly used lithium-ion batteries. Their specific energy is, however, far below that of the presented Al-water technology.

Table 3. Specific electric energy storage via Al-water hydrogen production reaction and PEM fuel cell compared to other storage means for surface and underwater marine vehicles as a function of operating time.

Application, Mission	Specific Energy (Wh/kg)					Remarks
	Without Fuel Cell Mass$^{(1)}$	With Fuel Cell Mass$^{(2)}$				
		Operating Time				
		1 hr	10 hr	100 hr	1000 hr	
Marine surface vessels, Al-water technology	2200	96	688	1803	2150	Al mass only. Water and air available
Marine underwater vehicles, Al-water technology	1165	92	538	1043	1150	Al and oxygen mass. Water available
Hydrides, underwater	267	73	211	260	267	Hydride and oxygen mass
Batteries, both surface and underwater	100-300	100-300	100-300	100-300	100-300	Battery mass$^{(3)}$

(1) Aluminum mass 0.455 kg/kWh
(2) Estimated system mass of cell and auxiliary equipment 10 kg/kW
(3) For high power and missions of long duration, batteries with specific energy of 100-150 Wh/kg such as rechargeable lithium-ion batteries are likely to be used

3.2 Marine vehicles and Sample calculations

The application of fuel cell technology for electrically operated marine vehicles has been gaining interest, and actual vessels apply this technology. IBI – International Boat Industry magazine reported in 2007 on a sailing yacht equipped with a 1 kW fuel cell [26]. Siemens Industries, Inc. has long been developing and installing PEM fuel cells for submarines [27]. The source of hydrogen is metal hydride whereas oxygen may be stored as liquid. It may also be produced from oxygen containing solids such as sodium chlorate.

As mentioned before, providing compact (high specific energy and high energy density) electric energy storage for underwater autonomous vehicles (UUVs, AUVs) is essential for enabling longer missions or larger space for instrumentation, as the use of batteries may occupy most of the vehicle space, leaving little space for instrumentation, as well as limiting the mission range and duration.

In the following section evaluation of the outcome of replacement of an existing battery power source by the present Al-water-fuel cell technology in a small AUV is presented.

The following data are available for this vehicle. Data on the battery characteristics were taken from the website of Bluefin Robotics [28]:

Total electric energy: 4.5 kWh.
Energy storage: lithium-polymer battery packs.
Endurance: 26 hours.
Specific energy: unpacked 200 Wh/kg; packed 80-120 Wh/kg (average 100 Wh/kg).
From these data one can deduce that the overall energy storage package weighs 45 kg and the average power is 173 W.

Using the Al-water-fuel cell technology for the same overall energy and average power will result in:
Fuel cell and reactor mass: 1.8 kg.
Activated aluminium mass: 2.1 kg.
Oxygen mass, stored as liquid: 1.9 kg; or stored in sodium chlorate: 4.2 kg.
Overall energy storage mass: about 4 kg for liquid oxygen storage or about 8 kg for sodium chlorate as the oxygen source.

This is a noticeable mass saving. Alternatively, for the same mass of the battery pack one could increase the operating time by a factor of about 5 to 11, namely from about 140 to almost 300 hours, depending on the oxygen storage method, compared to the original 26 hours.

4. TECHNOLOGY DEMONSTRATION

The combined technology of in-situ hydrogen production from the reaction of activated aluminum and water together with electric energy generation by a fuel cell has been demonstrated by designing and constructing a model boat (as well as a model car) with on-board hydrogen reactor, PEM fuel cell (Horizon H-30, rated power 30 W), and electric motor. Fed by 5 gram of activated aluminium powder the boat could operate for more than 40 minutes. The model boat and installation is presented in Fig. 4. A short video clip appears in the following link: http://youtu.be/IBbPL_c0mks

Fig. 4. A model boat as technology demonstrator for electric marine vehicle operation using on-board an Al-water hydrogen reactor and a PEM fuel cell.

4. SUMMARY

This work deals with the use of aluminum-water reaction for hydrogen and electric energy production and storage on-board marine vehicles. Using an original method for aluminum activation, it is demonstrated that high reaction rate and hydrogen production yield may be obtained at room temperature. The combination with a PEM fuel cell exhibits compact electric energy storage compared to batteries that may be essential for long range and long duration AUV operation. A model boat equipped with hydrogen reactor, fuel cell, and electric motor has been constructed and operated, demonstrating the technology.

References

1. Carreiro, L.G. and Burke, A.A., "Unmanned underwater vehicles", 7th Annual SECA Workshop and Peer Review, Naval Undersea Warfare Center, Newport, USA, September 12, 2006.
2. Linden, D. and Reddy, T.B., Handbook of batteries, McGraw-Hill Handbooks, 3rd Edition, 2002.
3. Aifantis, K.E., Hackney, S.A. and Kumar, R.V., Editors, High energy density lithium batteries: materials, engineering, applications, Wiley-VCH, Verlag GmbH & Co., Germany, 2010, p. 28.
4. The Department of Energy hydrogen and fuel cells program plan, an integrated strategic plan for the research, development, and demonstration of hydrogen and fuel cell technologies, USA, September 2011.
5. Züttel, A., "Hydrogen storage methods", Naturwissenschaften, **91** (2004), 157-172.
6. Jena, P., "Materials for hydrogen storage: past, present, and future", J. Phys. Chem. Lett., **2**/3 (2011), 206-211.
7. Zhou, L., "Progress and problems in hydrogen storage methods", Renewable and Sustainable Energy Reviews, **9** (2005), 395-408.
8. Felderhoff, M., Weidenthaler, C., von Helmolt, R. and Eberle, U., "Hydrogen storage: the remaining scientific and technological challenges," Phys. Chem. Chem. Phys., **9** (2007), 2643-2653.
9. Schlapbach, L. and Züttel, A., "Hydrogen-storage materials for mobile applications," Nature, **414** (2001), 353-358.
10. Satyapal, S., Petrovic, J., Read, C., Thomas, G. and Ordaz, G. "The U.S. Department of Energy's national hydrogen storage project: progress towards meeting hydrogen-powered vehicle requirements," Catalysis Today, **120** (2007), 246-256.
11. Chen, P. and Zhu, M., "Recent Progress in Hydrogen Storage", MaterialsToday, **11**/12 (2008), 36-43.

12. Perizzini, M. and Poli, R., Recent advances in hydride chemistry, Elsevier, Amsterdam, (2001), 537-539.
13. Principi, G., Agresti, F., Maddalena, A. and S. L. Russo, S.L., “The problem of solid state hydrogen storage”, Energy, **34** (2009), 2087-2091.
14. Klebanoff, L., and Keller, J., Final report for DOE metal hydride center of excellence, SAND2012-0786, Sandia National Laboratories, USA, 2012.
15. Vlaskin, M.S., Shkolnikov, E.I. and Bersh, A.V., "Oxidation kinetics of micron-sized aluminum powder in high-temperature boiling water", Int. J. of Hydrogen Energy, **36** (2011), 6484-6495.
16. Yavor, Y., Goroshin, S., Bergthorson, J., Frost, D., Stowe, R. and Ringuette, S., "Enhanced Hydrogen Generation from Aluminum-Water Reactions”, Int. J. of Hydrogen Energy, **38** (2013), 14992-15002.
17. Dupiano, P., Stamatis, D. and Dreizin, E.L., “Hydrogen Production by reacting water with mechanically milled composite aluminum-metal oxide powders,” Int. J. of Hydrogen Energy, **30** (2011), 4781-4791.
18. Razavi-Tousi, S.S. and Szpunar, J.A., "Effect of structural evolution of aluminum powder during ball milling on hydrogen generation in aluminum-water reaction", Int. J. of Hydrogen Energy, **38** (2013), 795-806.
19. Franzoni, F., Milani, M., Montorsi, L. and Golovichev, V., “Combined hydrogen production and power generation from aluminum combustion with water: analysis of concept”, Int. J. of Hydrogen Energy, **35** (2010), 1548-1559.
20. Ziebarth, J.T., Woodall, J.M., Kramer, R.A., and Choi, G., "Liquid phase-enabled reaction of Al-Ga and Al-Ga-In-Sn alloys with water", Int. J. of Hydrogen Energy, **36** (2011), 5271-5279.
21. Soler, L., Macanás, J., Muñoz, M., and Casado, J., "Aluminum and aluminum alloys as sources of hydrogen for fuel cell applications", Journal of Power Sources, **169**/1 (2007), 144-149.
22. Rosenband, V. and Gany, A., "Compositions and methods for hydrogen generation", US Patent No. 8,668,897 B2, March 11, 2014. China Patent No. ZL201080009706.4, April 30, 2014.
23. Rosenband, V. and Gany, A., “Application of activated aluminum powder for generation of hydrogen from water”, Int. J. of Hydrogen Energy, **35** (2010), 10898-10904.
24. Elitzur, S., Rosenband, V. and Gany, A., “Study of hydrogen production and storage based on aluminum-water reaction”, Int. J. of Hydrogen Energy, **39**/12 (2014), 6328–6334.
25. Elitzur, S., Rosenband, V. and Gany, A., “High energy density storage using in-situ hydrogen production”, AIAA-2013-3616, 11th International Energy Conversion Engineering Conference, San Jose, CA, USA, July 2013.
26. file:///D:/My%20documents/My%20Papers%20&%20Conferences/HIPER,%20Athens,%20Dec%203-5,%202014,%20Hi%20Perf%20Marine/World-first%20sea%20trials%20of%20fuel%20cell,%20IBI%2022-6-07.htm
27. http://www.industry.usa.siemens.com/verticals/us/en/marine-shipbuilding/brochures/Documents/SINAVY-PEM-Fuel-Cell-en.pdf
28. http://www.bluefinrobotics.com/

USE OF LNG AS PROPULSION FUEL IN GREEK TERRITORY

Dimitrios Pirounakis[1], Panagiotis Mizythras[1]

Research and Development Department of Hellenic Register of Shipping, 23, Akti Miaouli str. – 185 35 Piraeus, Greece

ABSTRACT

The establishment of stricter limits to the SOx emission in Emission Control Areas (ECA), such as Baltic Sea, North Sea and English Channel has increased the early implementation of green technologies on the ships which are active on ECA zones. Future expansion of these limits to areas which do not belong to ECA zones such as the Mediterranean Sea will necessitate the adoption of fuel efficient technologies or the use of alternative fuels. In terms of these requirements, this paper will describe the systems which are required for the use of liquefied natural gas as an alternative fuel on ships which are active in Greek Coastal Shipping. The properties of natural gas will be evaluated, as well as the demands and the hazards that may be present when using a new fuel in a country with an increased number o routes and vessels in its borders.

1 INTRODUCTION

Environmental protection is a world issue. As a result, the energy efficiency now affects every parameter of a ship design and is followed by an effort to reduce the emissions found in the exhaust gases of ships.

The main problem is the reduction of emissions of existing vessels. The first way to reduce the fuel consumption is by using innovative hull technologies at the bottom of the ship (Kodama, Kakugawa, Takahashi, & Kawashima, 2000) (Foeth, 2008) and to decrease the developed friction on the hull of the ship. Another way to decrease the emissions in existing shipping is to reduce the speed by developing slow-steaming technique (Lindstad, Asbjornslett, & Stromman, 2011). Except of the reduced fuel consumption, this technique will have impact to the ship's friction. Of course, the first solution can be applied only to new ship-buildings and the second has direct effect on the speed of the ship. The only recommended way to reduce the emissions of the existing ships is to interfere with the propulsion system of the ship. The contribution of these systems to the energy efficiency is taken into account when calculating the Energy Efficiency Design Index, as it is has been proposed by the International legislation. (IMO, 2011)

Modifications in the ship's machinery system have direct impact to emission reduction. The solutions that may be applied to the main engine of the ship can be distinguished in three categories. The first category includes an improvement of fuel combustion's efficiency by implementing technologies which reduce the emissions on their production. Implementation of these systems to the engine has effect only to a specific category of emission (e.g. NO_x).

Another way to decrease emissions of an engine is by using an after treatment technology, responsible for the collection and reduction of the emissions which are produced by the engine. This technology has direct application on thevessel and sufficient results to the ship's emissions. However, its disadvantages include the increased cost of the investment, the additional weight to the ship and the management of the chemical process waste products.

Finally, an alternative solution to the after-treatment system is the reduction of the harmful emission by targeting their source, the fuel. Low Sulphur Marine Gas Oil (LSMGO) and Ultra Low Sulphur Marine Gas Oil (ULSMGO) may be used as fine distillates of diesel oil for the propulsion of the ship. Removal of sulphur from the gas oil demands sufficient treatment of the fuel, increasing, however, the final fuel price (EMSA, 2010). In addition, the availability of such fuel distillates is uncertain in many places of interest. Other fuel sources that may be used for ship propulsion and have low sulphur content are bio fuels, LNG, LPG, methanol, or DME. In terms of research, innovative technologies may be used as hydrogen and nuclear propulsion. (McGill, Remley, & Winther, 2013)

This paper will investigate the solution of using LNG as an alternative fuel in ships. Boil-off gases of LNG were initially used as a fuel in marine engines of LNG carriers to reduce the natural gas venting to the atmosphere and utilize it for the propulsion of the ship. Therefore, the release of large quantities of natural gas that is harmful to the environment (Wuebbles & Hayhoe, 2002) is prevented and in addition, valuable quantities of natural gas are not wasted.

The use of LNG for ship's propulsion doesn't only require the relevant gaseous or dual-fuel engines, but additional systems to be installed for the proper storage and supply of the natural gas as well. Installation of these systems will depend on the installed engines and the type of ship. The objectives of this paper are to provide a comprehensive view of the systems which are required for LNG-fuelled ships, presenting as well the hazards that might be present. The implementation of LNG in existing commercial ship propulsion plants is evaluated in the "LNG-COMSHIP" project, evaluating the hazards and the systems required for using such technology in Greek shipping.

The selection of this technology will have direct impact to the emissions of the Greek shipping and the total emissions of Greece. The emissions in the Greek territory are uncertain due to the general lack of data, concerning the type of engines, their properties and ship movement information (Ministry of Environment, Energy and Climate Change, 2014). As a result, the emissions in the Greek territory can be only estimated by fuel-based methodologies. Emissions by Greek domestic and international shipping reached 12.9 million tons (12.4 million tons for CO_2), contributing to the European and Mediterranean emission inventory from shipping with 7.3% and 14.1% respectively (Tzannatos, 2010). Considering the amount of the emissions which are produced in the Greek territory, the implementation of new technologies and alternative fuels is necessary for the compliance of Greek Shipping to the International legislation.

2 INTERNATIONAL LEGISLATION IN EXHAUST GAS EMISSIONS

All these efforts for reduction of emissions and improvement of the energy efficiency of ships are also motivated by specific legislation. In 1997 the International Maritime Organization introduced Annex IV of MARPOL convention specifically for air pollution. The purpose was to limit the main air pollutants contained in ships' exhaust gases, including sulphur and nitrous oxides and to prohibit deliberate emissions of ozone depleting substances. Annex IV also regulated shipboard incineration and the emissions of volatile organic compounds from tankers (IMO, 2014).

In October 2008 a revision was adopted indicating a gradual reduction on emissions. The new revised regulations dictated that the maximum sulphur content in fuel was to be reduced from 4.5% m/m prior 1 January 2012, to 3.5% on and after 1 January 2012, and no later than 2018 the feasibility of reducing the limit further to 0.5% is to be discussed (IMO, 2014). It must be noted that these limits apply to the sulphur content of fuels and in case an exhaust gas cleaning system is installed on board the ship, an equivalent limit in g/ KWh is applied instead (MEPC.170(57), 2008). These specific limits have been implemented to the European legislation by the EU Sulphur Directive 1999/32, as amended by 2005/33/EC and 2012/33/EC, following the limitations which have been introduced by the IMO.

Progressive reduction in NOx emissions from marine diesel engines was also introduced. These limits are relative to the engine's speed and differ according to the date the ship was constructed. Engines with Tier I emission limit are destined for ships constructed from 1 of January 2000 to 31 December 2010 unless the engine is more than 5000KW or 90 lt displacement which makes is compulsory for ships constructed from 1 January 1990. Ships constructed on or after 1 January 2011 must be equipped with Tier II emission engines and from 2016, a date under discussion nowadays, ships operating in special designated areas shall be equipped with TIER III emission engines. These designated areas are called Emission Control areas and were also introduced through the revised MARPOL Annex VI (IMO, 2014).

The Emission Control Areas (ECAs) include areas such as the Baltic Sea, the US coasts and the Northern Sea. Areas such as the Mediterranean Sea are discussed to be included in the ECAs, an action that would lead to even stricter emission limits. Indicatively sulphur limits are reduced to 1.5% prior to July 2010, 1% m/m on and after 1 July 2010 and 0.1% after 1 January 2015. (IMO, 1973).

In order to ensure the reduction of ship emissions, every operator needs to comply with the limits set by IMO. There are many paths to follow when searching for the best solution and each operator shall weigh the advantages and disadvantages of each solution.

3 LNG PROPERTIES

Natural gas is considered the cleanest fossil fuel and is continuously implemented in various applications, either in the industry or in the marine technology. It is consisted primarily of methane and in atmospheric temperatures it remains in gaseous form. Storage and supply of gaseous fuels is always a challenge for every installation.

The only solution to increase the efficiency of energy content during its storage is to increase the density of the gaseous fuel by modifying the storage conditions of it. When gas is in high pressure or in liquefied form, the energy density is high enough to maintain a reasonable storage volume. However, engineers need to face the challenges which arise in each form. High pressure storage is inappropriate for large quantities as the required strength of the tank leads to unacceptable solutions. On the other hand, the liquefied form requires storage at cryogenic conditions. Between these forms, the liquid is always preferable due to its increased density and therefore the ability to transfer larger quantities of natural gas.

The cryogenic temperatures incorporate additional dangers that must be considered during the design of the safety systems that will be installed on board. The low temperatures can cause freeze burns in case of direct contact with human skin or even embrittlement to carbon steel if this metallic surface is under LNG exposure for a sufficient time.

Nevertheless, when LNG is released in the atmosphere, it evaporates rapidly and returns to its gaseous form. Even if natural gas is diluted fast in the environment, gaseous natural gas remains a source of hazards that will jeopardize the safety of the system if it is not addressed appropriately.

Natural gas is flammable between 5% and 15% volume concentration in the air. Below 5%, the concentration is unable to sustain proper combustion and on the contrary, above 15%, the concentration of oxygen in the atmosphere is insufficient. In order to trigger the combustion process, an ignition source is required. These limits shall be always taken under consideration during the design of safety systems. On the other hand, the auto-ignition temperature is higher compared to other fuels as shown in Table 1, increasing the safety of the fuel.

Table 1. Auto-ignition temperatures for fuels **(Pataki, et al., 1998)**

Fuel	Autoignition Temperature [^oC]
LNG	540
LPG	454-510
Ethanol	423
Methanol	464
Gasoline	257
Diesel	315
Fuel	(approximately)

Due to the increased speed of chemical reaction of natural gas with oxygen, the generated flames reach even higher temperatures (approximately 1330^{o}C) with high burn rate (12.5 m^2/minute) and heat of combustion (50.2 MJ/kg). (GIIGNL, 2009).

A system designed to handle and store natural gas in its liquefied form must consider the possible accidents that could occur. LNG spill is an accident that can cause injuries, damage to the hull or machinery equipment of the vessel and consequently lead to evaporation of LNG and dispersion of gas to the atmosphere. The consequences of this release depend on the quantity and velocity of the leakage.

The most undesirable hazard that may be caused by natural gas is fire. There are three types of fires which may be caused by a LNG leakage: flash fire, jet fire and pool fire. Flash fires describe a phenomenon of a sudden and intense combustion of a flammable mixture and are characterized by its short duration. The gas and oxygen mixture could be formed by direct leakage of natural gas, or by evaporation of accidentally pre-released LNG. Jet fires on the other hand require a pressurized release of natural gas, and their range is usually smaller than the rest types of fires. Although they are not the main threat to the public, jet fires are capable to initiate a disastrous sequence of events to the adjacent installations, known as “domino effect”. Finally the most common fire hazard is the pool fire. A pool fire is erupted when the evaporated LNG above an LNG spill is ignited. The size of the ignited pool depends on the spill and the burning rate. An assumption of the shape and size of the plume according to the diameter of the pool can be provided by considering the combustion Froude number and the dimensionless wind speed. (Webber, Gant, Ivings, & Jagger, 2010)

Besides fire, there are additional hazards that are involved when using LNG as fuel. Unless there is proper ventilation, a release of natural gas in either vapor or liquefied form, may cause the formation of a vapor cloud. When these clouds are formed in confined or congested spaces, there is a higher possibility for asphyxiation or/and explosion. In case that sufficient ventilation is provided to the space through openings or fans, the dilution speed of natural gas will be increased and the ignition probability will be reduced as well. Additional parameter that may affect the dilution is the temperature of the environment. While the vapor clouds have low temperature, they remain in the lower parts of the space. When the temperature of the vapor is increased, the density of the gas decreases and the gaseous fuel rises to the upper levels of atmosphere where its dilution speed is increased. In case that natural gas concentration at the atmosphere is in the flammable limits of the fuel, the danger of explosion is present.

Furthermore, when LNG is spilled onto water or any other high temperature surface, it is possible that a phase change may take place causing the liquid change to vapor rapidly, thus leading to a physical explosion called as “Rapid phase Transition” (RPT) explosion. This effect is most common when a jet of LNG impinges water surface and mixes in high turbulence with it. Even if the developed pressure is not high enough to cause any fatal accidents to humans, there are incidents of damaged equipment due to this phenomenon. (Sauter, Goanvic, & Ohba, 2004)

Finally, the potential of a BLEVE effect to take place on the tank shall be estimated. The BLEVE effect stands for Boiling Liquid Expanding Vapor Explosion effect. It refers to accidents caused by excessive heating of the LNG storage tank due to presence of fire nearby. The heat transfer from the fire will accelerate the evaporation rate of natural gas within the storage tank. Therefore, the increased pressure caused by the high boil-off gases production, plus the high temperature difference between the parts of the tank that will be exposed to the heat and the parts of the tank where LNG is stored will lead to excessive thermal stresses that challenge the mechanical strength of the tank. In case of a failure, the results of the effect will be catastrophic.

4 LNG BUNKERING PROCEDURE

Special attention is required when natural gas is supplied to the ship in liquefied form. LNG can be supplied on the ship with four different ways: on-shore LNG terminal, on-shore truck, off-shore LNG barge or removable cassettes. According to the existing regulations, bunkering operations shall be conducted only within the limits of the port, with the relevant permission.

The only existing terminal in Greek territory that has the capability to accept LNG from ships is located in Revithousa (DESFA, 2000). Additional ideas for offshore LNG terminals as well as an upgrade to the existing LNG terminal capacity has been proposed[1], in order to supply natural gas in liquefied form to ships. The investment on such terminals will also stimulate the interest of ship owners to invest in this technology.

Due to the increased number of islands and ports in Greece, the implementation of natural gas in Greek Coastal Shipping will depend on the LNG availability. Possible modifications in Revithousa’s LNG terminal will have the option to serve as one of the greatest ports of the Mediterranean sea, located in Piraeus. However, problems arise at coast lines and islands which are distant from main LNG terminals. The first solution that is proposed includes the use of a re-liquefication unit, capable to produce LNG when there is a connection to the natural gas network. This solution is preferable for ports located in the mainland. An alternative solution would be the development of small capacity LNG terminals and their supply with LNG via a small barge. Finally, another efficient way is the provision of removable tanks to the ships and with the assistance of a truck or a crane, their substitution on the vessel.

Besides the supply problem, additional problems arise during the bunkering procedure as well. The problems differentiate according to the final bunkering procedure selected. The existing procedures of LNG carriers during fuel loading may be followed for the bunkering of a permanently installed LNG storage tank as well. These procedures are quite demanding and require special training. The main problem of bunkering is the timeline and the duration of the procedure. Natural gas will be at an extremely low temperature and sufficient time is required for the preparation of the bunkering hoses and the pipelines on board. The preparation includes also check of each connection for its gas tightness and purging of bunkering hoses to ensure that no traces of oxygen will be met into the pipes thus creating a flammable atmosphere.

[1] European Commission: “List of projects submitted to be considered as potential Projects of Common Interest in energy infrastructure – GAS”

The supply of LNG will always include the use of one supply and one return line. An additional line may be used before and after bunkering, for the purging of the pipelines. The connection of the bunkering hoses to the ship shall be established by an internationally accepted standard, satisfying the direct connection and disconnection of the hoses and reducing the risk of failure caused by the variation of temperature.

A removable tank will reduce the problems of hoses connection during bunkering, as well as the time that is required for vessel's bunkering. On the contrary, the entire procedure of tank replacement demands high precision and means that facilitate the connection procedure so as to reduce possible hazards that will be raised from the procedure itself.

Except of the primary scope of refuelling, bunkering operation is required when the pressure of natural gas has been increased in dangerous levels. When natural gas is not consumed, the thermal loads of the environment will increase the boil-off gases production in the tank. As a result, the risk of activation of the tank's pressure relief valves is increased, releasing natural gas to the atmosphere. In addition, the cost of a refrigerating unit, responsible for cooling the boil-off gases is prohibitive, especially for an existing ship. Under these conditions, a refreshing of the stored liquefied natural gas will restore the pressure to the previous levels.

5 STORAGE SYSTEM

The storage of the LNG is a major challenge for the engineers in marine applications. The extremely low temperatures of the LNG dictate the use of special cryogenic materials that maintain their strength and mechanical properties when operating at these temperatures. The common structural steel is inappropriate for use and certain alloys of stainless steel, such as 304L is used instead.

According to IMO, there are three types of Storage tank designs (A, B & C) that are appropriate for use when transferring LNG. Types A and B have the advantage that they can utilize most of the cargo space as they adapt efficiently the shape and form of the vessel. Sufficient insulation shall be placed outside of the tank to keep the temperature of LNG low while the part of the ship where the tank will be installed will act as a safe barrier in case of leakage. A fatigue analysis method is required to be conducted, in order to ensure the reliability of tanks against wave loads and thermal stresses and study the crack propagation to the tank.

The type C is the third type of storage tank. Due to its construction, it has the ability to withstand pressures above atmospheric pressure, while the second shell of the tank acts also as a safety barrier against leakages. The ability of high design pressures is crucial when choosing a tank to be used as a mean of fuel storage in the case that LNG is used as a propulsion fuel. The downside of this tank is that it does not take advantage of the total space onboard a ship and presents dead spaces that cannot be exploited.

When deciding to use LNG as a fuel for the propulsion of ships, the cost of the required systems onboard needs to be carefully calculated so as to remain a competitive solution compared to other environmentally friendly technologies. Therefore, the use of reliquefication systems to maintain the LNG at its liquefied form will increase the capital cost of the investment and the weight of the installation. Consequently, such system needs to be avoided and alternative solutions for the management of boil-off gases shall be considered.

Considering the fact that a continuous gas flow from the tank needs to be directed to the engines, the evaporation process of the LNG is required in order to produce vapour. During the evaporation, the temperature of the LNG remains constant at a value that depends on the pressure of the natural gas vapour in the tank. The higher the pressure of the vapour is, the higher the temperature of the LNG. Moreover, when the LNG is maintained at a higher temperature, the temperature difference with the environment is decreased, thus decreasing the thermal transfer. In any case, the higher temperatures reduce the thermal stresses developed due to temperature differences and increase the structural strength of the tank. Consequently, type C tanks have a larger operating pressure window, and are preferred as a solution as they can manage potential pressure fluctuation during sailing.

Even though the design of the type C storage tanks resemblances the common pressure vessels, the philosophy of the design is completely different. There are two shells, the inner shell and the outer shell where the former is supported on the latter. The inner shell is in direct contact to the LNG and its temperature remains close to the cryogenic temperatures whereas the outer shell's temperature is closer to the environmental temperatures. This vast temperature difference leads to gigantic thermal stresses at the supports that connect the inner tank with the outer tank. Specifically, the outer shell is resisting the deformation due to contraction of the inner tank thus increasing the stresses and jeopardizing the integrity of the tank. The thermal stresses and thermal transfer needs to be calculated thoroughly via finite element modelling, incorporating the developed thermal loads besides the pressure loads of the tank.

The heat loads that will arrive to the tank will be responsible for the boil-off vapours production. Several models have been introduced to estimate the rate of the vapour production in the tank, depending on the pressure and the quantity of the stored LNG, the composition of the natural gas and the heat transfer by the external loads. (Adom, Zahidum Islam, & Ji, 2010). The heat loads that will arrive to the ships which operate in Greek seas will be increased due to the geographical location, increasing as well the production of vapour in the tank. The vapour production will be increased in case that these tanks will be exposed on the open deck to the solar radiation.

6 GAS SUPPLY SYSTEM

Natural gas will be stored in liquefied form on the ship. The storage pressure of the LNG will depend on the propulsion engine of the ship. If the required supply pressure of the natural gas to the engine is low, then LNG can be stored under pressure and no pumps or additional systems are required for its supply to the engine. Alternatively, the gas is possible to be stored at atmospheric pressure and an additional pressure build up unit can be used to increase the pressure up to the engine's supply pressure, increasing at the same time the space consumption and the weight of the installations on the ship.

Natural gas in the storage tank shall always be at in equilibrium with the LNG and shall cover the fuel demand of the engine continuously without allowing the pressure to overpass the design pressure of the installed tank. The heat transfer from the environment to the liquefied gas is limited due to the insulation of the storage tank in order to decrease the evaporation rate and ensure the safety of the tank against overpressure.

When natural gas is supplied to the engine, the pressure of the tank is reduced. In order to keep the pressure of the liquefied natural gas, the evaporation rate of the LNG shall be controlled, depending on the engine consumption and operational mode. It must be noticed that the pressure of LNG boil-of-gases affects the saturation temperature of the natural gas. When the pressure is increased, the saturation temperature is increased as well. As a result, the control of the evaporation rate is defined by the consumption of gas from the engines and the self-evaporation of the LNG due to the thermal loads which are delivered to the storage tank system.

The latent heat of LNG evaporation will be offered by a heat exchanger. Many manufacturers who provide such heat exchangers in the market call this unit as a “Pressure Built-up Unit” (PBU), derived by the scope of this unit. An additional heat exchanger is required to increase the temperature of natural gas before fuel is supplied to the engine preventing any undesirable thermal shocks. These systems shall be separated in order to increase the efficiency, responsiveness and sensitivity of the systems to the demanded loads.

The medium of the heat exchanger can be sea water, a hydrocarbon based heat transferred fluid or a solution of glycol water. The source providing the thermal energy to the medium could derive from high energy density means, such as heat losses of engine, or from a lower energy density means, such as the cooling mean for the refrigeration and/or air conditioning systems on the ship. As a result, these heat exchangers are capable to exploit heat sources with lower energy content.

Heat exchange installations are a serious techno-economical problem on the ship due to the increased weight and the volume which is required for these systems. Even if the liquefied natural gas has an extremely low temperature, the temperature of the thermal energy source will define the size of the heat exchanger.

7 SYSTEM SAFETY

Even if there is no specific legislation and rules about the installation and use of these systems, several guidelines have been published and discussed about the protection of the systems and the methods that should be established to ensure safety during their operation. (IMO, 2009) The guidelines cover the arrangement of the systems, the preventive measures that shall be taken into account to protect the personnel and the ship from any hazard and the alarms that will be necessary for the sufficient information of the responsible persons in case of emergency. The type of the systems that will be installed on the ship will depend on the phase of natural gas.

Storage tank of natural gas is required to be monitored. Pressure relief valves and safety procedures shall be installed to ensure the safety of the tanks. Each pipeline that will contain liquefied natural gas shall be insulated to reduce the direct contact of hull structure with the low temperature of LNG. On the other hand, the safety measures for the systems when natural gas is in vapour form are increased, monitoring for any possible leakages of fuel and providing the means for the proper venting of any entrapped natural gas.

Gas supply system requires a set of valves and filters for the proper interruption of the supply in case of emergency and for the maintenance of the entire system. The required valves are located usually to a separated compartment, sufficiently ventilated, due to the number of the connections to the supply system and the increased risk at their installation on the ship.

Furthermore, the machinery spaces which will host the dual fuel or gas fuelled engines require additional provisions for their safety. According to the IMO, the designs which are proposed are the *Inherently Gas-Safe Machinery Space* and the *Emergency Shutdown (ESD) Machinery Space.* The differences between these designs have to do with the type of gas pipelines (single or double walled), the pressure of the natural gas supply line, the ventilation and the arrangement of the space.

Besides the safety that should describe each system on the ship, additional safety systems shall be provided to ensure the safe operation of it. These systems will include the gas detection system, the gas inerting system and the fire extinguishing system. Every system that will be used shall be suitable for operation under explosive atmospheres and they shall have sufficient performance in marine environment. Additional, seperate venting system shall support any space or pipeline which contains natural gas in order to prevent undesirable release of gas to the main venting system of the ship.

8 ENGINE TECHNOLOGY

A ship using natural gas as fuel for its propulsion requires the equivalent propulsion engines so as to utilize the new fuel. Gas fuelled engines is not something new in the maritime community as they have been used for many years now at LNG Carriers. The boil-off gases of the LNG cargo are directed to the engines and get utilized for the propulsion of ships instead of HFO. The high auto ignition temperature of the natural gas (Table 1) allows the fuel to be combusted at a higher compression ratio than diesel engines, offering at the same time a cleaner combustion. (Papagiannakis, et al., 2010)

There are mainly four engine technologies using natural gas as fuel. The first type of technology is designed for spark ignition engines (SI engine), which operate with Otto's thermodynamic cycle and with a lean air – fuel ratio. This technology offers a reduction in the produced nitric oxides of almost 85%. (Burel, Taccani, & Zuliani, 2013) The natural gas can be injected prior to the inlet valve. When the inlet valve opens, the air – gas fuel mixture enters the chamber. The injection system can be single point or multi point, depending on where the injector is installed. The timing and duration of the injection is controlled through the Electronic Control Unit (ECU) of the engine according to the engine's load and speed. However, this engine requires the installation of a spark plug for the ignition of combustion. Due to the limits of thermodynamic cycle and the properties of fuel, gaseous spark – ignition engines require a larger displacement than compression-ignition engine to achieve the same power output. In addition, at part loads, engine appears to have lower volumetric efficiency than diesel engines. (Munde & Dalu, 2012) An alteration of the indirect injection engines are the direct injection engines where the injector is installed within the cylinder chamber. This solution offers higher BMEP levels, reduced knocking phenomena because of the better configuration on the injection timing, but requires a more complicated construction of the cylinder head as well as higher injection pressure. (Bakar, Kadirgama, Rahman, Sharma, & Semin, 2012)

The gas-diesel engines are designed to operate on a mixture of natural gas and diesel without the use of a spark plug. This type of engines is most commonly found at LNG carriers where HFO is consumed together with the boil-off gases. The gas- diesel ratio of the mixture depends on engines load and speed. At full load operation only HFO is used while in dual – fuel operation, a lower proportion of diesel is used for the ignition of flammable mixture. Due to the fact that natural gas needs to be injected in the combustion chamber, the pressure and velocity of the injection needs to be high to achieve sufficient turbulence in the chamber.

The fact that this type of engine requires a significant amount of diesel to be consumed simultaneously has a negative effect on the emissions found at the exhaust gases. Sulphur oxides as well as particulate matter remains above the strict emission limits that are set by the International Regulations in Tier III.

The development of this engine technology is the dual fuel engine. This type of engine is also easier to be applied to an existing diesel engine through retrofitting with reasonable costs. It is similar to the gas – diesel engine though the difference lies between the amounts of diesel required for the ignition of the combustion and the operating thermodynamic cycle. The proportion of diesel is significantly lower (near to 1%) of the total mixture and acts as a trigger for the combustion of the fuel mixture. It has also the ability to operate solely on diesel in case there is no availability of natural gas on board the vessel or the supply of natural gas has been terminated for safety reasons. The engine has also the ability to change between the diesel mode and the natural gas mode instantaneously. The timing of the pilot diesel injection defines the combustion timing of the mixture, giving a more reliable ignition and faster combustion of the combustible charge. This leads to reduced exposure time and to higher temperatures, thus reducing the amount of nitric oxides produced. In addition, the engine maintains the high compression ratio of its predecessor thus maintaining high efficiency.

When in gas mode the dual fuel engine operates in the Seiliger cycle[2] which is similar to the Otto cycle. However, when the engine operates in diesel mode, the thermodynamic cycle is changed to the Diesel Cycle. The following figures show the two cycles in a pressure – volume diagram (p-V).

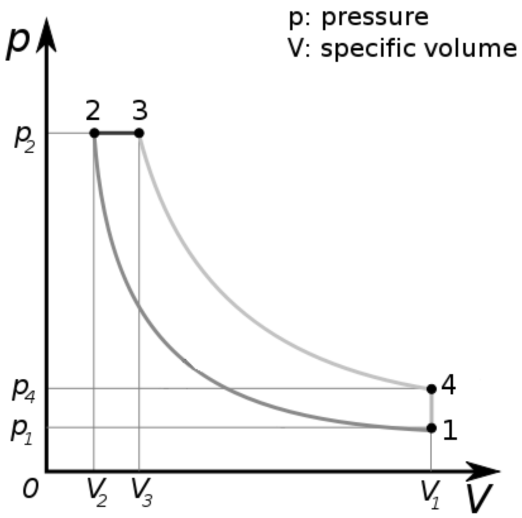

Figure 1. p-V diagram of Diesel cycle

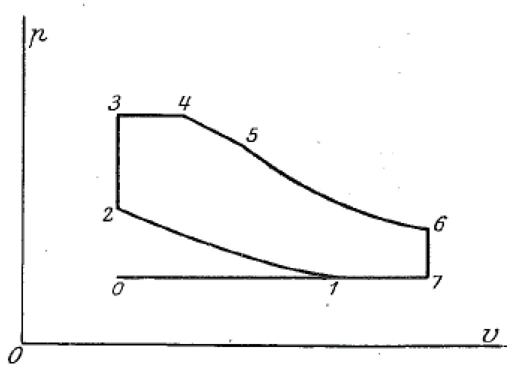

Figure 2. p-V diagram of Seiliger cycle **(Seiliger, 1922)**

The natural gas injection valve can be installed prior to the inlet cylinder valve. However, the diesel injector is modified accordingly in order to support the two operation modes. The injector needs to have a separate nozzle when injecting the pilot diesel fuel, equipped with smaller diameter holes so as to achieve the required spray distribution and turbulence. The main advantage of dual fuel engines is their compliance with the limits that have been set by the International legislation without the necessity of any after treatment technology to the ship. In addition, according to the manufacturers dual fuel engines provide the ability of low- pressure

[2] The Seiliger Cycle is also known as Trinkler Cycle, Sabathe Cycle or simply dual fuel cycle.

gas admission in medium speed engines (Nylund, 2014) which are used in the majority of ships in Greek coastal shipping. It is preferred that the supply pressure of natural gas to the engine is low and therefore no additional system is required to build-up the pressure.

Using fuels with different properties have the disadvantage of knocking effects during the combustion. (Selim, 2004) The effect of gaseous fuel to the operation of the engine has been evaluated and especially, how the natural gas affects the knocking effect on the engine. (Sahoo, Sahoo, & Saha, 2009) Further development in the direct diagnosis and control of such effects, as well as the optimization of the combustion in the chamber will result in minimization of the problems that are caused to the power output of the engine and the chamber.

9 CONCLUSIONS

The use of natural gas as fuel in Greek shipping is proposed for the reduction of the produced emission and as a step for a sustainable solution to the new limits defined in forthcoming legislation. Even if the hazards for maintenance and storage of natural gas are increased, sufficient training of the crew which participates in the operations and the proper design of the additional systems which will be used will reduce the considered risk.

The aforementioned systems are required on the ship for its propulsion with LNG. It is recommended to consider their application in Greek seas, an operational area with high marine traffic and part of the Mediterranean Sea which is under discussion to be included in future ECAs. Besides the hazards that may be included to its application, natural gas shall be considered as the safest fuel between other gaseous fuels due to its lower density, the high auto-ignition temperature and the gained experience from LNG carriers.

References

Adom, E., Zahidum Islam, S., & Ji, X. (2010). 'Modelling of Boil-Off Gas in LNG Tanks: A case Study'. International Journal of Engineering and Technology, 2 (4), p. 292-296.

Bakar, R. A., Kadirgama, K., Rahman, M. M., Sharma, K. V., & Semin. (2012). 'Application of Natural Gas for Internal Combustion Engines'. In Advances in Natural Gas Technology (pp. 453-478). Shanghai: InTech.

Burel, F., Taccani, R., & Zuliani, N. (2013). 'Improving Sustainability of Maritime Transport Through Utilization of Liquefied Natural Gas (LNG) for Propulsion'. Energy (57), 412-420.

DESFA. (2000). LNG Terminal 'Revithousa' - Marine procedures manual. Hellenic Gas Transmission System Operator S.A.

EMSA. (2010). 'The 0.1% sulphur in fuel requirement as from 1 January 2015 in SECAs - An assessment of available impact studies and alternative means of compliance.' Technical Report, European Maritime Safety Agency.

Foeth, E. J. (2008). 'Decreasing frictional resistance by air lubrication'. 20th International Hiswa Symposium on Yacht Design and Yacht Construction, Maritime Research Institute of the Netherlands (MARIN).

GIIGNL. (2009). LNG Custody Transfer Handbook. International Group of Liquefied Natural Gas Importers.

IMO. (1973). International Convention for Prevention of Pollution from Ships. IMO.

IMO. (2009). Interim Guidelines on Safety for Natural Gas-Fuelled Engine Installations in Ships. International Maritime Organization.

IMO. (2011). Ammendments to the Annex of the Protocol of 1997 to amend the international Convention for the Prevention of Pollution from ships, 1973, as modified by the Protocol of 1978 relating thereto. International Maritime Organization.

IMO. (2014). Prevention of Air Pollution from Ships. Retrieved from International Maritime Organization: http://www.imo.org/OurWork/Environment/PollutionPrevention/AirPollution/Pages/Air-Pollution.aspx

Kodama, Y., Kakugawa, A., Takahashi, T., & Kawashima, H. (2000). 'Experimental study on microbubbles and their applicability to ships for skin friction reduction'. Elsevier. Ship Research Institute. Tokyo.

Lindstad, H., Asbjornslett, B., & Stromman, A. (2011). 'Reductions in greenhouse gas emissions and cost by shipping at lower speeds'. Elsevier. Norwegian University of Science and Technology (NTMU); Norwegian Marine Technology Research Insitute (MARINTEK). Trondheim, Norway.

McGill, R., Remley, W., & Winther, K. (2013). Alternative Fuels for Marine Applications. IEA-AMF.

MEPC.170(57). (2008). Guidelines for Exhaust Gas Cleaning Systems. Marine Environment Protection Committee (MEPC). IMO.
Ministry of Environment, Energy and Climate Change. (2014). Annual Inventory Submission of Greece under the Convention and the Kyoto Protocol for Greenhouse and other Gases for the Years 1990-2012. Ministry of Environment, Energy and Climate Change.
Munde, G. G., & Dalu, R. (2012). ‘Compressed Natural Gas as an Alternative Fuel for Spark Ignition Engine: A Review’. International Journal of Engineering and Innovative Technology (IJEIT), 2(6), 92-96.
Nylund, I. (2014, January 28-33). ‘Low Pressure at Low Speed’. Marine in Detail.
Papagiannakis, R. G., Kotsiopoulos, P. N., Zannis, T. C., Yfantis, E. A., Hountalas, D. T., & Rakopoulos, C. D. (2010). ‘Theoretical Study of the Engine Parameters on Performance and Emissions of a Pilot Ignited Natural Gas Diesel Engine’. Energy(35), 1129-1138.
Pataki, G. E., Gargano, C., Valentino, W. F., Cahill, J., Helmer, M., & Boardman, J. (1998). Report on issues Regarding the Existing New York Liquefied Natural Gas Moratorium. Informative report, New York Energy Planning Board.
Sahoo, B. B., Sahoo, N., & Saha, U. K. (2009). ‘Effect of Engine Parameters and Type of Gaseous Fuel on the Performance of Dual-fuel Gas Diesel Engines - A critical review’. Renewable and Sustainable Energy Reviews(13), 1151-1184.
Sauter, V., Goanvic, J., & Ohba, R. (2004). ‘Evaluation of Rapid Phase Transition Between LNG and Water’.
Seiliger, M. (1922). Graphische thermodynamik und berechnen der verbrennungs – maschinen und turbinen. Berlin, Germany: Julius Springer.
Selim, M. Y. (2004). ‘Sensitivity of Dual Fuel Engine Combustion and Knocking Limits to Gaseous Fuel Composition’. Energy Conversion and Management(45), 411-425.
Tzannatos, E. (2010). ‘Ship emissions and their externalities for Greece’. Elsevier. University of Pireaus. Pireaus.
Webber, D. M., Gant, S. E., Ivings, M. J., & Jagger, S. F. (2010). ‘LNG source term models for hazard analysis’. HSE. Health and Safety laboratory. Derbyshire.
Wuebbles, D., & Hayhoe, K. (2002). ‘Atmospheric Methane: Trends and Impacts’. University of Illinois.

ON-GOING GaN SSPA FOR NAVAL RADAR TRANSMITTERS: A MMIC AMPLIFIER DESIGN

Evangelia A. Karagianni[1], Christina C. Lessi[2] and Christos N. Vazouras[1]

[1] Sector of Battle Systems, Naval Operations, Sea Studies, Navigation, Electronics and Telecommunications, Hellenic Naval Academy, Hatzikyriakou Ave., Piraeus, 185-39, Greece
[2] Department of Informatics and Telecommunications, National and Kapodistian University of Athens, Panepistimioupoli, Athens, 157-84, Greece

ABSTRACT

Solid state amplifier modules are of increasing interest for radar applications due to various advantages (as compared with tube transmitters), such as increased design flexibility, reduced size and power requirements and improved system reliability. In this paper the innovative GaN (as compared with GaAs) technique applied to power amplifiers is addressed. A novel design of a GaN Power Amplifier in the E/F frequency band (more traditionally termed S-band) is presented and the comparison with its counterpart GaAs confirms the forefront of Nitride Gallium technology.

1. INTRODUCTION

Solid State Power Amplifiers (SSPA) are increasingly used in radar system Power Amplifier Transmitters (PAT) instead of more conventional vacuum tube amplifiers, or sometimes, combined with them. Due to their relatively low power output, their primary areas of application include phased array systems (e.g. in active antenna modules) and continuous-wave Low Probability of Interception (LPI) systems, both of interest for shipborne radar applications, especially in warships. They are also used in parallel architecture PATs and pre-amplifier transmitter stages.

Currently, shipborne radar systems largely rely on either traditional vacuum tube based centralized transmitters or various distributed architectures employing SSPAs. Microwave tubes offer much greater peak or average output power and are the exclusive choice for high power systems, such as missile control radars where output peak power can be of the order of hundreds of kW. Tubes, namely magnetrons, are also a standard choice in single stage oscillator architectures for pulsed maritime radars with substantially lower but still high (up to a few tens of kW) output peak power levels, offering advantages of low cost, high efficiency and circuit simplicity. On the other hand, SSPAs are used in lower power systems (e.g. LPI ones), often in parallel architectures where several SSPAs are combined to achieve the total output power required. Such solutions offer, among others, significant improvement in reliability, along with better serviceability, depending on specific system design. Gallium arsenide (GaAs) MESFET-based devices represent a mature choice often used in commercial systems, while Gallium Nitride (GaN) devices appear quite promising for utilization in the next generation systems, due to their ability to produce higher RF output power at higher temperatures and high efficiency over larger bandwidths than traditional semiconductors, contributing to higher sensitivity and / or increased detection range, as well as improved reliability with lower cost and weight. Over the last decade, GaN has rapidly matured to the point that quite a number of products are commercially available (Wood et al 2012). In this paper, we focus on a new design to improve the performance of E/F frequency band which more traditionally termed S-band, radar systems for both military and civilian applications. Such designs are capable of replacing traditional Travelling Wave Tube or Cross Field Amplifiers (TWTAs or CFAs, respectively) with solid state devices. This design is applied in the frequency area of 2.9 – 3.1 GHz, which is usually allocated on a primary basis for maritime radio-navigation by national regulations, for example the Greek (FEK 399 2006) and U.S. (Frequency Allocation 2014) tables, in accordance with the ITU Radio Regulations.

2. MICROWAVE AMPLIFIER TECHNOLOGY AND ARCHITECTURE

Mission critical systems demand the absolute maximum reliability possible. A high level of reliability is critical to military microwave amplifier systems. By Turner (2013), it has been demonstrated that the modular design of solid SSPA can provide dramatically higher levels of system reliability in comparison with TWTA. For SSPAs, the advantage often follows an advance in Gallium Arsenide (GaAs) device technology. A higher power transistor enables the amplifier designer to increase the output power capability of an SSPA. On the other hand, solid state linearizer or predistortion circuits are now frequently used with TWTAs to improve distortion and make the TWTA's power transfer curve more closely approximate that of the SSPA. In recent years depressed collector techniques have improved the efficiency of TWTAs. Despite efficiency increases in SSPA and TWTA technology, both still suffer from relatively low overall efficiency, requiring high power supplies for operation. Any time low efficiency circuits consuming high power levels are encountered, thermal design becomes a major concern. In fact, as the reliability of both tubes and transistors improves, it is noted that amplifier system failures are often due to power supply and thermally related problems.

SSPA devices of parallel module architecture are based on parallel combination, using in-phase combiners, of several SSPA modules to achieve the desired output power level. High gain levels are achievable with this type of design (of the order of 70 dB or even higher). The parallel module concept may also be extended to the power supply, resulting in elimination of single points of failure in any active component within the SSPA; if one module fails, the SSPA can continue operation at reduced output power. Additional reliability and failover characteristics, such as field replaceable modules and redundant power supplies, are also feasible with this architecture.

In contrast, the TWTA is a single electron tube amplifier, which is often combined in cascade with a small signal SSPA to boost the overall gain of the amplifier, and a linearizer circuit usually at the input. Therefore a failure in any one of the three major building blocks can result in overall system failure.

The SSPA also has a decided advantage in operating voltage. An SSPA typically operates with a DC supply voltage in the +12 to +50 V DC range. At these voltage levels there exists a wide variety of reliable power supply solutions, including redundant power supply module implementations. Conversely, travelling wave tubes require supply voltages in the range of several thousand volts, which substantially increases complexity in the power supply subsystem. There are presently very few commercially available power supplies that produce these voltage levels, much less provide the redundancy of a modular N+1 power supply.

3. ADVANCES OF GaN TECHNOLOGY

Historically most modules are based on market available GaAs die, but more recently most companies have been working with the premier GaN die suppliers to develop a range of high power wide band amplifiers, ideally suited for ground and air jamming applications. As the reliability of the devices over the next few years improves, suppliers (Teledyne Microwave 2013) plan to push the advantages of GaN technology up in frequency to satisfy the need for improved efficiency in the X, Ku & K-Band communications market.

The high energy gap (3.4 eV) of the GaN compared with GaAs, as well as the high critical electric field (3.5 MV/cm), are the main properties that can support high voltage applications such as a high power amplifier. What is more, GaN is suitable for high current density applications because it has high charge density ($10^{13}/cm^2$) and high thermal conductivity (1.5 W/cm/K). High saturation velocity ($2.7x10^7$ cm/s) and medium mobility (1500 $cm^2/V/s$) are properties that allow the use of GaN in high frequencies applications.

GaN is a preferred technology for Low Noise Amplifier (LNA) applications because of the low minimum Noise Figure (NF) and the high OIP3 demands (over 40 dBm) available. Besides survivability and robustness, it can also support wide band applications.

Specifically for radar systems the key GaN MMIC T/R enables (a) Limiter reduction or elimination, (b) circulator elimination, (c) Improved NF & Resolution and (d) DC power distribution efficiency. As a result, the system benefits at cost, as well as range and volume.

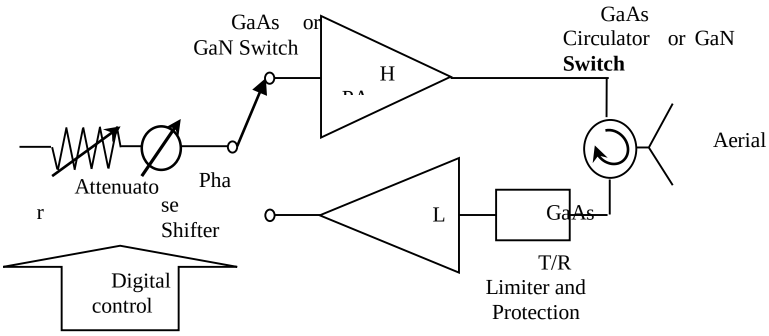

Figure 1. Typical T/R module components for both GaAs and GaN technologies

Active phased array antennas are antennas at which the transmit power is produced by many relatively low output T/R modules mounted directly on the antenna and they are discussed later on. An active phased array uses a special type of solid state transmitter module.

The RF block diagram of a typical T/R module is shown in Fig. 1. Amplitude and phase control are provided by a variable attenuator and a variable phase shifter. Since these components are placed at the input to the high power amplifier (HPA) and the output of the low noise amplifier (LNA), they have minimal impact on the radiated power and noise figure of the module. A switch follows these components to provide selection between transmit and receive functions. At the other end of the module, a circulator acts as a duplexer for transmit and receive. The remaining elements are the HPA and LNA. Additional requirements such as polarization diversity, transmit or receive linearity, waveform diversity and / or low phase and amplitude errors will add complexity to both the module design and its solid-state components. All components are assembled in one single T/R module. It is usual for the module to have self test and status features so that the overall performance of the system can be assessed (BITE). A limiter is sometimes added between the LNA and antenna. This reduces very strong incoming signals from jammers or large targets (with very high Radar Cross Section) close to the radar. The limiter also protects the receiver against duplexer failure. A simple limiter implementation may be achieved using two shunt P-I-N diodes with inverted polarities.

4. PHASED ARRAY RADARS

There are two types of phased arrays: Passive and Active. Passive phased arrays have a central transmitter and receiver, with phase shifters located at each radiating element or sub-array. The passive array is the least expensive phased array because of its low number and cost of components (Parker & Zimmermann 2002, EMS Technologies 2005). Active arrays use Transmit/Receive (T/R) modules to provide the last stage of amplification for transmitted signals, the first stage of amplification for receive signals, and provide both amplitude and phase control at each radiating element. Use of T/R modules in active arrays provides the advantages of amplitude control, low loss, and graceful degradation over passive arrays. Notwithstanding these advantages, high cost and low efficiency of the modules poses an obstacle to development of active phased array antennas.

The two types of phased arrays are shown in Fig. 2. The right side of the figure depicts a passive phased array. It is similar to a mechanically scanned antenna, in that it has a central transmitter and receiver along with a central feed network. Unlike a mechanically scanned antenna, it has an electronically controlled phase shifter immediately behind each radiating element. The phase shifters allow the beam to be steered electronically. On the left side of the figure is an active phased array block diagram. Note that it has a T/R module placed immediately behind each radiating element. Both these arrays offer several advantages over mechanically steered arrays. They have excellent beam agility, they are very reliable since they have no moving parts, and they minimize radar cross section. In the passive phased array, the only active elements are the phase shifters, which are extremely reliable. Furthermore, if they fail randomly, up to around 5% of the phase shifters can fail before the antenna's performance degrades enough to require replacement of the phase shifters.

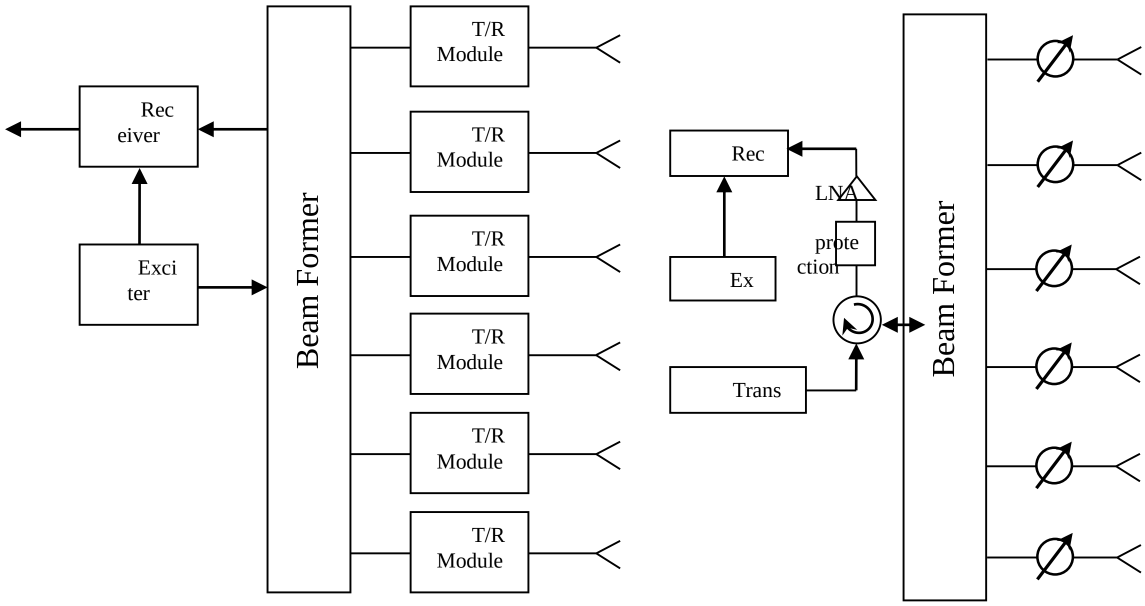

Figure 2. Block diagrams of active and passive phased arrays

Active Phased Array Radar Systems have many advantages compared to passive. They have low loss, higher sensitivity and they are more reliable employing graceful degradation. They also have increased capability (multiple digital beamforming and improved clutter attenuation). The Solid State T/R module is the key enabler of advanced Phaced Array Radar Systems. Regarding the disadvantages, a GaN MMIC T/R module improves system design tradeoffs such as range, resolution, efficiency, size and weight.

The first challenge for the T/R module designer is fitting all the components in a package that will fit in a radiating element spacing that will allow scanning without grating lobes. For example, Nuttinck et al (2002) proposed a scan requirement of ±60° limits the spacing of the radiators to a half wavelength. This limitation is particularly difficult to overcome as the frequency of operation increases. However, even for arrays operating at lower frequencies, the size requirements create problems due to the heat generated by the HPA. The high EIRP requirements of a radar phased array, coupled with the low power added efficiency (PAE) of solid-state HPAs, create a cooling challenge for the antenna designer. This problem is further complicated because the water cooling is located in the same space that is needed to distribute the DC power. Moreover, self heating of the HPA degrades its performance and limits its life (Stimson, 1998). Active phased array designers achieve the desired EIRP by power combining in the module and by increasing the number of T/R modules. Unfortunately, power combining in the module is limited by the degradation of module efficiency as the number of MMICS increases. For example, a single amplifier with PAE of 45% degrades to 30% when it is combined with a second amplifier (Zhang et all 2003). In addition, increasing the number of power amplifier MMICs increases the cost of the module. As a result, typical X-band HPA uses only one or two MMIC amplifiers (Lessi & Karagianni, 2014). Unlike ferrite phase shifters, the digital phase shifter used in a T/R module increases in size and loss as the phase resolution increases. As a result, the module designer uses the lowest possible resolution for the phase shifter. Unfortunately, decreasing the phase shifter resolution degrades the beam pointing accuracy and increases sidelobes. The SPDT switches included in T/R modules degrade output power due to load pulling as the antenna scans and the antenna radiating elements' VSWR degrades. Another disadvantage of distributed T/R modules is the increased cost and complexity of locating EMI filters at each T/R module (Kopp et al 2002).

5. MMIC DESIGN

The TGF2023-01 (Triquint Semiconductor 2013) is a discrete 1.25 mm GaN on SiC HEMT which operates from DC-18 GHz. The TGF2023-01 is designed using TriQuint's proven 0.25um GaN production process. This process features advanced field plate techniques to optimize microwave power and efficiency at high drain bias operating conditions. The TGF2023-01 typically provides 38 dBm of saturated output power with power gain of 18 dB at 3 GHz. The maximum power added efficiency has a typical value of 55% and a maximum value of 66% which makes the TGF2023-01 appropriate for high efficiency applications. Recently, the component was upgraded to TGF2023-2-01 which is recommended by the supplier as a substitute for all purposes; its equivalent or superior characteristics (including a power added efficiency of 71.6%) may be expected to allow for further design improvements.

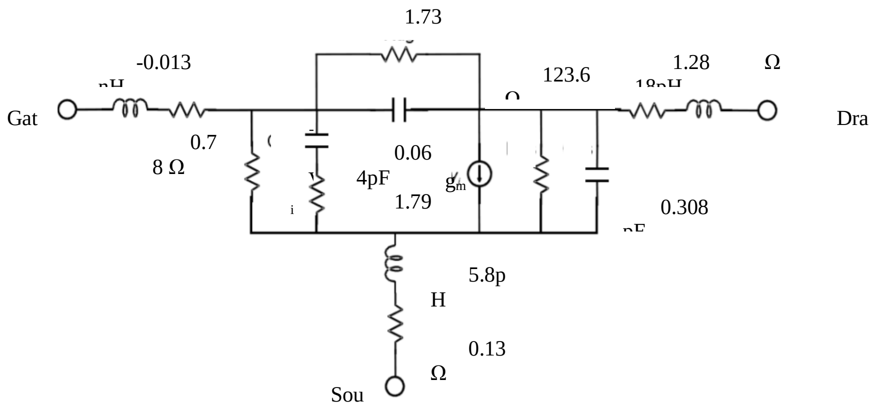

Figure 3. The linear model for 1.25 mm Unit GaN Cell with T_{au}=2.78 ps and g_m=0,27 S.

As depicted in Fig. 4, the amplifier design is based in a two stages topology. The first stage ensures a low overall noise level and the second stage a high overall gain level. Simulation results are presented in Figs 5-8.

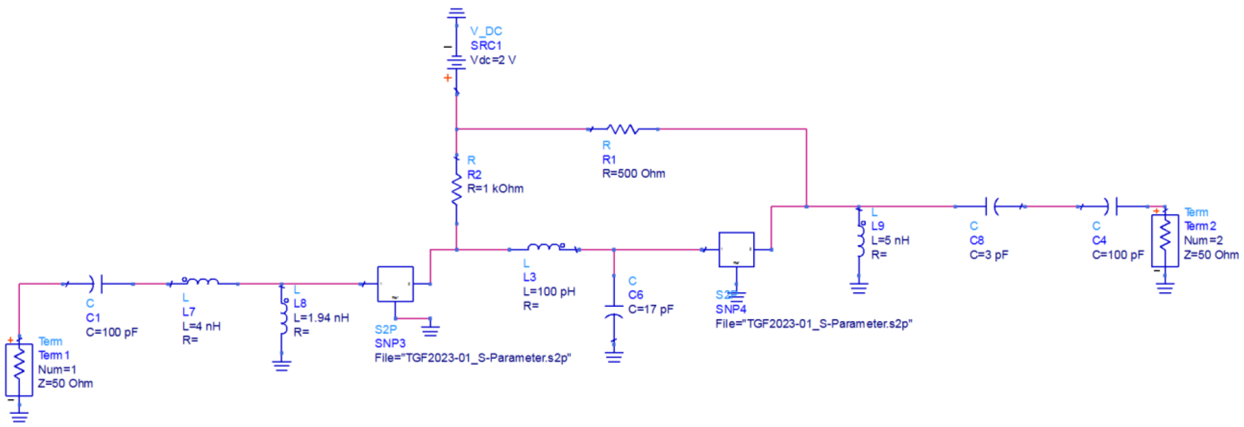

Figure 4. 3.1 GHz High Power Amplifier circuit.

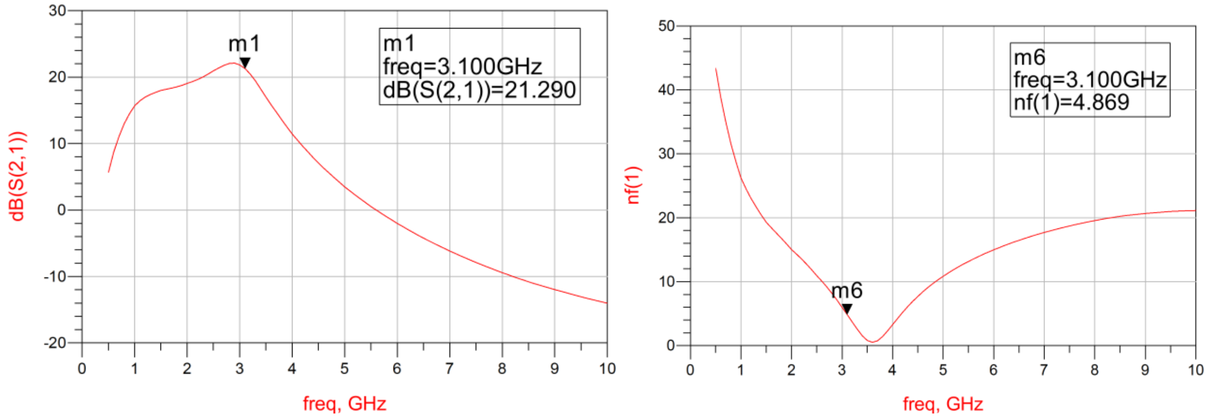

(a) (b)

Figure 5. (a) Gain and (b) Noise Figure

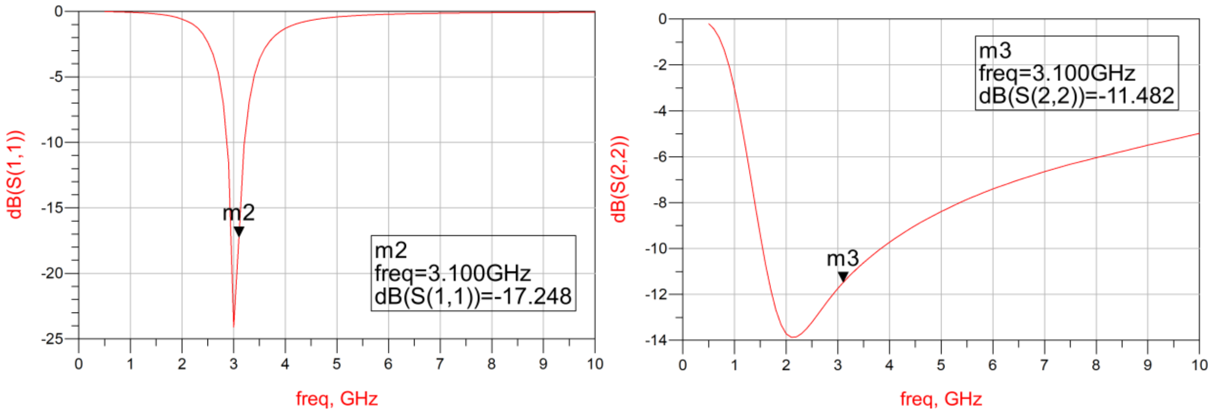

(a) (b)

Figure 6. (a) S11 and (b) S22 parameters

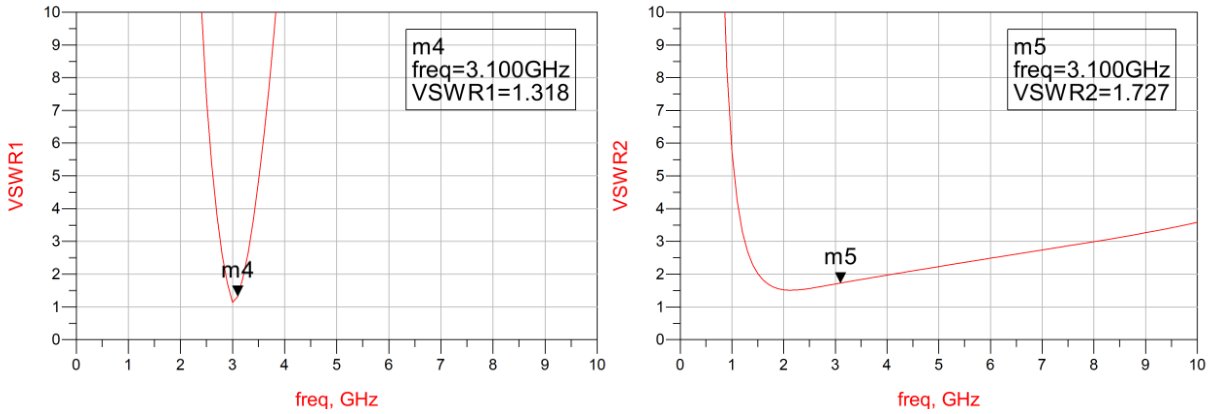

(a) (b)

Figure 7.(a) Input and b) Output VSWR

As shown by the simulation results, the proposed design exhibits optimized gain behaviour, along with quite satisfactory noise levels, throughout the whole operational S-band range of 2900MHz – 3100 MHz. As a matter of fact, the values of around 21 dB for gain and <5 dB for NF achieved are not very far from performance parameter bounds characterizing receiver LNA stages according to real system specs in the lower part of the F band (a realistic example would be about $G \geq 25$ dB and $NF \leq 4.7$ dB for frequencies below 3.5 GHz). This could imply potential interest in further investigation of similar GaN based designs for receiver amplifying stages as well. As may be seen from Figs 7-8, both input and output matching are quite satisfactory within the frequency range of interest, with the latter also exhibiting remarkable stability over a much larger frequency range. Finally, stability requirements are found to be met over a range of 0.5GHz to 10GHz.

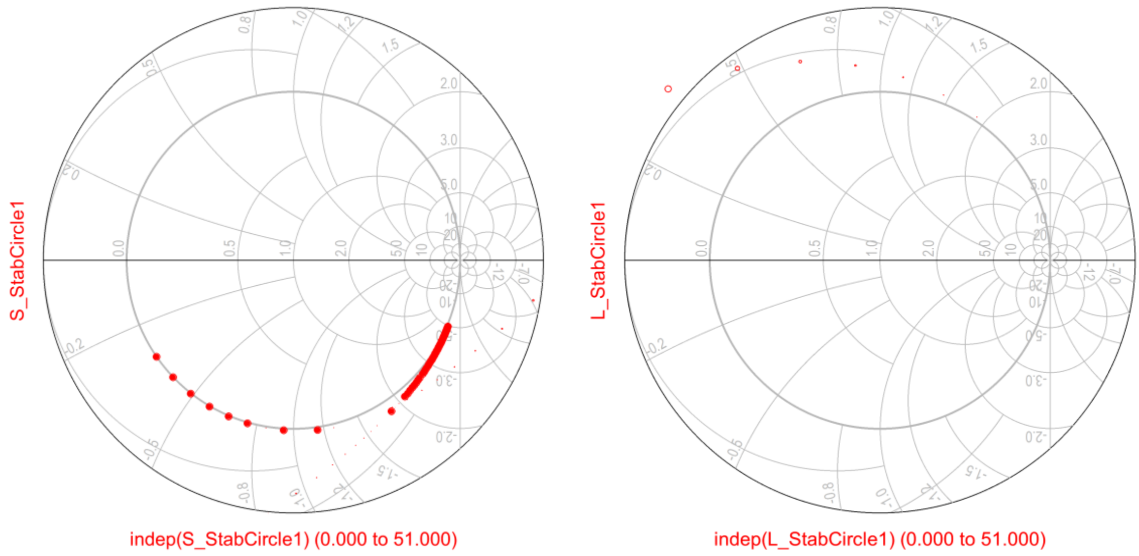

(a) **(b)**

Figure 8. (a) Input and (b) Output stability circles

6. CONCLUSIONS

A GaN solid state amplifier design in the S-band 2.9-3.1 frequency region has been presented. The two stage architecture adopted allows for combination of remarkable noise characteristics and excellent gain performance. Good matching and stability features have also been achieved over the frequency range of interest. Simulation results indicate the aforementioned behavior, appropriate for maritime radar transceiver applications, e.g. in parallel architecture. Its output CW power capability around 6 W makes it an attractive candidate as a single power amplifier output stage for continuous-wave LPI systems implementation, due to its efficiency and reliability characteristics. Additional improvement of noise characteristics would be an interest topic for further investigation to explore possible application as an LNA receiver stage.

References

G. W. Stimson (1998), Introduction to Airborne Radar. Raleigh, SciTech Publishing.

B. A. Kopp, M. Borkowski, & G. Jerinic (2002), Transmit/Receive Modules, IEEE Trans. Microwave Theory and Tech., vol. 50, pp. 827-834.

S. Nuttinck, E. Gebara, J. Laskar, B. Wagner & M. Harris (2002), RF Performance and Thermal Analysis of AlGaN/GaN Power HEMTs in Presence of Self-Heating Effects, IEEE MTT-S Int. Microwave Symp. Dig., pp. 921-924.

D. Parker & D. C. Zimmermann (2002), Phased Arrays - Part I: Theory and Architectures, IEEE Trans. Microwave Theory and Tech., vol. 50, pp.678-687.

A. P. Zhang, L.B. Rowland, E. B. Kaminsky, J. W. Kretchmer, V. Tilak, A. F. Allen, B. J. Edward (2003), Performance of AlGaN/GaN HEMTs for 2.8 and 10 GHz Power Amplifier Applications, IEEE MTT-S Int. Microwave Symp. Dig., pp. 251-254.

EMS Technologies (2005), Inc. Space and Technology, Passive Phased Arrays for Radar Antennas, White Paper, Atlanta.

FEK 399/B/3.4.2006 (2006) Greek National Frequency Band Allocation Regulation, Common Ministerial Decision.

DeTect Inc (2009), Advantages of a Solid-state based Radar System over a Magnetron-based Marine Radar System, r.ga.120903

Simon M. Wood, Ulf Andre, Bradley J. Millon, and Jim Milligan (2012), Hybrid and Monolithic GaN Power Transistors for High Power S-Band Radar Applications, IEEE 42nd European Microwave Symposium, Amsterdam, Netherlands.

Stephen D. Turner (2013) Reliability Advantages of Modular Solid State Power Amplifiers compared to Traveling Wave Tube Amplifiers, Paradise Datacom, Boalsburg, PA, USA

TriQuint Semiconductor (2013), TGF2023-01, 6 Watt Discrete Power GaN on SiC HEMT datasheet

Teledyne Microwave (2014), www.teledynewireless.com/products/SSPA/SSPA.aspx

Lessi, C. and Karagianni, E. (2014) An X-Band Low Noise Amplifier Design for Marine Navigation Radars, Int. J. Communications, Int. J. Communications, Network and System Sciences, 7, 75-82.

U.S. Federal Communications Commission (2014), FCC Online Table of Frequency Allocations, http://transition.fcc.gov/oet/spectrum/table/fcctable.pdf

DIRECT CURRENT TECHNOLOGY AS A MEANS TOWARDS INCREASED VESSEL EFFICIENCY

T. Kourmpelis, J. Prousalidis[1] and S. Dallas
[1] Corresponding Author, School of Naval Architecture & Marine Engineering, NTUA
E-mail : jprousal@naval.ntua.gr

ABSTRACT

The amount of electrical power that is used on-board has grown exponentially over the last years. This, in combination with the requirements for greener shipping, led researchers to consider new versatile and more efficient electric power distribution schemes as a means. Future ships, will enjoy the flexibility of electrical power distribution from different power generation modules to be connected to propulsion and ship service loads in any arrangement that supports the ships mission with maximum efficiency and reliability. This widespread electrification of ship systems introduces novel concepts, with a favorable one being the introduction of Direct Current. In this paper an Integrated Power System (IPS) with Medium Voltage Direct Current (MVDC) distribution for a modern cruise ship is presented. The model, consists of the power generation module, the power conversion modules, the DC distribution line, and the several distribution loads. The second part of the paper highlights whether the DC systems eliminate reactive power circulation and losses, and, hence, could improve ship efficiency indices in terms of the Energy Efficiency Design Index (EEDI). Also several other issues are taken into account and investigated, such as power quality problems and faults. To this end, some of the main results of the ongoing research project "DC-Ship" are presented and discussed.

NOMENCLATURE

EEDI	Energy Efficiency Design Index
EEOI	Energy Efficiency Operational Indicator
GHG	Greenhouse Gas
IMO	International Maritime Organisation
IPS	Integrated Power System
MECP	Marine Environmental Protection Committee
MVDC	Medium Voltage Direct Current
MCR	Maximum Continuous Rating (kW)
P_{ME}	Main Engine Power (kW)
P_{PTI}	Shaft Motor Power (kW)
P_{PTO}	Shaft Generator Power (kW)
SEEMP	Ship Energy Efficiency Management Plan
SFOC	Specific Fuel Oil Consumption (g $kW^{-1}h^{-1}$)

1. INTRODUCTION

The increasing need for more efficient ships, has led the researchers to start considering new versatile and more efficient power distribution architectures. Several studies have shown that the extensive electrification of ship systems, known as the All Electric Ship, if electric propulsion motors is used, can lead to a "greener" and more efficient ship. To this end, novel concepts are explored, with a promising one being the introduction of Direct Current Distribution abroad [1].

DC grids for shipboard power systems have shown resurgence in recent times, mainly due to the evolution of power electronic devices and because of the fact that recent trends in electric power consumption indicate an increasing use of DC-based power and constant-power loads [1],[2].

Moreover, the concept of Direct Current technology presents several advantages such as improved efficiency, ability to incorporate renewable energy sources and energy storage systems into the ship power plant, reduced size and rating of switchboards, increased reconfiguration capability and so on.

In this work, the Integrated Power System (IPS) of a cruise ship with Medium Voltage Direct Current (MVDC) distribution and electric propulsion is modelled and presented. The network topology resembles to the IPS that was constructed in [2], but is significantly altered, while being fairly generic. Furthermore, this paper deals with the method of calculation of the attained EEDI for ships using electric propulsion and specifically this specific power system configuration. Also, a case study is presented. Finally, several other issues regarding the operation of a DC grid are taken into account and investigated, such as power quality problems and faults.

2. GRID ARCHITECTURE

An Integrated Power System (IPS) is a novel power distribution architecture, where a common bus is used to supply both service and propulsion loads and instantly redistribute power as necessary. In contrast to a typical mechanical drive system, an IPS would not require different prime movers for the propulsion and the ship service systems, a fact that offers significant architectural flexibility and allows decentralization of the ships systems and component arrangements [2], [3]. A conceptual IPS with DC Power Distribution is shown in Figure 1. In this section, the ship power system is discussed and a detailed description of each component is given.

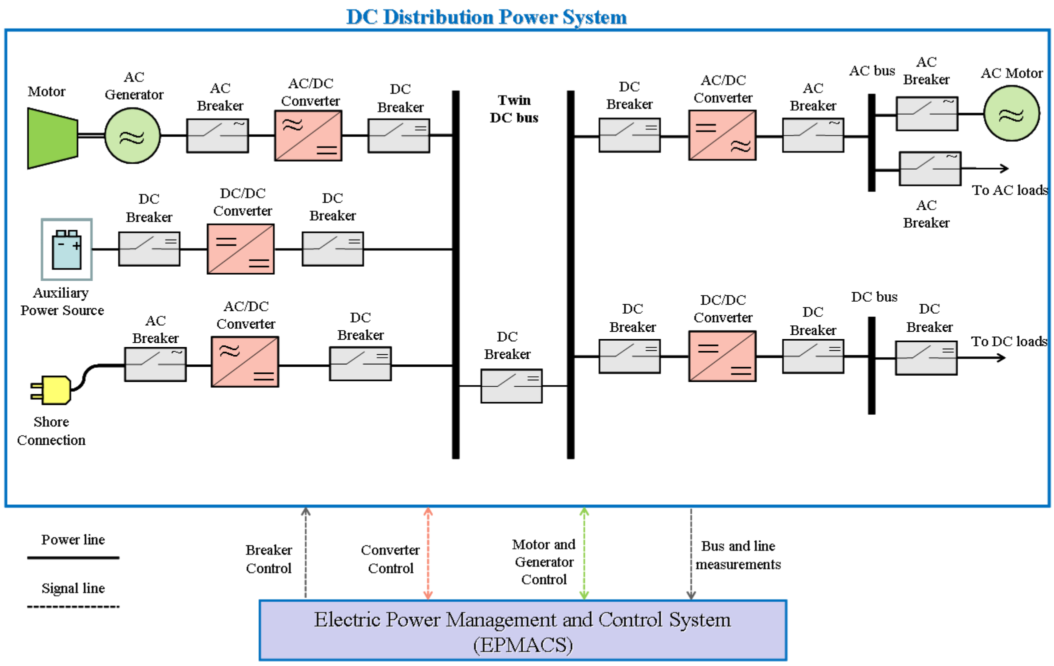

Figure 3: Conceptual DC Distribution Power System

2.1 Power Generation

The marine generators form the heart of the ship electrical design. That means that their careful selection is essential for a workable and economical system. When sizing, a marine generator cognisance must be given to the nature of the load. The generator often works on its own and is accordingly susceptible to large system load swings, loads causing distortion, the connection of motors and the connection of large heater elements for air conditioning systems. International maritime regulations [5], require at least two generators for a ship main electrical power system. The generators are normally driven by their own dedicated diesel engine but this can be expensive, taking up additional space that could be used for other purposes. For ships engaged on long sea voyages, it can be economically appealing to drive the generators from the main propulsion plant. International maritime regulations also require at least one electrical generator to be independent of the speed and rotation of the main propellers and associated shafting and accordingly at least one generator must have its own prime mover. In the system under study, there are three marine diesel generators and a shaft generator. Due to their differences in aspects of operation and design, each type of generator is discussed differently.

2.1.1 Diesel Generators

The main parts of a marine Diesel generator set are the Diesel prime mover, the speed governor, the synchronous machine and its exciter. The block diagram of a Diesel Generator is shown in Figure 2.

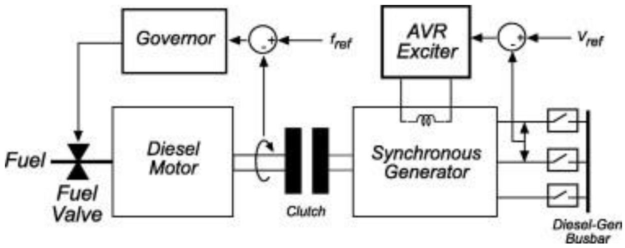

Figure 4: Diesel Generator Set block diagram

This system has two closed-loop feedback control systems: a speed feedback control system and an excitation feedback control system. These two feedback loops, ensure that the synchronous generator will operate at a steady speed and generate power at a fixed electrical frequency and voltage. The produced power is controlled via appropriate regulation of the field winding current. A detailed description of a diesel generator model can be found in [4].

2.1.2 Shaft Generators

A shaft generator is usually coupled to the ship mechanical shaft through a step-up gear. It is known to the worldwide bibliography as Shaft generator and according to its position, the type of coupling and the control equipment can be categorized into fourteen types [4]. It aims not only to produce electric power for the ship but, also, in certain cases to operate as a propulsion motor and assist the main motor engine. In typical fixed-speed shaft generator system, the generator is driven by the ship main engine, which is also driving the ship propeller. In this case, the grid frequency is tightly tied to propeller rotational speed. Any change in speed has a direct impact on network frequency. Thrust and ship speed can therefore only be controlled by propeller pitch, leading to undesired loading of the main engine, decreased efficiency and increased CO_2 emissions[6]. To eliminate these undesired effects the usage of an electrical drive is employed. A shaft generator drive (SGD) allows a wide speed range for the main engine. Propeller pitch and main engine speed can always be optimized for any desired sailing speed. The shaft generator drive maintains a stable voltage and frequency regardless of the main engine speed. When the SGD is placed between the shaft generator output and the distribution network, the shaft generator can be used independently of the shaft speed, enabling optimization of the ship operation for each route. The SGD also allows the shaft generator to run in parallel with the auxiliary generators. This means that the full benefits of lower specific fuel oil consumption (SFOC) for the main engine compared with the auxiliary engine can be fully exploited. If the auxiliary engines use marine diesel oil (MDO) instead of heavy fuel oil (HFO), the difference is even greater: the costs of lubrication oil and maintenance are relatively higher for auxiliary engines than for main engines [7].

2.2 DC Grid

The scheme that was used to implement the DC grid, comprised a twelve-pulse rectifier. This rectifier is simply yielded from the connection of two six-pulse thyristor bridges in series. The six-pulse rectifiers are supplied from the secondary and the tertiary of a three-winding transformer. The transformer winding connection is wye (Y) at the primary and wye (Y)-delta (Δ) at the two other windings (Figure 3). As a consequence, the voltage angle of the second group of thyristors would be 30-degrees lagging. Thus, multiples of sixth ±1 current harmonics which are present in the secondary and tertiary windings of the feeding transformer, will be cancelled in the primary winding and the remaining harmonic components will be of order: $h = 12n \pm 1$ on the AC side (current harmonics) and $h = 12n$ on the DC side (voltage harmonics). This results in major economy in the filters. High power filters are usually undesirable components because they are large and so they occupy useful space, the have reduced efficiency and important impact on power system stability. Moreover, filters provide fault current even after the circuit breakers are open. If the current magnitude is too large it can cause ancillary damage. Thus, a design balance must be met between voltage stability and excessive fault currents. This indicates that the filters used with power electronics need to be designed carefully as they can be used to mitigate faults in MVDC architectures [2], [3].

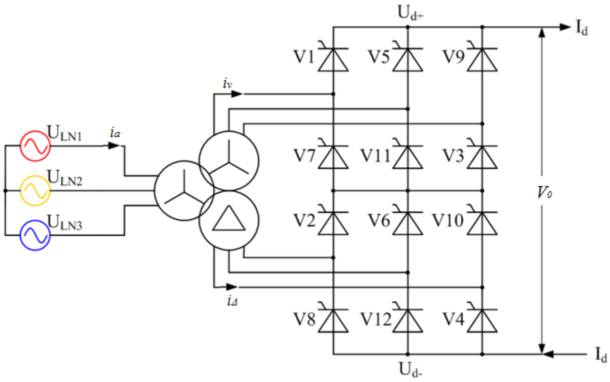

Figure 5: The twelve-pulse rectifier

The mean value of the output DC voltage, which is produced from the 12-pulse rectifier, is:

$$\bar{V_0} = \overline{V_{0Y}} + \overline{V_{0\Delta}} = \frac{3}{\pi}\int_{\alpha-\frac{\pi}{6}}^{\alpha+\frac{\pi}{6}} \sqrt{6}\tilde{V}_1 \cos(\omega t) d(\omega t)$$
$$+\frac{3}{\pi}\int_{\alpha-\frac{\pi}{6}}^{\alpha+\frac{\pi}{6}} \sqrt{6}\tilde{V}_1 \cos(\omega t) d(\omega t) = \frac{6\sqrt{6}}{\pi}\tilde{V}_1 \cos\alpha$$

Equation 1: Mean output DC voltage of the 12-pulse rectifier

The total input current i_a that flows through the primary of the transformer is calculated from eq. 2:

$$i_A = \left(\frac{N_2}{N_1}\right) i_Y + \left(\frac{N_3}{N_1}\right) i_\Delta = \frac{i_Y}{\alpha} + \frac{\sqrt{3}}{\alpha} i_\Delta.$$

Equation 2: Total input current at the primary of the three-winding transformer

2.3 Propulsion System

The Propulsion System consists of 2 x 8.5MW induction motors with slip frequency current control. A three-phase inverter connects each induction motor with the DC bus. The three-phase inverter is controlled with the hysteresis current control method. A block diagram of the propulsion system can be found at Fig. 4 below.

2.3.1 Induction Motor

The three-phase 12-pole 8.5MW induction motor is the propulsion drive. The voltage equations of the induction motor stator and rotor windings are given below. It is assumed that both induction motors are operating at the same phase voltage.

The 4th order transient model of the induction motor expressed in a reference frame rotating at the synchronous speed with the *q*-axis leading the d-axis by 90° is used. The differential equations forming the model of the generator are given in set of **Equations (3)-(10)**.

$$u_{sd} = r_s \cdot i_{sd} - \omega_s \cdot \Psi_{sq} + p\Psi_{sd} \tag{3}$$

$$u_{sq} = r_s \cdot i_{sq} + \omega_s \cdot \Psi_{sd} + p\Psi_{sq} \tag{4}$$

$$u_{rd} = r_r \cdot i_{rd} - (\omega_s - \omega_r) \cdot \Psi_{rq} + p\Psi_{rd} \tag{5}$$

$$u_{rq} = r_r \cdot i_{rq} + (\omega_s - \omega_r) \cdot \Psi_{rd} + p\Psi_{rq} \tag{6}$$

$$\Psi_{sd} = (L_{ls} + L_m) i_{sd} + L_m i_{rd} \tag{7}$$

$$\Psi_{sq} = (L_{ls} + L_m) i_{sq} + L_m i_{rq} \tag{8}$$

$$\Psi_{rd} = (L_{lr} + L_m) i_{rd} + L_m i_{sd} \tag{9}$$

$$T_e = \frac{3}{2}\frac{P}{2}(\Psi_{sd} i_{sq} - \Psi_{sq} i_{sd}) \tag{10}$$

Where, $p = \frac{d}{dt}$, $\frac{P}{2}$ is the number of pairs of poles, ω_s is the rotating speed of the reference frame and subscripts *{d}*, *{q}*, *{s}*, *{r}* denote *d*, *q* axis, stator and rotor, respectively.

Motion equation of the rotor is used to derive its rotating speed ω_r ,

$$J_m \frac{d\omega_r}{dt} = T_m - T_e \tag{11}$$

A more detailed analysis of induction motor operation can be found in [10] and [11].

2.3.2 Motor Drive

The three-phase IGBT/diode inverter is given by Matlab/SimPower Systems Toolbox. The gate input signal for controlled inverter consists of six firing signals for each IGBT, based on the inverter hysteresis current control output. The current control method applied here is the hysteresis control method [11]. Using this method the switching of the inverter does not depend only on an external control signal but also on the instantaneous currents in the circuit. The switching action is performed each time the current error reaches the limits of the hysteresis bandwidth defined in advance [12].

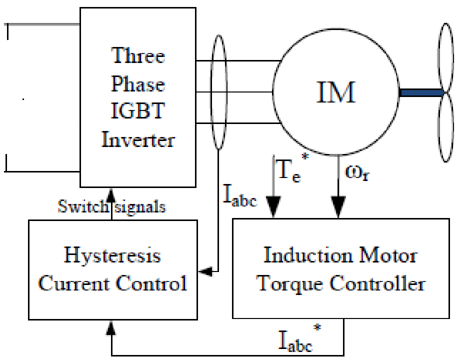

Figure 6: Propulsion motor and drive block diagram

3. ENERGY EFFICIENCY

3.1 IMO Regulations

Environmental pollution caused by ships, worldwide concern about air quality, greenhouse gas (GHG) emissions, and oil supplies have led to stricter emissions regulations and fuel economy standards[7]. Annex VI of the MARPOL Convention, adopted by the International Maritime Organization (IMO) in 1997, sets regulations for the prevention of air pollution (Cox, NOx, SOx, etc) caused by ships. The above conditions create the need for:

• the shipbuilding industry to continue optimizing traditional ship types with the goal of increased safety and environmental protection
• existing vessels to become more energy-efficient, in order to be competitive for the remaining of their life cycle.

Thus, according to the directives of the International Maritime Organization (IMO), the ship efficiency is to be quantitatively evaluated via the two following indices:
- Energy Efficiency Design Index (EEDI),
- Energy Efficiency Operation Index (EEOI).

Both indices express the ship efficiency in terms of the produced CO_2 per ship capacity and/or transport work, with the EEDI-index addressing new buildings, and the EEOI-index addressing existing ones. Moreover, in the near future all ships must have a well designed Ship Energy Efficiency Management Plan (SEEMP), the mission of which will be to monitor on-line and control the efficiency indices of the ship in an optimum way. The production of CO_2 is mainly due to the operation of the main propulsion engine(s) and of the auxiliary engines used as prime movers for the electric generators [6], [7].

3.2 EEDI for Ships with Electric Propulsion

The purpose of the EEDI is to provide a fair basis for comparison, to stimulate development of more efficient ships in general and to establish the minimum efficiency of new ships depending on ship type and size. The EEDI Calculation Guidelines describe in detail the formula for the EEDI calculation, but the formula was not applicable until recently for ships having electric propulsion. The ANNEX 17/RESOLUTION MEPC.233(65) [8], that was adopted on 17 May 2013 provides the guidelines for calculation of reference lines for use with the EEDI for cruise ships having non-conventional propulsion. These guidelines apply to cruise passenger ships that utilise diesel-electric propulsion, turbine propulsion, and hybrid propulsion systems. The reference line value for cruise passenger ships having non-conventional propulsion is formulated as:

$$\textit{Reference line value} = 170.84 \cdot b^{-0.214}$$

Equation 12: Reference Line calculation for vessels with non-conventional propulsion

where b represents the gross tonnage of the ship. To calculate the reference line, an index value for each cruise passenger ship having non-conventional propulsion is calculated using the following assumptions: The carbon emission factor is constant for all engines, including engines for diesel-electric and hybrid propulsion cruise passenger ships, i.e. $C_{F,ME} = C_{F,AE} = C_F = 3.1144$ g CO_2/g fuel. The carbon factor for hybrid propulsion ships equipped with gas turbines $C_{F,AE}$ is calculated as an average of the carbon factors of auxiliary engines (i.e. 3.1144 g CO_2/g fuel) and the carbon factor of gas turbines (i.e. 3.206 g CO_2/g fuel) weighted with their installed rated power. $P_{ME(i)}$ is reflected as 75 % of the rated installed main power ($MCR_{ME(i)}$). Where a ship only has electric propulsion $P_{ME(i)}$ is zero. The specific fuel consumption for all ship types, including diesel-electric and hybrid propulsion cruise passenger ships, is constant for all auxiliary engines, i.e. SFC_{AE}=215g/kWh. The specific fuel consumption for hybrid propulsion cruise passenger ships equipped with gas turbines SFC_{AE} is calculated as an average of the specific fuel oil consumption of the auxiliary engines (i.e. 215 g/kWh) and the specific fuel oil consumption of the gas turbines (i.e. 250 g/kWh) weighted according to their installed rated power. P_{AE} is calculated according to paragraph 2.5.6.3 of the 2012 Guidelines on the Method of Calculation of the Attained Energy Efficiency Design Index (EEDI) for new ships (resolution MEPC.212 (63)) [9] considering a given average efficiency of generator(s) weighted by power of 0.95. Innovative mechanical energy efficiency technology, shaft generators and other innovative energy efficient technologies are all excluded from the reference line calculation, i.e. $P_{AE,eff} = 0$ and $P_{eff} = 0$. $P_{PTI(i)}$ is 75% of the rated power consumption of each shaft motor divided by a given efficiency of generators of 0.95 and divided by a given propulsion chain efficiency of 0.92.

The equation for calculating the index value for cruise passenger vessels having non conventional propulsion is as follows:

$$Estimated\ Index\ Value = \frac{3{,}1144 \cdot 190 \sum_{i=1}^{nME} P_{ME} + C_{F,AE} \cdot SFC_{AE} \cdot (P_{AE} + \sum_{i=1}^{nPTI} P_{PTI(i)})}{GrossTonnage \cdot V_{ref}}$$

Equation 13: Estimated Index Value for ships using non-conventional propulsion

4. CASE STUDY

The investigated vessel is a cruise passenger ship, whose general characteristics are presented in Table 1 and it's electrical characteristics were analysed in section 2. The required ship propulsion power of 17MW is delivered by two induction motors rated at 8.5MW each, whereas three marine diesel generators of 5MW each and a shaft generator of 5MW are required for covering the ship electric energy demand. The ship is considered to in a route of 560NM which includes a part of 340NM inside ECA zones (60% sailing in ECA, 40% sailing in non-ECA). An example of this route is an itinerary between Portsmouth and Santander, Spain. Each part of the ship voyage lasts approximately 36h considering a sailing speed of 21 knots, 28h of sailing, 0.5h of maneuvering and 1h that remains in port.

Table 1. Cruise Ship Main Particulars

Characteristic	Value
Size	35000 GT
Length	220 m
Beam	28.2 m
Draft	7.0 m
Service Speed	21.0 knots
Deadweight	12500mt
Propulsion Power	17 MW
Aux. Power(Installed)	20 MW
Propulsion	Elect. Propulsion

The Energy Efficiency Design Index for the specific cruise ship was calculated regarding the assumptions that were made above in 3.2. The main advantages of the configuration that was discussed in section 2, which result in the reduction of the EEDI value are a) the usage of electric propulsion b) the utilization of shaft generators as auxiliary power and c) the specific DC grid configuration that reduces the total weight and volume of the electrical installations across the ship. The calculation results can be summarised at Fig. 5 below. In the suggested approach, the attained EEDI was calculated to **13,044** while the minimum required that was calculated from the reference line for this specific vessel is **18,052**. This means that the obtained EEDI is about 27% below the required index. Also, as it can be deduced from Figure 5, the investigated vessel will comply with all IMO regulations including the future ones.

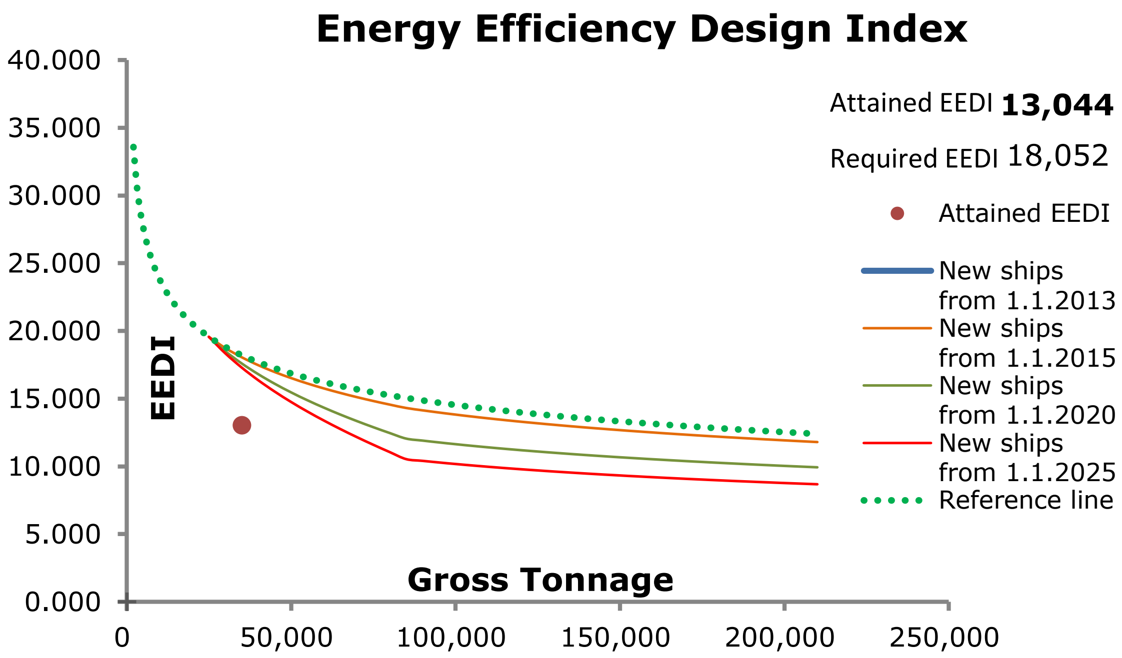

Figure 5: EEDI of the ship under study in contrast to reference lines of IMO.

5. CONCLUSIONS AND FUTURE WORK

The aim of this paper has been the modelling of an IPS with MVDC power distribution for a reference cruise passenger ship. Each component of the electric grid was separately discussed and presented regarding its role in the power distribution network. Also, an approach to determine the efficiency and environmental gains from DC power distribution was made. The technical measure that was used for this study was the Energy Efficiency Design Index (EEDI). The recent EEDI regulations for ships with electric propulsion were cited and a preliminary case study was presented to demonstrate the energy efficiency benefits that arise from this novel grid configuration. The findings indicated that new ships that will adopt this power distribution concept, will have sufficiently reduced EEDI and will comply with even stricter future regulations regarding CO_2 emissions.

Future work includes further deepening on All-Electric Ship power quality and stability issues, investigation of new techniques for MVDC grid optimal operation, further deepening on the impact of integrating DC technology upon the ship efficiency, and examination of the operation, maintenance and procurement costs of vessels with DC power distribution.

ACKNOWLEDGEMENTS

The authors wish to express their gratitude towards the European Commission for funding the MARINELIVE project (contract No 264057) within the FP7-REGPOT-2010-1 frame. The continuance of this research is co-financed by the European Union (European Social Fund) and Hellenic National funds through the Operational Program “Education and Lifelong Learning” (NSRF 2007-2013), Research Funding Program: ARISTEIA (EXCELLENCE), project “DC-Ship” (project code No 987).

References

1. REED, G., GRAINGER, B., SPARACINO, A. and MAO, ZH., ‘Ship to Grid’, IEEE Power & Energy Magazine *Vol. **10***, 2012.

2. KOURMPELIS T. and PROUSALIDIS J. ‘Setting a Computer Simulation Platform for Passenger Ships DC Power Distribution Networks’ , Design and Operation of Passenger Ships International Conference, London UK, 2013

3. PREMPRANEERAH, P., KARNIADAKIS G., and CHRYSSOSTOMIDIS, C., 'DC fault Protection in Shipboard Power systems using Z-Source Breakers', MIT SG 11-30, 2011.

4. LUO, L., 'The Control and Modeling of Diesel Generator Set in Electric Propulsion Ship', I.J. Information Technology and Computer Science, 2011.

5. 'Rules & Regulations for the Classification of Naval Ships 2013 Full Set', Vol. **2**, Part **10**, Lloyd's Register, 2013.

6. MEPC 59/INF.10 '2nd IMO GHG Study', IMO, 2009

7. MEPC.203(62) 'Inclusion of regulations on energy efficiency for ships in MARPOL Annex VI', IMO 2011

8. MEPC.233(65) RESOLUTION/ANNEX 17'Guidelines for calculation of reference lines for use with the EEDI for cruise passenger ships having non-conventional propulsion', IMO , 2013

9. MEPC.224(64), 'Amendments on the 2012 Guidelines of the Method of Calculation of the Attained Energy Efficiency Design Index(EEDI) for new ships' , IMO , 2012

10. MOHAN, N., UNDELAND, T., ROBBINS, W., 'Power Electronics: Converters, Applications, and Design', John Wiley & Sons, 2003.

11. MANIAS, S., 'Power Electronics', Symeon Publications, 2012.

12. IRFAN, M.M., PRASAD, P.H.K., RAO, P.V, Simulation of five-level five-phase SVPWM voltage source inverter, Power, Control and Embedded Systems, International Conference, 2010.

13. SMITH, P., FURSE, C. and GUNTHER, J., 'Analysis of Spread Spectrum Time Domain Reflectometry for Wire Fault Location', IEEE Sensors Journal, 2005

14. HANSEN, J.F., LINDTJORN J.O., MYKLEBUST, T.A. and VANSKA K., 'Onboard DC Grid', ABB, 2012.

15. BERNET, S., 'Recent Developments of High Power Converters for Industry and Traction Applications', IEEE Transactions on Power Electronics, 2000

16. PROUSALIDIS, J., 'Simulation tools for ship electric power and control system studies', Proceedings of 6th International Naval Exhibition and Conference, 2002.

17. PROUSALIDIS, J., MOUZAKIS P., 'Analysis of Electric Power Demands of Podded Propulsors', The Journal of Marine Engineering & Technology, 2010.

18. PROUSALIDIS J., PATSIOS C., TSOURAKIS G., ANTONOPOULOS G., KATSIKAS P., KARLOVITS N., BUCKNALL R., GREIG A., 'Comparison of DC vs AC via ship electric grid emulators', Proceedings of INEC 2014, Amsterdam (The Netherlands), 2014.